ODESSA ASTRONOMICAL PUBLICATIONS

Volume 30
(2017)

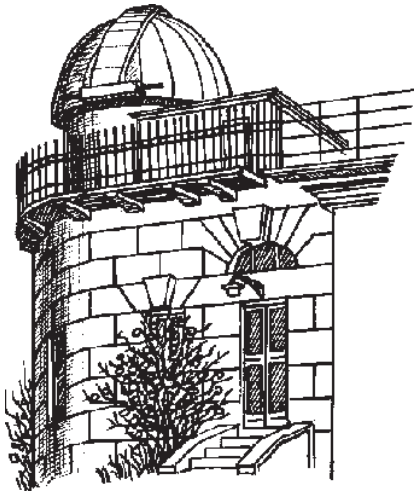

Astronomical Observatory
of I. I. Mechnikov Odessa National University

ODESSA ASTRONOMICAL PUBLICATIONS

Volume 30
(2017)

Address:
Astronomical Observatory, Odessa National University,
T. G. Shevchenko Park, Odessa, 65014, UKRAINE
Tel.: + 38 048 728-11-68
E-mail: astronomical_observatory@onu.edu.ua
http://www.astro-observ.odessa.ua

The electronic version of the journal is on the web page: http://oap.onu.edu.ua

Одесские Астрономические Публикации
Издается с 1946 года (издание возобновлено в 1993 г., №6)

Свидетельство о государственной регистрации печатного средства массовой информации: серия КВ № 14722-3693Р от 30.10.2008 г.
Журнал включен в список МОН Украины приказом МОНУ № 996 от 11.07.2017 г.

Печатается по решению Ученого совета НИИ "Астрономическая обсерватория" Одесского национального университета имени И.И.Мечникова от 20 июня 2017 г., протокол №6

Printed in UKRAINE
BAITE PUBLISHING COMPANY

ISSN 1810-4215

ODESSA ASTRONOMICAL PUBLICATIONS

Volume 30
(2017)

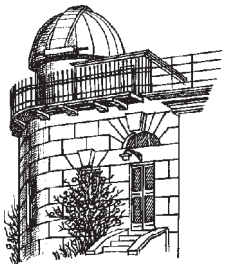

CONTENTS

Cosmology, gravitation, astroparticle physics, high energy physics

Astrophysics

Astroinformatics

Sun and Solar system

Memorial

COSMOLOGY, GRAVITATION, ASTROPARTICLE PHYSICS, HIGH ENERGY PHYSICS

DOI: http://dx.doi.org/10.18524/1810-4215.2017.30.114127

LIMIT VALUES AS AN UNIVERSAL METHOD OF DESCRIPTION OF PHYSICAL REALITY

Yu.L. Bolotin[1], V.A. Cherkaskiy[1], V.V. Yanovsky[2,3]

[1] A.I.Akhiezer Institute for Theoretical Physics, NSC KIPT NAS Ukraine, Kharkiv, Ukraine, *ybolotin@gmail.com*
[2] Institute for Single Crystals, NAS Ukraine,Kharkiv, Ukraine, *yanov50@gmail.com*
[3] V.N.Karazin Kharkiv National University,Kharkiv, Ukraine, *yanov50@gmail.com*

ABSTRACT. There are two main forms of cognition of Nature: empiric knowledge obtained from the experience, and theory as system of ideas and principles. Each of the two forms uses its own methods. While empirics or phenomenology is based on experiments, theory mostly deals with axiomatic approach. Every axiomatics starts from the principal question: what statements should be chosen as axioms? The present work uses the existence of limit values as the initial axiom. It is well known that the statement about the existence of minimum quantum of action $\hbar$ is sufficient to build all the Quantum Mechanics, likewise maximum velocity value c—for the Special Relativity. Similar approach can be realized in General Relativity as well, which can be built on the postulated existence of limit (maximum) power

$$\eta = \frac{c^5}{4G}.$$

It seems natural in context of this axiomatics to transit from the traditional Planck's units to the modified ones, i.e. from the set ($\hbar$, c, G) to ($\hbar$, c, η), with the latter containing exclusively limit values. The approach considered in the present paper opens new exciting possibilities for interpretation of the known results and obtaining the new ones.

Keywords: axiomatic approach, limit values, fundamental constants.

1. Introduction

The traditional approach to describe the reality was based on physical laws and seemed unshakable, but today it is changing before our very eyes. The new concept "it from bit" (Wheeler, 1986; Lloyd, 2005) step by step conquers its place in collective consciousness of the "physical community" (holographic principle, black hole thermodynamics, informational paradox), and number of its supporters continuously grows. Structure of the new paradigm can be briefly described in the following way.

States of a physical system should be treated as purely informational states. Space-time, where all physical processes are played out in the habitual picture of the world, now is "just" an object for realization of the informational states. The information (the bits) is now the only real thing.

Such a radical revision of the reality nature causes understandable prejudices, especially in view of undeniable achievements of the traditional physics. And the first question to rise is: why Nature uses two dominant approaches instead of one? It is possible that the two alternative approaches can contradict each other. Time reversibility of mechanics and time arrow in thermodynamics represent a well known example of such a contradiction. Hopefully Nature is sufficiently perceptive to avoid contradictions of that kind. It has apparently foreseen that all the adequate approaches to its description are somehow, yet mysteriously for us, linked.

In our opinion, the so-called limit values play an important role in search for those links. The statement about the existence of limit values can be used as a basis for physical axiomatics. It is well known that the Quantum Mechanics can be built basing on the existence of minimum quantum of action $\hbar$, Special Relativity—of maximum velocity c. Relatively recently it became clear that the analogous approach can be realized in general Relativity as well (Gibbons, 2002; Schiller, 2006), which can be built on postulate about existence of maximum force

$$F_{max} = \frac{c^4}{4G}.$$

The limit values are actual for all physical systems regardless their nature, and for every observer. The particular value of the limit is of less importance than the very fact of its existence. One should distinguish between two types of the limit values: the "fundamental" ones and all the others. The limit value is called fundamental if it cannot be deduced from the existing theories, and its existence can be used as a basis for fu-

ture theories. A classical example: finite value of propagation velocity for arbitrary signal in vacuum generates Lorentz transformations and consequently the Special Relativity.

Only finite limit values make interest. Appearance of singularities in a theory is commonly considered as a first signal of the fact that the theory has gone beyond its applicability limits and needs modernization. The latter implies taking into account the previously neglected effects, which would allow to make the theory free of the singularities.

An alternative point of view was formulated by Penrose as the "cosmic censorship principle": Nature always hides a naked singularity (Penrose, 1973). The space-time singularities appear in such places which are hidden from observers, like inner parts of black holes. In other words, the super-limit values are screened from us by the horizons, and the very limit is reached exclusively at the horizon. The present work is aimed to generalize the cosmic censorship principle to the level of the physical censorship one, having shown that a large number of fundamental limitations in both micro- and macro-physics is imposed by existence of the limit values. Treatment of those limitations in terms of the limit values opens new and interesting possibilities for axiomatic formulation of physics, which can be realized postulating existence of certain set of limit values.

2. The Maximum Force Principle

The role of the two fundamental values – the light speed c and Planck's constant $\hbar$ – is well known. We will now focus on the third fundamental constant— the limit force. The maximum force principle was first formulated in the paper of Gibbons (Gibbons, 2002): *I suggest that classical General Relativity in four space-time dimensions incorporates a Principal of Maximal Tension and give arguments to show that the value of the maximum tension is*

$$F_{max} = \frac{c^4}{4G} \approx 3.25 \times 10^{43} N. \tag{1}$$

The limit does not depend on the force nature and equally holds for gravitational, electromagnetic, nuclear, and all other forces. The statement about existence of maximum power is absolutely equivalent to the latter:

$$P_{max} = \frac{c^5}{4G} \approx 9.07 \times 10^{51} W. \tag{2}$$

Both quantities are components of the 4-vector

$$F^\lambda = \frac{dp^\lambda}{dt}.$$

The multiplier 1/4 does not play a principal role. Therefore, further, where it does not lead to confusion, we will omit numerical multipliers of the order of unity assuming that the approximate equality $A \approx B$ corresponds to the relation $\log A \approx \log B$.

The limit force and the limit power are invariants: if follows from invariance of the quantities c and G. Time dependence is not however excluded in general. The force limit takes place for every component of the 3−force, as well as for its absolute value.

The limit power has a trivial physical interpretation. Let us consider the power released in "annihilation" of a black hole of mass M. Minimum time required for realization of this process equals to the time interval needed for light signal to travel the distance equal to its "gravity radius"

$$t = \frac{2R_g}{c} = \frac{4MG}{c^3}$$

$$P = \frac{Mc^2}{4MG/c^3} = \frac{c^5}{4G}, \tag{3}$$

which exactly coincides with the above introduced limit power.

Here is another example to clarify the mechanism of the occurrence of the maximum force. In the Newtonian mechanics $F = dp/dt$, therefore

$$F_{max} = \frac{(\Delta p)_{max}}{(\Delta t)_{min}} \approx \frac{mc}{t_{Pl}} = \frac{mc^2}{l_{Pl}}. \tag{4}$$

At first sight one may expect that unlimited growth of the mass will give rise to arbitrarily great force. However, this is not true, and the limitation is bound up with the appearance of horizon at the increase of the mass on a fixed scale of length l_{Pl}. Indeed, omitting the numerical multipliers $O(1)$, we find the mass with the gravitational radius equal to the Planck length:

$$m \approx \frac{l_{Pl}c^2}{G} = \sqrt{\frac{\hbar G}{c^3}}\frac{c^2}{G} = \sqrt{\frac{\hbar c}{G}} = m_{Pl}. \tag{5}$$

Consequently, the maximum mass which can be used in (3) for preventing the appearance of the horizon is the Planck mass, so

$$F_{max} \approx \frac{m_{Pl}c^2}{l_{Pl}} = \frac{c^4}{G}. \tag{6}$$

The result (6) can be obtained in the form of the combination of the Planck units with the dimension of force:

$$F_{Pl} = m_{Pl}\frac{l_{Pl}}{t_{Pl}^2} = \sqrt{\frac{\hbar c}{G}}\sqrt{\frac{\hbar G}{c^3}}\frac{c^5}{\hbar G} = \frac{c^4}{G}. \tag{7}$$

Note that for the Planck mass the gravitational radius coincides with the Compton wavelength.

It should be emphasized that all our statements concern solely the case of dimension $D = N + 1 = 4$. It is

only in the space of dimension $D = 4$ that the Planck force is independent of $\hbar$:

$$F_{Pl(D)} = \frac{M_{Pl(D)} L_{Pl(D)}}{T^2_{Pl(D)}} = G_D^{-\frac{2}{D-2}} \hbar^{D-4} c^{\frac{D+4}{D-2}}. \quad (8)$$

More strictly the expression for the limit force (limit power) can be obtained in the frames of General Relativity (Schiller, 2005).

3. Modification of Planck's Unit System

Dimensional analysis is a powerful method which makes it possible to obtain results (both qualitative and quantitative) on the basis of general knowledge of the phenomenon under consideration. Dimensional analysis (along with symmetry considerations) is especially significant for construction of initial approaches to description of the systems for which any theory is absent at present. As it is well-known, many astonishing results have been achieved due to dimensional considerations which at first sight seem to be quite simple. There are even such results that are still not obtained in other, more rigorous way. A classical illustration of such a situation is quantum gravity. The latter has practically become a synonym of Planck-scale physics whose description to a considerable extent reduces to endless shuffle of fundamental constants. However, dimensional analysis is not all-powerful, and the results obtained with its help should be interpreted carefully.

Especially significant role in clarification and understanding of the foundations for the future theory of Planck-scale processes belongs to the Planck units. The Planck units represent fundamental physical scales of mass, length and time built by means of the fundamental constants $\hbar, c, G$ (Planck, 1899):

$$\begin{aligned} m_{Pl} &= \sqrt{\frac{\hbar c}{G}} \simeq 2.18 \times 10^{-8} kg, \\ l_{Pl} &= \sqrt{\frac{\hbar G}{c^3}} \simeq 1.6 \times 10^{-35} m, \\ t_{Pl} &= \sqrt{\frac{\hbar G}{c^5}} \simeq 5.39 \times 10^{-44} sec \end{aligned} \quad (9)$$

Planck units represent "natural" physical scales of mass, length and time, constructed from the fundamental constants $\hbar, c, G$. The three constants used to construct the Planck's units have different functional roles. While the first and the second of them represent limit values and lie in the foundations of Quantum Mechanics ($\hbar$) and Special Relativity (c), the Newtonnian constant (G) "just" fixes absolute value of the gravitational forces. It seems natural to make the set of fundamental constants more consistent and more efficient using exclusively limit values to construct the Planck units. In order to that, in addition to the limit values $\hbar$ and c, we introduce the limit power $\eta = P_{max}$, having made the substitution

$$G = \frac{c^5}{\eta}.$$

In other words, using the set $(\hbar, c, \eta)$ instead of $(\hbar, c, G)$, we get the modified system of Planck units (which consists only of the limit values):

$$\begin{aligned} m_{Pl} &= \sqrt{\frac{\hbar c}{G}} \rightarrow m_{Pl} = \sqrt{\frac{\hbar \eta}{c^4}}, \\ l_{Pl} &= \sqrt{\frac{\hbar G}{c^3}} \rightarrow l_{Pl} = \sqrt{\frac{\hbar}{\eta}} c, \\ t_{Pl} &= \sqrt{\frac{\hbar G}{c^5}} \rightarrow t_{Pl} = \sqrt{\frac{\hbar}{\eta}}. \end{aligned} \quad (10)$$

It should be emphasized again that the necessary condition for the existence of event horizon is finiteness of the realized power and of the speed of light. Thereat, as we have already noted, the magnitude of the limit value is less significant than the fact of its existence. It is easily seen that

$$\lim_{c \to \infty} R_g = \lim_{c \to \infty} \frac{2mG}{c^2} = 0; \quad (11)$$

$$\lim_{P_{max} \to \infty} R_g = \lim_{c \to \infty} \frac{2mc^3}{P_{max}} = 0. \quad (12)$$

In other words, at $\eta \to \infty$ or $c \to \infty$ the concept of gravitational radius and, consequently, the event horizon, becomes meaningless.

While considering the maximum force (maximum power) as a fundamental constant it is natural to use it instead of the gravitational constant. For instance, Newton's law of universal gravitation acquires the form

$$F = G\frac{mM}{R^2} = \frac{c^4 mM}{4F_{max} R^2} = \frac{1}{F_{max}} \frac{mc^2 \cdot Mc^2}{R^2} \quad (13)$$

Here the relation between the value of gravitational interaction and the maximum force becomes more transparent: a gigantic maximum force gives rise to a weak gravitational interaction. Naturally, if one chooses the gravitational constant G for the initial fundamental constant, the opposite statement will be true as well.

The choice of the maximum power as a new fundamental constant leads to the Planck scales which preserve their previous numerical values. However, such a changeover opens up interesting opportunities for interpretation of the estimates made using the modified Planck units, as well as for the obtaining the new results. Below we will give a number of examples.

4. Space-Time Foam

If the space is subject to quantum fluctuations, then the fluctuations should manifest in form of the uncertainties in measurements of different type (Ng & van Dam, 1994). Measurement of length is an important class of measurements. One can measure length of an interval measuring time of registration of the reflected signal. However the quantum fluctuations will generate uncertainty δl of the measured distance. Wigner (1957) showed that

$$\delta l^2 \geq \frac{\hbar l}{mc}. \tag{14}$$

Here m is the clock's mass. It may seem that increasing mass of the clock infinitely, one can eliminate influence of the quantum fluctuations. However, possibility to increase the clock's mass is strictly limited. The clock's characteristic size d is evidently limited by the very experiment's validity condition ($d \leq \delta l$), and on the other hand the clock's size must exceed its Schwarzschild radius $d > Gm/c^2$, preventing the transformation of the clock into a black hole, because otherwise the clock readings would be unavailable to us. It then follows that

$$\delta l \geq \frac{Gm}{c^2}. \tag{15}$$

Combining (14) and (15), one obtains (Karolyhazy, 1966)

$$\delta l \geq (l l_{Pl}^2)^{1/3} = l_{Pl}\left(\frac{l}{l_{Pl}}\right)^{1/3}, \quad l_{Pl} \equiv \sqrt{\frac{\hbar}{\eta}}c. \tag{16}$$

Similar relations can be obtained for measuring time intervals (Ng, 2001; 2002),

$$(\delta t)^2 \geq \frac{\hbar t}{mc^2}, \quad \delta t \geq \frac{Gm}{c^3} \tag{17}$$

where t is the measured time interval. By combining these two expressions we find

$$\delta t \geq \left(t t_{Pl}^2\right)^{1/3} \tag{18}$$

Relation (18) connects the minimum uncertainty during measurement of time with the measured time interval. The absolute value of uncertainty $\delta t \sim t^{1/3}$ rises, whereas its relative value $\delta t/t \propto t^{-2/3}$ diminishes. Now rewrite relations (16) and (18) in the form

$$\delta l \geq \left(\frac{l}{c}\frac{\hbar}{\eta}\right)^{1/3} c; \tag{19}$$

$$\delta t \geq \left(t\frac{\hbar}{\eta}\right)^{1/3} \tag{20}$$

which clearly shows that the existence condition for the minimum uncertainty during measurement of distance (time) is equivalent to the existence condition for the limit power which, in its turn, is dictated by the existence of the horizon.

To avoid confusion, we emphasize that in the first and in the second case it is not about the accuracy of the particular design of "ruler" or clock, and the universal limitations on the accuracy of the measurement of length and time, which are based on fundamental physical laws.

We should point out that the result (19) is closely linked to the holographic principle ('t Hooft, 1994; Susskind, 1995), according to which all the information contained in some region of space can be "recorded" (represented) on the boundary of the region.

Let us imagine that some volume l^3 is divided on parts (say, cubes) of the smallest size that is allowed by physical laws. It seems natural to assign one degree of freedom to each such elementary volume (recall dimensionless cell of phase volume of a quantum system $dpdq/(2\pi\hbar)^{3N}$). If the minimum uncertainty in measurement of distance l equals to δl, then the elementary volume component has volume $(\delta l)^3$ and number of degrees of freedom in the system equals $(l/\delta l)^3$. According to the holographic principle

$$(l/\delta l)^3 \leq \frac{l^2}{l_{Pl}^2}, \tag{21}$$

which immediately returns us to the result (19).

It is important to note that in derivation of (21) we used the holographic principle to find the expression for the minimum uncertainty δl. As we have seen above, existence of this fundamental characteristic directly follows from the physical censorship principle (the maximum force principle) and its value can be obtained without application of the holographic principle. Therefore with the same degree of certainty we can assert that the holographic principle represents a consequence of the quantum fluctuations of the space-time (J. Ng, 2003).

5. Maximum Acceleration

The existence condition for the traditional space-time in the presence of vacuum polarization (virtual processes of production and annihilation of pairs caused by quantum fluctuations) leads to limitation of proper acceleration relatively to the vacuum, or, in other words, to the occurrence of the maximum acceleration (Caianiello, 1981; Brandt, 1989; Papini, 2003; Wood, 1989).

The proper acceleration of the particle a in curved space-time is the scalar defined by the relation

$$a^2 = -c^4 g_{\mu\nu}\frac{Dv^\mu}{ds}\frac{Dv^\nu}{ds} \tag{22}$$

where $g_{\mu\nu}$ is the metric tensor, $v^\mu \equiv dx^\mu/ds$, the dimensionless four-velocity of the particle, D/ds is the

covariant derivative with respect to the line element on the world line of the particle,

$$\frac{Dv^\mu}{ds} \equiv \frac{dv^\mu}{ds} + \Gamma^\mu_{\alpha\beta} v^\alpha v^\beta \tag{23}$$

Here $\Gamma^\mu_{\alpha\beta}$ are the affine connections (the Christoffel symbols) of space-time with the metric $g_{\mu\nu}$, $ds^2 = g_{\mu\nu} dx^\mu dx^\nu$, the linear element of this space-time.

From the energy-time uncertainty principle it follows that the lifetime of the virtual pair particle-antiparticle (with the particle mass m) generated due to vacuum fluctuations, is $\approx \hbar/2mc^2$, whereas the distance covered during this time is $\approx \hbar/2mc$ (the Compton wavelength of the particles). If a virtual particle acquires the energy equal to its rest mass, it will be transformed into a real particle. When considering the rest system of a particle which is, generally speaking, non-inertial, we find that it undergoes the inertial force $F_{in} = |ma|$, where a is the proper particle acceleration. The work executed by the inertial force during the particle lifetime

$$A = ma \times \frac{\hbar}{2mc}.$$

If $A = mc^2$, then there arises acceleration

$$a = \frac{2mc^3}{\hbar} \tag{24}$$

At this acceleration, particles of the mass m will be copiously produced from the vacuum. The growth of acceleration will lead to the rise of the mass of the produced particles. What critical consequences may arise at unlimited growth of acceleration? If the value of acceleration is high enough, the produced particles can be transformed into black holes. This will occur in the case when the Compton wavelength of a particle (particle "size") $\hbar/mc$ is less than its Schwarzschild radius $2Gm/c^2$,

$$\hbar/mc < \frac{2Gm}{c^2} \tag{25}$$

From here it follows that the threshold for black hole formation is a mass of the order of the Planck mass $(\hbar\eta)^{1/2}/c^2$. By substituting $m = m_{Pl}$ into (1) we find

$$a_0 \approx \sqrt{\frac{\eta}{\hbar}}\, c \tag{26}$$

(as before, we omit the multipliers of the order of unity). At such an acceleration, production of black holes with the Planck mass due to vacuum polarization will result in breakdown of the traditional knowledge of the structure of space-time, and the acceleration concept itself will lose its conventional sense. Therefore, the value a_0 should be considered the maximum proper acceleration relatively to the vacuum. Note that the presence of the maximum acceleration leads to the formation of a horizon even in SR. In fact, from the viewpoint of SR, the length l of an object moving with the acceleration a is limited by the relation

$$l \le \frac{c^2}{2a}.$$

On the other hand, it cannot be less than $l \ge l_{Pl} = \sqrt{\hbar/\eta}c$. When using this inequality for acceleration one obtains

$$a \le c\sqrt{\frac{\eta}{\hbar}}$$

. As is seen, the maximum acceleration corresponds to the fundamental acceleration in the Planck system of units, and is a simple combination of the three limit values $\hbar, c, \eta$. The necessary condition for its existence is finiteness of all the three limit values : at $c \to \infty$, $\hbar \to 0$ or $\eta \to \infty$ the maximum acceleration is absent.

The presence of the maximum proper acceleration a_0 (33) automatically leads to the existence of the minimum radius of curvature $R_{\min}$ of the particle world lines. The radius of curvature of the world line is $R = c^2/a$ (since the centripetal acceleration during motion along the circle of the radius R is $a = v^2/R$). Therefore, the minimum radius of curvature has the form

$$R_{\min} = \frac{c^2}{a_0} \approx \left(\frac{\hbar G}{c^3}\right)^{1/2} = c\left(\frac{\hbar}{\eta}\right)^{1/2} \tag{27}$$

Again, we clearly see the key role of the horizon which produces the limit power and, as a consequence, the maximum proper acceleration and the minimum radius of curvature of the world line.

6. An Ideal Quantum Clock and Principle of Maximum Force

Achievement of required accuracy in any quantum measurement inevitably imposes certain limitations on characteristics of the device designed to perform it. All possible methods to measure the time always involve observation of some periodical physical process. As an example (following (Burderi, 2016)), consider a quantum clock based on observation of radioactive disintegration described by the following equation

$$\frac{dN}{dt} = -\lambda N \tag{28}$$

where $N(t)$ is the current number of radioactive particles in the sample. Average number of the decayed particles during the time interval $\Delta t \ll \lambda^{-1}$ is $\Delta N = \lambda N \Delta t$. It enables us to measure the time intervals calculating number of the decaying particles

$$\Delta t = \frac{\Delta N}{\lambda N} \tag{29}$$

The relative error of such a method of time measurement $\varepsilon = (\lambda N \Delta t)^{-1/2} = 1/\sqrt{\Delta N} \leq 1$. At first glance, it seems that increasing size of the quantum clock (the number N), we would gain unlimited improvement in accuracy of the time interval measurement. However, such a process is limited by the following condition: the rise of the clock mass must not lead to transformation of the clock into a black hole (i.e. to occurrence of horizon). Let us analyze the quantitative limitations which may be caused by this condition. By using the uncertainty principle $\Delta E \Delta t \geq \hbar/2$ we can transform (29) into the inequality

$$\Delta t \geq \frac{\hbar}{2\varepsilon^2 c^2} \frac{1}{M} \tag{30}$$

where $M = N m_p$ (with m_p corresponding to the mass of one particle) is the clock mass. If the clock radius R (the clock is assumed to be spherical) becomes less than the gravitational radius R_g, it will be impossible to use the clock for time measurements. The condition $R > R_g$ is transformed into

$$\frac{1}{M} > \frac{2G}{c^2 R} \tag{31}$$

When substituting (31) into (30) we obtain

$$\Delta t R > \frac{1}{\varepsilon^2} \frac{G}{c^4} \hbar \tag{32}$$

Treating R as uncertainty Δr in position of the physical object (the clock), which is the basis for the time measurement process, and taking into account that $\varepsilon \leq 1$, one finally obtains (Bolotin, 2016)

$$\Delta t \Delta r > \frac{G}{c^4} \hbar \tag{33}$$

The obtained inequality limits the possibility to determine the time and space coordinates of events to an arbitrary precision.

Let us analyze expression (44) using the notion of the limit force (Bolotin, 2016). For this purpose present it in the form

$$\Delta t \Delta r > \frac{1}{F_{\max}} \hbar \tag{34}$$

At the fixed Planck constant $\hbar$, it is only the limit force $F_{\max}$ defines the limitation imposed on the quantum clock size. If such a force is absent in the theory, i.e. $F_{\max} = \infty$, then $R_g \to 0$, and limitation for the quantum clock size is absent too. The main cause of the discussed limitation is the requirement $R > R_g$ equivalent to the condition preventing the formation of horizon. Therefore, the occurrence of the force $F_{\max}$ in relation (34) which can be achieved only at the horizon seems absolutely natural.

The structure of relation (34) does not contain any information concerning the process which has been the base for construction of the clock. This suggests the idea that this relation may be obtained from general considerations. To prove this statement let us use the uncertainty relation

$$\Delta x_{\min} \Delta p_{\max} \geq \frac{\hbar}{2} \tag{35}$$

Since

$$F_{\max} = \frac{\Delta p_{\max}}{\Delta t_{\min}},$$

we immediately obtain that the minimum size $\Delta x_{\min}$ of the clock necessary for measurement of the time intervals $\Delta t_{\min}$ obeys the limitation

$$\Delta x_{\min} \Delta t_{\min} \geq \frac{\hbar}{F_{\max}} = \frac{\hbar c}{\eta} \tag{36}$$

in complete correspondence with (45). This is just the relation that describes the structure of space-time foam! A simple form of relation (47) points to the fact that the limit values $\hbar, c, \eta$ have a fundamental character.

Certainly, the earlier obtained restrictions for the limits of measurability of distance and time (20) are in accord with relations (47). In fact, multiplication of the uncertainties (20) gives

$$\delta l \cdot \delta t \geq \left(\frac{l\hbar}{c\eta}\right)^{1/3} c \left(\frac{t\hbar}{\eta}\right)^{1/3} = (l \cdot t)^{1/3} \left(\frac{\hbar c}{\eta}\right)^{2/3} \tag{37}$$

Suppose that we are to measure the minimum scales of length and time, i.e. $l = \delta l$ and $t = \delta t$. In such a case (37) will reproduce relation (36).

7. Limit Relations in Information Theory

Limit values $\hbar, c, \eta$ control (or limit) rates of all physical processes and in particular information transmission rate. Exact value of this quantity goes far beyond all purely technological applications. Level of human society development to great extent is determined by information transmission and processing speed. In order to find the limit working speed of a computing devise one should take into account three aspects:

1. Uncertainty principle
2. Finite velocity of signal transmission
3. Necessity to prevent formation of a black hole (existence of the horizon)

In the considered example all the three limit values $(\hbar, c, \eta)$ work together leading to the following inequalities:

$$\Delta E \Delta t \geq \hbar, \quad \Delta t \geq L/c, \quad L > r_g = \frac{2MG}{c^2}. \tag{38}$$

It results in the following expression for the limit working speed v of arbitrary computing device (Gorelik, 2009):

$$v = \sqrt{\frac{c^5}{G\hbar}} = \sqrt{\frac{\eta}{\hbar}} = t_{Pl}^{-1}. \quad (39)$$

The information processing speed in arbitrary computing device is bounded by limit concentration of energy inside the device. The limit power η gives quantitative measure of this bound. At $\eta \to \infty$ (limitations are absent) the computing device could work with arbitrarily high performance.

Acknowledgements. This work was supported by SFFR, project n.32367.

References

Bolotin Yu.L. et al.: 2016, preprint (arXiv:1604.01945).
Brandt H.E.: 1989, *Foundations of Physics Letters,* **2**, 39.
Burderi L., Di Salvo T., Iaria R.: 2016, *Phys. Rev.,* **D93**, 064017.
Caianiello E.: 1981, *Lelt. Nuovo Gimento,* **32**, 65.
Gibbons G.W.: 2002, *Found. Phys.,* **32**, 1891.
Gorelik G.: 2009, preprint (arXiv:0910.3424).
Karolyhazy F.: 1966, *Il Nuovo Cimento,* **A42**, 390.
Lloyd S.:2005, preprint (arXiv:quant-ph/0501135).
Ng J., van Dam H.: 1994 *Mod. Phys. Lett.,* **A9**, 335.
Ng J.: 2001, *Phys. Rev. Lett.,* **86**, 2946.
Ng J.: 2002, *in Proc. of OCPA 2000, Editors: N.G.Chang et al. (World Scientific Publishing Company)*, 235; available at arXiv:0010234.
Ng J.: 2003, *Modern Physics Letters,* **A18**, 1073.
Papini R.: 2003, *Nuovo Gimento,* **B117**, 1325.
Penrose G.: 1973, *Ann. N. Y. Acad. Sci.,* **224**, 125.
Planck M.: 1899, *S.-B. Preu.Akad.Wiss.,* **5**, 440.
Schiller C.: 2005, *International Journal of Theoretical Physics,* **44**, 1629.
Schiller C.: 2006, *Motion mountain, Relativity*, **2**, 103, Edition 27.06, available at www.motionmountain.net.
't Hooft G.: 1994, Dimensional Reduction in Quantum Gravity, in Salamfestschrift, Editors: A. Ali, J. Ellis and S.Randjbar-Daemi (World Scientific Publishing Company) 284, available at arXiv:gr-qc/9310026.
Susskind L.: 1995, *J. Math. Phys.,* **36**, 6377.
Wheeler J.A.: 1986, *American Scientist,* **74**, 366.
Wigner E.P., 1957, *Rev. Mod. Phys.,* **29**, 255.
Wood W.R., Papini G., Cai Y.Q.: 1989, *Nuovo Gimento,* **B104**, 727.

DOI: http://dx.doi.org/10.18524/1810-4215.2017.30.114129

THE ABC OF COSMOGRAPHY

Yu. L. Bolotin[1], L. G. Zazunov[1,2], M. I. Konchatnyi[1,3], O. A. Lemets[1,4]

[1] A.I.Akhiezer Institute for Theoretical Physics,
National Science Center "Kharkov Institute of Physics and Technology",
Kharkov, Ukraine, *ybolotin@gmail.com*
[2]*lzazunov@gmail.com*
[3]*konchatnij@kipt.kharkov.ua*
[4]*oleg.lemets@gmail.com*

ABSTRACT. The basis of this work is the scheme for describing the universe, called the "cosmography" entirely based on the cosmological principle. Within the framework of such a scheme the parameters of any model that satisfies the cosmological principle (the universe is homogeneous and isotropic on large scale), can be expressed through cosmographic parameters. We demonstrate a number of advantages of the approach used before traditional methods

Keywords: cosmographic parameters, cosmography.

1. Introduction

The fundamental characteristics used to describe the evolution of the universe can be either kinematic if they are extracted directly from the space-time metric or dynamical if they depend on the properties of the fields that fill the universe. The dynamic characteristics are, of course, model dependent while the kinematic characteristics are more universal. In addition, the latter are free from the uncertainties arising when physical quantities such as, for example, energy densities are measured. It is for this reason that the kinematic characteristics are convenient for describing the current expansion of the universe. The kinematics of cosmological expansion of a homogeneous and isotropic universe has been called cosmography

In the early 60s of the last century, Alan Sandage (Sandage, 1962) defined as the primary goal of the cosmologists a search for two parameters, namely, the Hubble parameter and the deceleration parameter. However, an expansion with a constant acceleration is not the only possible realization of the kinematics of a nonstationary universe. As the universe evolves, the relative content of the components that fill it is changing and, as a consequence, the dynamics of expansion changes, hence the changes in acceleration. Thus, for a more complete description of the kinematics of cosmological expansion, it is useful to consider an extended set of parameters by including temporal derivatives of a higher-order scale factor (Visser, 2005; Dunsby et al., 2016; Bolotin et al., 2012):

$$
\begin{aligned}
lH(t) &\equiv \frac{1}{a}\frac{da}{dt};\\
q(t) &\equiv -\frac{1}{a}\frac{d^2a}{dt^2}\left[\frac{1}{a}\frac{da}{dt}\right]^{-2};\\
j(t) &\equiv \frac{1}{a}\frac{d^3a}{dt^3}\left[\frac{1}{a}\frac{da}{dt}\right]^{-3};\\
s(t) &\equiv \frac{1}{a}\frac{d^4a}{dt^4}\left[\frac{1}{a}\frac{da}{dt}\right]^{-4};\\
l(t) &\equiv \frac{1}{a}\frac{d^5a}{dt^5}\left[\frac{1}{a}\frac{da}{dt}\right]^{-5}.
\end{aligned}
\tag{1}
$$

The inclusion of higher derivatives from the scale factor, on one hand, reflects the continuous progress of observational cosmology, and, on the other, it is dictated by the need to describe the increasingly complex effects used for obtaining precise information.

2. The basic cosmographic relations

Let us give a number of useful relationships needed to describe the kinematics of cosmological expansion. The deceleration parameter is related to the Hubble parameter by the following relations:

$$
\begin{aligned}
lq(t) &= \frac{d}{dt}\left(\frac{1}{H}\right) - 1;\\
q(z) &= \frac{1+z}{H}\frac{dH}{dz} - 1;\\
q(z) &= \frac{1}{2}\frac{d\ln H^2}{d\ln(1+z)} - 1.
\end{aligned}
\tag{2}
$$

Derivatives $\frac{dH}{dz}$, $\frac{d^2H}{dz^2}$, $\frac{d^3H}{dz^3}$, $\frac{d^4H}{dz^4}$ and can be expressed through the deceleration parameter and other cosmo-

logical parameters as follows:

$$\begin{aligned}
\frac{dH}{dz} &= \frac{1+q}{1+z}H;\\
\frac{d^2H}{dz^2} &= \frac{j-q^2}{(1+z)^2}H;\\
\frac{d^3H}{dz^3} &= \frac{H}{(1+z)^3}\left(3q^2+3q^3-4qj-3j-s\right);\\
\frac{d^4H}{dz^4} &= \frac{H}{(1+z)^4}(-12q^2-24q^3-15q^4+32qj+\\
&+ 25q^2j+7qs+12j-4j^2+8s+l). \qquad (3)
\end{aligned}$$

Let $C_n \equiv \gamma_n \frac{a^{(n)}}{aH^n}$, where $a^{(n)} \equiv \frac{d^n a}{dt^n}$ is the n-th time derivative of the scale factor, $n \geq 2$ and $\gamma_2 = -1$, $\gamma_n = 1$ for $n > 2$. Then $C_2 = q$, $C_3 = j$, $C_4 = s \ldots$ For the derivatives of the parameters with respect to the redshift, the following relation takes place:

$$(1+z)\frac{dC_n}{dz} = -\frac{\gamma_n}{\gamma_{n+1}}C_{n+1} + C_n - nC_n(1+q). \quad (4)$$

Using $dz/dt = -(1+z)H$, the redshift derivatives can be converted into time derivatives.

3. Cosmography of cardassian model

Dunajski and Gibbons (Dunajski and Gibbons, 2008) proposed an original approach for testing cosmological models that satisfy the cosmological principle. Implementation of the method implies the following sequence of steps:

1. The first Friedman equation is transformed to the ODE for the scale factor. This is achieved by using the conservation equation for each component included in the model to find the dependence of the energy density on the scale factor.

2. The resulting equation is differentiated (with respect to cosmological time) as many times as the number of free parameters of the model.

3. The time derivatives of the scale factor are expressed through the cosmographic parameters.

4. By solving the obtained system of linear algebraic equations, we express all free parameters of the model through cosmographic parameters.

The procedure under consideration can be made more universal and effective if the system of Friedmann equations for the Hubble parameter H and its time derivative $\dot{H}$ is considered as a starting one. By differentiating the equation the required number of times (this number is determined by the number of free parameters of the model), we obtain a system of equations including higher time derivatives of the Hubble parameter $\ddot{H}, \dddot{H}, \ddddot{H}$ ... These derivatives are directly related to the cosmological parameters by the relations (3). We implement this procedure for the so-called Cardassian model, whose evolution is described by a system of equations (Freese and Lewis, 2002)

$$H^2 = A\rho + B\rho^n. \quad (5)$$

$$\dot{\rho} + 3H\rho = 0. \quad (6)$$

Here ρ is the density of nonrelativistic matter. Differentiating equation (5) with respect to the cosmological time and using (6), we construct a system of coupled equations

$$\begin{aligned}
&H^2 = A\rho_m + B\rho_m^n,\\
&-\tfrac{2}{3}\dot{H} = A\rho_m + Bn\rho_m^n,\\
&\tfrac{2}{9}\tfrac{\dot{H}}{H} = A\rho_m + n^2B\rho_m^n.
\end{aligned} \quad (7)$$

Using the solutions of this system and the time derivatives of the Hubble parameter (3), we find for constants B and n:

$$\begin{aligned}
&\tfrac{B\rho_0^n}{H_0^2} = \tfrac{1}{3}(1-2q_0)\\
&n = \tfrac{2}{3}\tfrac{j_0-1}{2q_0-1}.
\end{aligned} \quad (8)$$

These relationships solve the problem of finding cardassian model parameters. A similar procedure can be applied to any model that satisfies the cosmological principle

Otherwise, we must treat the time-dependent solution for the density ρ_m. It can be represented in the form

$$\frac{\rho_m}{\rho_c} = \frac{-n+\frac{2}{3}(1+q)}{1-n}, \quad \rho_c \equiv \frac{3H^2}{8\pi G}. \quad (9)$$

The current density ρ_{m0} can be found by substitution $q \to q_0$, $H \to H_0$.

It is interesting to note that the expression (7) for the parameter n coincides exactly with the parameter s, one of the so-called statefinder parameters $\{r, s\}$ (Sahni V. et al., 2003).

$$r \equiv \frac{\dot{a}}{aH^3}, \quad s = \frac{2}{3}\frac{r-1}{2q-1}. \quad (10)$$

The coincidence is obvious, since $r \equiv j$. The reason for the coincidence can be explained as follows. In any model with the scale factor $a \propto t^\alpha$, there are the simple relations for the cosmographic parameters q and j,

$$2q-1 = \frac{2-3\alpha}{\alpha}, \quad j-1 = \frac{2-3\alpha}{\alpha^2}. \quad (11)$$

In cardassian model $a \propto t^{\frac{2}{3n}}$, from which it follows that $s = n$.

4. Summary: advantages of cosmographic description

The proposed approach to finding the parameters of cosmological models has many advantages. Let's briefly dwell on them.

1. Universality: the method is applicable to any braid model that satisfies the cosmological principle. The procedure can be generalized to the case of models

with interaction between components (Bolotin et al., 2016).

2. Reliability: all the obtained results are accurate, since they follow from identical transformations.

3. The simplicity of the procedure.

4. Parameters of different models are expressed through a universal set of cosmological parameters. There is no need to introduce additional parameters.

5. The method provides an interesting possibility of calculating the highest cosmological parameters from the values of lower parameters known with a better accuracy.

6. The method presents a simple test for analyzing the compatibility of different models. The analysis consists of two steps. In the first step, the model parameters are expressed through cosmological parameters. The second step consists in finding the intervals of cosmological parameter changes that can be realized within the framework of the considered model. Since the cosmological parameters are universal, only in the case of a nonzero intersection of the obtained intervals, the models are compatible.

References

Sandage A.: 1962, *ApJ,* **136**, 319.

Visser M.: 2005, *Gen. Relat. Grav.,* **37**, 1541.

Dunsby P.K.S. et al: 2016, *Int. J. Geom. Methods, Mod. Phys.,* **13**, 1630002.

Bolotin Yu., Erokhin D., Lemets O.: 2012, *Phys. Usp.*, **55**, 876918.

Dunajski M. and Gibbons G.: 2008, *Class. Quant. Grav.,* **25**, 235012.

Freese K. and Lewis M.: 2002, *Phys. Lett. B,* **540** 1-8.

Bolotin Yu., Cherkaskiy V., Lemets O.: 2016, *Int. J. Mod. Phys.,* **D25**, No. 5, 1650056.

Sahni V. et al: 2003, *JETP Lett.,* **77**, 201.

DOI: http://dx.doi.org/10.18524/1810-4215.2017.30.114218

ΛGR CENTENNIAL: COSMIC WEB IN DARK ENERGY BACKGROUND

A.D.Chernin

Sternberg Astronomical Institute, Moscow University, Russia, *Arthur.Chernin@gmail.com*

ABSTRACT. The basic building blocks of the Cosmic Web are groups and clusters of galaxies, superclusters (pancakes) and filaments embedded in the universal dark energy background. The background produces antigravity, and the antigravity effect is strong in groups, clusters and superclusters. Antigravity is very weak in filaments where matter (dark matter and baryons) produces gravity dominating in the filament internal dynamics. Gravity-antigravity interplay on the large scales is a grandiose phenomenon predicted by ΛGR theory and seen in modern observations of the Cosmic Web.

Keywords: General Relativity, Cosmology, Dark Matter, Dark Energy, Cosmic Web.

1. Introduction

General Relativity theory with a non-zero cosmological constant(ΛGR) was introduced by Einstein in 1917, one hundred years ago. In 1922-24, the cosmological constant Λ was included Friedmann to his cosmological model where Λ was treated as an empirical parameter which should be measured in astronomical observations. Later, Gliner (1965) argued that the cosmological constant is a physical parameter characterizing some substance that fills the whole Universe with the constant density

$$\rho_\Lambda = \Lambda/(8\pi G),$$

where G is the Newtonian gravitational constant; the speed of light is $c = 1$ hereafter.

In 1998-99 observations with the Hubble Space Telescope (HST) made it possible to discover the positive cosmological constant at the largest observable distances of 1-3 Gpc (Riess et al., 1998; Perlmutter et al., 1999; 2011 Nobel prize in physics). In these studies, the current density of the cosmic fluid, mostly referred to as dark energy now, was determined to be

$$\rho_\Lambda \simeq 0.7 \times 10^{-29} g/cm^3.$$

Like the cosmological constant itself, the dark energy density is a fundamental time-independent parameter of the ΛGR.

A couple of years later dark energy of the same density was found in the Local Universe at rather modest distances of about 1-3 Mpc from us (Chernin et al., 2000). The earlier pioneering works of 1927-29 by Lemaître and Hubble were used for this purpose together with the recent HST data on the Local Universe (Karachentsev, 2005). These findings indicate that the dark energy density is the universal, both global and local, physical constant. Accordingly, all astronomical structures are treated now as embedded in the universal dark energy background.

In this presentation the local effects of dark energy are discussed on the scales from groups of galaxies to clusters, superclusters (or pancakes) and filaments. These objects are known as basic building blocks of the Cosmic Web. The interplay between dark matter and dark energy within these systems is in the focus of the discussion.

2. Matter/energy balance in the Universe

Dark matter was discovered in groups and clusters of galaxies in 1930-70s (see the book by Einasto, 2014, for a fresh systematic and complete review). The physical nature of dark matter is yet unknown. Most probably it is some kind of non-relativistic gas of particles that are not represented in the current Standard Model of fundamental physics. The present mean cosmological density of cosmic dark matter (see the above book) is now well measured,

$$\rho_{DM} \simeq 0.25 \times 10^{-29} g/cm^3.$$

The mean density of the ordinary (baryonic) matter of stars, interstellar medium, etc., is also known:

$$\rho_B \simeq 0.05 \times 10^{-29} g/cm^3.$$

It is seen from these data that the dark energy dominates in the matter/energy balance of the observed Universe.

A quantitative measure of the dark energy domination in the Universe is given by the ratio

$$X(t) = (2\rho_\Lambda)/(\rho_{DM} + \rho_B).$$

In Friedmann's model, the ratio X goes to zero when the cosmic time t goes to zero; and it goes to infinity when t goes to infinity (the coefficient 2 in this relation is explained below). Friedmann's theory enables one to find also that $X = 1$ at the cosmic age about 7 Gyr. After this moment, dark energy dominates in the expanding Universe.

3. Einstein's antigravity

As some kind of a fluid, dark energy has both the density (given above) and pressure. The relation between density and pressure (equation of state) for dark energy is rather special, namely:

$$P_\Lambda = -\rho_\Lambda.$$

Since the dark energy density ρ_Λ is positive, its pressure is negative. According to GR, the effective gravitating dark energy density is

$$\rho_{eff} = 3P_\Lambda + \rho_\Lambda = -2\rho_\Lambda < 0.$$

The negative effective density means that the dark energy produces negative gravity, or antigravity.

With the discovery of dark energy at the global distances, the antigravity force entered the cosmic scene; it was realized soon that the gravity-antigravity interplay is the major factor that controls the dynamics of the cosmological expansion. In a similar way, our astronomical findings at local distances of 1-10 Mpc (Chernin et al., 2000; 2003) show that Einstein's antigravity can dominate dynamically on relatively small, non-cosmological distances of ∼1-3 Mpc as well. Thus Einstein's antigravity is a universal omnipresent force which has the same rank among the forces of nature, as Newton's gravity does.

4. Dark energy and Cosmic Web

The Cosmic Web, as was first described a decade ago (see Einasto 2014 and references therein), is a vast network formed by all the galaxies of the Universe. The galaxies constitute three types of systems: (1) groups and clusters of galaxies, of 1-10 Mpc size; (2) superclusters, or pancakes, of the 10-20 Mpc size; (3) filaments with the length of 10-30 Mpc. Groups, clusters and superclusters form the nodes of the Web, and filaments link them together.

The geometry of the building blocks is of three types in accordance with their dimension: groups and clusters are 3D systems, superclusters are 2D ones, and filaments are 1D one-dimensional.

There are also three types of the building-block internal dynamics corresponding to different values of the density ratio

$$\langle X(t)\rangle = (2\rho_\Lambda)/\langle\rho_M\rangle;$$

here $\langle\rho_M\rangle = (\langle\rho_{DM}\rangle + \langle\rho_B\rangle)$ is the mean matter (dark matter and baryons) density of a block. The local ratio $\langle X\rangle$ is directly related to the internal block dynamics. Indeed, $\langle H\rangle = 1$ means that gravity of matter and antigravity of dark energy are equally strong in the system, so that the system is in the state of gravitational equilibrium. If $\langle X\rangle > 1$, then the system dynamics is dominated by dark energy antigravity. On the contrary, $\langle X\rangle < 1$ means that antigravity in the system is weak as compared to the gravity of matter (dark matter and baryons).

So there are three types of internal dynamics (characterized by $\langle X\rangle = 1,\ > 1,\ < 1$), as well as three geometry types of building blocks ($3D$, $2D$, $1D$). It seems reasonable to expect a one-to-one correspondence between those:

$$(3D \Leftrightarrow \langle H\rangle = 1),\ \ (2D \Leftrightarrow \langle H\rangle > 1),\ \ (1D \Leftrightarrow \langle H\rangle).$$

This may be considered as a new prediction of the ΛGR theory that may be checked and supported or disproved by observational data.

5. Conclusion: Three examples

Observational material on the building blocks of the Cosmic Web that are available in publications of the last decade may be used to verify the theory prediction above. Here are only three examples of the relevant data.

1) The Local Group: 3D

The Local Group of galaxies is the nearest to us gravitationally bound system that may be described theoretically in terms of a 3D matter ball embedded in the dark energy background (Chernin et al., 2000). According to observations, the matter mass of the ball is $M = 1.2 \times 10^{12} M_\odot$ and its radius is $R = 1.2$ Mpc (Karachentsev, 2005). The mean matter density in the group comes from these data: $\langle\rho_M\rangle = 3/4\pi M/R^3 \simeq\simeq \times 10^{-29} g/cm^3$.

This value is almost exactly equal to the (absolute) value of the dark energy effective gravitating density. Thus, the Local Group is indeed an example of a 3D system with $\langle X\rangle \simeq 1$.

Similar results with $\langle X\rangle \simeq 1$ and 3D are found also for the Virgo, Fornax, and Coma clusters of galaxies whose mass is 7 to 10 times larger than mass of the Local Group (Bisnovatyi-Kogan et al., 2012).

2) Local Pancake: 2D.

The Zeldovich Local Pancake (ZLP) is a supercluster of about 20 Mpc across that is seen as an expansion flow of giant galaxies. It has recently been studied with the HST observations (Karachentsev et al., 2013).

The flow involves 15 most luminous nearby galaxies (actually, these are galaxy groups like the Local Group) together with about 300 their fainter companions. The flow giants are moving away from the barycenter of the Local Group with the radial velocities from 100 to about 1000 $km\,s^{-1}$.

The ZLP is a 2D system: it occupies a flattened volume located near the Supergalactic Plane. The total matter mass of the ZLP is $M \simeq 8 \times 10^{13} M_{\odot}$. The density ratio is definitely larger than 1: $\langle X \rangle = 2\,\rho_{\Lambda}/\langle \rho_M \rangle \geq 10$. It means that dark energy antigravity dominates in the dynamics of this 2D system and ZLP is expanding with acceleration.

The change of the expansion rate can be characterized by the dimensionless deceleration parameter $q(R) = -\ddot{R}R/V^2$ borrowed from cosmology. The parameter proves to be negative for each of the ZLP individual galaxies at the present epoch of observations. Its mean value for the flow as a whole is $\langle q(R) \rangle \simeq -0.9$. A similar indications of dark energy domination may be expected in other 2D expanding superclusters.

3) Filament feeding a massive cluster: 1D.

The weak lensing detection of a large-scale filament funneling matter onto the core of the massive galaxy cluster MACSJ0717.5+3745 is recently reported (Jauzac et al., 2012). Its proper length is 18 Mpc and the mean matter density is $2 \times 10^{-27} g/cm^3$. Accordingly, the ratio $\langle X \rangle$ is of the order of 10^{-2} which means that dark energy dynamical effects are negligibly weak in the filament.

It may be expected that the dynamics of most other observed large filaments is as well strongly dominated by matter gravity.

To conclude, the basic building blocks of the Cosmic Web and the Web as a whole are embedded in the universal dark energy background. The background produces antigravity which is strong ($\langle H \rangle \geq 1$) inside clusters (3D) and superclusters or pancakes(2D) of galaxies. The strong antigravity effect is reliably observed inside typical systems of these kind. The antigravity is very weak ($\langle H \rangle << 1$), and gravity produced by matter (dark matter and baryons) dominates in large filaments (1D). Gravity-antigravity interplay is one of the most impressive phenomenon predicted theoretically by ΛGR that revealed itself in various modern observations of the Cosmic Web.

I am grateful to Alexander S. Silbergleit for important discussions.

References

Bisnovatyi-Kogan G.S., Chernin A.D.: 2012, *Astrophys. Space Sci.* **338**, 337.

Chernin A.D., Teerikorpi P., Baryshev Yu.V.: 2000, [astro-ph/0012021].

Chernin A.D. et al.: 2003, *Adv. Space Res.* **31**, 459.

Chernin A.D., Emelyanov N.V., Karachentsev I.D.: 2015, **MNRAS** *449*, 2069.

Einasto J.:2014, *Dark matter and Cosmic Web story.* World Sci., Berlin/Roma.

Gliner E.B.: 1966, *Sov.Phys. JETP* **22**, 378.

Jauzac E. et al.: 2014, *MNRAS* **426,**, 3360.

Karachentsev I.D.: 2005, *Astron. J.,* **129**, 178.

Perlmuter S., Aldering G., Goldhaber A. *et al.*: 1999, *Astrophys.J.*, **517**, 565.

Riess A.V., Filippenko A., Challis P. *et al.*: 1998, *Astron.J.,* **116**, 1009.

DOI: http://dx.doi.org/10.18524/1810-4215.2017.30.114219

QUANTUM MODEL OF A CHARGED BLACK HOLE

V.D. Gladush

Dnipro National University, Gagarin Ave, 725014, Ukraine,
vgladush@gmail.com

A canonical approach for constructing of the classical and quantum description spherically-symmetric configuration gravitational and electromagnetic fields is considered. According to the sign of the square of the Kodama vector, space-time is divided into R- and T-regions. By virtue of the generalized Birkhoff theorem, one can choose coordinate systems such that the desired metric functions in the T-region depend on the time, and in the R-domain on the space coordinate. Then, the initial action for the configuration breaks up into terms describing the fields in the T- and R-regions with the time and space evolutionary variable, respectively. For these regions, Lagrangians of the configuration are constructed, which contain dynamic and non-dynamic degrees of freedom, leading to constrains. We concentrate our attention on dynamic T-regions. There are two additional conserved physical quantities: the charge and the total mass of the system. The Poisson bracket of the total mass with the Hamiltonian function vanishes in the weak sense. A classical solution of the field equations in the configuration space (minisuperspace) is constructed without fixing non-dynamic variable. In the framework of the canonical approach to the quantum mechanics of the system under consideration, physical states are found by solving the Hamiltonian constraint in the operator form (the DeWitt equation) for the system wave function Ψ. It also requires that Ψ is an eigenfunction of the operators of charge and total mass. For the symmetric of the mass operator the corresponding ordering of operators is carried out. Since the total mass operator commutes with the Hamiltonian in the weak sense, its eigenfunctions must be constructed in conjunction with the solution of the DeWitt equation. The consistency condition leads to the ansatz, with the help of which the solution of the DeWitt equation for the state Ψ_{em} with a defined total mass and charge is constructed, taking into account the regularity condition on the horizon. The mass and charge spectra of the configuration in this approach turn out to be continuous. It is interesting that formal quantization in the R-region with a space evolutionary coordinate leads to a similar result.

Keywords: charged black holes, mass and charge functions, constraints, mass and charge operators, the compatibility condition.

1. Introduction

Spherically-symmetric systems of gravitational and electromagnetic fields represent the simplest configurations for check of the main ideas and results of quantum gravitation. They are a convenient testing ground for studying some of the problems arising from a rigorous consideration of a more complete theory. One of the main features general-relativistic configurations is their degeneracy. The general formalism of the canonical approach to degenerate systems was constructed by Dirac [1], which was then developed in many works (see, for example, [2,3,4]). Problems of the quantum description spherically-symmetric configurations gravitational and electromagnetic fields was considered in many work A general, geometrodynamical approach to the spherically symmetric gravitational field was developed in [5], which was then generalized to the case of a spherically symmetric configuration electromagnetic and gravitational fields in [6].

The proposed model is based on the observation that the classical spherically-symmetric configurations of electromagnetic and gravitational fields are stationary from the point of view of an external observer, have certain regions of space-time with dynamic behavior. This means that these regions do not allow a timelike vector Kodama (Killing) [7], which implies in these regions the evolution of the geometry of space-time in time. This evolution of a space-time geometry is also responsible for quantum-mechanical properties of the considered model of the charged black hole. Such models, with a fixed evolutionary time coordinate and space-like Killing vector were considered in [8, 9]. In this paper, on the basis of simple approach using the DeWitt equation and quantum mass and charge operators, a quantum description of the spherically symmetric configuration of the gravitational and electromagnetic fields is constructed, i.e. quantum model of a charged black hole with a continuous spectrum of masses and charge.

2. Classical description of the spherically-symmetric configuration of the gravitational and electromagnetic fields

Consider the spherically symmetric space-time $M^{(4)}$ with the metric

$$ds^2 = g_{\mu\nu}dx^\mu dx^\nu = \gamma_{ab}dx^a dx^b - R^2 d\sigma^2\,, \quad (1)$$
$$d\sigma^2 = d\theta^2 + \sin^2\theta d\alpha^2\,. \quad (2)$$

Here $R = R(x^a)$, $\gamma_{ab} = \gamma_{ab}(x^a)$ — 2D metric tensor, $\sqrt{-g} = \sqrt{-\gamma}R^2\sin\theta$, где $g = \det|g_{\mu\nu}|$, $\gamma = \det|\gamma_{ab}|$, $\mu,\nu = 0,1,2,3\,;\ a,b = 0,1$.

The total action for a system of gravitational and electromagnetic fields has the form

$$S = -\frac{1}{16\pi c}\int_{M^{(4)}}\left(\frac{c^4}{\kappa}\,{}^{(4)}R + F^{\mu\nu}F_{\mu\nu}\right)\sqrt{-g}d^4x\,. \quad (3)$$

Here ${}^{(4)}R$ is the scalar curvature of $M^{(4)}$ with respect to the metric $g_{\mu\nu}$, $F_{\mu\nu} = A_{\nu,\mu} - A_{\mu,\nu}$ is the electromagnetic field tensor, where $A_\mu = \{A_a, 0, 0\}$ is vector potential.

In the spherically symmetric case, after integrating over the angles and discarding the surface term, the action (3) can be represented in the form

$$S = -\tfrac{1}{4c}\int_{M^{(2)}}\left\{\tfrac{c^4}{\kappa}\sqrt{-\gamma}\left(R^2\,{}^{(2)}R + 2(\nabla R)^2 - 2\right) - \tfrac{2}{\sqrt{-\gamma}}R^2E^2\right\}d^2x\,, \quad (4)$$

where ${}^{(2)}R$ is scalar curvature $M^{(2)}$ (radially-time part $M^{(4)}$), $(\nabla R)^2 = \gamma^{ab}R_{,a}R_{,b}$. The reduced action is invariant under coordinate transformations $x^a = x^a(\acute{x}^b)$.

In a spherically-symmetric space-time there is a preferable reference system (RS). Tangents to world lines of this RS are proportional to Kodama's vector

$$\vec{K} = K^a\partial_a = -e^{ab}R_{,b}\partial_a\,. \quad (5)$$

It is easy to see that $\vec{K}R = K^a R_{,a} = 0$ and the Kodama vector satisfies the continuity equation $K^a_{;a} = 0$. For the free space, as well as for electrovacuum spaces, the Kodama vector is transformed into a Killing vector, which corresponds to the generalized Birkhoff theorem (Frolov, 1998).

Using an admissible coordinate transformation, we lead the metric (1) to the diagonal form

$$ds^2 = f(r,x^0)(dx^0)^2 - h(r,x^0)dr^2 - R^2(r,x^0)d\sigma^2\,, \quad (6)$$

where $f > 0, h > 0$. Then $\sqrt{-\gamma} = \sqrt{fh}$ and the action takes the form

$$S = \tfrac{1}{2c}\int\limits_{M^{(2)}}\left\{\tfrac{c^4}{\kappa}\sqrt{hf}\left\{\tfrac{R}{h}R_{,1}\left(\ln\left(fR\right)\right)_{,1} - \tfrac{R}{f}R_{,0}\left(\ln(hR)\right)_{,0} + 1\right\} + \tfrac{R^2}{\sqrt{fh}}E^2\right\}d^2x\,, \quad (7)$$

where $R_{,0} = \partial R/\partial x^0$, $R_{,1} = \partial R/\partial r$. In what follows we confine ourselves to the class of diagonal metrics.

Note that information about the structure of $M^{(2)}$ is contained in the square of the Kodama vector

$$(\vec{K})^2 = -(\nabla R)^2 = \frac{1}{h}\left(R_{,1}\right)^2 + \frac{1}{f}\left(R_{,0}\right)^2\,. \quad (8)$$

Light surfaces $R(r,x^0) = R_g = const$, for which $(\vec{K})^2 = -(\nabla R)^2 = 0$, divide $M^{(2)}$ into regions

R-regions $M^{(2)}_R \subset M^{(2)}$, when $(\vec{K})^2 > 0\,,$
T-regions $M^{(2)}_T \subset M^{(2)}$, when $(\vec{K})^2 < 0\,.$

In the R-region the surface $R(r,x^0) = const$ are timelike, and in the T-region is spacelike. In the T-region we sometimes use the notation $R = cT$. Using the generalized Birkhoff theorem, in the R-region we can choose a coordinate system (CS) in which γ_{ab} and R depend only on the space-like coordinate r. Similarly, in the T-region, there exists an CS in which γ_{ab} and R depend on the time-like coordinate x^0.

In the T-region it is convenient to go to the new variable

$$f(x^0) = \frac{N^2(x^0)}{h(x^0)}\,, \qquad A_1 = \phi\,, \quad (9)$$

so that the metric (6) takes the form

$$ds^2_T = \frac{N^2(x^0)}{h(x^0)}(dx^0)^2 - h(x^0)dr^2 - R^2(x^0)d\sigma^2\,. \quad (10)$$

In this case for the action (7) we get

$$S_T = \int\limits_{x^0\in M^{(2)}_T} L_T dx^0\,, \quad (11)$$

$$L_T = \tfrac{l}{2c}\left\{\tfrac{1}{N}\left[R^2\left(\phi_{,0}\right)^2 - \tfrac{c^4}{\kappa}\left(RR_{,0}h_{,0} + h\left(R_{,0}\right)^2\right)\right] + \tfrac{c^4}{\kappa}N\right\}\,, \quad (12)$$

where L_T is the Lagrangian of the reduced system. Here, $l = r_2 - r_1$ is a constant that arises as a result of integration over r in the range from r_1 to r_2, permissible transformations are $x^0 = x^0(\acute{x}^0)$.

Further, it is convenient to go over to the so-called characteristic variables $\{\xi = hR,\ R = cT,\ \phi\}$. Then the metric and Lagrange function of the T-region take the form

$$ds^2 = N^2\frac{R}{\xi}\left(dx^0\right)^2 - \frac{\xi}{R}dr^2 - R^2d\sigma^2\,, \quad (13)$$

$$L = \frac{l}{2c}\left\{\frac{1}{N}\left[-\frac{c^4}{\kappa}\dot{\xi}\dot{R} + R^2\dot{\phi}^2\right] + \frac{c^4}{\kappa}N\right\}\,. \quad (14)$$

In the case of the R-region, we pass to the variables

$$h(r) = \frac{N^2_R(r)}{f(r)}\,, \qquad \{\eta = fR, A_0 = \varphi\}\,, \quad (15)$$

in which the metric and Lagrange functions in the characteristic variables take the form

$$L_R = \frac{l}{2c}\left\{\frac{1}{N_R}\left[\frac{c^4}{\kappa}\acute{R}\acute{\eta} + R^2\acute{\varphi}\right]^2 + \frac{c^4}{\kappa}N_R\right\}, \qquad (16)$$

$$ds_R^2 = \frac{\eta}{R}(dx^0)^2 - N_R^2\frac{R}{\eta}dr^2 - R^2 d\sigma^2\,. \qquad (17)$$

From the Lagrangian (14) follows the primary constraint $P_N = \partial L/\partial\dot{N} = 0$ and momenta $P_i = \partial L/\partial\dot{q^i}$:

$$P_\xi = -\frac{c^3 l}{2\kappa N}\dot{R}\,, \quad P_R = -\frac{c^3 l}{2\kappa N}\dot{\xi}\,, \quad P_\phi = \frac{l}{cN}R^2\dot{\phi}\,. \qquad (18)$$

The Hamiltonian function $H = P_\xi\dot{\xi} + P_R\dot{R} + P_\phi\dot{\phi} - L$ leads to the secondary constraint in the T-region

$$H = \frac{Nc}{2l}\left\{-\frac{4\kappa}{c^4}P_\xi P_R + \frac{1}{R^2}P_\phi^2 - \frac{l^2c^2}{\kappa}\right\} \sim 0 \qquad (19)$$

in the characteristic variables.

The Maxwell equations following from actions (3) or (4) lead to to the relation $(R^2/NE)_{,b} = 0$. This implies the conservation law

$$\frac{R^2}{N}E = Q = const\,. \qquad (20)$$

It is natural to define the following function:

$$Q(N, R, \dot{\phi}) = \frac{R^2}{N}\dot{\phi} = \frac{c}{l}P_\phi\,. \qquad (21)$$

This function for a free electromagnetic field is conserved and is equal to the configuration charge inside the region of radius R. In what follows we will call it the charge function.

We introduce the mass function (Cahill,1970; Berezin, 1987; Gladush, 2012) by the relation:

$$M_f(\gamma_{ab}, R) = \frac{c^2}{2\kappa}R\left(1 + \gamma^{ab}R_{,a}R_{,b}\right)\,. \qquad (22)$$

In the R-region, it is related to the field energy of a spherical region of radius R. Its value for the free gravitational field is constant: $M_f = m$ and determines the mass that appears in the Newtonian limit of the gravitational field. In the T-region, it is conserved and in the used variables has the form

$$M_f = \frac{c^2}{2\kappa}\left(R + \frac{1}{N^2}\xi\dot{R}^2\right)\,. \qquad (23)$$

For the system under consideration, $M_f \neq const$. It can be shown that the quantity given by formula

$$M_{tot} = M_f + \frac{Q^2}{2c^2R} = const\,, \qquad (24)$$

is conserved and has the meaning of the total field mass of the spherical region of radius R taking into account a contribution of the electromagnetic field. In characteristic variables, as well as through momenta, it has the form

$$M_{tot} = \frac{c^2}{2\kappa}\left[R + \frac{1}{N^2}\left(\xi\dot{R}^2 + \frac{\kappa R^3\dot{\phi}^2}{c^4}\right)\right]\,, \qquad (25)$$

$$M_{tot} = \frac{1}{2l^2}\left[\frac{l^2c^2}{\kappa}R + \frac{4\kappa}{c^4}\xi P_\xi^2 + \frac{1}{R}P_\phi^2\right]\,. \qquad (26)$$

We write out the Poisson brackets of the dynamic quantities:

$$\{H, M_{tot}\} = \frac{2\kappa}{l^2c^4}P_\xi H \sim 0\,, \quad \{H, Q\} = \{M_{tot}, Q\} = 0\,.$$

The Lagrangian multiplier N can be excluded from the action (11), (12). Then the initial variational principle is transformed into the variational principle in the configuration space (Gowdy, 1970). We rewrite the Lagrange function (14) in the form

$$L_T = \frac{l}{2c}\left\{\frac{\mathfrak{T}}{N} + NU\right\}\,, \qquad (27)$$

where

$$\mathfrak{T} = -\frac{c^4}{\kappa}\dot{\xi}\dot{R} + R^2\dot{\phi}^2\,, \qquad U = \frac{c^4}{\kappa}\,. \qquad (28)$$

Then we have

$$\frac{\partial L_T}{\partial N_T} = \frac{l}{2c}\left\{-\frac{\mathfrak{T}}{N_T^2} + U\right\} = 0 \qquad (29)$$

This implies $N_T = \sqrt{\mathfrak{T}/U}$ and from (11) we obtain action for a geodesic in a minisuperspace

$$S = \frac{lc}{\sqrt{\kappa}}\int\sqrt{-\frac{c^4}{\kappa}d\xi dR + R^2\left(d\phi\right)^2} = \frac{lc}{\sqrt{\kappa}}\int d\Omega \qquad (30)$$

with the metric

$$d\Omega^2 = -\frac{c^4}{\kappa}d\xi dR + R^2\left(d\phi\right)^2\,. \qquad (31)$$

The geodesic equations obtained from here, together with the Hamiltonian constraint, are equivalent to the original system of Einstein's equations. It turns out that the corresponding configuration space with the metric (31 is flat, since the curvature tensor for the metric (31) vanishes. Let us write out the volume element defining the measure in the configuration space:

$$dV = \sqrt{-\det\|\Omega_{AB}\|}dq^1dq^2dq^3 = \frac{c^2}{2\kappa}Rd\xi dRd\phi\,. \qquad (32)$$

3. Quantum description of the spherically-symmetric configuration of the gravitational and electromagnetic fields

The quantum states of the field configuration under consideration are determined by the wave function $\Psi(R,\xi,\phi)$ on the minisuperspace with the coordinates $\{R,\ xi,\ phi\}$. The corresponding momentum operators in this representation have the form:

$$\hat{P}_R = -i\hbar\frac{\partial}{\partial R},\quad \hat{P}_\xi = -i\hbar\frac{\partial}{\partial \xi},\quad \hat{P}_\phi = -i\hbar\frac{\partial}{\partial \phi}\,. \quad (33)$$

The classical Hamiltonian, the total mass and charge functions lead to operators

$$\hat{H} = \frac{Nc}{2l}\left\{\frac{4\kappa\hbar^2}{c^4}\frac{\partial^2}{\partial R\partial\xi} - \frac{\hbar^2}{R^2}\frac{\partial^2}{\partial\phi^2} - \frac{c^2l^2}{\kappa}\right\}, \quad (34)$$

$$\hat{M} = \frac{1}{2l^2}\left(\frac{l^2c^2}{\kappa}R - \frac{4\kappa\hbar^2}{c^4}\frac{\partial}{\partial\xi}\xi\frac{\partial}{\partial\xi} - \frac{\hbar^2}{R}\frac{\partial^2}{\partial\phi^2}\right). \quad (35)$$

$$\hat{Q} = \frac{c}{l}\hat{P}_\phi = -i\frac{c\hbar}{l}\frac{\partial}{\partial\phi}\,. \quad (36)$$

For the Hermitian operator of the total mass, in the configuration space with measure (32) we use the following ordering of the operators: $\hat{P}_\xi\xi\hat{P}_\xi$. The following commutation relations hold

$$\left[\hat{H},\hat{M}\right] = -\frac{2\kappa\hbar^2}{l^2c^4}\frac{\partial}{\partial\xi}\hat{H}\sim 0\,,\quad \left[\hat{H},\hat{Q}\right] = \left[\hat{Q},\hat{M}\right] = 0\,.$$

States with a certain total mass and charge correspond to eigenfunctions and eigenvalues of the operators of total mass and charge:

$$\hat{M}\Psi_m = m\Psi_m\,,\qquad \hat{Q}\Psi_q = q\Psi_q\,. \quad (37)$$

They reduce to the following equations

$$\left\{\frac{c^2l^2}{\kappa}R - \frac{4\kappa\hbar^2}{c^4}\frac{\partial}{\partial\xi}\xi\frac{\partial}{\partial\xi} - \frac{\hbar^2}{R}\frac{\partial^2}{\partial\phi^2}\right\}\Psi_m = 2l^2m\Psi_m\,. \quad (38)$$

$$\frac{\partial}{\partial\phi}\Psi_q = \frac{iql}{c\hbar}\Psi_q\,. \quad (39)$$

From the last equation we obtain $\Psi_q = Ae^{i(ql/c\hbar)\phi}$. Now, the general wave functions of the DeWitt equation $\hat{H}\Psi = 0$ and the charge operator, also as general wave functions of the operators total mass and charge, can be represented in the form

$$\Psi = \psi(\xi,R)\,e^{i(ql/c\hbar)\phi}\,,\quad \Psi_m = \psi_m(\xi,R)\,e^{i(ql/c\hbar)\phi}\,.$$

The functions ψ and ψ_m satisfy the equations

$$\left(\frac{4\partial^2}{\partial R\partial\xi} + \frac{c^2q^2l^2}{\kappa\hbar^2}\frac{1}{R^2}\right)\psi = \frac{c^6l^2}{\kappa^2\hbar^2}\psi\,, \quad (40)$$

$$\left\{\frac{l^2c^2}{\kappa}R - \frac{4\kappa\hbar^2}{c^4}\frac{\partial}{\partial\xi}\xi\frac{\partial}{\partial\xi} + \frac{1}{R}\frac{q^2l^2}{c^2}\right\}\psi_m = 2ml^2\psi_m\,. \quad (41)$$

Next, we introduce Planckian and dimensionless quantities

$$m_{pl}^2 = c\hbar/\kappa,\ l_{pl}^2 = \hbar\kappa/c^3,\ q_{pl} = m_{pl}\sqrt{\kappa} = \sqrt{c\hbar}\,,$$

$\mu = m/m_{pl},\ \sigma = q/q_{pl},\ x = \xi/l_{pl},\ y = R/l_{pl},\ \chi = l/l_{pl}$.

Then, the system of equations (40), (41) can be rewritten as follows

$$\frac{\partial^2\psi}{\partial y\partial x} = \frac{\chi^2}{4}\left(1 - \frac{\sigma^2}{y^2}\right)\psi\,, \quad (42)$$

$$\frac{\partial^2\psi_m}{\partial x^2} = -\frac{1}{x}\frac{\partial\psi_m}{\partial x} + \frac{\chi^2}{4x}\left(y + \frac{\sigma^2}{y} - 2\mu\right)\psi_m\,. \quad (43)$$

A joint solution of this system, which regularly on the horizon, gives the wave function of configuration for the T-region in the state with a given mass m and a charge q

$$\Psi_{m,q} = CJ_0\left(\frac{lc}{l_{pl}^2}T\sqrt{hF_T(T,m,q)}\right)e^{i(ql/c\hbar)\phi}\,, \quad (44)$$

where $R = cT$ and

$$h = \frac{\xi}{R} = \frac{c^2}{2\kappa m}\xi_0F_T(T,m,q) > 0\,, \quad (45)$$

$$F_T(T,m,q) = -1 + \frac{2\kappa m}{c^3T} - \frac{\kappa q^2}{c^6T^2} > 0\,. \quad (46)$$

The functions h and $T = R/c$ in the initial metric (10) are arbitrary here. We note that the coefficient N does not enter the wave function $\Psi_{m,q}(h,T,\phi)$, which determines the probability amplitude of the given configuration $\{h,T,\phi;m,q\}$, that is, points $\{h,T,\phi\}$ in the configuration space for the given observables m,q. The mass and charge spectra in this approach are continuous. We note that formal quantization in the R-region with a spacelike evolutionary coordinate gives an analogous wave function.

References

1. Dirac P.: 1979, Lectures on quantum mechanics, in Principles of quantum mechanics, (Nauka, Moscow).
2. Sundermeyer K.: 1982, *Lec. Not. Phys.*, **V.169**.
3. Nesterenko V.V, Chervyakov A.M.: 1986, Singular Lagrangians, (JINR, Dubna), 102 p.
4. Gitman D., Tyutin I.: 1986, Canonical quantization of fields with constraints, (Nauka, Moscow), 216.
5. Kuchar K.: 1994, *Phys. Rev.*, **D50**, 3961.
6. Louko J. et. al.: 1996, *Phys. Rev.*, **D 54**, 2647.
7. Kodama H.: 1980, *Prog. Theor. Phys.*, **63**, 1217.
8. Nakamura K. et. al.: 1993, *Prog. Theor. Phys.*, **90**, 861.
9. Gladush V.: 2016, *Visn. Dnipr. univ.*, **24**, 31.
10. Frolov V.P., Novikov I.D.: 1998, Black Hole Physics. Netherlands: Kluwer Academic, 770 p.
11. Cahill M.E. et. al.: 1970, *J. Math. Phys.*, **11**, 1382.
12. Berezin B.A. et. al.: 1987, *JETP*, **93**, 1159.
13. Gladush V.D.: 2012, *STFI*, **1**, 48.
14. Gowdy R.: 1970, *Phys. Rev. D.*, **2**, 2774.

DOI: http://dx.doi.org/10.18524/1810-4215.2017.30.114223

QUANTIZATION OF THE SPHERICALLY SYMMETRIC CONFIGURATION OF THE GRAVITATIONAL AND ELECTROMAGNETIC FIELDS

M.G. Holovko, V.D. Gladush

Dnipro National University, Gagarin Ave, 725014, Ukraine,
dilmendar@gmail.com, vgladush@gmail.com

ABSTRACT. To construct a quantum model of a charged black hole (CBH), we introduce a modified description of the configuration of the electromagnetic and gravitational fields in a spherically symmetric space-time, which consists of T- and R- regions. We choose such coordinate system that the desired metric functions depend only on the time coordinate in the T-region, and on the space coordinate in the R-region. Then, the initial action for the configuration decays into terms which describe the fields in the T- and R-regions with the time and the space evolutionary coordinate respectively. We define new coordinates in the R- and T- regions, what allows us to unify the form of the Lagrangians, in each of them and carry out their uniform analysis. Then we construct the canonical formalism for obtained degenerate system according to the method of D.M.Gitman and I.V.Tyutin. It appears that system contains non-physical degrees of freedom. For their expicit separation we carry out the canonical transformation to new canonical variables. In these variables the constraints are reduced to the canonical form and physical part of the Hamilton function of the system is identically equal to zero. This leads to the fact that the desired wave function is determined only by the eigenvalue equations for the operators of observable physical quantities. According that considered system has only two observables – charge and mass of black hole – for further construction of quantum model of this system we introduce its mass and charge functions and find their expression in the new canonical variables. The solution of eigenvalue equations for corresponding operators leads to continuous spectra of charge and mass in considered model of CBH.

Keywords: black holes, mass function, charge function, Hamiltonian constraint, quantization, mass and charge operators.

1. Introduction

Spherically symmetric configurations of gravitational and other fields are the simplest models for testing the basic ideas and consequences of quantum gravity. They represent a convenient ground for studying some of the problems that arise at strict consideration of more complete theory. One of the main features of general-relativistic configurations is their degeneracy. The general formalism of the canonical approach to degenerate systems was constructed by Dirac (1979), which was developed in further works (see, for example, Sundermeyer, 1982; Nesterenko, 1986; Gitman, 1986; etc.). The problems of the classical and quantum description of spherically symmetric configurations of the gravitational and electromagnetic fields in the framework of the canonical approach were considered in many papers. A general, geometrodynamic approach to a spherically symmetric gravitational field was developed by Kuchar K. (1996), which was then generalized to the case of a spherically symmetric electromagnetic and gravitational configuration (Louko, 1996; Vaz, 2000). The proposed model is based on the observation that classical spherically symmetric configurations of electromagnetic and gravitational fields are stationary from the point of view of an external observer and have certain regions of space-time with dynamic behavior (T-regions). This means that these regions do not allow the time-like Killing vector, which implies in them the evolution of the space-time geometry in time. This evolution of space-time geometry is responsible for the quantum-mechanical properties of the model of a BH. Such models, with a fixed evolutionary time coordinate and a spacelike Killing vector, were considered in several works (Nakamura, 1993; Gladush, 2016; Holovko, 2017). In this paper constructed a quantum model of a charged black hole according to the method of D.M.Gitman and I.V.Tyutin (1986).

2. Classic description of CBH

The action for the gravitational and electromagnetic fields in space-time $V^{(4)}$ has the form

$$S_{tot} = -\frac{1}{16\pi}\int_{V^{(4)}}\left(\frac{c^3}{\kappa}R^{(4)} + \frac{1}{c}F_{\mu\nu}F^{\mu\nu}\right)\sqrt{-g^{(4)}}d^4x. \tag{1}$$

For a spherically symmetric configuration, the electromagnetic field tensor and the interval have the forms

$$F_{\mu\nu} = A_{\nu,\mu} - A_{\mu,\nu} \to F_{ab} = A_{b,a} - A_{a,b}, \tag{2}$$

$$ds^2 = h\left(x^0, r\right)\left(dx^0\right)^2 + g\left(x^0, r\right)dr^2 + R^2\left(x^0, r\right)d\sigma^2, \tag{3}$$

where $d\sigma^2 = d\theta^2 + \sin\theta d\alpha^2$ is the angular part of the metric; a, b = 0, 1. After integrating over the angles and discarding the surface term, the action (1) can be reduced to the form

$$\begin{aligned} S &= \int_{V^2}\left(\frac{c^3}{2\kappa}\sqrt{gh}\left[1 + \frac{RR_{,1}}{g}\left(\ln Rh\right)_{,1} - \right.\right. \\ &- \left.\left.\frac{RR_{,0}}{h}\left(\ln(gR)\right)_{,0}\right] + \frac{1}{2c}\frac{\left(A_{1,0} - A_{0,1}\right)^2 R^2}{\sqrt{gh}}\right)dx^2. \end{aligned} \tag{4}$$

Here $X_{,0} \equiv \partial X/\partial x^0$, $X_{,1} \equiv \partial X/\partial r$ denote the derivatives with respect to x^0 and x^1. Information on the structure of space is contained in the quantity $(\nabla R)^2 = g^{ab}R_{,a}R_{,b}$ The surface $R\left(x^0, r\right) = R_g = const$ for which $(\nabla R)^2 = 0$ divides V^4 into one T- and two R-regions. Moreover, $(\nabla R)^2 > 0$ in the T-region, and $(\nabla R)^2 < 0$ in the R-region. Using the generalized Birkhoff theorem, we can choose a coordinate system in the R-region in which h, g and R depend only on the spacelike coordinate r. Similarly, in the T-region there exists a coordinate system in which h, g and R depend only on the timelike coordinate x^0. Then the metrics in the R- and T-regions take the form:

$$ds_R^2 = h\left(r\right)\left(dx^0\right)^2 + g\left(r\right)dr^2 + R^2\left(r\right)d\sigma^2, \tag{5}$$

$$ds_T^2 = h\left(x^0\right)\left(dx^0\right)^2 + g\left(x^0\right)dr^2 + R^2\left(x^0\right)d\sigma^2. \tag{6}$$

In this case, the action (4) is divided in the sum $S = S_R + S_T$, where S_R and S_T are the actions defined in the R and T regions respectively. The Lagrangians corresponding to them have the form

$$L_R = \frac{\lambda_T}{2c}\frac{A_{0,1}^2R^2}{\sqrt{gh}} + \frac{\lambda_T c^3}{\kappa}\sqrt{gh}\left[1 + \frac{RR_{,1}}{g}\left(\ln Rh\right)_{,1}\right], \tag{7}$$

$$L_T = \frac{\lambda_R}{2c}\frac{A_{1,0}^2R^2}{\sqrt{gh}} + \frac{\lambda_R c^3}{\kappa}\sqrt{gh}\left[1 - \frac{RR_{,0}}{h}\left(\ln Rg\right)_{,0}\right]. \tag{8}$$

Here λ_T and λ_R – constants, obtained by integration of te action over coordinate x^0 in R-region and coordinate r in T-region. Since the Lagrangian is defined up to a constant factor, we further assume that $\lambda_R = \lambda_T = 1$ (meter).

It is convenient to introduce new variables in the R- and T- regions:

$$\begin{aligned} F_R &= -A_0, \qquad U_R = Rh, \qquad N_R = \sqrt{gh}\,, \\ F_T &= A_1, \qquad U_T = -Rg, \qquad N_T = \sqrt{gh}\,. \end{aligned} \tag{9}$$

In these variables, the Lagrangians (7) and (8) take a uniform form:

$$L = \frac{F_{,\alpha}^2R^2}{2cN} + sN\left(1 + \frac{R_{,\alpha}U_\alpha}{N^2}\right). \tag{10}$$

where $s = c^3/\kappa$, α – is the evolutionary parameter, which in each of the regions takes the form $\alpha = x^0 = ct$ or $\alpha = r$ respectively. For the considered configuration (10), the Hessian is zero. Therefore, the system is degenerate and the construction of the canonical theory is specific. In order to construct the canonical formalism for the considered dynamical system, we use the method of D.M.Gitman and I.V.Tyutin. We introduce an extended system of Lagrange equations for the system:

$$\dot{Q}^i = V^i, \qquad M_{ij}\dot{V}^j = K_i, \qquad P_i = \frac{\partial L}{\partial V^i}, \tag{11}$$

Here Q^i, V^i, P_i are the sets of generalized coordinates (F, R, U, N), velocities (V_F, V_R, V_U, V_N) and momenta (P_F, P_R, P_U, P_N),

$$M_{ij} = \frac{\partial^2 L}{\partial V^i \partial V^j}, \tag{12}$$

– the Hessian matrix of the system, and the quantities K_i are defined as follows:

$$K_i = \frac{\partial L}{\partial Q^i} - \frac{\partial^2 L}{\partial V^i \partial Q^j}V^j. \tag{13}$$

The Hamiltonian function for the extended Hamiltonian system is introduced as follows:

$$H = P_iV^i - L^V. \tag{14}$$

From equations $P_i = \partial L/\partial V^i$ we obtain expressions for the velocities V_F, V_R, V_U, and also the primary constraint $P_N = 0$. Demanding its preservation during the evolution of the system, we get a secondary constraint:

$$0 = \{P_N, H\} = -\frac{1}{s}\left(P_UP_R - s^2\right) - \frac{c}{2R^2}P_F^2. \tag{15}$$

The obtained constraint remains identically, and therefore no new constraints arise. The Poisson brackets of the found constraints are also equal to zero, so both of them are first-type constraints. This means that the Hamilton function contains non-physical degrees of freedom. For their explicit separation, we can make a canonical transformation to new canonical variables

$\left(q^i, p_i\right)$ with the following generating function of the second type:

$$G_2\left(\alpha, Q^i, p_i\right) = Fp_1 + \left(R - \tfrac{p_2}{s}\right)p_3 + \\ +2\sqrt{s^2RU + \tfrac{csU}{2R} - sUp_2} + Np_4. \quad (16)$$

Herefrom for the new canonical variables we obtain:

$$q^1 = F + \tfrac{sc}{R}\tfrac{P_F}{P_U}, \qquad q^2 = -\left(\tfrac{P_R}{s} + \tfrac{c}{R^2}\tfrac{P_F^2}{P_U}\right), \quad (17)$$
$$q^3 = \tfrac{UP_U^2}{s^2} - \tfrac{cP_F^2}{2sR}, \qquad q^4 = N;$$
$$p_1 = P_F, \qquad p_2 = s\left(R - \tfrac{UP_U^2}{s^2}\right),$$
$$p_3 = P_R - \tfrac{s^2}{P_U} + \tfrac{cs}{R^2}\tfrac{P_F^2}{P_U}, \qquad p_4 = P_N.$$

Old canonical variables are expressed in terms of new variables as follows:

$$F = q^1 + p_1\tfrac{p_3+sq^2}{p_2+sq^3}, \qquad R = q^3 + \tfrac{p_2}{s} \quad (18)$$
$$U = \left(\tfrac{p_3+sq^2}{s}\right)^2\left(q^3 + \tfrac{cp_1^2}{2(p_2+sq^3)}\right), \qquad N = q^4;$$
$$P_F = p_1, \qquad P_R = s\left(\tfrac{cp_1^2\left(p_3+sq^2\right)}{2(p_2+sq^3)^2} - q^2\right),$$
$$P_U = -\tfrac{s^2}{p_3+sq^2}, \qquad P_N = p_4.$$

In the new variables, the Hamilton function and the constraints take the form:

$$H = p_4V_N - \frac{sq^4p_3}{p_3+sq^2}, \quad (19)$$

$$p_3 = 0, \qquad p_4 = 0. \quad (20)$$

From the fact that in new variables the constraints have the canonical form, it means that the physical degrees of freedom are contained in the pairs of quantities $\left(q^1, p_1\right)$ and $\left(q^2, p_2\right)$.

3. Quantum description of CBH

Assuming for the Hamiltonian (19) that the constraints (20) are equal to zero, we find that the physical part of the Hamiltonian function is identically equal to zero. Therefore, for a quantum description of the system, its wave function is determined only by the eigenvalue equations for the operators of the observed physical quantities. For the considered system there are only two quantities: the mass and charge of the black hole. In the classical case, the charge is determined by the charge function as follows:

$$Z = \frac{R^2}{\sqrt{gh}}\left(A_{0,1} - A_{1,0}\right). \quad (21)$$

The total mass of the configuration has the form

$$M = \frac{s}{c}R\left(1 + \frac{R_{,0}^2}{h} - \frac{R_{,1}^2}{g}\right) + \frac{Z^2}{2c^2R}. \quad (22)$$

It has the meaning of the total field mass of a spherical region of radius R of the configuration in question, taking into account the contribution of the electromagnetic field. When changing to new coordinates in the R- and T-regions, and then transit to new canonical variables, we find:

$$M = \frac{p_1}{c}, \qquad Z = cp_2. \quad (23)$$

Then the corresponding operators of mass and charge will have the form:

$$\hat{M} = -\frac{i\hbar}{c}\frac{\partial}{\partial q^1}, \qquad \hat{Z} = -i\hbar c\frac{\partial}{\partial q^2}. \quad (24)$$

For the wave function of the configuration, it is necessary to solve the system of equations:

$$\begin{cases} i\hbar\frac{\partial\Psi}{\partial\alpha} = \hat{H}\Psi, \\ \hat{M}\Psi = m\Psi, \\ \hat{Z}\Psi = z\Psi. \end{cases} \quad (25)$$

Taking into account that the physical degrees of freedom are only described by pairs of canonical variables (q^1, p_1) and (q^2, p_2), we get:

$$\Psi = \Psi\left(q^1, q^2\right) = C\exp\frac{i}{\hbar}\left[mcq^2 + \frac{sq^1}{c}\right]. \quad (26)$$

Since this system has a solution for any values of m and z, the mass and the charge spectra of BH are continuous.

4. Conclusion

In the previous work of one of the authors (Gladush V., see the article in this collection), there was carried out a direct quantization of the constraints for the considered system. In this paper, according to the method of Gitman and Tyutin, quantization of considered system was carried out after separation of physical and non-physical degrees of freedom by suitable canonical transformation. This approach is consistent with the results of the geometrodynamic approach (Louko, 1996; Vaz., 2000). In the case of non-charged BH (z = 0), the result obtained is analogous to the result for the Schwarzschild black hole of the general geometrodynamic approach (Kuchar, 1996).

References

Dirac P.: 1979, Lectures on quantum mechanics, in Principles of quantum mechanics, (Nauka, Moscow).

Sundermeyer K.: 1982, *Lec. Not. Phys.*, **V.169**.

Nesterenko V.V, Chervyakov A.M.: 1986, Singular Lagrangians, in Classical dynamics and quantization, (JINR, Dubna), 102.

Gitman D., Tyutin I.: 1986, Canonical quantization of fields with constraints, (Nauka, Moscow), 216.
Kuchar K.: 1994, *Phys. Rev.*, **D50**, 3961.
Louko J., Winters-Hilt S.: 1996, *Phys. Rev. D*, **54**, 2647.
Vaz C., Witten L.: 2000, *Phys. Rev. D*, **63**, 24.
Nakamura K., Konno S., Oshiro Y.: 1993, *Prog. Theor. Phys.*, **90**, 861.
Gladush V.: 2016, *Visn. Dnipr. univ.*, **24**, 31.
Holovko M., Gladush. V.: 2017, Quantization of spherically symmetric gravitational field. International Conference "Astronomy and Space Physics", Kiev, 2017, 31.

DOI: http://dx.doi.org/10.18524/1810-4215.2017.30.115466

HIGH-ENERGY DIFFRACTION AND DUALITY RELATIONS

László Jenkovszky[1], István Szanyi[2]

[1] Bogolyubov Institute for Theoretical Physics, Nat. Ac. Sc. of Ukraine, Kiev, *jenk@bitp.kiev.ua*

[2] Uzhgorod National University, Uzhgorod, *sz.istvan03@gmail.com*

ABSTRACT. Relations between elastic and inelastic diffraction due to Regge factorisation and pomeron dominance are discussed in the light of the new phenomena discovered at the LHC in nearly forward scattering.

1. Introduction

At the LHC, in the nearly forward direction for the first time one can see the isolated pomeron, uncontaminated by secondary (non-leading) reggeon contributions. Elastic proton-proton scattering, single and double proton diffraction dissociation are related by factorization, as shown in Fig. 1. The input pomeron is a double pole in the j plane, lying on a non-linear trajectory. Deviation from the exponential diffraction cone are studied in details.

2. Elastic scattering

The scattering amplitude is a sum of four terms, two asymptotic (pomeron (P) and odderon (O)) and two non-asymptotic ones (secondary Regge pole contributions). P and f have positive C-parity, thus entering in the scattering amplitude with the same sign in pp and $\bar{p}p$ scattering, while the odderon and ω have negative C-parity, thus entering pp and $\bar{p}p$ scattering with opposite signs, as shown below:

$$A\left(s,t\right)_{pp}^{\bar{p}p} = A_P\left(s,t\right) + A_f\left(s,t\right) \pm \left[A_\omega\left(s,t\right) + A_O\left(s,t\right)\right], \tag{1}$$

where the symbols P, f, O, ω stand for the relevant Regge-pole amplitudes and the super(sub)script, evidently, indicate $\bar{p}p(pp)$ scattering with the relevant choice of the signs in the sum (1). This sum can be extended by adding more reggeons, whose role may become increasingly important towards lower energies; their contribution can be effectively absorbed by f and ω.

We treat the odderon, C-odd counterpart of the pomeron on equal footing, differing by its $C-$ parity and the values of its parameters (to be fitted to the data).

The main subject of our study is the pomeron, and it is a double pole, or DP [1, 2] lying on a non-linear trajectory, whose intercept is slightly above one. This choice is motivated by unique properties of the DP: it produces logarithmically rising total cross sections at unit pomeron intercept. The DP satisfies unitarity by reproducing itself (scaling) under s-channel unitarization. By letting $\alpha_P\left(0\right) > 1$, we allow for a faster rise of the total cross section[1], although the intercept is about half that of the DL model [3] since the double pole (or dipole) itself drives the rise in energy. Due to its geometric form (see below) the DP reproduces itself against unitarity (eikonal) corrections. As a consequence, these corrections are small, and one can use the model at the "Born level" without complicated (and ambiguous) unitarity (rescattering) corrections. DP combines the properties of Regge poles and of the geometric approach.

Regge trajectories are non-linear complex functions. In a limited range and with limited precision, they can be approximated by linear trajectories (which is a common practice, reasonable when non-linear effects can be neglected). This non-linearity is manifest e.g. as the "break" i.e. a change of the slope $\Delta B \approx 2$ GeV^{-2} around $t \approx -0.1$ GeV^2 and at large $|t|$, beyond the second maximum, $|t| > 2$ GeV^2, where the cross section flattens and the trajectories are expected to slow down logarithmically.

A simple mechanism of the diffractive dip-bump structure combining geometrical features and Regge behaviour was suggested in [2]. In that model, the dip is generated by the pomeron contribution. The relevant pomeron is a double pole arises from the interference between this dipole with a simple one, it is accompanied by. The dip-bump in the model shows correct dynamics, that is it develops from a shoulder, progressively deepening in the ISR energy region. As energy increases further, the dip is filled by the odderon contribution. At low energies the contribution from

[1] A supercritical pomeron trajectory, $\alpha_P(0) > 1$ in the DP is required by the observed rise of the ratio σ_{el}/σ_{tot}, or, equivalently, departure from geometrical scaling.

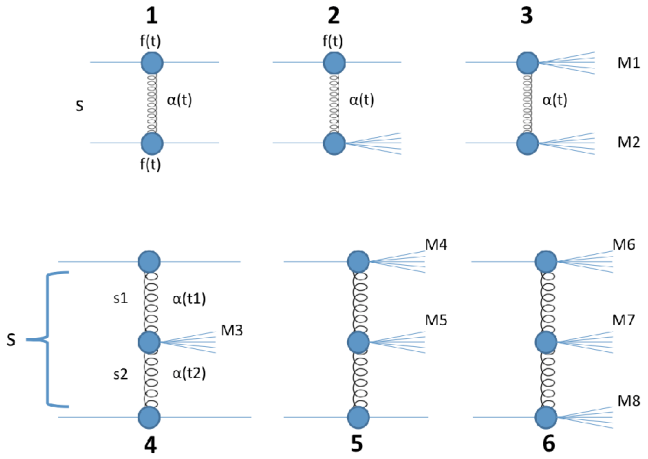

Figure 1: Diagrams for elastic scattering and diffraction dissociation (single, double and central).

non-leading, "secondary" reggeons is also present.

The dipole pomeron produces logarithmically rising total cross sections and nearly constant ratio of σ_{el}/σ_{tot} at unit pomeron intercept, $\alpha_P(0) = 1$. While a mild, logarithmic increase of σ_{tot} does not contradict the data, the rise of the ratio σ_{el}/σ_{tot} beyond the SPS energies requires a supercritical DP intercept, $\alpha_P(0) = 1 + \delta$, where δ is a small parameter $\alpha_P(0) \approx 0.05$. Thus DP is about "twice softer" then that of Donnachie-Landshoff's model [3], in which $\alpha_P(0) \approx 0.08$.

We use the normalization where

$$\frac{d\sigma}{dt} = \frac{\pi}{s^2}|A(s,t)|^2 \quad \text{and} \quad \sigma_{tot} = \frac{4\pi}{s}\Im m A(s,t)\Big|_{t=0}. \quad (2)$$

Neglecting spin dependence, the invariant proton(antiproton)-proton elastic scattering amplitude is that of Eq. (1). The secondary reggeons are parametrized in a standard way, with linear Regge trajectories and exponential residua, where R denotes f or ω - the principal non-leading contributions to pp or $\bar{p}p$ scattering:

$$A_R(s,t) = a_R e^{-i\pi\alpha_R(t)/2} e^{b_R t}\Big(s/s_0\Big)^{\alpha_R(t)}, \quad (3)$$

with $\alpha_f(t) = 0.70 + 0.84t$ and $\alpha_\omega(t) = 0.43 + 0.93t$.

The pomeron is a dipole in the $j-$plane

$$A_P(s,t) = \frac{d}{d\alpha_P}\Big[e^{-i\pi\alpha_P/2}G(\alpha_P)\Big(s/s_0\Big)^{\alpha_P}\Big] = \quad (4)$$

$$e^{-i\pi\alpha_P(t)/2}\Big(s/s_0\Big)^{\alpha_P(t)}\Big[G'(\alpha_P) + \Big(L - i\pi/2\Big)G(\alpha_P)\Big].$$

Since the first term in squared brackets determines the shape of the cone, one fixes

$$G'(\alpha_P) = -a_P e^{b_P[\alpha_P - 1]}, \quad (5)$$

where $G(\alpha_P)$ is recovered by integration, and, as a consequence, the pomeron amplitude Eq. (4) can be rewritten in the following "geometrical" form

$$A_P(s,t) = i\frac{a_P\ s}{b_P\ s_0}[r_1^2(s)e^{r_1^2(s)[\alpha_P-1]} - \varepsilon_P r_2^2(s)e^{r_2^2(s)[\alpha_P-1]}], \quad (6)$$

where $r_1^2(s) = b_P + L - i\pi/2$, $r_2^2(s) = L - i\pi/2$, $L \equiv \ln(s/s_0)$.

The main features of the nonlinear trajectories are: 1) presence of a threshold singularity required by $t-$channel unitarity and responsible for the change of the slope in the exponential cone (the so-called "break") near $t = -0.1$ GeV^2 [4], and 2) logarithmic asymptotic behaviour providing for a power fall-off of the cross sections in the "hard" region. The combination of theses properties, however is not unique.

2.1. Diffraction minimum (dip-bump)

Fig. 2 (a) shows the pp and $\bar{p}p$ total elastic scattering cross section calculated from the model (values of parameters see in [5]). Figure 2 (b) shows the ratio of the real to imaginary part of the forward amplitude. The model with a linear trajectory describes reasonably the data a wide range of collision energies for pp and $\bar{p}p$. Figures 3 (a,b,c) show the fitted $\bar{p}p$ and pp differential cross sections and predictions for three different center of mass energies are shown. The yellow area exhibits the statistical uncertainty on the calculations, described earlier. Calculations are characterized by an approximately exponential fall-off in the range $0 < |t| < 8$ GeV^2, with the slope changing around $-t \approx 0.6$ GeV^2. The dip moved towards lower momentum transfer and became almost filled by the odderon.

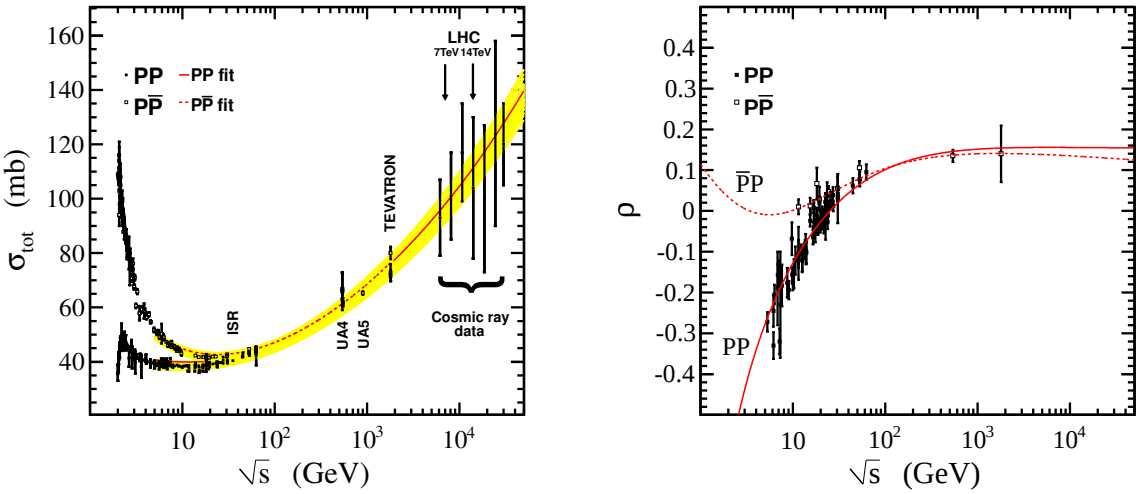

(a) (b)

Figure 2: (a) Total pp and $\bar{p}p$ cross sections calculated from the model, fitted to the data in the range $\sqrt{s} = 5$ — 30 TeV and 5 GeV — 1.8 TeV, respectively. (b) Ratio of the real to imaginary part of the forward amplitude for pp and $\bar{p}p$, calculated from the model and fitted to the data.

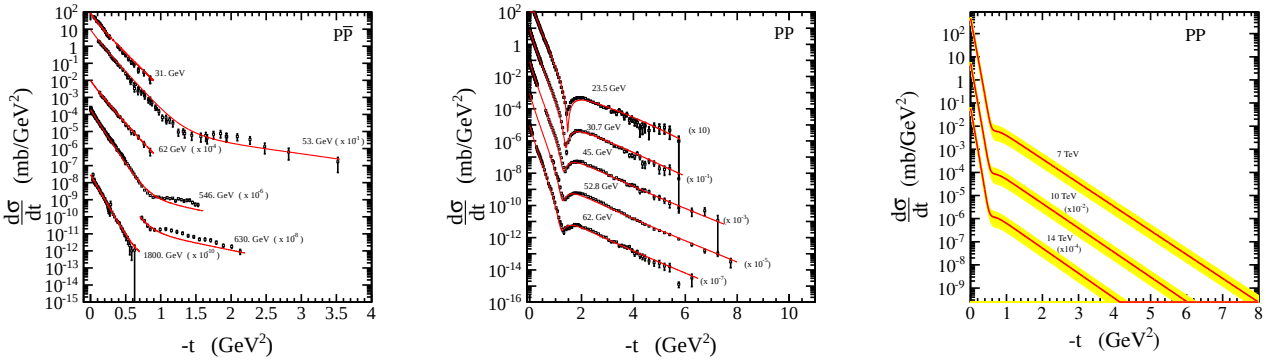

(a) (b) (c)

Figure 3: (a) $\bar{p}p$ differential cross sections calculated from the model, fitted to the data in the range $-t = 0.1$ — 8 GeV^2. (b) pp differential cross sections calculated from model fitted to the data. (c) predictions for the pp differential cross section calculated from the model for three different LHC energies.

2.2. Low-$|t|$ "break" and proton shape

The diffraction cone of high-energy elastic hadron scattering deviates from a purely exponential dependence on t due to two structures clearly visible in proton-proton scattering: the so-called "break" (in fact, a smooth curve with a concave curvature) near $t = -0.1$ GeV^2, whose position is nearly independent of energy and the prominent "dip" – diffraction minimum, moving slowly (logarithmically) with s towards smaller values of $|t|$, where s and t are the Mandelstam variables. The physics of these two phenomena are quite different. As illustrated in Fig. 4, the "break" is likely a reflection due to the "pion cloud", which controls the "static size" of nucleon. This effect, first observed in 1972 at the ISR, was interpreted [4, 6, 7] as the manifestation of t-channel unitarity, generating a two-pion loop in the cross channel, Fig. 5, and was referred to by Bronzan [8] as the "fine structure" of the pomeron. The dip (diffraction minimum), on the other hand, is generally accepted as a consequence of s-channel unitarity or absorption corrections to the scattering amplitude. As such, dip location reflects the "size" of proton, moving towards smaller $|t|$ values as the total cross section increases with energy.

The departure from the linear exponential behavior was confirmed by recent measurements by the TOTEM Collaboration at the CERN LHC, first at 8 TeV (with a significance greater then 7σ) [9] and subsequently at 13 TeV [10]. At the ISR the "break" was illustrated by plotting the local slope $B(t)$ for several t-bins at fixed values of s.

At the LHC the effect appears of the same order of magnitude and is located near the same value of t. Different from the ISR [11], TOTEM quantifies the deviation from the exponential by normalizing the measured cross section to a linear exponential form, (see Eq. (9) below). For the sake of completeness we will exhibit this "break effect" both in the normalized form and for $B(t)$.

The new LHC data from TOTEM at 8 TeV confirm the conclusions [4, 6, 7] about the nature of the break and call for a more detailed analysis and better understanding of this phenomenon. The new data triggered intense theoretical work in this direction [14, 13, 12], but many issues still remain open. Although the curvature for $B(t)$, both at the ISR and the LHC is concave, a convex behavior cannot be excluded in other reactions and/or new energies. While the departure from a linear exponential was studied in details both at the ISR and LHC energies, an interpolation between the two is desirable to clarify the uniqueness of the phenomenon. This is a challenge for the theory, and it can be done within Regge-pole models. Below we do so by adopting a simple Regge-pole model, with a pomeron and two secondary reggeons, f and ω exchanges. The odderon may also be present. However its contribution at low $|t|$ is too small to be identified unambiguously.

Having identified [4, 6, 7] the observed "break" with a two-pion exchange effect, we investigate further two aspects of the phenomenon, namely: 1) to what extent is the "break" observed recently at the LHC a "recurrence" of that seen at the ISR (universality)? 2) what is the relative weight of the Regge residue (vertex) compared to the trajectory (propagator) in producing the "break"? We answer these questions by means of a detailed fit to the elastic proton-proton scattering data in the relevant kinematic range $0.05 < -t < 0.35$ GeV^2 ranging between the ISR energies ($23.5 \leq \sqrt{s} \leq 62.5$ GeV), and those available at the LHC.

As shown by Barut and Zwanziger [15], t-channel unitarity constrains the Regge trajectories near the threshold, $t \to t_0$ by

$$\Im\, \alpha(t) \sim (t - t_0)^{\Re\, \alpha(t_0)+1/2}, \tag{7}$$

where t_0 is the lightest threshold, $4m_\pi^2$ in the case of the vacuum quantum numbers (pomeron or f meson). Since the asymptotic behavior of the trajectories is constrained by dual models with Mandelstam analyticity by square-root (modulus $\ln t$): $\mid \frac{\alpha(t)}{\sqrt{t \ln t}} \mid_{t\to\infty} \leq$ const, (see [4] and references therein), for practical reasons it is convenient to approximate, for the region of t in question, the trajectory as a sum of square roots. Higher thresholds, indispensable in the trajectory, may be approximated by their power expansion, *i.e.* by a linear term, matching the threshold behavior with the asymptotic.

At the ISR, the proton-proton differential cross section was measured at $\sqrt{s} = 23.5, 30.7, 44.7, 52.8$ and 62.5 GeV [16]. In all the above energies the differential cross section changes its slope near $-t = 0.1$ GeV^2. By using a simple Regge-pole model we have mapped the "break" fitted at the ISR onto the LHC TOTEM 8 TeV data. The simple Regge-pole model is constructed by a leading supercritical pomeron and two secondary, f and ω contributions.

The detailed results of fits and the parameters see in [17]. To demonstrate the important features more clearly, we show the results of the mapping in higher resolution in Fig. 6 and Fig. 7. In Fig. 6, we exhibit the shape of local slopes, defined by

$$B(s,t) = \frac{d}{dt} \ln(d\sigma/dt)\,, \tag{8}$$

at six s values. To better demonstrate the quality of our fit and to anticipate the comparison with the LHC data, we also present in Fig. 7 the ISR data in normalized form as used by TOTEM [9]:

$$R = \frac{d\sigma/dt}{d\sigma/dt_{ref}} - 1, \tag{9}$$

where $d\sigma/dt_{ref} = Ae^{Bt}$, with A and B constants determined from a fit to the experimental data.

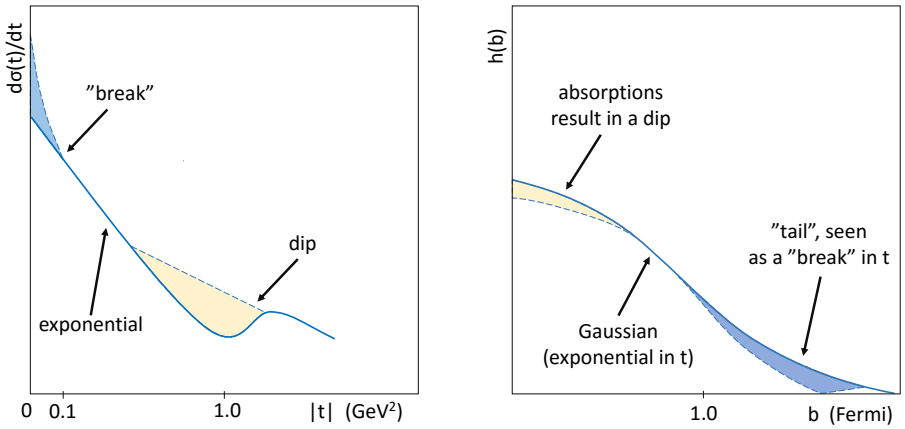

(a) (b)

Figure 4: The "break" followed by a single diffraction minimum ("dip") and maximum, shown both as function in t and its Fourier transform (impact parameter representation), in b.

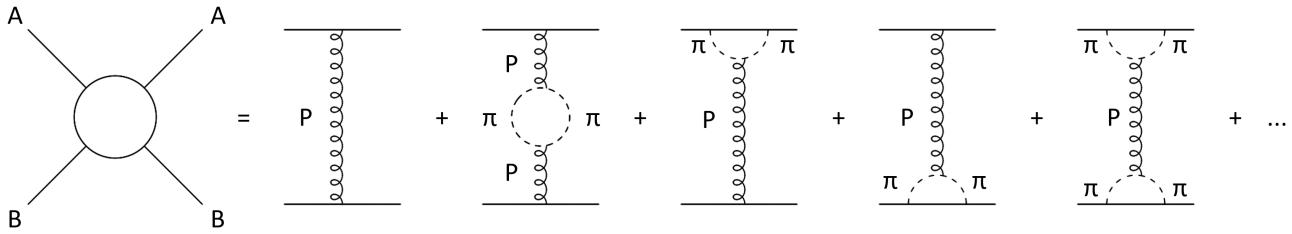

Figure 5: Diagram for elastic scattering with t-channel exchange containing a branch point at $t = 4m_\pi^2$.

Both Fig. 6 and Fig. 7 re-confirm the earlier finding that the "break" can be attributed the presence of two-pion branch cuts in the Regge parametrization. The effect of pion cloud manifest itself most importantly through the Regge residue, rather then the pomeron trajectory.

3. Diffraction dissociation, single (SD) and double (DD)

In most of the papers SD is calculated from the triple Regge limit of an inclusive reaction, as shown in Fig. 8.

In that limit, the double diffraction cross section can be written as

$$\frac{d^2\sigma}{dtdM_x^2} = \frac{G_{13,2}^{PP,P(t)}}{16\pi^2 s_0^2}\left(\frac{s}{s_0}\right)^{2\alpha_P(t)-2}\left(\frac{M^2}{s_0}\right)^{\alpha_P(0)-\alpha_P(t)}.$$

This approach has two shortcomings. The first one is that it leaves outside the small-M^2 resonance region. The second one is connected with the fact that whatever the pomeron, the (partial) SD cross section overshoots the total one, thus obviously conflicting with unitarity. Various ways of resolving this deficiency are known from the literature, including the vanishing (decoupling) of the triple pomeron coupling, but none of them can be considered completely satisfactory.

We instead follow the idea [18] according to which the reggeon (here, the pomeron) is similar to the photon and that the reggeon-nucleon interaction is similar to deep-inelastic photon-nucleon scattering (DIS), with the replacement $-Q^2 = q^2 \to t$ and $s = W^2 \to M_x^2$. There is an obvious difference between the two: while the C parity of the photon is negative, it is positive for the pomeron. We believe that while the dynamics is essentially invariant under the change of C, the difference between the two being accounted for by the proper choice of the parameters. Furthermore, while Jaroszewicz and Landshoff [14], in their pomeron-nucleon DIS structure function (SF) (or Pp total cross section) use the Regge asymptotic limit, we include also the low missing mass, resonance behaviour.

It is evident that Regge factorization is essential in both approaches (triple Regge and the present one). It is feasible when Regge singularities are isolated poles. While the pre-LHC data require the inclusion of secondary reggeons, at the LHC we are in the fortunate situation of a single pomeron exchange (pomeron dominance) in the t channel in single and double diffraction (not necessarily so in central diffraction, to be treated elsewhere). Secondary Regge pole exchanges will appear however, in our dual-Regge treatment of Pp scattering (see below), not to be confused with the the t channel of pp. This new situation makes diffraction

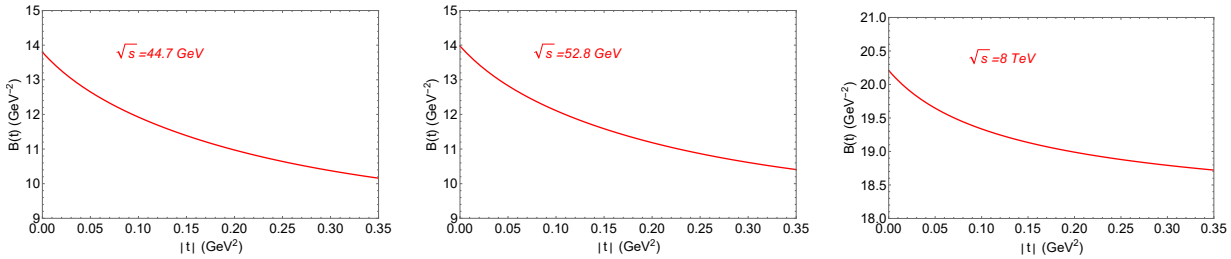

(a) 44.7 GeV (b) 52.8 GeV (c) 8 TeV

Figure 6: Local slopes.

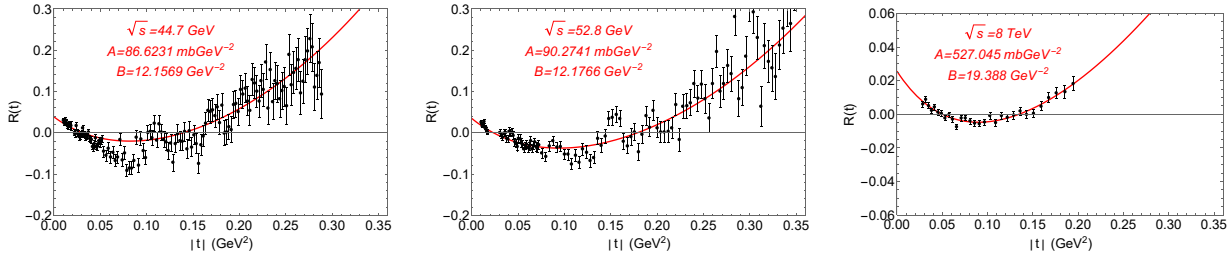

(a) 44.7 GeV (b) 52.8 GeV (c) 8 TeV

Figure 7: $R(t)$ ratios.

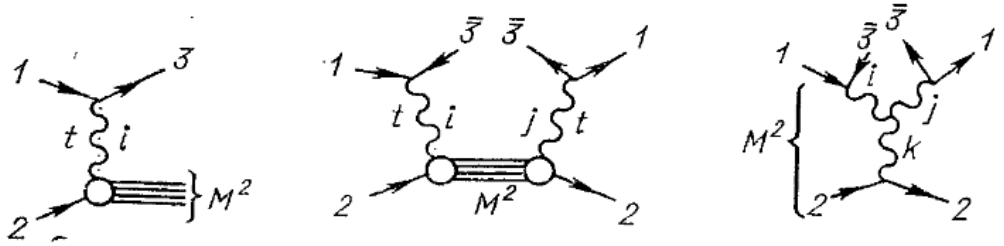

Figure 8: From SD to the triple Regge limit.

at the LHC unique in the sense that for the first time Regge-factorization is directly applicable. We make full use of it.

Diffraction is limited both in the missing mass (coherence), $\xi \lesssim 0.05$ and in t ("soft" collisions). There is a transition region in t from "soft" to "hard" collisions, with a possible dip-bump structure between the two. To be sure, in our analysis we leave outside these interesting but controversial points, concentrating on the "first" cone with clear exponential behaviour.

With the advent of the LHC, diffraction, elastic and inelastic scattering entered a new area, where it can be seen uncontaminated by non-diffraction events. In terms of the Regge-pole theory this means, that the scattering amplitude is completely determined by a pomeron exchange, and in a simple-pole approximation, Regge factorization holds and it is of practical use!

3.1. A compilation of basic formulae

This subsection contains a compilation of the main formulae used in the calculations and fits to the data.

The single diffraction (SD) dissociation cross section is:

$$2 \cdot \frac{d^2\sigma_{SD}}{dtdM_x^2} = {F_p}^2(t) {F_{inel}}^2(t, M_x^2) \left(\frac{s}{M_x^2}\right)^{2(\alpha(t)-1)}. \tag{10}$$

Double diffraction (DD) dissociation cross section:

$$\frac{d^3\sigma_{DD}}{dtdM_1^2 dM_2^2} = N_{DD} {F_{inel}}^2(t, M_1^2) {F_{inel}}^2(t, M_2^2) \times \left(\frac{ss_0}{M_1^2 M_2^2}\right)^{2(\alpha(t)-1)}. \tag{11}$$

with the norm $N_{DD} = \frac{1}{4A_{el}}$, and the inelastic vertex:

$${F_{inel}}^2(t, M_x^2) = A_{res} \frac{1}{M_x^4} \sigma_T^{Pp}(M_i^2, t) + C_{bg}\sigma_{Bg}, \tag{12}$$

where the pomeron-proton total cross section is the sum N^* resonances and the Roper resonance, with a relevant norm factor R (we remove the t dependent $f_{res}(t)$ out of the sum):

$$\sigma_T^{Pp}(M_x^2, t) = R \frac{[f_{res}(t)]^2 \cdot M_{Roper} \left(\frac{\Gamma_{Roper}}{2}\right)}{\left(M_x^2 - M_{Roper}^2\right)^2 + \left(\frac{\Gamma_{Roper}}{2}\right)^2} + \\ + [f_{res}(t)]^4 \sum_{n=1,3} \frac{\mathcal{I}m\, \alpha(M_x^2)}{(2n + 0.5 - \mathcal{R}e\, \alpha(M_x^2))^2 + (\mathcal{I}m\, \alpha(M_x^2))^2}, \tag{13}$$

and the background corresponding to non-resonance contributions:

$$\sigma_{Bg} = \frac{f_{bg}(t)}{\frac{1}{(M_x^2 - (m_p + m_\pi)^2)^\varsigma} + (M_x^2)^\eta}, \tag{14}$$

Integrated cross sections are calculated as:

$$\frac{d\sigma_{SD}}{dt} = \int_{M_1^2}^{M_2^2} \frac{d^2\sigma_{SD}}{dtdM_x^2} dM_x^2 \tag{15}$$

for SD and:

$$\frac{d\sigma_{DD}}{dt} = \int\int_{f(M_{x_1}^2, M_{x_2}^2)} \frac{d^3\sigma_{SD}}{dtdM_{x_1}^2 dM_{x_2}^2} dM_{x_1}^2 dM_{x_2}^2 \tag{16}$$

for DD.

We calculate also fully integrated cross sections:

$$\sigma_{SD} = \int_0^1 dt \int_{M_{th}^2}^{0.05s} dM_x^2 \frac{d^2\sigma_{SD}}{dtdM_x^2}, \tag{17}$$

$$\sigma_{DD} = \int_0^1 dt \int\int_{\Delta\eta > 3} dM_{x_1}^2 dM_{x_2}^2 \frac{d^3\sigma_{DD}}{dtdM_{x_1}^2 dM_{x_2}^2} \tag{18}$$

and

$$\frac{d^2\sigma_{DD}}{dM_{x_1}^2 dM_{x_2}^2} = \int_0^1 \frac{d^3\sigma_{DD}}{dtdM_{x_1}^2 dM_{x_2}^2} dt. \tag{19}$$

3.2. Fitting procedure

The model contains 12 parameters, a large part of which is fixed either by their standard values (e.g. those of Regge trajectories, except for the pomeron slope, whose slope exceeds the "standard" value to meet the SD data) or are set close to the previous fits [18].

The elastic data and Regge theory fix the parameters $s_0, \alpha(0)$, α', A_{el}, b_{el}.

The data at larger $|t|$, with the dip-bump structure and subsequent flattening of the cross section, both in elastic scattering and in SD may indicate the onset of new physics and the transition to hard scattering, implying a non-exponential residue and/or a non-linear pomeron trajectory, that goes beyond the present study.

Single diffraction dissociation (SD) is an important pillar in our fitting procedure. The following parameters were fitted to the SD data: A_{res}, C_{bg}, R, b_{res}, b_{bg}, ς, η. As input data we use double differential cross sections $\frac{d^2\sigma_{SD}}{dtdM^2}$ versus M_x^2 at $|t| = 0.05$ GeV^2; b)single differential cross sections $\frac{d\sigma_{SD}}{dt}$ vs. t; c) fully integrated cross sections versus energy $\sqrt{s}$.

Central exclusive diffraction (Diagram 6. in Fig. 1) was calculted recently in [19].

4. Conclusions

At the LHC, in the diffraction cone region ($t < 1$ GeV^2) proton-proton scattering is dominated (over 95%) by pomeron exchange (quantified in [5]). This enables full use of factorized Regge-pole models.

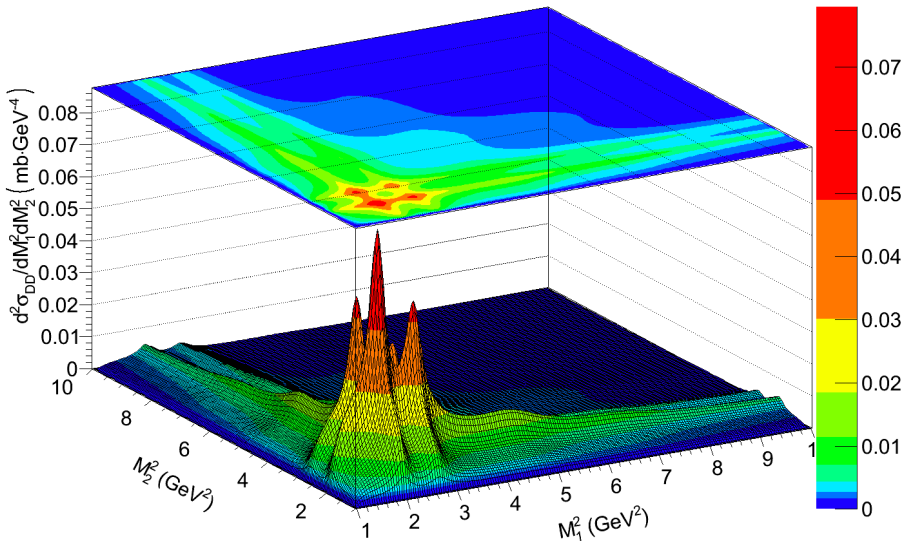

Figure 9: Double differential DD cross section as function of M_1^2 and M_2^2, integrated in t;, see Eq. (11).

Contributions from non-leading (secondary) trajectories can (and should be) included in the extension of the model to low energies, e.g. below those of the SPS.

Acknowledgements. L.J. thanks the organizers of the Gamov Conference for their hospitality. The work of I.Sz. was supported by HDFU (UMDSZ).

References

[1] R. Fiore *et al.* Int. J. Mod. Phys., A24, 2551-2559 (2009); arXiv:hep-ph/0812.0539.

[2] L.L. Jenkovszky and A.N. Vall, ITP Preprint, Kiev 1974; Czech. J. Phys. B, **26**, 447 (1976).

[3] S. Donnachie and P. Landshoff, Phys. Lett., **B 123**, 345 (1983); Nucl. Phys. **267**, 690 (1985).

[4] G. Cohen-Tannoudji *et al.*, Nuov. Cim., **5**, 957 (1972).

[5] L.L. Jenkovszky, A.I. Lengyel, D.I. Lontkovsky, Int. J. Mod. Phys. A, **26**, 4755 (2011); arXiv:1105.1202.

[6] C.-I Tan and D.M. Tow, Phys. Letters B. **53B**, 452 (1975).

[7] U. Sukhatme, Chung-I Tan, and Tran Thanh Van, Z. Phys. C, Particles and Fields, **1**, 95 (1979).

[8] J.B. Bronzan, *Fine structure of the Pomeron*, in Symposium on the Pomeron, ANL report, ANL/HEP 7327, p.34, (Argonne National Laboratory, 1973).

[9] TOTEM Collab. (G. Antchev *et al.*), Nucl. Phys., **B 899** 527 527 (2015); arXiv:1503.08111.

[10] M. Deile, *Elastic and Total Cross-Section Measurements by TOTEM*, Contribution at the 17. Conference on Elastic and Diffractive Scattering, (Prague, Czech Republic, 2017).

[11] B. Barbiellini *et. al.*, Phys. Lett. **B39**, 663 (1972).

[12] L. Jenkovszky, I. Szanyi, Phys. Part. Nuclei Lett., **14**, 687 (2017); arXiv:1701.01269.

[13] D.A. Fagundes, L. Jenkovszky, E.Q. Miranda, G. Pancheri, P.V.R.G. Silva, Int. J. Mod. Phys. A **31**, 1645022 (2016); arXiv:1509.02197.

[14] L. Jenkovszky and A. Lengyel, Acta Phys. Pol., **B 46**, 863 (2015); arXiv:1410.4106.

[15] A.O. Barut and D.E. Zwanziger, Phys. Rev. **127**, 974 (1962).

[16] http://durpdg.dur.ac.uk/review/pp2/exphtml/CERNISR.shtml

[17] L. Jenkovszky, I. Szanyi and C.-I Tan. *Shape of Proton and the Pion Cloud*, arXiv:1710.10527.

[18] R. Fiore *et al.* Phys. Rev. D **83**, 056014 (2011); arXiv:056014; R. Fiore *et al.*, Yad. Fizika, **77** 1535 (2014); arXiv:1011.0664.

[19] R. Fiore, L. Jenkovszky and R. Schicker, EPJ C **76(1)** 1-10 (2016); arXiv:1512.04977.

DOI: http://dx.doi.org/10.18524/1810-4215.2017.30.114229

CORRELATION OF THE NUMBER OF IMAGES OF AN N-POINT GRAVITATIONAL LENS AND THE NUMBER OF SOLUTIONS OF ITS SYSTEM

A.T. Kotvytskiy[1,2], S.D. Bronza[2],V.Yu. Shablenko[1]

[1] Karazin Kharkov National University,
Svobody Square 4, Kharkiv, 61022, Ukraine, *kotvytskiy@gmail.com*
[2] Ukrainian State University of Railway Transport,
Feierbakh Square 7, 61050, Kharkiv, Ukraine *bronza_semen@mail.ua*

ABSTRACT. In this paper, we study the correlation between the number of solutions of a system of lens equations and the number of source images that a gravitational lens has. We defined the concept of an image in a gravitational lens. To find the set of solutions of a system of lens equations, we applied methods of algebraic geometry.

Keywords: Lens: gravitational lenses, images, solutions; Algebraic geometry: resultant, Bezout theorem.

1. Introduction

One of the main theoretical problems of gravitational lensing is the study of images. This problem is studied in some publications (Bliokh et al., 1989; Zakharov, 1997; Schneider, 1999). The images in these publications are studied mostly by numerical methods, sometimes with elements of an analytical description. In this paper, we study the images of a point source in N-point gravitational lens analytically. In this paper, we continue to investigate gravitational lenses by methods of algebraic geometry. The results obtained by these methods previously published in (Kotvytskiy & Bronza, 2016; Kotvytsky et al., 2016; Kotvytskiy et al., 2017; Bronza & Kotvytskiy, 2017).

2. Images in gravitational lensing

In astrophysical literature, the concept of an image in a gravitational lens is usually not defined. In terms of empirical astrophysics this concept is obvious. However, the absence of a definition can lead to ambiguous understanding of the concept and a different interpretation of some results, for example, the theorem on the odd number of images (Zakharov, 1997; Schneider, 1999). The terminology developed in algebraic geometry enables us to define the concept of an image in a gravitational lens. Based on this definition, we can refine certain known statements and formulate new ones.

The equation of N-point lens (in dimensionless form) has the form:

$$\vec{y} = \vec{x} - \sum_i m_i \frac{\vec{x} - \vec{x}_i}{|\vec{x} - \vec{x}_i|^2}, \qquad (1)$$

where $\vec{x}_i$ - are the radius vectors of the point masses entering the lens, and m_i, $\sum_i m_i = 1$ − their dimensionless masses.

Equation (3) in the coordinate form has the form:

$$\begin{cases} y_1 = x_1 - \sum\limits_{i=1}^{N} m_i \frac{x_1 - a_i}{(x_1 - a_i)^2 + (x_2 - b_i)^2} \\ y_2 = x_2 - \sum\limits_{i=1}^{N} m_i \frac{x_2 - b_i}{(x_1 - a_i)^2 + (x_2 - b_i)^2} \end{cases}, \qquad (2)$$

where a_i and b_i are the coordinates of the radius-vector $\vec{l}_i$, i.e. $\vec{l}_i = (a_i, b_i)$.

The system (2) is a system of two rational equations (over the field of real numbers) in two variables. Equations (2) are given in Cartesian coordinates on the plane. In terms of algebraic geometry, the image of a source in N-point gravitational lens can be defined as follows:

Definition. An image of a point source in N-point gravitational lens will be called the real solution of system (2) without regard to multiplicity. The set of images is the set of different real solutions of this system.

Let us investigate the set of real solutions of system (2). We transform the equations of the system to polynomial form:

$$\begin{cases} F_1(x_1, x_2, y_1) = 0 \\ F_2(x_1, x_2, y_2) = 0 \end{cases} \qquad (3)$$

The equations of system (3) will be studied over the field of complex numbers.

The system (3) is defined in. System (3) is not equivalent to system (2), but it follows from it.

We can compute the set of solutions of system (2) from the set of real solutions of system (3) if we remove solutions from it in which system (2) is not defined. These solutions are the coordinates of the point masses.

We directly check out that the points with coordinates (a_i, b_i), $i = 1, ..., N$, are solution of system (3), but system (2) is not defined in these points.

Let f_1 and f_2 be the left-hand sides of the first and second equations of system (2), $M(f_1, f_2)$ be the solution set of system (2), $V(F_1, F_2)$ be the solution set of system (3), and $ReV(F_1, F_2) \subset V(F_1, F_2)$ the subset of its real solutions, then relation:

$$M(f_1, f_2) = ReV(F_1, F_2) / \{\cup (a_i, b_i)\}. \qquad (4)$$

From the theorem on the structure of the set of solutions of a system of polynomial equations, see (Arzhancev, 2003) it follows that the set $V(F_1, F_2)$ can be represented in the form

$$V(F_1, F_2) = \left(V^0(F_1, F_2)\right) \cup \left(V^1(F_1, F_2)\right), \qquad (5)$$

where $V^1(F_1, F_2)$ is the set of solutions depending on single parameter, and $V^0(F_1, F_2)$ is the discrete set of solutions of system (3). The dimension $\dim V^1(F_1, F_2) = 1$, $\dim V^0(F_1, F_2) = 0$.

There are several theorems that answer the question: is the set empty, see for example (Walker, 1950; Kalinina, 2002)? In (Bronza & Kotvytskiy, 2017), we present an algorithm that allows us to describe this set analytically, if it is not empty. If the set $V^1(F_1, F_2)$ is not empty, then the equations of system (3) have a common component. The equation of the general component can be obtained from its analytical description.

The set $M(f_1, f_2)$ can be represented in the form: $M(f_1, f_2) = \left(M^0(f_1, f_2)\right) \cup \left(M^1(f_1, f_2)\right)$, where $M^0(f_1, f_2) = ReV^0(F_1, F_2) / \{\cup (a_i, b_i)\}$ and $M^1(f_1, f_2) = ReV^1(F_1, F_2) / \{\cup (a_i, b_i)\}$.

It is known that the set $M^1(f_1, f_2)$, for a point source in single-point lens is not empty, see for example (Bliokh et al., 1989; Zakharov, 1997; Schneider, 1999), coincides with $V^1(F_1, F_2)$, see (Bronza & Kotvyskiy, 2017) and is Einstein ring. But for a point source in symmetric 2-point lens, we proved (Bronza & Kotvyskiy, 2017) that the set $M^1(f_1, f_2)$ is empty and put forward hypothesis: for N-point lens this set is empty for $N > 1$.

To study the set of solutions $V^0(F_1, F_2)$ of system (3) we use the Bezout theorem, see for example (Walker, 1950), (Kalinina, 2002; Arzhancev, 2003; Reid, 1988).

Theorem 1. The number of intersection points of plane curves Φ_1 and Φ_2 is equal to $n \cdot m$, where $m = \deg \Phi_1$ and $n = \Phi_2$, if the curves: not have common components, are defined over an algebraically closed field, are considered on the projective plane, points of intersection are counted taking into account the multiplicity.

The Bezout theorem, in our case, is equivalent to the following

Theorem 2. The system of polynomial equations

$$\begin{cases} \Phi_1(X_0 : X_1 : X_2) = 0 \\ \Phi_2(X_0 : X_1 : X_2) = 0 \end{cases} \qquad (6)$$

has in the projective plane CP^2, counting multiplicity, exactly $m \cdot n$ solutions, where, $m = \deg \Phi_1$ and $n = \Phi_2$, if $\gcd(\Phi_1, \Phi_2)$ belongs to the coefficient field C.

In the equations of system (3) we pass to homogeneous coordinates, which are projective. Let:

$$\begin{cases} x_1 = \frac{X_1}{X_0} \\ x_2 = \frac{X_2}{X_0} \end{cases} \qquad (7)$$

The system (7) defines surjective mapping, $\Im : C^2 \to CP^2$, which defines the left-hand sides of the equations of system (6):

$$\begin{cases} \Phi_1(X_0 : X_1 : X_2) = X_0^{2N+1} F_1\left(\frac{X_1}{X_0}, \frac{X_2}{X_0}, y_1\right) \\ \Phi_2(X_0 : X_1 : X_2) = X_0^{2N+1} F_2\left(\frac{X_1}{X_0}, \frac{X_2}{X_0}, y_2\right) \end{cases}, \qquad (8)$$

The functions $\Phi_1 = \Phi_1(X_0 : X_1 : X_2)$ and $\Phi_2 = \Phi_2(X_0 : X_1 : X_2)$ are homogeneous functions of degree $2N + 1$. The triple of complex numbers $(X_0 : X_1 : X_2)$ is the coordinates of the point and specifies point $p \in CP^2$. The triple $(\lambda X_0 : \lambda X_1 : \lambda X_2)$ specifies the same point if $\lambda \neq 0$. If, at least one of the coordinates of the point p is equal to zero, say that this point is irregular. Otherwise, the point is called regular.

The set of points CP^2 one of the coordinates, which is equal to the number $h \neq 0$, is called affine map on CP^2 and denoted by $A^2(h)$. The complement of $CP^2 \backslash A^2(h)$ consists of an one-dimensional complex projective subspace, which is called infinitely distant line of the affine map $A^2(h)$, see for example (Arzhancev, 2003; Reid, 1988). The infinitely distant line of any affine map $A^2(h)$ is evidently irregular.

For example, if we set Theorem 3. In a situation of general position (the Jacobian of the system of lens equations is not equal to zero), the number of point images in N-point gravitational lens has parity opposite to the parity of the number N., then the set of points CP^2 with coordinates $(1 : X_1 : X_2)$ will be affine map of $A^2(1)$, and the infinity of the straight line of this map will be given by equation $X_0 = 0$.

We have

Theorem 3. In a situation of general position (the Jacobian of the system of lens equations is not equal to zero), the number of point images in N-point gravitational lens has parity opposite to the parity of the number N.

In the proof of Theorem 2 we use the following

Lemma. The number of irregular solutions of system (6), on line $X_0 = 0$, is $2N$.

Proof. Using (8), we reduce the system (6) to the form:

$$\begin{cases} (X_1 - X_0 y_1) \prod_{i=1}^{N} [\Gamma_i] - X_0^2 \sum_{j=1}^{N} m_j (X_1 - X_0 a_j) \times \\ \qquad \times \prod_{i=1, i\neq j}^{N} [\Gamma_i] = 0 \\ (X_2 - X_0 y_2) \prod_{i=1}^{N} [\Gamma_i] - X_0^2 \sum_{j=1}^{N} m_j (X_2 - X_0 b_j) \times \\ \qquad \times \prod_{i=1, i\neq j}^{N} [\Gamma_i] = 0 \end{cases}, \tag{9}$$

where $\Gamma_i = (X_1 - X_0 a_i)^2 + (X_2 - X_0 b_i)^2$.

Let $X_0 = 0$. We have:

$$\begin{cases} X_1 \prod_{i=1}^{N} \left(X_1^2 + X_2^2\right) = 0 \\ X_2 \prod_{i=1}^{N} \left(X_1^2 + X_2^2\right) = 0 \end{cases} \Rightarrow \begin{cases} X_1 \left(X_1^2 + X_2^2\right)^N = 0 \\ X_2 \left(X_1^2 + X_2^2\right)^N = 0 \end{cases} \tag{10}$$

$$\Rightarrow \left(X_1^2 + X_2^2\right) = 0 \Rightarrow X_1 = \pm i X_2 \Rightarrow \begin{cases} X_1 = a \\ X_2 = \pm a \end{cases} \tag{11}$$

Finally we have two N-fold solutions: $P_1 = (0 : a : ia)$ and $P_2 = (0 : a : -ia)$.

Proof of Theorem 2. For the degrees of the polynomials of systems (3) and (6) we have: $\deg F_1 = \deg F_2 = \deg \Phi_1 = \deg \Phi_2 = 2N + 1$. By Bezout's theorem, the system of equations (6) has $(2N+1)^2$ solutions, which include an even number $2q$ of complex conjugate solutions and $P = 2N$ irregular solutions. Therefore, the number of real solutions of system (6).

$$card\left(ReV^0(F_1, F_2)\right) = (2N+1)^2 - 2q - P = \tag{12}$$

$$= (2N+1)^2 - 2q - 2N = 4N^2 + 2N + 1 - 2q.$$

From the fact that the restriction of the inverse mapping $\Im^{-1} : CP^2 \to C^2$ to the affine map $A^2(1)$ is a bijection that is given by the equations: $X_0 = 1, X_1 = x_1, X_2 = x_2$, we have:

$$card\left(M^0(f_1, f_2)\right) = card\left(ReV^0(F_1, F_2)\right) - N = \tag{13}$$

$$= 4N^2 + N + 1 - 2q.$$

In a situation of general position, the point source is not on the caustic, therefore, all elements of the set $ReV(f_1, f_2)$ are different. In this case, each point of the set $ReV(f_1, f_2)$ is, by definition, an image. It follows from (13) that the parity of the number of images is opposite to the parity of the number N. The theorem is proved.

Theorem 3 does not contradict the theorem on the oddness of the number of images in transparent lenses (Bliokh, 1989).

In the special case, for 1-point lens the number of images is: $4N^2 + N + 1 - 2q = 6 - 2q$ - even number; for 2-point lens: $4N^2 + N + 1 - 2q = 19 - 2q$ - odd number, and so on.

5. Conclusions

In this article, we applied methods of algebraic geometry to determine number of images in gravity lens. Proved that the parity of the number of images is opposite to the parity of the number.

References

Arzhancev I.V.: 2003, Basisy Grebnera i systemy algebraicheskikh uravneniy [in Russian]. Letnyaya shkola, Sovremennaya matematika. Moskow, P. 68.

Bliokh P.V. & Minakov A.A.: 1989, Gravitational Lenses [in Russian], Naukova Dumka, Kiev.

Bronza S.D.: 2016, *Zbirnik naukovih prats, Kharkiv, UkrURT*, 68 [in Russian].

Bronza S.D., Kotvytskiy A.T.: Mathematical bases of the theory of N-point gravity lens.

Bronza S.D., Kotvytskiy A.T.: 2017, *The Journal of Kharkiv National University, ser. Physics*, **26(1121)**, 6.

Kalinina E.A., Uteshev A.Yu.: 2002, *Teoria isklyucheniya, SPBU, Saint Petersburg*, 72.

Kotvytskiy A.T., Bronza S.D.: 2016, Odessa Astron. Publ., **29**, 31.

Kotvytskiy A.T., Bronza S.D., Vovk S.R.: 2016, *The Journal of Kharkiv National University, ser. Physics*, **24(1119)**, 55.

Kotvytskiy A.T., Bronza S.D., Nerushenko K.Yu., Shablenko V.Yu.: 2017, *Zbirnik naukhovih prats VI Mizhregionalnoyi naukovo-praktichnoyi konferencii "Astronomiya i syogodennya", Vinnitsya*, [in Ukrainian], 198.

Lang S.: Algebra. Columbia University. New York, 1965.

Reid Milies A.: 1988, *Undergraduate Algebraic Geometry*, 151.

Schneider P., Ehlers J., Falco E.E.: 1999, *Gravitational lenses*, 560.

Van Der Waerden B.L.: 1971, Algebra I, II, P. 456.

Walker R.J.: 1950, Algebraic curves, P. 236.

Zakharov A.F.: 1997, *Gravitacionnye linzy i mikrolinzy*, 328.

DOI: http://dx.doi.org/10.18524/1810-4215.2017.30.115803

SPIN AND MODEL DETERMINATION OF EXTRA NEUTRAL GAUGE BOSONS AT LHC AND ILC*

A.A. Pankov[1,2,3], A.V. Tsytrinov[3]

[1] Institute for Nuclear Problems, Belarusian State University, Minsk, 220030, Belarus, *pankov@ictp.it*

[2] Gelepov Laboratory of Nuclear Problems, Joint Institute for Nuclear Research, Dubna, 141980, Russia

[3] Abdus Salam ICTP Affiliated Centre and Technical University of Gomel, Gomel, 246746, Belarus, *tsytrin@rambler.ru*

ABSTRACT. Heavy neutral gauge Z' bosons are predicted by many models of physics beyond the Standard Model. If a new neutral gauge boson is discovered at the LHC in the clean Drell-Yan channel, the characterization of its spin and couplings will proceed via measuring production rates and angular distributions of the decay products. We study the discrimination between a Z' boson (spin-1) against the Randall-Sundrum graviton resonance (spin-2) and spin-0 resonance (sneutrino) with the same mass and producing the same number of events in the cross section. The next step would be to measure its properties to identify the underlying theory that gave rise to the Z'. We discuss in this context the foreseeable sensitivity to Z's of fermion-pair production observables at the ILC with polarized beams, especially as regards the potential of distinguishing different Z' models once such deviations are observed.

Keywords: Elementary particles, Standard Model, physics beyond the Standard Model, extra neutral gauge bosons.

1. Introduction

Electroweak theories beyond the Standard Model (SM) based on spontaneously broken extended gauge symmetries naturally envisage the existence of heavy, neutral, vector bosons Z'. The variety of the proposed Z' models is somewhat broad, and for definiteness in the sequel we shall focus on the so-called $Z'_{\rm SSM}$, Z'_{E_6}, $Z'_{\rm LR}$ and $Z'_{\rm ALR}$ models (Langacker, 2008). Particular attention has recently been devoted to the phenomenological properties and the search reaches on such scenarios, and in some sense we may consider these Z' models as representative of this New Physics (NP) sector.

A typical manifestation of the production of such states is represented by (narrow) peaks observed in the cross sections for processes among SM particles at high energy accelerators, for example, in the dilepton invariant mass distributions for Drell-Yan (DY) process $pp \to Z' \to \ell^+\ell^- + X$ with $\ell = e, \mu$ at the CERN LHC hadronic colliders. Current experimental search limits on $M_{Z'}$ at 95% C.L., at the LHC with $\sqrt{s} = 13$ TeV using ≈ 36 fb^{-1} in DY, generally range in the interval 3.8–4.5 TeV, depending on the particular Z' model being tested (Aaboud, 2017).

Clearly, the eventual discovery of a peak should be supplemented by the verification of the spin-1 of the assumed underlying Z', vs. the alternative spin-2 and spin-0 hypotheses corresponding, e.g., to exchanges of a Randall-Sundrum graviton resonance or a sneutrino. This kind of analysis relies on appropriate angular differential distributions and/or angular asymmetries. Finally, once the spin-1 has been established, the particular Z' scenario pertinent to the observed signal should be identified, see, e.g., Refs. (Osland, 2008), (Osland, 2009). From studies of Drell-Yan processes at the LHC with a time-integrated luminosity of 100 fb^{-1}, it turns out that one can expect, at the 5-σ level, discovery limits on $M_{Z'}$ of the order of 4–4.5 TeV, spin-1 identification up to $M_{Z'} \simeq 2.5$–3.0 TeV and potential of distinction among the individual Z' models up to $M_{Z'} \simeq 2.1$ TeV (95% C.L.).

An alternative resource for the observation of virtual heavy gauge boson exchanges should be represented by the next generation e^+e^- ILC, with center of mass energy $\sqrt{s} = 0.5$–1 TeV and typical time-integrated luminosities $\mathcal{L}_{\rm int} \sim 0.5$–1 ab^{-1}, and the really high precision measurements that will be possible there. Indeed, the baseline configuration envisages a very high electron beam polarization (larger than 80%) and positron beam polarization of order 60% (MoortgatPick, 2005).

We will here focus on the fermion-antifermion pro-

*The complete paper is to be published in Journal of Physics: Conference Series

duction reactions at the polarized ILC (Osland, 2009):

$$e^+ + e^- \to f + \bar{f}, \qquad f = e, \mu, \tau, c, b. \qquad (1)$$

Particular emphasis will be given to the comparison between the cases of unpolarized and polarized initial beams, as regards the expected potential of ILC in identifying the Z' models of interest here, for $M_{Z'}$ values beyond the limits accessible at the LHC. Concerning the Z' mass, we will follow the scenario where the Z' mass range is above the LHC discovery limit and, here, with $M_{Z'}$ unknown, both discovery and identification reaches should be assessed for the ILC.

2. Discovery of the Z' bosons

In the absence of available data, the assessment of the expected 'discovery reaches' on the various Z's needs the definition of a 'distance' between the NP model predictions and those of the SM for the basic observables that will be measured. The former predictions parametrically depend on the Z' mass and its corresponding coupling constants, while the latter ones are calculated using the parameters known from the SM fits. Such a comparison can be performed by a standard χ^2-like procedure. We divide the full angular range into bins and identify the basic observables with the polarized differential angular distributions for processes (1), $\mathcal{O} = \mathrm{d}\sigma(P^-, P^+)/\mathrm{d}z$, in each bin. Correspondingly, the relevant χ^2 can symbolically be defined as:

$$\chi^2(\mathcal{O}) = \sum_f \sum_{\{P^-,\ P^+\}} \sum_{\text{bins}} \frac{[\mathcal{O}(\text{SM} + Z') - \mathcal{O}(\text{SM})]^2_{\text{bin}}}{(\delta\mathcal{O}_{\text{bin}})^2}. \qquad (2)$$

To derive the expected 'discovery' limits on Z' models at the ILC, for the 'annihilation' channels in Eq. (1), with $f \neq e, t$, we restrict ourselves to combining in Eq. (2) the $(P^-, P^+) = (|P^-|, -|P^+|)$ and $(-|P^-|, |P^+|)$ beam polarization configurations, that are the predominant ones. For the Bhabha process, $f = e$, we combine in (2) the cross sections with all four possible polarization configurations, i.e., $(P^-, P^+) = (|P^-|, -|P^+|)$, $(-|P^-|, |P^+|)$, $(|P^-|, |P^+|)$, $(-|P^-|, -|P^+|)$. Numerically, we take for the electron beam $|P^-| = 0.8$ and for the positron beam $|P^+| = 0.6$.

Regarding the ILC energy and the time-integrated luminosity (which, for simplicity, we assume to be equally distributed among the different polarization configurations defined above), we will give explicit numerical results for c.m. energy $\sqrt{s} = 0.5$ TeV with time-integrated luminosity $\mathcal{L}_{\text{int}} = 500$ fb^{-1}, and for the 'ultimate' upgrade values $\sqrt{s} = 1.0$ TeV with $\mathcal{L}_{\text{int}} = 1000$ fb^{-1}. The assumed final state identification efficiencies governing, together with the luminosity, the expected statistical uncertainties, are: 100% for e^+e^- pairs; 95% for l^+l^- events ($l = \mu, \tau$); 35% and 60% for $c\bar{c}$ and $b\bar{b}$.

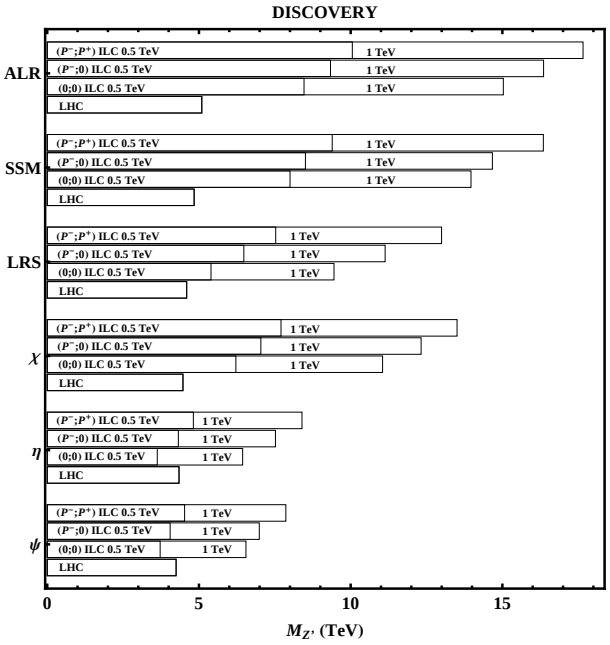

Figure 1: Discovery reaches on Z' models obtained from combined analysis of the unpolarized and polarized processes (1) (95% C.L.) at the ILC with $\sqrt{s} = 0.5$ TeV (1 TeV) and $\mathcal{L}_{\text{int}} = 500$ fb^{-1} (1000 fb^{-1}), compared to the results expected from Drell-Yan processes at the LHC at the 5-σ level. Three options of polarization are considered at the ILC: unpolarized beams, $P^- = P^+ = 0$; polarized electron beam, $|P^-| = 0.8$; both beams polarized, $|P^-| = 0.8$ and $|P^+| = 0.6$.

As for the major systematic uncertainties, they originate from errors on beam polarizations, on the time-integrated luminosity, and the final-state reconstruction and energy efficiencies. For the longitudinal polarizations, we adopt the values $\delta P^-/P^- = \delta P^+/P^+ = 0.25\%$, rather ambitious, especially as far as P^+ is concerned, but strictly needed for conducting the planned measurements at the permille level. As regards the other systematic uncertainties mentioned above, we assume for the combination the (perhaps conservative) lumpsum value of 0.5%. The systematic uncertainties are included using the covariance matrix approach.

The Fig. 1 includes a comparison with the discovery potential of the LHC with luminosity 100 fb^{-1}, from the Drell-Yan processes $pp \to l^+l^- + X$ ($l = e, \mu$) (at the 5-σ level). These values provide a representative overview of the sensitivities of the reach in $M_{Z'}$ on the planned energy and luminosity, as well as on beam polarization.

3. Distinction of Z' models

Basically, in the previous subsection we have assessed the extent to which Z' models can give values of e^+e^- differential cross sections that can *exclude* the SM hypothesis to a prescribed C.L. Such 'discovery reaches' are represented by upper limits on Z' masses, for which the observable deviations between the corresponding Z' models and SM predictions are sufficiently large compared to the foreseeable experimental uncertainties on the cross sections at the ILC).

However, since different models can give rise to similar deviations, we would like to determine the ILC potential of identifying, among the various competing possibilities, the source of a deviation, should it be effectively observed. These ID-limits should obviously be expected to lie below the corresponding ILC discovery reaches and, for an approximate but relatively simple assessment, we adapt the naive χ^2-like procedure applied in the previous subsection.

To this purpose, we start by defining a 'distance' between pairs of Z' models, i and j with i, j denoting any of the SSM, SM, ALR, LRS, ψ, η, χ, but $i \neq j$. We assume for example model i to be the 'true' model, namely, we consider 'data' sets obtained from the dynamics i, with corresponding 'experimental' uncertainties, compatible with the expected 'true' experimental data. The assessment of its distinguishability from a j model, that we call 'tested' model, can be performed by a χ^2 comparison analogous to (2), with the χ^2 defined as:

$$\chi^2(\mathcal{O})_{i,j} = \sum_f \sum_{\{P^-,\ P^+\}} \sum_{\text{bins}} \frac{\left[\mathcal{O}(Z_i') - \mathcal{O}(Z_j')\right]^2_{\text{bin}}}{\left(\delta_i \mathcal{O}_{\text{bin}}\right)^2}. \quad (3)$$

Here, we study a scenario where the Z' mass cannot be known *a priori*, e.g., the Z' is too heavy to be discovered at the LHC (say, $M_{Z'}$ >4–5 TeV), but deviations from the SM predictions can still be observed at the ILC. Actually, models with different Z' masses and coupling constants can in principle be the source of a deviation from the SM predictions observed at the ILC. With the coupling constants held fixed numerically at the theoretical values pertinent to the Z_i' and Z_j' models under consideration, the χ^2_{ij} of Eq. (3) becomes a function of the two masses, $M_{Z_i'}$ and $M_{Z_j'}$, both assumed to lie in the respective ILC discovery ranges.

Finally, Fig. 2 shows the comparison of identification reaches or distinction bounds on the Z'-models considered in Fig. 1, together with the corresponding bounds on $M_{Z'}$ obtained from the process $pp \to l^+l^- + X$ at the LHC with c.m. energy 14 TeV and time-integrated luminosity 100 fb^{-1}. We assume, for the ILC, the same c.m. energy, luminosty and beam polarization as in Fig. 1. The figure speaks for itself, and in particular clearly exhibits the roles of the ILC parameters.

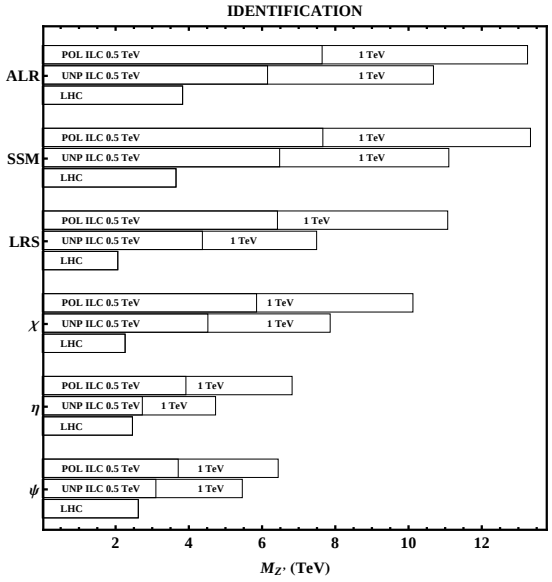

Figure 2: Comparison of the Z'-model distinction bounds on $M_{Z'}$ obtained from combined analysis of the unpolarized and polarized processes (1) at the ILC with $\sqrt{s}$ = 0.5 TeV (1 TeV) and $\mathcal{L}_{\text{int}}$ = 500 fb^{-1} (1000 fb^{-1}), compared to the results expected from Drell-Yan processes at the LHC at 95% C.L. Two options of polarization are considered: unpolarized beams $P^- = P^+ = 0$ and both beams are polarized, $|P^-| = 0.8$ and $|P^+| = 0.6$.

4. Concluding remarks

We find that one might be able to distinguish among the considered Z' models at 95% C.L. up to $M_{Z'} \simeq$ 3.1 TeV (4.0 TeV) for unpolarized (polarized) beams at the ILC (0.5 TeV) and 5.3 TeV (7.0 TeV) at the ILC (1 TeV), respectively. In particular, the figure explicitly manifests the substantial role of electron beam polarization in sharpening the identification reaches. Positron polarization can also give a considerable enhancement in this regard (if measurable with the same high accuracy as for electron polarization), although to a more limited extent in some cases.

Acknowledgements. This research has been partially supported by the Abdus Salam ICTP (TRIL Programme), the Belarusian republican foundation for fundamental research and the Belarusian state programme of scientific research "Convergence-2020".

References

Langacker P.: 2009, *Rev. Mod. Phys.*, **81**, 1199.
Aaboud M. et al.: arXiv:1707.02424 [hep-ex].
Osland P., Pankov A.A., Paver N., Tsytrinov A.V.: 2008, *Phys. Rev.* D, **78**, 035008.
Osland P., Pankov A.A., Tsytrinov A.V., Paver N.: 2009, *Phys. Rev.* D, **79**, 115021.
Moortgat-Pick G.A. et al.: 2008, *Phys. Rept.*, **460**, 131.

DOI: http://dx.doi.org/10.18524/1810-4215.2017.30.114259

CORES IN DARK MATTER HALOES WITH ANISOTROPIC OSIPKOV-MERRITT DISTRIBUTION AND MAXIMAL PHASE-SPACE DENSITY

A.V. Rudakovskyi[1,2]

[1] Bogolyubov Institute of Theoretical Physics,
Metrologichna Str. 14-b, 03680, Kyiv, Ukraine, *rudakovskyi@bitp.kiev.ua*
[2] Taras Shevchenko National University of Kyiv, Faculty of Physics,
Glushkova ave. 2, Kyiv, Ukraine

ABSTRACT. This paper describes the developed model of dark matter cored density profiles. This model was recently proposed by Dmytro Iakubovskyi (Iakubovskyi & Rudakovskyi, in preparation). It has only one extra parameter – the maximal value f_{max} of phase-space distribution function – that turn a cusped Navarro-Frenk-White density profile into a cored one. This paper focuses on the estimation of the influence of velocity anisotropy on the cored density profile by using the Osipkov-Merritt model. The density profiles of the typical dwarf-spheroidal galaxy for different masses of fermionic dark matter particle and different anisotropy parameters r_a was calculated. It was obtained that the influence of velocity anisotropy on the cored density profile is small.

Keywords: Dark matter, core, Navarro-Frenk-White profile, Eddington transformation, Osipkov-Merritt model, dwarf spheroidal galaxy.

1. Introduction

The nature of dark matter particles is one of the most important questions of astroparticle physics and cosmology. The dark matter particle candidates could be classified into two groups: warm dark matter (WDM) particles with relativistic initial velocities (Bisnovatyi-Kogan & Novikov, 1980) and cold dark matter (CDM) with non-relativistic initial velocities (Blumenthal et al, 1984). The standard cosmology ΛCDM model can predict well the large-scale structure of the Universe. But there is no solid evidence that the ΛCDM predictions are successful on the small scales.

The recent numerical simulations of cold dark matter suggest the density distribution of dark matter in the haloes can be described by the Navarro-Frenk-White (NFW) profile (Navarro, Frenk, White, 1996; Navarro, Frenk, White, 1997):

$$\rho_{NFW}(r) = \frac{\rho_0}{\frac{r}{r_s}\left(1+\frac{r}{r_s}\right)^2} \quad (1)$$

where r_s and ρ_0 are the parameters of the halo. The parameters concentration C_{200} and halo mass M_{200} are rather used. The M_{200} is the mass of sphere with average density 200 times larger than the critical density of the Universe. The radius of this sphere r_{200} is connected with r_s as the $r_{200} = C_{200} r_s$.

The Navarro-Frenk-White profile has a singularity (cusp) at $r = 0$. But the observations (see, e.g. de Block, 2010) prefer the much flatter shape of density profile (core with constant density near the center of the halo). The cores could be naturally produced by the feedback of supernovae (Navarro, Eke, Frenk, 1996; Pontzen & Governato, 2012), in the fermionic (see, e.g., Ruffini & Stella, 1983) or self-interacting dark matter paradigm (e.g. Kamada et al., 2017). In this paper, we focus on the fermionic particles as DM candidates.

According to the Liouville theorem, the phase-space density of fermionic warm dark matter cannot be larger than some maximal value f_{max}. This fact leads to the limits on the mass of DM particle (Tremaine & Gunn, 1979; Boyarsky et al., 2009). The previous analytical models of dark matter haloes as self-gravitating fermionic gas (Ruffini & Stella, 1983; Bilic & Viollier, 1997; Merafina & Alberti, 2014; Chavanis, Lemou, Mehats, 2015; Domcke & Urbano, 2015; Vega & Sanchez, 2016; Arguelles et al., 2016; Di Paolo, Nesti, Villante, 2017) require non-trivial assumptions about the temperature of dark matter and their distribution function. In this paper, we propose the method of calculating cored density distributions without such disadvantages. We used such cosmological constants from the*Planck* satellite : $\Omega_0 = 0.307$, $h = 0.678$, $\Omega_\Lambda = 0.693$, $\Omega_b = 0.0483$ (Planck collaboration, 2016).

This paper is structured as follows. Sec. 2.1 briefly

describes the model of cored density profiles proposed by Dmytro Iakubovskyi (Iakubovskyi & Rudakovskyi, in preparation). Sec. 2.2 focuses on the developed model, which includes velocity anisotropy according to Osipkov-Merritt model. Finally, Sec 3. presents short discussion and conclusion.

2. Methods

2.1. Isotropic halo density profiles

If the velocity distribution of the dark matter particles is isotropic (the distribution function depends only on the energy of the particle), the phase-space density distribution is connected with density profile by the Eddington transformation (Binney & Treemaine, 2008) :

$$f(E) = \frac{1}{\pi^2\sqrt{8}} \frac{\mathrm{d}}{\mathrm{d}E} \int_E^0 \frac{\mathrm{d}\rho}{\mathrm{d}\Phi} \frac{d\Phi}{\sqrt{E-\Phi}}. \qquad (2)$$

where E is total energy, $E = \frac{v^2}{2} + \Phi(r)$, v is velocity of the dark matter particle, $\Phi(r)$ is gravitational potential. The gravitational potential is defined as:

$$\Phi(r) = 4\pi G_N \int_0^r \frac{\mathrm{d}x}{x^2} \int_0^x \rho(y) y^2 \mathrm{d}y, \qquad (3)$$

where G_N is gravitational constant.
The phase-space density corresponding to the NFW profile is infinite at the center of the halo. But the phase-space density of the fermionic gas cannot exceed the maximal phase-space density (Boyarsky et al., 2009):

$$f_{max} = \frac{g m_{FD}^4}{2(2\pi\hbar)^3} \qquad (4)$$

where g is internal degrees of freedom of fermions (we assume that $g = 2$), m_{FD} is the mass of the fermion particle.
Hence, following method of obtaining the cored density profile was proposed. This method is based on the assumption that the mass density follows NFW law at large scale and phase-space density distribution function is limited by maximal value f_{max}. The phase-space density distribution function corresponding to staring NFW profile is calculated. Assuming that the DM particle mass is m_{FD}, we truncate obtained distribution function $f(E)$ by the maximal value f_{max}:

$$f_{tNFW}(E) = \begin{cases} f_{NFW}(E), & f(E) < f_{max} \\ f_{max}, & f(E) \geq f_{max} \end{cases} \qquad (5)$$

The truncated phase-space density distribution function can be converted to the modified truncated matter density profile:

$$\rho_{tNFW}(r) = 4\pi \int_{\Phi(r)}^0 f_{tNFW}(E) \sqrt{2\left(E - \Phi(r)\right)} \mathrm{d}E \qquad (6)$$

New truncated density profile $\rho(r)$ corresponds to the new gravitational potential and new phase-space density distribution function. Hence, the required cored density profile can be obtained iteratively. It was obtained that the 5 iterations are enough for convergence of truncated density profiles.
The dwarf spheroidal galaxies are the objects with highest average phase-space density (Boyarsky et al., 2009). I assume that the density profile of dwarf spheroidal galaxy on large scales is similar to the NFW profile with parameters $M_{200} = 10^8 M_\odot$ and $C_{200} = 30$. I choose the possible values of DM particle mass as $m_{FD} = 250, 500, 1000, 2000$ eV and ∞ (this case corresponds to the NFW profile at all radii). The obtained density profiles are depicted on Figure 1.

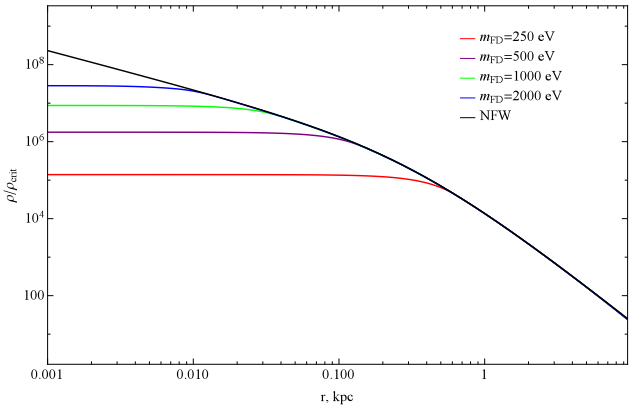

Figure 1: Cored halo density profiles of typical dwarf spheroidal galaxy for fermionic dark matter particles with masses $m_{FD} = 250, 500, 1000, 2000$ eV. Velocity distribution is isotropic. NFW profile corresponds to the $m_{FD} = \infty$, its parameters are $M_{200} = 10^8 M_\odot$ and $C_{200} = 30$ respectively.

2.2. Cored density profile in Osipkov-Merritt model

The anisotropy of velocities in the halo is described by the parameter $\beta(r) = 1 - \frac{\sigma_t^2(r)}{\sigma_r^2(r)}$, where σ_t and σ_r are tangential and radial velocity dispersions. The density profiles in previous sections were obtained in the assumption that $\beta = 0$ ($\sigma_r = \sigma_t$). In this section, we estimate the influence of anisotropy on cored profile by using the Osipkov-Merritt model (Osipkov, 1979; Merritt, 1985; Binney & Tremaine, 2008). The Osipkov-Merritt model is based on the assumption that the phase-space density distribution function depends on the isolated integral of motion $Q = E + \frac{L^2}{2r_a^2}$, where E is the energy, L is angular momentum, r_a is anizotropy radius (parameter of the halo). The anisotropy parameter in this model is $\beta = 1 - \frac{\sigma_t^2}{\sigma_r^2} = 1 - \frac{1}{1+\frac{r^2}{r_a^2}}$. For $r \ll r_a$ the velocity distribution is isotropic, and anisotropic

for large radii. The case $r_a \to \infty$ corresponds to the isotropic velocity distribution.
Denoting the $\rho_Q(r) = \left(1 + \frac{r^2}{r_a^2}\right)\rho(r)$, the Eddington's transformation changes to:

$$f(Q) = \frac{1}{\pi^2\sqrt{8}} \frac{\mathrm{d}}{\mathrm{d}Q} \int_Q^0 \frac{\mathrm{d}\rho_Q}{\mathrm{d}\Phi} \frac{\mathrm{d}\Phi}{\sqrt{Q-\Phi}}. \quad (7)$$

The phase-space density distribution function $f(Q)$ is truncated by f_{max}:

$$f_{tNFW}(Q) = \begin{cases} f(Q), & f(Q) < f_{max} \\ f_{max}, & f(Q) \geq f_{max} \end{cases} \quad (8)$$

Than truncated density profile is calculated as follows:

$$\rho_{tNFW}(r) = \frac{4\pi}{\left(1 + \frac{r^2}{r_a^2}\right)} \int_{\Phi(r)}^0 f_{tNFW}(Q)\sqrt{2\left(Q - \Phi(r)\right)}\mathrm{d}Q. \quad (9)$$

In this paper 5 iterations was used in iterative process (similarly to previous section). The obtained results for typical dwarf spheroidal galaxy, $m_{FD} = 500$ eV and $r_a = 0.25, 0.5, 1$ kpc is depicted on Fig. 2.

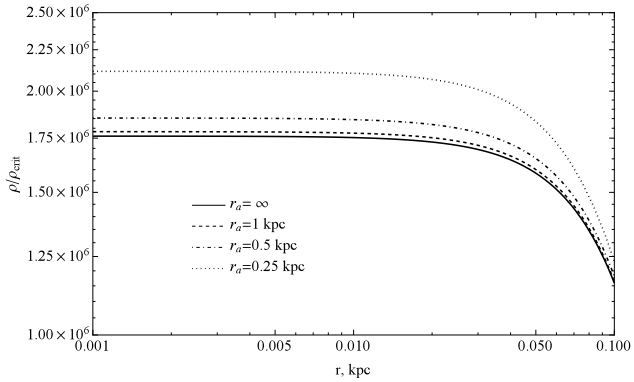

Figure 2: Cored density profiles of typical dwarf spheroidal galaxy with anisotropy radiuses $r_a = 0.25, 0.5, 1, \infty$ kpc and $m_{FD} = 500$ eV. $r_a = \infty$ corresponds to the isotropic cored halo.

3. Discussion and conclusion

This paper focuses on the development of the iterative method of calculation of the cored halo density profile for fermionic dark matter particles (proposed by Dmytro Iakubovskyi; Iakubovskyi & Rudakovskyi, in preparation). According to this method, the phase-space density distribution $f(E)$ (corresponding to the NFW profile) was calculated by using the Eddington transformation. Then $f(E)$ was truncated phase-space density by some maximal value f_{max} and recalculated corresponding truncated mass density ρ_{tNFW}. This procedure was iterated until ρ_{tNFW} converges. On large scales ρ_{tNFW} is well described by NFW profile. But near the center of the halo, the density is flattening. This core corresponds to the degenerate fermionic dark matter gas, which phase-space density cannot exceed some maximal values f_{max}. The obtained shape of ρ_{tNFW} is analogous to the results of the simulations in (Shao et al., 2013; Maccio et al., 2013).
The cored density profile is characterized by core radius r_c. In this paper the core radius is defined as $\rho_{tNFW}(r_c) = \frac{1}{4}\rho_{tNFW}(0)$. In this paper the density profile of typical dwarf spheroidal galaxy is assumed on large scales as described by NFW with parameters $M_200 = 10^8 M_\odot$, $C_{200} = 30$. It was found for this halo that $r_c \simeq 0.03$ kpc for $m_{FD} = 2000$ eV, $r_c \simeq 0.2$ kpc for $m_{FD} = 500$ eV, $r_c \simeq 0.7$ kpc for $m_{FD} = 250$ eV. Obtained density profiles showed the decreasing density of core $\rho_{tNFW}(0)$ with increasing the mass of DM particle. The difference in M_{200} of initial NFW profile and M_{200} of obtained cored density profile for dwarf spheroidal galaxy does not exceed 10% .
The influence of velocity anisotropy on the cored density profile was estimated by using the Osipkov-Merritt (OM) model. OM model assumes that the distribution function depends on isolated integral of motion $Q = E + \frac{L^2}{2r_a^2}$ instead of E. The natural assumption is that the smallest value of anisotropy parameter r_a must be comparable with the core radius of isotropic halo r_c. This assumption is based on the fact that central parts of haloes seem to be isotropic (Boyarsky et al., 2009). In this paper I focus on the $m_{FD} = 500$ eV, hence the minimal $r_a = 0.25$ kpc was chosen. It was obtained that the influence of anisotropy on a radius of a core is negligible for all tested r_a. The density in the core is increased maximum by 20 % in the presence of velocity anisotropy. For $r_a \geq 1$ kpc the difference between the anisotropic and isotropic density profiles is negligible.

Developed model of cored density profile combined with the models of baryonic feedback processes and observations of dwarf spheroidal galaxies can be used for constraining mass of fermionic dark matter particle candidate.

Acknowledgements. I thank Dmytro Iakubovskyi for useful comments. The work of A. R. was partially supported by the Program of Cosmic Research of the National Academy of Sciences of Ukraine, the grant 6F of the Department of Target Training of the Taras Shevchenko Kiev National University under the National Academy of Sciences of Ukraine.

References

Arguelles C.R. et al.: 2016, preprint (arXiv:1606. 07040).
Bilic N. & Viollier R.D.: 1997, *Phys. Lett. B*, **408**, 75.
Binney J. & Tremaine S.: 2008, Galactic Dynamics: Second Edition. (Princeton Univ. Press, Princeton)

Bisnovatyi-Kogan G.S. & Novikov I.D.: 1980, *Sov. Ast.*, **24**, 516.
de Block W.J.G.: 2010, *A&A*, **2010**, 789293.
Blumenthal G.R. et al.: 1984, *Nature*, **311**, 517.
Boyarsky O., Ruchayskiy O., Iakubovskyi D.: 2009, *JCAP*, **0903**, 005.
Chavanis P.-H., Lemou M., Mehats F.: 2015, *Phys.Rev.D*, **92**, 123527.
Di Paolo C., Nesti F., Villante F.L.: 2017, preprint (arXiv: 1704.06644)
Domcke V. & Urbano A.: 2015, *JCAP*, **1501**, 002.
Kamada et al.: 2017, *Phys.Rev.Lett.*, **119**, 111102.
Maccio A.V. et al.: 2013, *MNRAS*, **428**, 3715.
Merafina M. & Alberti G.: 2014,*Phys. Rev.D.*, **89**, 123010.
Merritt D.: 1985, *Astron. J.*, **90**, 1027.
Navarro J.F, Eke V.R., Frenk C.S.: 1996, *MNRAS*, **283**, 72.
Navarro J.F., Frenk C.S., White S.D.M.: 1997, *ApJ*, **490**, 493.
Navarro J.F., Frenk C.S., White S.D.M.: 1996, *ApJ*, **462**, 563.
Osipkov L.P.: 1979, *Pis'ma v Astron. Zhur.*, **5**, 77.
Planck collaboration: 2016, *A&A*, **594**, A13.
Pontzen A. & Governato F.: 2012, *MNRAS*, **421**, 3464.
Shao S. et al: 2013,*MNRAS*, **430**, 2346.
de Vega H.J. & Sanchez N.G.: 2016, *IJMPA*, **31**.

DOI: http://dx.doi.org/10.18524/1810-4215.2017.30. 114263

DETERMINATION OF THE GALAXY CLUSTER ORIENTATION USING X-RAY IMAGES BY FOCAS METHOD

S.Yu. Shevchenko[1], A.V. Tugay[2]

[1] Schmalhausen Institute of Zoology,
Bohdan Hmelnitskiy St., 15, Kyiv, Ukraine, *astromott@gmail.com*
[2] Astronomy and Space Physics Department, Faculty of Physics,
Taras Shevchenko National University of Kyiv,
Glushkova ave., 4, Kyiv, 03127, Ukraine, *tugay.anatoliy@gmail.com*

ABSTRACT. In our work we considered orientations of bright X-ray halos of the galaxy clusters (mainly Abell clusters). 78 appropriate clusters were selected using data from Xgal sample of extragalactic objects in XMM-Newton observation archive. Position angles and eccentricities of these halos were calculated applying FOCAS method. No privilegd orientations were found.

Keywords: Galaxies: clusters; X-rays: galaxies: clusters.

1. Introduction

One of the interesting tasks of the extragalactic astronomy is a search of dedicated directions in the galaxies and their clusters orientations. The catalog of Abell Cluster Objects (Abell et al., 1989) is the main catalog of galaxy clusters. It contains the most of closest and brightest clusters which are the most suitable for both optical and X-ray observations. Galaxy orientations in 247 rich Abell clusters were studied by Godlowski et al. (2010) and Panko et al. (2013) with corresponding statistical data analysis and simulations. Orientation of the galaxies from relatively small sample can be numerically described by the distribution of anisotropy parameter. This parameter was calculated for edge-on galaxies in Parnovsky & Tugay (2007) and for nearby galaxy groups in Godlowski et al. (2012). Galaxies orientation in the nearby groups was studied by Pajowska et al. (2012).

X-ray images of galaxy cluster halos could be easily approximated by ellipses, so they are well suitable to study such large-scale orientation. We use XMM-Newton archive based sample of X-ray extragalactic objects X-Gal (Tugay, 2012). In the previous work (Tugay et al., 2016) the orientation of 30 X-ray southern clusters from PF catalog (Panko & Flin, 2006) was determined using the method of image isophotes approximation by ellipses. In this work we estimated orientation of the whole sky sample of X-ray brightest galactic clusters with more accurate FOCAS method (Jarvis& Tyson, 1981).

2. Method

Primarily X-Gal sample, comprised by about 5 000 objects was examined to find the brightest galaxy clusters. As a result 77 clusters were selected applying the precondition of the most right in X-Ray band. We used $1x10^{-11}$ - 110^{-12} mW/m^2 interval for the flux in 2-10 keV range. The major part of these objects (70%) turned out to be Abell clusters. Redshifts of our clusters are in the range from z=0,02 to 0,3 (i.e. their distances reaches up to 1 Gpcs). XMM-Newton imaging data (in FITS format) were retrieved from LEDAS (LEicesterDatabase andArchiveService) and processed by XMM-SAS software. The next step was to use these data to calculate clusters X-Ray halo position angles (PA), eccentricities and their inaccuracies using FOCAS algorithm. Results are shown in Tables 1 and 2. The clusters in the tables are arranged by right ascension. For the obtained results we determined equatorial coordinates of the clusters orientation effective vector $\vec{n_A}$ (Fig. 1). Vector $\vec{n}$ points to the cluster center. Vector n_z points to Northen celestial pole (0, 0, 1). Cluster ellipsoid projection is given on the Fig. 2, where $\vec{n_A}$ vector is the direction of the main axis of visible image. Direction of the third ellipsoid axis n_3 is not known. But it is known that the cluster ellipticity is insignificant and if there is measurable eccentricity of the cluster then it would be in the range of existing axis n_A and n_N. In general case, spatial orientation of the vector $\vec{n_3}$ is perpendicular to $\vec{n_A}$ and hence within single-valued conversion of $\vec{n_3}$ it is possible to use vector $\vec{n_A}$ instead. Hence vector $\vec{n_A}$ was used to describe possible orientations of the cluster. It was determined from the following equations:

$$\begin{cases} \vec{n_N} \cdot [\vec{n} \times \vec{n_Z}] = 0 \\ \vec{n_N} \times \vec{n} = 0 \end{cases} \quad (1)$$

$$\begin{cases} \vec{n_A} \times \vec{n} = 0 \\ \vec{n_A} \times \vec{n_N} = cos(PA) \end{cases} \quad (2)$$

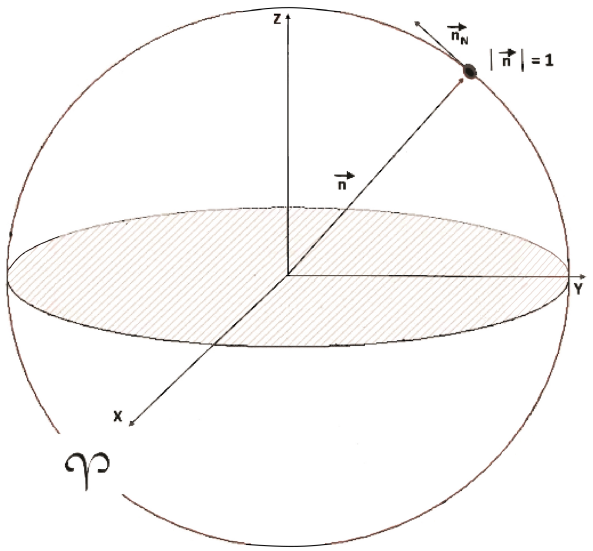

Figure 1: Cluster orientation directions.

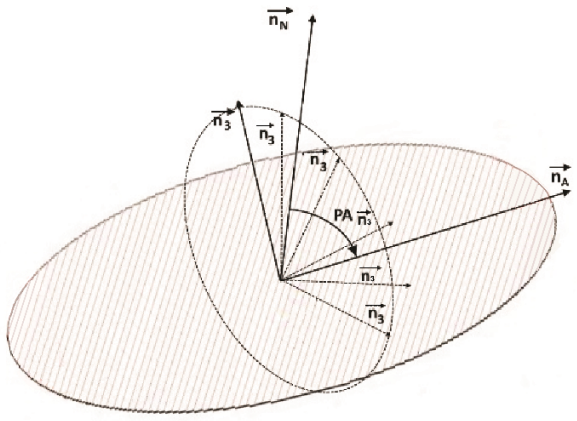

Figure 2: X-Ray halos orientation directions plane projections.

Table 1: Orientations and Eccentricities of X-Ray halos.

Name	PA	e
ACO 2700	25 ± 11	0.51 ± 0.2
ACO 119	110 ± 3	0.09 ± 0.01
ACO 122	84 ± 2	0.713 ±0.327
ACO 2984	84 ± 1	0.52 ± 0.4
ACO 399	63 ± 15	0.31 ± 0.1
ACO 401	53 ± 1	0.39 ± 0.25
ACO 3112	71 ± 5	0.62 ± 0.5
ACO 3158	82 ± 4	0.212 ± 0.01
ACO S 384	38 ± 20	0.36 ± 0.25
ClG 0422-09	19 ± 1	0.079 ± 0.01
ACO 496	8 ± 3	0.2 ± 0.1
ClG 0451-03	71 ± 8	0.17 ± 0.02
MCXC J0528.9-3927	46 ± 39	0.28 ± 0.16
MCXC J0532.9-3701	88 ± 1	0.19 ± 0.14
ACO 3378	111 ± 20	0.45 ± 0.21
ACO 3391	107 ± 3	0.22 ± 0.04
ACO 3404	45 ± 2	0.47 ± 0.3
ZwCl 0735+7421	42 ± 11	0.15 ± 0.08
ClG 0745-1910	76 ± 2	0.17 ± 0.46
ACO 653	46 ± 3	0.36 ± 0.2
ACO 689	46 ± 34	0.14 ± 0.01
ACO 773	103 ± 5	0.37 ± 0.25
ACO 901A	41 ± 20	0.36 ± 0.27
ACO 907	45 ± 22	0.42 ± 0.3
ZwCl 1021+0426	35 ± 9	0.46 ± 0.4
ACO 1084	20 ± 6	0.51 ± 0.33
ACO 1201	25 ± 15	0.5 ± 0.2
ClG J1115+5319	66 ± 5	0.25 ± 0.02
ACO 1413	4 ± 2	0.63 ± 0.35
MCXC J1206.2-0848	59 ± 25	0.24 ± 0.17
ZwCl 1215+0400	144 ± 9	0.49 ± 0.15
ACO S 700	8 ± 3	0.07 ± 0.01
ACO 3528	10 ± 1	0.6 ± 0.4
ACO 1651	99 ± 3	0.35 ± 0.27
ACO 1656	73 ± 3	0.18 ± 0.1
ACO 1663	48 ± 39	0.3 ± 0.2
ACO 1664	157 ± 5	0.48 ± 0.25
2E 2975	60 ± 15	0.28 ± 0.25
1325-5737	45 ± 33	0.17 ± 0.1
ACO 3558	43 ± 16	0.47 ± 0.3
ACO 1750N	140 ± 25	0.379 ± 0.24
ACO 3560	26 ± 14	0.32 ± 0.27
ACO 3562	150 ± 29	0.31 ± 0.14
ACO 1775	136 ± 40	0.31 ± 0.23
ACO 3571	84 ± 2	0.3 ± 0.01
ClG J1347-1145	11 ± 6	0.15 ± 0.08
ACO 1835	10 ± 5	0.21 ± 0.16
ACO 3581	69 ± 7	0.2 ± 0.06
1419+2511	30 ± 3	0.45 ± 0.3
NGC 5718 Group	61 ± 2	0.22 ± 0.15
ClG J1504-0248	147 ± 17	0.1 ± 0.06
ACO 2050	141 ± 34	0.47 ± 0.25
ACO 2052	135 ± 6	0.48 ± 0.3
ACO 2051	64 ± 8	0.25 ± 0.03
ACO 2055	12 ± 12	0.31 ± 0.13
ACO 2063	8 ± 4	0.25 ± 0.06
ACO 2204	7 ± 5	0.087 ± 0.01
ClG J1720+2638	70 ± 3	0.38 ± 0.01
MCXC J2011.3-5725	60 ± 15	0.28 ± 0.25

Table 2: The same as Table 1 for the last clusters.

Name	PA	e
ACO 3667	8 ± 8	0.76 ± 0.08
2MAXI J2014-244	9 ± 1	0.52 ± 0.45
ACO 3693	39 ± 23	0.12 ± 0.08
ClG J2129+0005	24 ± 1	0.5 ± 0.3
ACO 3814	65 ± 23	0.56 ± 0.27
2217-1725	71± 6	0.22±0.2
ACO 3854	37 ± 22	0.51 ± 0.37
ACO 3856	39 ± 10	0.56 ± 0.31
ACO S 1101	121 ± 2	0.45 ± 0.3
ACO 3992	2 ± 2	0.37 ± 0.1
ACO 2597	37 ± 1	0.17 ± 0.05
ACO 4010	148 ± 4	0.148 ± 0.01
ACO 2626	156 ± 5	0.67 ± 0.06
ACO 2667	133 ± 27	0.403 ± 0.28
ACO 2670	132 ± 35	0.23 ± 0.14
ACO 13	60 ± 20	0.41 ± 0.1
0018-0053	149 ± 2	0.12 ± 0.05
ClG 0016+16	67 ± 24	0.18 ± 0.02

Table 3: Coordinate codes for clusters with long designations.

Name	Coordinate code
1RXS J132441.9-573650	1325-5737
2XMM J141830.6+251052	1419+2511
XMMXCS J221656.6-172527.2	2217-1725
2XMMi J001737.3-005239	0018-0053

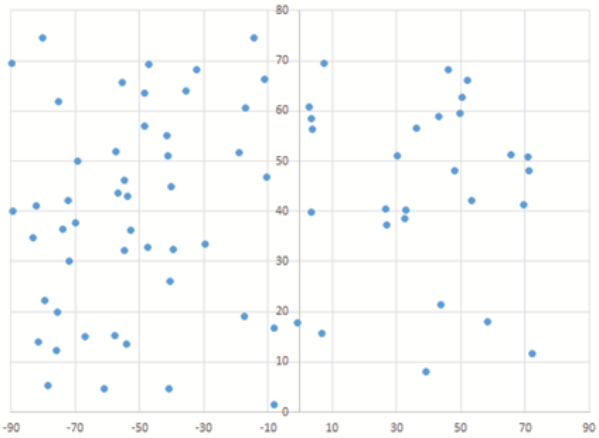

Figure 3: Distribution of the X-Ray halos orientation directions for RA and DEC.

3. Results and conclusion

Orientation and Eccentricities of X-Ray halos are presented in Tables 1-2 and the distribution of the $\vec{n}_A$ orientation (RA, Dec) is given on Fig. 3. To check possible anisotropy the range of the right accession and declination of the $\vec{n_A}$ was split into 10 degree intervals. Then using Kolmogorov's criterion we determined maximal mean deviations for clusters number in each interval and hence further verified probability of the clusters orientation anisotropy. Uniformity of the distribution was assessed using above Kolmogorov's criterion. Application of this criterion enables with probability up to 95% to accept hypothesis that Local Universe in the range up to about 1 Gpcs is isotropic. Further comparisons of the X-ray halos alignments and galaxies clusters orientation in optical band might be required and useful in the next works.

Acknowledgements. The authors are thankful to Elena Panko for discussions related to this work. This research retrieved data from NASA's Astrophysics Data System and LEDAS archive of XMM-Newton observations.

References

Abell G.O., Corwin H.G., Olowin, R.P.: 1989, *ApJS*, **70**, 1.
Godlowski W., Piwowarska P., Panko E., Flin P.: 2010, *ApJ*, **723**, 985.
Godlowski M., Panko E., Pajowska P., Flin P.: 2012, *JPhSt.*, **16**, 3901.
Jarvis J.F., Tyson J.A.: 1981, *AJ*, **86**, 476
Pajowska P., Godlowski M., Panko E., Flin P.: 2012, *JPhSt.*, **16**, 4901.
Panko E., Piwowarska P., Godlowska J., Godlowski W., Flin P.: 2013, *Ap.*, **56**, 322.
Parnovsky S., Tugay A.: 2007, *JPhSt.*, **11**, 366.
Tugay A.: 2012, *Odessa Astron. Publ.*, **25**, 142.
Tugay A., Dylda S., Panko E.: 2016, *Odessa Astron. Publ.*, **29**, 34.

DOI: http://dx.doi.org/10.18524/1810-4215.2017.30.114270

DISCONNECTED REGIONS OF STABLE CIRCULAR ORBITS IN PRESENCE OF MASSIVE SCALAR FIELD

O.S. Stashko[1], V.I. Zhdanov[2]

[1] Taras Shevchenko National University of Kyiv, Physical Faculty, Kiev, Ukraine, *alexander.stashko@gmail.com*

[2] Taras Shevchenko National University of Kyiv, Astronomical observatory, Kiev, Ukraine, *ValeryZhdanov@gmail.com*

ABSTRACT. We study circular orbits around a static spherically symmetric configuration of General Relativity in presence of a nonlinear massive scalar field (SF). The problem deals with a family of solutions to Einstein – SF equations with the SF potentials that are negative for some SF values in order to consider black hole configurations. We show that, for some parameters of the family, there can exist two disconnected regions of stable circular orbits around the configuration. Such regions can exist both for black hole and for naked singularities.

Keywords: classical black holes, naked singularities, scalar fields, accretion disks.

1. Introduction

Scalar field (SF) is often used in the General Relativity to study models of the dynamical dark energy (Novosyadlyi et al. 2013), so it is natural to look for the SF effects in astrophysical objects. Here we look for such effects in stable circular orbits (SCO) distributions around spherically symmetric configuration. It is well known that SCO form a connected structure in Schwarzschild and Kerr black hole space-times of General Relativity. It was shown by Chowdhury et al. (2012) that, in presence of the linear massless scalar field, there can exist disconnected regions of SCO separated by a ring of unstable orbits. Examples of gaps in the SCO distribution have been found by Stuchlík & Schee (2010); Pugliese et al. (2013, 2017); Vieira et al. (2014); Boshkayev et al. (2016) in presence of naked singularities (NS). We wonder, is NS always necessary for the existence of such a discontinuous SCO structure?

The aim of this paper is to present examples with a non-trivial self-interaction potential $V(\phi)$ of the massive scalar field ϕ showing that the disconnected SCO structure can exist in the black hole (BH) space-time as well. We study test-body circular orbits in static spherically symmetric asymptotically flat space-times of General Relativity in presence a non-linear SF minimally coupled with gravity. Note that our black hole solutions discussed below involve potentials that are negative in some regions, so they do not contradict to the no-scalar-hair theorem (Bekenstein 1998).

We shall use a well known method (see, e.g., Bronnikov 2001, Bronnikov & Shikin 2002, Azreg-Aïnou 2010) of generation of special spherically symmetric solutions to these equations along with corresponding potentials. Investigation shows the occurrence of the disconnected SCO distribution, both in case of BH and/or NS, for certain domain of the family parameters. At the same time, the other choice of the parameters can lead to the absence of discontinuities in the SCO distribution. Here we present main results of a numerical investigation; more detailed presentation can be found in our preprint (Stashko & Zhdanov 2017) and will be published elsewhere.

2. Basic relations

The metric of a general spherically symmetric space-time in static region can be written as

$$ds^2 = A(x)dt^2 - \frac{dx^2}{A(x)} - r^2(x)dO^2, \qquad (1)$$

and we say that x_0 is a point of a center if $r(x_0) = 0$ and $r(x) > 0$ for $x > x_0$. The center x_0 appears to be a simple root of $r(x)$ (Bronnikov 2001, Bronnikov & Shikin 2002, Azreg-Aïnou 2010).

The Einstein equations in presence of a self-interacting minimally coupled scalar field ϕ can be derived from the action functional

$$S = S_{GR} + \int d^4x\sqrt{|g|}\,[g^{\mu\nu}\phi_{,\mu}\phi_{,\nu} - 2V(\phi)] \quad , \qquad (2)$$

where S_{GR} is the standard gravitational action of the General Relativity ($c = 8\pi G = 1$), and $V(\phi)$ is a self-interaction potential to be specified below. The joint system of equations for A, r, ϕ under the conditions of spherical symmetry and asymptotic flatness is reduced to a system of equations (Azreg-Aïnou 2010),

which represent a general solution in an implicit form in terms of arbitrary $r(x)$. Thus, we use the "inverse" method (Bronnikov 2001, Bronnikov & Shikin 2002) to generate families of special solutions: we fix $r(x)$, and look for $A(x), \phi(x)$ and $V(\phi)$. This problem is solved uniquely under the conditions of the asymptotic flatness, where $V(\phi)$ is defined parametrically. In particular,

$$A(x) = r^2(x) \int_x^\infty \frac{2x' - C}{r^4(x')} dx', \tag{3}$$

where for the integration constant we have $C = 6m$, and $m > 0$ is the mass of the whole configuration.

Further we make a particular choice

$$r(x) = x \left[1 - \left(\frac{x_0}{x} \right)^N e^{-\mu(x - x_0)} \right], \tag{4}$$

where $x_0 \geq 0$, $N > 1$, and $\mu > 0$ is related to the scalaron mass $\mu/2$. The latter follows from the estimate (Stashko & Zhdanov 2017)

$$V(\phi) \sim \frac{\mu^2}{8} \phi^2 \tag{5}$$

for small ϕ (and any fixed N) on account of asymptotic relations for $x \to \infty$.

We use the general results of Azreg-Aïnou (2010) showing that (a) if $x_0 \geq 3m$, then $A(x) > 0, x > x_0$, and we have a naked singularity at $x \to x_0$; (b) if $x_0 < 3m$, then we have a BH solution: there exist a point $x_h > x_0$ (the horizon) such that $A(x_h) = 0$ and $A(x) > 0$ for $x > x_h$. For numerical estimates we choose further the units of length so as to have $C = 1$. The SF potentials that correspond to (4) for different values of the parameters are shown on Fig.1. For $x_0 < 0.5$ (BH case) they have a form of the Mexican hat and they are not positive everywhere; for $x_0 \geq 0.5$ (NS case) the potentials are not bounded from below.

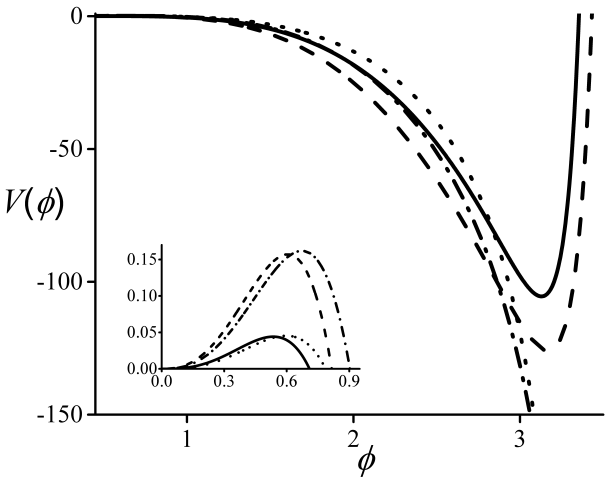

Figure 1: Scalar field potentials in cases of BH ($x_0 = 0.45$, $\mu = 0$: $N = 4$ – solid, $N = 5$ – dashed) and NS ($x_0 = 0.55$, $\mu = 0$: $N = 4$ – dotted, $N = 5$ – dash-dot). Smaller panel shows details of the graphs near the origin $\phi = 0$. which cannot be seen on the scale of the larger panel. We note that the potential graph of the intermediate case $x_0 = 0.5$ (not shown here) is completely similar to the case of $x_0 > 0.5$.

3. Regions of SCO

We are interested in time-like geodesics of the static region, where $A > 0$, $r > 0$. We shall concentrate on the case shown in Fig.2: here X_r, $r = 1, 2, 3$ represent limiting radii of different regions of the stable circular orbits. Namely, the radial coordinates $x : X_3 < x < \infty$ correspond to the infinite outer ring of circular orbits, and $x : X_1 < x < X_2$ correspond to the inner ring (if it exists), which is separated off the outer region by a prohibited area $X_2 < x < X_3$, where either there is no circular orbits or they are unstable. In case of the spherically symmetric space-time metric (1) the investigation of geodesics is reduced to the equations of one-dimensional classical particle motion in a field with effective potential $U_{eff}(x, L) = L^2 U_1(x) + U_2(x)$, where

$$U_1(x) = \frac{A(x)}{r^2(x)}, \quad U_2(x) = A(x). \tag{6}$$

At the points of minima of U_{eff} we have $U'_{eff} = 0$, $U''_{eff} > 0$ yielding

$$L^2 = F(x), \quad F'(x) > 0, \tag{7}$$

where

$$F(x) = -U'_2/U'_1 .$$

The roots of the equation (7) in the region where $F'(x) > 0$, $F(x) > 0$ correspond to SCO with different radii. The double roots of (7) yield double minima of U_{eff} with fixed L. Simple analysis on account of the explicit form of $r(x)$ (see Stashko & Zhdanov 2017) shows that in order to have non-connected regions of SCO one must have a positive maximum of $F(x)$. Then the limiting radii of the SCO regions can be found either as roots of the second derivative $F''(x)$, of as roots of the function $F(x)$ itself. Using the equation (3) one can find an explicit form of $F(x)$ and its derivatives in terms of $r(x)$ so as to find these roots numerically.

The conditions that guarantee the existence of separated SCO regions can be violated at bifurcation points in the space of parameters x_0, N, μ. These can be two types of the bifurcations:

(I) when the point of the maximum becomes negative

$$F'(X) = 0, \quad F(X) = 0, \quad F''(X) < 0; \tag{8}$$

(II) when the maximum of $F(x)$ disappears: it merges together with a point of minimum to yield an inflection point:

$$F'(X) = 0, \quad F''(X) = 0, \quad F(X) > 0. \tag{9}$$

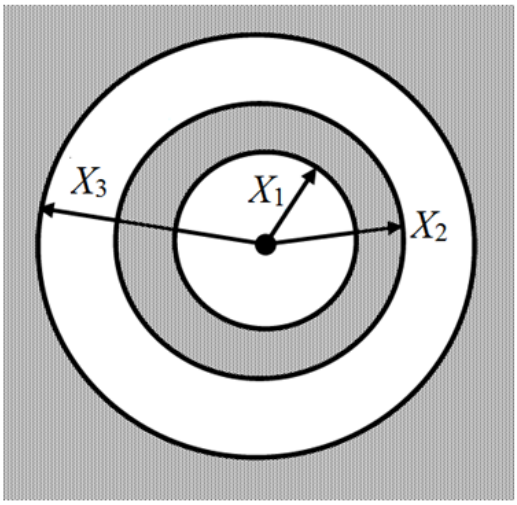

Figure 2: Shaded area: regions of stable orbits. White area: no stable orbits.

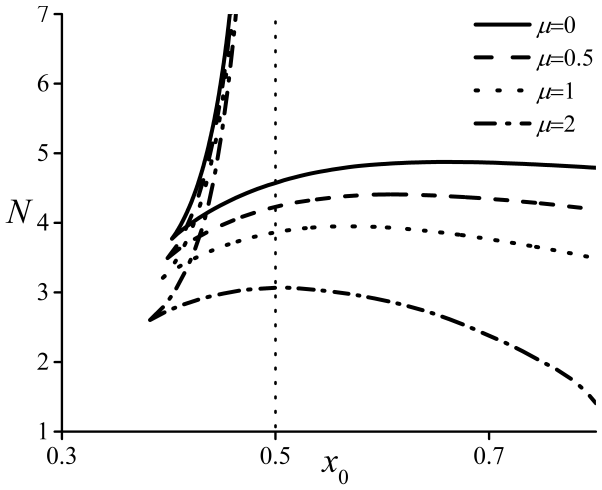

Figure 3: Cusp-like bifurcation curves limiting the regions of parameters where SCO form separate inner rings as in Fig.2. For any choice of the family parameters N, x_0 inside a cusp (to the right of the curves) the configuration has two different non-connected regions of SCO.

We performed this analysis in case of the family of solutions that correspond to the generating function (4). Fig.3 shows the resulting bifurcation cusp-like curves in the plane of parameters N, x_0 for several μ. The region for $x_0 < 0.5$ (to the left of the vertical dotted straight line) describes the BH cases; this region contains the whole left branch of the "cusp" and a part of the lower branch. We note that for sufficiently small x_0 (sufficiently small SF effects) there is no disconnected SCO regions.

4. Conclusions

We studied special solutions of the joint system of Einstein equations and SF equations with various nonzero self-interaction potentials. The solutions describe isolated static spherically symmetric configurations with an asymptotically flat space-time and a positive total mass. These solutions deal with either NS in the center of the configuration, or with BH. The family includes the Schwarzschild metric as limiting case $x_0 = 0$ and $V \equiv 0$. In the BH case, the scalar field potentials $V(\phi)$ have the form of the Mexican hat; they are bounded from below. The potentials are infinitely negative for some SF values in case of NS.

The main outcome of this paper is that separated (disconnected) ring-like structures of stable circular orbits do exist for some family parameters in the BH space-times. Analogous feature was first revealed by Chowdhury et al. (2012) in case of the massless linear scalar field dealing with NS at the center. The well-known BH-no-hair theorem (Bekenstein 1998) does not prohibit the BH case, if the scalar field potential is not positive everywhere; this is just the case of our solutions. It is also important to note that occurrence of NS does not necessarily imply the existence of the discontinuous structures. There is no any universal situation with the scalar field as concerned the existence of the non-connected SCO regions, either in the BH or NS case.

Acknowledgements. This work has been supported in part by the Department of target training of Taras Shevchenko National University of Kyiv under National Academy of Sciences of Ukraine (project 6Φ).

References

Azreg-Aïnou M., 2010, *GRG*, **42**, 1427.
Bekenstein J.D.: 1998, Black Holes: Classical Properties, Thermodynamics and Heuristic Quantization. ArXiv:gr-qc/9808028.
Boshkayev K. et al.: 2016, *PRD*, **93**, id.024024.
Bronnikov R.A.: 2001, *PRD*, **64**, id.064013.
Bronnikov K.A., Shikin G.N.: 2002, *Gravit. Cosmol.*, **8**, 107.
Chowdhury A.N. et al.: 2012, *PRD*, **85**, id.104031.
Novosyadlyi B., Pelykh V., Shtanov Yu., Zhuk A.: Dark energy and dark matter of the universe: in three volumes. Ed. V. Shulga, Vol. 1: Dark matter: Observational evidence and theoretical models (Kiev, Akademperiodyka, 2013) [arXiv:1502.04177].
Pugliese D. et al.: 2013, *PRD*, **88**, id.024042.
Pugliese D. et al.: 2017, *Eur. Phys. J. C*, **77**, id.206.
Stashko O.S., Zhdanov V.I.: 2017, arXiv:1702.02800v2.
Stuchlík Z., Schee J.: 2010, *Class. Quant. Grav.*, **27**, id. 215017.
Vieira R.S.S. et al.: 2014, *PRD*, **99**, id.024035.

DOI: http://dx.doi.org/10.18524/1810-4215.2017.30.114271

STATISTICAL ANALYSIS OF LARGE-SCALE STRUCTURE OF UNIVERSE

A.V. Tugay

Astronomy and Space Physics Department, Faculty of Physics,
Taras Shevchenko National University of Kyiv,
Glushkova ave., 4, Kyiv, 03127, Ukraine, *tugay.anatoliy@gmail.com*

ABSTRACT. While galaxy cluster catalogs were compiled many decades ago, other structural elements of cosmic web are detected at definite level only in the newest works. For example, extragalactic filaments were described by velocity field and SDSS galaxy distribution during the last years. Large-scale structure of the Universe could be also mapped in the future using ATHENA observations in X-rays and SKA in radio band. Until detailed observations are not available for the most volume of Universe, some integral statistical parameters can be used for its description. Such methods as galaxy correlation function, power spectrum, statistical moments and peak statistics are commonly used with this aim. The parameters of power spectrum and other statistics are important for constraining the models of dark matter, dark energy, inflation and brane cosmology. In the present work we describe the growth of large-scale density fluctuations in one- and three-dimensional case with Fourier harmonics of hydrodynamical parameters. In result we get power-law relation for the matter power spectrum.

Keywords: Cosmology: theory, cosmology: large-scale structure of Universe.

1. Introduction

Large-scale structure of the Universe (LSS) is thought to be a composite of galaxy clusters, superclusters, voids, walls and filaments. It is very hard to detect extragalactic filaments with current observational facilities (Tugay, 2014), although future projects such as ATHENA and SKA (Kale et al., 2016) gives some perspectives. Attempts to build filament network on Sloan Digital Sky Survey data were performed in (Tugay, 2014) and (Chen et al., 2016) using the method of density ridges. X-ray space observatories gives us new findow for LSS studying. First results of X-ray galaxy distribution based on XMM-Newton observations were get in (Elyiv et al., 2012) and (Tugay, 2012). Extragalactic filaments and other LSS details could be found in future with ATHENA observations (Nandra et al., 2013; Nevalainen, 2013). This may be also possible due to ATHENA detection and observations of 3.5 keV emission line of sterile neutrino decay (Neronov & Malyshev, 2016). Until there are no enough observer galaxy positions to recover internal structure of single filaments, the main way of LSS studying is estimation of general statistic parameters of extragalactic object distribution, such as correlation function, power spectrum and other. Such parameters should be predicted from cosmological theoretical models including the theory of growth of primordial density perturbations (Bernardeau et al., 2002).

In this work we consider simple case of gravitational instability, apply power law assumption for Fourier harmonics of perturbations and derive a relation for power spectrum.

2. Starting equations

LSS formation can be described in Newtonian gravity by the equations of Poisson, Euler and continuity:

$$\Delta\phi = 4\pi G\rho \tag{1}$$

$$\frac{d(\rho\vec{v})}{dt} + (\vec{v}\cdot\nabla)(\rho\vec{v}) = -\rho\nabla\phi \tag{2}$$

$$\frac{d\rho}{dt} = -\rho\nabla\cdot\vec{v} \tag{3}$$

We will consider velocity field as irrotational. This allows us introduce velocity potential and divergence:

$$\overrightarrow{u} = -\nabla\Phi, \theta = \nabla\cdot\overrightarrow{u} \tag{4}$$

Then we can write continuity equation as

$$\dot{\delta} + \theta = 0 \tag{5}$$

And Euler equation as

$$\dot{\overrightarrow{u}} + (\overrightarrow{u}\cdot\nabla)\overrightarrow{u} = -\nabla\Phi \tag{6}$$

or

$$\dot{\theta} + \nabla\phi + (\overrightarrow{u} \cdot \nabla)\overrightarrow{u} = 0 \tag{7}$$

Let's take the divergence from the last equation and use the continuity equation. We will get single equation for continuous matter in own Newton gravity field:

$$\ddot{\delta} + H^2\delta + \nabla(\overrightarrow{u} \cdot \nabla)\overrightarrow{u} = 0 \tag{8}$$

where H is inverse character time of the system. It may be close by order of value to Hubble constant but not necessary. To analyse LSS evolution we will onsider density contrast as superposition of plane waves:

$$\delta = \sum_m \delta_m e^{i(k_m x + \omega_m t)} \tag{9}$$

In the linear approximation we can neglect the last term in (8). We will then find the solution for exponential growth of all modes with character time t=1/H. Below we will solve the equation (8) in one-dimentional and three-dimentional weakly non-linear case.

3. One-dimentional case

In this case velocity field has single component and the values of θ and Φ ane connected with it by simple spatial derivative:

$$u = -\frac{d\Phi}{dx}, \theta = -\frac{d^2\Phi}{dx^2} \tag{10}$$

Now equation (8) can be written as

$$\ddot{\delta} + H^2\delta + \theta^2 + u\frac{d\theta}{dx} = 0 \tag{11}$$

Now we can write plane wave decompositin for Φ, u and θ:

$$\Phi = \sum_m \Phi_m e^{i(k_m x + \omega_m t)} \tag{12}$$

$$u = \sum_m u_m e^{i(k_m x + \omega_m t)} \tag{13}$$

$$\theta = \sum_m \theta_m e^{i(k_m x + \omega_m t)} \tag{14}$$

Let's substitute last expression to (11) and perform Fourier transformation. We will keep one θ in the third term and $d\theta/dx$ in the fourth term unchanging. We will get the next expression for harmonics.

$$\delta_m(H^2 - \omega_m^2) + \theta_m \cdot \theta + u_m \cdot \frac{d\theta}{dx} = 0 \tag{15}$$

It can be shown, suprisingly, that in one dimentional case there is simple expression between harmonic amplitudes of u, θ and $d\theta/dx$ such as

$$\theta_m \cdot \theta = u_m \cdot \frac{d\theta}{dx} \tag{16}$$

So we have

$$\delta_m(H^2 - \omega_m^2) + 2\sum_m \theta_m^2 e^{i(k_m x + \omega_m t)} = 0 \tag{17}$$

This means that $\theta_m = 0$ and we can not consider nonlinear dynamics with out assumptions in one dimentional case. (Abell, Corwin & Olowin, 1989)

4. Three-dimentional case

Let's write nonlinear term in (8) in tensor notations

$$\nabla(\overrightarrow{u} \cdot \nabla)\overrightarrow{u} = u_{p,q}u_{q,p} + u_q u_{p,pq} \tag{18}$$

and change velocity field with scalar potential:

$$\nabla(\overrightarrow{u} \cdot \nabla)\overrightarrow{u} = \Phi_{,pq}\Phi_{,qp} + \Phi_{,q}\Phi_{,ppq} \tag{19}$$

Then equation (8) takes form

$$\ddot{\delta} + H^2\delta + (\nabla \otimes \overrightarrow{u}) \cdot (\nabla \otimes \overrightarrow{u}) + \overrightarrow{u} \cdot \nabla\theta = 0 \tag{20}$$

or

$$\ddot{\delta} + H^2\delta + \Phi_{,pq}\Phi_{,qp} + \Phi_{,q}\Phi_{,ppq} = 0 \tag{21}$$

Direct tensor product of nabla operator and vector velocity field can be written for plane waves (remember (4)):

$$\nabla \otimes \overrightarrow{u} = \frac{u_p}{dx_q} = \frac{d}{dx_q}(-ik_p\Phi) = -k_p k_q \Phi \tag{22}$$

Double scalar product of such two tensors is equal to

$$(\nabla \otimes \overrightarrow{u}) \cdot (\nabla \otimes \overrightarrow{u}) = \sum_{p,q} k_p^2 k_q^2 \Phi^2 = k^4\Phi^2 \tag{23}$$

Now let's find the derivatives in the last term in (21) in the plane wave assumption:

$$\Phi_{,q} = -\overrightarrow{u} = i\overrightarrow{k} \cdot \Phi \tag{24}$$

$$\Phi_{,pp} = \frac{d}{dx_p}(-ik_p \cdot \Phi) = -k^2\Phi = -\theta \tag{25}$$

$$\nabla\theta = -k^2\overrightarrow{u} = k^2\nabla\Phi \tag{26}$$

$$\overrightarrow{u} \cdot \nabla\theta = -i\overrightarrow{k}\Phi \cdot (-k^2\overrightarrow{u}) = ik^2\overrightarrow{k}\Phi \cdot (-i\overrightarrow{k})\Phi = k^4\Phi^2 \tag{27}$$

Applying all above derivatives, equation (8) takes form

$$\ddot{\delta} + H^2\delta + 2k^4\Phi^2 = 0 \tag{28}$$

or for Fourier harmonics

$$\delta_m(H^2 - \omega_m^2) + 2k_m^4\Phi_m^2 = 0 \tag{29}$$

In the opposition to one-dimentional case, now we can get non-trivial result with additional assumptions. First, let's suppose that LSS is periodical in the cube with side equal to L. Then we have straight expression for wavenumber: $k_m = 2\pi m/L$. Second, suppose powerlaw relation of harmonics of velocity potential: $\Phi_m = \Phi_0 m^\gamma$. The last term in (29) must be constant. This gives us

$$k_m^4\Phi_m^2 = (2\pi m/L)^4 \cdot \Phi_0^2 m^{2\gamma} \tag{30}$$

and finally

$$\gamma = -2 \tag{31}$$

So we get inverse power law relation for matter power spectrum which is well agreed with standard cosmological model and analysis of galaxy observations (Tegmark et al., 2004):

$$P = P_0(k/k_0)^{-2} \tag{32}$$

5. Results and conclusion

Matter power spectrum parameters were found in this work in simple analytical model. More general case will be considered in the next work under wider assumptions for different functional relations for Fourier harmonics of density and velocity field.

Acknowledgements. The author is thankful to V.Zhdanov for the general idea of such study. This research has made use of NASA's Astrophysics Data System.

References

Bernardeau F., Colombi S., Gaztanaga E., Scoccimarro R.: 2002, *PhR*, **367**, 1.
Chen Y.-C., Ho S., Brinkmann J. et al.: 2016, *MNRAS*, **461**, 3896.
Elyiv A., Clerc N., Plionis M.: 2012, *A& A*, **537**, 131.
Kale, R., Dwarakanath, K.S., Vir Lal D. et al.: 2016, *JApA*, **37**, 31.
Nandra K., Barret D., Barcons X. et al.: 2013, *arXiv:1306.2307*.
Neronov A., Malyshev D.: 2016, *PhRvD*, **93**, 3518.
Nevalainen J.: 2013, *AN*, **334**, 321.
Tegmark M., Blanton M.R., Strauss M.A. et al.: 2004, *ApJ*, **606**, 702.
Tugay A.V.: 2012, *Odessa Astron. Publ.*, **25**, 142.
Tugay A.V.: 2014, *AASP*, **4**, 42.

ASTROPHYSICS

DOI: http://dx.doi.org/10.18524/1810-4215.2017.30.117154

ZIRCONIUM ABUNDANCES IN THE CENTRAL PART OF THE dSph FORNAX GALAXY

S. M. Andrievsky[1,2], S. A. Korotin[1,4], V. Hill[3], A. V. Zhukova[4]

[1] Astronomical Observatory, Odessa National University,
Shevchenko Park, 65014 Odessa, Ukraine, *andrievskii@ukr.net*
[2] GEPI, Observatoire de Paris, PSL, Research University, CNRS, Univ Paris Diderot, Sorbonne Paris Cité, Place Jules Janssen, 92195 Meudon, France
[3] Université Côte d'Azur, Observatoire de la Côte d'Azur, CNRS, Laboratoire Lagrange, Bd de l'Observatoire, CS 34229, 06304, Nice Cedex 4, France
[4] Crimean Astrophysical Observatory, Nauchny, 298409, Crimea

ABSTRACT. We derived LTE zirconium abundance in a sample of 81 giant stars in dwarf spheroidal Fornax galaxy. The LTE synthesis was used for this aim. We obtained the lower Zr abundance in Fornax galaxy comparing to the relevant value in the thick/thin disc of the Milky Way. We note that this result may be affected by the NLTE effects that decrease the real zirconium abundance.

Keywords: stars: abundances – galaxies: individual: Fornax – galaxies: evolution – galaxies: dwarf – galaxies: formation

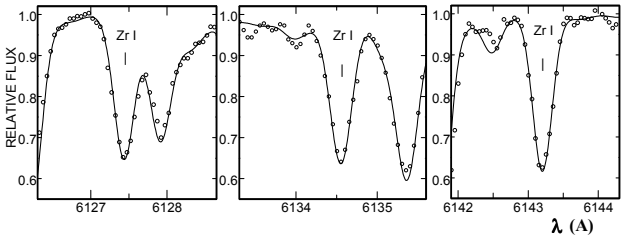

Figure 1: Synthetic and observed spectra of three zirconium lines for the star BL211 (the best zirconium abundance is (Zr/H)=2.14). Circles – observed spectrum, continuos line – synthetic spectrum.

1. Introduction.

Dwarf spheroidal galaxy Fornax is one of the most luminous satellites of the Milky Way. Its stellar population was studied spectroscopically by many authors. In particular, Letarte et al. (2010) and Lemasle et al. (2014) determined abundances of α- and some s-process elements in the giants of this stellar system. Among s-process elements zirconium was not studied in the stars of this galaxy. Therefore we decided to fill in this gap.

2. Sample of the stars

The sample of our program stars has been previously investigated by Letarte et al. (2010). The spectra were secured with ESO VLT facilities with resolving power of about 20000 in the two ranges: 5340–5620 Å, and 6120–6701 Å. 81 RGB stars were selected in the central part of Fornax dSph galaxy. In this article we report the results of determination of zirconium abundnace. We used stellar parameters and iron abundance determined by Letarte et al. (2010). The program stars and their iron abundance are listed in Table 2 together with our LTE abundance of Zr (see next sections).

3. Abundance determination details.

As we have already mentioned Letarte et al. did not derive abundance of zirconium. From the light s-process element they give abundance only for yttrium. We performed LTE profile synthesis for the three Zr I lines: 6127, 6134 and 6143 Å using SYNTHV code (Tsymbal 1996). Blending lines of other species were taking into account by using the Vienna Atomic Line Database (VALD, Kupka et al. 1999).[1] An example of the profile fitting is given in Fig. 1. Table 1 contains an information about zirconium line parameters used in our calculations. Zirconium abundance in our program stars is listed in Table 2.

[1] http://vald.astro.univie.ac.at/ vald3/php/vald.php

Table 1: Zirconium line parameters.

El	λ (Å)	log gf
Zr I	6127.48	–1.06
Zr I	6134.59	–1.28
Zr I	6143.25	–1.10

4. Results and discussion.

It is generally accepted that zirconium nuclei are produced in the higher-mass AGB stars (Prantzos et al. 1990, Raiteri et al. 1992). Production rate of the first-peak (Sr, Y, Zr) elements depends also on the metallicity of the AGB star. Metal-poor AGB stars produce a larger amount of the *s*-process peak nuclei.

The ratio [Zr/Fe] in our program stars appears to be below the value which is predicted by the Galaxy model of chemical evolution for the thick/thin disc (Bisterzo et al. 2017) (see Fig. 2).

Battistini & Bensby (2016) having analysed 311 stars in the solar neighbourhood found an increase of zirconium abundance in the Galactic thin and thick disc with metallicity decrease. Their mean [Zr/Fe] value in the metallicity region from about –1 to –0.5 is approximately 0.3–0.4 dex which is significanly higher than the mean value from the Fornax star sample. On contrary, Reddy et al. (2003) analysed 181 F and G dwarfs from Galactic disc, and their result on zirconium shows that at least up to [Fe/H] ≈ -0.7 there is no sign of an increase of abundance of this element with iron abundance decrease. The similar result was published also by Brewer & Carney (2006). The situation with zirconium becomes even more entangled if we take into account that in the different studies the different Zr lines were used to derive abundance of this element (for instance, Battistini & Bensby (2016) employed Zr I 4687 Å, 4739 Å, and Zr II 4208 Å, 5112 Å lines, while we used set of the red zirconium lines). Could such a discrepancy in the literature data be the result of ignoring of the NLTE corrections? There is a very limited information in the literature concerning the NLTE corrections for zirconium LTE abundance derived from different lines. Here one can mention only the paper of Velichko et al.(2010), who provided some limited data on corrections that should be applied to abundances derived from Zr I 4687 Å, Zr II 4208 Å, and 5112 Å lines in cool giants. According to those authors corrections are of about 0.2–0.3 dex, and they should even increase the LTE abundances (later authors published erratum where they informed that they used wrong ionization potential for Zr I). Nevertheless, those authors say (but without quantitative estimates) that observed red zirconium lines should be weakened due to the NLTE effects, what means that our result on LTE zirconium

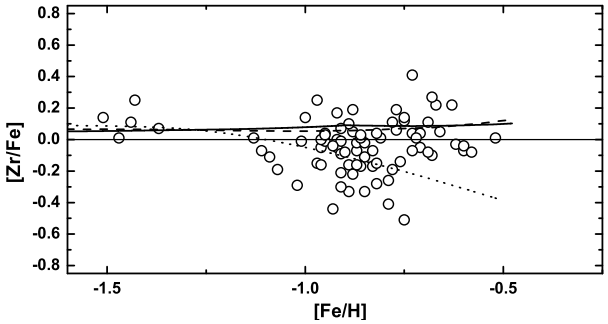

Figure 2: [Zr/Fe] vs. [Fe/H]. Circles – our stars, the model data are from Bisterzo et al. (2017). Continuous line – thin disk, dashed line – thick disk, dotted line – halo.

"underabundance" in the Fornax giants (Fig. 2) may be just an artefact. In our analysis we used Zr I 6127, 6134 and 6143 Å, for which no information about NLTE effect exists in the literature. Taking into account that different zirconium lines were used by the different authors to derive abundance in dSph Fornax galaxy and in the Milky Way, and no reliable data on the NLTE corrections for zirconium abundance derived from those lines exist in the literature, we leave the question about the detected difference in zirconium abundance in Fornax galaxy and the Milky Way stars open.

Acknowledgements. We are thankful to Dr. Sara Bisterzo for her kind help with theoretical modeling data. SMA is thankful to the Universite Côte d'Azur, Observatoire de la Côte d'Azur, CNRS, Laboratoire Lagrange administration for their hospitality during his visit in 2016, and financial support, and also for the partial financial support from the SCOPES grant No. IZ73Z0-152485, which is also acknowledged by SAK.

References

Battistini C., Bensby T.: 2016, *A&A*, **586**, A49.
Bisterzo S., Travaglio C., Wiescher M., Käppeler F., Gallino R.: 2017, *ApJ*, **835**, 97.
Brewer M.-M., Carney B.W.: 2006, *AJ*, **131**, 431.
Busso M., Gallino R., & Wasserburg G. J.: 1999, *ARA&A*, **37**, 239.
Kupka F., Piskunov N., Ryabchikova T. et al.: 1999, *A&AS*, **138**, 119.
Lemasle B., de Boer T.J.L., Hill V., et al.: 2014, *A&A*, **572**, A88.
Letarte B., Hill V., Tolstoy E. et al.: 2010, *A&A*, **523**, A17.
Prantzos N., Hashimoto M., Nomoto K.: 1990, *A&A*, **234**, 211.
Raiteri C.M., Gallino R., Busso M.: 1992, *ApJ*, **387**, 263.

Table 2: Program stars, their metallicity and abundances of Zr and Ba. (El/H)=log ϵ(El)+12.00; [El/H] = $(El/H)_{star} - (El/H)_{Sun}$.

Star	[Fe/H]	(Zr/H)	[Zr/Fe]	Star	[Fe/H]	(Zr/H)	[Zr/Fe]
BL038	–0.88	1.76	0.05	BL185	–0.71	1.92	0.04
BL045	–1.09	1.39	–0.11	BL190	–0.79	1.39	–0.41
BL052	–1.02	1.28	–0.29	BL195	–0.97	1.87	0.25
BL065	–1.43	1.41	0.25	BL196	–1.07	1.33	–0.19
BL076	–0.85	1.63	–0.11	BL197	–0.89	1.54	–0.16
BL077	–0.79	1.54	–0.26	BL203	–0.83	1.69	–0.07
BL079	–0.52	2.08	0.01	BL204	–1.00	1.73	0.14
BL081	–0.62	1.94	–0.03	BL205	–0.69	2.01	0.11
BL084	–0.85	1.41	–0.33	BL208	–0.66	1.98	0.05
BL085	–2.59	–	–	BL210	–0.76	1.69	–0.14
BL091	–0.96	1.58	–0.05	BL211	–0.67	2.14	0.22
BL092	–0.95	1.63	–0.01	BL213	–0.93	1.62	–0.04
BL096	–0.75	1.33	–0.51	BL216	–0.77	1.88	0.06
BL097	–0.92	1.67	0.00	BL218	–0.60	1.92	–0.07
BL100	–0.93	1.22	–0.44	BL221	–0.86	1.74	0.01
BL104	–0.96	1.63	0.00	BL227	–0.91	1.75	0.07
BL113	–0.75	1.96	0.12	BL228	–0.88	1.49	–0.22
BL115	–1.47	1.13	0.01	BL229	–0.71	1.83	–0.05
BL123	–0.97	1.47	–0.15	BL233	–0.68	1.81	–0.10
BL125	–0.73	1.90	0.04	BL239	–0.91	1.47	–0.21
BL132	–0.89	1.37	–0.33	BL242	–1.11	1.41	–0.07
BL135	–0.95	1.68	0.04	BL247	–0.82	1.62	–0.15
BL138	–1.01	1.57	–0.01	BL250	–0.68	2.18	0.27
BL140	–0.87	1.65	–0.07	BL253	–0.73	1.79	–0.07
BL141	–0.82	1.49	–0.28	BL257	–0.58	1.93	–0.08
BL146	–0.92	1.62	–0.05	BL258	–0.60	1.95	–0.04
BL147	–1.37	1.29	0.07	BL260	–0.87	1.56	–0.16
BL148	–0.63	2.18	0.22	BL261	–0.86	1.76	0.03
BL149	–0.91	1.59	–0.09	BL262	–0.78	1.92	0.11
BL150	–0.83	1.59	–0.17	BL266	–1.44	1.26	0.11
BL151	–0.86	1.56	–0.17	BL267	–0.72	1.88	0.01
BL155	–0.75	1.98	0.14	BL269	–0.81	1.79	0.01
BL156	–1.13	1.47	0.01	BL278	–0.73	2.27	0.41
BL158	–0.87	1.70	–0.02	BL279	–1.51	1.22	0.14
BL160	–0.95	1.67	0.03	BL295	–0.69	1.82	–0.08
BL163	–0.77	2.01	0.19	BL300	–0.92	1.84	0.17
BL166	–0.89	1.80	0.10	BL304	–0.96	1.47	–0.16
BL168	–0.88	1.90	0.19	BL311	–0.78	1.62	–0.19
BL171	–0.90	1.61	–0.08	BL315	–0.82	1.81	0.04
BL173	–0.85	1.72	–0.02	BL323	–0.91	1.38	–0.30
BL180	–0.91	1.67	–0.01				

Reddy B.E., Tomkin J., Lambert D.L., Allende Prieto C.: 2003, *MNRAS*, **340**, 304.

Tsymbal V.V.: 1996, Model Atmosph. and Spectr. Synth., eds.: S. J. Adelman, F. Kupka, W.W. Weiss, San Francisco, *ASP Conf. Ser.*, 108.

Velichko A., Mashonkina L., Nilsson H.: 2010, *AstL*, **36**, 664.

DOI: http://dx.doi.org/10.18524/1810-4215.2017.30.118521

STATISTICALLY OPTIMAL MODELING OF FLAT ECLIPSES AND EXOPLANET TRANSITIONS. THE "WALL-SUPPORTED POLYNOMIAL" (WSP) ALGORITMS

Andrych K.D.[1,2], *Andronov I.L.*[2], *Chinarova L.L.*[3,2]

[1] Department of Theoretical Physics and Astronomy, Odessa National University
[2] Department of Mathematics, Physics and Astronomy, Odessa National Maritime University
[3] Astronomical Observatory, Odessa National University
katyaandrich@gmail.com, tt_ari@ukr.net, llchinarova@gmail.com

ABSTRACT. The methods for determination of the characteristics of the extrema are discussed with an application to irregularly spaced data, which are characteristic for photometrical observations of variable stars. We introduce new special functions, which were named as the "Wall-Supported Polynomial" (WSP) of different orders. It is a parabola (WSP), constant line (WSL) or an "asymptotic" parabola (WSAP) with "walls" corresponding to more inclined descending and ascending branches of the light curve. As the interval is split generally into 3 parts, the approximations may be classified as a "non-polynomial splines".

These approximations extend a parabolic/linear fit by adding the "walls" with a shape, which asymptotically corresponds to the brightness variations near phases of the inner contact. The fits are compared to that proposed by Andronov (2010, 2012) and Mikulasek (2015) and modified for the case of data near the bottom of eclipses instead of wider intervals of the light curve. The WSL method is preferred for total eclipses showing a brightness standstill. The WSP and WSAP may be generally recommended in a case of transit eclipses, especially by exoplanets. Other two methods, as well as the symmetrical polynomials of statistically optimal order, may be recommended in a general case of non-total eclipses.

The method was illustrated by application to observations of a newly discovered eclipsing binary GSC 3692-00624 = 2MASS J01560160+5744488, for which the WSL method provides 12 times better accuracy.

Keywords: variable stars; eclipsing binary; minima timings; O-C analysis; TYC 3692-624-1 = Gaia DR1 505352827074254080 = GSC 03692-00624 .

1. Introduction

The O-C analysis is the most popular method of studies of period variations (cf. Tsesevich 1970, 1971, Kreiner et al. 2001, Andronov et al., 2017). Many astronomers observe stars only during relatively short intervals near extrema (minima of eclipsing binaries or maxima of the pulsating variables) instead of the complete light curves.

Currently in the AAVSO (2017) and BAA (2011) user guides, the Times of Minima (or Maxima, the letter "M" is the same) are abbreviated to "ToM". This needs adequate methods of modeling, which will provide best quality of approximation.

In the pre-computer era, the most popular was method of chordes by Pogson, where the approximation of points on the graph was made manually. More advanced method was proposed by Herzsprung, where the mean curve was estimated by binning the data in to time (or phase) intervals and then linearly interpolated. Such a curve was shifted and scaled to the particular data to obtain individual extrema timings.

These historical methods were discussed in numerous monographs and textbooks (e.g. Tsesevich 1970, 1971).

In the computer era, one may expect to make "physical" modeling using the code based on the method by Wilson & Devinney (1971) and its improvements (e.g. Zoła, Kolonko & Szczech,1997; Zoła et al., 2010; Prša & Zwitter, 2005). Or to use a simplified physical model (e.g. Andronov & Tkachenko 2013).

However, the number of the parameters in these models is still too large. So one may get approximations of nearly the same quality for a relatively large region in the parameter space. Thus "phenomenological" approximations are still valid for a dominating majority of variable stars.

Andronov (1987) elaborated software based on periodic cubic splines, which allows determination of the local or global approximations and, particularly, of the characteristics of extrema. More functions were reviewed by Andronov (2005).

Specially for (generally) asymmetric maxima of pulsating variables, Marsakova & Andronov (1996) proposed an algorithm of "Asymptotic parabolae" (AP), which was used for a compilation of the catalogue of characteristics of extrema of a group of the Mira-type stars (Andronov & Marsakova, 2006).

However, Chinarova & Andronov (2000) used an algebraic polynomial approximation of a degree corresponding to a minimum error estimate of timing.

Previous methods were typically based on the assumption of smooth functions, whereas eclipses definitely show begin and end not only in EA-type (Algol) systems (Samus et al. 2017), but also in EB-type (β Lyr) and even EW-type (W UMa) systems (Andronov 2012a, 2012b; Tkachenko, Andronov & Chinarova, 2016).

Thus it is natural either to apply non-polynomial splines to a complete phase light curve, or to make local approximations near the extrema.

In this paper, we compare approximations using "old" and "new" sets of functions for statistically optimal modeling of symmetrical minima of eclipsing binary stars.

2. The Observations

The methods are illustrated by application to one "flat" minimum of the eclipsing binary GSC 3692-00624 = 2MASS J01560160+5744488 (Devlen, 2015). From the complete data set, we extracted a "full" (HJD 2455506.28847 – .43138, n=43) and "part" (HJD 2455506.32250 – .40077, n=24) intervals.

As previous algorithms were effective for "smooth" minima, here we concentrate on the "flat" minima characteristic for transits of stars and exoplanets.

3. The Methods

3.1. Asymmetrical polynomials

The basic method of the approximation is based on algebraic polynomials. They are included in popular electronic tables in the Microsoft, Open/Libre, Kingsoft offices, GNUmeric and others. However, these approximations are only shown on graphs, without a possibility of getting precise coefficients and error estimates of them.

Algebraic polynomials were implemented for the minima determination in the software VSCalc (Breus, 2006) and PERANSO (Vanmunster, 2015) with an user freedom to choose the degree of the polynomial. Generally, these polynomials are asymmetrical for $m > 3$.

Typically, the duration of observations is much less than the time from some "adopted" starting point (e.g. ad in the Julian Date (JD)). Thus it is suitable to rescale the time argument t to the symmetrical interval $[-1,+1]$:

$$u = 2\cdot(t-t_{n_1})/(t_{n_2}-t_{n_1})-1 \qquad (1)$$

Here t_{n_1} and t_{n_2} are times of the beginning and end of the interval of observations. Thus

$$x_P(t) = \sum_{\alpha=1}^{m} C_\alpha \cdot u^{\alpha-1} \qquad (2)$$

These functions are generally asymmetrical in respect to the moment of extremum, thus may be used for studies of pulsating variables as well.

In our program MAVKA (Multi-Analysis of Variables by Kateryna Andrych), we have used various approximations, not only the ordinary algebraic polynomials.

The preliminary version was introduced by Andrych et al. (2015).

3.2. Symmetric polynomials

Another set of functions on time t are symmetric algebraic polynomials

$$x_{SP}(t) = \sum_{\alpha=1}^{m} C_\alpha \cdot v^{2(\alpha-1)} \qquad (3)$$

for different m. Here $v = u - u_e$ is the shift from the argument of symmetry $u_e = C_{m+1}$.

Because of this specific form, the symmetric polynomial defined by (m+1) parameter is of the degree 2(m-1) instead of m for the generally asymmetrical algebraic polynomial. So the parabola (degree 2) is defined by 3 parameters in both cases. But next steps in the degree of 2 require 1 or 2 parameters, respectively.

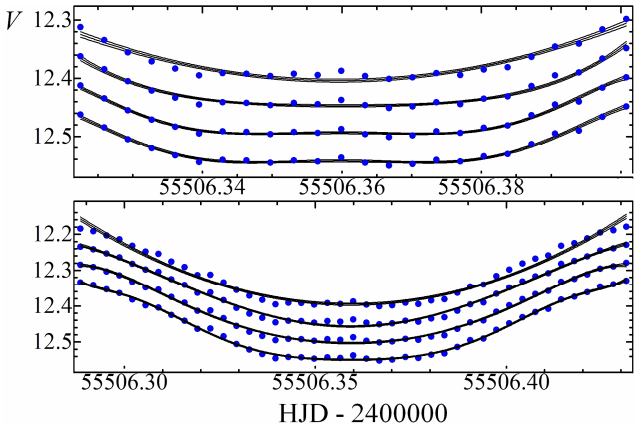

Figure 1: "Symmetric polynomial" approximations for "part" (up) and "full" (down) intervals of the same eclipse. The approximations are shown for the number of parameters $m = 3,4,5,6$ (from up to down) with an artificial shift of 0.05^{m}.

Such an approximation coincides exactly with an algebraic polynomial of order 0 (constant, m=1) and 2 (parabola, m=2). The parameters $C_1..C_m$ are determined using the LS (Least Squares) method with further improvement of C_{m+1} using differential corrections (cf. Andronov 1994, 2003). Numerical experiments show that sometimes there may be "inverse" variations, typically at the borders and at a mid-eclipse, if observationally it is flat enough.

The symmetrical polynomial fits are shown in Fig. 1 for different number of parameters. The $\pm 1\sigma$ "error corridors" for $x_{SP}(t)$ are shown as well, but are typically comparable to the thickness of line. As expected, the increase of the number of parameters leads to smaller deviations of the data from the fit, but the minimum becomes split. Thus the point of symmetry u_e, which should correspond to the minimum, formally corresponds to the maximum brightness surrounded symmetrically by deeper local minima.

3.3. Non-integer degrees as asymptotic fits

Andronov, Tkachenko & Chinarova (2017) tested many functions and modifications and ranged them according to the quality of approximation. There are two families of functions describing the shape (synonyms: "pattern", "form") of the eclipse. The first suggests a limited width of the eclipse (Andronov, 2010, 2012a)

$$G_A(z) = \begin{cases} 1-(1-|z|^{\beta})^{1.5}, & \text{if } |z|\le 1, \\ 0, & \text{if } |z|>1, \end{cases} \qquad (4)$$

where $z = (u-u_e)/\Delta = v/\Delta$ is dimensionless time, u_e is again an argument of extremum, Δ is the eclipse half-width. This approximation is called NAV ("New Algol Variable".

The second family corresponds to a formally unlimited width (Mikulášek et al., 2011, Brat et al., 2011):

$$G_M(z) = (1-\exp(-\vartheta))^{\gamma} \quad , \tag{5}$$

where $\vartheta(z) = z^2/2$ corresponds to a Gaussian function for $\gamma = 1$. Despite existence of advanced functions, this simplest function was used recently for studies of GAIA observations of eclipsing variables (Mowlavi et al., 2017).

An improved function (Mikulášek, 2015) may be decomposed into Mac-Laurin series (Andronov et al., 2016):

$$\vartheta(z) = \cosh(z) - 1 = \frac{z^2}{2} \cdot (1 + \frac{z^2}{12} + \frac{z^4}{360} + ...) \tag{6}$$

A restricted form of these functions is below:

$$G_A(z) = \frac{3}{2}|z|^{\beta} - \frac{3}{8}|z|^{2\beta} + ... \tag{7}$$

$$G_M(z) = \vartheta^{\gamma} \cdot (1 - \frac{\gamma\vartheta}{2} + \frac{(3\gamma^2+\gamma)}{24}\vartheta^2 + ...) \tag{8}$$

At the bottom of the eclipse, far of its borders, the most important are the first terms. Thus the restricted approximations are

$$x_A(z) = C_1 + C_2|v|^{\beta} + C_3|v|^{2\cdot\beta} \tag{9}$$

$$x_M(z) = C_1 + C_2|v|^{\beta} + C_3|v|^{2+\beta} \tag{10}$$

So the difference is only in the third term. For the compatibility, we adopt $\beta = 2\gamma$. Hereafter we call these approximations as NAVs and Ms, respectively. Besides the three coefficients seen in the formulae, there are two more coefficients $(u_e = C_{m+1}$ and $\beta = C_{m+2})$, which are determined by differential corrections after searching for a minimum of the test function

$$\Phi = \sum_{k=n_1}^{n_2} w_k \cdot (x_k - x_C(u_k))^2 \tag{11}$$

at a grid. The total number of parameters here is $m_p = m + 2$. As we do not extrapolate, the minimum is expected to be inside of the selected interval of observations $t_e \in [t_{n_1}, t_{n_2}]$, $u_e \in [-1,+1]$.

The parameter $\beta \in [1,5]$. Formally, the upper limit may be set to infinity, but the listed value is enough for minimization on a grid, and may be corrected to (e.g.) larger values using differential corrections.

Similarly, for the family of functions

$$G_{SP}(z) = 1 - (1-z^2)^{\gamma} = \gamma z^2 + \frac{\gamma(\gamma-1)}{2}z^4 + \frac{\gamma(\gamma-1)(\gamma-2)}{6}z^6 ... \tag{12}$$

(Andronov, 2012b) one may get a subset of "symmetric polynomial" (SP) approximation with integer powers:

$$x_{SP}(z) = C_1 + C_2 u^2 + C_3 u^4 + C_4 u^6 + ... \tag{13}$$

The approximation (12) was recently applied by Juryšek et al. (2017) for studies of a large sample of eclipsing binaries with changing inclination in the LMC .

The unbiased estimate of the root mean squared (r.m.s.) deviation of the data from the fit

$$\sigma_0 = \sqrt{\frac{\Phi}{n - m_p}} \tag{14}$$

As will be shown below, these analytical functions produce apparent waves, like the Gibbs phenomenon in the trigonometric polynomial fits of the complete phase light curves (e.g. Andronov, Tkachenko & Chinarova, 2016). However, during the transits or total eclipses, it is natural to split the data at the intervals of inner contacts.

3.4. "Wall-Supported" Functions

This series of functions we call "wall-supported" (WS), assuming some symmetrical basic function $V(v)$ for the integral of total minimum, and another symmetrical function $W(v)$ outside.

We tested different approximations. The corresponding plots are shown in Figures 2 and 3 for "part" and "full" data sets, respectively. The smoothing functions are shown in Fig. 4 and 5.

Taking into account a limb darkening, we initially suggested a "Wall-Supported Parabola"

$$x_{WSP}(u) = C_1 + C_2 \cdot v^2 + C_3 \cdot W_+(|v| - \delta) \tag{15}$$

Here the "Wall" function of $\varsigma = |v| - \delta$

$$W_+(\varsigma) = \begin{cases} 0, & \text{if } \varsigma \le 0 \\ W(\varsigma), & \text{if } \varsigma > 0 \end{cases} \tag{16}$$

Here u_s, u_f – are the arguments of "start" and "finish", respectively. Obviously, the argument of extremum is $u_e = (u_s + u_f)/2$, $u_s = u_e - \delta$, $u_f = u_e + \delta$, and the half duration of the middle part $\delta = (u_f - u_s)/2$.

To determine "non-linear" parameters in each approximation, we computed of the test function Φ on a grid.

The lines of equal level of Φ at the two-parameter diagrams for the NAV method applied to a simplified physical model were presented by Tkachenko (2016).

To study test functions for our models, we preferred to change the type of presentation, taking into account a locally paraboloidal shape of the test function. Thus, in our program, we made a following routine for the 2D-plots. The test function was computed over a grid (201×201). Then we computed a dimensionless value

$$p = \sqrt{(\Phi - \Phi_{\min})/(\Phi_{\max} - \Phi_{\min})}, \tag{17}$$

which we expect to represent a set of equal levels better than (typically) without the square root. For an exact paraboloid, the constant step in p leads to concentric ellipses with a constant step in each fixed direction from the center. The interval [0,1] for p is split into $N_p = 10$ subintervals, inside each of them the color linearly changes from blue to yellow.

This makes an abrupt change of color between the subintervals. Such a kind of presentation allows to get advantages of the "gradient" and "lines" styles.

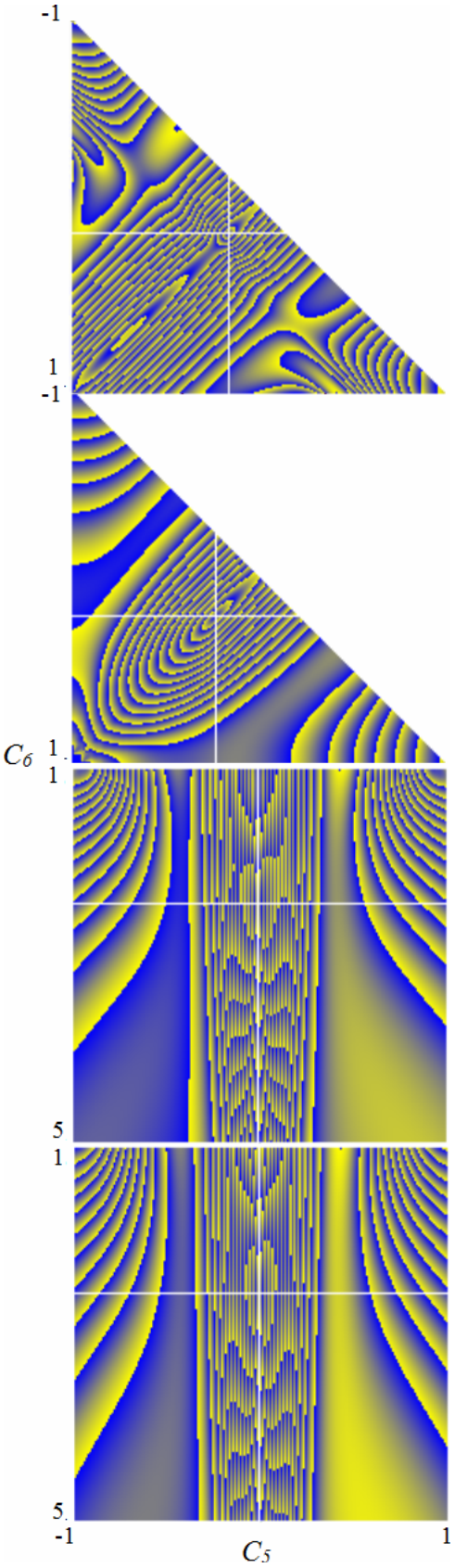

Figure 2: The dependence of the test function on the parameters C_5 ("scaled" time from –1 to 1) and C_6 , for "full" data, depending on the model (up to down): WSP, WSL (C_5=u_s, C_6=u_f), "NAVs" (Eq. (9)), "Ms" (Eq. (10)) (C_5=u_e, C_6=β). The white cross shows the minimum.

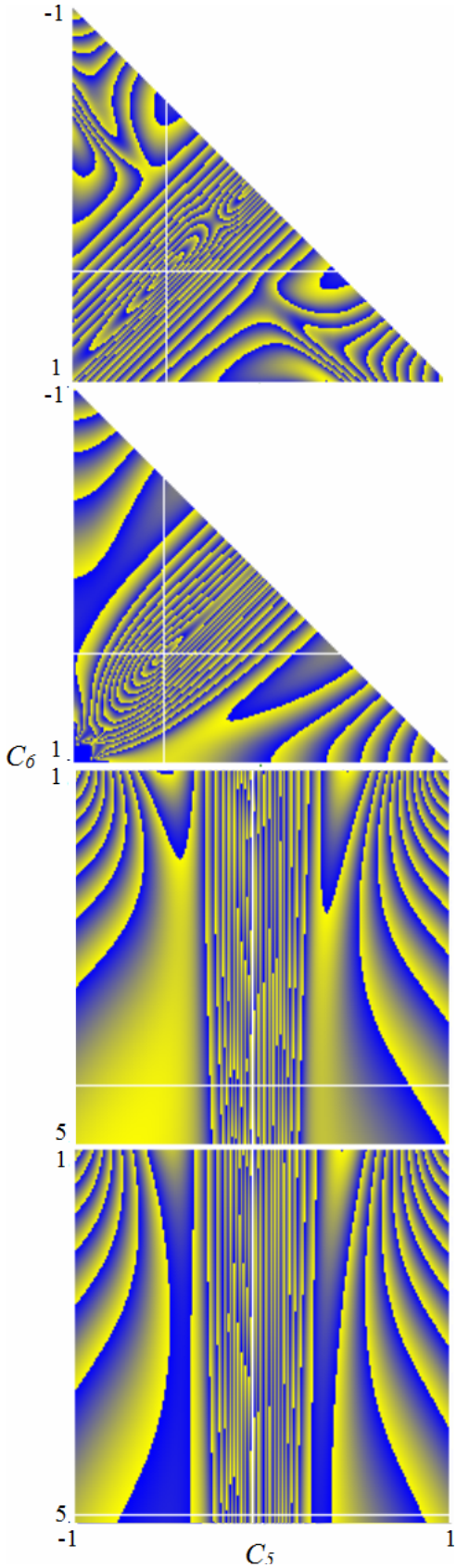

Figure 3: The dependence of the test function on the parameters C_5 ("scaled" time from –1 to 1) and C_6 , for "part" data, depending on the model (up to down): WSP, WSL (C_5=u_s, C_6=u_f), "NAVs" (Eq. (9)), "Ms" (Eq. (10)) (C_5=u_e, C_6=β).

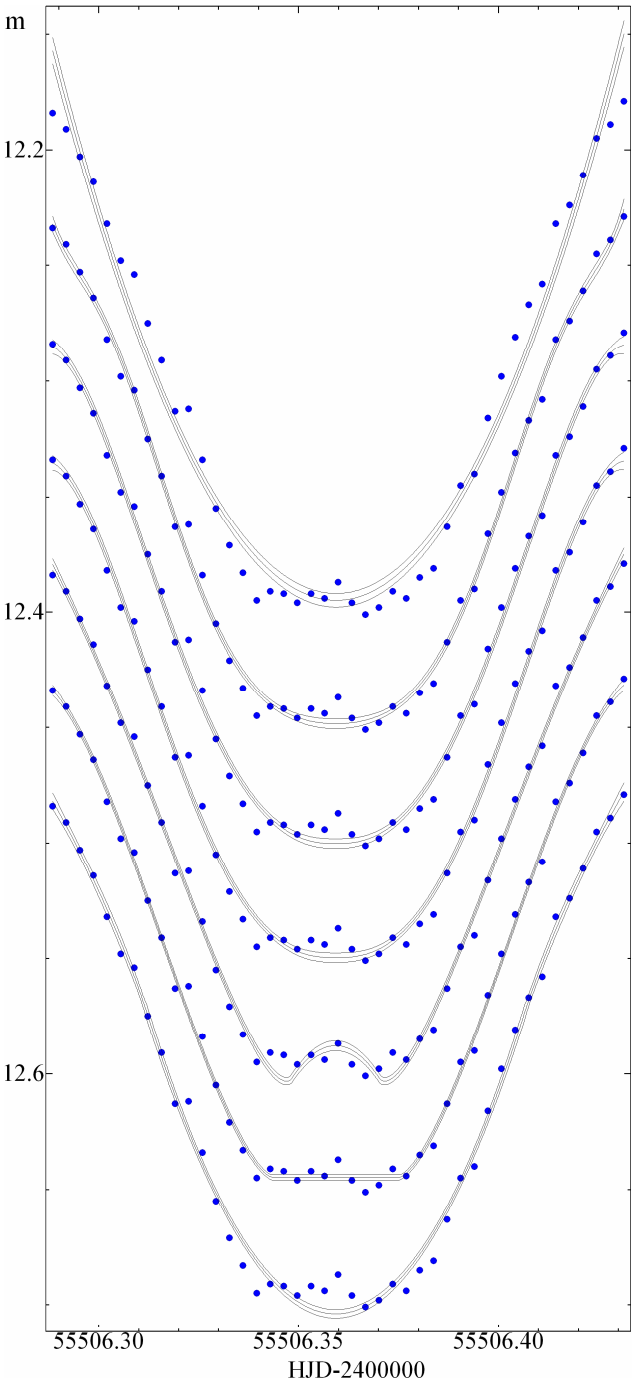

Figure 4: Approximations of the "full" data using the methods (up to down, as the graphs):

x_C	t_e	±	m_e	±	σ_0	m_p
P	369	494	9484	296	1294	3
SP	925	240	9843	211	561	5
NAVs	259	268	10002	208	599	5
Ms	259	263	9959	206	588	5
WSP	234	220	8790	217	523	5
WSL	248	**188**	9450	**134**	**426**	5
WSAP	264	294	10393	187	663	5

With the bold font, we mark the minimal error estimates among the different approximations. Time t_e is as 10^6(HJD-2455506.359), brightness m_e=10^5 (V-12.3), the error estimates are scaled similarly.

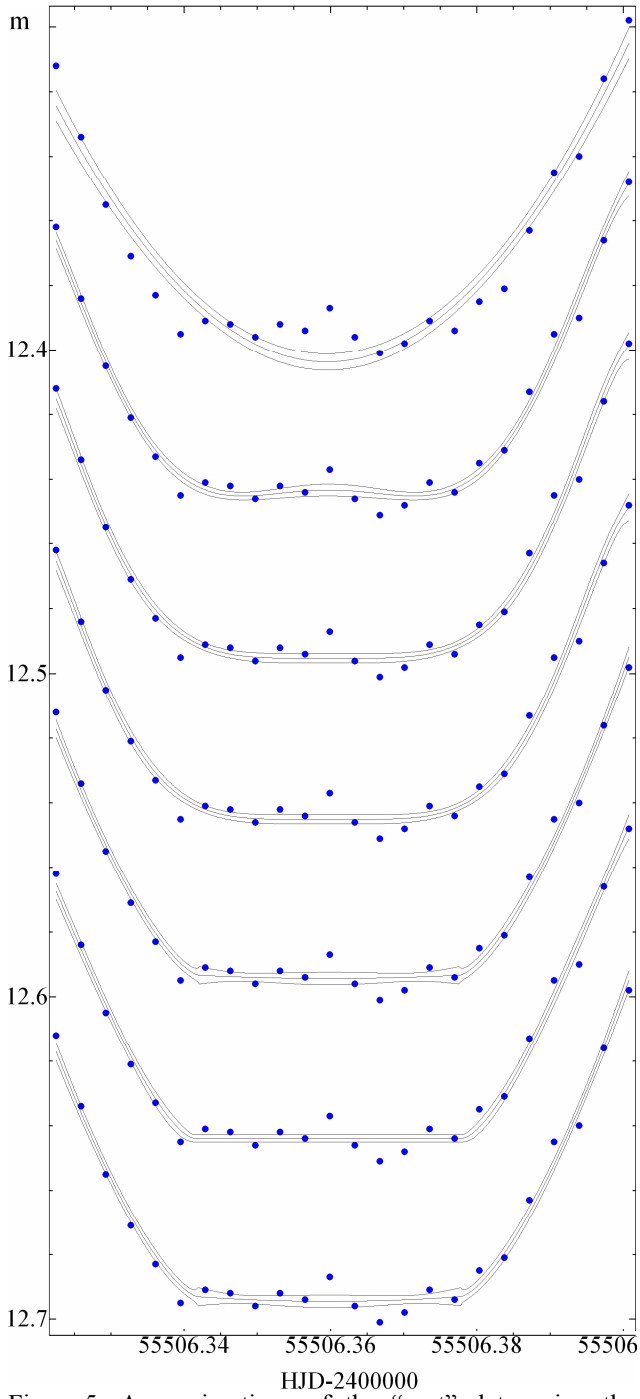

Figure 5: Approximations of the "part" data using the methods (up to down, as the graphs):

x_C	t_e	±	m_e	±	σ_0	m_p
P	504	637	10369	256	836	3
SP	1132	272	9326	183	416	5
NAVs	744	283	9517	145	437	5
Ms	734	281	9501	142	432	5
WSP	800	267	9431	193	425	5
WSL	684	**272**	9380	**124**	**415**	5
WSAP	800	266	9447	193	425	5

With the bold font, we mark the minimal error estimates among the different approximations. The scaling is as in Fig. 4.

As the "wall function", we initially adopted $W_1(\varsigma) = \varsigma^{1.5}$ as theoretically expected for the asymptotic behavior of the light curve near inner and outer contacts, except for the rare case of equal radii, when the power index is 1 for the inner contact (cf. Andronov, 2012a, Andronov & Tkachenko, 2013). More simple, than WSP, appeared a "Wall-Supported Line" (WSL) with a constant

$$x_{WSL}(u) = C_1 + C_2 \cdot (\varsigma^{1.5})_+ + C_3 \cdot (\varsigma^{3.5})_+ \quad (18)$$

Here again the index "+" means that the function is non-zero only for positive argument.

Finally, we introduce an "Asymptotic Parabola" (AP) (Marsakova & Andronov, 1996) base (Eq. 19):

$$x_{WSAP}(u) = \begin{cases} C_1 + C_2 \cdot v^2, & \text{if } v \le \delta, \\ C_1 + C_2 \cdot (2|v| - \delta)\delta + C_3 \cdot \varsigma^{1.5}, & \text{if } v > \delta \end{cases}$$

Obviously, the dependence is on time, other variables (u, v, ς) are related and introduced for suitability.

4. Discussion

Previous methods were typically based on the assumption of smooth functions, whereas eclipses definitely show begin and end not only in EA-type (Algol) systems (Samus et al. 2017), but also in EB-type (β Lyr) and even EW-type (W UMa) systems (Andronov 2012a, Tkachenko et al. 2016). Thus it is natural either to apply non-polynomial splines to a complete phase light curve, or to make local approximations near the extrema.

Contrary to partial eclipses with relatively smooth variations, during the transits of smaller stars or especially exoplanets, we introduces non-polynomial spline approximations with interval split at (unknown) moments of the inner contacts. This significantly inproves the quality of approximations using the analytical functions.

After numerical tests, we conclude that, for the flat minimum, the best function is WSL ("Wall-Supported Line"), which corresponds to the minimal error estimates either in time, or magnitude. The timing accuracy is better for a "full" data set (0.000188^d), which is by a factor of 12 better than the original estimate presented in the discovery paper: Min II HJD 2455506.3590±0.0023 (Devlen, 2015) using the old method of Kwee & van Woerden (1956) .

The simple "wall" function $W_1(\varsigma) = (\varsigma^{1.5})_+$ for WSL is adequate for the "short" series with data points at the very bottom of ellipse. but, for "long" series, one may see a distinct change of the sign of the second derivative, thus one has to add one more parameter. We propose to use a "corrected" function $W_2(\varsigma) = (\varsigma^{1.5} \cdot (1 + \lambda\varsigma^2))_+$.

However, for the middle part corresponding to the total eclipse, there may be a variety of functions $V(u)$, and it is possible to choose the best in the program.

These methods are "turned to" symmetrical eclipses. For the pulsating variables, see Andronov et al. (2014).

5. Conclusions

The described algorithms are realized in the software MAVKA, which is open for further improvements. It may be effectively used for determination of characteristics of individual minima of eclipsing binary stars with a possibility to choose the method providing the best accuracy for a given data set.

References

AAVSO: 2017, https://sites.google.com/site/aavsoebsection/determining-time-of-minimum
Andronov I.L.: 1987, *PAICz*, **70**, 161.
Andronov I.L.: 1994, *Odessa Astron. Publ.*, **7**, 49.
Andronov I.L.: 2003, *ASPC*, **292**, 391.
Andronov I.L.: 2005, *ASPC*, **335**, 37.
Andronov I.L.: 2010, Int. Conf. KOLOS-2010 Abstr. Booklet, Snina, Slovakia, 1, http://www.astrokarpaty.net/kolos2010abstractbook.pdf
Andronov I.L.: 2012a, *Ap*, **55**, 536.
Andronov I.L.: 2012b, Częstochowski Kalendarz Astronomiczny 2013, 133, (2012arXiv1212.6707A).
Andronov I.L. et al.: 2003, *Astron.Astroph.Trans.*,**22**, 793.
Andronov I.L. et al.: 2014, *AASP*, **4**, 3.
Andronov I.L. et al.: 2017, *ASPC*, **511**, 43.
Andronov I.L., Marsakova V.I.: 2006, *Ap*, **49**, 370.
Andronov I.L., Tkachenko M.G.: 2013, *Odessa Astron. Publ.*, **26**, 204.
Andronov I.L., Tkachenko M.G., Chinarova L.L.: 2016, *OEJV*, **176**, 35.
Andronov I.L., Tkachenko M.G., Chinarova L.L.: 2017, *Astrophysics*, **60**, 57.
Andrych K.D., Andronov I.L., Chinarova L.L., Marsakova V.I.: 2015, *Odessa Astron. Publ.*, **28**, 158.
BAA: 2011, "Eclipsing Binary Observing Guide", http://www.britastro.org/vss/EBHandbook11.pdf
Brát L., Mikulášek Z., Pejcha O.: 2012, http://var2.astro.cz/library/1350745528_ebfit.pdf
Breus V.V.: 2003, *Odessa Astron. Publ.*, **16**, 24.
Chinarova L.L., Andronov I.L.: 2000, *Odessa Astron. Publ.*, **13**, 116.
Devlen A.: 2015, *OEJV*, **171**, 1.
Juryšek J. et al.: 2017, *A&A*, doi:10.1051/0004-6361/201730655
Kreiner J.M., Kim Chun-Hwey, Nha Il-Seong: 2001, "An Atlas of O-C Diagrams of Eclipsing Binary Stars", Cracow, Poland, 2001aocd.book.....K .
Kwee K.K., van Woerden H.: 1956, *BAN*, **12**, 327,
Marsakova V.I., Andronov I.L.: 1996, *Odessa Astron. Publ.*, **9**, 127.
Mikulášek et al., 2011, *ASPC*, **451**, 111.
Mowlavi N. et al: 2017, *A&A*, **606A**, 92.
Prša A., Zwitter T.: 2005, *ApJ*, **628**, 426.
Samus' N.N. et al.: 2017, *ARep*, **61**, 80.
Tkachenko M.G.: 2016, *AASP*, **6**, 73.
Tkachenko M.G., Andronov I.L.: Chinarova L.L.: 2016, *JPhSt*, **20**, 4902.
Tsesevich V.P.: 1970, "Peremennye zvezdy i sposoby ikh issledovaniia.", Moskva: Nauka, 240 p. 1970pzsi.book....T
Tsesevich V.P.: 1971, "Instationary stars and methods of their investigation. Eclipsing variables", Moskva: Nauka, 352 p. 1971isme.conf....T
Vanmunster T.: 2015, PERANSO Light Curve and Period Analysis Software. http://www.peranso.com
Zoła S., Kolonko M., Szczech M.: 1997, *A&A*, **324**, 1010.
Zoła S. et al.: 2010, *MNRAS*, **408**, 464.

DOI: http://dx.doi.org/10.18524/1810-4215.2017.30.118314

IONISATION LOSS AND SHOCK EXCITATION OF $^{44}_{20}$Ca I AND $^{44}_{20}$Ca II ATOMS IN COLD REMNANTS OF TYPE II SUPERNOVAE

D.N.Doikov[1], S.M.Andrievsky[2,3]

[1] Odessa National Maritime University, Dep. of Mathematics, Physics and Astronomy, Odessa, Ukraine, *doikov@mail.bg*
[2] Astronomical Observatory, Odessa National University, and Isaac Newton Institute of Chile Odessa, Shevchenko Park, 65014 Odessa, Ukraine, *andrievskii@ukr.net*
[3] GEPI, Observatoire de Paris, PSL, Research University, CNRS, Univ. Paris Diderot, Sorbonne Paris Cite, Place Jules Janssen, 92195 Meudon, France

ABSTRACT. The light emission ("glow") of cold dusty plasma of the remnant of SN1987A was confirmed by the Hubble Space Telescope observations on 7th January, 1995. In particular, Ca I and Ca II lines were recorded and identified in the spectrum of the supernova's envelope. The period of complete hydrogen recombination in the remnant is 800 days. Thus, it is only radioactive decay that could be a primary source of the plasma light emission at the moment of observation. This paper describes the conditions of shock excitation and recombination of $^{44}_{20}$Ca resulted from the decay of radioactive $^{44}_{22}$Ti travelling in the remnant's cold dust. The over-ionisation in the remnant resulted from the motion of the $^{44}_{20}$Ca recoil nucleus, as well as its impact on the spectrum formation, was studied. It has been shown that the calcium lines are formed by the $^{44}_{20}$Ca II ion in the inner layers of the remnant. We have reached the conclusion that the Ca I/Ca II lines strength ratio corresponds to the isotopic abundance ratio $[^{40}_{20}\mathrm{Ca}]/[^{44}_{20}\mathrm{Ca}]$ in type II supernova remnants.

Keywords: SN1987A remnant, radioactive elements, spectroscopy of Ca I and Ca II.

1. Introduction

Calcium is an alpha-process element along with oxygen, neon, magnesium, silicon, sulphur, argon and titanium. The major source of calcium production in space is the synthesis in type II, Ib and Ic supernovae, as well as in exploding white dwarfs which are progenitors of type Ia supernovae. Large amounts of the stable isotope ^{40}Ca are synthesised in such processes. Its estimated abundance among other stable isotopes on Earth is about 97%. The stable isotope ^{44}Ca also makes a marked contribution, but its origin differs from the mechanism of synthesis of the most common isotope on the Earth. Exploding supernovae enrich the interstellar gas with various chemical elements, including calcium. Subsequently, the interstellar medium provides the raw material for the formation of new generation stars. Yellow supergiants with high luminosity, hence visible at long distances from the Sun, are the most relevant to studying the distribution of calcium in the Galactic disc. Cepheids are also among these objects. The lines of neutral and ionised calcium can be identified in the visible, near-ultraviolet and near-infrared portions of their spectra. As the ionised calcium lines in the near-ultraviolet spectral region are very strong, they cannot be used to determine the calcium abundance in the afore-mentioned stars. An example of calcium distribution in the Galactic disc inferred from the quantitative analysis of the spectra of a large number of Cepheids is presented in Fig. 1.

Cepheids are relatively young objects, hence their average calcium abundance at the galactocentric distance, which is close to the distance of the Sun from the Galactic centre (about 8 kiloparsecs), slightly exceeds the calcium abundance in the solar atmosphere.

As mentioned above, the ionised calcium lines in the near-ultraviolet spectral region cannot be used to precisely determine the calcium abundances in the atmospheres of stars with chemical compositions which do not differ much from that one of the solar atmosphere. However, the situation changes dramatically when we determine the chemical composition of extremely low-metallicity stars. Such stars can be found, for instance, in the halo of our Galaxy. With declining total metal content in a star its calcium abundance also decreases. It results in weakening of subordinate lines which generally serve as indicators of the calcium abundance in stars with normal metallicity. Thus, for extremely low-metallicity stars it is only feasible to use the ionised calcium lines in the near-ultraviolet spectral region (which are sufficiently weak in the spectra of such objects).

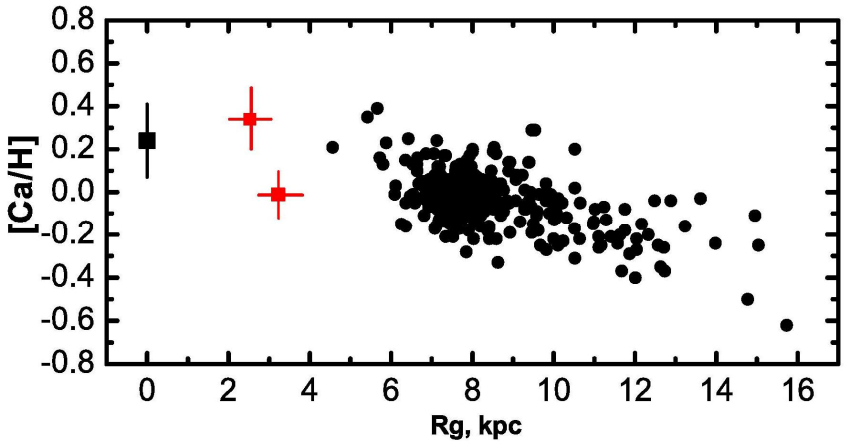

Figure 1: The radial distribution of calcium abundance in the Galactic disc inferred from the analysed spectra of Cepheids (marked with circles and two red squares based on the data reported in Andrievsky et al., 2014). The calcium abundance in the centre of the disc was adopted from the literature. The positions of two Cepheids which are the closest to the Galactic centre are marked with squares. The Y-axis shows [Ca/H] = log (Ca/H)$_*$ – log (Ca/H)$_{Sun}$ where the first term is attributed to the star while the second one – to the Sun; log (Ca/H) is the logarithm of the ratio of calcium to hydrogen concentration in the object's atmosphere. The X-axis presents Rg which is the distance from the Galactic centre expressed in kiloparsecs.

Table 1: The abundances of Ti, Sc and Ca isotopes (as reported by Popov et al., 2014; Jerkstrand et al., 2011) at the instant of ejection of the SN1987A envelope, as well as their estimated amounts at the present time expressed in solar masses.

Studies	$^{47}_{22}$Ti	$^{46}_{22}$Ti	$^{44}_{22}$Ti	$^{43}_{21}$Sc	$^{44}_{20}$Ca	$^{42}_{20}$Ca	$^{40}_{20}$Ca
Popov et al. (2014)	$5.25 \cdot 10^{-4}$	$4.86 \cdot 10^{-5}$	$1.73 \cdot 10^{-3}$	$5.75 \cdot 10^{-5}$	$5.91 \cdot 10^{-4}$	$5.91 \cdot 10^{-5}$	$6.23 \cdot 10^{-2}$
Jerkstrand et al. (2011)		$8.6 \cdot 10^{-4}$	$1.5 \cdot 10^{-3}$	$1.2 \cdot 10^{-6}$			0.043
Present study			10^{-3}		$1.0 \cdot 10^{-3}$		

2. Calcium atoms in the supernova remnant

The ionized calcium lines can be observed not only in the stellar spectra, but also in the ejecta spectra. The type II supernova remnants cool down noticeably while they expand. The formation of dust grains starts just under a year after the explosion. According to Kozasa et al. (1988), the formation of the dust component is only possible in the presence of condensation nuclei which are diatomic molecules. The rates of gas-phase reactions and nucleation decline significantly with time due to a drastic reduction in the material density. Within several decades, the particle density in the supernova remnants makes 10^4–10^6 cm^{-3}. The average thermodynamic temperatures of the ejecta, measured by the intrinsic infrared emission of the dust particles, are within the range of 30–70 K. When the blast wave moves rapidly away from the remnant, the intensity of hard radiation from the forward shock gradually decreases. For the remnants of SN1987A and Cas A, the International Gamma-Ray Astrophysics Laboratory (INTEGRAL) observations enabled us to reveal the evidence of radioactive decay of the titanium isotope which undergoes a two-phase series of β-process according to the following scheme:

$^{44}_{22}$Ti → $^{44}_{21}$Sc through the capture of a K-shell electron 1s ($p + e^- \rightarrow n + \nu_e$); the half-life of $^{44}_{22}$Ti is 48 years;

$^{44}_{21}Sc^* \rightarrow {}^{44}_{20}$Ca with emission of γ-quanta (67.9, 7, 4 and 1157 keV), positron e^+ and with transfer of a considerable momentum to the $^{44}_{20}$Ca nucleus; the half-life of the excited $^{44}_{21}Sc^*$ nucleus is 6 hours.

The decay phase described in item 1 is finished once the $^{44}_{21}$Sc nucleus has been formed. At the instant of time when the $^{44}_{21}$Sc nucleus is formed, it emits an electron neutrino. The nucleus gains a little recoil momentum (2–4 eV). The second phase of the radioactive decay, described in item 2, results in the transfer of high recoil kinetic energy of about 0.61–1.14 MeV to the $^{44}_{20}$Ca nucleus which acquires the velocity of around 10^5–10^6 m/s. When colliding with electrons and atoms of the cold supernova remnant, this energy is sufficient for either collisional ionisation or transition to an excited state. It is known that the total mass of the supernova remnant is M=19$M_\odot$, and its material density is $n \sim 10^{11} - 10^{12}$ m^{-3}. The change in the chemical composition of the supernova remnant envelope is an important effect of the processes specified in items 1 and 2. The initial isotopic composition of SN1987A that we are interested in is adapted from Popov et al. (2014) and given in Table 1.

At the present time, the stable isotope $^{40}_{20}$Ca abundance in the ejecta is an order of magnitude higher than that one of the $^{44}_{20}$Ca isotope. The remnant has greatly cooled down due to its expansion. Atoms of the primordial calcium, which is more abundant, have low

thermal velocities. Taking into account the given estimates, the average number of collisions of the $^{44}_{20}Ca$ isotope with the atoms of the supernova remnant material per unit of time can be calculated:

$$< z \geq = < v > \sqrt{2}\pi\sigma^2 n \approx 10^6 \cdot 1.41 \cdot 3.14 \cdot 2.64 \cdot 10^{-20} 10^{12} \approx 0.16\ \mathrm{s}^{-1} \quad (1)$$

The time interval between binary collisions $t_{binary} = \frac{1}{<z\geq}$ under the given physical conditions is $t \approx 6$ s. It far exceeds the characteristic time of radiative transitions associated with the atomic excitation. Before another mutual collision with atoms and electrons of the surroundings, the Ca I atom and Ca II ion efficiently interact with the radiation field exclusively. In the next section of the paper, we will estimate the energy losses due to excitation and ionisation of cold gas in the supernova remnant caused by the Ca I atom and its ion Ca II.

2.1. Ionisation loss in the cold remnants of SN1987A and Cas A

It is known that cold regions of supernova remnants comprise free radioactive atoms, molecules and dust containing radioactive components. Ionisation loss in the cold remnant is one of the ways their radioactivity manifests itself. The Ca I atom and its ion Ca II may be the sources of ionisation in the above-discussed decay chain. Given the recoil nucleus kinetic energy of 0.6 MeV and a rough non-relativistic approximation of the Bethe-Bloch formula, we can use its exact expression:

$$-\left(\frac{dW}{dx}\right)_{ion} = \frac{4\pi z^2 e^4 n_e}{m_e v^2}\left\{ln\frac{2m_e v^2}{I} - \beta^2 - ln(1-\beta^2)\right\} \quad (2)$$

where n_e is the electron density in the remnant; z_e is the charge of the particle ($z = 20$ for the calcium atom); v is the particle's velocity; β is the relativistic component which equals $\frac{v}{c}$, in our case $\beta \sim 0.01$; $\left(\frac{dW}{dx}\right)_{ion}$ is specific ionisation loss per unit of distance; I is the characteristic full ionisation potential, $I = (13.6$ eV)$\cdot z = 13.6 \cdot 20$ eV $= 270$ eV. The concentration of calcium ions at the forward propagating shock is many orders of magnitude lower than their concentration in the supernova remnant. The $^{44}_{20}$Ca isotope concentration is directly related to the number of decayed $^{44}_{22}$Ti nuclei. Ionisation loss in the material can be expressed as the linear energy loss L:

$$L = \frac{2\pi e^4 z^2 M n_e}{E m_e} \ln\left(\frac{4Em_e}{MI(z)}\right) \approx 2\ eV/10\ \mathrm{km} \quad (3)$$

Given the dimensions of the envelope, it can be deduced that all kinetic energy of calcium atoms is lost in radiative-loss processes. Let us determine the range of l_0 wherein the radiative loss diminishes the initial energy by a factor of e:

$$l_0 = \frac{4.31 \cdot 10^{26}}{n_e Z^2 \ln(183/Z^{1/3})} \approx 4.31 \cdot 10^{13}\mathrm{cm} \quad (4)$$

Physical dimensions of the envelope – remnant of SN 1987A are sufficient to ensure that the $^{44}_{20}$Ca atom transfers almost all kinetic energy in the form of radiative loss to ionise atoms of the remnant material. The process of ionisation of surroundings by the $^{44}_{20}$Ca ion involves binary collisions. In between such collisions, this ion interacts with the radiation field, and when reaching the outer layers of the envelope, its recombination takes place. By the time of recombination (which involves the capture of surrounding "cold" electrons), the $^{44}_{20}$Ca ion velocity decreases significantly down to the thermal velocity value. At this instant, it mixes with other calcium isotopes. The kinetic energy of positrons is proportional to the recoil energy of the $^{44}_{20}$Ca nuclei. The total energy loss of positrons in the remnant makes 10^{36} erg/s. Upon reaching the critical velocity, a positron collides with a cold electron that results in their annihilation and formation of two γ-quanta. The interaction between γ-quanta and gas is rather weak, but these γ-quanta heat the remnant's dust particles to some extent.

2.2. Triple recombination of the $^{44}_{20}$Ca II ions in SNR 1987A

The recombination coefficient α of the $^{44}_{20}$Ca II ion at its concentration N_i with the density of electrons density N_e and neutral atoms N_a in the thin remnant's envelope can be expressed as follows:

$$\frac{dN_i}{dt} = -\alpha N_\varepsilon N_\iota + \beta N_r N_a \quad (5)$$

Here the value β defines the ionisation coefficient of neutral atoms and molecules. To make the capture of an electron by a positively charged ion possible, the kinetic energy of their collision should convert into the energy carried away by the photon. In this case, the recombination cross-section contains the factor $\left(\frac{e^2}{hc}\right)^2$. The most accurate formula (5) for determination of the triple shock-recombination coefficient was inferred in the study by Smirnov (1968) by adjusting the level population of a given atom in the k^{th} state. We assume that N_k and N_n are the densities of atoms in relevant states; N_e is the density of electron states; v is the velocity of electrons; σ_{nk} is the cross-section of the transition of an excited atom from the state n to the state k. The product of the values in angle parentheses is averaged using the Maxwellian distribution function. The value γ_{nk} is the probability of the photon emission per unit of time when a given atom transits from the state n to the state k.

$$\frac{dN_k}{dt} = \sum_n \langle N_e v_e \sigma_{nk}\rangle - N_k \sum_n \langle N_e v_e \sigma_{nk}\rangle + \sum_n \langle N_n \gamma_{nk}\rangle - N_k \sum_n \langle \gamma_{nk}\rangle \quad (6)$$

If the recombination time is noticeably longer that the time interval between collisions of electrons, $\frac{dN_k}{dt} = 0$. In this case, the recombination process can be deemed to be quasi-stationary. As reported in the study referred above, at rather low temperatures the level population can be written as a Boltzmann distribution function. In this case, $N_k \sim e^{-E_{k/kT}}$. If the density of electrons is equal to the density of atoms at low temperatures, then allowing for the collisions with hydrogen, these equations will deliver the estimated coefficient of the shock-radiative recombination $\alpha \sim 10^{-6} cm^3/s$ at

N_e~10^{12} and T~30 – 60 K. If the mean free path of the $^{44}_{20}$Ca II ion is about one metre or greater, then the ion will have sufficient time to recombine prior to the next collision. At low temperatures, the energy of the $^{44}_{20}$Ca II ion collisions with free electrons is consistent with the ionisation energy. The shock-recombination and photo-recombination processes ought to be considered separately as they are not correlated.

We assume that the electron binding energy is E_0. A travelling $^{44}_{20}$Ca II ion undergoes predominantly binary collisions with the atoms of H I, He I, C I, N I, O I, Sc I and Ti I, as well as with electrons. When transiting to the reference system related to the travelling Ca ion, we can deduce that the ion is quiescent while the aforedescribed atoms and electrons have similar velocity 10^8 cm/s. At the instant of collision of the $^{44}_{20}$Ca II ions with any of the above mentioned atoms, a diatomic quasi-molecule is formed. If the adiabatic approximation whereby the motion of nuclei is neglected is true for this molecule, then the following expression is fair: $\frac{\omega Z_1 Z_2}{\mu v^2} \ll 1$ where ω is the energy difference between the investigated states; μ is the reduced mass of the quasi-molecule; v is the relative velocity. In other words, the adiabaticity of collisions is postulated when the Coulomb interaction potential is far lower than the kinetic energy of the incident atom. When $^{44}_{20}$Ca II is travelling in the envelope, this condition is met unless the ion reaches dense outer regions. In such regions the triple recombination is the most likely as the concentrations of hydrogen and helium are orders of magnitude higher than in the region of localisation of iron peak elements.

2.3. Calcium recombination in binary collisions

Incident electrons play a pivotal role in the $^{44}_{20}$Ca II recombination processes. At the time of the shock electron-ion recombination in low-temperature and low-density plasma of the supernova remnant, an electron is in a highly excited state. Thus, the recombination coefficient is defined by the rates of inelastic radiative transitions from highly excited states to the ground state. Let us give the triple recombination coefficients for the atoms of the alkali metals at T = 250K. For the electron density N_e~$10^8$and particle density of 10^{13} cm^{-3} the correspondent's coefficient's is $\alpha \approx 7.8 \cdot 10^{-11}$ and $2.6 \cdot 10^{-6}$. For the low-density plasma, the Born cross-section of inelastic transition is $\sigma = \frac{4\pi e^2}{h^2 v^2}|d_z|^2 L$ where L is the Coulomb logarithm that is not correlated with the relative velocity; d_z is the dipole moment operator. The production formulae can be inferred from the partition function counting all the states:

$$\sigma = \frac{4\pi}{3}\left(\frac{e^2}{hv}\right)^2 L(r^2), \qquad \alpha = const\,\frac{e^4}{h^2}\left(\frac{m}{T}\right)^{1/2}\frac{e^4}{T^2}\frac{e^6 N_i}{T^2} \quad (7)$$

In the study by Smirnov (1968) the constant is 1/3.

Let us present semiempirical recombination coefficients α for the Ca I atom and its ion Ca II in the radiation field of the supernova remnant at temperatures within the range of 10–1000K:

$$\alpha(T) = 27.9\left(\frac{T}{100}\right)^{-0.647};\ \text{Ca I: } \alpha(T) = 5.58\left(\frac{T}{100}\right)^{-0.683}$$

and the rate of photoionization resulted from Melender (2007) is as follows: Ca I: $(3.4-4.3)\cdot 10^{-10}$; Ca II: $(1.3-2.6)\cdot 10^{-12} s^{-1}$. The spontaneous velocities of the allowed dipole transitions can be written as per Landini (1972) and Melender (2007):

$$A_{ij}^{E1} = 2.6774 \cdot 10^9 \left(E_i - E_J\right)^3 \frac{1}{g_i} S_{ij}^{E1}\ (s^{-1}) \quad (8)$$

2.4. Characteristic time of the recombination transitions

The time at which an electron reaches the level with the binding energy of order of ~ T is denoted by τ_b; the time of recombination is denoted by τ_c. The rates of transitions from the state n to the state k, free-bound and bound-free transitions are denoted by ω_{nk}, ω_{cb} and ω_{bc}, respectively. With a rather high density of the supernova remnant the principle of detailed balance is fairly reasonable as the first approximation. Then, the time of transitions can be expressed as the continuum τ_c:

$$\tau_c = \frac{1}{\omega_{b0}}\frac{g_c}{g_0} \approx \frac{1}{N_e <v\sigma> e^6 N_i}\frac{T^3}{e^6 N_i},\ \ \alpha = \left(\frac{1}{\tau N_\varepsilon}\right) \quad (9)$$

An alternative formulation of the Born approximation may be a relevant expression which factors in the energy difference between the recombination transitions from the level with the principal quantum number n to the ground (zero) level with the quantum number 0. In atomic units, the mass of an electron is used as a unit of mass; hence, the energy difference between the excited q_n and ground q_0 levels can be written as follows:

$$q_0 - q_n = \sqrt{2E_0} - \sqrt{2E_n} \approx \frac{2\Delta E}{\sqrt{E_0}} \quad (10)$$

where E_0 and E_n represent the electron energy before and after collision; ΔE is the atom's excitation energy. The following formula can be an additional validity criterion for the Born approximation: $\frac{a\Delta E}{\sqrt{E_0}} \ll 1$. Usage of this criterion significantly simplifies further calculations of the recombination process involving the $^{44}_{20}Ca$ II ion.

Using adiabaticity as a criterion, Bethe deduced a formula for recombination cross-section per one ionised atom (Haykawa, 1969):

$$\sigma_{on} = \frac{8\pi}{v_0^2}(D_x)_{0n}^2 Ln\frac{v'}{|v_0 - v_n|},\ \ D = \sum_i r_i \quad (11)$$

where D is the dipole moment operator; v_0 and v_n are the velocities of the incident electron before and after collision, respectively; v' is the average effective velocity in the region of invalidity of the Born approximation. The $^{44}_{20}$Ca II ion recombination coefficient can be estimated using observations of the structure of the supernova remnant's envelope and localization of the main fraction of the radioactive titanium isotope $^{44}_{22}$Ti performed during Hubble observations of SNR1987A on 7th January, 1995, can be used. In most models of the supernova remnant, the radioactive titanium is concentrated in the same region as iron. The average number density of the iron atoms N_{Fe} at the time of observations was 10^4 cm^{-3}. The electron density N_e is about 0.14 N_{Fe}.

In the same region, 60% of the total $^{44}_{22}$Ti and other heavy elements are found. The mixing ratio between the layers is insignificant; hence, the abundance of $^{44}_{22}Ti$ in other layers is lower. In outer layers containing H and He atoms, the respective density reaches 10^{12} –10^{13} particles per cm^3. At the same time, titanium is absent in these layers while $^{44}_{20}$Ca II penetrating these layers recombines into a neutral $^{44}_{20}$Ca I atom.

2.5. Formation of the remnant spectrum in the ultraviolet (UV), optical and near-infrared (NIR) regions

The Hubble Space Telescope observations of SNR 1987A were conducted in the spectral region from 200 to 800 nm. The observations proved that the escaping radiation spectrum corresponds to the thermodynamic temperature which is 300 K higher than reported by the observations of the dust emission in the infrared region. The formation of the UV and optical radiation fluxes of sufficient intensity requires highly efficient conversion of the radioactive decay energy into the thermal energy of the envelope. In other words, γ-quanta, positrons and recoil nuclei should be thermalized. Taking into account that at present the level of radioactive decays remains practically unaltered while the density and abundance decreased t^3 times, the current abundance is two-three orders of magnitude lower than observed in 1995.

However, γ-quanta and X-rays easily escape from the remnant thereby slightly heating the dust. Thus, positrons with energy of about 0.6 MeV and $^{44}_{20}$Ca recoil nuclei with the kinetic energy of the same order are expected to be the key contributors to the energy balance of the envelope. The subsequent excitation of atoms and molecules occurs via three channels:

The first channel is induced by the UV and other shortwave quanta of the radiation field and results in the formation of the lines of Mg I, Mg II (282.5 nm), Fe II (373 nm), O II (372.7 nm), Ca II((397.3 nm, 730.63 nm).

The second channel is related to the ionization loss due to positron and $^{44}_{20}$Ca recoil nucleus deceleration. The fluxes of energy formed by these shock excitation sources throughout the remnant make up about $4{\cdot}10^{36}$erg/s. The total volume of the envelope at the moment of observations was $V = 10^{50}$ cm^3 (or 30 erg s^{-1}cm^{-3}). The probability of electron transitions from the excited levels to the adjacent levels is significantly higher than the likelihood of recombination transitions. Thus, within the range of radiative losses L_0, the $^{44}_{20}$Ca atom will be in the ionised state while the density of atoms and free electrons in the envelope will decline. It means that calcium is more likely to be in the ionised state rather than in the neutral state as far as the end of the decelerating path. When the kinetic energy of the atom becomes comparable to the particle thermal-motion energy, the recombination of the ion into the neutral Ca atom occurs. In this case, the methods for calculation of the detailed balance for quantum bound states can be employed. The optical and infrared transitions of the neutral atoms of the supernova remnant were analysed in accordance with the data reported by Jerkstand et al. (2011). One of the ways to independently determine the mass fraction of calcium produced by the decay chain is to estimate the ionised and neutral Ca line strengths and their ratios.

The third channel is associated with the cascade transitions caused by the high rate of excitation of $^{44}_{20}$Ca atoms, as well as target atoms in the initial phase of the recoil nucleus motion. These transitions are displayed mainly in the hard UV region, and after conversion by the iron atoms they form an observed field of the remnant radiation in the optical and infrared regions of the spectrum.

The non-thermal source of energy supply resulting from the radioactive decays in the supernova remnant produces excessive scattered non-thermal radiation which is not typical for the diffusion radiation in nebulae. On the other hand, the supernova remnant is quantitatively characterized by the same physical parameters as the nebulae. The absence of the central compact source of hard quanta is offset by the inner radioactive transformations. This effect leads to collisions, induces ionization loss in the remnant and forms a radiation field of sufficient intensity. The Ca II/ Ca I line strength ratio is an important indicator of the radioactive decay processes in the investigated physical system "cold gas + radioactive isotopes". However, this question requires in-depth investigation and should be the focus of a separate paper.

3. On the possibility of the presence of calcium molecular compounds in the supernova cold envelope

Most of diatomic molecules are formed within one year after the explosion. Compounds with rather high ionisation potential are of special interest as the shortwave radiation does not destroy, but only excite the molecules. Both absorption and emission lines are formed: the former belong to the optical and near-infrared regions while the latter represent emission in the far infrared and radio regions. Another condition for the existence of diatomic molecule is the presence of inhomogeneous clumps caused by the Rayleigh-Taylor instability when the material falls on the iron nucleus. Later, these clumps isolate themselves and exhibit densities which are several orders of magnitude higher than the density of the surrounding gas. The probability of the formation of dust and molecules in these clumps is higher. One year later, the dust particles accounting for these clumps efficiently absorb hard UV and X-ray radiation. This enables the dust to screen molecules from quanta which cause their dissociation. The envelope inhomogeneities, which had already isolated within 10–12 years after the explosion, were studied by Varosi & Dwek (1999). Statistical distribution of these inhomogeneities by the data size made it possible to estimate their average size using a sample of one thousand recorded data units. The clumps themselves gradually expand due to their excessive internal pressure. Enhancing the sensitivity of instruments, as well as allowing for the geometric factor, results in the increased number of recorded clumps. Observations of old remnants of type II supernovae confirm these conclusions.

Table 2: The spectroscopic molecular constants for CaO (in cm^{-1})

State	T_{00} – Term energy	State weight (g_i)	Internuclear distance (A)	B_e	α_ε	ω_e	$\omega_e x_e$
$X^1\Sigma$	0.0	1	1.822	0.44452	0.00338	733.4	5.28
$A^1\Pi$	8225	2	2.097	0.3353	0.0015	556.2	2.30

The cellular structure in the envelope should be further considered with the application of the formalism suggested by Varosi & Dwek (1999). We suggest that the spherical approximation should be solved first to determine the lines of elements best suitable for the physical and observational analyses, and then the problem should be solved using a relevant Monte-Carlo method to allow for the specific cellular structure of the object observed.

4. Isotopic composition of the SN1987A envelope

The strengths of molecular lines in the supernova remnant and at the forward shock have greatly increased recently while the X-ray and infrared radiation fluxes have declined. Apart from the suggested criterion for the selection of isotopes by the Ca II and Ca I atomic line strength ratio, let us consider the possibility of the determination of the isotopic shift in the molecules involving $^{44}_{20}$Ca , $^{42}_{20}$Ca and $^{40}_{20}$Ca isotopes while the isotopic ratio gradually changes due to the radioactive $^{44}_{22}$Ti decay.

The isotopic shift in the diatomic molecules depends on the atomic mass numbers. As reported in Herzberg (1949), such a correlation can be expressed as a function of molecular constants of compounds in the parent molecule containing, for instance, $^{40}_{20}$Ca, and the ratio given by the following formula:

$$\rho = \sqrt{\mu_{^{44}_{20}\mathrm{Ca}} \Big/ \mu_{^{40}_{20}\mathrm{Ca}}} = \sqrt{44/40} \approx 1.05.$$

From all diatomic molecules involving calcium isotopes formed in the envelope we select molecules with the maximum ionisation potential and the highest sensitivity to the isotopic shift ρ. The selected molecules should have the highest density and population of the excited levels both at present and in the future. Molecules selected in such a manner ought to exhibit well-measured absorption lines in the UV, visible and NIR regions of the remnant's spectrum. Among diatomic molecules containing Ca atoms in the stellar spectra, the CaO molecule is the most stable with the dissociation potential D_0 = 5–6.11 eV. According to the survey results and new findings reported in Pavlenko & Schmidt (2015), the dissociation energy of the CaH molecule is 1.686–1.974 eV. The detection of the CaC molecule is expected though its ionisation coefficient is an order of magnitude lower than that one of CaH. Thus, the calcium oxide (CaO) molecule appears to be most suitable for the determination of the isotopic shift of spectral lines. The ratios reported in Jorgensen (1994) and Herzcberg (1949) can be applied to perform an assessment of the isotopic shift. It is reasonably convenient to conduct such an analysis for the band heads reported in Doikov et al. (2017) for the transition $A^1\Pi \rightarrow X^1\Sigma$ using the molecular constants given in Table 2 below. The vibrational band-head shift in this case is 4.9183021 cm^{-1} or 4.1 Å in the near-infrared region. In the optical band, this shift will be an order of magnitude less and within the accuracy of spectrometric measurements.

5. Conclusion

The present paper shows the feasibility of observing and identifying the lines of neutral and singly ionised calcium. The availability of the lines of this element for the observations and its involvement in the radioactive decay chain $^{44}_{22}\mathrm{Ti} \xrightarrow{85\,y} {}^{44}_{21}\mathrm{Sc} \xrightarrow{6\,h} {}^{44}_{20}\mathrm{Ca}$ enables us to use the calcium isotope as a chemical marker of the evolution processes in the ejecta of supernova remnants. Different molecular lines appear in the remnant's spectrum after 20–30 years after the supernova explosion. In this regard, the CaO molecule is of special interest. We suppose that the ^{44}Ca/^{40}Ca isotopic abundance ratio may be inferred from the CaO molecular lines using high-resolution spectroscopy.

References

Andrievsky, S.M., Martin, K. P., Kovtuykh, V.V. et al.: 2016, *MNRAS*, **461**, 4256.

Doikov D.N., Savchuk N.V., Yushchenko A.V.: 2017, Odessa Astron. Publ., **30**, 69.

Landini M., Monsignori B.C., Fossi: 1972. *A&A*, **7**, 291.

Melender M., Bautista M.A., Badnell N.R.: 2007, *A&A*, **469**, 1208.

Kozasa T., Yasegava H. and Nomoto K.: 1989, *ApJ*, **344**, 325.

Jerkstand A., Fransson C. and Kozma C.: 2011, *A&A*, **530**, A45, 1-23.

Jorgensen U.G.: 1994, *A&A*, **284**, 179.

Hayakawa S.: 1969, Cosmic ray physics. Nuclear and astrophysics aspects. J. Wiley & Sons. N.Y.

Herzberg G.: 1949, Spectra and Molecular Structure. Van Norst. Reinhold, N.Y.

P'equignot D. and Aldovandi S.M.: 1986, *A&A*, **161**, 169.

Popov M.V., Filina A.A. et al.: 2014, *ApJ*, **783**, 43(Spp).

Pavlenko Ya.V., Schmidt M.: 2015, *Kinem. and Phys. of Cel. Bod.*, **31**, issue 2, 90.

Smirnov B.M.: 1968, Atomic collision and elementary processes in plasma, Moscow: Atomizdat.

Varosi F. & Dwek E.: 1999, *ApJ*, **523**, 265.

DOI: http://dx.doi.org/10.18524/1810-4215.2017.30.114273

RADIOACTIVE MOLECULES IN SN1987A REMNANT

D.N.Doikov[1], N.V.Savchuk[1], A.V.Yushchenko[2]

[1]Odessa National Maritime University, Dep. of Mathematics, Physics and Astronomy Odessa, Ukraine, *doikov@mail.bg*

[2]Sejong University, Seoul, Republic of Korea, *avyushchenko@gmail.com*

ABSTRACT. The investigation of SN1987A remnant is complicated due to absence of the source of ionizing radiation, which should excite the remnant's atoms and molecule. X-ray radiation from the shock wave front and, in accordance with recent observations, the intensity of X-rays significantly decreased during the last year made the backlighting of remnant. At the same time the intensity of molecular lines emission, localized near the front, abruptly increased. The remnant itself can be detected at the longer wavelength due to IR emission of dust component. One of the outburst's results was the synthesis of radioactive isotope $^{44}_{22}Ti$. Its decay time is 85 years, the total mass of synthesized atoms is near the mass of Jupiter. The thermochemical analysis shows that during the last two years the remnant creates a set of diatomic molecules, which will be not a subject of thermal dissociation later. One of these molecules is the radioactive titanium oxide – $^{44}_{22}Ti^{16}_{8}O$.

We investigate the properties of diatomic molecules $^{44}_{22}Ti^{16}_{8}O$ and $^{44}_{21}Sc^{16}_{8}O$ before and after the radioactive decays of $^{44}_{22}Ti$ and $^{44}_{21}Sc$. For oxides $^{44}_{22}Ti^{16}_{8}O$ and $^{44}_{21}Sc^{16}_{8}O$ the spectroscopic constants were calculated using the isotopic shifts with respect to well known $^{48}_{22}Ti^{16}_{8}O$ and $^{48}_{21}Sc^{16}_{8}O$ molecules. The isotope $^{44}_{22}Ti$ captures the electron from internal level. The result is the synthesis of new molecule $^{44}_{21}Sc^{16}_{8}O$. $^{44}_{21}Sc$ decays after 6 hours and creates the stable isotope $^{44}_{20}Ca$, hard X-ray and γ-quanta and positron (e^+). Additional result is the dissociation of molecule and the synthesis of stable neutral isotope $^{44}_{20}Ca$ after the sequence of decays $^{44}_{22}Ti \rightarrow {}^{44}_{21}Sc \rightarrow {}^{44}_{20}Ca$.

We found the energetic properties of transient molecules $^{44}_{22}Ti^{16}_{8}O$ and $^{44}_{21}Sc^{16}_{8}O$. We first estimated the probabilities of radioactive transitions in the molecule $^{44}_{22}Ti^{16}_{8}O$ during its transition to $^{44}_{21}Sc^{16}_{8}O$. We calculated the molecular transitions which allow to point the electronic, vibrational and rotational transitions during the decay $^{44}_{22}Ti \rightarrow {}^{44}_{21}Sc$. The obtained results permit us to predict the new spectral lines and bands detection in the spectrum of SN1987A remnant. It will be emitted by transient molecules and can be identified in future observations.

Keywords: SN1987A remnant, radioactive molecules.

1. Introduction

The supernova explosion 1987A in the Magellanic Clouds was the closest type IIb supernova. The availability of this object for a large number of modern ground-based and space telescopes allowed us to stand up its adequate physical model. During the last 30 years, the structure of the shock wave front, created by an asymmetric explosion, is an important source of information on the surrounding supernova interstellar medium. The front of the shock wave formed X-ray radiation, causing the emission of relic cocoon from which the progenitor was formed as well as the dust remnant. Observations of the IR excess of the remnant allowed obtaining the chemical composition, optical characteristics and particle size distribution. Frank et al. (2016) observed a correlation of energy fluxes in the X-ray and IR spectral regions. The chemical composition and optical characteristics of solid particles were found from observations.

Infrared fluxes from the remnant were first observed one year after the explosion, when the temperature of discarded envelope was noticeably decreased. The basic thermodynamic parameters of remnant were described in a simple, Sedov approximation (Zeldovich & Raizer, 1966). Detailed calculations of the reaction rates taking into account the pressure, concentration of the substance, and temperature in the shell have led to the conclusion that the use of the thermochemical equilibrium approximation at the time frames within 360-900 days after the explosion is justified.

The self-consistent scheme of equations of the kinetics of nucleation of the solid phase in the supernova remnant can be solved. It showed that the formation of dust particles is effective when the diatomic molecules are accepted to be condensation centers. That is why with great certainty it can be accepted that the diatomic molecules were formed simultaneously with dust. Unfortunately, the line spectra of molecules during the indicated period of remnant's evolution were not detected because of the strong dominance of other radiation sources. Later the physical conditions of the shell are such that the formation of diatomic molecules and dust becomes not effective.

Rough estimates show that the total mass of the dust in SNR1987A residue until recently was no more than one solar mass, and the mass of the molecular component can be as high as several solar masses. According to the solution of the thermochemical equilibrium equations for the gas mixture in the remnant, virtually all metals are first

linked into diatomic molecules and then are condensed to the dust (Kozasa et al., 1989). In an atomic form, they can be observed only near the remnant's surface, where due to X-ray illumination, the presence of a shock front, the dissociation of molecules and the evaporation of dust are more intense than inside it. At present time, according to the Sedov's equations and the observations of IR radiation of dust, the average thermodynamic temperature of the remnant is not higher than 100 K, and the concentration of molecules and particles reaches 10^6-10^8 cm^{-3} and below. Under such conditions, only rotational levels can be excited in diatomic molecules, the intensity of which sharply increases against the significant recent drop of the X-ray and IR radiation.

The absence of a high temperature compact source in the remnant's center makes it impossible to excite the vibrational-rotational electronic transitions in diatomic molecules located inside the shell. Purely rotational transitions of molecules can be intensive only under the specific ratios between the Franck-Condon and Henle-London factors. Such conditions are rarely satisfied and are valid only for molecules in which the dipole moment is sufficiently small or zero.

The physical conditions for intense rotational transitions of molecules arise near the shock wave front of and near the surface of the remnant. In these cases, the conditions for shock excitation of the rotational levels of diatomic molecules exist. The similar physical conditions are also valid for regions of the interstellar medium behind the shock wave front.

The probabilities of radiative and impact transitions are high in the regions near the remnant's surface. It is caused by its high intrinsic speed in the interstellar space. Such physical conditions exist at all stages of the remnant's evolution. In this regard, it is clear that the radioastronomical observations will be always important for determining the location of supernova remnants, the shock waves generated by them, and the relict cocoon, which in the past led to the formation of a progenitor star. To perform the spectral diagnostics and to determine the chemical composition of the cold remnant, it is necessary to use the lines of atomic transitions as well as the lines of vibrational-rotational transitions of diatomic molecules.

The only source of excitation of various electronic states of atoms and molecules can be the decay of radioactive isotopes. Modern satellite observations revealed the significant enrichment of supernova remnants of type II with radioactive isotopes – the products of asymmetric supernova explosions. In particular, a significant content of the isotope $^{44}_{22}Ti$ was found.

This review is devoted to the physical signs of the presence of radioactive isotopes in supernova remnants, which can manifest themselves in the form of atomic and molecular lines and bands, and can be observed. Here after we give the review and the new results obtained by authors are presented. Conclusions are drawn about the future observations of supernova remnants. We introduce a new type of molecules and call it Radioactive Molecules.

2. Radioactive Molecules

Molecules in which the nucleus of at least one of the atoms is unstable will be called radioactive. In the overwhelming majority of cases, the radioactive decay of atoms entering the molecule does not give any spectroscopic manifestations, characteristic of diatomic molecules. The molecular spectra are not observed. The decaying nucleus acquires a recoil energy that is many orders of magnitude higher than the energy of the molecular bound, namely several electron volts. That is why the products of such decays exist in an atomic form and increase the fraction of the atomic component in the remnant's chemical composition. However, there is a small group of radioactive nucleus that can carry out electronic capture and do not acquire recoil energy at the time of capture.

In this case, the molecule's internal structure changes. The nucleus of a lower atomic number and charge appears. Here after we will be interested in such changes in the structure of diatomic molecules, for which an electronic transition is allowed and the selection rules are satisfied. In the case of electron K-capture by the nucleus of a radioactive isotope, first the redistribution of electronic and nuclear states occurs in the initial molecule, second a finite diatomic molecule is formed. Depending on the characteristic times of these processes, electronic transitions occur, in particular, similar to vibrational-rotational transitions in usual (non-radioactive) molecules.

For experimental spectroscopy of radioactive diatomic molecules, it is important to know the location of the lines and bands in the emission spectrum. Absorption spectra in this paper are not considered because of the physical and astrophysical features of the objects studied, noted in the previous section.

2.1. Radioactive Molecules in SNR1987A

The information about the initial and boundary conditions of the explosion of the progenitor star allowed to carry out quantitative calculations of the main average thermodynamic quantities, the chemical composition of gas and dust in SNR1987A. A sharp increase in the sensitivity threshold of the recording equipment in the x-ray and gamma wavelength regions made it possible to detect the quanta responsible for the radioactive decay of the isotope of titanium in the chain of radioactive transformations of the type $^{44}_{22}Ti \overset{85\,y}{\longrightarrow} {}^{44}_{22}Co \overset{6\,h}{\longrightarrow} {}^{44}_{22}Ca$ (Grebenev et al., 2012). In this chain of decays, the radioactive isotope of titanium $^{44}_{22}Ti$ forms diatomic molecules: $^{44}_{22}Ti^{16}_{8}O, {}^{44}_{22}Ti^{12}_{6}C, {}^{44}_{22}Ti^{14}_{7}N, {}^{44}_{22}Ti^{1}_{1}H$.

The main part of $^{44}_{22}Ti$ is bound by these diatomic molecules and does not occur in free form. Here after we begin with the molecule $^{48}_{22}Ti^{16}_{8}O$. In spectroscopy of stellar atmospheres this molecule is known for more than 60 years. Its molecular constants were determined by experimental methods and theoretical ab initio calculations. The most studied titanium isotope $^{48}_{22}Ti$ is stable to radioactive decays. To determine the molecular constants of the radioactive molecule of interest, namely $^{44}_{22}Ti^{16}_{8}O$, we use the results obtained by Hertzberg (1949), formulas and data on them. Jorgensen (1994) & Dobrodey (2001) refined the

molecular data and used them to calculate the molecular lines of different titanium isotopes.

Titanium isotopes that we are interested in, namely those with an excess of protons in the nucleus, were not considered earlier. Titanium molecules were important to determine the average absorption coefficient in the atmospheres of cold stars. Molecular bands and lines with the isotope of interest to us, $^{44}_{22}Ti$, in stellar atmospheres are not found. It is radioactive and can be formed effectively only during strong asymmetrical supernova explosions. The planning of observations of molecular bands and their lines in the SN1987A remnant requires the consideration of state of the remnant at present time and in the forthcoming years.

There are no specific sources of excitation of molecular bands and lines. There is no central source of energy in the form of a relativistic object that pushes the widening remnant with a wide range of photons. External illumination by hard radiation from the front of the shock wave only leads to partial dissociation of diatomic molecules in the near surface layer of the residue and does not excite the molecules that are of interest to us. The average thermodynamic temperature of the remnant is 30-60 K. This value was found using IR observations of the dust in remnant. Under these conditions, practically all diatomic molecules under discussion are in the main "frozen" state.

Under these physical conditions, we have an initial radioactive molecule in the ground state. The values of vibrational quantum numbers are zero and the rotational lines can be calculated from the isotopic shift of molecular vibrations inside the vibrational bands for molecules with stable isotopes of titanium ($^{44}_{22}Ti$). It will be shown that the radioactive processes associated with the isotope of titanium lead to a significant change in the quantum state of the molecules.

2.2. Electronic capture in radioactive molecules

The physical phenomena considered below are valid for all molecules which include radioactive isotopes experiencing electron capture at the time of nuclear transformation. From the point of view of future spectroscopic observations, the most interesting isotopes are those with a half-life period much longer than the characteristic time of the electronic transition of the molecule from the excited state to the ground one. As it was noted in the previous section, there are no sources of external excitation in the SN1987A remnant due to low average thermodynamic temperatures. The infrared field of radiation caused by dust particles can only affect the formation of weak rotational lines.

The total Coulomb energy of an atom (or a molecule) will decrease because of a decrease in the charge of the nucleus – the product of the nuclear transformation. The stored potential energy of the molecule is comparable to the molecular binding energy and to the energies of all types of electronic molecular transitions. The excess of the Coulomb potential energy leads to the fact that the state of the initial molecule proves to be unstable and the transition to the stable state of the daughter molecule is forced.

Following the previous sections, the initial radioactive molecule is $^{44}_{22}Ti^{16}_{8}O$, and the daughter radioactive molecule is $^{44}_{21}Sc^{16}_{8}O$. The half-life of scandium is $T_{1/2} = 6^h$, the molecule will exist during the time sufficient to emit a certain number of emission quanta. To date, there is no reliable data on recombination transitions to a hole in a 1s shell of titanium and then scandium, which are part of different molecules. Under low temperatures and low concentrations of the remnant's substance, the probability of such recombination is comparable to the probabilities of purely molecular emission transitions.

The main part of the energy of the radioactive transition accompanying the electron capture in the marked titanium molecules is estimated from the mass difference between $^{44}_{22}Ti$ and $^{44}_{21}Sc$, taking into account the total energy of the captured electron (0.512 Mev) minus the ionization energy 1s of the level $^{44}_{22}Ti$, the total energy of the emitted neutrino (0.1 MeV) and the recoil energy of the nucleus of the newly formed $^{44}_{21}Sc$ -E_{Sc}.

$$E_{Sc} = \frac{(h\nu)^2}{2Mc^2} \approx 2 - 4\ eV \qquad (1)$$

Until recently, it was believed that all types of neutrinos do not have a rest mass like quanta of electromagnetic radiation. The observed oscillations of the energy of these particles led to the understanding that they have infinitesimal rest masses at the upper threshold of the sensitivity of the our hardware. In this case, the formula for E_{Sc} remains valid, taking into account the small correction for the rest mass of the electron neutrino.

3. Electronic transitions in radioactive molecules

The calculation of electronic transitions in diatomic radioactive molecules is to find the wave functions of the initial and final states of two radioactive diatomic molecules, one of whose nuclei participates in the radioactive transformation. For example, $^{44}_{22}Ti^{16}_{8}O \rightarrow {}^{44}_{21}Sc^{16}_{8}O$. The method to choose or calculate molecular constants consists in taking into account the kinematic features and quantum characteristics of the excited and ground levels of radioactive diatomic molecules before and after their excitation in the cold supernova remnant.

In some cases it is convenient to carry out calculations of the spectroscopic properties of titanium oxide on the basis of previously chosen molecular constants (Herzberg, 1949; Huber and Herzberg, 1979; Jorgensen, 1994; Dobrodey, 2001). To implement the electronic transition, the selection rules and statistical sums must be taken inti account. Here after we shall consider only allowed dipole transitions.

3.1. Emission characteristics of transition molecules. The molecule $^{44}_{22}Ti^{16}_{8}O$

The molecule $^{48}_{22}Ti^{16}_{8}O$ will become the starting point of our analysis of the spectroscopic properties of the molecule $^{44}_{22}Ti^{16}_{8}O$. In laboratory experiments, as well as in spectroscopy of stellar and planetary atmospheres, the molecular spectra of $^{48}_{22}Ti^{16}_{8}O$ have been studied in detail. Laboratory experiments on the measurement of spectroscopic constants are also known. Following the method proposed by Jorgenssen (1994), we will search the emission properties of $^{44}_{22}Ti^{16}_{8}O$ using the known parameter of isotopic shift between the $^{48}_{22}Ti$ and $^{44}_{22}Ti$ nuclei in the indi-

cated oxides ρ according to the formula $\rho = \overline{\frac{\mu_{48}}{\mu_{44}}} = 1.011075$, where μ_{48} and μ_{44} are the specific masses of the molecules $^{48}_{22}Ti^{16}_{8}O$ and $^{44}_{22}Ti^{16}_{8}O$, respectively.

As a first step, we find an isotopic shift of the rotational line when the isotope $^{48}_{22}Ti$ is replaced by the isotope $^{44}_{22}Ti$ in the titanium oxide.

$$\begin{aligned}\Delta\nu_r\ J'' &= \nu_{44}\ v,J'' - \nu_{44}\ v,0 - \nu_{48}\ v'',J'' - \nu_{48}\ v'',0\\ &= F_v^{44}\ J' - F_v^{44}\ J'' - F_v^{48}\ J' - F_v^{48}\ J''\\ &= \Delta F_v^{48}\ J' - \Delta F_v^{48}\ J''\\ &= \rho^2-1\ B_e' - \rho^3-1\ \alpha' u'\ J'\ J'+1\\ &\quad + \rho^4-1\ D_e' - \rho^5-1\ \beta' u'\ J'^2(J'+1)^2\\ &\quad - \rho^2-1\ B_e'' - \rho^3-1\ \alpha'' u''\ J''\ J''+1\\ &\quad + \rho^4-1\ D_e'' - \rho^5-1\ \beta'' u''\ J''^2(J''+1)^2\end{aligned}$$

The isotopic shift $\Delta\nu_v(v'')$ relative to the center of the vibrational band for these molecule depends on the molecular constants and the displacements relative to the upper $\Delta G_v(v''$ and the lower $\Delta G_v(v')$ states of the vibrational levels in the molecule $^{48}_{22}Ti^{16}_{8}O$

$$\begin{aligned}\Delta\nu_v(v'') &= \Delta G_v(v') - \Delta G_v\ v''\\ &= \rho-1\ \ u^{\dagger}\omega_e' - u''\omega_e''\\ &\quad - \rho^2-1\ \ u'^2 x_e\omega_e' - u''^2 x_e\omega_e''\\ &\quad + \rho^3-1\ \ u'^3 y_e\omega_e' - u''^3 y_e\omega_e''\end{aligned}$$

Thus, we find the true position of the line (its wave number) in the molecule $^{44}_{22}Ti^{16}_{8}O$ using the expression

$$\nu'\ v'',J''\ = \nu\ v'',J''\ + \Delta\nu_v(v'') + \Delta\nu_r(J'').$$

In this paper we consider cold remnants, and therefore we will only be interested in transitions that lead to the emission of photons. Small values of emission fluxes from cold gas-dust formations are caused by remoteness of the studied objects or by a small concentration of the molecules studied. We will search for possible intense bands in which the molecules emit with higher probability and energy. In order to relate the quantum transitions in the radioactive decay under consideration to emission, the upper limit of the population of the upper excited levels is assumed equal to N.

Here N is the number of decaying isotopes in the given molecules. Without the loss of physical meaning, the population of the excited level can be assumed equal to the number of decaying atoms $^{44}_{22}Ti$. In order to quantitatively determine the number of $^{44}_{22}Ti^{16}_{8}O$ molecules, after determining the position of the center of the vibrational band $\nu'\ v'',J''$ it is necessary to calculate the integral emission coefficient of the electron-vibrational band (Kuznetsova, 1980; Kuzmenko, 1984)

$$k\ v',v''\ = \frac{hc\nu_{v'v''}}{4\pi} A^{nm}_{v'v''} N_{nv'} \qquad (2)$$

$$A^{nm}_{v'v''} = \frac{64\pi^4\nu^3_{v'v''}}{3h}\frac{S_e(r_{v'v''})q_{v'v''}}{(2-\delta_{0,\Lambda'})} \qquad (3)$$

We take into account that this process is going only in one direction and the use of local thermodynamic equilibrium for the calculation of populations is not required in the problem under consideration. In this case, $N_{nv'}$ will be considered equal to N. The coefficients of spontaneous, electron-vibrational transitions with emission $A^{nm}_{v'v''}$ are taken into account without the discussion of induced transitions.

Let us calculate the wave numbers of the lines ν in the electron-vibrational-rotational spectrum arising during the transition from one quantum state to another:

$$\begin{aligned}\nu = \ T_e' - T_e''\ &+ G\ v'\ - G\ v''\\ &+ F\ J'\ - F\ J''\end{aligned} \qquad (4)$$

The first term is called the wave number ν_e of the electronic transition and has a dimension of cm^{-1}. Accordingly, the first two summands are called the beginning of the strip and are denoted as $\nu\ v',v'' = \nu_e + G\ v' - G\ v''$. The initial point of this will be levels with zero rotational energy, i.e. J^'=0, J^'=0. The substitution of the values of molecular constants in the formula (4) makes it possible to calculate the wave number ν for the quanta created by the radioactive β process in the transition like $^{44}_{22}Ti^{16}_{8}O \rightarrow {}^{44}_{21}Sc^{16}_{8}O$.

Using the molecular constants for the well-studied molecules $^{48}_{22}Ti^{16}_{8}O$ and $^{48}_{21}Sc^{16}_{8}O$ according to Jorgenssen (1994) & Herzberg (1949) it is possible to estimate the positions of head's bands and lines of $^{44}_{22}Ti^{16}_{8}O$ and $^{44}_{21}Sc^{16}_{8}O$ molecules as a result of the isotopic shift.

3.2. Selection of excited and ground states in radioactive molecules

The transition of initial radioactive molecule to the excited state before the subsequent radiative transition in the newly formed daughter molecule will be considered in three steps. During the first step, the original molecule with a radioactive core resides in the frozen ground state with zero values of the vibrational quantum number. As noted in the introduction, this is due to the fact that at present time the remnant has a molecular-dust component with an average thermodynamic temperature of the order of 30-60 K.

One-third of the original radioactive titanium $^{44}_{22}Ti$ has already turned into the isotope $^{44}_{20}Ca$, existed in an atomic form. The remaining two-thirds are represented as diatomic molecules. In particular, $^{44}_{22}Ti^{16}_{8}O$. During the second step, at the moment of K-electron capture by a nucleus $^{44}_{22}Ti$ with a filled 1s molecular orbital, the total quantum number J changes by one, the electron shells are rearranged almost instantaneously, simultaneously with this the electronic dipole moment changes. At time intervals in order of magnitude equal to or shorter by 2-3 orders of magnitude, the charge of the titanium nucleus decreases, A nucleus $^{44}_{21}Sc$, whose lifetime is 6^{h}, arises.

It is obvious that for radiative transitions we have sufficient time. Quantum electronic transitions arise. Electronic transitions can be divided into molecular and cascade-recombination to 1s level. At the same time, the lifetime of molecular transitions can take 10^{-8} seconds to reach the main level of the newly formed molecules $^{44}_{21}Sc^{16}_{8}O$. That is why the molecular transition succeeds either during or

after the cascade recombination transition to the 1s-vacancy.

Direct spectroscopic measurements of the recombination transition in a given molecule gave a value of 2478 eV and a dissociation energy of D_0 = 9.5 eV (Dobrodey 2001). The last, third step is the destruction of the molecule $^{44}_{21}Sc^{16}_{8}O$, obtaining a significant recoil energy from the positron emitted from the nucleus $^{44}_{21}Sc$ and the formation of the atom $^{44}_{20}Ca$. During the third step, the movement of the atom $^{44}_{20}Ca$ in the remnant at high speed causes the ionization losses in it.

3.3. Preliminary calculations

The calculation of quantum transitions in radioactive molecules should be started with the determination of molecular constants of the excited $^{44}_{22}Ti^{16}_{8}O$ and of the basic $^{44}_{21}Sc^{16}_{8}O$ molecules. All molecular constants for the main lower levels of $^{48}_{22}Ti^{16}_{8}O$ were revised by Dobrodey (2001). To the lowest singlet states are $a^1\Delta, d^1\Sigma^+$, and the triplet -$X^3\Delta, E^3\Pi$. The energies of the electron terms are: T_e= 3565, 3435, 0, and 13713, respectively. For the molecule $^{44}_{21}Sc^{16}_{8}O$ the doublet transitions $A^2\Pi \rightarrow X^2\Sigma$ (574-730 nm) and $B^2\Sigma \rightarrow X^2\Sigma$ (450-577 nm) are well known. The chemical ties in $^{44}_{22}Ti^{16}_{8}O$ and $^{44}_{21}Sc^{16}_{8}O$ molecules are created by configurations formed by the interaction of valence P and D oxygen shells ($2p^4$), titanium ($3d^2$) and scandium ($3d^1$) shells.

In this case, a large number of quantum states of a diatomic molecule arise as a whole, with different values of the projection of the orbital angular momentum onto its internuclear axe. Namely, $\Sigma^+, \Sigma^\pm, \Sigma^-, \Pi^+, \Pi^+, \Pi^\pm, \Pi^-, \Delta^+, \Delta^-,$ and Φ terms. To determine the configuration of the excited and ground levels in a radioactive molecule, it is also necessary to be guided by the rules for selecting the molecular transitions.

These selection rules are formally analogous to the rules for individual atoms and their ions, in fact supplemented by the projections of the angular and spin moments on the nuclear axis of the diatomic molecule. For the basic and nearest excited molecular levels, we can restrict ourselves to the following rules:

$\boldsymbol{\Delta S = 0}$**.** Molecular transitions of different multiplicity are forbidden.

$\boldsymbol{\Delta\Sigma = 0}$**.** The projection of the spin on the internuclear axis of the molecule should not change.

$\boldsymbol{\Delta\Omega = 0, \pm 1}$ The sum of the projections on the internuclear axis of the spin and orbital angular momentum can vary only in this ratio.

$\boldsymbol{\Delta\Lambda = 0, \pm 1}$ The projection of the orbital angular momentum on the internuclear axis varies within the framework of this equation.

The application of selection rules for radioactive molecules is difficult because of the fact that only singlet and triplet multiplets appear in titanium oxide, while they are doublets in scandium oxide. Those either transitions will be forbidden, or after electron capture by a titanium nucleus 1s-electron, the electron configuration changes so rapidly that the electron from the initial electronic configuration find its position in the newly formed molecule $^{44}_{21}Sc^{16}_{8}O$.

According to the law of energy conservation, the nearest electronic configuration of this molecule must have the energy of the electronic term T_e of the original molecule $^{44}_{22}Ti^{16}_{8}O$. The use of the molecular constants of diatomic molecules permits to find the energy characteristics of all types of allowed transitions. Then the value of the initial energy of the electronic term of the excited state, together with the molecular constants, is chosen for $^{44}_{22}Ti^{16}_{8}O$. And the ground lower state corresponds to the basic doublet level $^{44}_{21}Sc^{16}_{8}O$.

3.4. Selection of molecular constants

Molecular constants of the excited state are chosen in accordance with the ground state of titanium oxide using the physically valid value of the electron term T_e. The used values are pointed in Table 1.

Usually, the electronic structure of a molecule changes almost instantly in comparison with the vibration and rotation of nuclei. This can lead, in our case, to a ban on dipole and rotational transitions in accordance with the above selection rules and to the appearance of purely rotational transitions. In our case, at least, the transition from the triplet to the doublet states is forbidden. Then rotational energy is calculated using the formulas:

$$E'_j = hB_{e1}j\ j-1\ - hD_{e1}j^2(j-1)^2 \qquad (5)$$

$$E''_j = hB_{e2}j\ j+1\ - hD_{e2}j^2(j+1)^2 \qquad (6)$$

Here the anharmonicity of the rotation of diatomic molecules is taken into account. The rule for selecting rotational levels is written as $\Delta j = \pm 1$. In the case of radiation as a result of rotational transitions, we have $\Delta j = 1$. This means the replacement of the rotational quantum number j by j-1. Then the energy of quantum emitted as a result of radioactive transformation of these molecules is:

$$\Delta E = hB_{e2}j\ j+1\ - hD_{e2}j^2\ j+1\ ^2 - hB_{e1}j\ j-1\ + hD_{e1}j^2(j-1)^2 \qquad (7)$$

3.5. Radiation in the vibrational bands

Another variant of the transition state of the radioactive molecule will be the presence of vibrational transitions. In practice, they are allowed within any permitted electronic transition. Any excited electronic state is associated with a change (most often an increase) of the distance between the nuclei r_e. The values of the potential energy for vibrational motion of nuclei near the equilibrium points for better physical clarity will be first written as the Morse potential:

$$E\ r\ = D_e\{1 - e^{-\alpha\ r\ -r_e}\ )\}^2 \qquad (8)$$

Where D_e is the dissociation potential of the molecule, r_e is the equilibrium distance between the nuclei of molecule, β is the conditional force constant determined by the known values of the molecular constants using the formula $\alpha = 2\pi\nu_e\ \sqrt{\frac{\mu}{2D_e}}$, μ is the reduced mass of the radioactive molecule. In the case of the β-decay processes under con-

Table 1. Molecular constants of the molecules $^{44}_{22}Ti^{16}_{8}O$ and $^{44}_{21}Sc^{16}_{8}O$ in the ground state in accordance with Dobrodey (2001) & Jorgensen (1994).

Molecule	*State*	T_e	ω_ε	$\omega_e x_e$	B_e	α_e	$D_e 10^{-7}$	$\beta_e 10^{-9}$	r_e	ν_{00}	D_0
$^{44}_{22}Ti^{16}_{8}O$	$X^3\Delta$		*1009*	*4.2*	*0.53*	*0.033*	*6.03*	*3.4*			*55413.42*
$^{44}_{21}Sc^{16}_{8}O$	$X^2\Sigma$	*0*	*964.9*	*4.5*	*0.52*	*0.00034*	*5.8*	*1.67*			*56266.73*

sideration as an electron capture by a radioactive titanium atom, in the first approximation the reduced mass remains unchanged. The mass change does not exceed the electron mass. The difference of the vibrational energies within the electronic transition in the first approximation is represented in the form:

$$E_{v'} - E_{v''} = D'_e \left(1 - e^{-\alpha'(r_{v'v''} - r_{e'})}\right)^2 - D''_e \left(1 - e^{-\alpha'' r_{v'v''} - r_{e''}}\right)^2 \quad (9)$$

Assuming that $\alpha = \alpha' = \alpha'' = \frac{\alpha' + \alpha''}{2}$, and making the substitutions $F_1 = e^{\alpha r_{e'}}$, $F_2 = e^{\alpha r_{e''}}$,

$$P = F_1^2 D'_e - F_2^2 D''_e,$$
$$Q = F_1 D'_e - F_2 D''_e,$$
$$R_{v'v''} = D'_e - D''_e - E_{v'} - E_{v''}, \quad x = e^{-\alpha r_{v'v''}}$$

we obtain a quadratic equation in which *x* is unknown:

$$Px^2 - 2Qx + R_{v'v''} = 0 \quad (10)$$

The roots of this quadratic equation obtained can be written as the following values of $r_{v'v''}$:

$$r_{v'v''} = -\frac{1}{\alpha} \ln x \quad (11)$$

The simplest estimate of the molecular transition can be the difference in the energies of the lower zero states in molecules $^{44}_{22}Ti^{16}_{8}O$ and $^{44}_{21}Sc^{16}_{8}O$ – ΔE_0:

$$\frac{\Delta E_0}{hc} = \frac{1}{2}(\omega'_\varepsilon - \omega''_\varepsilon) - \frac{1}{4}(\omega'_\varepsilon x'_e - \omega''_\varepsilon x''_e) \quad (12)$$

Substitution of molecular constants from Table 1 gives a value $\frac{\Delta E_0}{hc}$ =43.8 cm^{-1} which corresponds to a wavelength λ = 2.287983 cm. This wavelength is available for observation by radio telescopes. Let us find the necessary Morse potentials of the initial excited state from the molecular data of the ground state of $^{44}_{22}Ti\,^{16}_{8}O$ and the final ground state of $^{44}_{21}Sc^{16}_{8}O$.

Calculations of the vibrational structure of E(r) are usually considered in the form of a Rydberg-Klein-Riesz potential (the so-called RKR potential). Let E(r) be determined by the Morse potential. The energy difference between the vibrational levels of the molecule is comparable to the calculated recoil energies of the E_R nucleus. Then the source of excitation of the vibrational levels of the molecule is the transfer of kinetic energy to the scandium nucleus at the moment of radioactive transformation of titanium.

4. M-L-K emission in radioactive atoms and molecules

Let us consider such a process in the first approximation of a hydrogen-like atom. Namely, the energy difference between the electrons of the first ground level in $^{44}_{22}Ti$ and $^{44}_{21}Sc$. In the atomic system of units, we can write down that the energy of electron at the first quantum level is the function of atomic number:

$$E = -\frac{1}{2}\left(\frac{Z}{n}\right)^2, \Delta E = -20.5 \text{ eB} \quad (13)$$

Thus, during the radioactive transition, the formed daughter molecule $^{44}_{21}Sc^{16}_{8}O$ receives an additional energy of the electrostatic field equal to 20.5 eV. Part of this energy is sufficient for quantum transitions in the formation of a daughter molecule. We can also estimate the closest position of the first level in $^{44}_{21}Sc$ atom:

$$< r >= \frac{1}{2Z}\left(3n^2 - l\,(l+1)\right) = 0.36\ A. \quad (14)$$

As it was noted above, the description of the localization of the 1s^1 orbital near the titanium nuclei and also the scandium gives a relatively accurate value of ΔE. However, the observed wavelength of the recombination X-ray line $^{44}_{21}Sc$ does not correspond to formula (10) and requires the consideration of various types of molecular interactions. The titanium atom and then scandium atom after electron capture in a highly excited ionized states. It leads to cascade of X-ray transitions between the following levels: L-K, M-K, H-L.

The average probabilities of L-K transitions are 68.4%, M-L – 22.2%, and H-K – 2%. In some cases, for light nuclei, the energy of these transitions is not transferred to quanta corresponding for the indicated transitions, but are spent on the extraction of one or more electrons out of the molecule. This process is called the Auger effect. The probability of this effect is small in the discussed process. We note only that in some cases the result of Auger effect is the ionization of molecule, in others the molecule dissociates due to the detachment of the valence electrons participating in the molecular interactions.

X-ray quanta, after their emission, also transmit a certain kinetic energy to the nucleus of the recoil of radioactive scandium, sufficient for excitation of the vibrational levels of the scandium oxide $^{44}_{21}Sc^{16}_{8}O$.

5. Conclusion

The effective pollution of cold gas-dust nebulas can be associated with their enrichment in radioactive isotopes of

chemically active elements produced by remnants of supernovae, stellar winds of giants, supergiants and cosmic rays. The important feature of explosive processes in type II supernovae is the asymmetry. It was first proposed by Zeldovich and Chechetkin (Popov et al., 2014). Numerous theoretical models for calculating the abundances of chemical elements as a result of asymmetric explosions were proposed.

These calculations found that one of the manifestations of the asymmetric explosion is the presence of specific isotopes: $^{44}_{22}Ti$ and other. The pointed titanium isotope forms diatomic molecules. The registration of radioactive species in cold supernova remnants is a new task for molecular spectroscopy. In this review the possibility of detection of isotopic nuclei on molecules during radioactive decays was shown. It should be noted that in earlier investigations the supernova remnants were studied mainly using the radiation of shock-wave fronts.

Taking into account the remoteness of shock wave fronts from actual remnants, for several decades the shock waves highlighted the gas and dust in supernova remnant and gave us the possibility of diagnosis of interstellar medium. The registration of traces of radioactive emissions is associated exclusively with the presence of nonstable isotopes in supernova remnants. Therefore, together with dust particles analysis, the radioactivity is the only source of information about the chemical composition of cold remnants.

The radioactivity of $^{44}_{22}Ti$ is manifested in the form of emission of specific quanta, some of them are similar to those emitted by individual atoms in the γ and X-ray energy diapasons. This review shows that the remaining quanta are of a molecular nature. Namely, they are formed as a result of cascade transitions, after K-capture by the nucleus $^{44}_{22}Ti$ of the 1s electron in the molecule as a result of its strong excitation. We give the set of energy intervals of the emission lines:

1. Cascade transitions 3-4 keV
2. Cascade transitions 30-40 eV;
3. Molecular transitions caused by the presence of recoil energy of the nucleus $^{44}_{21}Sc$ 2-4 eV;
4. Transitions in molecules during the radioactive decay of $^{44}_{22}Ti$ isotope ($^{44}_{22}Ti^{16}_{8}O$ – $^{44}_{21}Sc^{16}_{8}O$). The wavelengths of these lines are close to 2 cm;
5. Radiation due to ionization losses as a result of the motion of $^{44}_{20}Ca$ atom, whose nucleus is the end of a chain of radioactive decays similar to $^{44}_{22}Ti \rightarrow {}^{44}_{21}Sc \rightarrow {}^{44}_{20}Ca$.

Thus, the very fact of detection of emission transitions in the spectral ranges listed above will be the basis for identifying this type of radioactive decay. The determination of the activity of these radioactive elements and their effective amount, and also the time series observations, allows us to reconstruct the physical picture of stellar explosion. The detection of CaI and CaII recombination lines arising during the ionization losses makes it possible the precise identification of atoms and ions of $^{44}_{20}Ca$ isotope in cold remnants.

References

Dobrodey N.V.: 2001, *A&A*, **365**, 642.

Frank K.A., Zhekov S.A., Park S. et al.: 2016, *ApJ*, **829**, 40.

Grebenev S.A., Lutovinov A.A., Tsygankov S.S.: 2012, *Nature*, **490**, 373.

Herzberg G.: 1949, Spectra and Molecular Structure (Van.Norst.Reinhold, N.Y.).

Huber K.P., Herzberg G.: 1979, Spectra and Molecular Structure (Van. Norst. Reinhold, N.Y.).

Jorgensen U.G.: 1994, *A&A*, **284**, 179.

Kozasa T., Yasegava H., Nomoto K.: 1989, *ApJ*, **344**, 325.

Kuznetsova L.A., Kuzmenko N.E. Kuziakov Ia.Ia., et al.: 1980, Probabilities of optical transitions of diatomic molecules (Nauka, Moscow, in Russian).

Kuzmenko N.E., Kuznetsova L.V., Kuziakov Yu.Ia.: 1984, .The Framk-Condon Factors in diatomic molecules (MGU Publ. Moscow, in Russian).

Popov M.V., Filina A.A., Baranov A.A. et al.: 2014, *ApJ*, **783,** 43.

Zel'dovich Ya.B., Raizer Yu.P.: 1966, The physics of shock waves and high temperature hydrodynamics phenomena (Nauka, Moscow, in Russian).

DOI: http://dx.doi.org/10.18524/1810-4215.2017.30.114274

MOLYBDENUM AND RUTHENIUM ABUNDANCES IN COOL STARS OF THE GALACTIC DISC

T.I.Gorbaneva, T.V.Mishenina

Astronomical Observatory, Odessa National University, Odessa, Ukraine
clumpstars@ukr.net, tmishenina@ukr.net

ABSTRACT. We revise the molybdenum and ruthenium abundances in FGK stars with metallicities ranging from −1.0 < [Fe/H] < +0.3. The observed stars belong to the substructures of the Galaxy. The observations were conducted using the 1.93 m telescope at Observatoire de Haute-Provence (OHP, France) equipped with the echelle type spectrographs ELODIE and SOPHIE. The results are based on analyses of spectra that have a typical S/N ~ 100-300 and a resolution of 42 000. These estimates were obtained using synthetic spectra computed with LTE model atmosphere.

Keywords: stars: abundances – stars: late-type – Galaxy: disc – Galaxy: evolution.

Mo and Ru as neutron-capture elements are produced by three different processes, namely the rapid and slow neutron capture process (respectively, the r and s processes) and the p-process. In this work we present and discuss the observations Mo and Ru abundances for FGK dwarfs, located in the Galactic disc with metallicity −1 < [Fe/H] < +0.3. The data obtained will allow exploring ways of production and enrichment by Mo and Ru of the galactic substructures and the Galaxy generally.

1. Observations and atmospheric parameters

The high-resolution echelle spectrographs SOPHIE (R = 75000) and ELODIE (R = 42000) on board 1.93m telescope of OHP (France) for the wavelengths range 4400–6800 ÅÅ were used. Spectral processing carried out by (Katz et al., 1998; Galazutdinov, 1992).

The effective temperatures T_{eff}, the surface gravities logg, the microturbulent velocity V_t, and metallicities of the studied stars were determined earlier in our paper (Mishenina et al., 2013). Effective temperatures T_{eff} were estimated by the line depth ratio method (Kovtyukh et al., 2003). Surface gravities lg g were obtained by two methods: parallaxes and ionization balance of iron.

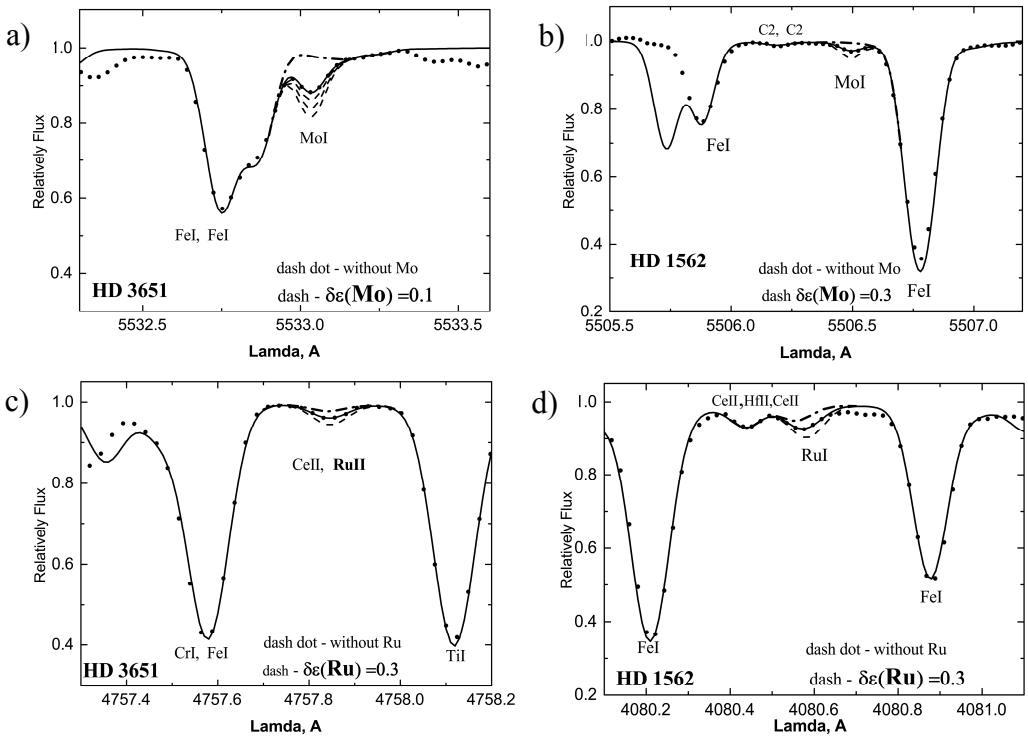

Figure 1: Comparison of synthetic and observed spectra in the region of MoI and RuI lines. Dotted line: observations; solid black lines marked the spectra calculated for the resulted abundances.

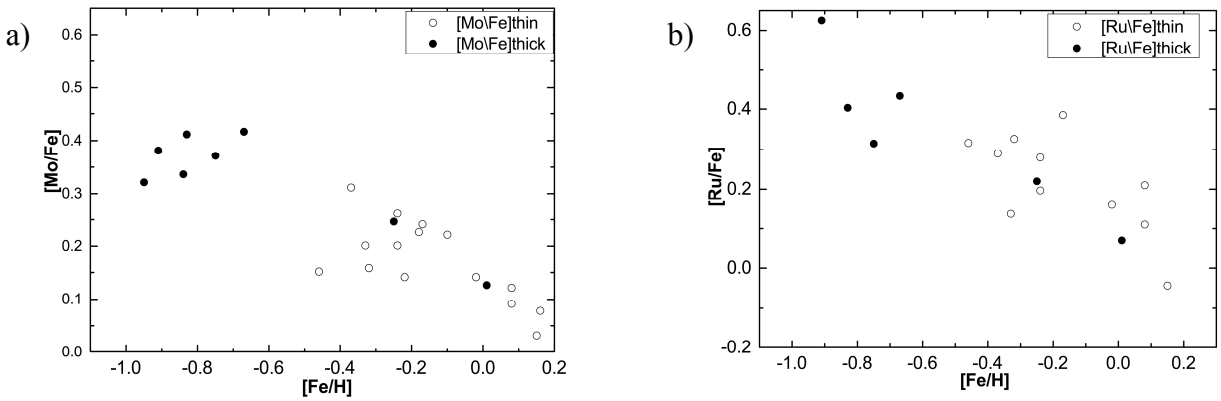

Figure 2: The run of [Mo/Fe], [Ru/Fe] with [Fe/H]

2. Abundances

The following lines, detected in the spectra of the Sun, were considered for abundance determinations in star spectra: λ5506.493, λ 5533.031 for MoI and λ4080.594, λ4584.443, and λ4757.848 for RuI. Determination of the Mo and Ru abundances was made by STARSP LTE spectral synthesis code (Tsymbal, 1996). We used lines, which are weak and do not require to take into account the hyperfine or isotopic structure. The example of comparison of synthetic and observed spectra for MoI and RuI line is shown in Fig. 1.

3. Results and conclusions

Rapid (r) and slow (s) captures of neutrons to some extent describe the behavior of heavy elements. However, recent observations of the distribution of heavy elements in the oldest stars show the limits of this approach, in particularity, overabundance of Mo and Ru (Peterson, 2011). Some stars require processes with a neutron mean density between these processes, which are called the intermediate i process (Jones et al., 2016). Abundances and behavior of underinvestigated elements, such as molybdenum and ruthenium in stars of different metallicities and in various components of the Galaxy permits to study their contribution to enrichment in stars of thin and thick disks and to investigated the sources of their origin.

Here we investigated a small number of stars of galactic discs, and we can preliminary draw conclusions :

1) the abundances of the molybdenum and ruthenium decrease with increasing metallicity in both discs,

2) the abundance of these elements in the thick disc is higher than in the thin one.

In the future, we plan to make a determination of Mo and Ru abundances for a larger number of stars and also we will be performed an analysis from the point of view of the theories of nucleosynthesis and chemical evolution.

Acknowledgments. This work was supported by the Swiss National Science Foundation (SCOPES project No. IZ73Z0-52485).

References

Jones S., Ritter C., Herwig F. et al.: 2016, *MNRAS*, **455**, 3848.
Galazutdinov G.A.: 1992, Preprint SAO RAS, n92.
Katz D., Soubiran C., Cayrel R. et al.: 1998, *A&A*, **338**, 151.
Kovtyukh V., Soubiran C., Belik S. et al.: 2003, *A&A*, **411**, 559.
Mishenina T., Pignatari M., Korotin S. et al.: 2013, *A&A*, **552**, 128.
Peterson R.: 2011, *ApJ*, **742**, id.21.
Tsymbal V.V.: 1996, *ASP Conf. Ser.*, **108**, 198.

DOI: http://dx.doi.org/10.18524/1810-4215.2017.30.117155

CIRCUSTELLAR MATTER ACTIVITY IN AE/BE HERBIG STAR MWC 614

N.Z. Ismailov, A.N.Adigezalzade, U.Z.Bashirova

N. Tusi Shamakhy Astrophysical Observatory of Azerbaijan National Academy of Sciences, Y.Mamedaliyev settl., Shamakhy, Azerbaijan, AZ 5626
hadigozalzade@gmail.com

ABSTRACT. The results of spectral observations of the Herbig Ae/Be type star HD 179218 are presented. Two wave-like cycles of variability in the parameters of hydrogen lines Hα and Hβ with a characteristic time of ~ 40 days are revealed. The first wave of variations is deeper; the branches of decreasing and increasing the spectral parameters of the lines are more clearly expressed. At the time of the first minimum, in the profile of the emission line Hα the appearance and disappearance of additional blue and red emission components are observed. At the same time, narrow absorption components were discovered in the Hβ line. Possible mechanisms of the observed variability of the star are discussed.

Key words: stars: variables: Herbig Ae/Be – stars: circumstellar matter – stars: individual – HD179218

1. Introduction

The Herbig Ae/Be type stars (HAe/Be) are pre-main sequence (PMS) objects of intermediate mass 2-10 $M_{\odot}$ and are considered to be the progenitors of Vega type stars, which are surrounded with a residual protoplanetary disks. Spectral monitoring of individual objects has shown that in the spectra of these stars are observed variable emission and absorption lines (Praderie et al., 1986; Pogodin, 1994; Rodgers et al., 2002; Mora et al., 2004). The same features are also characteristic of classical T Tauri stars (CTTS) (Johns at al., 1995; Schisano et al., 2009; and references therein). It is known that in young stars, emission lines, as well as some absorption lines, are formed in the circumstellar disks or in the envelopes of the stars. Such circumstellar matter can often participate in accretion, polar outflows, winds and other forms of disk interaction with the central star. Tracking the variation in the observed spectral lines makes it possible to perform diagnostics of the physical processes that are occurring in the stellar atmosphere and in the circumstellar environment. In young stars, in particularly, these processes can directly affect the formation of the planets and their evolution. Consequently, one of the important problems in the study of the early stage of evolution of stars is the study of the characteristics of the circumstellar structure and the processes of interaction of the central star with the surrounding matter.

HD 179218 (MWC 614, Sp B9-A2) is an isolated HAe/Be type star. Despite the fact that the star is relatively bright comparatively to other HAe stars, it has been studied less. Only when the star was included in the catalog of The et al. (1994), it became the subject of active research. The circumstellar surroundings of the star were studied by IR photometry and speckle interferometry by (Millan-Gabet et al., 2001), (Prizkal et al., 1997), which did not reveal closely spaced components. Spectral studies of the star were performed by Miroshnichenko et al. (1998) and in more detail (Kozlova, 2004; Kozlova et al., 2017).

According to the classification of (Meeus et al., 2001), the spectral energy distribution (SED) of the star belongs to group I, i.e. starting with the infrared band K and further there is an excess of radiation excited in the dust. On the (Mendigutıa et al., 2012) the profile of the line Hα is consisting of a stable single-peak structure. Perhaps the star has a close companion, about 2.5 arcsec apart (Wheelwright et al., 2010; Fedele et al., 2008) showed that the star has two dust rings at distances of 1 AU and 20 AU, and the space between from 1 to 6 AU from the star filled with gas. The magnetic field of the star was measured by Hebrig et al. (2009) where on the data 2008 they have got about 51 ± 30 G.

The purpose of this paper is to carry out monitoring of the spectral variability of the star on spectral lines of hydrogen obtained in the visual range of spectrum.

2. Observations

Spectral observations of the star were performed at the Cassegrain focus of the 2 m Karl Zayss telescope of ShAO of Azerbaijan NAS by using an echelle spectrometer constructed on the base of the spectrograph UAGS (Ismailov et al., 2013). As a light detector we have used a CCD with 530x580 elements. Observations were performed in the range λ 4700-6700 Å. The spectral resolution is R = 14000. The mean signal to noise level in the region of the line Hα is S/N = 80-100, and in the region of the line Hβ, is S/N = 30-40. Reduction and calibration of the spectrograms is performed in the DECH programs (Galazutdinov, 1992). The method of

observations and material processing is described in more detail in the work of Ismailov et al. (2013).

Observations were conducted for the season May-September 2015. In total, 28 pairs of spectrograms were obtained for 28 nights of observations. For to control of instrument stability and position measurements the spectra of standard stars HR 7300 and HR 7734 for each night were obtained. The equivalent widths EW, the bisector radial velocities V_{bis}, the radial velocities at the peak of the line Vp, the half-widths FWHM (full width at half maximum), the central depths R_λ (intensities) of lines Hα, Hβ, HeI λ5876 Å, D1, D2 NaI, SiII λ6347, 6371 Å, [OI] λ 6300, 6363 Å and diffuse interstellar bands DIB λ 5780 and 5797 Å were measured.

The average error in the intensity measurements as a function of the S/N level was 0.4-0.5% in the region of the Hα line and up to 1% in the region of the Hβ line. Depending on the S/N level, errors in equivalent widths measurements, for example, were from 3% for Hα, up to 30% for [OI] λ 6300, 6363 Å lines. The average error in measuring the radial velocities for individual spectral lines in the spectra of standard stars does not exceed ± 1.5-2.0 km/s.

3. Results

3.1. The line Hα.

This line has a complex structure which consists of an emission component that is superimposed on the core of broad photospheric absorption. The structure of the emission component varies from night to night, sometimes in both the red and blue wings of the line, additional emission components appear and disappear. Figure 1 shows all overlaying profiles of the Hα line, as well as the variation in the root-mean-square deviation σ from the average in intensity for a given value of the radial velocity. Here (and further for other line profiles) the ordinate is given by the ratio relative intensity I/Ic, where I – the intensity at a given wavelength of the spectrum, and Ic – the continuum intensity at the same wavelength. Hence it can be seen that the main variability in the central emission occurs at the peak, and also to a lesser extent on both wings. It is also seen that the intensity varied on the blue wing is noticeably larger than on the red wing.

For radial velocities, we measured the displacement of the central peak of the emission component (Vp), the shift of the line center at half of the residual intensity (bisector velocity V_{bis}). The photospheric wings of the line are very wide and at the continuum level they have a maximum displacement of -1000 km/s and +1000 km/s in blue and red wings, respectively.

Since, as in the blue and red wings of the line, additional emission components appear and disappear from time to time, which could distort the wings of the emission profile, the measured V_{bis} velocity could not always reflect the real displacement of the center of the common emission structure in the line Hα. We also considered for the analysis the character of variation in the radial velocities at the peak of the main emission component.

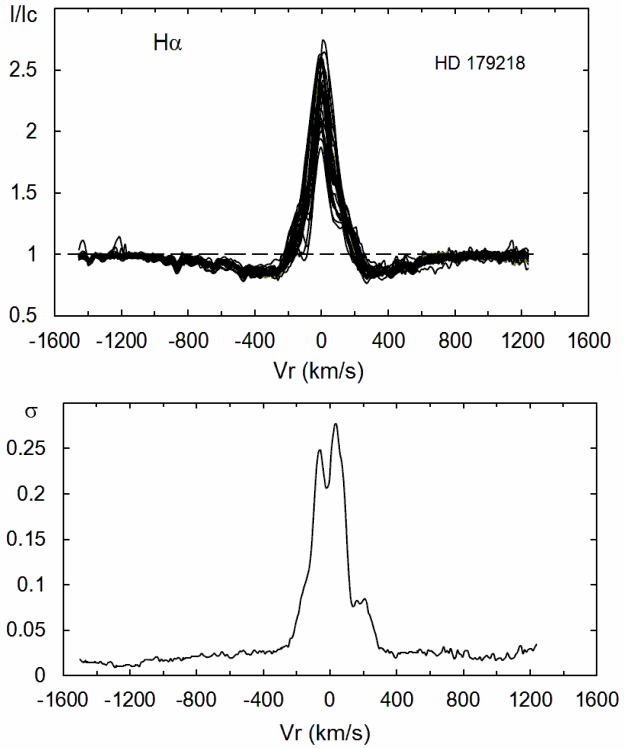

Figure 1: The overlaying profiles of the line Hα (top panel) and variation in the root-mean-square deviation σ of the intensity versus of the radial velocities (bottom panel). Here I – is the intensity at the given wavelength of the spectrum, and Ic – the intensity of the continuum at the same wavelength.

Figure 2 shows the variation with time of the radial velocities V_{bis} and Vp, as well as the equivalent widths of the emission component of the line Hα. As can be seen from these diagrams, both radial velocities and equivalent widths clearly show a wavy-like variation. The variation in the EW of the emission component demonstrates two waves of variation and return to the previous value, where first wave of event is deeper. Both of these waves of variation have duration of about 40 days, in which the general course of the reduction and then the return to the initial position is traced. Analogous variations show the radial velocities Vbis and Vp. In addition, within each 40-day wave-like variations in Vbis and Vp, variability with a small amplitude with a characteristic time of 10 to 20 days is distinguished. The total interval of variations in the parameters Vbis and Vp from peak to peak is 40 km/s and 20 km/s, respectively, while the amplitude of a single small wave in Vbis is about 15-20 km/s, while in Vp it is about 10 km/s. The minima of the EW parameter in time coincide well with the minima of the radial velocity of the Vp, and do not completely coincide with the minima of Vbis. It is seen that equivalent widths are not sensitive to shorter cycles of 10-20 days, which are observed at the radial velocities of the line Hα.

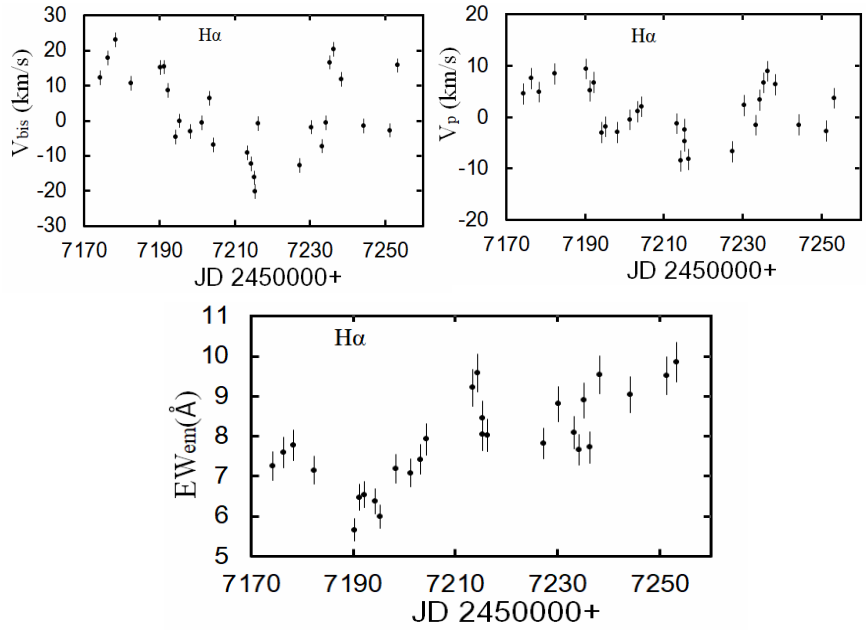

Figure 2: Variation of radial velocities Vbis (upper left panel), Vp (upper right panel) and equivalent widths (bottom panel) of emission component in the line Hα. The values of the vertical bars are corresponding to the average error of parameters.

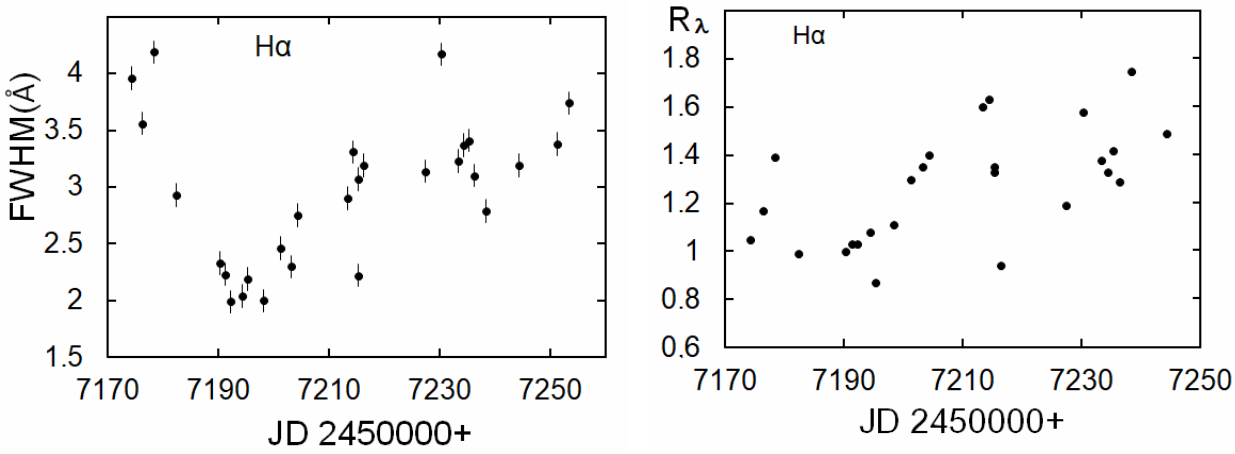

Figure 3: Variation in time of the parameters FWHM (left panel) and R_λ (right panel) of the emission component of the line Hα.

Figure 3 shows the diagram of variations of the half-width FWHM (full width at half maximum) and the absolute value of the intensity R_λ = | 1-I/Ic | of the emission component of the line Hα. As indicated below, the profile of the line sometimes corresponds to Type III according to (Reipurth et al.,1996). This means that the intensity of the emerging additional emission components do not exceed half of intensity of main the emission component. Therefore, the effect of these additional components on the value of the half-width should be negligible. Consequently, the variation in the parameter FWHM and R_λ, rather, is not directly related to the appearance of additional emission components in the line.

From Fig. 3 can be seen that a wavy-like variation in parameters FWHM and R_λ is also observed. The first, deeper wave is continued about 40 days, then followed not so good distinct second wave, which also is occured about 40 days. Each of these waves is expressed by a minimum, areas of decrease and increase in the parameters (EW, FWHM, R_λ, Vp) of the central emission. The first wave of variation is most distinctly revealed. It is characterized by a deeper minimum, where the branch of decreasing of the line parameters was observed in the time interval JD 2457174 – 2457192, and the branch of increasing – in the interval JD 2457194 -2457216 (see also Figures 2 and 3).

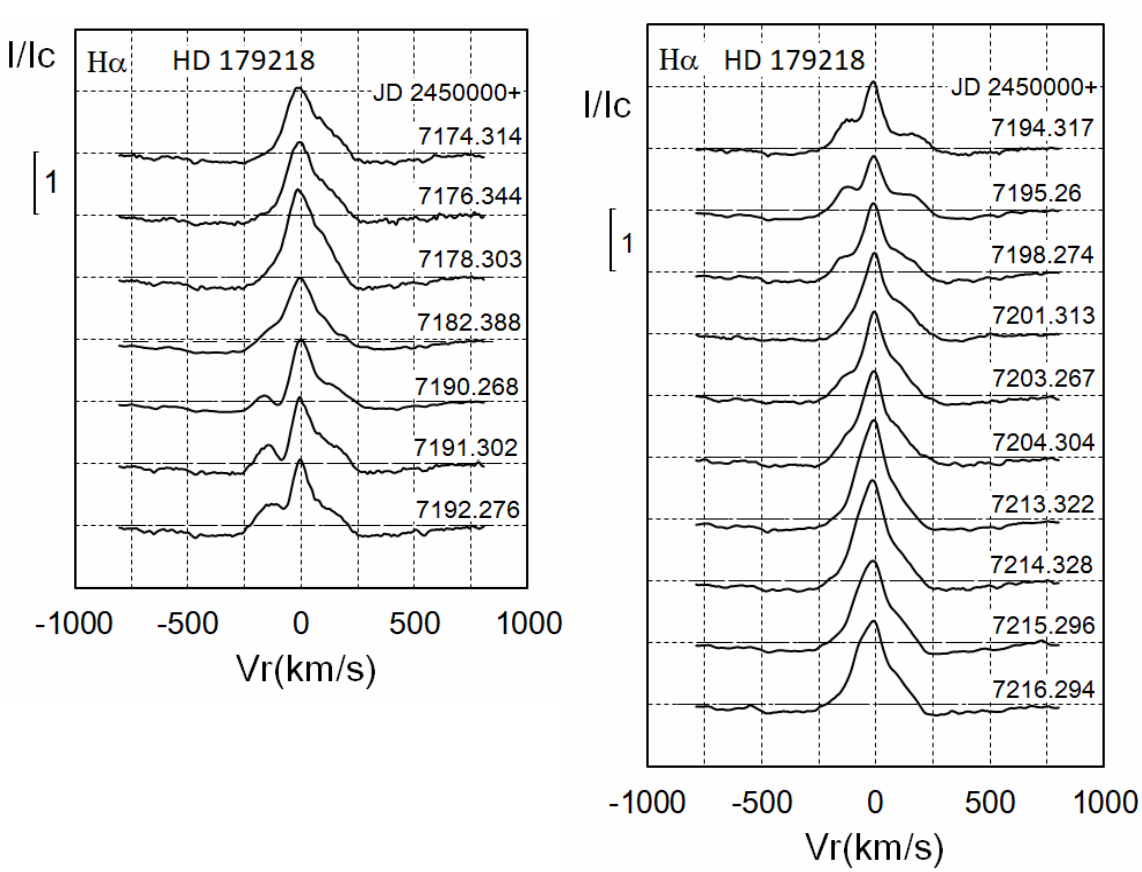

Figure 4: Variations in the profile of the emission component of the line Hα for the descending and ascending branches over 42 days of observations in the first wave-like variations (see Fig. 4).

Figure 4 shows all profiles of the line Hα, obtained in the time interval of about 42 days, when it is occured first deep minimum of variations of parameters of the line. For this time variations in the profile of the line Hα is well traced. The left panel in Fig. 4 corresponds to the time interval in which the spectral parameters are decreased, and the right panel to the time interval for increasing these parameters. As seen from the left panel of Fig. 4, starting from JD 2457190.268 over the next three nights three profiles show the appearance of a clearly marked blue and a weakerly expressed red emission components. As can be seen, in the beginning we have a profile with a central emission component. With the appearance of additional emission components on the blue and red wing, the structure of the profile is transformed from type I to type III according to the scheme of Reipurth et al. (1996). However, the obtained profile is not completely represented in type III according to the indicated classification scheme, because a central emission simultaneously produces an emission component with a blue and a red wings. The displacements of the appeared blue and red components relative to the line core are approximately symmetrical and in different dates are consisting from ± 150 to ± 200 km/s.

The second panel in Fig. 4 on the right shows the results of the continuation of this series of observations, where the same split structure remains in the next 3-4 nights (JD 2457194-2457198). Such a split structure of emission component is observed until night JD 2457198, then on the remaining nights there are profiles with single emission peak. The observed type of the line profile is unstable and was observed only at the minimum of the parameters of the main emission component (see Fig. 1-3). Thus, in just 8 days (JD2457190-2457198) of observations, during the first wave of decreasing in the parameters of the line Hα, it was success to observe the course of the appearance and disappearance of additional emission components.

We also considered the profiles of the line Hα in the time interval of the second wave of parameter variations at JD 2457216-2457253. Among these profiles there are no profiles showing an explicit splitting into different components as in the minimum of the first wave-like of variations. There is a faint hint of the existence of an additional component on the red wing of Hα emissions only in dates JD 2457227 – 2457230. All other line profiles in this time interval are single peaks.

3.2. Line Hβ

In the line Hβ mainly we have observed a wide photospheric profile, on which at some nights are superimposed weak emission peaks. In most cases, such emission peaks are located symmetrically with respect to the line center, and have displacements about from -150 to -270 km/s in blue and from +150 to +250 km/s in the red wings, respectively.

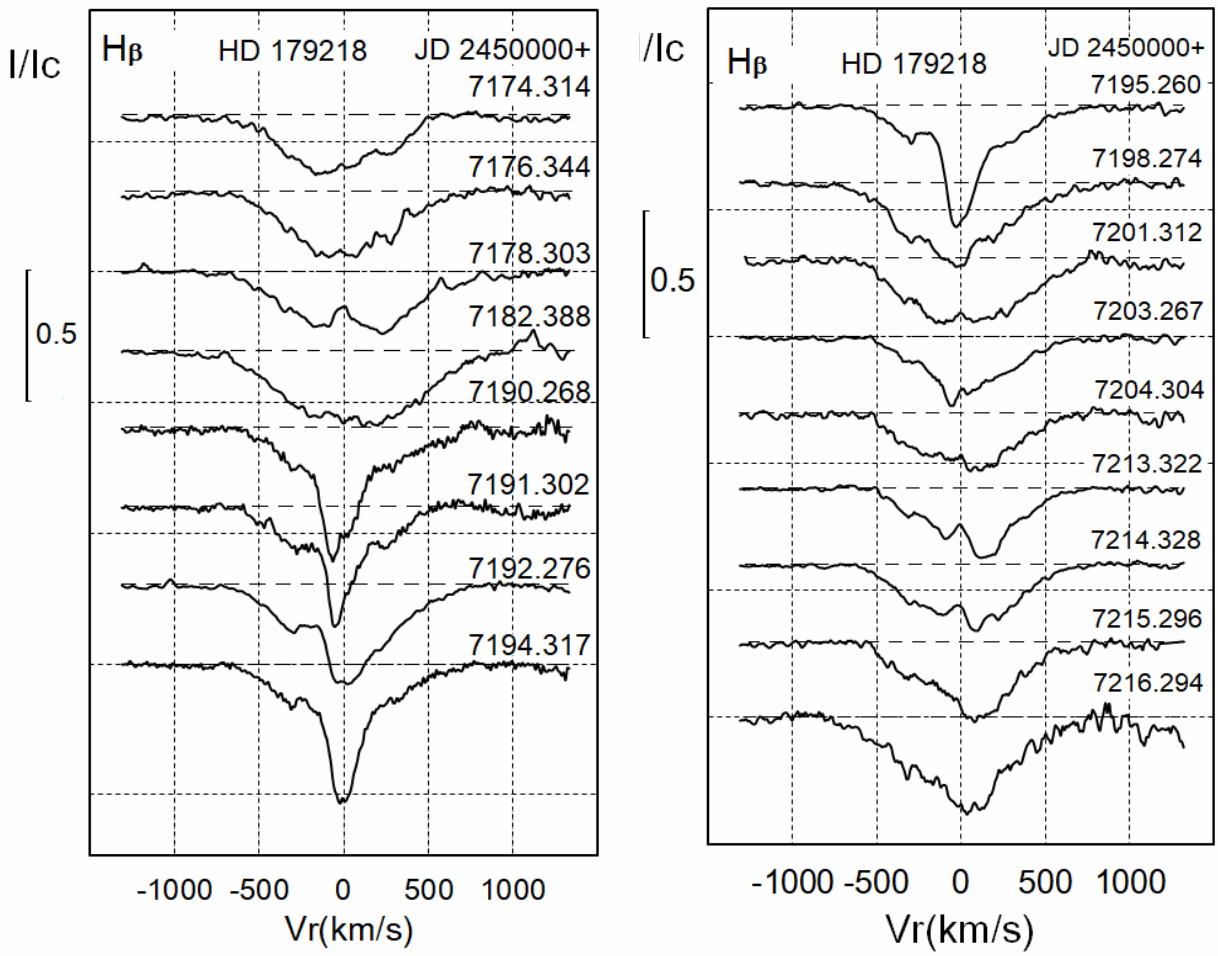

Figure 5: The profiles of the line Hβ obtained at the first wave of variations in the spectral parameters of the line. The left panel corresponds to the time of fall, the second panel, the increase in the spectral parameters of the line.

Among the obtained profiles of the line Hβ, a great interest is represented the profiles and spectral parameters, obtained during of the first wave-like decreasing. In Fig. 5 is shown profiles of the line Hβ, which are obtained on dates, when the spectral parameters in the line Hα were degreased during for the first wave-like variation (JD 2457174 – 2457216). At the beginning, the wide photospheric profiles of the line Hβ with a smooth core and without any special details is observed. As can be seen, with a minimum of the spectral parameters, in JD 2457190-2457195, a significant variation in the profile of the Hβ line is observed – the depth of the line increases, the core becomes narrow and deep, and a weak emission component is superimposed on the wide wings. Such a structure is observed at the line Hβ just at the time when an additional emission component appears in the line Hα (see Fig. 4). Such a coincidence by the dates of these events in the lines Hα and Hβ indicates that in both cases is operated a common mechanism of variability. From the right panel of Fig. 5 shown that after leaving the minimum at JD 2457198, the profile of the Hβ line gradually returns to its original position.

In the Figure 6 shown the diagrams of the time variations in the spectral parameters Vp – the radial velocity of the deepest absorption component, FWHM-absorption half-width, EW-equivalent width absorption, R_λ – depth (intensity) of the line Hβ. As you can see, here too, with the first wave of variations in JD 2457174 – 2457216, a significant variations in the specified line parameters is noticeable. The equivalent width of absorption is increased, the FWHM is sharply reduced, the intensity of the line has increased. The radial velocities of the line peak over the whole observation season give a significant shift from -100 to +100 km/s. The wave-like variation is best observed here in the parameter R_λ.

Figure 6 shows the diagrams of the variations in the spectral parameters Vp-the radial velocity of the deepest absorption component, FWHM-absorption half-width, EW-equivalent absorption width, Rλ-depth (intensity) of the Hβ line with time. As you can see, here too, with the first wave of variations in JD 2457174 – 2457216, a significant variation in the specified line parameters is noticeable. The equivalent width of absorption is increased, the half-width is sharply reduced, the intensity of the line has increased. The radial velocities of the line peak over the whole observation season give a significant shift from -100 to +100 km / s. The wave-like variation is best observed here in the parameter R_λ of the line.

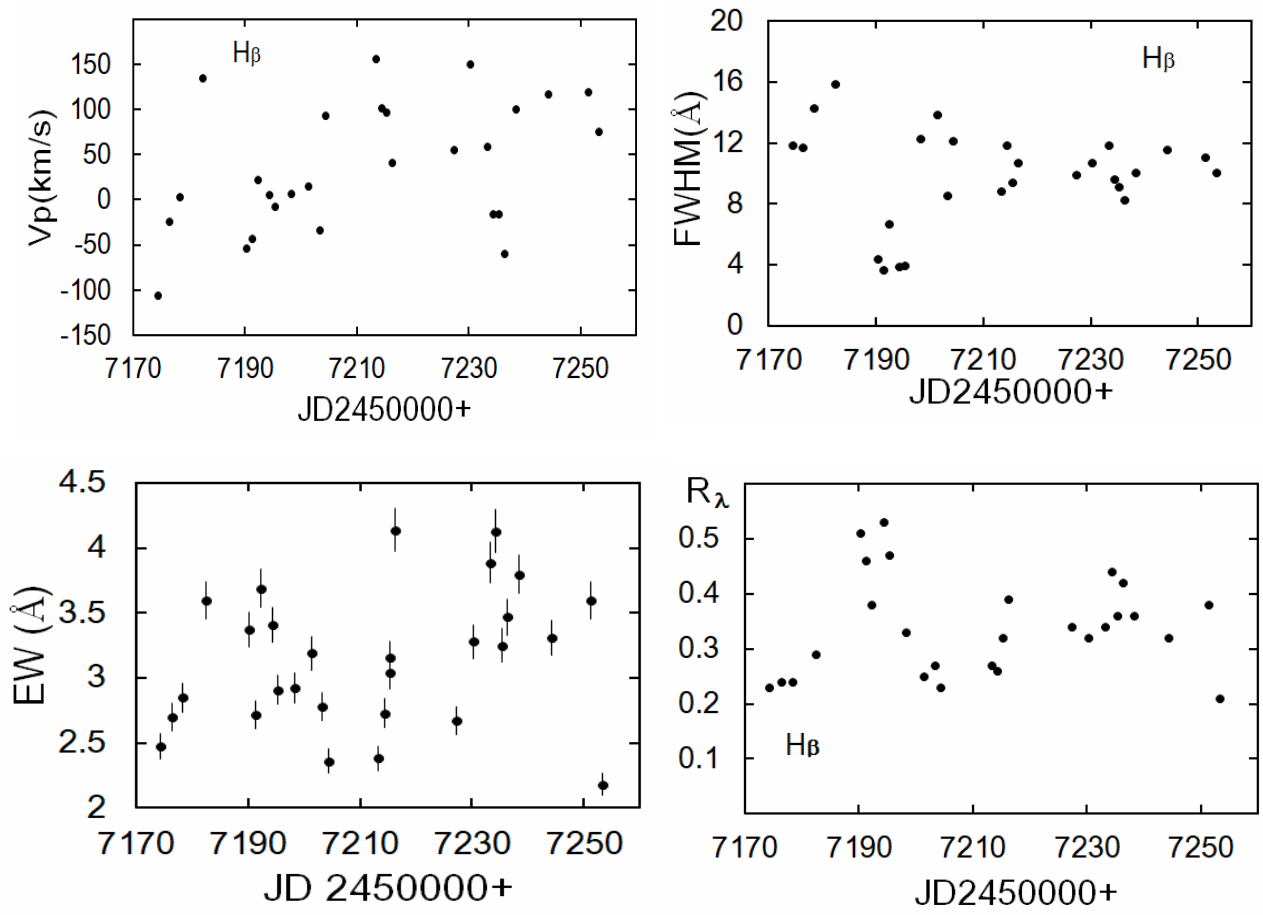

Figure 6: The time variation of the radial velocity of the peak Vp (upper left panel), half width FWHM (upper right panel), equivalent width EW (lower left panel) and intensity R_λ (lower right panel) of the line Hβ.

4. Conclusion

The rotation velocity of HD 179218 in (Bernacca et al., 1970) is 60 km/s, and (Guimaraes et al., 2006) gives the value υsin i = 72 ± 5 km/s. According to (Dent et al., 2005) the angle of inclination to the axis of rotation of the star is about 40°. Then, if we consider the observable minimum characteristic time equal to 10 days, for the rotation velocity of the star we obtain υ = 112 ± 8 km/s and for the star radius R*- about 22 $R_\odot$, which is not reasonable and differs significantly from the data of (Alecian et al., 2008) (~4.8 $R_\odot$). An even greater discrepancy is obtained for the radius if we take the angle i = 20°, as suggested by Leinert et al. (2004). This means that the observed cycle of about 10 days can not be a period of axial rotation of the star. Remaind that the characteristic time of 10 days is obtained from the variation in the radial velocities of the peak of dominant emission component and the intensity of the line. Therefore, it should be assumed that it arises in the outer parts of the disk. However, if the observed 10-day activity is related to the axial rotation of the disk, it can be assumed that such a variation could occur at the boundary between the matter accretion and outflow. Then one of the assumptions of the cause of the observed variations in the emission lines of the star may be the existence of a stellar magnetosphere. In favor of the possibility of the existence of magnetospheric accretion, the star is also proposed in the work of (Mendigutıa et al., 2017). The main indicator existence of the magnetosphere of the star is the strength of magnetic field. In classical T Tauri stars, for which the presence of the magnetosphere is assumed, the magnitude of the magnetic field is several KGs (see, for example, Bouvier et al., 2007). However, the result of measuring the magnetic field of star HD 179218 shows the existence of a weak magnetic field (Hebrig et al., 2009).

It is also possible that a star can be a spectral-binary or multiple system. In fact, it is difficult to explain the observed wave-like variation of the radial velocities and other parameters of the line Hα. (Kozlova et al., 2017) showed that the dependence of the brightness V on the color index V-I has two separate distributions. This fact is accepted by the authors in favor of the binarity of the star. The time of our observations from May to September 2015 corresponds to the minimum of the 4000-day cycle of variability founded by (Kozlova et al., 2017). Therefore, the observed features of the variation in the spectrum in the line Hα can be related to the moment of the star's stay at the minimum of the 4000-day cycle. Then the results obtained by us, perhaps, are a kind of unique event and can be observed only in the minima of the 4000-day cycle. Our observations have shown that in order to

elucidate these questions it is necessary to perform a more dense series of photometric and spectral observations of the star.

Based on the results obtained in this paper, we can draw the following conclusions:

1. There are two wave-like variations lasting about 40 days each, in the parameters of the emission component of the Hα line in the spectrum of the star HD 179218. The first wave is deeper, the second is relatively less significant, and possibly distorted by fluctuations.

2. An unusual variation in the profile of the Hα line near the minimum in the descending and ascending branches of the first wave of variations in the spectral parameters was observed. At the entrance to the minimum and during the passage of the minimum, appearance and disappearance of additional emission components in the line Hα was detected. The displacement of each components corresponds to approximately ± 150 km/s. During the rest of the observation time, such profiles were no longer detected.

3. With the first wave of variations, the parameters of the Hβ line showed a synchronous variation in time with the line Hα. At the time of appearance of additional emission components near the line Hα, narrower and deeper components appear at the line Hβ.

4. Within each 40-days wave-like variations, a small amplitude fluctuation of the radial velocities of the peak of the emission component and the intensity of the Hα line with a characteristic time of about 10-20 days is observed. Also, the half-widths and intensities of the line Hβ more clearly demonstrate the existence of 10-20 day wave-like variations.

References

1. Alecian E., Catala C., Wade G. A. et al.: 2008, *MNRAS*, **385,** 391.
2. Bouvier J., Alencar S.H.P., Harries T.J. et al.: 2007, in: *Protostar and Planets V*, Univ. Arizona Press, p. 479.
3. Dent W.R.F., Greaves J.S., Coulson I.M.: 2005, *MNRAS*, **359,** 663.
4. Fedele D., Van den Ancker M.E., Acke B. et al.: 2008, *Astron. and Astrophys.*, **491**, 809.
5. Galazutdinov G.A.: 1992, *Prepr. of the Special Astrophysical Observatory*, **№.92**.
6. Guimaraes M.M., Alencar S.H.P., Corradi W.J.B., Vieira S.L.A.: 2006, *Astron. and Astrophys.,* **457,** 581.
7. Johns C.M., & Basri G.: 1995, *AJ*, **109,** 2800.
8. Hebrig S., Stelzer B., Schöller M. et al.: 2009, *Astron. and Astrophys.*, **502,** 283.
9. Ismailov N.Z., Bahaddinova G.R., Kalilov O.V., Mikailov Kh.M.: 2013, *Astrophys.Bull.*, **68,** №2, 196.
10. Kozlova O.V.: 2004, *Astrophys.*, **47,** № 3, 287.
11. Kozlova O.V., Alekseev I.Yu.: 2017, *ASP Conf. Ser.*, **510**, 153.
12. Leinert Ch., van Boekel R., Waters L.B.F.M. et al.: 2004, Astron. and Astrophys., **423**, 537.
13. Mora A., Eiroa C., Natta A. et al.: 2004, *A&A*, **419,** 225.
14. Miroshnichenko A.S., Bjorkman K.S., Mulliss C.L. et al.: 1998, PASP, **110,** 883.
15. Mendigutía I., Eiroa C., Montesinos B., Mora A., Oudmaijer R.D., Merín B., Meeus G.: 2011, *A&A*, **529,** A34.
16. Mendigutıa I., Oudmaijer R.D., Mourard D., Muzerolle J.: 2017, *Monthly Notices Royal Astron. Soc*., **464,** 1984.
17. Mendigutıa I., Mora A,, Montesinos B. et al.: 2012, *A&A*, **543,** A59.
18. Millan-Gabet R., Schloerb F.P., Traub W.A.: 2001, *Ap.J.*, **546,** 358.
19. Praderie F., Simon T., Catala C., Boesgaard A.M.: 1986, *ApJ*, **303,** 311.
20. Pogodin M.A.: 1994, *A&A*, **282,** 141.
21. Pirzkal N., Spillar E.J., Dyck H.M.: 1997, Ap.J., **481,** 392.
22. Rodgers B.,Wooden D.H., Grinin V. et al.: 2002, *ApJ*, **564,** 405.
23. Schisano E., Covino E., Alcalá J.M. et al.: 2009, *A&A*, **501,** 1013.
24. The P.S., De Winter D., Perez M.R.: 1994, *A&ASS*, **104,** 315.
25. Wheelwright H.E., Oudmaijer R.D., Goodwin S.P.: 2010, *Monthly Notices Royal Astron. Soc.,* **401,** 1199.

DOI: http://dx.doi.org/10.18524/1810-4215.2017.30.117671

UPDATED LIGHT ELEMENTS OF 10 RRAB STARS IN THE ANTLIA, CAELUM AND SCULPTOR CONSTELLATIONS

A.Kolotsey, M.Atroschenco, S.A.Dubrouski, I.I.Baluk

The Regional Centre of Technical Creativity of Children and Youth (RCTCCY)
36A Oktyabrya Avenue, Gomel 246010 Belarus
toliman@tut.by; balig@tut.by; bis6411@gmail.com

ABSTRACT. This paper presents the results of verification of the periods and other characteristics of 10 variable stars. The All Sky Automated Survey (ASAS) data have been used in this verification study. 10 RRab stars in the Antlia, Caelum and Sculptor constellations have been investigated. The study was performed using the software package developed by S.A.Dubrouski and V.P.Goranski.

ASAS J043516-4112.4

The star was discovered by G.Pojmański in 2002 [1]. In 2015 the star was described in the paper by G.Torrealba [2]. The period of the star has been refined by I.I.Baluk. The UCAC4 position of the star: RA = 04h35m16.45s; Dec =
-41º12´33˝.4. The star's catalogue identifiers: the 2MASS identifier – J04351645-4112333; the GSC identifier – 07582-00453; the USNO identifier – B1.0 0487-0041252; the UCAC4 identifier – 244-004867; the ASAS identifier – J043516-4112.4. The star's variability type: RRab. The peak brightness is 12.68m (in the V band); the minimum brightness is 13.02m (in the V band). The star's light ephemerides are plotted in Figure 1. M – m = 23%.

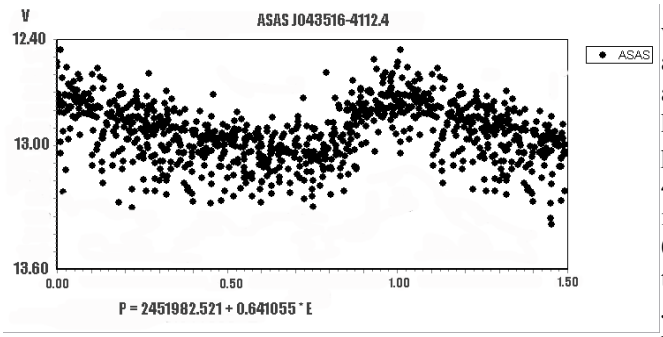

Figure 1

ASAS J042716-4828.0

The star was discovered by G.Pojmański in 2002, and further investigated by D.M.Szczygieł, G.Pojmański and B.Pilecki [3], as well as by G.Torrealba, M.Catelan and A.J.Drake [4]. An individual investigation of the star was conducted by I.I.Baluk. The UCAC4 position of the star: RA = 04h27m16.34s; Dec = -48°28´04˝.0. The star's catalogue identifiers: the 2MASS identifier – J04271633-4828040; the GSC identifier – 08072-01147; the USNO identifier – B1.0 0415-0035016; the UCAC4 identifier – 208-004473; the ASAS identifier – J042716-4828.0; the CD identifier – 48 1347. The star's variability type: RRab. The peak brightness is 11.53m (in the V band); the minimum brightness is 12.22m (in the V band). The star's light elements are depicted in Figure 2. M – m = 21%. The Blazhko effect is barely noticeable.

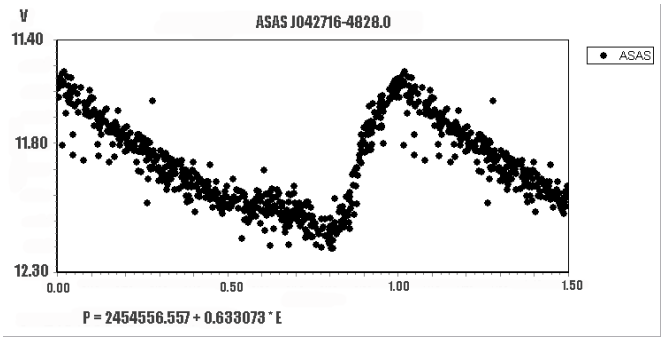

Figure 2

ASAS J042014-4236.2

The star was discovered by G.Pojmański in 2002 [5]; it was further investigated by D.M.Szczygieł, G.Pojmański and B.Pilecki [6], as well as by G. Torrealba, M. Catelan and A.J.Drake [7]. An individual investigation of the star has been conducted by Anastasia Kolotsey. The UCAC4 position of the star: RA = 04h20m14.26s; Dec = -42°36´10˝.5. The star's catalogue identifiers: the 2MASS identifier – J04201425-4236105; the GSC identifier – 07584-00479; the USNO identifier – B1.0 0473-0053076; the UCAC4 identifier – 237-004452; the ASAS identifier – J042014-4236.2. The star's variability type: RRab. The peak brightness is 13.20m (in the V band); the minimum brightness is 14.25m (in the V band). The star's ephemerides are presented in Figure 3. M – m = 20%.

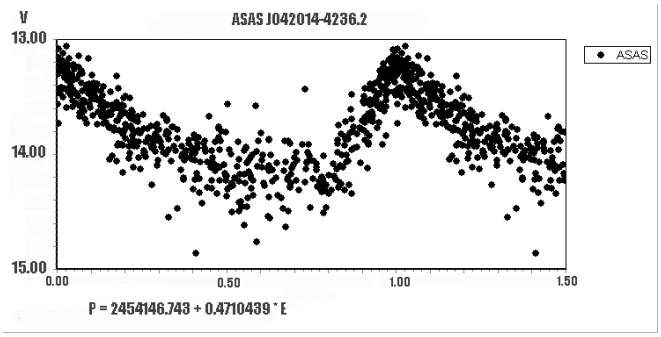

Figure 3

BK Ant, ASAS J094415-3939.7

The star was investigated by W.Strohmeier and I.Patterson in 1969 [8]; its further study was conducted by G.Pojmański in 2002 [9]. The star was also investigated by N.N.Samus in 2008 [10], and later by D.M.Szczygieł, G.Pojmański and B.Pilecki in 2009 [11]. Anastasia Kolotsey has reported the results of her individual investigation of the star. The UCAC4 position of the star: RA = 09h44m14.80s; Dec = -39°39′41″.0. The star's catalogue identifiers: the 2MASS identifier – J09441481-3939411; the GSC identifier – 07697-00594; the USNO identifier – B1.0 0503-0193681; the UCAC4 identifier – 252-037970; the ASAS identifier – J094415-3939.7. The star's variability type: RRab. The peak brightness is 11.83m (in the V band); the minimum brightness is 12.35m (in the V band). The star's ephemerides are plotted in Figure 4. M – m = 21%.

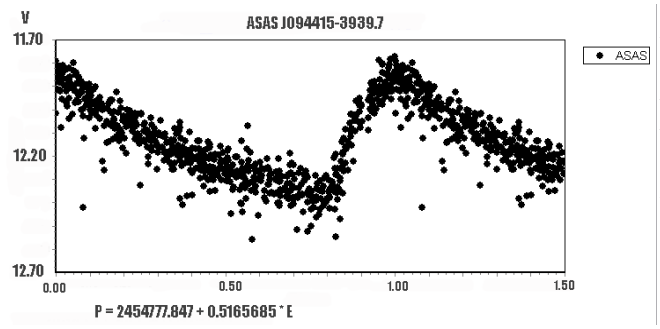

Figure 4

BN Ant, ASAS J095706-3917.4

The star was studied by W.Strohmeier, R.Knigge and H.Ott in 1965 [12]. G.Pojmański conducted further investigation of the star in 2002 [13]; his results were extended by E.V.Kazarovets, N.N.Samus, O.V.Durlevich, N.N.Kireeva and E.N.Pastukhova in 2008 [14]; D.M.Szczygieł, G.Pojmański and B.Pilecki in 2009 [15]; and G.Torrealba, M.Catelan, A.J.Drake, S.G.Djorgovski, R.H.McNaught, V.Belokurov, S.Koposov, M.J.Graham, A.Mahabal, S.Larson and E.Christensen in 2015 [16]. Milena Atroschenco has reported the results of her individual investigation of the star. The UCAC4 position of the star: RA = 09h57m05.98s; Dec = -39°17′26″.4. The star's catalogue identifiers: the 2MASS identifier – J09570598-3917264; the GSC identifier – 07694-02169; the USNO identifier – B1.0 0507-0211233; the UCAC4 identifier – 254-041200; the ASAS identifier – J095706-3917.4. The star's variability type: RRab. The peak brightness is 11.68m (in the V band); the minimum brightness is 12.93m (in the V band). The star's ephemerides are presented in Figure 5. M – m = 14%.

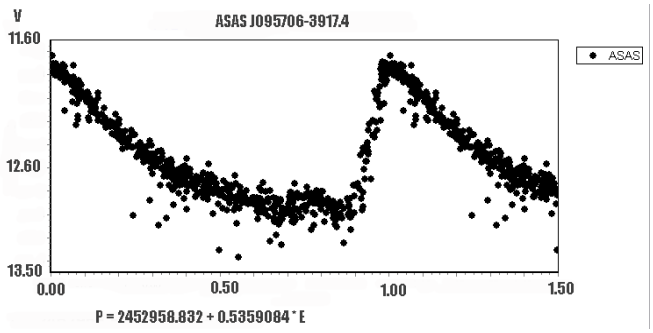

Figure 5

SS Ant, ASAS J093911-2633.1

The star was investigated by Emily Hughes Boyce in 1936 [17] and later by V.P.Tsesevich, M.S.Kazanasmas [18]; G.Pojmański [19]; N.N.Samus, E.N. Pastukhova and O.V.Durlevich [20]; D.M.Szczygieł, G.Pojmański and B.Pilecki [21]; G.Torrealba, M.Catelan, A.J.Drake, S.G.Djorgovski, R.H.McNaught, V.Belokurov, S.Koposov, M.J.Graham, A.Mahabal, S.Larson and E.Christensen [22]. The study of the star has been updated by I.I.Baluk. The UCAC4 position of the star: RA = 09h39m10.96s; Dec = -26°33′08″.2. The star's catalogue identifiers: the 2MASS identifier – J09391095-2633080; the GSC identifier – 06610-01195; the USNO identifier – B1.0 0634-0256695; the UCAC4 identifier – 318-060956; the ASAS identifier – J093911-2633.1. The star's variability type: RRab. The peak brightness is 12.81m (in the V band); the minimum brightness is 14.25m (in the V band). The star's ephemerides are plotted in Figure 6. M – m = 15%. The Blazhko effect is visible.

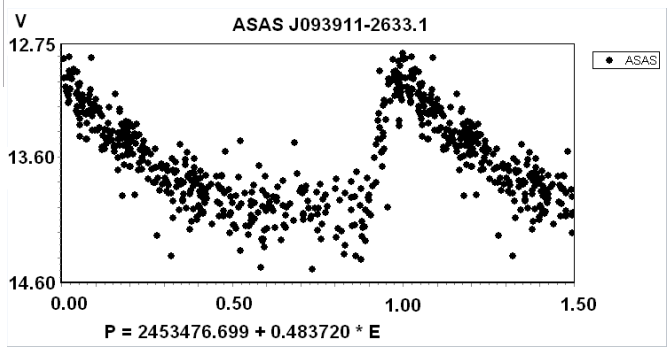

Figure 6

AL Pic, ASAS J044131-5216.6

The star was investigated by Willem Jacob Luyten in 1938 [23]. The results were later extended by G.Pojmański [24]; P.Wils and A.Sodor [25]; E.V.Kazarovets, N.N.Samus, O.V.Durlevich, N.N.Kireeva and E.N.Pastukhova [26]. I.I.Baluk has presented the results of his individual study of the star. The UCAC4 position of the star: RA = 04h41m30.80s; Dec = -52°16′37″.0. The star's catalogue identifiers: the 2MASS identifier – J04413082-5216370; the

GSC identifier – 08082-00469; the USNO identifier – B1.0 0377-0058120; the UCAC4 identifier – 189-004707; the ASAS identifier – J044131-5216.6. The star's variability type: RRab. The peak brightness is 12.80m (in the V band); the minimum brightness is 14.11m (in the V band). The star's ephemerides are depicted in Figure 7. M – m = 25%. The Blazhko effect was detected by I.I.Baluk: P1 = 34.1715 d (Figure 8).

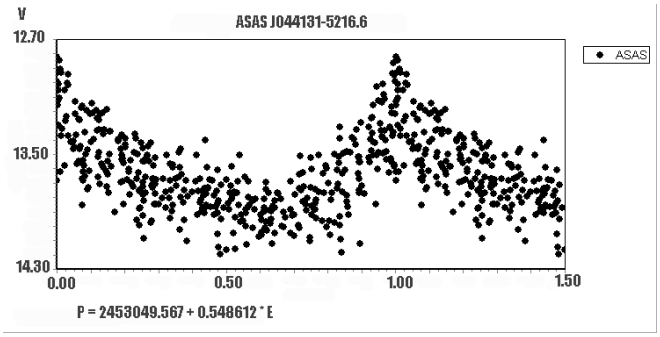

Figure 7

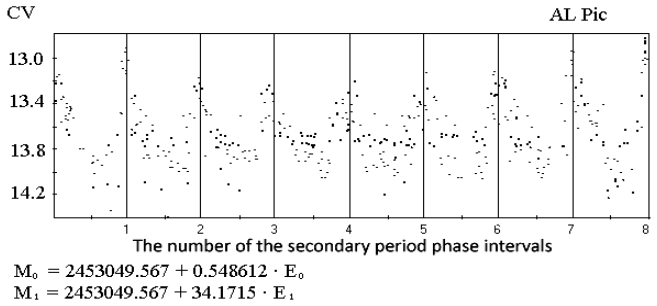

Figure 8

TW Cae, ASAS J045319-3131.9

The star was investigated by G.Pojmański in 2002 [27]. Its further study was performed by E.V.Kazarovets, N.N.Samus, O.V.Durlevich, N.N.Kireeva and E.N.Pastukhova [28]; G.Torrealba, M.Catelan, A.J.Drake, S.G.Djorgovski, R.H.McNaught, V.Belokurov, S.Koposov, M.J.Graham, A.Mahabal, S.Larson and E.Christensen [29]. I.I.Baluk has reported the results of his individual study of the star. The UCAC4 position of the star: RA = 04h53m19.31s; Dec = -31°31′56″.6. The star's catalogue identifiers: the 2MASS identifier – J04531930-3131566; the GSC identifier – 07046-01634; the USNO identifier – B1.0 0584-0060796; the UCAC4 identifier – 293-005838; the ASAS identifier – J045319-3131.9. The star's variability type: RRab. The peak brightness is 12.70m (in the V band); the minimum brightness is 13.75m (in the V band). M – m = 25%. The star's period shows variations. The star's ephemerides are presented in Figure 9.

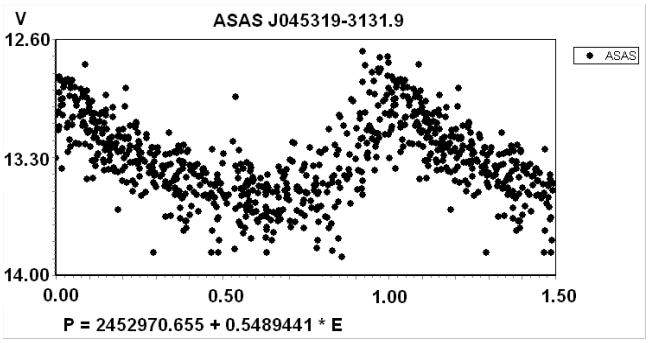

Figure 9

UZ Ant, ASAS J110520-3856.8

The star was investigated by Luis E. Erro in 1940 [30]. Further investigations of the star were conducted by N.N.Samus, E.N.Pastukhova and O.V.Durlevich [31]. The results of an individual study of the star have been reported by I.I.Baluk. The UCAC4 position of the star: RA = 11h05m20.16s; Dec = -38°56′46″.4. The star's catalogue identifiers: the 2MASS identifier – J11052026-3856462; the GSC identifier – 07725-00690; the USNO identifier – B1.0 0510-0243867; the UCAC4 identifier – 256-051914; the ASAS identifier – J110520-3856.8. The star's variability type: RRab. The peak brightness is 13.00m (in the V band); the minimum brightness is 14.40m (in the V band). M – m = 21%. The star's period shows variations. The star's ephemerides are plotted in Figure 10.

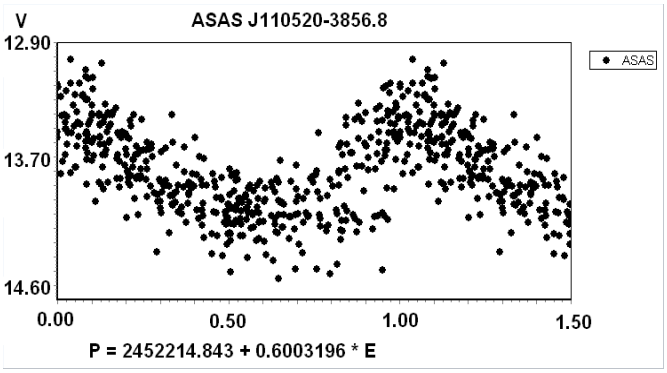

Figure 10

WY Ant, ASAS J101605-2943.7

The star was investigated by Cecilia Payne-Gaposchkin [32], as well as by V.P.Tsesevich and M.S.Kazanasmas [33]; J. Lub [34]; G.Pojmański G. [35]; D.M.Szczygieł, G.Pojmański and B.Pilecki [36]; G.Torrealba, M.Catelan, A.J.Drake, S.G.Djorgovski, R.H.McNaught, V.Belokurov, S.Koposov, M.J.Graham, A.Mahabal, S.Larson and E.Christensen [37]. I.I.Baluk has presented the results of his study of the star. The UCAC4 position of the star: RA = 10h16m04.95s; Dec = -29°43′42″.4. The star's catalogue identifiers: the 2MASS identifier – J10160494-2943423; the GSC identifier – 06630-01689; the USNO identifier – B1.0 0602-0242795; the UCAC4 identifier – 302-061329; the ASAS identifier – J101605-2943.7. The star's variability type: RRab. The peak brightness is 10.31m (in the V band); the minimum

brightness is 11.23m (in the V band). M – m = 15%. The star's period shows variations within the interval JD 2451700 – 2455300; P = 0.5743448d. The star's ephemerides are plotted in Figure 11.

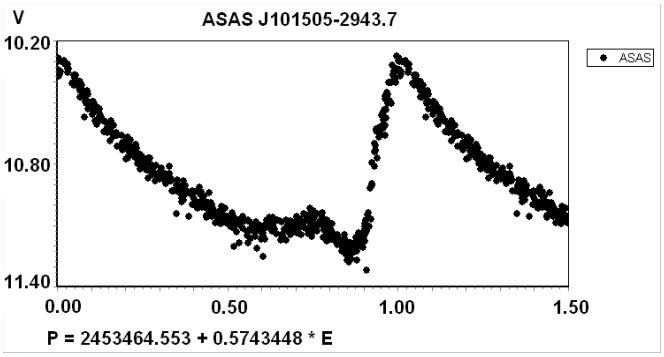

Figure 11

Acknowledgements. The authors are grateful to S.M.Andrievsky, N.N.Samus and I.S.Bryukhanov for their kind attention and help.

References

1. Pojmański G.: http://adsabs.harvard.edu/abs/2002AcA....52..397P
2. Torrealba G.: http://nunuku.caltech.edu/cgibin/getcssconedb_id_phase.cgi?ID=3041027014747&PER=0.64105&PLOT=plot
3. Szczygieł D. M., Pojmański G., Pilecki B.: http://adsabs.harvard.edu/abs/2009arXiv0906.2199S
4. Torrealba G., Catelan M., Drake A.J.: http://adsabs.harvard.edu/abs/2015MNRAS.446.2251T
5. Pojmański G.: http://adsabs.harvard.edu/abs/2002AcA....52..397P
6. Szczygieł D. M., Pojmański G., Pilecki B.: http://adsabs.harvard.edu/abs/2009arXiv0906.2199S
7. Torrealba G., Catelan M., Drake A.J.: http://adsabs.harvard.edu/abs/2015MNRAS.446.2251T
8. Strohmeier W., Patterson I.: http://adsabs.harvard.edu/abs/1969IBVS..330....1S
9. Pojmański G.: http://adsabs.harvard.edu/abs/2002AcA....52..397P
10. Samus N.N.: http://adsabs.harvard.edu/abs/2008IBVS.5863....1K
11. Szczygieł D. M., Pojmański G., Pilecki B.: http://adsabs.harvard.edu/abs/2009arXiv0906.2199S
12. Strohmeier W., Knigge R., Ott H.: http://adsabs.harvard.edu/abs/1965IBVS..115....1S
13. Pojmański G.: http://adsabs.harvard.edu/abs/2002AcA....52..397P
14. Kazarovets E. V., Samus N. N., Durlevich O. V., Kireeva N. N., Pastukhova E. N.: http://adsabs.harvard.edu/abs/2008IBVS.5863....1K
15. Szczygieł D.M., Pojmański G., Pilecki B.: http://adsabs.harvard.edu/abs/2009arXiv0906.2199S
16. Torrealba G., Catelan M., Drake A. J., Djorgovski S. G., McNaught R. H., Belokurov V., Koposov S., Graham M. J., Mahabal A., Larson S., Christensen E.: http://adsabs.harvard.edu/abs/2015MNRAS.446.2251T
17. Boyce Emily Hughes: http://adsabs.harvard.edu/abs/1936BHarO.903...28B
18. Tsesevich V.P., Kazanasmas M.S.: http://adsabs.harvard.edu/abs/1971afcv.book.....T
19. Pojmański G.: http://adsabs.harvard.edu/abs/2002AcA....52..397P
20. Samus N.N., Pastukhova E.N., Durlevich O.V.: http://adsabs.harvard.edu/abs/2007PZ.....27....6S
21. Szczygieł D.M., Pojmański G., B. Pilecki: http://adsabs.harvard.edu abs/2009arXiv0906.2199S
22. Torrealba G., Catelan M., Drake A. J., Djorgovski S. G., McNaught R. H., Belokurov V., Koposov S., Graham M. J., Mahabal A., Larson S., Christensen E.: http://adsabs.harvard.edu/abs/2015MNRAS.446.2251T
23. Luyten Willem Jacob: http://adsabs.harvard.edu/abs/1938POMin...6....1L
24. Pojmański G.: http://adsabs.harvard.edu/abs/2002AcA....52..397P
25. Wils P., Sodor A.: http://adsabs.harvard.edu/cgi-bin/nph-data_query?bibcode=2005IBVS.5655.... 1W&db_key=AST&link_type= ABSTRACT&high=57c41da3cd31283
26. Kazarovets E.V., Samus N.N., Durlevich O.V., Kireeva N.N., Pastukhova E.N.: http://adsabs.harvard.edu/cgi-bin/nph-data_query?bibcode=2009yCatp018586300K&db_key=AST&link_type=ABSTRACT&high=57c41da3cd32417
27. Pojmański G.: http://adsabs.harvard.edu/cgi-bin/nph-data_query?bibcode=2002AcA....52..397P&db_key=AST&link_type=ABSTRACT&high=57e3e9f7d215013
28. Kazarovets E.V., Samus N.N., Durlevich O.V., Kireeva N.N., Pastukhova E.N.: http://adsabs.harvard.edu/cgi-bin/nph-data_query?bibcode=2015IBVS.6151....1K&db_key=AST&link_type=ABSTRACT&high=57e3e9f7d219175
29. Torrealba G., Catelan M., Drake A.J., Djorgovski S.G., McNaught R.H., Belokurov V., Koposov S., Graham M.J., Mahabal A., Larson S., Christensen E.: http://adsabs.harvard.edu/cgi-bin/nph-data_query?bibcode=2015MNRAS.446.2251T&db_key=AST&link_type=ABSTRACT&high=57e3e9f7d220641
30. Erro Luis E.: http://adsabs.harvard.edu/cgi-bin/nph-data_query?bibcode=1940BHarO.913.... 1E&db_key=AST&link_type=ABSTRACT&high=57e3e9f7d227308
31. Samus N.N., Pastukhova E.N., Durlevich O.V.: http://adsabs.harvard.edu/cgi-bin/nph-data_query?bibcode=2007PZ.....27....6S&db_key=AST&link_type=ABSTRACT&high=57e3e9f7d210343
32. Payne-Gaposchkin Cecilia: http://adsabs.harvard.edu/cgi-bin/nph-data_query?bibcode=1952AnHar.115..189P&db_key=AST&link_type=ABSTRACT&high=57e3e9f7d218654
33. Tsesevich V.P., Kazanasmas M.S.: http://adsabs.harvard.edu/cgi-bin/nph-data_query?bibcode=1971afcv.book.....T&db_key=AST&link_type=ABSTRACT&high=57e3e9f7d230043
34. Lub J.: http://adsabs.harvard.edu/cgi-bin/nph-data_query?bibcode=1977A%26AS...29..345L&db_key=AST&link_type=ABSTRACT&high=57e3e9f7d232538
35. Pojmańskic G.: http://adsabs.harvard.edu/cgi-bin/nph-data_query?bibcode=2002AcA....52..397P&db_key=AST&link_type=ABSTRACT&high=57e3e9f7d201770
36. Szczygieł D. M., Pojmański G., Pilecki B.: http://adsabs.harvard.edu/cgi-bin/nph-data_query?bibcode=2009AcA....59..137S&db_key=AST&link_type=ABSTRACT&high=57e3e9f7d202914
37. Torrealba G., Catelan M., Drake A.J., Djorgovski S.G., McNaught R.H., Belokurov V., Koposov S., Graham M.J., Mahabal A., Larson S., Christensen E.: http://adsabs.harvard.edu/cgi-bin/nph-data_query?bibcode=2015MNRAS.446.2251T&db_key=AST&link_type=ABSTRACT&high=57e3e9f7d204020

DOI: http://dx.doi.org/10.18524/1810-4215.2017.30.114279

SHORT SOFT Γ-RAY BURST SPECTRAL EVOLUTION

V. N. Kondratyev[1,2]

[1] Physics Department, Taras Shevchenko National University of Kyiv, 03022-UA Kyiv, Ukraine, *vkondrat@univ.kiev.ua*

[2] Bogolubov Laboratory of Theoretical Physics, JINR, 141980, Dubna, Russia

ABSTRACT. Short Soft Gamma-Ray bursts are considered as neutron star crust magnetoemission. Statistics of temporal burst properties are shown to display universal features.

Keywords: Soft gamma repeaters. – neutron stars: magnetic field, magnetar.

1. Introduction

The discovery of soft gamma repeaters (SGRs) is associated with pioneering observations of soft gamma-ray burst from SGR 1806-20 on 1979 January 7 by KONUS experiment on the Venera 11 and Prognoz-7 spacecrafts (Mazets et al. 1981). Such repeating outbursts of a short-duration (~ 100 ms), soft-spectrum (below < 100 keV) and super-Eddington luminosity, i.e., L~10^3 – 10^4 L_{Edd} ($L_{Edd} \approx 10^{38}(M_{NS}/M_\odot)$ ergs/s with neutron star (NS) M_{NS} and solar M_0 masses, see, e.g., (Kondratyev 2002), represent general activity of these pulsars. Such burst emissions tend to concentrate into short intervals (weeks to months) of intense activity separated by relatively long (years) quasi-regular quiescent periods with associated sub-Eddington persistent X-ray luminosity $L_X \sim 10^{34.5} - 10^{36}$ erg/s. More rarely, SGRs emit giant flares that last for minutes and display very hard X- and gamma-ray spectra, extending into the MeV range, enormous energy release and associated with pioneering observations of the famous 1979 March 5 event related to SGR0526_66 (Mazets et al., 1979).

Many observed SGR properties strongly support the magnetar concept suggesting an ultra-magnetized stellar media with magnetic induction strength H up to *tera-tesla*. Such a magnetization can be understood, e.g., as an effect of the magneto-rotational instabilities and/or "dynamo action" processes which might operate in fast rotating stars (Kondratyev, 2014). Respectively, SGR activity is well explained within such `magnetar' concept.

Detailed analysis of burst light curves can provide more constrain for theoretical models and burst triggering mechanisms. In this contribution the randomly jumping interacting moments (RJIM) model (Kondratyev, 2002) is further extended for an analysis of SGR bursts. Particular attention is paid for spectral evolution.

2. Neutron Star Crust Magnetoemission

The RJIM model applications for magnetodynamics simulations in NS crust has already been described by Kondratyev (2002). We briefly remind that in simulations of demagnetization dynamics we use a very general form for magnetic moments m of atomic nuclei $m = \mu I g$ with the nucleon magneton μ, nuclear spin I and g-factor g. Atomic nuclei occupied a volume V_D contribute to the magnetization $Q = m/V_D$. Taking $g = 3$ for nuclear component of magnetic induction we get

$$Q = 1.5 \text{ TG } In /(10^{13} \text{ g/cm}^3), \quad (1)$$

In a case of comparable sizes for nucleus and occupied volume V_D (i.e., $n \sim 10^{13,5}$ g/cm^3) internuclear interaction is ferromagnetic (Kondratyev&Lutz, 1999; Kondratyev, 2002).

We consider adiabatically decreasing in time crust magnetic field H. For certain local field values b_i nuclear magnetic response peculiarities give rise to stepwise change of NS crust magnetization on a value proportional to nuclear spin ΔI (Kondratyev, 2002). The corresponding excess of magnetic pressure is estimated as

$$\Delta P = H \Delta Q = 10^{23} \text{ At} \quad (2)$$
$$(H/\text{TT})\,(\Delta I\, n/\, 10^{13} \text{ g/cm}^3) .$$

and evolves in a crust with a linear speed $c_m \sim 10^8$ cm/s , for more details see (Kondratyev 2002). Then for outer crusts of a linear size, $l_{crust} \sim 100$ m, an estimate of the pressure jump region spanning time, $t_{av} \sim l_{crust} / c_m \sim 0.1$ ms, is consistent with the rising time for giant flares of SGR (Mazets et.al 1979, Kondratyev 2002, Svinkin et.al 2015). Such magnetic pressure jump excites magnetoplasma waves (i.e., Alfvén waves). Since the Alfvén velocity of is close to the speed of light c, the linear size of the strongly excited magnetosphere region exceeds the value $R_{ex} \sim l_{crust}\, c/c_m \sim 10$ km , comparable to NS radius. Subsequent development and cooling of photon-electron-positron plasma via gamma-ray emission from this region generates a short-duration (~ 100 ms) SGR-burst event with rising $\sim 10^{0.5}$ ms and decaying ~ 10 ms fronts of light curve (Kondratyev, 2002).

For a field strength $H \sim 3$TT, typical magnitar crust density $n \sim 10^{13,5}$ g/cm^3, and avalanche linear size of order of outer NS crust thickness, 100 m (i.e., volume of magnetization jump V_a about 10^6 m^3) the amount of released energy $\Delta E = \Delta P\, V_a$ is consistent with an energy of soft gamma-ray bursts, as is obtained from Eq. (2). These values determine burst duration time T. Therefore, quantity $x = t_{av}/T \sim l_{av}/V_a \sim T^{2/3}$

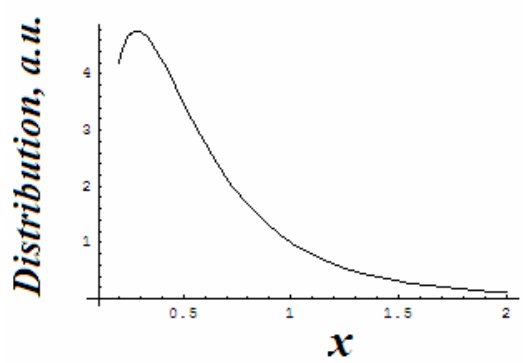

Figure 1: The time ratio x (in units of x_0) distribution (see text).

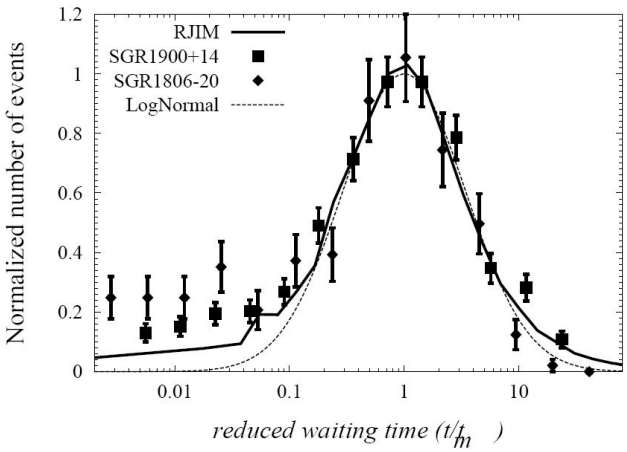

Figure 2: The reduced waiting time distribution between the successive RXTE/PCA bursts from SGR 1900+14 (squares) (Gogus et.al. 1999) and SGR 1806-20 (diamonds) (Gogus et.al. 2000) are compared with the waiting time distribution between avalanches (solid curve). The dashed line represents the fit to the lognormal distribution of the width 3.6.

is distributed according to $[W(x^{-3/2})/x^{5/2}]dx$ where $W(T)$ gives T-distribution. As is seen in Fig. 1 short front rising time relative to value T has higher probability. Such a feature is caused by linear scale for burst front while the duration is determined by volume.

It is worthy to notice in this regards the delayed emission of softer gamma-ray component. Such a time lag is due to cooling of photon-electron-positron plasma in magnetosphere. The Alfvén waves damping and energy loss of respective accelerated electrons lead to softening of emitted radiation. Corresponding time scale is given by region of excited magnetosphere $R_{ex} \sim 10$ km and for multiple wave propargation is estimated as $t_{lag} \sim 1$ ms.

For a constant change rate $\dot{B}$ of the magnetic field the inter-avalanche field interval is proportional to the time interval (i.e. waiting time) between the induced bursts. Taking the respective normalized values, i.e. inter-burst time and inter-avalanche field, we compare the theoretical predictions with observations in Fig. 2. As seen in Fig. 2 for different SGRs the waiting time distributions as a function of the reduced time obey universal function. The data are well reproduced by simulations and fitted at a maximum by the lognormal function. Such a property points out the single time scale for SGR-burst triggering processes. Within RJIM model such a time-scale is determined by the ratio of the disorder parameter R and the field change rate $\tau = R/\dot{B}$. Therefore, the scaling with respective time leads to an universal function.

4. Conclusion

We considered magnetoemission of inhomogeneous nuclear matter relevant for neutron star crusts. As is seen erratic jumps in crusts magnetotransport result in excitations of the Alfvén waves in magnetoplasma that leads to gamma-ray bursts. The properties of such bursts are favorably compared with activity of Soft Gamma Repeaters. As is shown considered mechanism of SGR short burst emission suggest relatively small rising time front and a time lag for softer gamma-ray component.

Acknowledgements. This work is supported in part by Integral scientific data center and the Alexander von Humboldt Foundation.

References

Gogus E. et.al. 1999 *Ap.J Letters* **526**, L93.
Gogus E. et.al. 2000 *Ap.J Letters* **532**, L121.
Kondratyev V.N, Lutz H.O 1999 *Eur.Phys.J.D* **9**, 483.
Kondratyev V.N 2002 *Phys.Rev.Lett*. **88**, 221101.
Kondratyev V.N.:2014, *EPJ A*. **50**, 7.
Mazets E.P., et.al., 1979 *Nature (London)* **282**, 587.
Svinkin D. S. et.al. 2015 *Mon. Not. R. Astron. Soc.* **447**, 1028.

DOI: http://dx.doi.org/10.18524/1810-4215.2017.30.114335

SYNTHESIS OF MAGNETIZED NUCLEI AT SUPERNOVA EXPLOSION

V.N.Kondratyev [1,2], U.M.Nurtayeva [2,4], A.Zh.Zhomartova [2,4], T.V.Mishenina [3]

[1] Physics Department, Taras Shevchenko National University of Kyiv, 03022-UA Kyiv, Ukraine, *vkondrat@univ.kiev.ua*
[2] BLTP, JINR, 141980-RU Dubna, Russia
[3] Astronomical Observatory, Odessa National University, 65014-UA Odessa, Ukraine
[4] Department of Experimental Methods in Nuclear Physics, MEPhI NRNU, Moscow, Russia

ABSTRACT. Influence of magnetorotational instabilities in astrophysical plasma at supernova explosion on synthesis of chemical elements is investigated. At field strength less than 10 teratesla nuclear magnetic susceptibility exhibits linear regime with enhanced nuclear binding energy for open shell nuclei. Effects of ultra-strong nuclear magnetization are demonstrated to enhance the portion of titanium product. The relation to an excess of titanium isotopes revealed from the Integral mission data and galactic chemical evolution is discussed.

Keywords: Stars: supernovae, magnetic field. – Nucleosynthesis: abundances, the Galaxy chemical evolution.

1. Introduction

Ultrastrong magnetic fields exceeding *teratesla* (TT) arise at core-collapse supernova (SN) explosion (Kondratyev 2014), in magnetar crusts and heavy ion collisions. Nuclides produced in such processes contain an information on matter structure and explosion mechanisms. In this work we analyze effect of relatively *weak* magnetic field in nuclear structure and discuss possibilities for using radionuclides to probe internal regions of respective sites.

Interaction of nucleon magnetic moment m_N with a field H leads to a shift of energy levels $\Delta = m_N H$. Dramatic change in nuclear structure corresponds to conditions of level crossing. The nuclear level spacing $\Delta E \sim 1$ MeV gives respective field strength scale $\Delta H_{cross} \sim \Delta E / \mu_N \sim 10$ TT. Here μ_N denotes the nuclear magneton. In a case of smaller strengths $H < 10$ TT one can use a linear approximation, cf., (Kondratyev & Korovina, 2015). In next section we demonstrate that magnetic susceptibility at a field strength of teratesla exceeds significantly respective ground state *g*-factor corresponding to vanishing magnetic induction. Effect of magnetic field in nuclear composition is considered in sect. 3. Conclusions are in sect. 4.

2. Structure of magnetized atomic nuclei

The single-particle (sp) Hamiltonian H_α for nuclei within non-relativistic approximation and a linear limit in a weak magnetic field **H** reads

$$H_\alpha = H_\alpha^0 - (g_\alpha^o \mathbf{l} - g_\alpha \mathbf{s}) \omega_L \qquad (1)$$

for protons α=p and neutrons α=n with well known g-factors g_α. Here H_α^0 represents the sp Hamiltonian for isolated nuclei, **l** and **s** denote operators of the orbital momentum and spin. An interaction of nucleon dipole magnetic moment with magnetic field is represented by terms containing the vector $\omega_L = \mu_N H$.

The nuclear binding energy $\Delta B = \Sigma_{occ}\, e_i$ is given as a sum over occupied levels i of sp eigen energies e_i. By making use of angular momentum representation for spherical nuclei one can write the change of binding energy in magnetic field as

$$\Delta B_\alpha = \kappa_\alpha \omega_L, \kappa_\alpha = \Sigma_{i\text{-}occ}\, \kappa^i_\alpha \qquad (2)$$
$$\kappa^i_\alpha = \Sigma_{m,s} |<lm, ½\, s|jm_j>|^2 (g_\alpha^o\, m + g_\alpha\, s),$$

where $<lm, ½\, s|jm_j>$ represents the Clebsch-Gordan coefficient.

Thus, values *k* are significantly different from nuclear *g*-factors corresponding to an interaction of nuclear magnetic moment in a ground state with magnetic field. Within the shell model nuclear magnetic moment is determined by a valent unpaired nucleons and associated nuclear g-factor is given by values of Eq. (2) and determined for states with maximum spin projection m_j of positive and negative signs for protons and neutrons, see Tables 1.

Table 1. Susceptibility parameter κ for iron shell closure region. Contributions of Z protons and N neutrons are indicated by κ_p and κ_n .

Z	κ_p	*N*	κ_n
20	0.00	20	0.00
21	5.793	27	1.913
22	9.931	26	3.279
23	12.414	25	4.099
24	13.241	24	4.373
25	12.414	23	4.099
26	9.931	22	3.279
27	5.793	21	1.913
28	0.00	28	0.00

Evidently, such strong nuclear magnetization leads to an increase of binding energy. As is seen from Eqs. (3) and in

Table 1 open shell nuclei experience maximum of such extra binding. For protons effect is about 3 times larger as compared to neutrons. Consequently, composition of stable nuclei in magnetic field is modified. For instance, for often considered isobars ^{44}Z, e.g., ^{44}Sc and ^{44}Ti, from Table 1 we have ($k_{\rm Ti}$ - $k_{\rm Sc}$) = 3.32 and at a field strength H= 2.5 TT the nucleus ^{44}Ti is stronger bound than ^{44}Sc. It is worthy to recall here that ^{44}Ti becomes the most tightly bound nucleus at H = 20 TT, see (Kondratyev, 2014; Kondratyev & Korovina, 2015). For a weak field limit we notice similar results obtained from consideration within the covariant density functional theory (Pena Arteaga et al., 2011) and shell correction approach (Kondratyev & Korovina, 2015) which exclude an interaction of total magnetic moment of a nucleus with magnetic field.

3. Synthesis of magnetized nuclei

Such a magnetic medication of nuclear structure affects nuclide production at respective explosion. Nuclear statistical equilibrium (NSE) approach gives useful tool used very successfully for description and analysis of abundances of iron group and nearby nuclides for over half a century (Woosley, Heger & Weaver, 2002). At such conditions nuclide yield is determined mainly by the binding energy of corresponding atomic nuclei. The magnetic effects in the NSE were considered by Kondratyev (2014, and refs. therein). Recall that at temperatures ($T \le 10^{9.5}$ K) and field strengths ($H \ge 0.1$ TT), the magnetic field dependence of relative output value $y = Y(H)/Y(0)$ is determined by a change in the binding energy of nuclei in a field H and can be written in the following form

$$y = \exp\{\Delta B / kT\} \approx \exp\{\kappa\, \omega_{\rm I}/kT\}. \qquad (3)$$

We used here Eq. (2).

We consider examples of iron group and titanium. Such a choice of double magic and anti-magic nuclei at vanishing magnetization gives a clear picture of magnetic effects in the formation of chemical elements and fundamental conclusions about transmutation and synthesis of nuclei in ultramagnetized plasma.

It is worthy to recall in this regards there is a significant excess as compared to model predictions of Ti nuclei abundance obtained in direct observations of SN remnants (Kondratyev & Korovina, 2015). Furthermore, there is the difference between Ti abundance revealed from galactic chemical evolution (GCE) predictions and the Ti content observations in stars (Kondratyev&Mishenina 2016). Till now, none of the existing GCE codes does not describe the observational trend of [Ti/Fe] vs. [Fe/H]. This is primarily due to the difficulties in calculating of the present theoretical stellar yields from massive supernovas that are the main source for titanium probably. This means that improved of the core collapse supernovae nucleosynthesis predictions from realistic models are required. Among others, this needs a detailed study of the role of rotation and magnetic fields (Mishenina et al., 2017).

As is seen from Eqs. (2), (3) and Table 1 an excess on order of magnitude corresponds to field strength of several TT. As is evident from Eqs. (2) maximum of magnetic susceptibility κ corresponds to half filled shells. In case of iron closure $1f_{7/2}$ shell such a condition is met at Z=N=24. Then significant value of parameter $\kappa_{\rm Cr}$ = 17.33 implies strong magnetic enhancement in production of ^{48}Cr nuclde. The radioactive decay chain ^{48}Cr→ ^{48}V→ ^{48}Ti gives rise to an excess of major titanium isotope.

4. Conclusion

We employ arguments of nuclear statistical equilibrium to study nucleosynthesis at magnetorotational supernova explosion. As is shown binding energy of nuclei with open shells increases at relatively weak fields corresponding to linear nuclear magnetic response Such a property suggests possible mechanism of additional titanium enrichment when taking into account the increased yield of anti-magic nuclides in ultramagnetized astrophysical plasma. As is seen on an example of the radioactive isotope ^{44}Ti the direct observational data, see sect. 1, confirm such an enrichment which can be understood in terms of magnetic effects. The resulting enrichments of M44 isobars are collaborated with observational data (Kondratyev, 2014; Magkotsios, 2010). The proton magnetic reactivity dominates in a change of binding energy, see Eq. (2). Noticeable increase in production of ^{48}Cr leads to increasing volume of stable titanium isotopes, as well. At the same time a yield of iron and calcium isotopes can be expected unchanged because of the proton shell closure, see Eqs. (2), (3) and Table 1.

Acknowledgements. This work is supported in part by Integral scientific data center and by the Swiss National Science Foundation (SCOPES project No. IZ73Z0152485).

References

Kondratyev V.N.: 2014, *EPJ A ,* **50**, 7.
Kondratyev V.N., Korovina Yu.V.: 2015, *JETP L,* **102**, 131.
Kondratyev V.N., Mishenina T.V.: 2016, *OAP,* **29**, 60.
Magkotsios G., Timmes F.X., Hungerford A.L. et al.: 2010, *ApJS*, **191**, 66.
Mishenina T., Pignatati M., Côté B. et al.:2017, *MNRAS*, **469**, 4378.
Peña Arteaga D., Grasso M., Khan E., Ring P.: 2011, *Phys. Rev. C*, **84**, id.045806.
Woosley S.E., Heger A., Weaver T.A.: 2002, *Rev. Mod. Phys.,* **74**, 1015.

DOI: http://dx.doi.org/10.18524/1810-4215.2017.30.114346

PHASE PLANE ANALYSIS OF THE PHOTOMETRICAL VARIATIONS OF LONG-PERIOD VARIABLES

Kudashkina L.S., Andronov I.L.

Department of Mathematics, Physics and Astronomy,
Odessa National Maritime University, Odessa, 65029 Ukraine
kuda2003@ukr.net, tt_ari@ukr.net

ABSTRACT. Using the phase plane diagrams, the phase light curves of a group of the Mira-type stars and semi-regular variables are analyzed. As generalized coordinates x and $\dot{x}$, we have used m – the brightness of the star and its phase derivative. We have used mean phase light curves using observations of various authors. The data typically span a large time interval (nearly a century). They were compiled from the databases of AAVSO, AFOEV, VSOLJ, ASAS and approximated using a trigonometric polynomial of statistically optimal degree. As the resulting approximation characterizes the auto-oscillation process, which leads to a photometrical variability, the phase diagram corresponds to a limit cycle.

For all stars studied, the limit cycles were computed. For a simple sine-like light curve, in e.g., L_2 Pup, the limit cycle is a simple ellipse. In a case of more complicated light curve, in which harmonics are statistically significant, the limit cycle has deviations from the ellipse.

In an addition to a classical analysis, we use the error estimates of the smoothing function and its derivative to constrain an "error corridor" in the phase plane.

Keywords: Mira-type stars, semi-regular variables, limit cycle, phase plane diagrams.

1. Introduction

The pulsations of long-period variable stars – Mira-type, semi-regular variables studied are significantly worse than, for example, of the cepheids, because of the difficulties associated with the complex interaction of pulsations and convection, and strong nonlinear effects, leading to the formation of shock waves and the mass loss, with the problems of the transfer of the radiation in a cool extended atmospheres with a high degree of non-adiabatic pulsations due to the commensurate dynamic and thermal time scales for these stars.

The dynamic time scale τ_h characterizes the rate of change of parameters of stars with the motions with velocities comparable to the velocitie of sound v_s. The order of magnitude $\tau_h \propto \frac{R}{v_s}$, where R – the characteristic size of the star. For equilibrium star this time is order to time of free fall:

$$t \propto R^{3/2} / \sqrt{GM}\,. \qquad (1)$$

From these considerations, for example, in the work (Kudashkina & Marsakova, 2013) for stars R Aql, R Hya and T UMi, the time of the change of pulse period has been estimated "to zero" at the time of compression of the layers of the star due to the termination of helium burning in the layered source. Also the radius was estimated, from which begins the compression, for a range of stellar masses 0.9-1.5 $M_\odot$.

The thermal time scale τ_{th} determines the rate of cooling or heating of the star. When cooled in the absence of nuclear burning

$$\tau_{th} \propto \frac{U}{L} \propto \frac{GM^2}{RL}, \qquad (2)$$

since the energy U the order of the gravitational energy of a star.

On the asymptotic giant branch (AGB), to which belong the investigated star, the star consists of a degenerate carbon-oxygen core and two layer sources (helium and hydrogen), positioned very close to each other. Above them is an extended hydrogen envelope.

The small thickness of the layered sources cause thermal flashes. Here, the stars are divided into two stages: early (EAGB) is the time interval between the end of helium burning in the core and the first thermal pulse of the helium layer source, and "thermally pulsing regime of the He-burning shell" (TPAGB) is the thermally pulsed burning mode in the helium layer. At the stage of a TPAGB the star is getting brighter in M_{bol}. Some theoretical calculations show that, for example, zirconium stars over a range of luminosity and temperature correspond to the early stages of AGB when helium burning occurs stationary. At the same time, several observational features say, rather, in favor of finding these stars in more evolved evolutionary stage on the AGB (Kudashkina, 2003).

The different studies show that long-period variables pulsate in a fundamental fashion and in the first overtone. The latter is especially for semi-regular variables, but a significant part of the Mira-type stars are the overtone pulsators. In particular, in the article of Fadeev (1993) is that EAGB stars represent a homogeneous group of fundamental pulsators with periods from 10 to 400 days, while the TPAGB stars show different pulsation proper-

ties, depending on the initial mass. So for a range of masses from 2 to 3 solar the ultimate period of the first overtone of about 300 days, and 430 days, respectively for 2 and 3 $M_{\odot}$. Depending on the initial mass and surface luminosity, these stars pulsate in the fundamental mode, either in the first overtone. Some objects show variability of either optical, or maser emission (e.g. Kudashkina & Rudnitskij (1988).

Indirect dependence of the pulsation properties from surface luminosity is also seen in the various photometric dependencies. For example, the three-dimensional diagram of the photometric parameters: the period (P), the amplitude of light (Δm), the slope of the ascending branch of the light curve (dm_i/dt) were obtained (Kudashkina (2015).

The most significant correlation shows the dependence of the slope of the ascending branch of the period and amplitude.

$$dm_i/dt = -\underset{\pm 0.0075}{0.0633} + \underset{\pm 0.000021}{0.000165}\,P - \underset{\pm 0.00134}{0.00642}\,\Delta m\,. \quad (3)$$

This study is the next step in the study of the photometric parameters of long-period variables – Mira-type stars and the semi-regular and relative objects – which can be used as an additional criterion the classification of these stars to the EAGB and TPAGB stages.

2. Results

It is known that the mode of oscillation corresponds to a periodic limit cycle, i.e. a closed phase trajectory to strive for all of the close trajectory over time. We calculated limit cycles for 19 long-period variables and 5 stars of RV Tau-type, based on the mean light curves, averaged over a long period of time. As generalized coordinates of the phase plane are taken m – brightness of the star and its phase derivative. That is, the curve of evolution of the brightness of the star in the phase space $m = \Phi(\varphi, m_0)$ is a solution of the equation

$$\frac{dm}{d\varphi} = F(m), \quad (4)$$

where m_0 is the value at $\varphi=\varphi_0$.

For approximation of the phase curve was used trigonometric polynomials

$$m(\varphi) = C_1 + \sum_{j=1}^{M}(C_{2j}\cos(j\varphi) + C_{2j+1}\sin(j\varphi)), \quad (5)$$

moreover, the optimal value of the degree M is determined by the Fisher test with a critical probability of "false alarm" (FAP=False Alarm Probability) 10^{-3}.

The phase derivative in radians calculated simple

$$\dot{m}(\varphi) = \sum_{j=1}^{M} j\cdot(-C_{2j}\sin(j\varphi) + C_{2j+1}\cos(j\varphi)), \quad (6)$$

That is, upon differentiation, the amplitude of the harmonic is multiplied by j. Usually this leads to a greater increase in the relative statistical error of the derivative compared to the signal.

The examples of the phase portraits of the stars made using an improved version of the program FDCN (Andronov, 1994) and are shown in Fig. 1-17. Also the mean light curves are shown for several stars. For the analysis, we have used visual observations from the AAVSO, AFOEV and VSOLJ international databases, the ASAS survey, as well as the original observations by Whitelock et al. (2000) and Maffei &Tosti (1999).

Theoretically, for sinusoidal oscillations, the phase portrait is an ellipse with different units of measurement on axes – magnitude and magnitude "the radian" or "the period". Deviations from the ellipse expected for non-sinusoidal waves, i.e. if the degree of the trigonometric polynomial M >1. The calculation is performed in the cycle phase, the results for m, $\dot{m}$ are displayed with "3σ" corridors of errors on both coordinates. Naturally, the extreme points on each coordinate line "corridors of errors" for the other coordinate converge to a point like the letter Ж. Therefore, as the corridor of errors, use of external (and internal) part of the corridors of the errors for the two variables.

The list of stars and the basic data are given in table 1.

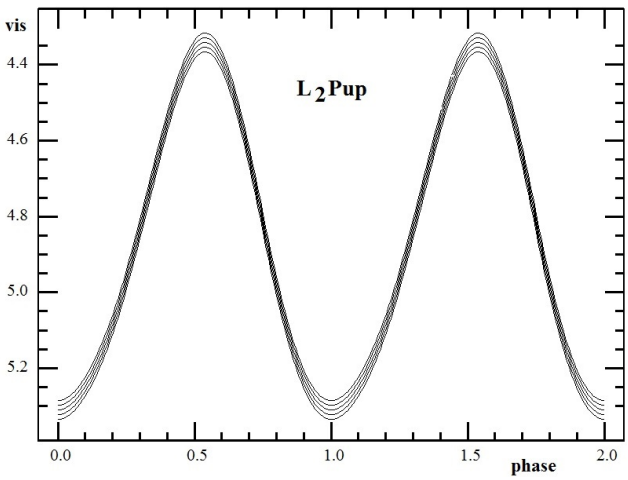

Figure 1: The mean light curve of L_2 Pup.

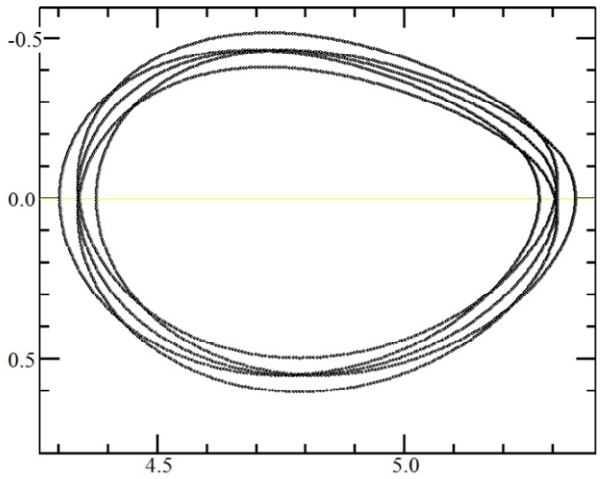

Figure 2: Phase portrait of L_2 Pup.

4. Conclusion

For the semi-regular variable S Per, as well as for L_2 Pup limit cycle is almost a perfect ellipse, despite the fact

that the individual cycles of the oscillations are not quite regular. For Mira-type stars, with more regular oscillations, but a complex form of the light curve, limit cycles deviate strongly from the ellipse.

For U Mon (RV-type star), the phase portraits are shown for short and long cycles of variability. We can see, that the short-period cycle is more stable and regular then the long-period.

Table 1: The list of stars and their basic data

N	**Star**	**Type**	**Spectral type**	Period, d
1	S Car	M	M2-M3e	150.07
2	U Her	M	M6.5e-M9.5e	406.74
3	X Oph	M	K1IIIv comp	332.37
4	R Aql	M	M5e-M9e	280.84
5	S Ori	M	M6.5e-M9.5e	414.46
6	Omi Cet	M	M5e-M9e	333.6
7	S Scl	M	M7-M8IIIe	367
8	RR Aql	M	M6e-M9	390.78
9	X CrB	M	M5e-M7e	241.1
10	U UMi	M	M6e-M8e	325.9
11	U Cyg	M	C7.2e-C9.2	465.49
12	V Cyg	M	C5.3e-C7.4e	421.27
13	BG Cyg	M	M7e-M8e	288.1
14	AM Cyg	M	M6e	371.9
15	R Leo	M	M6e-M9.5e	312
16	L_2 Pup	SRb	M5e	137.17
17	S Per	SRc	M3Iae-M7	816.8
18	W Hya	SRa	M7.5e-M9ep	381.7
19	Y CVn	SRb	C5,4J(N3)	267
20	RV Tau	RV	G2eIa-M2Ia	78.73
21	U Mon	RV	F8eIb-K0pIb (M2)	92
22	EP Lyr	RV	A4Ib-G5p	82.95
23	R Sge	RV	G0Ib-G8Ib	71.57
24	DF Cyg	RV	G5-K4I-II	776.4

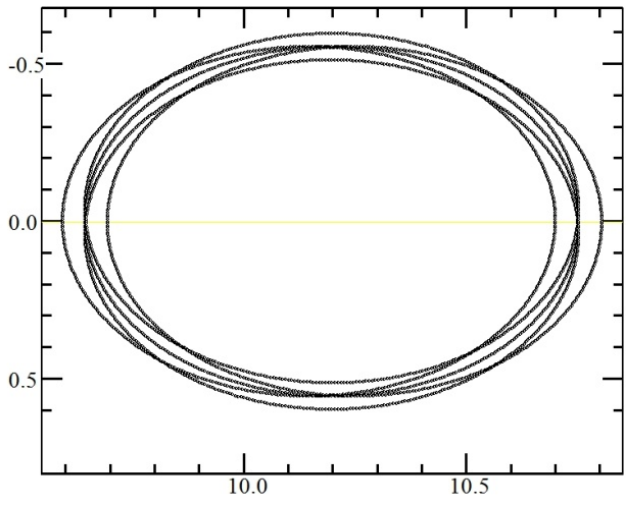

Figure 3: Phase portrait of S Per.

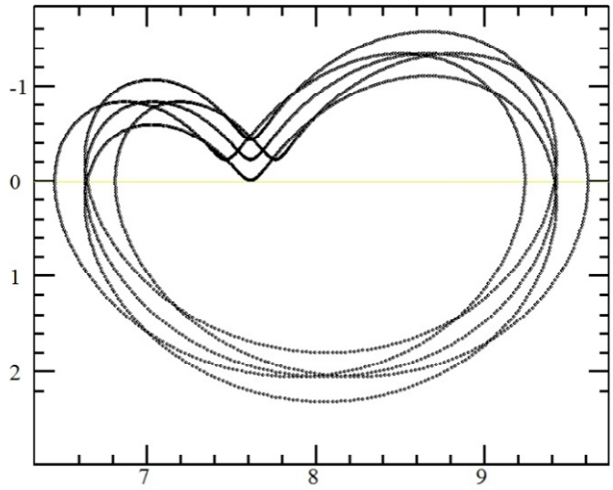

Figure 4: Phase portrait of W Hya.

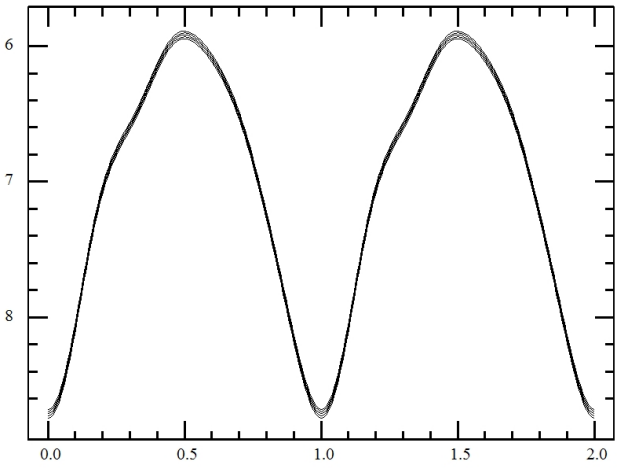

Figure 5: The mean light curve of S Car.

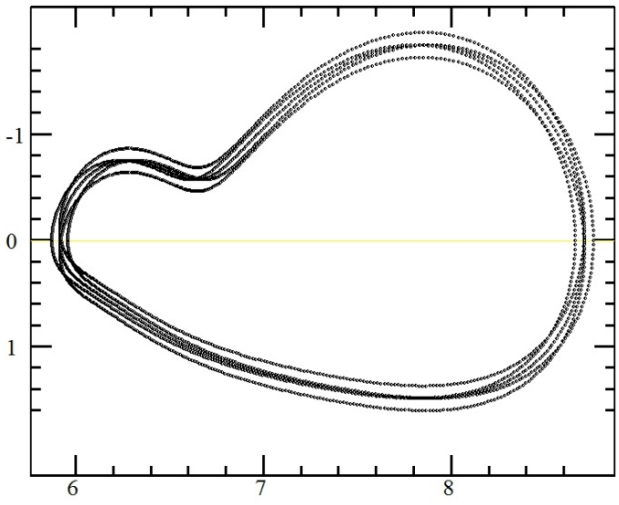

Figure 6: Phase portrait of S Car.

It was previously determined the value of *s* – the degree of the trigonometric polynomial. It is equal to 1 for L_2 Pup (Kudashkina, 2016); 2 for S Car, R Aql (Kudashkina & Andronov, 1996), S Ori (Kudashkina, 2016); 5 for U Her (Kudashkina & Andronov, 1996).

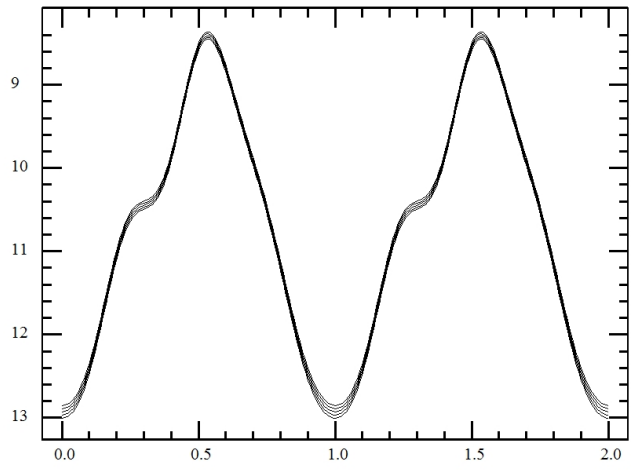

Figure 7: The mean light curve of S Ori.

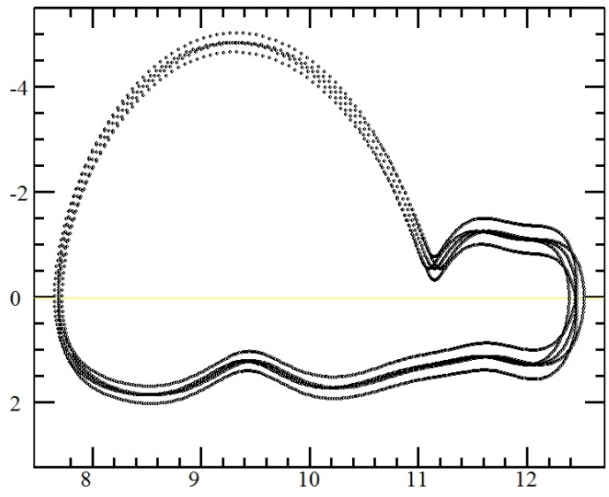

Figure 10: Phase portrait of U Her.

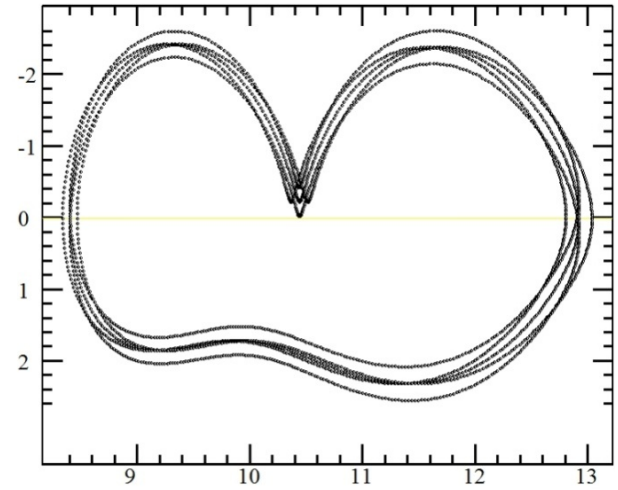

Figure 8: Phase portrait of S Ori.

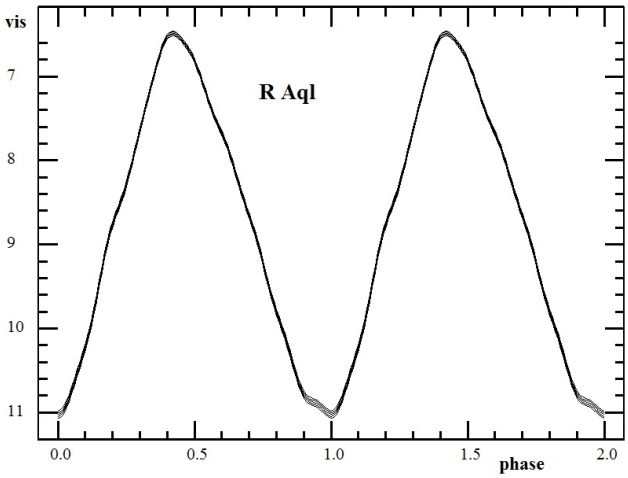

Figure 11: The mean light curve of R Aql.

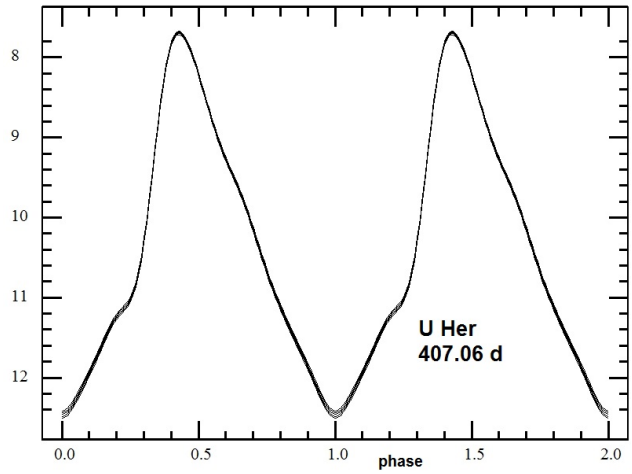

Figure 9: The mean light curve of U Her.

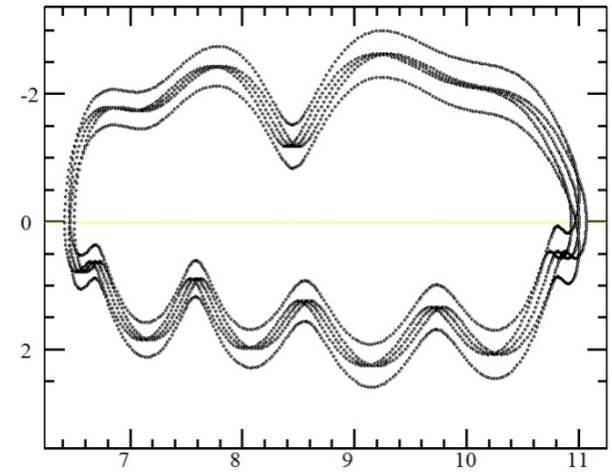

Figure 12: Phase portrait of R Aql.

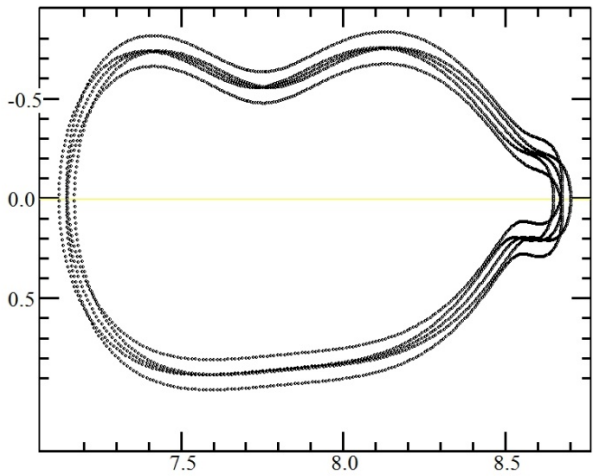

Figure 13: Phase portrait of X Oph.

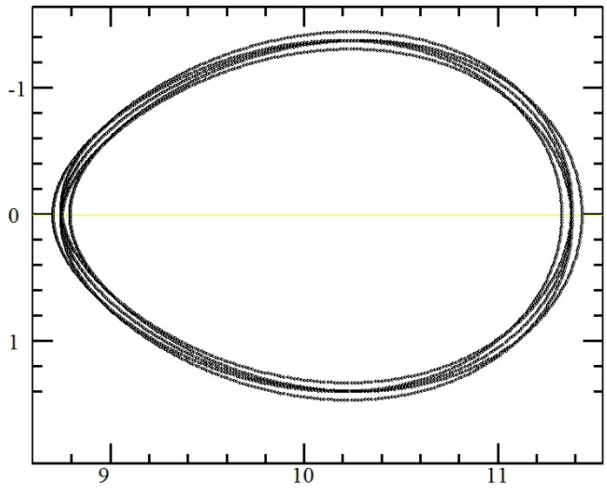

Figure 14: Phase portrait of U UMi.

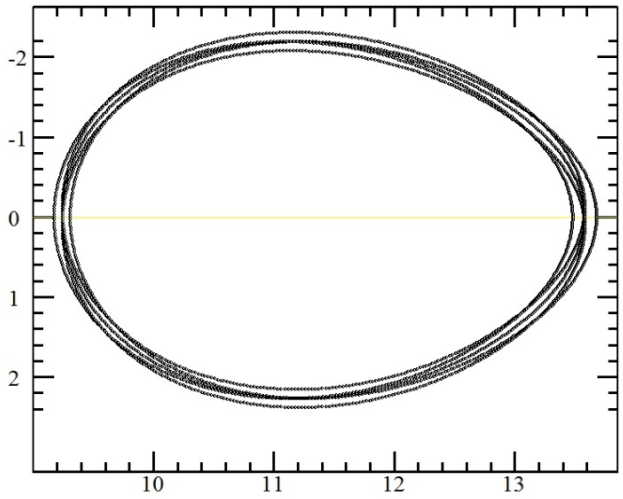

Figure 15: Phase portrait of X CrB.

Acknowledgements. This work is performed in the framework of the "Stellar Bell" part (pulsating variable stars) of the "Inter-Longitude Astronomy" project (Andronov et al., 2003, 2014, 2017). We acknowledge observations from the AAVSO (http://aavso.org), AFOEV (http://cdsarc.u-strasbg.fr/afoev), VSOLJ (http://www.kusastro.kyoto-u.ac.jp/vsnet/VSOLJ) and ASAS (http://www.astrouw.edu.pl/asas) databases.

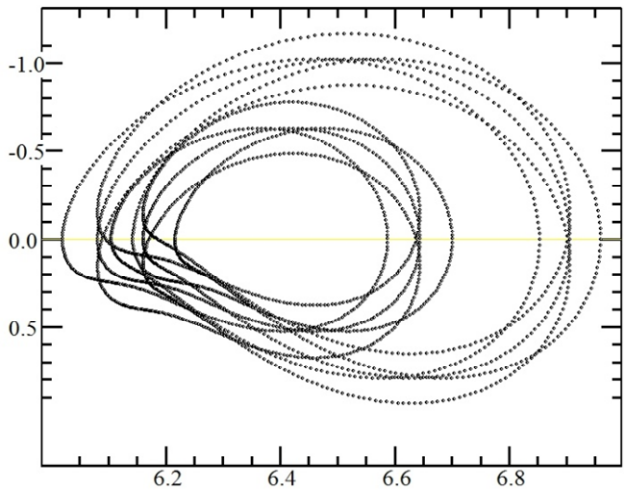

Figure 16: Phase portrait of U Mon.

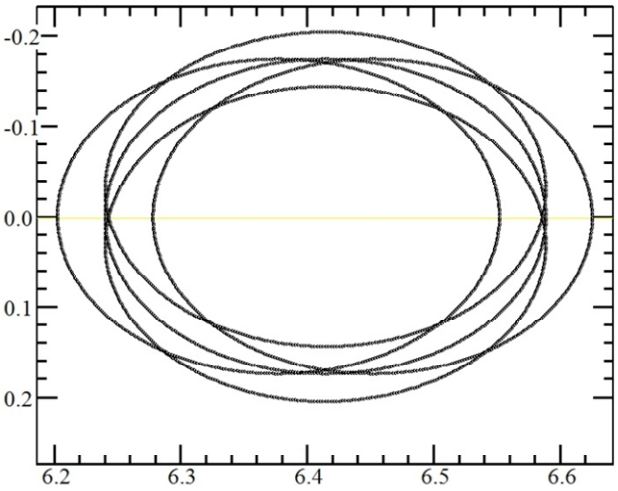

Figure 17: Phase portrait of U Mon with a half period.

References

Andronov I.L.: 1994, OAP, 7, 49.
Andronov I.L. et al.: 2003, Astron.Astroph.Trans.,22, 793
Andronov I.L. et al.: 2017, ASPC, 511, 43
Andronov I.L., Marsakova V.I., Kudashkina L.S., Chinarova L.L.: 2014, AASP, 4, 3.
Fadeyev Yu. A.: 1993, Astrophys. Space Sci., 210, 261.
Kudashkina L.S.: 2003, KFNT, 19, 193.
Kudashkina L.S.: 2015, Częstochowski Kalendarz Astronomiczny 2016, ed. Bogdan Wszolek, 265. (ptma.ajd.czest.pl/publikacje_elektroniczne/cka16.pdf)
Kudashkina L. S.: 2016, Częstochowski Kalendarz Astronomiczny 2017, ed. Bogdan Wszolek, 151. (ptma.ajd.czest.pl/publikacje_elektroniczne/cka17.pdf)
Kudashkina L. S., Andronov I.L.: 1996, OAP, 9, 108.
Kudashkina L. S., Marsakova V. I.: 2013, Częstochowski Kalendarz Astronomiczny 2014, ed. B.Wszolek, 243. (ptma.ajd.czest.pl/publikacje_elektroniczne/cka14.pdf).
Kudashkina L.S., Rudnitskij G.M.: 1988, Perem. Zvezdy, 2, 6, 925.
Maffei P., Tosti G.: 1999, 2013yCat.2320....0M
Whitelock P.A., Marang F., Feast M.: 2000, MNRAS, 319, 728.

DOI: http://dx.doi.org/10.18524/1810-4215.2017.30.114371

PHYSICAL PARAMETERS OF PROTOPLANETARY DISK SURROUNDING IRAS 22150+6109 YOUNG STAR

Kuratova A.K.[1,2], Zakhozhay O.V.[1,3], Kuratov K.S.[1,2], Zakhozhay V.A.[4], Miroshnichenko A.S.[1,5]

[1] National Center of Space Researches and Technologies, Almaty, Kazakhstan *aizhik03@gmail.com*

[2] Al-Farabi Kazakh National University, Almaty, Kazakhstan, *keneskenkuratov@gmail.com*

[3] Main Astronomical Observatory NAS of Ukraine, Kyiv, Ukraine *zakhozhay.olga@gmail.com*

[4] Kharkov National University named after V.N.Karazin, Kharkov, Ukraine *zkhvladimir@mail.ru*

[5] The University of North Carolina, Department of Physics and Astronomy, Greensboro, USA, *a_mirosh@uncg.edu*

ABSTRACT. IRAS 22150+6109 star belongs to L 1188 star forming region in Perseus, according to [1] located at distance of 910 pc from the Sun. Photometric observations in the visible range that were carried out in 1997-1999 have revealed the following features of the object: source variability 0.2^m, interstellar absorption reaches the value of $A_V = 2^m$ [2], visual brightness of $V \approx 10.8^m$ [3]. In near IR region (JHK bands) the emission excess is observed around 1^m in comparison with visible range: $J \approx 9.8^m$, $H \approx 9.7^m$, $K \approx 9.6^m$ [4]. Flux data in four bands contained in WISE catalog [5], confirmed the further increase of IR-excess in wavelength range of 3.4-21 μm. According to AKARI catalog [6] where the emission fluxes are in wavelength range of 18-160 μm, IR-flux increase continues nearly about 60 μm, thereafter it starts to decrease. Such star's spectral energy distribution (SED) is typical in the presence of dust disk surrounding it.

According to the analysis of color average data in optical range and optical spectrum, star's spectral class can be determined as B2-B3 of initial main sequence [7]. Fundamental parameters assessment according to [8] is as follows: weight – 6.5±0.5 M_{sun} and radius – 5 R_{sun}.

The aim of the work is to carry out the analysis of star's coherent astrophysical parameters and on their basis to determine parameters of the disk surrounding it.

1. Astrophysical characteristics of IRAS 22150+6109 star

Distinguishing characteristic of stars evolution before output on the main sequence is the presence of circumstellar matter, often in the disk form, from the material of protostar cloud. However, thermodynamics of disk surrounding it depends on star's definite parameters value that is important for obtaining the agreed parameters between it, surrounding it disk and observed spectral energy distribution.

For object's fundamental parameters determination the modern scale of stars astrophysical parameters was used (except radii easily determined from represented data), one of recent variations is contained in electronic form as summary table[1] compounded, generally, according to works data [9, 10]. Apparent stellar magnitude value in the band $V = 10.64^m \pm 0.06^m$ [3] is consistent with previously calculated weight 6.5±0.5 M_{sun} [8] and absolute visual stellar magnitude values $M_V = -1.5^m$ and B2V spectral type, on the condition that the studied system is located at the distance from the Sun in 950 pc, and its interstellar absorption is equal to $A_V = 2.2^m$. At these parameters the star radius should be equal to 3.7 R_{sun} rather than 5 R_{sun} as it was fore-quoted in the work [11]. Divergence of these values can be explained by the fact that the star has not yet passed to main sequence. In this case its radius can be slightly larger than the one with which it falls on main sequence, and remaining parameters nearly correspond to star's zero age values. At the same time, there are several fundamentals to assign the studied object to young systems where the disks can exist. Effective temperature value equal to $T_{eff} \approx 20\,000$ K corresponds to star assessed parameters.

2. Circumstellar disk parameters that follow from SED system

2.1. Simulation method of SED from the star and protoplanetary disk

Calculating SED from the system it was expected that emission flux on all wavelengths is the sum of fluxes from the star and from the disk. Flux from the star was calculated in black-body approximation using effective

temperatures and radii described above. Emission flux from disk was determined by expression:

$$F_{disk} = d^{-2} \int_{R_{in}}^{R_{out}} B_\nu(T_r)\, Q_\nu\, 2\pi r\, \mathrm{d}r,$$

$$Q_\nu = 1 - \mathrm{e}^{-\tau}; \quad \tau = \Sigma_r\, \kappa_\nu,$$

where r – radial distance in disk, d – distance from the system to the Sun, $B_\nu(T_r)$ – Planck function, R_{in} and R_{out} – inner and outer radius of the disk, respectively. Q – dust particles radiation efficiency, τ – disk optical thickness that is the product of surface density Σ_r depending on the distance from the star, and absorption coefficient κ_ν depending on frequency ν. Absorption coefficient was calculated with Mie theory (as in [12] work) for flush particles composed from astronomical silicates of 0.1 – 100 μm dimensions. Relation of gas mass to dust mass was excepted equal to 100. Surface density and disk temperature change with the distance under the laws (as in [13] work):

$$\Sigma_r = \Sigma_{in} \left(\frac{r}{R_{in}}\right)^p,$$
$$T_r = T_{sub} \left(\frac{r}{R_{sub}}\right)^q,$$

where p and q – surface density radial change and effective temperature exponents, respectively. R_{sub} – distance from the system center where disk temperature is equal to 1500 K – dust particles sublimating temperature [14].

2.2. Simulation results and analysis

Simulation of SED from central stars was carried out using above described algorithm and geometrical models [15, 16]. In fluxes from disks calculation it was assumed that disk's minimal inner radius is equal to the distance from the star surface on which conditions of temperature balance the dust particles will sublimate (for studied system parameters R_{sub} = 2 AU). Surface density radial change exponent p varied from 0 to –1.5, in increments of 0.5. Effective temperature radial change exponent q varied from –0.35 to –0.75, in increments of 0.01. Inclination angle value (i) varied from 0° to 60° in increments of 10°. Disk's inner and outer radii values R_{in} and R_{out} varied from minimal inner radius value to 1000 AU (in increments of 1 AU) and to 2000 AU (in increments of 10 AU), respectively.

Model that has best match with the observations was selected using minimum value determination χ^2,

$$\chi^2 = \sum_{i=1}^{n} \left(\frac{F_{obs,i} - F_{mod,i}}{\sigma_{obs,i}}\right)^2,$$

where $F_{obs,i}$ – observed flux, $\sigma_{obs,i}$ – observation error, $F_{mod,i}$ – model flux for every wavelength.

Figure 1 shows approximation result of observed SED of IRAS 22150+6109 system and calculations results according to stated algorithm. Distribution curve of SED IRAS 22150+6109 system has minimal value χ^2 over star parameters obtained in previous section and disk characteristics: R_{in} = 135 ± 15 AU, R_{out} = 850 (+1000/–250) AU, p = –0.5 (+0.5/–1.0), q = –0.65 ± 0.1 and inclination angle to observer = 20°–40°. Disk weight should not be less than 4% of star weight. Model parameters error was determined from system parameters values with which χ^2 does not exceed minimal value more than on 10%.

3. Conclusion

As it follows from above described researches, Herbig Ae/Be star and surrounding it disk are included in IRAS 22150+6109 system. Hence, the age of such system does not exceed Kelvin-Helmholtz time of 200 thous.years, according to its power-mode dependence on stellar mass (7 M_{sun}) with –2.8 exponent (see, e.g. [8, 17]). Stellar radius exceeds typical for moment of passing on main sequence, and dimensions of circumstellar disk significantly differ from analogous protoplanetary disks of solar type stars: $R_{in} \approx 135$ a.e. and $R_{out} \geq 600$ a.e. Such systems are significantly larger than Solar system.

Protoplanetary disks around stars with such mass evolve sufficiently fast. Whereby, disk loses the gas and main part of its mass. Therefore, massive disk presence around such a star means that this system is one of few observable on this stage of stellar evolution.

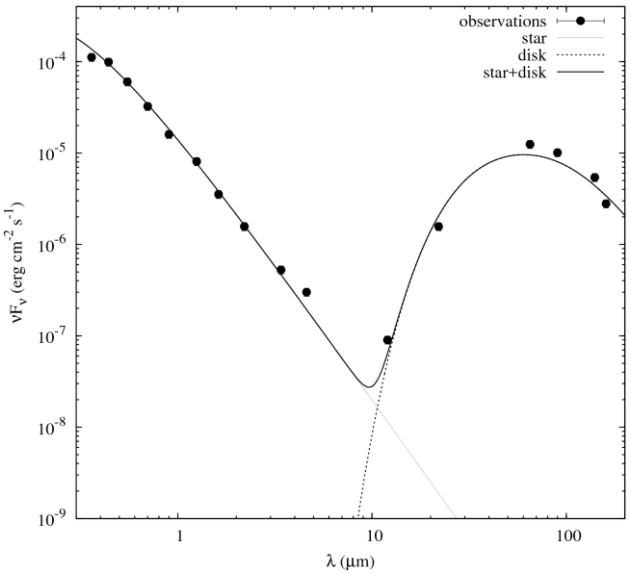

Figure 1: Observed (points) and SED calculation values of the star with didk surrounding it and calculation values of star SED with disk surrounding it approximated by two functions, the first (left) is the Planck curve (describing star's SED), and the second (right – IR-excess by means of circumstellar disk).

References

1. Abruham P., Dobashi K., Mizuno A. et al.: 1995, *Astron. Astrophys.*, **300**, 525.
2. Kuratov K.S.: 2004, *Transact., Nat., Academ., Kazakhst.*, **4**.
3. Hog E., Fabricius C., Makarov V.V. et al.: 2000, *Astron. Astrophys.*, **355**, L27.

4. Cutri R.M. et al.: 2003, *ADC Collection of Electronic Catalogues*, **2246**.
5. Wright E.L., Eisenhardt P.R.M., Mainzer A.K. et al.: 2010, *Astron. Astrophys.*, **140**, 1868.
6. Murakami H., Baba H., Barthel B. et al.: 2007, *PASJ*, **59**, 369.
7. Zakhozhay O.V., Miroshnichenko A.S., Kuratov K.S., et al.: 2017, *Proc. of the conf. The B[e] Phenomenon: Forty Years of Studies. ASP Conf. Ser.*, **508**, 191.
8. Palla P., Stahler S.V.: 1993, *Astrophys. J.*, *418*, 414.
9. Pecaut M.J., Mamajek E.C.: 2013, *Astrophys. J. Suppl. Ser.*, **208**, 9.
10. Pecaut M.J., Mamajek E.C., Bubar E.: 2012, *Astrophys. J.*, **746**, 154.
11. Straizhys V., Kuriliene G.: 1981, *Astrophys. Sp. Sci.*, **80**, No. 2, 353.
12. Zakhozhay O., Zapatero Osorio M.R., Bejar V., Boehler Y.: 2017, *MNRAS*, **464**, 1108.
13. Zakhozhay O.V.: 2017, *Kinem. and Phys. of Cel. Bod.*, **33**, is. 4, in press.
14. Dullemond C. P., Dominik C., Natta A.: 2001, *ApJ*, **560**, 957.
15. Zakhozhay V.A., Zakhozhay O.V., Vidmachenko A.P.: 2011, *Kinem. and Phys. of Cel. Bod.*, **27**, 140.
16. Zakhozhay O.V., del Burgo C., Zakhozhay V.A.: 2015, *Adv. in Astron. and Space Phys.*, **5**, 33.
17. Surdin V.G.: 2001, Birth of stars. M: URSS, 264 p.

DOI: http://dx.doi.org/10.18524/1810-4215.2017.30.114351

Hα AND Hβ PROFILE VARIATIONS IN THE SPECTRA OF THE STAR 55 CYG

Y.M. Maharramov

Shamakhy Astrophysical Observatory, Azerbaijan National Academy of Sciences, Yu. Mammadaliyev settlement, Shamakhy district, Republic of Azerbaijan
y_meherremov@rambler.ru

ABSTRACT. We study the variability of the Hα and Hβ lines in the spectra of 55 Cyg based on observations acquired in 2014 on the 2-m telescope of Shamakhy Astrophysical Observatory. In this work line profiles of Hα and Hβ are described extensively and compared with early observations. The profile of Hα line vanishes or almost vanishes in the spectra on some epochs again. Our observations showed that when the Hα line disappeared or weaken sharply in the spectra, the HeI and Hβ line are redshifted, but no synchronous variabilities were observed in other spectral lines (CII and others) formed in deeper layers of the stellar atmosphere. In addition, the profiles of the Hα and Hβ lines have been analysed, as well as their relations with possible conditions of the atmosphere of 55 Cyg.

We revealed that the structures of photospheric (CII, HeI etc.) absorption line profiles, as well as Hβ line, their radial velocities and equivalent widths are variable.

These events may be associated with a manifestation of the non-stationarity of the atmosphere or non-sphericity of the stellar wind.

Keywords: Supergiant star, stellar atmosphere, P Cyg profile, Hα and Hβ line profiles.

1. Introduction

HD198478 (55 Cyg) is a hot supergiant of spectral type B3Ia with the following parameters (Wilson, 1953; Barlow & Cohen, 1977; Gies & Lambert, 1992; Crowther et al., 2006; Markova & Puls, 2008):

m_v= 4.86 mag, T_{eff}=17500K, $M/M_\odot$=11, $R/R_\odot$=49, log $L/L_\odot$=5.31, log$g$=2.10, V_{rad}= –7.2 km/s, ξ=20 km/s, *vsini*=61 km/s, *d*=0.97 kpc

It is believed that this star belongs to Cyg OB7 association (Crowther et al., 2006).

Studying of the photospheric lines of 55 Cyg Hutchings (1970) revealed interesting facts: different elements typically different radial velocities, while the same lines show strong variations with time. In addition, Underhill (1960) described radial velocity variations of 30 km/s, but in these changes no found periodicity.

Later, Granes (1975) collected 34 spectra, based on spectral observations of the star over 15 consecutive nights, and found that the radial velocity curves oscillate with a period of four-to-five days, in addition to photospheric motions on timescales about three times longer. Kraus et al. (2015) studied the interplay between pulsations and mass loss in the blue supergiant 55 Cyg. They modeled the H, HeI, SiII, and SiIII lines using the non-local thermal equilibrium atmosphere code FASTWIND and derived the photospheric and wind parameters. In addition, they searched for variability in the intensity and radial velocity of photospheric lines and performed a moment analysis of the line profiles to derive frequencies and amplitudes of the variations. The Hα line varies with time in both intensity and shape, displaying various types of profiles: P Cyg, pure emission, almost complete absence, and double or multiple peaked. They also observed changes in the ionization rate of SiII and determined the multiperiodic oscillation in the HeI absorption lines, with periods ranging from a few hours to 22.5 days, and interpreted the photospheric line variations in terms of oscillations in p-, g-, and strange modes. Authors suggested that these pulsations can lead to phases of enhanced mass loss.

The profile of Hα line in the spectra of 55 Cyg is also highly variable.

Underhill (1960) remarked that in her spectra the Hα line maintained a P Cyg profile, but with highly variable strength. Ebbets (1982) noted that during one of his observations, Hα line showed additional faint emission wings, which were not visible anymore in the spectrum.

As seen, researchers noted that, Hα line in 55 Cyg indicates fast variable structure, but the sequence of observations was irregular and inadequate to trace in detail the changes in the spectra. Therefore they noted that more and systematic observations are needed to investigate this supergiant.

In the present paper we analyzed variations of the Hα and Hβ lines.

We also investigated the variabilities of the CII (6578.05 Å, 6582.88 Å), and HeI (5875.72 Å) lines which formed deeper effective layers in the atmosphere of this star. Our main aim is to study the observed peculiarities of these lines in the spectra.

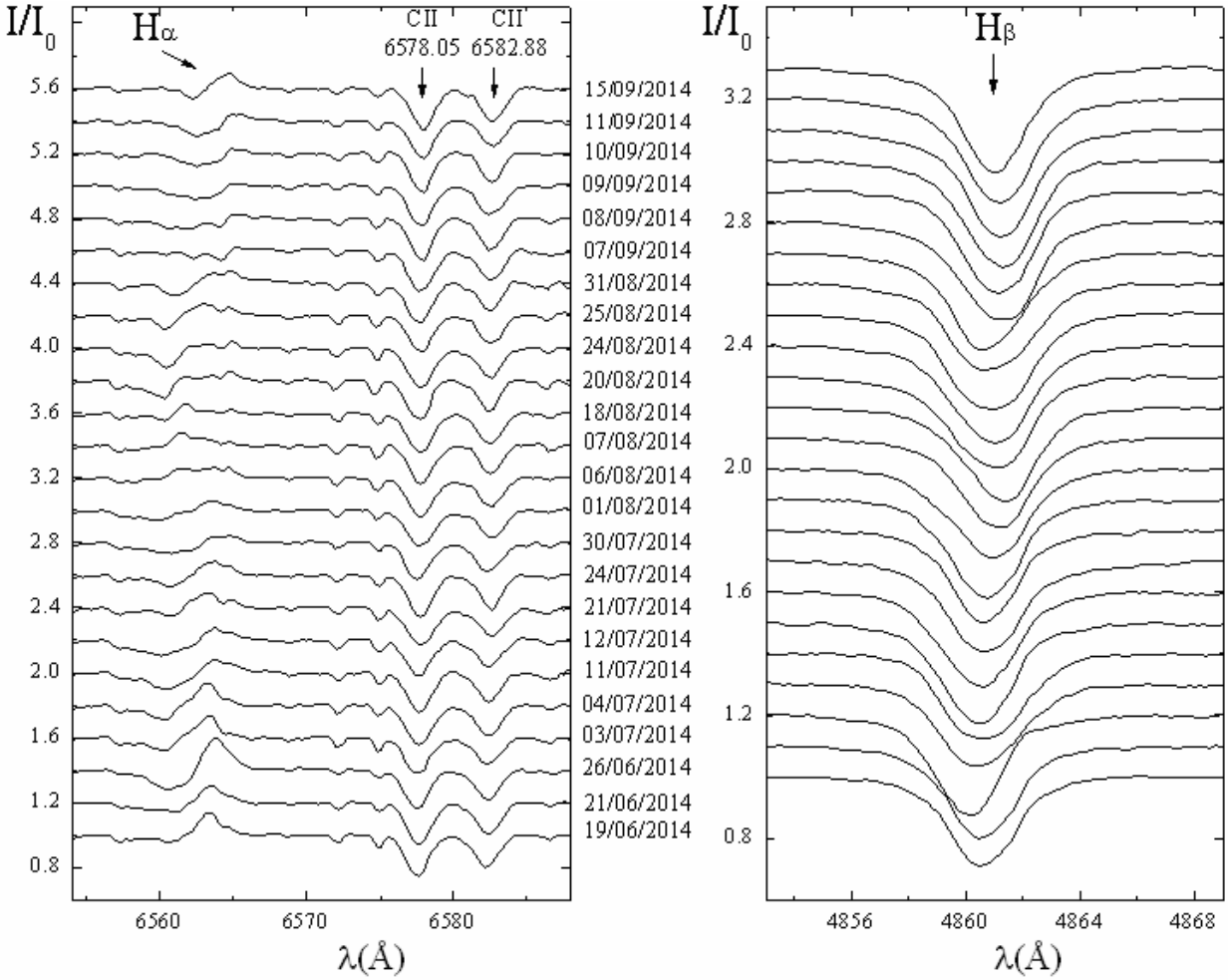

Figure 1: Profiles of the Hα, CII and Hβ lines in the spectra of 55 Cyg observed in 2014.

2. Observations and Data processing

Spectral observations of 55 Cyg were acquired during from June 19, 2014 to September 15, 2014 using a CCD detector in the echelle spectrometer mounted at the Cassegrain focus of the 2-m telescope of the Shamakhy Astrophysical Observatory (Mikailov et al., 2005). The spectral resolution was R = 15000 and the spectral range is λλ4700-6700ÅÅ. One to two spectra of the target star were obtained on each night. The signal-to-noise ratio was S/N =150-200. The average exposure was 600-900 s, depending on the weather conditions.

The Echelle spectra were processed with the standard technique using the DECH20 software package (Galazutdinov, 1992). The reduction of the spectra, which included the continuum placement, the construction of dispersion curves (from the spectra of a hollow-cathode Th+Ar lamp or radial velocity standard stars), spectrophotometric and position measurements was performed using this package.

In addition to the observations of the target star, in order to check the stability of the instrument we also obtained numerous spectra of standard stars, the daily sky solar spectrum, and comparison spectra. Thus, we recorded the spectrum of a thorium-argon lamp for wavelength calibration. The stability of the wavelength scale was verified by measuring the wavelength centroids of OI and H_2O sky lines. The long term accuracy achieved for the wavelength calibration is of the order of 1 km/s as derived from the spread of measured radial velocities of telluric lines in the spectra. The measurement error for the equivalent widths (W) does not exceed 5%, and error of the radial velocity (Vr) is of the order of ±2 km/s. Here, (Vr) are velocities of the absorption and emission peaks in the selected lines. Note that appropriate heliocentric corrections were included during data processing.

3. Results

The Hα line varies with time in both intensity and shape, displaying various types of profiles: normal P Cyg, pure absorption, pure emission, double or triple-peaked emission and complete absence.

We found that the complete absence of Hα line profile is real and recurrent. The Hβ line profiles and the radial velocities change during the observation period. When the Hα line disappears or weaken sharply the HeI and Hβ lines are redshifted.

When the Hα line disappeared in the spectra, no significant variabilities were observed in other spectral lines (except HeI and Hβ) formed in deeper layers of the stellar atmosphere.

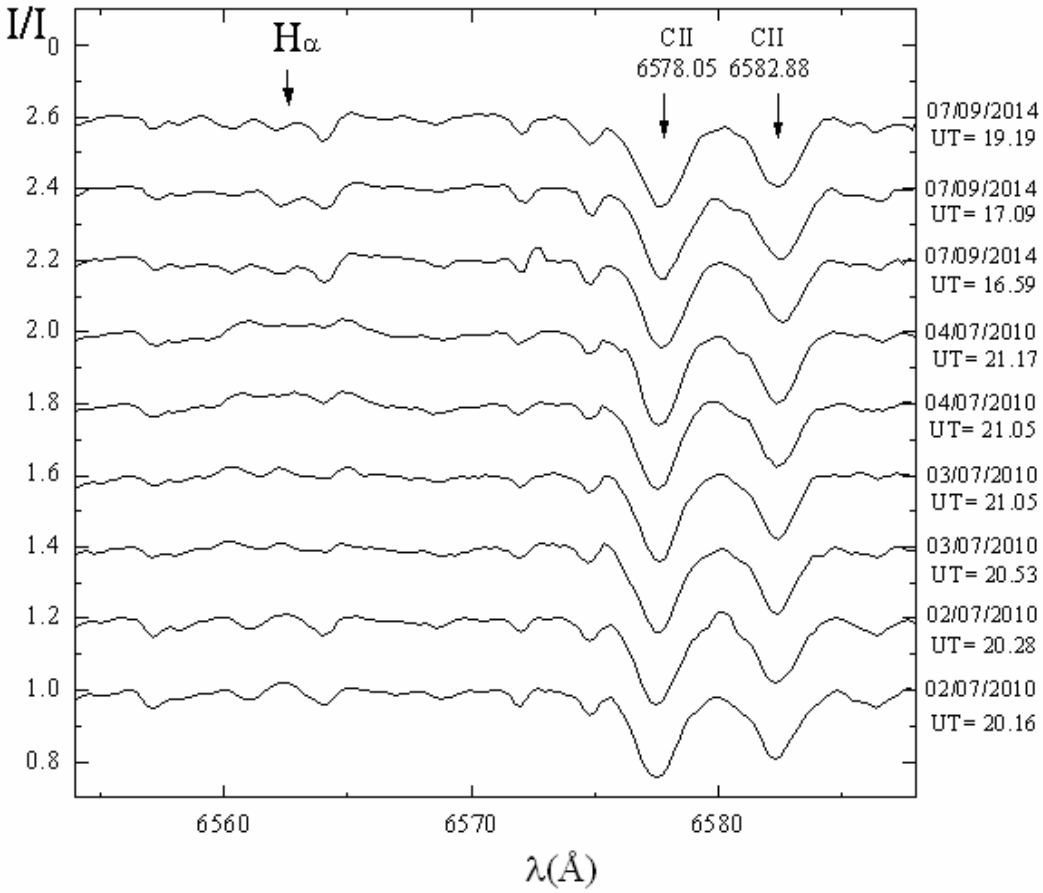

Figure 2: Hα and CII profiles in the individual spectra of 55 Cyg observed in 2010 and 2014.

In addition, in several spectra the emission components of Hα line are observed to be double or triple (Fig. 1).

During the observational period hydrogen and photospheric absorption line profiles and their radial velocities exhibited variations. The radial velocities measured from the absorption line cores vary with time and with the line intensity.

4. Data Analysis

It is known that the Hα line in the spectra of B supergiants has a clear P Cyg-type profile.

Our observations show that the most pronounced variability in the spectra of 55 Cyg are noticeable in the intensity and profiles of the Hα line. The following shapes of the Hα profile were observed: normal P Cyg profile; normal P Cyg-type profile with double-peaked in emission; normal P Cyg-type profile with triple-peaked in emission; pure emission profile; pure absorption profile; complete absence.

Fig. 1 shows the spectra of 55 Cyg in the wavelength ranges covering the Hα and Hβ regions observed in 2014. Here, the spectra obtained on 20/08/2014, and 09/09/2014 are shown individual profiles, only on 07/09/2014 are averaged three expositions, but the rest of them are averaged two expositions taken during single nights. The spectra are shifted vertically by an amount that ensures better visibility. On the right of Hα the profiles of the CII resonance doublet are seen. Vertical lines represent the laboratory position of the lines.

Hα shows variations in strength in both the absorption and emission components of the P Cyg profile (see Fig.1). The pattern of variability in 2014 can be described in the following qualitative way:

P Cyg profile with weak absorption, slowly evolves into P Cyg with deep components, later both components are weaken relatively, absorption components are broader and emissions is observed a double-peaked, only emission with triple-peaked is seen, later weaker absorption and emission components with triple-peaked are observed, both components (emission with double-peaked) are deeper, on September 07, 2014, the Hα disappeared, and on September 08, 2014, the Hα line became faint, on September 09, 2014, the absorption component became stronger and later emission component also became stronger, at last on September 15, 2014, normal P Cyg profile of Hα is observed again. As can be seen here more interesting event is the disappearance of Hα profile from the spectra. All spectral measurements presented in Table 1.

Note that similar patterns were observed in 2010 (Maharramov, 2013). So, the first time the Hα line alone is absent from the spectra on July 02-04, 2010, and no spectral features are observed at this wavelength (6562.816 Å), except for weak atmospheric lines and noise. In those spectra, all the other lines typical for hot supergiants such as 55 Cyg, apart from Hα, are observed, including Hβ. In addition, at those times we revealed that the Hβ equivalent width increased and a shift of this line toward the red is observed when Hα is absent.

Table 1. Values of the radial velocity (Vr), equivalent width (W), and depth (R) or residual intensity (r) in the Hα line.

Date	JD 2450000+	Vr(abs) km/s	Vr(em) km/s	W(abs) Å	W(em) Å	R(abs)	r(em)
2014 Jun.19	6828.40	–83	43	0.15	0.25	0.04	1.14
Jun.21	6830.41	–73	47	0.20	0.19	0.06	1.10
Jun.26	6835.34	–92	55	0.36	0.41	0.11	1.20
Jul.03	6842.29	–105	39	0.22	0.23	0.08	1.13
Jul.04	6843.29	–104	33	0.24	0.24	0.09	1.13
Jul.11	6850.32	–93	50 98	0.34	0.18	0.10	1.08 1.06
Jul.12	6851.31	–113	50 98	0.38	0.14	0.10	1.07 1.05
Jul.21	6860.31	–88	28 101	0.16	0.21	0.05	1.09 1.05
Jul.24	6863.26	–88	48 89	0.21	0.18	0.07	1.08 1.06
Jul.30	6869.27	–88	47 96	0.27	0.08	0.06	1.04 1.05
Aug.01	6871.29	–118	42 91	0.22	0.11	0.06	1.06 1.04
Aug.06	6876.33	-	–54 42 88	-	0.25	-	1.06 1.06 1.06
Aug.07	6877.31	-	–53 7	-	0.17	-	1.08 1.05
Aug.18	6888.31	–113	–41 40 91	0.07	0.08	0.05	1.05 1.01 1.02
Aug.20	6890.31	–118	–49 33 89	0.24	0.12	0.11	1.03 1.03 1.06
Aug.24	6894.21	–105	35 93	0.31	0.06	0.12	1.02 1.04
Aug.25	6895.23	–108	11 87	0.13	0.17	0.09	1.07 1.05
Aug.31	6901.22	–89	40 88	0.15	0.20	0.07	1.06 1.07
Sep.07	6908.21	-	-	-	-	-	-
Sep.08	6909.26	?	?	?	?	?	?
Sep.09	6910.16	–21 20	106	0.37	0.02	0.08 0.07	1.01
Sep.10	6911.16	–15	93	0.23	0.03	0.08	1.02
Sep.11	6912.13	–19	92	0.27	0.06	0.09	1.04
Sep.15	6916.26	–28	84	0.09	0.15	0.06	1.09

Furthermore, Kraus et al. (2015) discovered that Hα profile almost completely disappears from the spectrum again, and in their data they recognized it in 2012, July, 24 and in 2013, July, 26. Authors speculated that the wind conditions of 55 Cyg may have changed, because no earlier observational work on this star mentions phases in which the wind emission swamps the photospheric absorption line.

We noted above that on September 07, 2014, the Hα profile is absent from the spectrum of 55 Cyg again. Therefore, we suggest that this behavior is recurrent process.

Unfortunately, weather conditions before July 02-04, 2010 and September 07, 2014, did not make it possible to obtain spectra of the star 55 Cyg, which could shed light on the transition moments of this interesting process.

In order to investigate the short term variability in the Hα profile, all individual spectra obtained on July 02-04, 2010, and on September 07, 2014 were processed separately. These data are presented in Fig. 2. As can be seen the Hα profile can be variable on a time scale of hours.

In Table 1 the radial velocities, equivalent widths and the depths (and residual intensities) of absorption and emission components of Hα are presented. Our measurements show

Table 2. Measurements of the radial velocity, equivalent width and depth of the Hβ, CII, and HeI lines.

Date	JD 2450000+	CII6578.05Å		CII6582.88Å		HeI5875.72Å		Hβ		
		Vr km/s	W Å	Vr km/s	W Å	Vr km/s	W Å	Vr km/s	W Å	R
2014 Jun.19	6828.40	–9	0.50	–9	0.40	–13	0.77	–38	0.93	0.29
Jun.21	6830.41	–8	0.53	–11	0.40	–13	0.77	–41	1.00	0.30
Jun.26	6835.34	–10	0.47	–12	0.38	–20	0.76	–7	1.01	0.33
Jul.03	6842.29	–9	0.47	–10	0.35	–14	0.82	–47	0.99	0.26
Jul.04	6843.29	–8	0.54	–9	0.41	–9	0.89	–35	1.02	0.28
Jul.11	6850.32	–8	0.48	–8	0.35	–15	0.84	–40	1.07	0.33
Jul.12	6851.31	–9	0.46	–13	0.35	–14	0.85	–34	1.06	0.31
Jul.21	6860.31	–2	0.54	–4	0.41	–9	0.77	–35	0.96	0.29
Jul.24	6863.26	–5	0.51	–6	0.41	–12	0.78	–38	0.97	0.30
Jul.30	6869.27	–15	0.47	–15	0.40	–13	0.83	–30	1.07	0.32
Aug.01	6871.29	–6	0.51	–8	0.37	–6	0.84	–15	1.03	0.29
Aug.06	6876.33	–9	0.53	–11	0.40	–5	0.77	1	0.93	0.29
Aug.07	6877.31	–9	0.48	–9	0.32	2	0.81	9	1.01	0.31
Aug.18	6888.31	–12	0.53	–15	0.41	–9	0.85	–14	1.04	0.30
Aug.20	6890.31	–11	0.47	–20	0.34	–12	1.00	–15	1.09	0.32
Aug.24	6894.21	–9	0.52	–14	0.39	–6	0.88	–26	1.09	0.30
Aug.25	6895.23	–10	0.47	–12	0.35	–15	0.83	–39	1.08	0.28
Aug.31	6901.22	–16	0.52	–18	0.31	–24	0.83	–48	1.08	0.31
Sep.07	6908.21	–17	0.53	–17	0.37	–7	0.85	–4	1.30	0.32
Sep.08	6909.26	–11	0.50	–18	0.38	–10	0.89	–13	1.05	0.33
Sep.09	6910.16	–14	0.53	–23	0.40	–5	0.87	–14	1.16	0.34
Sep.10	6911.16	–12	0.44	–12	0.30	–7	0.83	–17	1.19	0.35
Sep.11	6912.13	–11	0.47	–12	0.31	–8	0.84	–19	1.14	0.33
Sep.15	6916.26	–8	0.51	–11	0.43	–11	0.83	–21	1.09	0.34

that the spectral parameters (W, R, r) and radial velocities of the absorption and emission components of the Hα line, as well as the parameters of lines of other elements, also vary with time (see Table 1 and 2). The largest variations are displayed by the emission component of the Hα line, which indicates changes of the physical condition in the expanding stellar envelope.

As seen from the Table 1 the significant changes happened in the radial velocity and spectral parameters of the Hα line. Fig.1, and Table 1 show that sometimes, Hα line absorption component is observed shifted toward the red side with a velocity of –15 km/s. Table 1 also shows that the radial velocity of the "blue" component of the absorption line Hα varies within from –118 to –15 km/s. The radial velocity of the Hα line blue emission component varies within the range of –54 ÷ +106 km/s. We have determined that the equivalent width, and depth (or the residual intensities in emission) of the absorption component of the Hα line vary within 0.07-0.38 Å, and 0.04-0.12, the emission component varies within 0.02-0.41 Å, and 1.00-1.20, respectively. Also, we noted above that Hα shows absorption and emission components with double or triple-peaked. If so to speak, the intensity inversions in the emission part of the Hα profile are observed and these are especially interesting.

To investigate the reason for variability of the Hα profile other lines (Hβ, lines of CII and HeI and others) were analyzed in the spectra. As can be seen in Fig. 1, Table 2 when the disappearance of Hα line is observed, the Hβ line is shifted toward the red simultaneously, and the Hβ equivalent width increases. The Hβ line profile also shows structural changes. Table 2 shows that radial velocity, equivalent width, and depth of the Hβ line varies within from –48 to 9 km/s, 0.93-1.30 Å, and 0.26-0.35, respectively.

Fig. 1, and Table 2 show that the shape of the CII lines change relatively during observations, as well as the radial velocities of the these lines varied between from –23 to –2 km/s. The equivalent width varies within 0.44-0.54 Å (for CII 6578.05Å) and 0.31-0.43 Å (for CII 6582.88Å).

The investigation of the HeI 5875.72 Å line showed that the radial velocity and equivalent width of this line varies between from –24 to 2 km/s and 0.76-1.00 Å (Table 2), and its profile also changed relatively (Fig. 3). As can be seen in Table 2 when the disappearance of Hα line is observed, the HeI line is also shifted toward the red simultaneously.

We also looked through the NaID doublet lines in the spectra (Fig. 3). Significantly structural changes had not been found in these profiles and the radial velocity varied between –12±2 km/s.

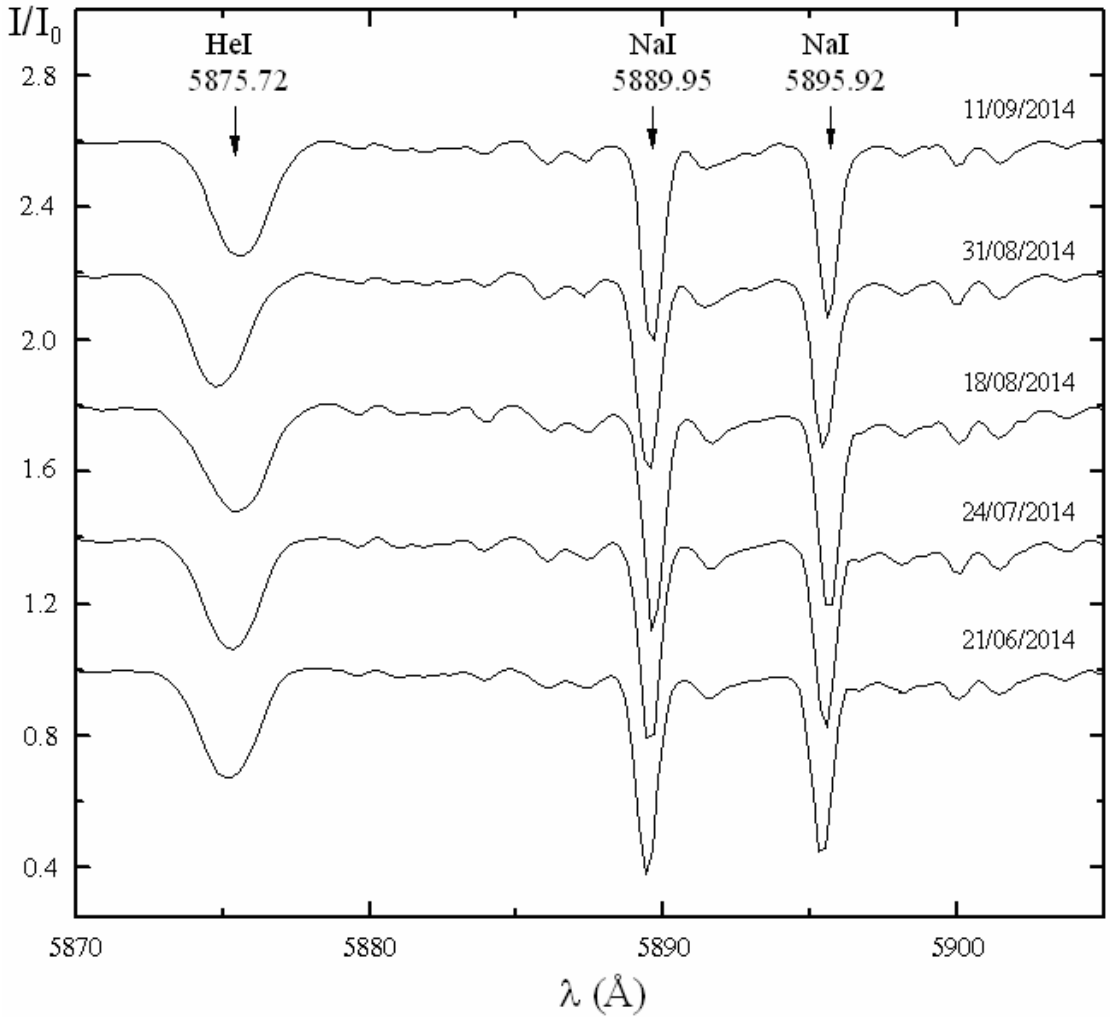

Figure 3: HeI and NaID doublet line profiles of 55 Cyg on different dates

Our measurements show that the line-profile variability (LPV) detected manifests itself by variations in velocity and line-strength, i.e. equivalent width. In particular, we found that the equivalent width, determined by means of line-flux integration within the profiles, varies within ±15 % around a mean value of 0.50 Å (for CII 6578.05 Å) and 0.35 Å (for CII 6582.88 Å), as well as, for HeI 5875.72 Å varies within ±15 % around a mean value of 0.83 Å. All these indicate the variability of the Hβ, CII and HeI lines.

It has been revealed that the variability of radial velocity and equivalent widths of Hβ line, as well as the radial velocities of averaged CII and HeI 5875.72 Å lines indicate repeating features.

There appears to be no clear correlation between variations in RVs and change in equivalent width. Fourier analysis performed for the 2014 spectroscopic series did not detect any periodicity for these lines.

In addition, we measured radial velocities of all photospheric absorption lines (CII, HeI, FeII, FeIII, AlIII, SiII, SiIII, NII, NeI, SII etc.) in the spectra and averaged them, and determined for mean velocity Vr′ =–8.5 km/s.

5. Discussion

The profile of the Hα line observed in the atmosphere of the supergiant 55 Cyg indicates rapidly variable structure. The dramatic variations previously reported in 55 Cyg (Underhill, 1960; Hutchings, 1970; Granes, 1975) are also seen in our data. Fig.1 showed that Hα exhibited the normal P Cyg type profile shape in most case. Our spectra enabled us to study the fine structure of the Hα line. The red-shifted absorption seen occasionally in Hα, is more likely of wind origin and suggests the presence of matter infall at the base of the wind (Markova et al., 2008). Our observations showed that the Hα line disappeared on September 07, 2014, again (Fig. 1), which is a manifestation of some recurrent processes in the star atmosphere.

The first time a similar variability pattern is revealed in 2010 by us (see Fig. 2). In 2010, we suggested that, when the matter of the stellar wind moves away from the observer, the central frequencies of the emission and absorption components can coincide and cancel each other out, making the Hα line disappear (Maharramov, 2013). Hα line profile completely disappeared from the spectrum in 2014 again. It shows that in particular case the wind emission was reduced so that it compensated by

coincidence for the absorption of Hα line. These events may be a manifestation of a non-stationary atmosphere of the star or a non-spherical stellar wind (Rosendhal 1973, Sobolev 1947, 1985). Note that, at the time of the disappearance of the Hα line or when it becomes faint (in 2014 September 07-08), the HeI and Hβ lines are redshifted, and their radial velocities are –7 km/s, –10 km/s for HeI, –4 km/s and –13 km/s for Hβ, respectively (Table 2). These observations may provide an evidence for the fact that in those epochs, the layer of matter where HeI and Hβ form move from away the observer and later move to the observer with too lower velocity. That is, if we take into account the velocity of mass center (Vr′=–8.5 km/s), in this case the very upper layers of the star atmosphere where HeI, Hβ, and Hα form are in the contraction phase and is non-stationary.

Also if we take into account the velocity of mass center (Vr′=–8.5 km/s), then in phases of disappearance of Hα we observe that the deeper layers (NII, SiIII, SII, AlIII and others) of the atmosphere is almost quiet, the layers where CII and SiII form are relatively expanding. It indicates that the layers where CII and SiII form are in the relatively expansion phase, and the lower layers are in the quiet phase. Therefore we suggest that disappearance of Hα is, so to speak, the mixed conditions phase of the atmosphere. Sometimes, we observed that the Hα line shows only pure absorption component and later absorption and too small emission feature (on 2014 September 9-11). It indicates that the physical conditions in the stellar atmosphere and envelope are changeable. It is known that, the variable stellar wind in the supergiants is caused by the pulsation (Cox 1983). If the dramatic changes of the Hα profile in the spectra of 55 Cyg are associated with the pulsation, they should occur periodically. But the amount of obtained data and their inconsistency in observation time does not make it possible to find such period in this study. On the other hand Kraus et al. (2015) noted that if the compensation of emission and absorption components of the Hα line were periodic, the possible period would be on the order of about one year.

As mentioned above, the photospheric absorption lines are variable. For instance, it was revealed that the relatively variability happens in the structures of CII (6578.05 Å, 6582.88 Å) and HeI 5875.72 Å lines, as well as in the other photospheric lines. Variability of the absorption lines indicates that disturbances are also occurring fairly deep in the atmosphere of the star. In particular and as also noted by Kraus et al. (2015), the results from the moment analysis suggest pulsations as the most reliable cause for the observed line profile variability in HeI and CII lines.

We suggest that the LPV of the photospheric lines are basically caused by non-radial pulsation (Kaufer et al., 1997).

In addition, the changes of the radial velocities and equivalent widths of lines Hβ, HeI and CII have been revealed (see Table 2). Sometimes, the relatively large changes in radial velocity of the photospheric absorption (CII and HeI) lines are caused by the pulsation instability (Markova, & Valchev 2000). For a more precise determination of pulsation period of star the systematic observations of this star is necessary.

Hence, observations obvious show that the Hα profile of 55 Cyg is rapid variable. We suggest that these changes may be a manifestation of complex motions in the atmosphere of this star. Especially, the disappearance of Hα line is not accompanied by synchronous changes of the spectral parameters of the other lines formed in deeper layers of the stellar atmosphere, except HeI and Hβ.

We suggest that the variations are explained probably by stellar wind properties and/or pulsations mechanisms (Kraus et al., 2015; Cox, 1983; Kaufer et al., 1997).

6. Conclusions

The Hα profile presented a complicated structure and a time variation for 55 Cyg star. For the first time in 2010, we observed that the profile of the Hα disappeared in the spectra. As this behaviour was observed in 2014 again we consider that this behavior is recurrent.

We suggest that in this particular case when the matter of the stellar wind moves away from the observer the absorption component of Hα is redshifted, and at that time the central frequencies of the emission and absorption components can coincide and cancel each other out, which may lead to the disappearance of Hα line profile.

We revealed that when the Hα line disappears or weaken sharply the HeI and Hβ lines are redshifted.

Our observations showed that the photospheric (CII, HeI etc.) line profile shapes and RVs change differently with time. We suggest that these changes in the spectra are caused by non-radial pulsations (Markova & Puls, 2008; Kaufer et al., 1997).

References

Barlow M. J., & Cohen D.: 1977, *Astrophys. J.*, **213**, 737.

Cox J.P.: 1983, "*Theory of Stellar Pulsation*", Mir, Moscow (in Russian).

Crowther P. A., Lennon D. J., & Walborn N. R.: 2006, *Astron. & Astrophys*., **446**, 279.

Ebbets D.: 1982, *Astrophys. J., Suppl. Ser.,* **48**, 399.

Galazutdinov G.A.: 1992, *Prepr. SAO RAS*, **92**, 2.

Gies D. R., & Lambert D. L.: 1992, *Astrophys. J*., **387**, 673.

Granes P.: 1975, *Astron. & Astrophys*., **45**, 343.

Hutchings J.B.: 1970, *Mon. Not. R. Astron. Soc*., **147**, 161.

Kaufer A., Stahl O, Wolf B. et al.: 1997, *Astron. & Astrophys*., **320**, 273.

Kraus M. et al.: 2015, *Astron. & Astrophys*., **581**, A75, 1.

Maharramov Y.M.: 2013, *Astronomy Reports*, **57**, 303.

Markova N., Prinja R. K., Markov H. et al.: 2008, *Astron. & Astrophys*., **487**, 211.

Markova N. & Puls J.: 2008, *Astron. & Astrophys*., **478**, 823.

Markova N. & Valchev T.:2000, *Astron. & Astrophys*., **363**, 995.

Mikailov Kh.M., Khalilov V.M., Alekberov I.A.: 2005, *Tsirk. ShAO*, **109**, 21.

Rosendhal J.D.: 1973, *Astrophys. J*., **186**, 909.

Sobolev V.V.: 1947, "*Moving Envelopes of Stars*", Leningrad.

Sobolev V.V.: 1985, "*Course in Theoretical Astrophysics*", Moscow, Izdatel'stvo Nauka.

Underhill A. B.: 1960, *Publ. Dom. Astrophys. Observ*., **11**, 353.

Wilson R.E.: 1953, *Carnegie Institution of Washington D.C., Publ*., 601.

DOI: http://dx.doi.org/10.18524/1810-4215.2017.30.114355

THREE GIANTS – MEMBERS OF THE OPEN CLUSTER M 67

T.Mishenina[1], V.Klochkova[2], V.Panchuk[2], N.Basak[1], V.Kovtyukh[1], S.Korotin[1,3], A.Velichko[4]

[1] Astronomical Observatory, Odessa National University, 65014-UA Odessa, Ukraine
tmishenina@ukr.net

[2] Special Astrophysical Observatory, Nizhnij Arkhyz, 369167, Russia

[3] Crimean Astrophysical Observatory, Nauchny, 298409, Crimea

[4] V. N. Karazin Kharkiv National University, Kharkiv, Ukraine

ABSTRACT. We determined the atmospheric parameters and chemical composition of the three giants, which are members of the open cluster M 67. The high resolution spectra (R = 60 000) were obtained with the echelle spectrograph NES mounted on the 6-meter telescope of the SAO RAS Obtained variations in Na and Zr abundances are within the determination errors. The Li abundance suggest a depletion of Li in the course of stellar evolution. For studied giants, the iron abundances derived from the neutral and ionized iron lines have not shown any significant discrepancies. The [Ba/Fe] values are close to the solar ones.

Keywords: stars: abundances – stars: atmospheres – Galaxy: open clusters and associations: individual: M 67

1. Introduction

The open cluster M 67 (NGC 2682) was discovered by Johann Gottfried Koehler in 1779 and is one of the best studied open clusters (OCs). It is also one of the oldest known Galactic clusters with an estimated age of about 4.3 Gyr (Pietrukowicz, 2006), it lies at a distance between 800 and 900 pc away (e.g. Sarajendini *et al.*, 2009), and has the reddening value E(B–V) = 0.041±0.004 (Taylor, 2007). M 67 contains a high percentage of blue stragglers, stars which are bluer and more luminous than the main-sequence turn-off point of the cluster (Pribulla et al 2008); for this cluster, the turn-off occurs near B−V = 0.55, and V = 13.0.

Our target stars, namely 84, 141, 151 (Fagerholm, 1906) show enhancement in CN band strengths and are 'clump' giants (Pagel, 1974). Carraro *et al.* (1996) evaluated the mass loss in M 67 based on the determinations of masses of the clump stars and RGB giants. Due to a small offset as d[B–V] = 0.01 mag, it was unfeasible to use the clump stars to infer the efficiency of mass loss along the RGB phase. They also reported that there was no evidence for a dependence of the mass-loss rate from RGB stars on metallicity.

Tautvaišienė *et al.* (2000) analyzed spectra of six core helium-burning 'clump' stars and three giants in M 67 to detect any signs of extra mixing associated with the He-core flash. They claim that the metallicity of M67 is close to solar ([Fe/H] = −0.03±0.03, the carbon is depleted by about 0.2 dex, nitrogen is enhanced by about 0.2 dex and oxygen is unaltered. The mean C/N and $^{12}C/^{13}C$ ratios are lowered to the values of 1.7±0.2 and 24±4 in the giants and to the values of 1.4±0.2 and 16±4 in the clump stars. The results obtained enabled to suggest that extra mixing of CN-cycled material to the stellar surface takes place after the He-core flash. Abundances of other elements in investigated stars were found to be close to the solar ones.

Our goal is to re-determine the parameters and chemical composition of the three clump stars of the M 67 cluster. The stars in question are shown on the Hertzsprung-Russell diagram for M 67 presented in Fig. 1; the V and B–V values have been adopted from Geller *et al.* (2015).

2. Observations and radial velocities

The main characteristics of the M 67 cluster stars, as well as the observational data, are given in the Tables 1, 2, respectively.

The spectral data have been obtained with the echelle spectrograph NES (Panchuk *et al.*, 2006, 2017) mounted on one of the Nasmyth focus platforms of the 6-meter telescope of the SAO RAS. NES provides a resolving power of R≥60000 within the wavelength region 3200-10000 ÅÅ. The reduction of stellar spectra, as well as the measurement of radial velocities VR, has been performed using the DECH20 software package (Galazutdinov, 1992).

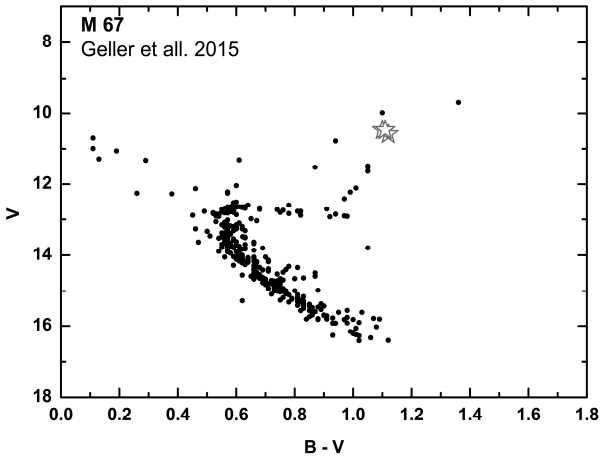

Figure 1: The H-R diagram for M 67; the V and B–V data have been taken from Geller *et al.* (2015). Clump giants marked as asterisks.

Mathieu *et al.* (1986) have reported that the M 67 mean radial velocity VR = 33.5±2.8 km/s (for 65 cluster member stars). It can be seen that there is good agreement between our VR values and those obtained by other authors (Table 2).

3. Parameter determination

The effective temperatures T_{eff} were estimated by calibration of line-intensity ratios – T_{eff} (Kovtyukh *et al*., 2006); the results are presented in Table 3.

To determine the gravity log g we used two methods: iron ionisation equilibrium (IE) and parallaxes (Pi). The obtained log g values are given in Table 4.

For two stars (namely, 84 and 141), we have obtained a noticeable difference in the value of gravity values, which is associated with use of two different methods. Further computations of elemental abundances have been performed using log g derived under conditions of ionization equilibrium for iron.

It should be noted that when using the parallax, we encountered a certain problem with parallax measurements can result in different distances to objects, which in turn leads to different values of gravity. For example, the parallax for the star 84 is 0.00097 and corresponds to the distance to the object 1030 pc. For the star 141, the parallax is 0.00088 and the relevant distance is 1136 pc. For the star 151 the parallax was markedly different from those for the two other target stars: the parallax for 151 is 0.00240; that means the determined distance, which is 417 pc. The latter distance value differs significantly from the distances to this cluster estimated earlier (e.g. Sarajendini *et al.*, 2009), as well as from the data obtained recently by Viani & Basu (2017), who have reported that from the resulting isochrones that fit the M 67 cluster, the age range is between 3.6 and 4.8 Gyr while the distance is between 755 and 868 pc.

Microturbulent velocity V_t was determined from independence of an abundance log A(Fe) from equivalent width EW for Fe I lines. The metallicity [Fe/H] was adopted as the iron abundance determined from Fe I lines.

All the parameters, which we have obtained, are presented in Table 5.

4. Chemical abundance determination

The elemental abundances were determined using Castelli & Kurucz's (LTE) models; the Kurucz WIDTH9 code was used for the LTE determination of Si, Ca, Ni, Fe, Zn, Y, Zr, La, Ce, Pr, Nd and Sm abundances; the modified latest version of STARSP (Tsymbal, 1996) was employed for the LTE determination of Li and Eu abundances; and the modified MULTI code (Carlsson, 1986; Korotin *et al*., 1999) was used for the NLTE determination of O, Na, Al, Mg, Ca and Ba abundances. The spectrum synthesis fitting of the Mg and Na lines to the observed profiles for 141 star is shown in Figs. 2, 3.

The elemental abundances [El/Fe] as function of metallicity [Fe/H] for the investigated stars are depicted in Fig. 4.

Table 1. The main characteristics of the target M67 giants

Star	star(2)	star(3)	alpha	Delta	V	B-V	Sp
84	6492	1074	8:48:28.54	12:03:58.7	10.59	1.12	G8III
141	6485	1010	8:48:38.72	11:59:18.6	10.48	1.11	K2 III
151	6494	1084	8:48:42.03	12:05:09.0	10.48	1.10	G8III

the name of stars have been taken from: (1) – Fagerholm (1906), (2) – Montgomery *et al.* (1993), (3) – Sanders (1977); the V, B–V and Sp Type data have been adopted from Geller *et al.* (2015) and Pribulla *et al.* (2008), respectively.

Table 2. Observations and radial velocities VR (km/s)

Star	Spec	λ (Å)	date	VR_{our}	VR_1	VR_2	VR_3
84	S34902	4500-6000	24.04. 2002	34.4	34.1	33.8	-
141	S39508	5275-6765	15.04. 2003	33.9	32.7	-	33.0
151	S39602	5275-6765	16.04. 2003	33.9	33.7	-	-

VR_1 have been taken from Geller *et al.* (2015); VR_2 – from Jacobson *et al.* (2011); VR_3 – from Yong *et al.* (2005).

Table 3. T_{eff} estimates

Star	T_{eff}	σ_1 ±	σ_2 ±	n
84	4755	28.7	64	5
141	4755	13.0	71	26
151	4745	17.6	75	18

where σ_1 is SEM, σ_2 is the individual error, n is the number of relevant calibrations.

Table 4. Surface gravity determinations

Star	T_{eff}	Pi	V	BC	log g(Pi)	log g (IE)
84	4755	0.00097	10.59	-0.433	2.25	2.7
141	4755	0.00088	10.48	-0.433	2.12	2.7
151	4745	0.00240	10.48	-0.439	2.98	2.8

where Pi have been adopted from SIMBAD, GAIA collaboration (2016); the Bolometric correction (BC) from Flower (1996).

Table 5. The parameters obtained for the target stars

Star	Spec	T_{eff}	log g	Vt	[Fe/H]
84	34902	4755	2.7	1.4	0.01
141	39508	4755	2.7	1.4	0.01
151	39602	4745	2.8	1.3	0.04

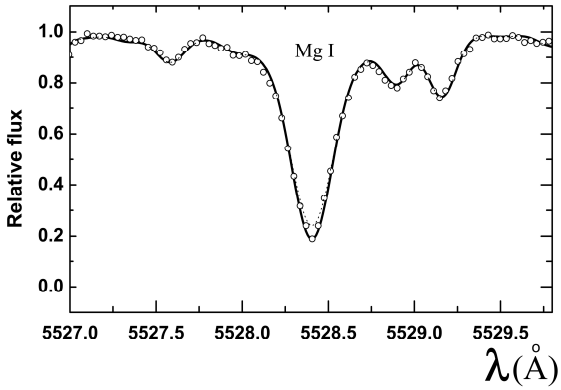

Figure 2: Observed (circles) and calculated (NLTE, solid, and LTE, dashed lines) spectra in the region of Mg I line for 141 star.

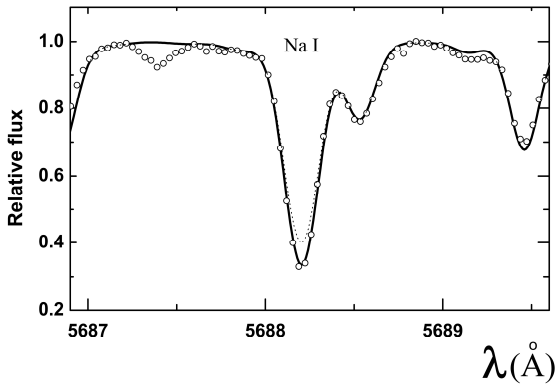

Figure 3: Observed (circles) and calculated (NLTE, solid, and LTE, dashed lines) spectra in the region of Na I line for 141 star.

To determine the systematic errors in the elemental abundance resulting from uncertainties in the atmospheric parameter determinations, we derived the elemental abundance of star 141 (T_{eff}/4755, log g/2.7, V_t/1.4, [Fe/H]/0.01) for several models with modified parameters (δT_{eff}=±50 K, δ log g= ± 0.2, δV_t=±0.1).

The total uncertainty due to parameter and EW errors for Fe I, Fe II are 0.06, 0.08, respectively. The determination accuracy varies from 0.06 to 0.15 dex.

A comparison of our data with the results of other authors is given in Table 6.

In general, there is good agreement between our determinations and those of other authors for all parameters, except for the gravity.

5. Results and discussions

We have compared our determinations with those of other authors; as an example, Fig. 5 illustrates the results of the comparison of our data for the star 84 with the data obtained by Tautvaišienė *et al.*, (2000).

The authors have found that the stars 84, 141 and 151 show a slight overabundance of Na (+0.17, +0.24 and +0.22, respectively) and underabundance of Zr (–0.18, –0.19, –18, respectively).

Sodium. The target three stars have been also studied by Jacobson *et al.* (2011). For the M 67 stars 84, 141 and 151 the authors have reported slightly different individual values of [Na/Fe], such as -0.06, 0.15, and 0.10, respectively. According to our LTE determinations, the Na abundances are 0.03, 0.11, and 0.08, respectively, these values are fairly similar to the determinations by Jacobson *et al.* (2011). Yong *et al.* (2005) have reported an overabundance of Na ~ +0.30 for the cluster M67. In all the afore-mentioned studies, the Na I lines λ 5682.64, 6154.23 and 6160.75 Å were used for the Na abundance determinations.

In so doing, despite the difference (about 0.2 dex) in the sodium abundance obtained by Tautvaišiene *et al.* (2000) and Jacobson *et al.* (2011), the equivalent widths EW of the lines 6154.23 and 6160.75 Å, e.g., for the star 84, given in both these paper are similar, the EWs are 84 and 110 mÅ, and 82 and 106 mÅ, respectively.

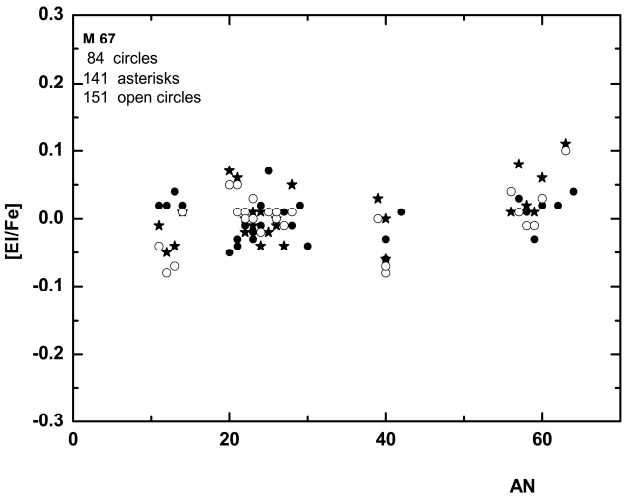

Figure 4: [El/Fe] vs. [Fe/H] for the target stars

Table 6. A comparison of our findings with the results of other authors

#	Star	T_{eff}	log g	[Fe/H]	reference
1	84	4755	2.7	0.01	This work
		4702	2.40	-	Kordoratis *et al.*, 2013
		-	2.56	-	Pace *et al.*, 2012
		4650	2.5	0.00	Jacobson *et al.*, 2011
		4750	2.4	-0.02	Tautvaisiene *et al.*, 2000
2	141	4755	2.7	0.01	This work
		4700	2.4	0.09	Jacobson&Friel, 2013
		-	2.56	-	Pace *et al.*, 2012
		4700	2.4	0.08	Jacobson *et al.*, 2011
		4730	2.4	-0.01	Tautvaisiene *et al.*, 2000
3	151	4745	2.8	0.04	This work
		4740	2.62	-	Meszaros *et al.*, 2013
		4700	2.4	-0.02	Jacobson *et al.*, 2011
		4760	2.4	-0.03	Tautvaisiene *et al.*, 2000

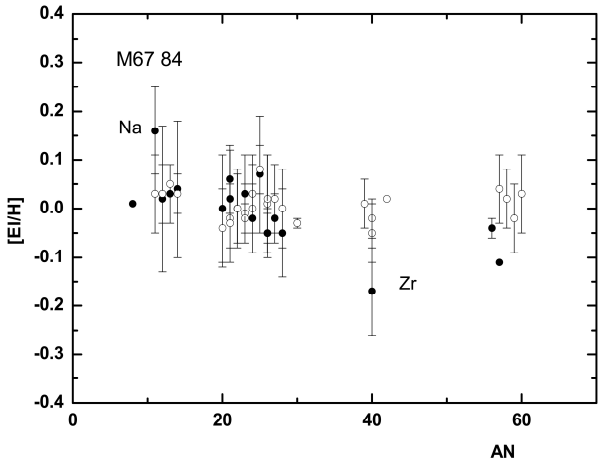

Figure 5: A comparison of our data for the M 67 cluster star F84 (open circles) with those obtained by Tautvaišienė *et al*. (2000) (full circles).

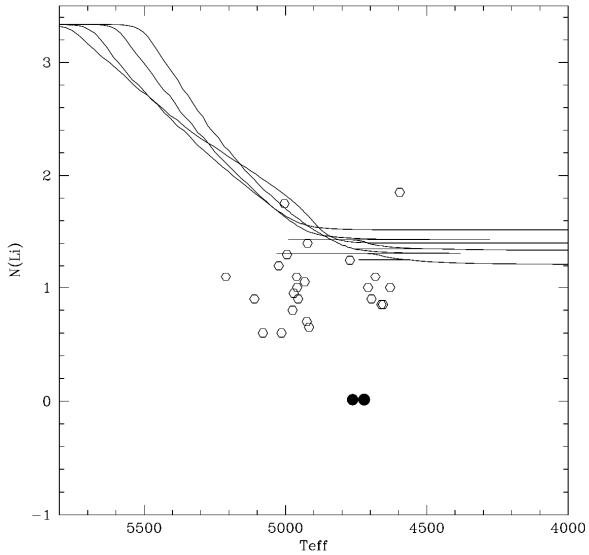

Figure 6: Li abundance vs. T_{eff}; our data are marked with full circles; trend lines illustrate the calculations performed by C. Charbonnel for the Li abundance after the first dredge-up; and the data obtained by Mishenina *et al*. (2006) for the clump giants are marked with open circles.

Zirconium. For the target stars, Jacobson *et a*l. (2011) found underabundance of Zr equal to –0.18, –0.16 and –0.10, respectively. Later, Jacobson *et al*. (2013) have re-determined the zirconium abundances and obtained an average value <[Zr/Fe]> of –0.01 ± 0.07 for the M67 cluster. Yong *et al*. (2005) have found [Zr/Fe] = −0.28 ± 0.03 for M67; however, Maiorca *et al*. (2011) have obtained [Zr/Fe] = +0.04 ± 0.05. While in the studies by Tautvaišienė *et al*. (2000), Jacobson *et al*. (2011, 2013), Yong *et al*. (2005), as well as in our study, the same Zr I lines, namely 6134.57, 6140.46, 6243.18, 6313.03 Å were used, Maiorca *et al*. (2011) used the UV Zr II lines, namely 4050.32, 4208.98, 4379.74 Å.

According to our Zr abundance determinations, there is a slight deficit of Zr for the three target stars: the mean underabundance from Zr I lines is –0.05 ± 0.01 and from Zr II lines <[Zr/Fe]> is – 0.02 ± 0.01.

Thus, in the studied stars in M67, the differences observed in elemental abundance, in particular of sodium and zirconium, depend on the individual approach of different authors and are within the errors of determination.

Now, let us consider the behavior of several elements (Li, Fe, Ba), which are especially manifested in OC's stars.

Lithium. Clump giants have shown Li abundances slightly lower than the upper limit of the first dredge up (Fig.6). We have only determined the upper limit of the Li abundance, which is about 0.0 in our stars (141 and 151). These values corroborate the Li abundance of star 141 (0.0) obtained by Pace *et al.* (2012). This value corresponds to a greater depletion of Li during the evolution of stars due to the presence of additional mechanisms that change the lithium abundance and operate inside stars (for example, meridional circulation or diffusion) or are the result of deeper mixing.

The iron problem. Yong *et al.* (2004) and Shuler *et al.* (2004) have found remarkable discrepancies between the iron abundances determined with Fe I and Fe II lines in the dwarf stars in the young clusters Hyades, Pleiades and M34. Till now the cause of that is unknown: NLTE effects (Yong *et al.*, 2004) for lines Fe II are negligible; blended lines are not used. We applied the same lines of Fe I and Fe II as in above mention papers and obtained the same iron abundances from lines of both species (within the given accuracy of determinations).

The Ba puzzle. The observed Ba overabundance in young OC's may be due to different causes: 1) additional enrichment with s-process elements from low mass AGB stars (d'Orazi *et al.*, 2009) or with i-process elements (Mishenina *et al.*, 2015); 2) NLTE corrections (Reddy & Lambert, 2015), but LTE correction is small, < 0.05 dex; 3) chromospheric activity or microturbulent velocity Vt (Reddy & Lambert, 2017). And if the study of influence of chromospheric activity on Ba line intensity can be reasonable, then the variation of the turbulent velocity by 3 times for one line, moreover having a depth of line formation of about log τ = –2 in solar atmosphere, has no substantial grounds. So, there is no definitive answer about the origin of Ba overabundance for today. Our [Ba/Fe] values are from 0.01 to 0.04 dex, it is near solar value. M 67 is old cluster and this is the expected result.

6. Conclusion

- The results which we have obtained show good agreement with the data reported by other authors.
- Variations in sodium and zirconium abundances are within the given accuracy of determinations.
- The Li abundance determinations suggest a greater depletion of lithium in the course of stellar evolution.
- For M 67 giants, the iron abundances derived from the neutral and ionized iron lines have not shown any significant discrepancies.
- M 67 is found to be an old open cluster with the [Ba/Fe] values close to the solar ones.

References

Carlsson M.: 1986, *Uppsala Astron. Obs. Rep.,* **33**.
Carraro G., Girardi L., Bressan A., Chiosi C.: 1996, *A&A*, **305**, 849.
Castelli F., Kurucz R.: 2004, preprint (ArXiv:0405087).
d'Orazi V., Magrini L., Randich S. et al.: 2009, *ApJ,* **693**, L31.

Flower P. J.: 1975, *A&A*, **41**, 391.
Fagerholm, E.: 1906, Ueber den Sternhaufen Messier 67 *Ph.D. thesis,* Uppsala Univ.
Gaia Collaboration: 2016, *A&A*, **595,** id.A2.
Galazutdinov G.: 1992, *Preprint SAO RAS*, n **92.**
Geller A., Latham D., Mathieu R.: 2015, *AJ*, **150**, id.97.
Jacobson H., Pilachowski C., Friel E.: 2011, *AJ*, **142**, id.59.
Jacobson H., Friel E.: 2013, *AJ*, **145**, id.107.
Kordopatis G., Gilmore G., Steinmetz M. et al.: 2013, *AJ*, **146**, id.134.
Korotin S., Andrievsky S., Luck R.: 1999, *A&A*, **351**, 168.
Kovtyukh V., Soubiran C., Bienaymé O. et al.: 2006, *MNRAS*, **371,** 879.
Kupka F., Piskunov N., Ryabchikova T. et al.: 1999, *A&A Suppl. Ser,* **138**, 119.
Maiorca E., Randich S., Busso M. et al.: 2011, *ApJ,* **736**, id.120.
Mathieu R., Latham D., Griffin R., Gunn, J.: 1986, *AJ*, **92**, 1100.
Mészáros Sz., Holtzman J., García Pérez A. et al.: 2013, *AJ*, **146**, id.133.
Mishenina T., Bienaymé O., Gorbaneva T. et al.: 2006, *A&A*, **456**, 1109.
Mishenina T., Pignatari M., Carraro G. et al.: 2015, *MNRAS*, **446**, 3651.
Montgomery K., Marschall L., Janes K.: 1993, *AJ*, **106**, 181.
Pagel B. E. J.: 1974, *MNRAS*, **16**7, 413.
Pace G., Castro M., Meléndez J. et al.: 2012, *A&A*, **541**, id.A150.
Panchuk V., Klochkova V., Najdenov I., Yushkin M.: 2006, *Proc. of the Joint Discuss. n.4 IAU general Assembly of 2006.* Ana I. Gómez de Castro and Martin A. Barstow (eds.), 179.
Panchuk V., Klochkova V., Yushkin M. 2017, *Astron. Rep.,* **61**, 820.
Pietrukowicz P.; Kaluzny J., Krzeminski W.: 2006, *MNRAS*, **365**, 110.
Pribulla T., Rucinski S., Matthews J. et al.: 2008, *MNRAS*, **391**, 343.
Reddy A., Lambert D.: 2015, *MNRAS*, **454,** 1976.
Reddy A., Lambert D.: 2017, preprint (ArXiv:170707051)
Sanders W. L.: 1977, *A&A Suppl. Ser.,* **27**, 89.
Sarajedini A., Dotter A., Kirkpatrick A.: 2009, *ApJ,* **698**, 1872.
Schuler S., King J., Hobbs L., Pinsonneault M.: 2004, *ApJ,* **602**, L117.
Tautvaišiene G., Edvardsson B., Tuominen I., Ilyin I.: 2000, *A&A*, **360**, 499.
Taylor B. J.: 2007, *AJ***, 133**, 370.
Tsymbal V.: 1996, *ASP Conf. Ser.,* **108**, 198.
Viani L., Basu S.: 2017, preprint (ArXiv:1705.06761).
Yong D., Lambert D., Allende Prieto C., Paulson D.: 2004, *ApJ*, **603**, 697.
Yong D., Carney B., Teixera de Almeida M.: 2005, *AJ*, **130**, 597.

DOI: http://dx.doi.org/10.18524/1810-4215.2017.30.114365

3D NUMERICAL HYDRODYNAMICAL MODELS OF THE PRECESSING THICK ACCRETION DISK AND ON- AND OFF-STATE GENERATIONS IN MICROQUASARS

V.V. Nazarenko, S.V. Nazarenko

Astronomical Observatory, Odessa National University,
Shevchenko Park, Odessa, 65014, Ukraine, *nazaret@te.net.ua*

ABSTRACT. The thick accretion disk and donor's wind on the example of CYG X-1 are computed. The main aim of the present simulations is to calculate the precessing thick accretion disk and ON- and OFF-state generation by the methods of 3D numerical hydrodynamics. The main task of the present research is to investigate the dependencies of the central disk temperature and mass accretion rate versus time. Non-stationary Euler's hydrodynamical equations are resolved by astrophysical variant of large-particle method by Belotserkovskii & Davydov. The ON- and OFF-state generation for the precessing thick accretion disk was setting. The correlation between radio flux and X-ray was setting. Our present calculations also show that in the cases of the thick accretion disk the jet velocities will be close to 0.24 -0.26 of light speed (see for instance SS433) and on contrary in the cases of a thin accretion disk jet velocities will be close to 0.98 -0.99 of light speed (see for instance CYG X-1).

Keywords: Stars: binaries – stars: jets – methods: numerical – hydrodynamics.

1. Introduction

In the present report we have continued to simulate ON- and OFF-states in microquasars. In our previous works we have modelled ON- and OFF-states on the base of thin accretion disk and microquasar CYG X-1. In these works the simulation of ON- and OFF-states on the base of long precession Nazarenko & Nazarenko (2014), the simulation of low/hard and high/soft states in accretion discs of microquasars and quasars on base of undefined precession Nazarenko & Nazarenko (2015) and the simulations of a radiation-driven jet launch and disappearing over low/hard state Nazarenko & Nazarenko (2016) were made.

In our present work we will simulate the thick accretion disk (the disk with the radiation pressure) and on this base the ON- and OFF-states will br simulated on the example of microquasar CYG X-1. For this purpose we have modelled the slaved precession of accretion disk and the donor's wind. We hope that in the precession thick accretion disk having been blown by the donor's wind two states in the disk's centre will begin to be generated – with the high and low density and temperature.

2. The numerical algorithm

To compute the thick accretion disk models, we have calculated the mass flow from the initial state to a steady one. To this end, we have used non-stationary Euler equations of hydrodynamics which are solved using the astrophysical variant of the large-particle method by Belotserkovskii & Davydov (1982). The distinction between astrophysical and standard applications of the large-particle method consists in the use of the internal energy at the first time substep in the astrophysical variant of the code.

In the computations, we have used a Cartesian coordinate system in which the X-axis lies on the line of centres. In this coordinate system, the donor position is 0.0, 0.0, 0.0, and that of accretor is 1.0, 0.0, 0.0. In the computations, we have factored in the gravity force and gas pressure of the binary components, as well as the Coriolis and centrifugal forces of the orbital motion. We calculated the gravity of the binary components in the approximation of the Roche model. We set the orbits of the binary components to be circular. To make an accretion disk to be thick one we have calculated radiation pressure z-component, $F_{rad,z}$, in the disk volume. Here we explicitly imply that the radiation pressure is differently from zero in the disk volume along z-axis only.

$$F_{rad,z} = \frac{\alpha \cdot H_z}{c} \quad , \tag{1}$$

where α is the coefficient of Thomson scattering, H_z is radiation flux along z-axis and c is light speed.

In this work and in the presented computations, we have employed the following dimensionless units. The density is expressed in units of 10^{11} particles per cm^{-3}; all distances are given in units of the orbital separation;

the temperature is given in units of eV. In the computations, the velocities are expressed in units of V_{orb} while in the figures presented in this paper, we have employed km s^{-1} as the velocity units. The time is expressed in such units that the orbital period is equal to 2π.

The code in use in the present paper is belonging to so-called methods of 'through account'. The last means that all the features of flow (shock, shock front, discontinuities and et cetera) are calculated through the single algorithm.

For the simulations presented in this work, RC has been calculated accordingly to the model for the radiative cooling of a low-density plasma with cosmic abundances in the ionisation equilibrium described in Cox & Daltabuit (1971).

The description of the used numerical algorithm in details one may see in Nazarenko & Nazarenko (2014, 2015, 2016).

In the present research the space resolution of the numerical grid in use was about of 5000 ÷ 6000 Schwarzcshild radii. In the real microquasars the hot disk corona and jets are produced on the highness the hot disk corona and jets are produced on the highness order of 50 ÷ 100 Schwarzcshild radii. It means that our space resolution is very low to produce hot corona really from quantitative point of view. But from quality point of view our present simulation may be very real since we can not to make the space resolution to be as in the real microquasars because of the very large computer expenses (we must cover all the disk space by one numerical grid).

The computations have been performed using FORTRAN 9.1. We have also employed the double-precision operations in the calculations.

3. The results

The plan of our present calculations is such that initially up to 36.5 precession period we were simulated the thin precession accretion disk (with the slaved precession) and after it, beginning with 36.5 precession period we start to calculate radiation pressure (Z-component only) into accretion disk. By this reason the disk become thick one very rapidly (on dynamic time scale) and after it we continue our calculation up to 41.5 precession period in order to see the disk properties over sufficiently long time.

To show the disk plane and vertical structure of the calculated thick accretion disk we are plotted the cross-section of the calculation area by X-Y plane lying on the disk plane (see Fig.1, Fig.2) and by the Z-X plane lying on the line of centres (see Fig.3, Fig.4) for times of 37.01 (Fig.1, Fig.3) when the temperature is high in the disk's centre and for times of 38.61 (Fig.2, Fig.4) when the temperature is low in the disk's centre). As one can see from these pictures the vertical size of disk is practically equal to the orbital disk size. By the other words we really see the thick disk on Fig.3, Fig.4. These figures also show that some features are present in the disk – here we have in mind in first turn the presence of funnel along the disk rotation axis, placed in the direction to contrary of the disk rotation vector. As we may see from the Fig.3, Fig.4 the present disk have approximately the cylindrical symmetry and the symmetry axis is the disk rotation one. These figures also show that the disk plane is always parallel to the donor's plane and it means that the slaved precession is working absolutely exactly.

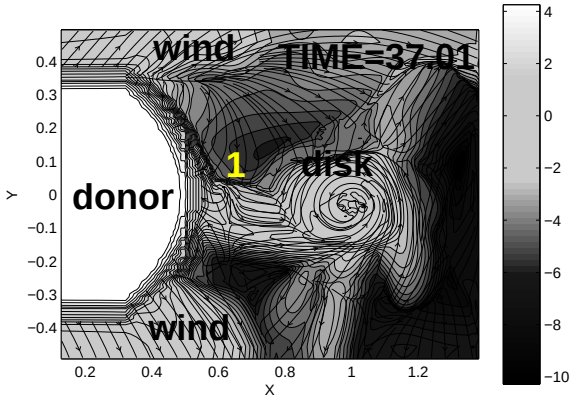

Figure 1: The disk plane structure on time of 37.01.

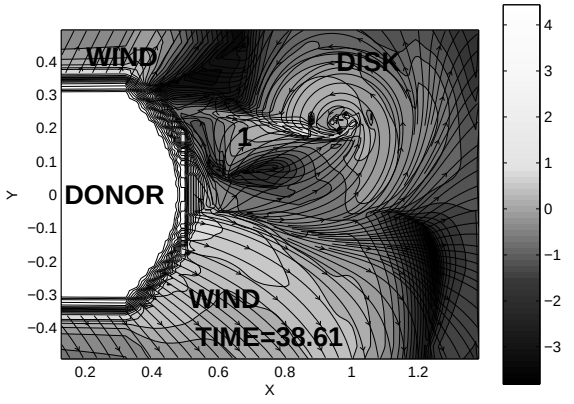

Figure 2: The disk plane structure on time of 38.61.

The essential parameters of a disk in the present calculation are the central disk's temperature and mass accretion rate. As easy to see the most interest is presented the dependencies of these values versus time. We show these dependencies in Fig.5 and Fig.6 in which

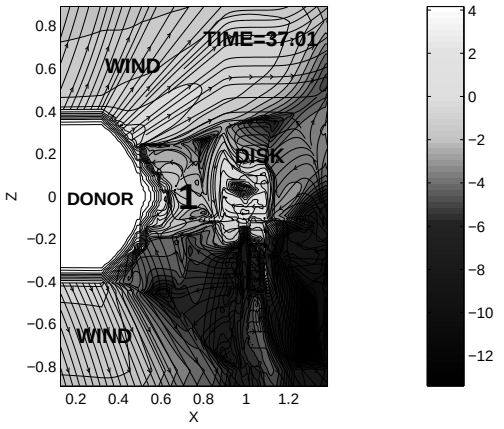

Figure 3: The vertical disk structure on time of 37.01.

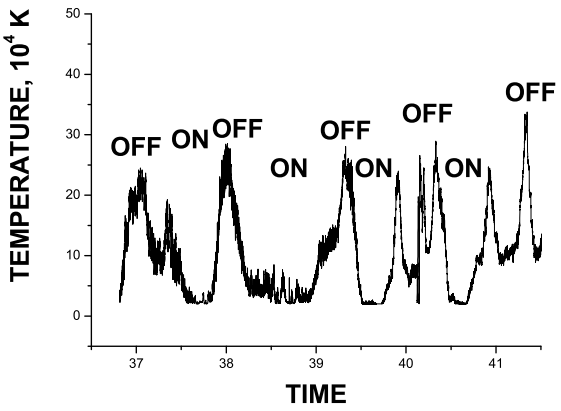

Figure 5: The central disk temperature versus time.

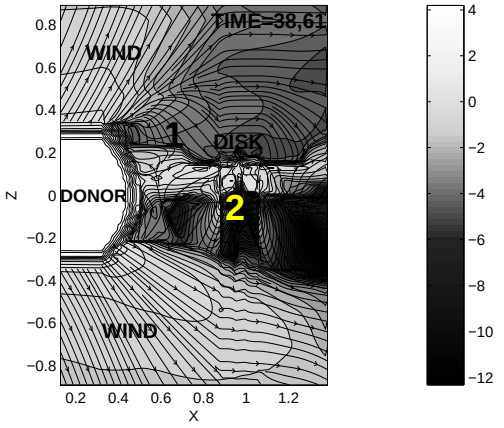

Figure 4: The vertical disk structure on time of 38.61.

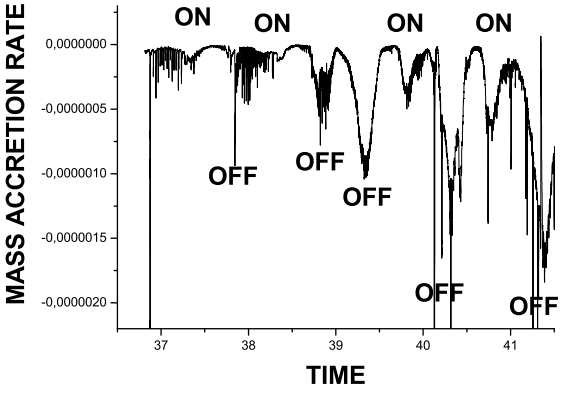

Figure 6: The mass accretion rate versus time.

mass accretion rates are given in units of solar mass in year and times are given in units of precession period which in turn is equal to 2.56 of the orbital period. As we can see from Fig.5 and Fig.6 the temperature and mass accretion rate time behaviours are such that these values have the maximal magnitudes in the view of sharp pics and the region of low magnitudes on the bottom of the dependencies. We have interpreted such the bottoms and sharp pics as ON- and OFF-states production in our calculations. As easy to see temperature and mass accretion rate correlates between a each other. It in turn means that in our calculations radio flux correlates with X-ray flux. Such the correlation coincides with the observed that of in CYG X-3 Fabrika (2004).

As one can see from Fig.5 and Fig.6 the amplitudes of temperature increasing over OFF-states are order of $5 \div 7$ relatively ON-states. For comparison, in the case of thin disk (see Nazarenko & Nazarenko, 2014; 2015; 2015) these amplitude were equal to $100 \div 200$. It show that in the case of the thick accretion disk the jet velocities will be much less relatively a thin disk. By the other words, it means that in the case of the thick accretion disk the jet velocities will be close to 0.24 -0.26 of light speed (see for instance SS433).

We may also to see from Fig.1-4 that over OFF-states the disk is strong compressed by the wind and on contrary over ON-states the disk is very extended towards the disk plane. Such the time and space disk behaviours over ON- and OFF-states prompts clear the mechanism to generate ON- and OFF-states that is working in the present research: this mechanism is follows – over the precession of thick disk having been blown by the wind this disk sometimes is strong compressed by the wind and sometimes this compression is very small. By this reason in the first case we see OFF-states generation since in high density disk the region in the disk centre along the disk rotation

axis is optically thick and due to this circumstance the temperature in this region becomes to be very high because of the action of the disk viscosity which is transformed the kinetic energy of the disk rotation in the thermal one. In the case when the wind-disk compression is small, the density in a disk is decreased, the region in the disk centre becomes to be relatively optically thin, and due to the action of radiation cooling the temperature in this region is very rapidly decreased. Thus, the mechanism stated above working in terms of optically and geometrically thick accretion disk produced the correlation between central disk temperature and mass accretion rate. This mechanism was also working in our previous works (Nazarenko & Nazarenko, 2014; 2015; 2016) in which the model of optically and geometrically thin accretion disk simulated and in which the anticorrelation between central disk temperature and mass accretion rate occurs.

4. Summary and conclusions

1. The correlation between X-Ray and radio flux calculated in the present research is similar to that of observed in CYG X-3 Fabrika (2004).

2. Our present calculations show that in the cases of the thick accretion disk the jet velocities will be close to 0.24 -0.26 of light speed (see for instance SS433) and on contrary in the cases of thin accretion disk jet velocity will be close to 0.98 -0.99 of light speed (see for instance CYG X-1).

References

Belotserkovskii O.M., Davydov Yu.M.: 1982, *The large particles code in gas dynamics, Moscow, Nauka,* 391.

Cox D. P., Daltabuit E.: 1971, *ApJ*, **167**, 113.

Fabrika, S.: 2004, *Astrophys. and Space Phys. Rev.*, **12**, 1.

Nazarenko V.V., Nazarenko S.V.: 2014, *Odessa Astron. Publ.*, **27**, 137.

Nazarenko V.V., Nazarenko S.V.: 2015, *Odessa Astron. Publ.*, **28**, 171.

Nazarenko V.V., Nazarenko S.V.: 2016, *Odessa Astron. Publ.*, **29**, 82.

DOI: http://dx.doi.org/10.18524/1810-4215.2017.30.114366

MULTI-WAVELENGTH MONITORING OF THE CHANGING-LOOK AGN NGC 2617 DURING STATE CHANGES

V.L.Oknyansky [1], C.M.Gaskell [2], N.A.Huseynov [3], Kh.M.Mikailov [3], V.M.Lipunov [1,4], N.I.Shatsky [1], S.S.Tsygankov [5], E.S.Gorbovskoy [1], A.M.Tatarnikov [1], V.G.Metlov [1], K.L.Malanchev [1], M.B.Brotherton [6], D.Kasper [6], P.Du [7], X.Chen [8], M.A.Burlak [1], D.A.H.Buckley [9], R.Rebolo [10], M.Serra-Ricart [10], R.Podesta [11], H.Levato [12]

[1] M.V.Lomonosov Moscow State University, Sternberg Astronomical Institute, Moscow, Russian Federation, *oknyan@mail.ru*

[2] Department of Astronomy and Astrophysics, University of California, Santa Cruz, USA

[3] Shamakhy Astrophysical Observatory, National Academy of Sciences, Pirkuli, Azerbaijan

[4] M.V. Lomonosov Moscow State University, Physics Department, Moscow, Russian Federation

[5] Tuorla Observatory, Department of Physics and Astronomy, University of Turku, Piikkiö, Finland

[6] University of Wyoming, Laramie, USA

[7] Institute of High Energy Physics, Chinese Academy of Sciences, Beijing, China

[8] School of Space Science and Physics, Shandong University , Shandong, China

[9] The South African Astronomical Observatory, Observatory, South Africa

[10] The Instituto de Astrofisica of Canarias, Tenerife, Spain

[11] OAFA, National University of San Juan, San Juan, Argentina

[12] ICATE, National University of San Juan, San Juan, Argentina

ABSTRACT. Optical and near-infrared photometry, optical spectroscopy, and soft X-ray and UV monitoring of the changing-look active galactic nucleus NGC 2617 show that it continues to have the appearance of a type-1 Seyfert galaxy. An optical light curve for 2010–2017 indicates that the change of type probably occurred between 2010 October and 2012 February and was not related to the brightening in 2013. In 2016 and 2017 NGC 2617 brightened again to a level of activity close to that in 2013 April. However, in 2017 from the end of the March to end of July 2017 it was in very low level and starting to change back to a Seyfert 1.8. We find variations in all passbands and in both the intensities and profiles of the broad Balmer lines. A new displaced emission peak has appeared in Hβ. X-ray variations are well correlated with UV–optical variability and possibly lead by ~2–3 d. The *K* band lags the *J* band by about 21.5 ± 2.5 d and lags the combined *B* + *J* bands by ~25 d. *J* lags *B* by about 3 d. This could be because J-band variability arises predominantly from the outer part of the accretion disc, while *K*-band variability is dominated by thermal re-emission by dust. We propose that spectral-type changes are a result of increasing central luminosity causing sublimation of the innermost dust in the hollow bi-conical outflow. We briefly discuss various other possible reasons that might explain the dramatic changes in NGC 2617.

Keywords: AGN, CL AGN, X-ray, UV, optical, photomery, spectroscopy

1. Introduction

NGC 2617 is a typical representative of the objects called "Changing Look" AGNs (CL AGNs), that is, active galactic nuclei changing their spectral type (their Seyfert type). Before 2013, NGC 2617 received relatively little attention, since significant variability was not detected, and optical spectra were obtained only twice: in 1994 (Moran, Halpern & Helfand, 1996) and in 2003 (the 6dFGS spectrum). According to these spectra NGC 2617 could be classified as Sy 1.8. In 2013 spectra showed a dramatic change in the profiles of the Balmer lines compared with the 2003 spectra and NGC 2617 showed a type 1 Seyfert spectrum (Shappee et al., 2013). Since then NGC 2617 has been intensively studied (Shappee et al., 2014; Fausnaugh et al., 2017) by photometric and spectral monitoring during 2013-2014. In 2016 we started our monitoring as a continuation of the monitoring of Shappee et. al., but we carried out not only new photometric observations at X-ray, UV, optical, IR, but also processed MASTER archival observations from 2010 and archival *Swift* observations from 2013. The results of our multi-wavelength monitoring up to June 2016 are given in Oknyansky et al. (2017). We have continued our multi-wavelength monitoring of NGC 2617 from September 2016 to July 2017. We present here preliminary new results from this.

2. Observations

As in Oknyansky et al (2017; see details there), our new observational data includes IR *JHK* photometry (IR-camera Astronircam (Nadjip et al., 2017) of 2.5-m telescope of the SAI Caucasus Mountain Observatory), optical photometry (MASTER Global Robotic Net (Lipunov, 2010; Kornilov, 2012), AZT-5, Zeiss-600 ShAO, *Swift/UVOT*), UV photometry (*Swift/UVOT*), X-ray observations in the 0.3–10 keV band (S*wift/XRT*), optical spectrophotometry with the 2-m Zeiss telescope of the ShAO. In the 2016-2017 season, additional CCD photometric observations were added from a Zeiss-600 telescope with the Apogee Aspen CG42 CCD camera system at the Crimean Station of the SAI MSU, the 1-m telescope at Weihai Observatory China (see details, for example, Guo et al., 2014), and also for optical spectroscopy from the 2.3-meter WIRO telescope (for details see: *physics.uwyo.edu/~WIRO/Longslit/long_slit.html*).

3. Multi-wavelength light curves

Fig. 1 shows multi-wavelength light curves. The *B*-band magnitudes were obtained with different telescopes (see figure caption) and have not yet been reduced to a common system to remove small systematic differences.

One can see that there are fast components of variability with several brightenings and a slow decline in brightness. From the end of the March 2017 until the end of the observing season at the end of the July NGC 2617 was in very low state with a small amplitude of UV and optical variability. The correlation of the variability in different wave bands can be clearly seen as well as some difference in UV/optical and X-ray relative amplitudes of the last brightening. We used the same method for determining time delays as in our previous papers (see details in Oknysnaky et al., 2017). Our cross-correlation analysis confirms the high degree of correlation between the UV and X-ray variability but with a small lag about 3 days.

The new IR *JHK* data are in agreement with our previously determined lags between the optical and IR (Oknyansky et al., 2017). Fig. 2 shows UVW1 (*Swift*) variability compared with the *K*-band variability shifted by 24 days and with the amplitude scaled to the UVW1 variability. More details on our cross-correlation analysis will be given in a future paper.

4. Spectroscopic observations

In the 2016-2017 observational season we procured spectra of NGC2617 in the Hα and Hβ regions with 2 instruments: the 2.3-m WIRO telescope (8 dates) and 2-m ShAO telescope (7 dates). The times of spectroscopic observations a re shown by arrows at the top of Fig. 1.

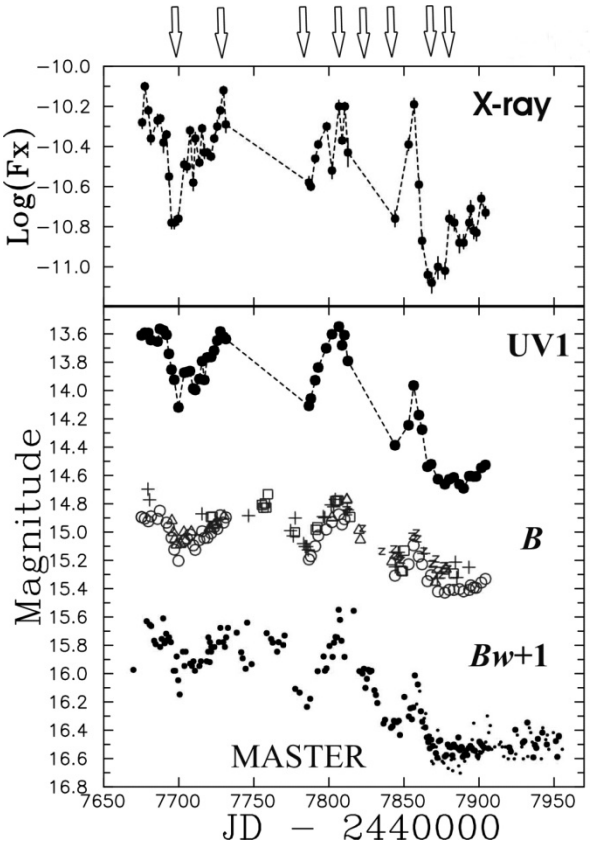

Figure 1: Multiwavelength light curves for NGC 2617. The top panel shows the log of the X-ray flux in ergs/cm^2/s obtained with the *Swift*/XRT. The bottom panel shows (from top to bottom) UV1 = UVW1 magnitudes obtained with *Swift/UVOT*; ***B*** = *B* magnitudes obtained with the AZT-5 (+) and the Zeiss-600 (z) of the Crimean Station of the SAI, the Zeiss-600 of ShAO (squares), the 1-m telescope of Weihai Observatory (triangles), and from the *Swift* (open circles)**;** $\boldsymbol{B_w + 1}$ = unfitered ***W*** data data obtained with MASTER-SAAO and MASTER – IAC (filled circles), and MASTER-OAFA (points) reduced to the ***B*** band and shifted on 1^m for clarity. Arrows show times of spectroscopic observations

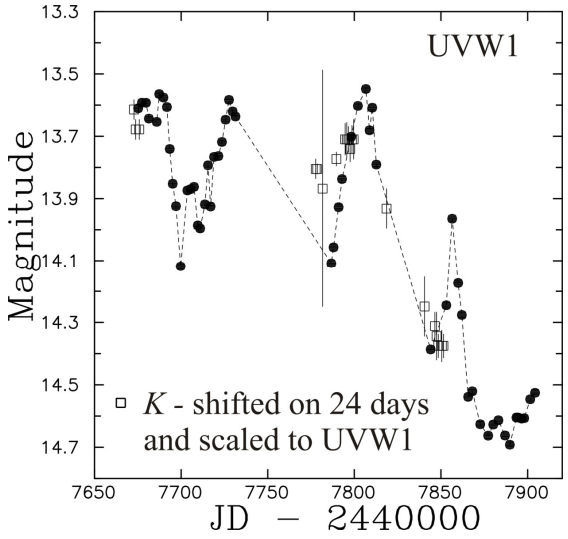

Figure 2: Light curves: points – **UVW1** (*Swift/UVOT*) and squares – *K* (2.5-m telescope of CMO SAI) shifted on -24 days and scaled to UVW1 following a linear regression.

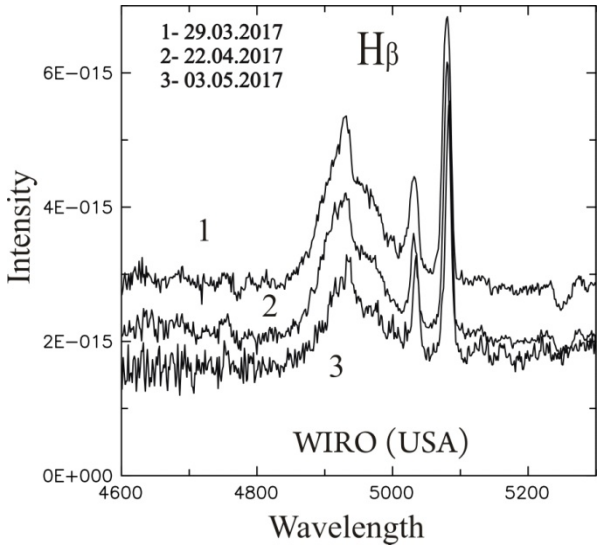

Figure 3: Calibrated spectra of NGC 2617 in Hβ region for 3 dates obtained with 2.3-m WIRO telescope. The intensity is in erg/s/sm^2/Å, the wavelength in Å.

For each date we usually obtained 3 spectra in Hα and Hβ regions and averaged the calibrated spectra for each date. Details will be described in a forthcoming paper. In Fig. 3 we show as an example just 3 of our spectra in the Hβ region obtained in WIRO. These spectra show how the intensity of Hβ was decreased from 2017 March 29 to 2017 May 3. From our photometry the deepest minimum at all wavelengths was at April 27-28. As was shown by Fausnaugh et al. (2017) the delay between the optical continuum and Hβ variability is about 6 days. This is in a good agreement with our results. In our last spectra Hβ still has a very low broad component but we suspect that NGC 2617 is going to change its spectral type back to a Seyfert 1.8 very soon.

5. Discussion

The most important question about CL AGNs is why they show the changes in luminosity and Seyfert type. We believe that the reason for the significant change in the luminosity of NGC 2617 is probably not a change in absorption alone. We propose that a change in the energy-generation rate led to a change in absorption. What caused the observed change in energy generation remains the main mystery as does the nature of AGN variability in general.

We interpret the *K*-band emission as being due to re-radiation by dust while the *J*- and *H*-band emission is due to a combination of radiation from the outer accretion disk and re-radiation by the hot dust. We have proposed that the dusty clouds are located in a hollow bi-conical outflow of which we see only the near side (Oknyansky et al., 2015; 2017). We have noted that this model can explain cases of changing Seyfert type. Gaskell & Harrington (2017) have proposed that changes in Balmer line profiles such as observed in NGC 2617 are due to clumps in the dusty outflow partially blocking the broad-line region.

We do not think that a tidal disruption event caused by a star passing too close to a massive black hole can be a common mechanism for CL AGNs, since the rate of tidal disruptions is very low. An alternative possibility is that a star does not get close enough to the black hole to be totally disrupted and a less dramatic event might happen. If the stellar orbit is bound and highly eccentric, just like some stars in the centre of our own Galaxy, repeated flares should occur. (Campana et al., 2015; Ivanov and Chernyakova, 2006).

6. Conclusions

We have assembled optical light curves of NGC 2617 from 2010 from the MASTER Global Robotic Network, and optical, UV, and X-ray light curves from 2013 onwards based on *Swift* archival data. We have obtained recent spectroscopic and photometric (from NIR toX-ray) monitoring of NGC 2617 in 2016-2017.

We find that NGC 2617 remains in a high state (i.e., it appears as a Seyfert 1), but from the end of the March till the end of July 2017 the object was in very low level of brightness and variability. We suspect that it was then in a transition state and could soon be changing its type back to Sy 1.8.

We continue to find that light-travel-time delays increase with wavelength. The new IR data obtained from October 2016 to May 2017 confirm our published (2016) result of a delay of the *K* band of ~ 24 days relative to UV/optical.

Acknowledgements. Thanks to P.B. Ivanov for useful discussions, thanks to the *Swift*, WIRO and MASTER teams for organizing the observations, to A.M. Cherepashchuk and N.S. Dzhalilov for supporting our observations. This work was supported in part by the Russian Foundation for Basic Research through grant 17-52-80139 BRICS-a and by the BRICS Multilateral Joint Sci-

ence and Technology Research Collaboration grant #110480. MASTER and ASTRONIRCAM works were supported in part by the M.V.Lomonosov Moscow State University Development Program (equipment). MASTER observations were supported throw RSF grant 16-12-00085 and by the National Research Foundation of South Africa (MASTER-SAAO).

References

Campana S., Mainetti D., Colpi, M. et al.: 2015, *A&A*, **581,** 11.

Fausnaugh M.M., Grier C.J., Bentz M.C. et al.: 2017, *ApJ,* **840**, 97.

Gaskell C.M. & Harrington P.Z.: 2017, *MNRAS* submitted (arXiv:1704.06455).

Guo D.-F., Hu S.-M., Tao J. et.al.: 2014, *RAA*, **14**, 923.

Ivanov P.B. & Chernyakova M.A.: 2006, A&A, **448**, 843.

Kornilov V., Lipunov V., Gorbovskoy E. et al.: 2012, *ExA*, **33**, 173K.

Lipunov V., Kornilov V., Gorbovskoy E. et al.: 2010, *Advances in Astronomy*, **2010**, 30L.

Moran E.C., Halpern J.P., Helfand D.J.: 1996, *ApJS*, **106**, 341.

Nadjip A.E., Tatarnikov A.M., Toomey D.W. et al.: 2017, *Astrophys. Bull*., **72,** 382.

Oknyansky V.L., Gaskell C.M., Shimanovskaya E.V.: 2015, *Odessa Astron. Publ.,* **28**, 175.

Oknyansky V.L., Gaskell C.M, Huseynov N.A. et al.: 2017, *MNRAS*, **467,** 1496.

Shappee B.J., Prieto J.L., Nugent J. et al.: 2013, *The Astronomer's Telegram*, **5010**.

Shappee B.J., Prieto J.L., Grupe D. et al.: 2014, *ApJ*, **788**, 48.

DOI: http://dx.doi.org/10.18524/1810-4215.2017.30.114369

THE PECULIARITIES IN O-TYPE GALAXY CLUSTERS

E.A. Panko[1], S.I. Emelyanov[2]

[1] Department of Theoretical Physics and Astronomy,
I.I. Mechnikov Odessa National University, Odessa, Ukraine,
panko.elena@gmail.com

[2] Kalinenkov Astronomical Observatory,
V.O. Suckomlinsky Nikolaev National University, Nikolaev, Ukraine

ABSTRACT. We present the results of analysis of $2D$ distribution of galaxies in galaxy cluster fields. The Catalogue of Galaxy Clusters and Groups PF (Panko & Flin) was used as input observational data set. We selected open rich PF galaxy clusters, containing 100 and more galaxies for our study. According to Panko classification scheme open galaxy clusters (O-type) have no concentration to the cluster center. The data set contains both pure O-type clusters and O-type clusters with overdence belts, namely OL and OF types. According to Rood & Sastry and Struble & Rood ideas, the open galaxy clusters are the beginning stage of cluster evolution. We found in the O-type clusters some types of statistically significant regular peculiarities, such as two crossed belts or curved strip. We suppose founded features connected with galaxy clusters evolution and the distribution of DM inside the clusters.

Keywords: Galaxies: clusters: morphological types.

1. Introduction

The fundamental problem of modern extragalactic astronomy and cosmology is the scenario of structure formation. The most popular concordance ΛCDM model describes the Universe as a spatially flat, homogeneous and isotropic in a large scale. In the model large-scale structures of Universe were formed from the primordial adiabatic, nearly scale invariant random fluctuations (Silk, 1968; Peebles & Yu, 1970; Sunyaew & Zeldovich, 1970). Modern simulations, from well quoted *Millennium Simulation* (Springel et al., 2005) to *Illustris Project* (Vogelsberger et al., 2014, Artale et al., 2017), show complex structure of sheets and filaments with clusters of galaxies at the intersections of this filamentary structure. The comparison the results with observation data give us the way to reliable scenario.

Galaxies in the galaxy clusters were and remain the confident optical markers of structure of clusters and their components. The features of distribution of galaxies inside the cluster can be described as the morphological type of the cluster. From the beginning time of galaxy clusters study they were divided to types according some schemes. Panko (2013) summarized the classical schemes, including both famous Bautz – Morgan (1970), Rood – Sastry (1971) ones and less popular López-Cruz at al. (1997) and López-Cruz & Gaztanaga (2001) approach. Improved and integrated scheme (Panko, 2013) allows to assign the morphological types corresponding to cluster "concentration" (from C – compact, to I – intermediate, and O – open), "flatness signs" (L – line or F – flat, and no symbol if no indication of "flatness sign" is present) and the role of bright galaxies (cD or BG, if the bright cluster members role is significant). Other peculiarities are noted as P. "Flatness signs" can correspond to filamentary substructure or preferential plane in cluster. The designations can be combined, for example CFcD or ILP. Note, the clusters CL-type were not found (Panko, 2013). The fact can be understanding taking into consideration the direction of evolution of galaxy clusters from O-type (independently from "flatness signs") to C-type (Struble & Rood, 1982). This way of evolution is confirmed by increase the ellipticity with redshift for low-redshift galaxy clusters and groups (Biernacka et al., 2009). According to ellipticity determination (Panko & Flin, 2006) the "flatness signs" – belts and strips – can be connected with DM distribution inside the clusters and/or between nearest large-scale structures, as was founded by Dietrich et al. (2012) for A222 and A223 clusters. Some years before hot gas filament connecting both clusters was traced in X-ray by Werner et al. (2008). The compound filamentary structure of DM inside the cluster can be reflected in regular peculiarities, in particulary as crossing belts or curved strips. We supposed such regular peculiarities can by founded in clusters with all types of concentration and select open galaxy clusters as observational data for first step of our study.

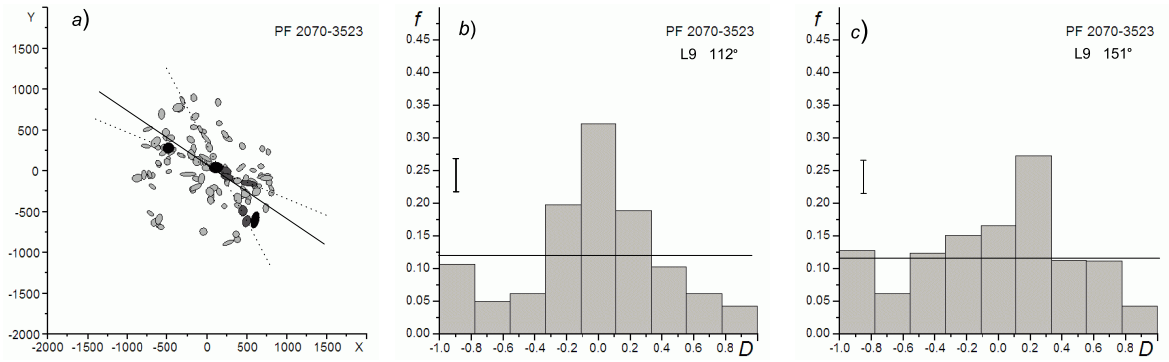

Figure 1: The map of galaxy cluster PF 2070-3523 with crossing $L9$ belts (a), dotted lines note the directions for first (112°) and second (151°) belt, solid line shows the direction of main axe of cluster. The panels (b) and (c) show the weighted densities in the bands across the belt for both cases, solid line corresponds to mean weighted density, vertical bar illustrates the SD.

2. Observational Data and Mapping

Our study based on "A Catalogue of Galaxy Clusters and Groups" (Panko & Flin 2006, hereafter PF). The PF Catalogue was constructed on Münster Red Sky Survey Galaxy Catalogue (Ungrue et al. 2003) as the observational basis. The full information in the PF Catalogue contains the list of galaxies in the cluster field for each PF galaxy cluster. Information for galaxies includes RA_{2000} and Dec_{2000}, r_F magnitude, major and minor axes and positional angle of major axis of galaxy best-fitted ellipse accordingly to MRSS (Ungrue et al. 2003).

We created the "The Cluster Cartography set" (Panko & Emelyanov, 2015, hereafter CC) for quick detail study of morphology of galaxy clusters. The cluster map is constructed in rectangular coordinates recalculated into arcseconds. The symbols on the map illustrate the galaxy shape and orientation in the projection on the celestial sphere, but size of symbol corresponds to galaxy magnitude; calculation bases on MRSS data. Additional brightest galaxies can be marked by darker shades of gray (Fig. 1, b and Fig. 1, c).

CC allows us to find the overdense regions as circles on case of C- and I-types of clusters or as belts/strips for L and F clusters. In the last case the clusters is divided to N bands. N can be 3, 5, 7, 9 or 11 and the width of each band is $1/N$ part of diameter of cluster. The numbers of galaxies in the bands are recalculated to weighted densities of galaxies (Panko & Emelyanov, 2015). It allows to describe overdense features as $L11$ or $L9$ for L-clyster and $F7$ or $F5$ for F-clusters (the numeral part corresponds N).

The map of PF 2070-3523 with crossing belts is shows in Fig. 1, a. Note the direction of major axis is in concordantly with directions of the belts (solid and dashed lines in Fig. 1, a). The distributions of waited density of galaxies for two $L9$ belts are shown in Fig. 1, b and Fig. 1, c. The central maximum in Fig. 1, b is significant, the cluster can be attributed to $F7$ type also. The case shown in Fig. 1, c corresponds to second overdense strip, so classification $L9$ is valid, without regard to asymmetry of histogram.

3. The Types of Peculiarities in Open Galaxy Clusters

The PF Catalogue contains 453 rich galaxy clusters without "boundary effects" connected with bounds of MRSS. Their previous classification was made by Panko and Gotsulyak (in preparation), and 254 PF galaxy clusters were attributed to O-type. The list was the observational base of present study. All clusters were mapped by CC. Common distribution open clusters according to subtypes is presented in Table 1. 6 clusters from 254 have feebly marked concentration to the center (last lines in Table 1) without peculiarities.

Table 1: Open PF galaxy clusters

Type	Number	BG	P
O	153	7	33
OF	59	6	5
OL	21	3	8
OLxF	15	5	5
IO	1		
OI	5		
All	254 (248)	21	51

For 153 pure O-type clusters 7 ones have peculiarities connected with positions of brightest galaxies (BCM). For example in PF 0016-3529 the brightest

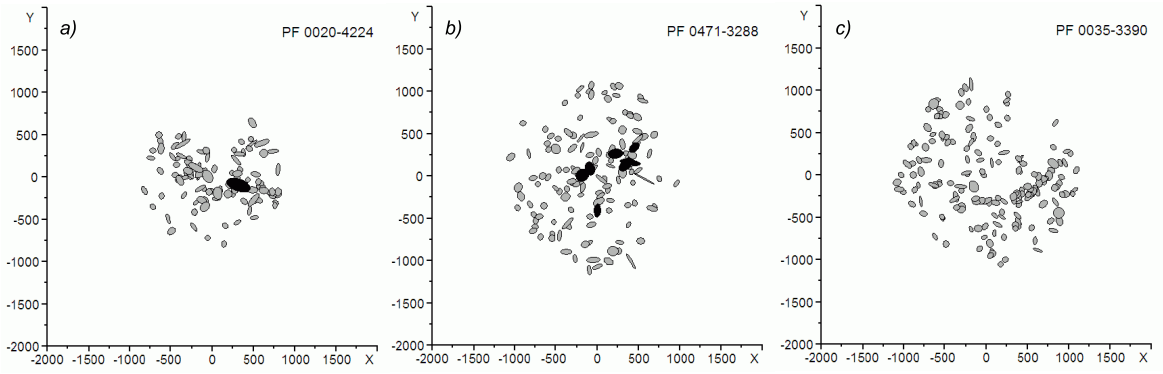

Figure 2: The examples of crossed belts, enhanced the orientation of the brightest galaxy (a), the positions of brightest galaxies (b)and curved strip (c) in open galaxy clusters.

galaxy placed in the center of clusters and difference in magnitudes between first and second BCM is $0^m.4$. Certainly, it is not *cD* galaxy, but the situation is not usual for *O*-type. In PF 0020-4224 (Fig. 2, *a*) the brightest galaxy is on the cross of two belts and have difference with second BCM $1^m.4$. Formally the difference notes to *cD* definition for PF 0020-4224. More, the alignment of brightest galaxy along to the main belt in the cluster notes to especial role of the brightest galaxy in PF 0020-4224 evolution. In *OL* and *OF* cluster peculiarities in BCM positions were found in 6 and 3 cases correspondingly. Another case BCM peculiarities we can illustrate in Fig. 1, *a* and Fig. 2, *b*: positions of tree and more BCM are connected with overdense regions. Crossed belts in open clusters were found in 15 cases and we recognized theirs as significant subtype. We suppose it reflects the *DM* filaments inside the cluster. Another types of peculiarities, Y-form overdense region (PF 0017-6446)or curved strips (Fig. 2, *c*). Other peculiarities connect with weak seen overdense regions with BCM.

4. Conclusion

We found the significant regular peculiarities in open galaxy clusters. More than 1/3 of cluster in our input list have filamentary substructure, both rectilinear and curved. We found 15 galaxy clusters with crossed overdense belts attributed to special type of peculiarity. Other peculiarities are rare, however Y-type overdense regions are confirmed by positions of BCM. We suppose the founded features note to nonuniform distribution of *DM* in the open clusters. The direction of overdense region must be connected with the orientations of galaxies in it. On the other hand, preferential directions connect with positions of nearest neighbors, and we can trace large-scale structure around galaxy clusters.

Acknowledgements. This research has made use of NASA's Astrophysics Data System.

References

Artale M.C., Pedrosa S.E., Trayford J.W. et al.: 2017, *MNRAS*, **470**, 1771.
Bautz P. & Morgan W.W.: 1970, *ApJ*, **162**, L149.
Biernacka M., Flin P., Panko E.: 2009, *ApJ*, **696**, 1689.
Dietrich J.P., Werner N., Clowe D., et al.: 2012, *Nature* **487**, 202.
Dressler A.: 1980 *ApJ*, **236**, 351.
López-Cruz O., Yee H.K.C., Brown J.P., et al.: 1997, *ApJ*, **475**, L97.
López-Cruz O. & Gaztanaga E.: 2001, *arXiv:astroph/0009028*.
Mo H.J., Yang X., van den Bosch F. C., Katz N.: 2005, *MNRAS*, **363**, 1155.
Panko E. & Flin P.: 2006, *J. Astr. Data*, **12**, 1.
Panko E.: 2013, *Odessa Astron. Publ.*, **26**, 90.
Panko E.A., Emelyanov S.I.: 2015, *Odessa Astron. Publ.*, **28**, 135.
Panko E., Flin P.: 2014, *Odessa Astron. Publ.*, **27**, 32.
Peebles P.J.E., Yu J.T.: 1970, *ApJ*, **162**, 815.
Rood H.J., Sastry G.N.: 1971, *PASP*, **83**, 313.
Silk J.: 1968, *ApJ*, **151**, 459.
Springel V., White S.D.M., Jenkins A. et al.: 2005, *Nature*, **435**, 629.
Struble M.F., Rood H.J.: 1982, *AJ*, **87**, 7.
Sunyaev R.A., Zeldovich Ya.B.: 1970, *Astroph. Sp. Sci.*, **7**, 3.
Vogelsberger M., Genel S., Springel V. et al.: 2014, *MNRAS*, **444**, 1518.
Werner N., Finoguenov A., Kaastra J.S.: 2008, *A&A*, **482**, L29.
Ungrue R., Seitter W.C. & Duerbeck, H.W.: 2003, *J. Astr. Data*, **9**,1.

DOI: http://dx.doi.org/10.18524/1810-4215.2017.30.114374

STELLAR ACTIVITY CYCLES: WHY DO WE NEED IN THE LONG-TERM MEASUREMENTS OF THE MAGNETIC FIELD?

S.I. Plachinda[2], V.V. Butkovskaya[1]

[1] Main Astronomical Observatory of National Academy of Sciences, Kyiv, Ukraine, *psi1951@yahoo.com*

[2] Crimean Astrophysical Observatory, Nauchny, Crimea

ABSTRACT. Solution of the two important problems requires a study of long-term behavior of the magnetic field on stars with nondegenerate matter: firstly, to define the role of the magnetic field on different evolutionary stages of stars; secondly, to know the influence of the star's activity on space weather in the habitable zone. This brief review summarizes the first results of the long-term magnetic field measurements on selected stars.

Key words: stars: activity – stars: late-type – stars: magnetic fields.

1. Introduction

Today we have a wide range of outstanding issues associated with the magnetization of the stellar matter: the origin of the stellar magnetism, the role of the magnetic field in the star formation and evolution, their rotational structure, mass loss, coronal activity and others activity phenomena.

Stellar activity cycles like the solar cycles have been found almost half a century ago. During this period, researchers have crystallized a number of important problems: measuring the duration of the activity cycles, the interplay between activity cycles, evolutionary status and stellar rotation, the variability of activity cycle duration and multicycles, and so on. Despite the facts that the regular, generally photometric, monitoring of some objects is carried out for decades, and the long-time datasets obtained by the space telescopes allow to discover short (0.5-6 years) cycles of activity for thousands of stars, the most of the task remain unsolved.

We present here the brief review of the first results of long-term measurements of the magnetic field on the selected stars.

2. Long-term variability cycles of selected stars

Radic et al. (1998) have found that the younger, more active stars "tend to become fainter as their HK emission increases, whereas the older, less active stars tend to become brighter as their HK emission increases, as the Sun does during its activity cycle."

The Sun. The absolute values of the General Magnetic Field (GMF) of the Sun as a star varies with the phase of the 11-year sunspot cycle. Today it is well known that in an epoch of the maximum of the solar activity (a maximal number of sunspots, a maximal flux in the chromospheric Ca II HK emission, a maximal visual photometric brightness, and so on) the GMF reaches its maximum ($\sim \pm 2$ G) and in an epoch of the minimum solar activity GMF reaches its minimum ($\sim \pm 0.2$ G). In other words, the variability of the GMF of the Sun as a star correlates with the phase of the sunspot cycle.

61 Cyg A. First results of the investigation of long-term magnetic field behavior on the old solar-like K-dwarf star 61 Cyg A was published by Saikia et al. (2016). 61 Cyg A shows Ca II emission periodicity in the time interval of about 7.3 years (Baliunas et al. 1995). But in spite of the above mentioned conclusion by Radic et al. (1998) in the case of 61 Cyg A Saikia et al. (2016) supposed a weak anti-correlation between the absolute value of the longitudinal magnetic field $|B_l|$ and the S-index of the calcium chromospheric emission.

β **Aql.** For the next stage in the evolution of solar-like stars, convective subgiants, first long-term measurements of the longitudinal magnetic field have been performed by Butkovskaya et al. (2017). The authors have carried out the spectropolarimetric observations of β Aql ($V_{\rm mag} = 3.7$, G8 IV-V) over 51 nights from 1997 to 2015. The results of this investigation is shown in Figure 1.

The upper panel of Figure 1 shows averaged in 10 bins V-brightness, which are phased with suspected activity period of about 969 d. The photometric data was taken from the All Sky Automated Survey (ASAS) and includes 344 measurements.

In the bottom panel of Figure 1 the total range of magnetic field variation, $\Delta B = B_{\rm max}$ - $B_{\rm min}$, folded in phase with the 969 d period are presented. One can

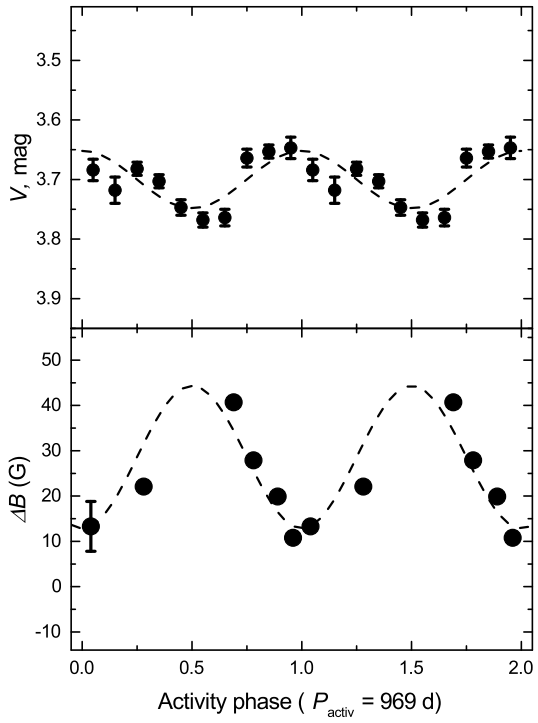

Figure 1: *Upper panel*: The V-brightness averaged in 10 bins phased with the 969 d activity period. The least-square sinusoidal fit is shown by the dashed line. *Bottom panel*: The range of magnetic field ΔB calculated using the magnetic field values falling in the same phases of the activity period. The SD = 5.5 G of these ΔB values from the fitting curve is shown as an error bar around the first value. The best least-square sinusoidal fit to ΔB is shown by the dashed line.

see that the maximum of ΔB fitting curve coincides in phase with the brightness minimum.

Vega. For more than six decades Vega has been accepted as a standard star in the near infrared, optical, and ultraviolet spectrum bands. Vasil'ev et al. (1989a) shows that the flux density E5556 produced by the emission of Vega at the wavelength $\lambda = 5556$ Å, varies with a period of 23 – 25 years. This variability has been investigated in detail by Merezhin (2001), but the results of his study remained unrecognized. Butkovskaya et al. (2011) have analyzed their long-term spectral data and have verified the long-term variability cycle of Vega. They have found the cycle duration of 7697 ± 157 d (21.28 year) and have concluded that the spectral and photometric standard Vega is a variable star. However, the physical mechanism of the long-term periodicity should be investigated. Also, the question "Does the magnetic field of Vega vary during the 21-year period?" should be answered.

3. Discussion and Conclusions

In contradiction with the solar correlations of the brightness, Ca II HK chromospheric emission and the range of the magnetic field variation, 61 Cyg A shows a weak anticorrelation between the cyclic magnetic field variation and Ca II HK chromospheric emission and β Aql shows the anticorrelation between the cyclic magnetic field variation and V-brightness.

On the other hand, the rapid increase in the number of discovered planetary systems strengthens the importance of the question of space weather on planets in the Habitable Zone (HZ). The possibility of origin of life on a planet in the HZ depends strongly on the magnetic activity of the hosting star whose activity level depends on the phase of the Hale cycle.

"The HZ is the circumstellar region inside which a terrestrial planet can hold permanent liquid water on its surface" (Selsis et al., 2007). NASA: "Conditions on the Sun and in the solar wind, magnetosphere, ionosphere and thermosphere that can influence the performance and reliability of space-borne and ground-based technological systems and can endanger human life or health."

Planets in the HZ of active stars can be exposed to high levels of X-ray and UV radiation and high-energy particle fluxes from the stellar wind or coronal mass ejections. Such high emissions are the result of the stellar magnetic activity and they can induce important thermal and non-thermal atmospheric losses to space, potentially able to strip the whole atmosphere. Therefore, to study the impact of the hosting star activity on the magnetosphere of planets the knowledge of the range of variability of the magnetic field of the hosting star is required.

As the duration of the activity cycles in stars of different spectral classes can reach several decades, long-term spectropolarimetric observations are required to detect these cycles and to investigate cyclical changes of the magnetic field.

References

Baliunas S.L., Donahue R.A., Soon W.H. et al.: 1995, *ApJ*, **438**, 269.

Butkovskaya V., Plachinda S., Valyavin G. et al.: 2011, *Astron. Nachr.*, **332**, 956.

Butkovskaya V.V., Plachinda S.I., Bondar' N.I., Baklanova D.N.: 2017, *Astron. Nachr.*, in press.

Merezhin V.P.: Vega. Analiz i interpretatsiya dannykh nablyuenii (Vega. Analysis and Interpretation for Observations), Kazan: Fen, 2001.

Radick R.R., Lockwood G.W., Skiff B.A. et al.: 1998, *ApJSS*, **118**, 239.

Saikia S.B., Jeffers S.V., Morin J. et al.: 2016, *A&A*, **594**, A29.

Selsis F., Kasting J.F., Levrard B. et al.: 2007, *A&A*, **476**, 1373.

Vasil'ev, I.A. et al.: 1989, *IBVS*, **3308**.

DOI: http://dx.doi.org/10.18524/1810-4215.2017.30.115819

IMPROVED EPHEMERIS OF POORLY STUDIED ECLIPSING BINARY GSC 3950-00707 = 2MASS J20355082+5242136

S.V. Savastru[1], V.I. Marsakova[1,2,3], K.D. Andrych[2,3], P. Dubovsky[4]

[1] Richeleu Liceum,
Odessa, Ukraine, *svsodessa@gmail.com*

[2] Odessa Mechnikov National University,
Odessa, Ukraine, *v.marsakova@onu.edu.ua, katyaandrich@gmail.com*

[3]Department "Mathematics, Physics and Astronomy",
Odessa National Maritime University, Odessa, Ukraine

[4]Vihorlat Observatory and Astronomical Observatory on Kolonica Saddle
Slovak Republik, *var@kozmos.sk*

ABSTRACT. We made our CCD-observations of GSC 3950-00707 by using the telescope Celestron-14 of Vihorlat Observatory and Astronomical Observatory on Kolonica Saddle. The moments of minima were calculated by using the symmetrical polynomial fit. We also analyzed the observations from automated surveys ASAS-SN and found 3 mean minima by using trigonometrical polynomial fit. The analysis of our observations and data from the surveys allows to conclude that it is the W UMa-type variable and its published period value is not accurate. We analyzed the O-C curve and corrected the elements.

Keywords: eclipsing variable stars; W UMa – type; individual: GSC 3950-00707.

1. Introduction

The eclipsing binary GSC 3950-00707 was discovered as the second variable in the field of V2551 Cyg (Devlen, 2009). There are only 2 publications concerning GSC 3950-00707 (Devlen, 2009; Hübscher, 2016). In the paper (Devlen, 2009) its light curve was built and the elements

$$\text{Min I (HJD)} = 2454232.5278(\pm 0.0004) + 0.4120(\pm 0.0001) \times E$$

were obtained. It was classified as EW variable (eclipsing, W UMa-type).

In the paper (Hübscher, 2016), only 1 minimum was listed for the variable.

Now we present the study of GSC 3950-00707 by using our CCD and archival data from sky survey ASAS-SN (Kochanek, et al., 2017)

2. Observations and O-C analysis

The observations were obtained by the Ukrainian observation group during the international Astrocamp "Variable-2017" (that was held by Vihorlat Observatory in Humenne at their observation station at the Kolonica saddle (Kudzej & Dubovsky, 2017)). The observations that performed on 20 and 22.07.2017 cover only 70% of the phase curve with the gap in one of the minima. So the additional observations were made on 29.09.2017 by Pavol Dubovsky. We used the telescope Celestron Edge HD CGE Pro 1400 (14 inch-diameter) and CCD-camera MII G2-1600. In this paper. we present the correction of the ephemeris based on our the observations in the R-filter.

Four minima were determined from our CCD-observations by applying the symmetrical polynomial fit of statistically optimal degree (Andrych et al., 2016).

We also analyzed the observations from automated survey ASAS-SN (Kochanek et al., 2017). We divided the all data for our object in this survey into 3 intervals of observations (and for each interval we calculated values of the period and the initial epoch according to mean minimum by using trigonometrical polynomial fit (of 4 and 6 degrees) in the FDCN program (Andronov, 1994).

In the Table 1, all moments of minima of GSC 3950-00707 are listed. There are two minima taken from Devlen (2009); Hübscher (2016), which we assign as primary ones (since in the curve by Devlen (2009), the minima have approximately equal depth and division into primary and secondary shows only their parity), our minima (in this term, 1 primary minimum and 3 secondary ones) and 3 mean minima obtained by using ASAS-SN observations. The mean minima we assign as the secondary ones and we take to account their O-C with the shift of 0.5P.

O-C curve built by using all these moments of minima is presented in Fig. 1. It shows that the period and initial epoch by Devlen (2009) are not perfect. We made two approximations of O-C: simple linear (1) and weighted linear (2) with squared reversal accuracy of the moment as the weights. According to the coefficients of linear approximation of the O-C curve, we obtained the corrected elements:

$$\text{Min I (HJD)} = 2457310.64970\pm0.00056 + (0.41198165\pm0.00000020)\cdot E \quad (1)$$

$$\text{Min I (HJD)} = 2457310.64891\pm0.00032 + (0.41198158\pm0.00000012)\cdot E \quad (2)$$

According to our light curve in the R-filter built according to our elements (2) that shown in Fig 2, the minima from literature probably are not primary, so, in the final elements. the initial epoch is shifted by -0.5P.

3. Conclusion

We collected 9 moments of minima and corrected the period by using the O-C curve.

Our CCD-observations show that the secondary minimum is flat, indicating a total eclipse in a system of components which are very different in sizes and masses.

Acknowledgements. Our special thanks to organizers of Astrocamp "Variable-2017", especially, Igor Kudzej and Pavol Dubovsky.

We also are grateful to I.L. Andronov for helpful discussions.

This research is a part of the project "Inter – Longitude Astronomy" (Andronov et al., 2017).

References

Andrych K.D., Andronov I.L., Chinarova L.L. et al.: 2016, *Odessa Astron. Publ.*, **28**, p. 158.

Andronov I.L.: 1994, *Odessa Astron. Publ.*, **7**, p. 49.

Andronov I.L. et al.: 2017, *ASPC*, **511**, 43.

Devlen A.: 2009, *Peremennye Zvezdy Prilozhenie*, **9**, No. 23.

Kochanek C.S., Shappee B.J., Stanek K.Z. et al.: 2017, *Publications of the Astronomical Society of Pacific*, **129**, 104502.

Kudzej I., Dubovsky P.: 2017. Available at: *http://www.astrokolonica.sk/podujatia/variable/variable-2017*.

Hübscher J.: 2016, *Information Bulletin on Variable Stars*, No. **6157**, 1.

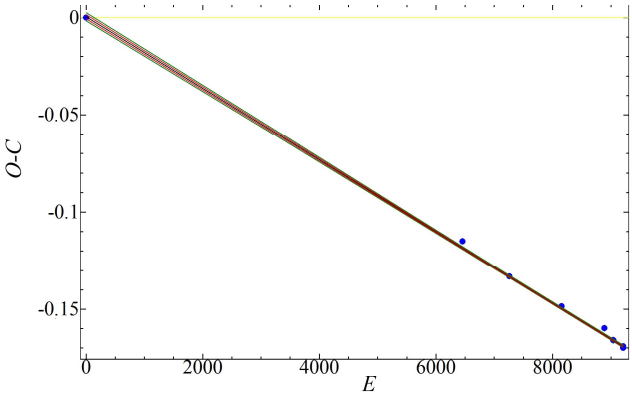

Figure 1: O-C curve by using different data (see Table 1) and its weighted linear approximation. Red and green lines show the 1 and 2 standard deviations, respectively.

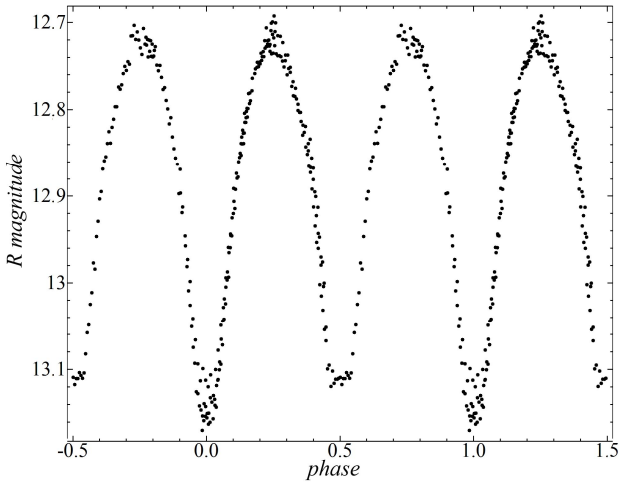

Figure 2: CCD-observations at Celestron-14 (R-filter), phase light curve with new elements (2).

Table 1: Moments of minima and O-C according to the elements of Devlen (2009) and our elements (2)

Source of data	Moments of minima	Cycle number (*E*)	O-C for (Devlen, 2009)	Period	O-C for our elements (2)	Primary /secondary
(Devlen, 2009)	2454232.5280 ±0.0004	0	0	0.4120 ±0.0006	-0.0005	II
(Hübscher, 2016)	2456891.4612 ±0.0006	6454	-0.1148		0.0036	II
ASAS-1 (J.D. 24557084-24557334)	2457222.4850 ±0.0008	7257.5	-0.1330	0.411975 ±0.000002	0.0001	I
ASAS-2 (J.D. 24557453-24557717)	2457590.3856 ±0.0013	8150.5	-0.1484	0.411983 ±0.000004	0.0012	I
ASAS-3 (J.D. 24557826-24557950)	2457893.6062 ±0.0017	8886.5	-0.1598	0.411964 ±0.000016	0.0033	I
Our CCD-observations 20.07.2017	2457955.4002 ±0.0003	9036.5	-0.1658		0.0001	I
Our CCD-observations 22.07.2017	2457957.4600 ±0.0003	9041.5	-0.1660		0.0000	I
Our CCD-observations 29.09.2017	2458026.26009 ±0.0003	9208.5	-0.1699		-0.0008	I
Our CCD-observations 29.09.2017	2458026.46696 ±0.0002	9209	-0.1690		0.0000	II

DOI: http://dx.doi.org/10.18524/1810-4215.2017.30.114380

MODEL OF MAGNETIC DEGENERATE DWARF

S.V. Smerechynskyi, D.V. Dzikovskyi

Department of Astrophysics, Ivan Franko National University of Lviv, Ukraine, *sviatoslav.smerechynskyi@lnu.edu.ua*

ABSTRACT. The macroscopic characteristics of the degenerate dwarves were calculated based on the equation of state of a spin-polarized electron gas at $T = 0K$ as well as at finite temperatures. It was shown that the spin-polarization cause an increase of the radius and mass in comparison with the characteristics of standard Chandrasekhar model. Within adopted model, the value of critical mass was estimated, by which an instability due to general relativity effects occurs. Parameters of model are: the relativistic parameter x_0 at stellar center, the chemical composition parameter $\mu_e = \langle A/Z \rangle$, the degree of spin-polarization ζ, the dimensionless temperature of core $T_0^* = k_B T_c / m_0 c^2$ and its radius $\xi_0 = R_c/R$ (R_c is the core radius, R is the radius of a dwarf). The inverse problem for a sample of massive dwarfs was solved using the known masses and radii and the parameters x_0, T_0^* were found for fixed values of spin-polarization.

Key words: degenerate dwarf, critical mass, relativistic parameter, spin-polarization.

PACS 97.20Rp, 97.60Bw

1. Introduction

The theory of the degenerate dwarfs was developed by S. Chandrasekhar in the 40-th years of the XX century, where the idea of R. Fowler's about mechanism of their stability and degeneration of electron subsystem [1, 2] was used. The Chandrasekhar model is two-component – it is a completely degenerate relativistic electron gas at absolute zero temperature and the static nuclear subsystem, which is considered as continuous classic medium. It has two parameters – the relativistic parameter $x_0 = (3\pi^2 n_0)^{1/3}\hbar/m_0 c$ (where n_0 is the number density of electrons in the stellar center of star, m_0 is the rest mass) and the chemical composition parameter $\mu_e = \langle A/Z \rangle$ (A is the mass number, Z is the number of protons in the nuclear)[3].

The standard Chandrasekhar model corresponds to non-magnetic massive dwarf, in which electron subsystem is in the paramagnetic state. At the same time from the observations are well known dwarfs with the masses which are very close to the Chandrasekhar limit $M_{ch} \approx 1.44 M_\odot$ or even exceed it [4]. Among these dwarfs can be stars with both weak and strong magnetic fields. The model of magnetic dwarf provides a simple interpretation of features of "super-Chandrasekhar" dwarfs and the existence of super-bright Ia type supernova.

Generalization of Chandrasekhar model for the case of finite temperature and consideration of magnetic field allows simultaneously to take into account the influence of these important factors on dwarfs. We constructed the model with five dimensionless parameters – the relativistic parameter x_0 at stellar center, the chemical composition parameter μ_e, the degree of spin-polarization ζ, the dimensionless core temperature $T_0^* = k_B T_c / m_0 c^2$ (the value $T_0^* = 1$ corresponds the temperature in stellar center $6.04 \cdot 10^9 K$) and the dimensionless core radius $\xi_0 = R_c/R$. Rough estimates of temperature of the degenerate dwarfs, which was obtained on the basis of their low luminosity, give the value of the order $10^6 \div 10^7$ K. Such factors, as the incomplete degeneration of electron subsystem, radiation pressure, and the thermal motion of nuclei, should be considered in the consistent theory of internal structure of these stars [5, 6].

In this work we consider model of magnetic dwarf at both absolute zero as well as finite temperature. We do not consider explicitly a magnetic field, which in the local approximation is assumed to be homogeneous. We restrict the consideration of the model, where the average occupation number of electrons $n_{\mathbf{k},s}(r)$ depends on the projection of the spin direction on the magnetic field [7].

2. The spin-polarized model at $T = 0K$

Let's consider an uniform model of the ideal relativistic degenerate electron gas, which consists of N electrons in the volume V influenced by a stable external magnetic field in the thermodynamic limit: $N, V \to \infty$, $N/V = const$.

In this model exists one selected direction, namely the direction of the vector of magnetic field intensity, and we assume that $n_{\mathbf{k},1/2} > n_{\mathbf{k},-1/2}$.

The value

$$\zeta_{\mathbf{k}} = \frac{1}{n_{\mathbf{k}}}(n_{\mathbf{k},1/2} - n_{\mathbf{k},-1/2}) \tag{1}$$

determines a degree of polarization of the electron gas,

where

$$n_{\mathbf{k}} = n_{\mathbf{k},1/2} + n_{\mathbf{k},-1/2}. \tag{2}$$

From here we will assume, that the degree of spin-polarization does not depend on the wave vector,

$$\zeta = \frac{1}{n}(n_+ - n_-), \quad n = n_+ + n_-, \tag{3}$$

where $n_\sigma = N_\sigma V^{-1}$ is the number density with given projection of the spin on the direction of the field. From the equation (3) we find, that

$$\begin{cases} n_+ = \dfrac{1}{2}\, n(1+\zeta), \\ n_- = \dfrac{1}{2}\, n(1-\zeta). \end{cases} \tag{4}$$

From the normalization condition $\sum_{\mathbf{k},s} n_{\mathbf{k},s} = N$ we obtain the expressions for the Fermi wave numbers, which correspond to different projection of the spins:

$$\begin{aligned} &k_F^\sigma = k_F \lambda_\sigma, \quad \lambda_+ = (1+\zeta)^{1/3}, \\ &\lambda_- = (1-\zeta)^{1/3}, \quad k_F = (3\pi^2 n)^{1/3}. \end{aligned} \tag{5}$$

The equation of state in the spatially two-component homogeneous case of the electron-nuclear model at $T = 0K$ has a parametric representation [7]:

$$\begin{aligned} &P = \sum_\sigma \frac{\pi m_0^4 c^5}{3h^3} \mathcal{F}(x_\sigma), \ \mathcal{F}(x_\sigma) = 4 \int\limits_0^{x_\sigma} \frac{dy\, y^4}{(1+y^2)^{1/2}}, \\ &\rho = m_u \mu_e \sum_\sigma n_\sigma = \frac{m_u \mu_e}{6\pi^2} \left(\frac{m_0 c}{\hbar}\right)^3 \sum_\sigma x_\sigma^3, \\ &\sigma = (+,-), \end{aligned} \tag{6}$$

where x_σ is the relativistic parameter in our model.

To obtain the equation of state for inhomogeneous model, we should perform the replacement $x \to x(r), P_\sigma \to P_\sigma(r)$, $\rho \to \rho(r)$, $x_\sigma \to x_\sigma(r)$.

According to the formulae (5)

$$x_\sigma(r) = x(r)\lambda_\sigma, \tag{7}$$

where $x(r) = \hbar k_F(r)(m_0 c)^{-1}$ corresponds to the Chandrasekhar model with paramagnetic subsystem.

Let us consider the mechanical equilibrium of star

$$\frac{dP(r)}{dr} = -G\,\rho(r)\frac{M(r)}{r^2}, \quad \frac{dM(r)}{dr} = 4\pi r^2 \rho(r), \tag{8}$$

where $P(r)$ is the pressure on the sphere of radius r, $\rho(r)$ is local density, $M(r)$ is a mass inside that sphere. The system of equations (8) is reduced to the nonlinear differential equation of second order for $x(r)$

$$\begin{aligned} &\frac{1}{r^2}\frac{d}{dr}\left\{ r^2 \left[\frac{\lambda_+^5}{\sqrt{1+x^2(r)\lambda_+^2}} + \frac{\lambda_-^5}{\sqrt{1+x^2(r)\lambda_-^2}} \right] \times \right. \\ &\left. \times\, x(r)\frac{dx}{dr} \right\} = -G(m_u\mu_e)^2\, \frac{64\pi^2 m_0^2 c^4}{3(hc)^3} x^3(r) \end{aligned} \tag{9}$$

in which λ_+, λ_- are the parameters, mentioned above, moreover $\lambda_+^3 + \lambda_-^3 = 2$.

In a general case at arbitrary value of the parameter ζ, the equation (9) also can be reduced to the equation of the standard Chandrasekhar model using the substitution

$$\begin{aligned} &\sum_{\sigma=\pm} \lambda_\sigma^3 \{(1+x^2(r)\lambda_\sigma^2)^{1/2} - 1\} = \varepsilon_0^\zeta y(\xi), \ \xi = \frac{r}{\lambda} \\ &\text{where} \\ &\varepsilon_0^\zeta = \sum_{\sigma=\pm} \lambda_\sigma^3 \{(1+x_0^2(r)\lambda_\sigma^2)^{1/2} - 1\}. \end{aligned} \tag{10}$$

To rewrite the right side of the equation (9) in terms of $y(\xi)$, let's determine $x(r)$ from the equation (10). We reduce this expression to the biquadratic equation

$$ax^4 - bx^2 + c = 0, \tag{11}$$

where

$$\begin{cases} a = (\lambda_+^8 - \lambda_-^8)^2, \\ b(y) = 2\{(\lambda_+^8 + \lambda_-^8)[(\varepsilon_0^\zeta y)^2 + 4\varepsilon_0^\zeta y] + \\ \quad + 4(\lambda_+\lambda_-)^3(\lambda_+^5 + \lambda_-^5)\}, \\ c(y) = [(\varepsilon_0^\zeta y)^2 + 4\varepsilon_0^\zeta y]\{[(\varepsilon_0^\zeta y)^2 + 4\varepsilon_0^\zeta y] + \\ \quad + 4(\lambda_+\lambda_-)^3\}. \end{cases} \tag{12}$$

The equation (11) has four real roots – two positive and two negative. The physical meaning have only positive roots. From them we choose that one, which in the limit $\zeta \to 0$(when $\lambda_+, \lambda_- \Rightarrow 1$) is a positive root of quadratic equation $c(y) - b(y)x^2 = 0$, because in this limit $a \Rightarrow 0$. Thus we find, that

$$x(r) = 2^{-1/2}(\lambda_+^8 - \lambda_-^8)^{-1}[b(y) - \varphi(y)]^{1/2}, \tag{13}$$

where

$$\begin{aligned} &\varphi(y) = \{b^2(y) - 4ac(y)\}^{1/2} = 4(2 + \varepsilon_0^\zeta y)(\lambda_+\lambda_-)^3 \times \\ &\times \{(\lambda_+\lambda_-)^2[(\varepsilon_0^\zeta y)^2 + 4\varepsilon_0^\zeta y] + (\lambda_+^5 + \lambda_-^5)^2\}^{1/2}. \end{aligned} \tag{14}$$

The equation (9) in a dimensionless form is

$$\begin{aligned} \frac{1}{\xi^2}\frac{d}{d\xi}\left(\xi^2 \frac{dy}{d\xi}\right) = -\{\sqrt{2}(\lambda_+^8 - \lambda_-^8)^{-1} \times \\ \times\, (\varepsilon_0^\zeta)^{-1}[b(y) - \varphi(y)]^{1/2}\}^3. \end{aligned} \tag{15}$$

and satisfies the boundary conditions $y(0) = 1, y'(0) = 0$ and the condition $y(\xi) \geq 0$. The scale factor λ is determined by the expression

$$\frac{32\pi^2 G}{3(hc)^3}\left\{ m_u \mu_e m_0 c^2 \lambda \frac{\varepsilon_0^\zeta}{2} \right\}^2 = 1, \tag{16}$$

which in the limit $\zeta \to 0$ coincides with the result of the standard model [3]. The dependence of the solutions of equation (15) on the relativistic parameter and the

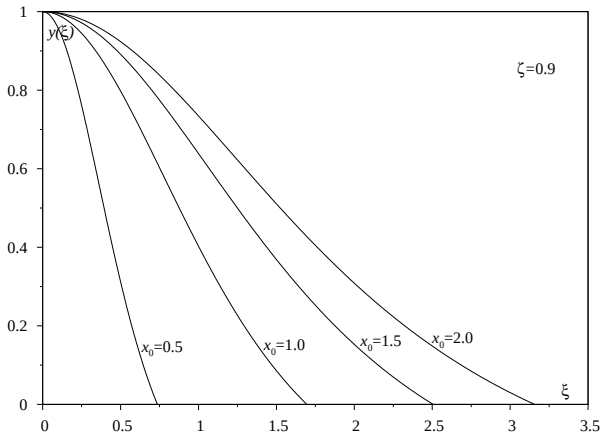

Figure 1: The solutions of equation (9) at fixed value $\zeta = 0.9$ for four values of x_0.

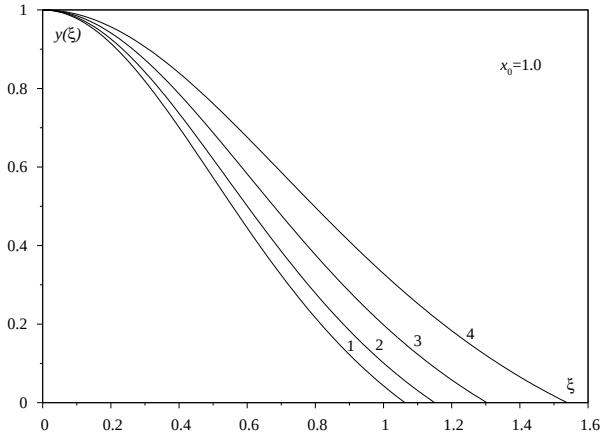

Figure 2: The solutions of equation (9) at fixed value $x_0 = 1.0$ ($\zeta = 0$ – curve 1, $\zeta = 0.2$ – curve 2, $\zeta = 0.4$ – curve 3, $\zeta = 0.6$ – curve 4)

.

degree of spin-polarization is illustrated in figures 1 and 2. The total mass of a star is the function of parameters x_0, μ_e, ζ:

$$M(x_0,\mu_e|\zeta) = \frac{M_0}{\mu_e^2}\mathcal{M}(x_0|\zeta),$$
$$\mathcal{M}(x_0|\zeta) = \xi_1^2(x_0|\zeta)\left|\frac{dy}{d\xi}\right|_{\xi=\xi_1(x_0|\zeta)} = 2.01824\cdots. \quad (17)$$

The radius of a star is determined by

$$R(x_0,\mu_e|\zeta) = \lambda\xi_1(x_0|\eta) = 2R_0\frac{\xi_1(x_0|\zeta)}{\mu_e\varepsilon_0^{\zeta}}. \quad (18)$$

Here

$$R_0 = \left(\frac{3}{2}\right)^{1/2}\frac{1}{4\pi}\left(\frac{h^3}{cG}\right)^{1/2}\frac{1}{m_0 m_u} = 1.12\cdot 10^{-2}R_\odot,$$
$$M_0 = \left(\frac{3}{2}\right)^{1/2}\frac{1}{4\pi}\left(\frac{hc}{Gm_u^2}\right)^{3/2} m_u = 2.89M_\odot \quad (19)$$

are the scale factors, $\xi_1(x_0|\zeta)$ is the dimensionless radius of star, which corresponds to the condition $y(\xi_1(x_0|\zeta)) = 0$.

The "mass-radius" relations obtained in the standard (solid curve) and spin-polarized models at different values of the parameter ζ are shown in fig. 3.

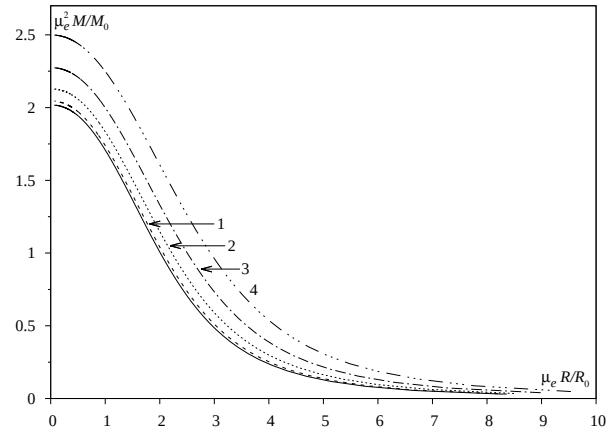

Figure 3: "Mass-radius" relation at different value ζ ($\zeta = 0$ – solid curve, $\zeta = 0.2$ – curve 1, $\zeta = 0.4$ – curve 2, $\zeta = 0.6$ – curve 3, $\zeta = 0.8$ – curve 4)

.

3. Influence of finite temperature effects on the spin-polarized model

In this section we briefly consider a model, which differs from the standard Chandrasekhar model by simultaneous accounting of magnetic field and finite temperature effects in the ideal relativistic electron systems. Here a dwarf is considered as spherically symmetric object, consisting of two regions – isothermal core with temperature T_0^* and radius R_c (occupies almost all volume of star) and a thin surface region, where the radial temperature distribution is approximated in the form $T^*(r) = T_0^*(\sqrt{1+x^2(r)} - 1)\varepsilon_0^{-1}(x_c)$. By the averaging of temperature throughout the volume of a dwarf, as it is shown in [5, 6], the equation of model can be approximately represented in the reduced form:

$$P_{red} = \sum_\sigma \mathcal{F}_\sigma(r)\left\{1 + \frac{4}{3}\pi^2\left(\frac{T_0^*}{\varepsilon_0(x_0)}\right)^2\cdot S(x_0,\xi_0)\right\}, \quad (20)$$

where

$$S(x_0,\xi_0) = \varepsilon_0(x_0)\left\{\int_0^R dr\, r^2 x^3(r)\right\}^{-1}\times$$
$$\times\left\{\int_0^{R_c} dr\, r^2 f(x(r)) + \int_{R_c}^{R} dr\, r^2\times\right. \quad (21)$$
$$\left.\times\, f(x(r))\frac{(\sqrt{1+x^2(r)}-1)^2}{\varepsilon_0^2(x_c)}\right\},$$

$$f(x(r)) = \frac{x^4(r)[r + x^2(r)][\sqrt{1 + x^2(r)} - 1]^2}{\mathcal{F}(x(r))},$$
$$\varepsilon_0(x_c) = \sqrt{1 + x_c^2} - 1, \quad x_c = x(R_c),$$
$$\mathcal{F}(x(r)) = x(r)(2x^2(r) - 3)\sqrt{1 + x^2(r)} + $$
$$+ 3\ln[x(r) + \sqrt{1 + x^2(r)}].$$

Here $\mathcal{F}(x(r))$ is the contribution of the ideal degenerate relativistic electron gas, R is the radius and $\xi_0 = R_c/R$ is the dimensionless radius of star, x_c is the value of the relativistic parameter on the edge of the isothermal core. Here the averaging is carried out using the mechanical equilibrium equation solutions at $T = 0K$ [3], and contribution to the pressure of finite temperature effects is considered as a correction. Using the reduced equation (20) and the dimensionless variables (10), the equation of state can be rewritten in the form, which was obtained in the previous section

$$\frac{1}{\xi^2}\frac{d}{d\xi}\left(\xi^2\frac{dy}{d\xi}\right) = -\{\sqrt{2}(\lambda_+^8 - \lambda_-^8)^{-1}\times \times (\varepsilon_0^\zeta)^{-1}[b(y) - \varphi(y)]^{1/2}\}^3. \quad (22)$$

However, the new scale λ is determined by:

$$\frac{32\pi^2 G}{3(hc)^3}\left\{m_u\mu_e m_0 c^2 \lambda \frac{\varepsilon_0^\zeta}{2}\right\}^2 = \eta, \quad (23)$$

where

$$\eta = 1 + \frac{4}{3}\pi^2\left(\frac{T_0^*}{\varepsilon_0(x_0)}\right)^2 \cdot S(x_0, \xi_0). \quad (24)$$

Since the equilibrium equation does not contain the temperature as a parameter, the macroscopic characteristics of a star, such as mass and radius, can easily be rewritten in the following form:

$$R(x_0, \mu_e, \zeta|\xi_0, T_0^*) = R_0\frac{\xi_1(x_0|\zeta)}{\mu_e\varepsilon_0^\zeta}\eta^{1/2},$$
$$M(x_0, \mu_e, \zeta|\xi_0, T_0^*) = \frac{M_0}{\mu_e^2}\mathcal{M}(x_0|\zeta)\eta^{3/2}. \quad (25)$$

Figures 4, 5 illustrate the dependence of mass and radius on the relativistic parameter x_0 at fixed values of the polarization parameter ζ, the dimensionless radius ξ_0 and different values of the dimensionless core temperature T_0^*. The temperature effects become more significant with decreasing of the relativistic parameter, i. e. decreasing dwarf mass. As can be seen from the figures, our model is not appropriate for low-mass dwarfs, because in such stars the temperature effects can not be considered as a correction. Therefore the branches of curves for which a mass are monotonically decreasing function of the relativistic parameter are non-physical. On the other hand in the region of large values of relativistic parameter, i. e. for massive dwarfs, the temperature effects are not significant.

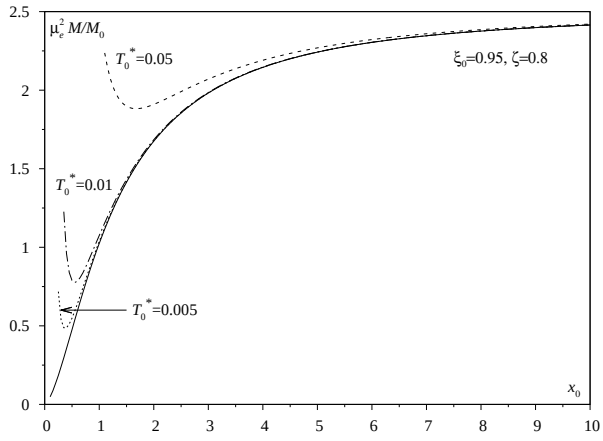

Figure 4: Dependence of dwarf's mass M on the relativistic parameter x_0 at fixed value of the dimensionless radius ξ_0 and the polarization parameter ζ for different values of the dimensionless temperature T_0^* (solid curve – $T_0^* = 0$).

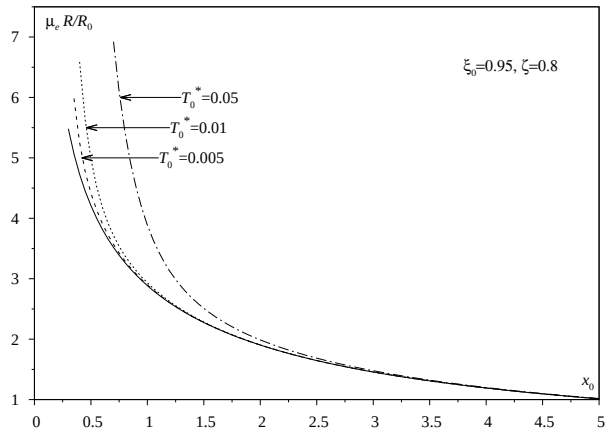

Figure 5: Dependence of dwarf's radius R on the relativistic parameter x_0 at fixed value of the dimensionless radius ξ_0 and the polarization parameter ζ for different values of the dimensionless temperature T_0^* (solid curve – $T_0^* = 0$).

We have used the sample of white dwarfs of DA spectral type from SDSS DR4 [8] and formed the subsample of the massive dwarfs with masses $M \geq 0.3M_0$ ($M \geq 0.87M_\odot$), because for such objects our model is appropriate (the temperature effects are small), on the other hand such objects can have strong enough magnetic fields.

Using the known values of masses and radii of the dwarfs, we can find from the system of equations (25) two parameters of the model x_0, T_0^*. At the same time other parameters are considered as free. The parameter μ_e is close to 2.0, we have taken the values from the work [5] for the same sample of objects. In the massive

dwarfs the isothermal core occupies almost all volume of the star [6], so the parameter ξ_0 must be close to one. In this work, we have taken the value $\xi_0 = 0.99$.

The dependence of the dimensionless temperature T_0^* on the relativistic parameter x_0 for (as an example) five massive dwarfs at the values of the spin-polarization $\zeta = 0.10; 0.15; 0.20; 0.25; 0.30$ is shown in fig. 6. As can be seen from the figure, with increasing parameter ζ, i. e. models with stronger magnetic field, central temperature of dwarf considerably drops, and the relativistic parameter in its center slowly increases.

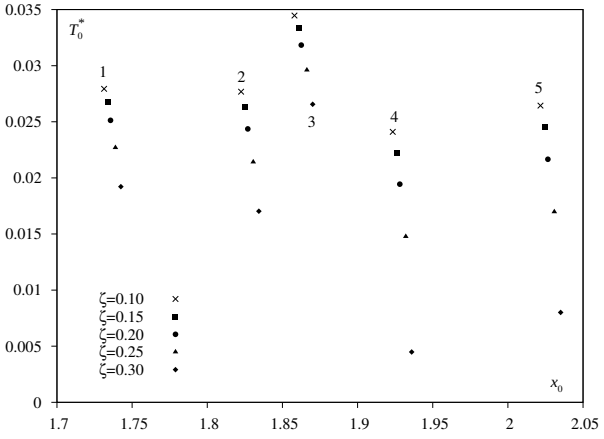

Figure 6: Dependence of the dimensionless temperature T_0^* on the relativistic parameter x_0 for the group of massive dwarfs at different values of the spin-polarization ζ (the dwarf 1 – $M = 0.870M_\odot$, $R = 0.0103R_\odot$, $T_{eff} = 38630K$; 2 – $M = 0.871M_\odot$, $R = 0.0094R_\odot$ $T_{eff} = 10330K$; 3 – $M = 0.871M_\odot$, $R = 0.0097R_\odot$, $T_{eff} = 19270K$; 4 – $M = 0.901M_\odot$, $R = 0.00963R_\odot$, $T_{eff} = 26120K$; 5 – $M = 0.931M_\odot$, $R = 0.0093R_\odot$, $T_{eff} = 27460K$).

In table 1 is shown the obtained data from the observations for the massive dwarfs (columns 2-4) [8], as well as determined parameters of the model [5], taking into account only incomplete degeneration of electron gas (columns 6-7), and considered here model, which also takes into account spin-polarization (columns 9-18). x_0^0 and $\tilde{\mu}_e$ are the values of the relativistic parameter in the stellar center and the average chemical composition parameter for the absolute cold white dwarf in the Chandrasekhar model (columns 5 and 8).

4. Critical mass and stability

For the massive dwarf at absolute zero temperature the relativistic parameter is sufficiently high ($x_0 \geq 10$). In the ultrarelativistic limit the equation of state of electron subsystem has a polytropic character,

$$P(r) \Rightarrow \frac{\pi m_0^4 c^5}{3h^3} \cdot x^4(r) \cdot \frac{(\lambda_+^4 + \lambda_-^4)}{2} \cdots . \qquad (26)$$

Therefore for calculation of the dwarf's mass, taking into account the general relativity effects, we can use the approximate dependence between energy and mass of a star which is similar to that of Zeldovich and Novikov [9] for the paramagnetic state of electrons. For the case of our model

$$E \cong \{AM - BM^{5/3}\}\rho_c^{1/3} + CM\rho_c^{-1/3} - \\ - DM^{7/3}\rho_c^{2/3} - \frac{m_0 c^2}{\mu_e m_u} M, \qquad (27)$$

where M is the mass of dwarf, ρ_c is the central density. The first three terms in the right side of this equation correspond to Newton approximation, and the term $(-DM^{7/3}\rho_c^{2/3})$ approximately takes into account the contribution of general relativity effects. Here is used the following notations:

$$A = k_1 K,\ B = k_2 G,\ C = k_3 \frac{m_0^2 c^3}{\hbar(\mu_e m_H)^{2/3}}, \\ D = k_4 \frac{G^2}{c^2},\ K = \frac{3^{1/3}\pi^{2/3}}{4} \cdot \frac{\hbar c}{(m_u \mu_e)^{4/3}} \cdot \frac{(\lambda_+^4 + \lambda_-^4)}{2}, \qquad (28) \\ k_1 = 1.75579,\ k_2 = 0.639001, \\ k_3 = 0.519723,\ k_4 = 0.918294.$$

For convenience in the following calculations we rewrite energy and mass in dimensionless form (in units E_0, M_0)

$$M = \frac{M_0}{\mu_e^2}\mathcal{M}(x_0|\zeta), \\ E = \frac{E_0}{\mu_e^3}\mathcal{E}(x_0|\zeta), \quad E_0 = \frac{GM_0^2}{R_0}, \qquad (29) \\ \rho_c^{1/3} = x_0 \left(\frac{m_u \mu_e}{3\pi^2}\right)^{1/3} \frac{m_0 c}{\hbar} \equiv x_0 \delta.$$

With dimensionless variables the formula (27) is transformed to the following form:

$$\mathcal{E}(x_0|\zeta) \cong \left\{ \frac{k_1 (3\pi^2)^{1/3}}{4} \left(1 + \frac{2}{9}\zeta^2\right) \mathcal{M}(x_0|\zeta) - \right. \\ \left. - k_2 \left(\frac{3\pi}{4}\right)^{1/3} \mathcal{M}^{5/3}(x_0|\zeta) \right\} \frac{x_0}{(3\pi^2)^{1/3}} + \\ + \frac{k_3}{x_0}\mathcal{M}(x_0|\zeta)\,(3\pi^2)^{1/3} - \\ - \frac{k_4\, x_0^2}{(4\pi)^{2/3}} \frac{m_0}{m_u \mu_e} \mathcal{M}^{7/3}(x_0|\zeta) - \mathcal{M}(x_0|\zeta). \qquad (30)$$

From the equilibrium condition $\frac{\partial}{\partial x_0}\mathcal{E}(x_0|\zeta) = 0$ we find biquadratic equation for mass as a function of the relativistic parameter at small values ζ:

$$\left(1 + \frac{2}{9}\zeta^2\right) \frac{k_1}{4} - \frac{k_2}{(4\pi)^{1/3}} \mathcal{M}^{2/3}(x_0|\zeta) - \frac{k_3\,(3\pi^2)^{1/3}}{x_0^2} - \\ - \frac{k_4}{(2\pi^2)^{1/3}} \cdot \frac{x_0\, m_0}{m_u \mu_e} \mathcal{M}^{4/3}(x_0|\zeta) = 0. \qquad (31)$$

Table 1: The microscopic parameters and the macroscopic characteristics for the massive degenerate dwarfs of spectral type DA from the catalog SDSS DR4 [8]. Symbol "-" corresponds to the cases when no solutions found.

№	R/R_0	M/M_0	T_{eff}, K	x_0^0	$\tilde{x}_0$	$\tilde{T}_0^*$	$\tilde{\mu}_e$	$\zeta = 0.10$		$\zeta = 0.15$		$\zeta = 0.20$		$\zeta = 0.25$		$\zeta = 0.30$	
								x_0	T_0^*	x_0	T_0^*	x_0	T_0^*	x_0	T_0^*	x_0	T_0^*
295	0.74623	0.34989	34020	2.6079	2.3959	0.030982	2.0221	2.3915	0.030364	2.3953	0.027776	2.3973	0.023905	2.4026	0.017152	-	-
362	0.85193	0.30832	24440	2.0468	1.9322	0.021003	2.0218	1.9277	0.020514	1.9306	0.018215	1.9323	0.014622	1.9363	0.0071401	-	-
555	0.79354	0.3291	23240	2.296	2.1654	0.02363	2.0206	2.1609	0.022898	2.1643	0.020128	2.1661	0.015746	2.1709	0.005436	-	-
650	0.79354	0.3291	26140	2.296	2.1654	0.02363	2.0206	2.1609	0.022898	2.1643	0.020128	2.1661	0.015746	2.1709	0.005436	-	-
728	0.88187	0.30832	30090	2.0468	1.8528	0.026291	2.0218	1.8482	0.026253	1.8509	0.024739	1.8527	0.022552	1.8564	0.019157	1.8602	0.013811
780	0.8719	0.30139	18340	1.9732	1.861	0.020378	2.0225	1.8564	0.019971	1.8592	0.01784	1.861	0.014528	1.8647	0.0079835	-	-
944	0.86686	0.30485	18760	2.0095	1.883	0.021713	2.0221	1.8784	0.021361	1.8813	0.019327	1.883	0.016233	1.8868	0.010592	-	-
1001	0.77463	0.33603	25450	2.3914	2.25	0.024951	2.0207	2.2456	0.024155	2.2492	0.021273	2.251	0.016724	2.256	0.0062781	-	-
1005	0.8469	0.31178	18830	2.0851	1.9552	0.022433	2.0215	1.9507	0.022007	1.9536	0.019822	1.9554	0.016486	1.9594	0.010226	-	-
1025	0.83167	0.32217	27460	2.2074	2.0262	0.026704	2.0208	2.0217	0.026437	2.0248	0.024499	2.0266	0.021661	2.0309	0.016974	2.0351	0.0080077
1430	0.8567	0.31178	26120	2.0851	1.9279	0.024358	2.0215	1.9234	0.024103	1.9263	0.022221	1.9281	0.019438	1.932	0.01477	1.936	0.0044897
1451	0.77463	0.33603	27670	2.3914	2.25	0.024951	2.0207	2.2456	0.024155	2.2492	0.021273	2.251	0.016724	2.256	0.0062781	-	-
1513	0.82719	0.31871	22180	2.1654	2.0306	0.023264	2.021	2.0261	0.022763	2.0293	0.020428	2.031	0.016853	2.0353	0.0099731	-	-
1902	0.92357	0.30139	38630	1.9732	1.736	0.027763	2.0225	1.7314	0.027935	1.7338	0.026779	1.7356	0.025126	1.7389	0.022694	1.7425	0.019218
2003	0.8719	0.30139	20450	1.9732	1.861	0.020378	2.0225	1.8564	0.019971	1.8592	0.01784	1.861	0.014528	1.8647	0.0079835	-	-
2237	0.85694	0.30485	13980	2.0095	1.9095	0.019557	2.0221	1.905	0.018998	1.9079	0.016558	1.9096	0.012618	1.9135	0.00084474	-	-
2383	0.82719	0.31871	23290	2.1654	2.0306	0.023264	2.021	2.0261	0.022763	2.0293	0.020428	2.031	0.016853	2.0353	0.0099731	-	-
2724	0.85193	0.30832	19960	2.0468	1.9322	0.021003	2.0218	1.9277	0.020514	1.9306	0.018215	1.9323	0.014622	1.9363	0.0071401	-	-
2836	0.89115	0.32217	58380	2.2074	1.8626	0.034161	2.0208	1.858	0.034468	1.8608	0.033375	1.8625	0.031834	1.8663	0.029604	1.8701	0.026559
2893	0.89208	0.30832	36820	2.0468	1.8271	0.027619	2.0218	1.8225	0.027679	1.8252	0.026317	1.827	0.024365	1.8306	0.021414	1.8343	0.017033
2914	0.7836	0.33603	28100	2.3914	2.2182	0.027283	2.0207	2.2138	0.026729	2.2173	0.024275	2.2191	0.020582	2.224	0.01392	-	-
3016	0.82656	0.32564	31420	2.2509	2.0505	0.028143	2.0207	2.0461	0.027924	2.0492	0.026047	2.051	0.023322	2.0554	0.018923	2.0596	0.011319
3035	0.882	0.30139	27420	1.9732	1.8352	0.022304	2.0225	1.8307	0.022068	1.8334	0.020252	1.8351	0.017537	1.8388	0.012921	-	-

in the Newton approximation for large relativistic parameter

$$\mathcal{M}_H(x_0|\zeta) \cong \left(1+\frac{2}{9}\zeta^2\right)^{3/2}\left(\frac{k_1}{k_2}\right)^{3/2}\frac{\pi^2}{4} - \\ -\left(1+\frac{2}{9}\zeta^2\right)^{1/2}\frac{k_3\,k_1^{1/2}}{k_2^{3/2}}\frac{6\sqrt{3}\pi^{7/6}}{x_0^2}+\cdots. \quad (32)$$

Taking into account the general relativity effects leads to a decrease of the dwarf's mass. In particular, for $\zeta = 0$ there is such value $x_0^{(0)}$ when $\frac{\partial}{\partial x_0}\mathcal{M}(x_0|0)=0$. This value determines the critical mass allowed for white dwarf and it can be found as a root of the equation

$$\frac{2k_3\,(3\pi^2)^{1/3}}{x_0^3} - \frac{k_4}{(2\pi^2)^{1/3}}\cdot\frac{m_0}{m_u\mu_e}\mathcal{M}^{4/3}(x_0|0)=0, \quad (33)$$

where $\mathcal{M}(x_0|0)$ is solution of the equation (31) at $\zeta = 0$. The instability of paramagnetic dwarf occurs in the point $x_0^{(0)}$. The critical mass of corresponding dwarf is less than the Chandrasekhar limit $\mathcal{M}_{ch} = \left(\frac{k_1}{k_2}\right)^{3/2}\frac{\pi^{1/2}}{4}$. In the case $\zeta \neq 0$ the solution

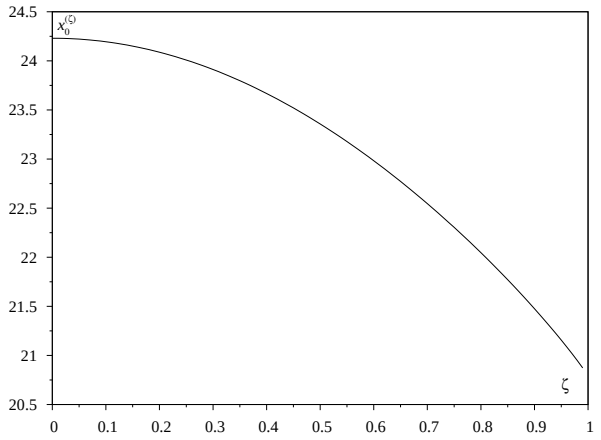

Figure 7: Dependence of the critical relativistic parameter $x_0^{(\zeta)}$ on the parameter ζ.

of equation (31) can exceed the Chandrasekhar limit and maximum mass (when the instability occurs) is achieved by some $x_0^{(\zeta)}$. The values $x_0^{(\zeta)}$ and $\mathcal{M}(x_0|\zeta)$ are determined by the equations (31) and

$$\frac{2k_2\,(3\pi^2)^{1/3}}{x_0^3} - \frac{k_4}{(2\pi^2)^{1/3}}\cdot\frac{m_0}{m_u\mu_e}\mathcal{M}^{4/3}(x_0|0)=0. \quad (34)$$

The dependence of critical value of the relativistic parameter $x_0^{(\zeta)}$ and the dimensionless mass $\mathcal{M}(x_0|\zeta)$ on the parameter ζ are shown in figures 7, 8. As we can see, the consideration of spin-polarization of electron gas in the model of white dwarf structure can yield dwarfs with masses exceeding the Chandrasekhar limit up to 40%. The critical value of relativistic parameter in stellar center (i.e. central density) decreases with increasing polarization parameter and in the model with fully polarized electron subsystem is equal to 20.9.

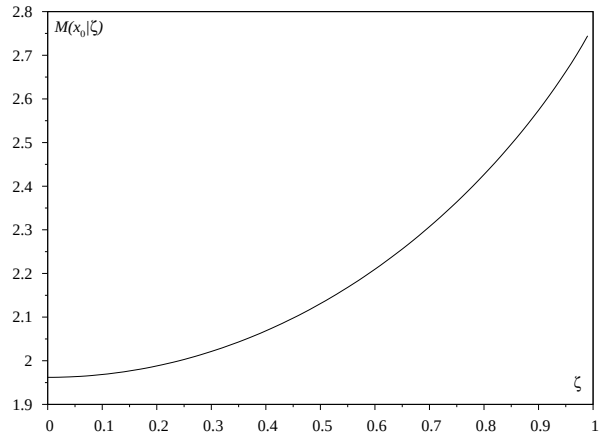

Figure 8: Dependence of dimensionless mass $\mathcal{M}(x_0|\zeta)$ on the parameter ζ.

5. Conclusions

In our work we have shown that the degree of spin-polarization and the influence of finite temperature effects of the electron subsystem can affect the macroscopic characteristics of degenerate dwarf, in particular increase the radius and especially the mass comparing with the standard Chandrasekhar model. The influence is stronger on dwarfs with low masses and is weak for massive ones. We have found the parameters of subsample of massive dwarfs in the model, where both the temperature effects and spin-polarization are taken into account. In the frame of our model we have examined the influence of general relativity effects on the critical mass of degenerate dwarf at which the instability occurs and have shown that it can exceed the Chandrasekhar limit up to 40%, what allows to explain the existence of super-Chandrasekhar white dwarfs.

References

[1] Chandrasekhar S.: 1931, *Astrophys. J.*, **74**, 81.

[2] Chandrasekhar S.: 1935, *Mon. Not. Roy. Astron. Soc.*, **95**, 676.

[3] Vavrukh M.V., Tyshko N.L., Smerechynskyi S.V.: 2010, *Journal Of Physics Studies*, **14**, n.4, 4901.

[4] James R.A.: 1964, *Astrophys. J.*, **140**, 552.

[5] Vavrukh M.V., Smerechinskii S.V.: 2012, *Astronomy Reports.*, **56**, n.5, 363.

[6] Vavrukh M.V., Smerechinskii S.V.: 2013, *Astronomy Reports.*, **57**, n.2, 913.

[7] Vavrukh M.V., Dzikovskyi D.V., Tyshko N.L.: 2015, *Odessa Astron. Publ.*, **28**, N1, 82.

[8] Tremblay P.-E., Bergeron P., Gianninas A.: 2011, *Astroph. J.*, **738**, 128.

[9] Shapiro S.L., Teukolsky S.A.: Black Holes, White Dwarfs and Neutron Stars. Cornell University, Ithaca, New York, 1983.

DOI: http://dx.doi.org/10.18524/1810-4215.2017.30.115463

EFFECTS OF THE MASS TRANSFER AND PRESENCE OF THE THIRD COMPONENTS IN CLOSE BINARY STELLAR SYSTEMS

D. E. Tvardovskyi[1], V.I. Marsakova[1,2], I.L. Andronov[2]

[1] Odessa I. I. Mechnikov National University
Odessa, Ukraine, dtvardovskyi@ukr.net, vmarsakova@onu.edu.ua

[2] Department "Mathematics, Physics and Astronomy", Odessa National Maritime University
Odessa, Ukraine, tt_ari@ukr.net

ABSTRACT: In our research, we have studied 6 close binary stellar systems which are eclipsing variables of β Lyrae and W Ursae Majoris types of variability. We have studied their O-C curves. To build them, we used moments of minima, listed in the BRNO database. Also, we used ones, which we obtained as the result of processing of observational data taken from AAVSO database. As the result of the O-C analysis, we detected that all of these stars have parabolic O-C curves, which might be caused by mass transfer from one component to another. In an addition, 3 from researched stars (U Peg, V0523 Cas and WZ Cyg) have superimposed parabolic and cyclic O-C changes that could be caused by presence of the third components in the systems. Also, we calculated minimal possible masses of third components, rates of the mass transfer for these systems and corrected the ephemerides.

Key words: eclipsing binaries, O-C curve, β Lyrae type, W Ursae Majoris type, ephemerid; stars (individual): WZ Cyg, V0388 Cyg, SX Aur, BF Aur, U Peg, V0523 Cas.

1. Objects of study

We have selected the variables for the analysis of periods changes using several main criteria. We chose the stars, observable through the small telescope during the most part of the year from Europe. Therefore, the selected stars have to:

- be bright enough (no fainter than 12–14 magnitude in the primary minimum);
- be located in the northern hemisphere of the sky;
- have short period (less than two days);
- have large enough amplitude of variability;
- have significant cyclic or secular period changes.

In an addition, the selected stars should be described at least in one research, in which we can find masses of the system's components (Bell, Adamson & Hilditch, 1987; Borkovits et al., 2005; Giuricin & Mardirossian, 1981; Lee et al., 2011; Kallrath & Strassmeier, 2000; Samec, Faulkner & Williams, 2004).

In this paper, we discuss 6 eclipsing binary stars: BF Aur, SX Aur, U Peg, V0388 Cyg, V0523 Cas and WZ Cyg. All of them are close binary systems, in which two components are deformed by their gravitational interaction.

2. Observational data and moments of minima

We used observations from different sources. Most of them were international databases, such as American Association of Variable Stars Observers (AAVSO) [http://www.aavso.org/], Brno Regional Network of Observers (BRNO) [http://var.astro.cz/ocgate/] and Northern Sky Variability Survey (NSVS) (Woźniak et al, 2004). The information about coordinates, constellations, spectral types and others was taken from the "General Catalogue of Variable Stars" (GCVS) (Samus et al., 2017).

For the variable V0523 Cas we also used our own observations obtained in filter R during international Astrocamp "Variable-2017" (http://www.astrokolonica.sk/en/events/variable/).

From the AAVSO database, we used the observations in the filters V, B, R and the visual ones for the variable stars BF Aur, SX Aur, U Peg, V0523 Cas and V0388 Cyg. Observations from the NSVS (in R-band) we used for WZ Cyg.

To collect the long series of minima, we used a large collection of ones for different eclipsing binary stars made by many authors and published in different articles on the web service BRNO [http://var.astro.cz/ocgate/].

Also, we processed all available observations by using the symmetrical polynomial fit (Andrych et al., 2015). That procedure was done for our own observations and those taken from the AAVSO database or from the NSVS, if there was not enough data in AAVSO. Phenomenological modeling of eclipses was reviewed by Andronov, Tkachenko & Chinarova (2017).

3. Methodic and hypothesis

3.1. O-C analysis

For all available moments of minima, we calculated values of O-C. Then, we built the O–C curves. For the stars with cyclic period changes (which we interpret as periodic within errors of observations), we defined the period and amplitude of the O–C changes.

The period and other parameters have been determined using the non-linear least squares fit, which takes into account simultaneously the algebraic polynomial trend, as well as multi-harmonic periodic wave. For this purpose, we have also used the program MCV (Andronov & Baklanov, 2004), which realizes the algorithm of fitting of the observations with the general formula:

$$x_C(t) = \sum_{k=1}^{p+1} C_k (E - E_0)^{k-1} + \sum_{j=1}^{s} (C_{p+2j} \cos(jw(\mathrm{E} - E0)) + Cp{+}2j{+}1 \sin(jw(\mathrm{E} - E0))), \quad (1)$$

where x_C is the value of function (in our case function is O–C), E is the cycle number, E_0 is the fixed value of E, which we set as initial, $w = {}^{2\pi}/_{T}$ is the rotation frequency, T is the period of changes of orbital period (P) of binary system; j, k, p, s are the integer numbers. The first part describes an algebraic polynomial trend of degree p and the second one – a trigonometric polynomial of power s. The coefficients C_i, $i = 1 \ldots (p + 1 + 2s)$, which may be determined using the least squares method (Andronov, 2003). The O–C curves and their approximations are shown at Fig. 1. The coefficients of the polynomial trend were used for the correction of the ephemerids.

In the case of parabolic trend $(p = 2)$, two coefficients (C_1 and C_2) mean the same as in the previous case. The coefficient (C_3) defines the rate of the secular period changes (Andronov, 1991, 2003).

Corrected ephemerids are listed in Table 1.

3.2. The rate of the mass transfer

If the star has a parabolic O–C curve or a cyclic one with parabolic trend, its period changes steadily. As the result of the O–C analysis, we detected that six of the researched stellar systems have secular period changes, which we interpreted as the mass transfer from one of the components to another. To calculate the rate of the mass transfer, we used the formula (Huang, 1963).

$$\dot{M} = \frac{1}{3}\frac{\dot{P}}{P}\frac{M_1 M_2}{(M_1 - M_2)} = \frac{1}{3}\frac{P'}{P^2}\frac{M_1 M_2}{(M_1 - M_2)}, \quad (2)$$

In this formula: $M = M_1$ is the rate of the mass transfer (measured in solar masses per day), M_1, M_2 are masses of the components in close binary system, P is the period of variability, $\dot{P}$ is the derivative of the period with time, $P' = 2C_3$ is the derivative of the period with cycle number (e.g. Andronov, 1991).

3.3. The third components hypothesis

For three systems, we detected cyclical period changes as the result of the analysis of the O–C curve. We interpret as periodic within errors of observations and supposed that they might be caused by the presence of a hypothetical third component (star or planet) in each of these systems. In our hypothesis, this component, because of its gravity, makes the binary system rotate around the common barycenter and causes the well-known light-time effect (Wolf, 2014).

In our model, we suppose that the distance between two components of binary system is much less than distance from binary system to the third component. So we can take the binary system as a single object with mass $M_1 + M_2$. Therefore, we can describe the motion of the binary system and the third body with these formulas:

$$A^3 = \frac{GMT^2}{4\pi^2} = \frac{G(M_1 + M_2 + M_3)}{\omega^2} \quad (3)$$

$$a_{12} = c\tau = A\frac{M_3}{M_1 + M_2 + M_3}\sin i \quad (4)$$

Formula (3) is the third Kepler's law; formula (4) comes from barycenter position (Tatum, 2017). In these formulas M_1, M_2, M_3 are masses of the components, i is angle of the orbit's inclination, A is semi major axis of the third component relatively to the binary system, a_{12} is semi major axis of the binary system relatively to the common barycenter, τ is the semi-amplitude of the O–C curve, T is the orbital period of the third component, ω is the angular velocity that corresponds T. There are three constants: G is the gravitational constant; c is the speed of light.

So we obtain:

$$\sin i = \frac{c\tau(M_1 + M_2 + M_3)}{AM_3} \quad (5)$$

We do not know neither $\sin i$, nor M_3. Therefore, we tabulated mass with a small step and then computed the sine of the inclination angle. Since sine of any angle cannot be more than unity, it gives us the limit of minimal mass of the third component. Thus, we built graphs, which show us relations between the mass of the third component and the orbit inclination (Fig. 2). Minimal masses of possible third components are listed in Table 2.

In addition, we calculated the errors of the minimal mass of the third body and the rate of the mass transfer by using formulas below. To obtain them, we used standard methods, which are described (Korn & Korn, 2000).

Formula of the error of the mass transfer:

$$\sigma\dot{\mathrm{M}} = \dot{\mathrm{M}}\sqrt{\left(2\frac{\sigma P}{P}\right)^2 + \left(\frac{\sigma P'}{P'}\right)^2 + \left(\frac{\sigma M_1}{M_1} - \frac{\sigma M_1}{M_1 - M_2}\right)^2 + \left(\frac{\sigma M_2}{M_2} + \frac{\sigma M_2}{M_1 - M_2}\right)^2} \quad (6)$$

where $\sigma\dot{\mathrm{M}}$ is the statistical error of the mass transfer, $\Delta\dot{\mathrm{M}}$ is the shift and similarly for other parameters.

To obtain the errors for minimal mass of the third component we use the similar approach.

Formula of the minimal mass error of the third component may be expressed as:

$$\sigma M_3 = \frac{M_3}{\frac{1}{M_3} - \frac{2}{3M}}\sqrt{\left(\frac{\sigma\tau}{\tau}\right)^2 + \frac{4}{9}\left[\left(\frac{\sigma M_1}{M_1}\right)^2 + \left(\frac{\sigma M_2}{M_2}\right)^2 + \left(\frac{\sigma T}{T}\right)^2\right]} \quad (7)$$

Δ and σ mean the same as in formula (6).

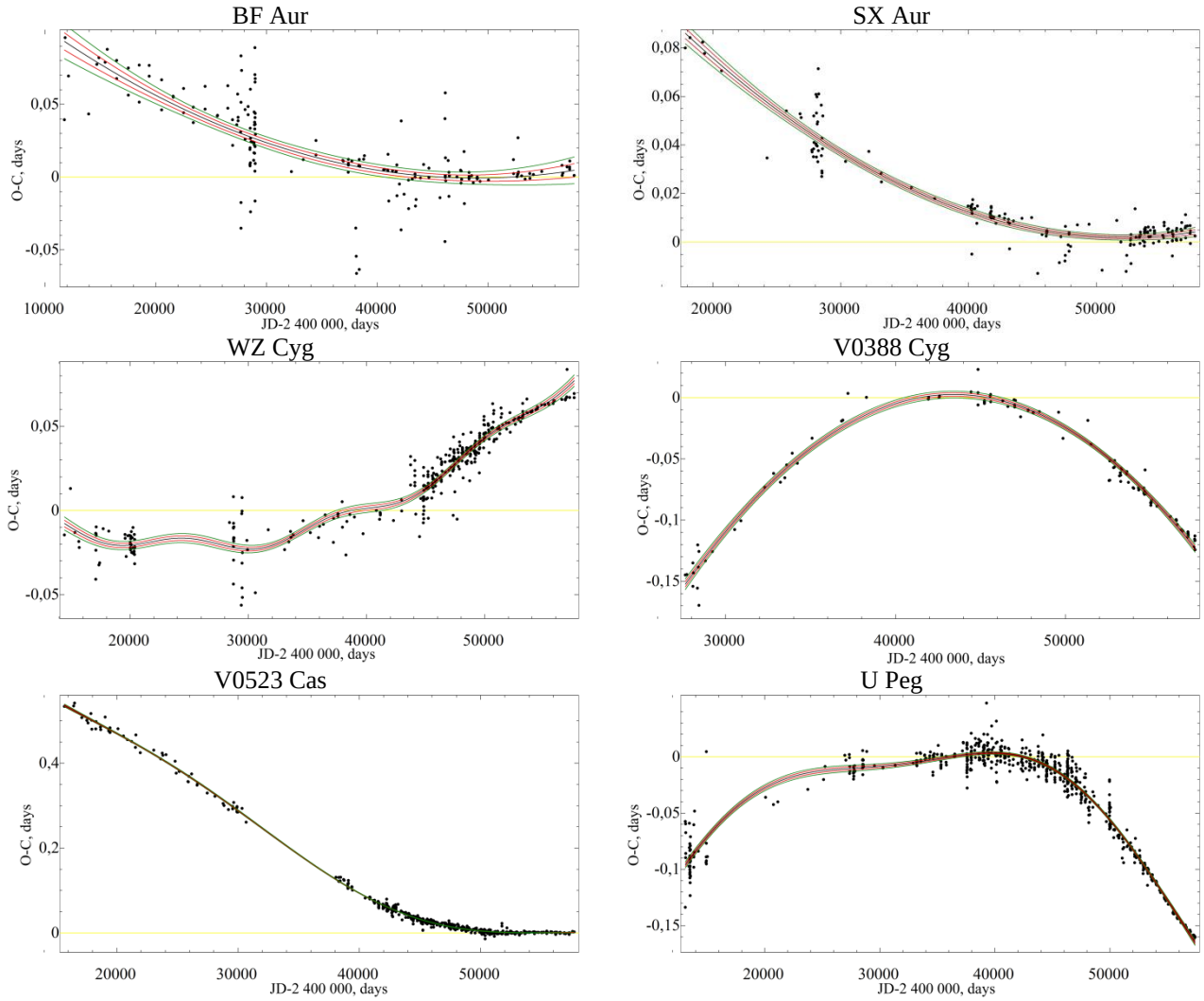

Figure 1: O–C curves for the studied systems. On the horizontal axis we set Julian date without 2400000; on the vertical one – value of O-C. Designation of each system indicated near corresponding curve. Solid lines show approximations, which take into account simultaneously the algebraic polynomial trend, as well as multi-harmonic periodic wave (using the MCV program (Andronov & Baklanov, 2004)). Red and green lines correspond to confidence interval of one and two root-mean-square deviations.

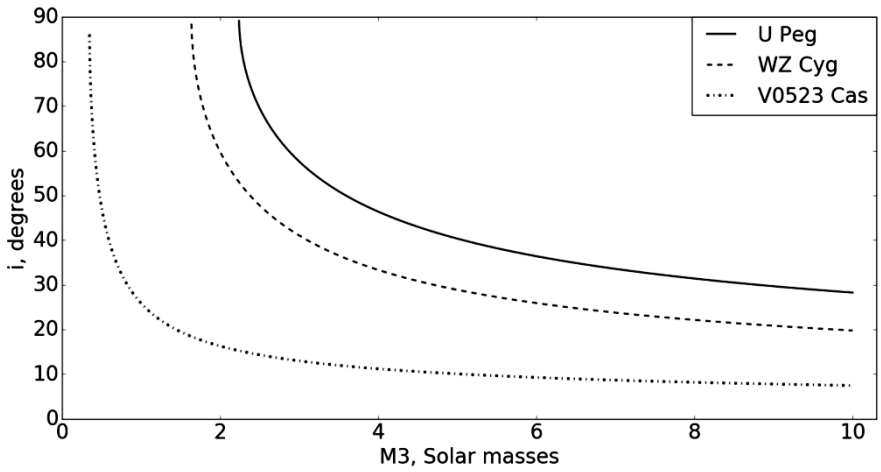

Figure 2: Dependence of orbital inclination of the third component on its mass (measured in solar masses) for the systems U Peg, WZ Cyg and V0523 Cas.

Table 1. Ephemerides before and after correction. Here E is the number of cycle. BJD means that the value was corrected for the Earth motion around the Sun (barycentric corrections).

Stellar system	Ephemerid before correction (GVCS [13]) Min I BJD – 2400000	Ephemerid after correction Min I BJD - 2400000
V0388 Cyg	$41953.3373+0.8590372\cdot E$	$(41953.337\pm0.003)+(0.8590372\pm 2\cdot10^{-7})\cdot E-(48\pm2)\cdot10^{-11}\cdot E^2$
BF Aur	$52500.950+1.5832232\cdot E$	$(52500.947\pm0.002)+(1.5832249\pm 2\cdot10^{-7})\cdot E+(17\pm3)\cdot10^{-11}\cdot E^2$
SX Aur	$52500.3179+1.2100855\cdot E$	$(52500.3119\pm0.0008)+(1.2100872\pm 7\cdot10^{-8})\cdot E+(105\pm8)\cdot10^{-12}\cdot E^2$
WZ Cyg	$40825.475+0.5844659\cdot E$	$(40825.6081\pm0.0007)+(0.58446590\pm7\cdot10^{-8})\cdot E+(1\pm0.4)\cdot10^{-10}\cdot E^2$
U Peg	$36511.66823+0.37478143\cdot E$	$(47070.5200\pm0.0005)+(0.37477680\pm3\cdot10^{-8})\cdot E-(4.8\pm0.2)\cdot10^{-10}\cdot E^2$
V0523 Cas	$57330.111+0.2336933\cdot E$	$57330.148+0.2337238\cdot E+(7.66\pm0.08)\cdot10^{-9}$

Table 2. Calculated characteristics of the period changes, minimal masses of the third components and the rates of the mass transfer for researched systems.

The name of the stellar system	The mass of the binary system	Period of the period changes	Semi-amplitude of the cyclic period changes	Minimal mass of the third body	The rate of the mass transfer
	Solar masses	days	Days	Solar masses	Solar masses per year
SX Aur	16 (Bell, Adamson & Hilditch, 1987)	—	—	—	$(3.1\pm0.3)\cdot10^{-7}$
U Peg	1.5 (Borkovits et al., 2005)	22633±1114	0.084±0.003	0.32±0.13	$(-3.7\pm0.3)\cdot10^{-8}$
V0388 Cyg	4.5 (Giuricin & Mardirossian, 1981)	—	—	—	$(-2.7\pm0.3)\cdot10^{-7}$
WZ Cyg	2.6 (Lee et al., 2011)	17196±1045	0.0047±0.0009	0.123±0.06	$(2.0\pm0.3)\cdot10^{-7}$
BF Aur	10.1 (Kallrath & Strassmeier 2000)	—	—	—	$(-1.7\pm1.5)\cdot10^{-6}$
V0523 Cas	1.18 (Samec, Faulkner & Williams, 2004)	33976±867	0.03071±0.00057	0.343±0.006	$(7.6\pm0.8)\cdot10^{-8}$

4. Conclusions

Our main results are given in Tables 1 and 2.

The rates of the mass transfer in the studied systems SX Aur, and U Peg are in a good agreement with results of other authors (Bell et al., 1987), (Borkovits et al., 2005). For WZ Cyg, we obtained the value, which is three times smaller than in (Lee et al., 2011). This can be caused by low accuracy and little quantity of data taken by us and other authors from older researches. For BF Aur and V0388 Cyg, we calculated the mass transfer rates for the first time.

For 3 systems (SX Aur, U Peg and V0523 Cas), the third components were suspected by other authors (Borkovits et al., 2005; Lee et al., 2011; Samec, Faulkner & Williams, 2004) but for U Peg the masses of the third component haven't been estimated earlier by other authors. For WZ Cyg, our results concerning periods of period changes are in good agreement with (Lee et al., 2011) (within our errors). Mass of the third body were estimated for WZ Cyg (Lee et al., 2011) it is comparable in order of values with our estimates. For V0523 Cas our estimation of the mass of the third body is approximately 20 percent smaller than one in (Samec, Faulkner & Williams, 2004).

As we can see from the Table 2, the majority of the third components have masses like stars. This fact may be caused by low accuracy of eclipse moments, especially moments that calculated decades ago (we analyzed the data obtained during about 100 years). This low accuracy does not allow to detect small period changes due to planet gravitation. But the usage of the international databases of observations and minima of eclipsing variable stars is very helpful for the analysis of the long-term period changes of these objects.

The alternative hypothesis for the explanation of cyclic period changes are discussed in (Zhu et al., 2012) and (Borkovits et al., 2005). They are magnetic activity of the second component of binary system or, in case stable changes and cyclic variations, cyclic changes in mass transfer. Confirmation or refutation of our hypothesis requires continuous spectroscopic observations of these systems.

We made similar calculations for other three systems (Tvardovskyi & Marsakova, 2015).

Acknowledgments. We are grateful to amateur astronomers for their observations published in the AAVSO and BRNO international databases that made this research possible. This work is a part of the international campaigns "Inter-Longitude Astronomy" (Andronov et al., 2017) and "Astroinformatics" (Vavilova et al., 2017).

References

Andronov I.L.: 1991, *"Struktura i evolyuciya peremennykh zvezd"* (in Russian, "Structure and evolution of variable stars"). Odessa, 1991, 48 p.

Andronov I.L.: 2003, *ASPC*, **292**, 391.

Andronov I.L., Andrych K.D., Antoniuk K.A. et al.: 2017, *ASPC*, **511**, 43.

Andronov I.L., Baklanov A.V.: 2004, *Astron. School's Rep.*, **5**, 264.

Andronov I.L., Tkachenko M.G., Chinarova L.L.: 2017, *Astrophysics*, **60**, 57.

Andrych K.D. Andronov I.L., Chinarova L.L. et al.: 2015, *Odessa Astron. Publ.*, **28**, 158.

Bell S.A., Adamson A.J., Hilditch R.W.: 1987, *Monthly Notices of the Royal Astronomical Society*, **224**, 649.

Borkovits T., Elkhateeb M.M., Csizmadia Sz., et al.: 2005, *Astronomy & Astrophysics*, **441**, 1087.

Giuricin G., Mardirossian F.: 1981, *Astrophysics and Space Science*, **76**, 1, 111.

Lee Jae Woo, Kim Seung-Lee, Lee Chung-Uk et al.: 2011, *A. J.*, **142**, 1, 7.

Kallrath J., Strassmeier K.G.: 2000, *A&A*, **362**, 673.

Korn G., Korn T.: 2000, Mathematical Handbook for Scientists and Engineers: Definitions, Theorems, and Formulas for Reference and Review, General Publishing Company, 1151P.

Samec R. G., Faulkner D. L., Williams D. B.: 2004, *A. J.*, **128**, 2997.

Samus N.N. Kazarovets, E.V.; Durlevich, O.V.; et al.: 2017, *ARep*, **61,** 80, General Catalogue of Variable Stars (GCVS). [E-resource]. Available from: http:// www.sai.msu.su/gcvs

Tatum J.B.: 2017, *Physics topics. Celestial Mechanics*. [E-resource]. Available from: http://astrowww.phys. uvic.ca/~tatum/celmechs/

Tvardovskyi D.E., Marsakova V.I.: 2015, *AASP*, **5**, 75.

Vavilova I.B. et al.: 2017, *IAUS*, **325,** 361.

Woźniak P.R., Vestrand W.T., Akerlof C.W. et al.: 2004, *A. J.*, **127**, 2436. [E-resource]. Available from: http:// skydot.lanl.gov/nsvs/nsvs.php.

Wolf M.: 2014, *Contributions of the Astronomical Observatory Skalnaté Pleso*, **43**, 3, 493.

Zhu Liying, Qian Sheng-Bang, Li Linjia: 2012, *Publ. Astron. Soc. Japan*, **64**, art. id. 94.

DOI: http://dx.doi.org/10.18524/1810-4215.2017.30.114381

PHOTOMETRY AND BLAZHKO EFFECT IN RR LYR-TYPE STAR AE LEO

S.N. Udovichenko, L.E. Keir

Astronomical Observatory, Odessa National University,
Odessa, Ukraine, *udovich222@ukr.net*

ABSTRACT. The photometric observations for the RR Lyr-type star AE Leo in the Astronomical station near Odessa using the 48-cm reflector AZT-3 and the CCD photometer equipped with the V filter have been carried out. The light curves shows variable amplitude of light maxima and the moderate Blazhko effect. The analysis of the O-C light maxima for our observations and the ASAS, NSVS data indicates the secular period changes.

Keywords: Stars: oscillations - stars; variables: RR Lyr-type stars: individual: AE Leo.

1. Introduction

AE Leo (AN 1935.0206, GSC 1437.00734, NSVS 10338360), ($\alpha_{J2000.0}$ = $11^h26^m12.2^s$; $\delta_{J2000.0}$ = $+17°39'39.7''$) The variability of the star was found by Morgenroth in 1935, as a variable star in list of the 31 new variables (Morgenroth, 1935). The finding chart for this star was published by N.E.Kurochkin (1949). The star thoroughly was investigated by L.Meinunger, which determined the primary period and 32 times of light maxima, using the old photographic plates from 1913 to 1961 years (Meinunger, 1961). The visual observations in 20 century were carried out by B.N.Firmanyuk and V.G.Derevyagin in 1987, Huebscher et al., in 1989 (Paschke, 2008). Now AE Leo is known as RR Lyr-type RRab star (GCVS) with amplitude $11.^m6 - 12.^m8$ (P) and period $0.^d626723$ (Samus et al., 2011).

2. Observations

To study the physical explanation for the Blazhko effect, we have to get as much as possible detailed observations of RR Lyr-type stars. The photometric CCD observations of AE Leo in Astronomical station near Odessa in observation season 2013,2015,2017 years have been carried out.

Two stars were chosen as comparison and check stars (comp=UCAC4 539-050620, Vcomp=$14.^m157$ (APASS, 2010), check=UCAC4-539-050615). The 48 cm reflector AZT-3 with the f/4.5 Newtonian focus and CCD photometer with chip Sony ICX429ALL (600x800 pixels), equipped with V filter, Peltier cooler were used (Udovichenko, 2012). The hermetic housing and thermoelectric (Peltier) cooler provide a temperature difference between the sensor CCD and the environment of about -40^{o}C, and the temperature was supported by a constant. The exposure time for variable and comparison stars for the most part were chosen to except a saturation of frame and consist 90 sec. More then 3900 CCD frames were gathered during 28 nights.

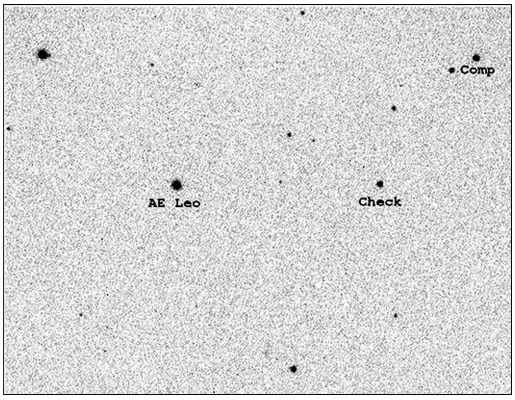

Figure 1: The finding chart AE Leo with the comparison and check stars marked.

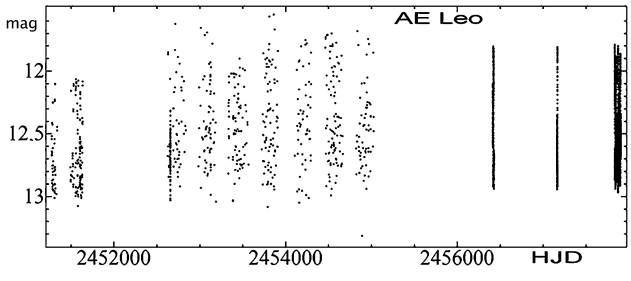

Figure 2: The all data set of observations with NSVS and ASAS data.

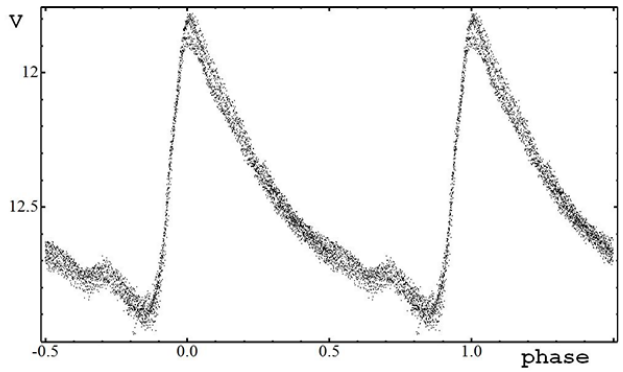

Figure 3: The phase curves of AE Leo from our observations. The moderate Blazhko modulation of amplitude reach about 0.13 mag

The standard reductions of the CCD frames were carried out using the MUNIPACK (Motl, 2009-17) software. The procedures for the aperture photometry is composed of the dark-level and flat-field corrections and determination of the instrumental magnitude and precision. To convert the differential magnitudes to the corresponding magnitudes of the variable, were used the comparison star V magnitude from APASS-catalog (2010). The finding chart with comparison and check stars are shown in Fig. 1, the all set of observations one in Fig. 2. The errors on individual data points vary between 0.005 mag to 0.02 mag.

3. Frequency analysis

For all our observations of AE Leo were determined the magnitudes comparatively of comparison star. The frequency analyses were performed using a package of computer programs with single-frequency and multiple-frequency techniques by using utilize Fourier as well as multiple-least-squares algorithms (program Period04, Lenz and Breger, 2004). The pulsation period was determined with this package as the highest peak on the Fourier amplitude spectra. The all light curves AE Leo with pulsating period are shown on fig.3. These phase curves were computed from elements:

$$MaxHJD = 2419839.549 + 0.6267074 * E.$$

The value in maxima of the light curves vary from 11.77 mag to 11.90 mag, moderate Blazhko modulation of amplitude reach about 0.13 mag and no phase-shift modulations. The maxima of the pulsation cycles were determined for our analysis. The data of ASAS (Pojmanski, 2002) and NSVS (Wozniak, 2004) so were used for determinations of the light maxima (Fig. 4).

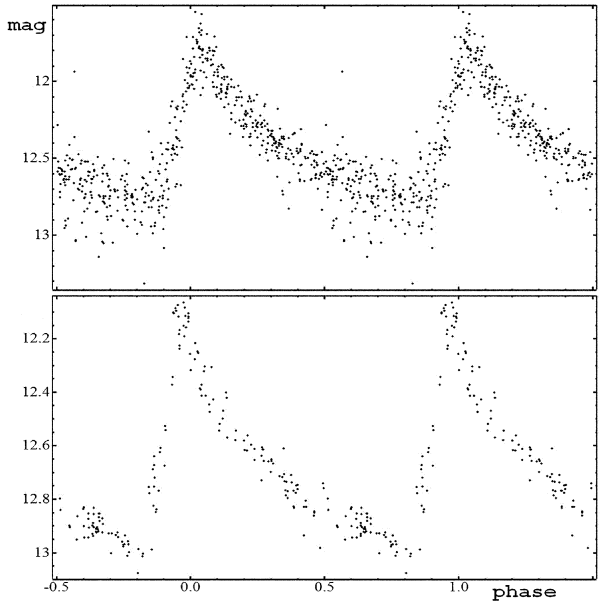

Figure 4: The phase curves of AE Leo from NSVS (bottom) and ASAS (top) data.

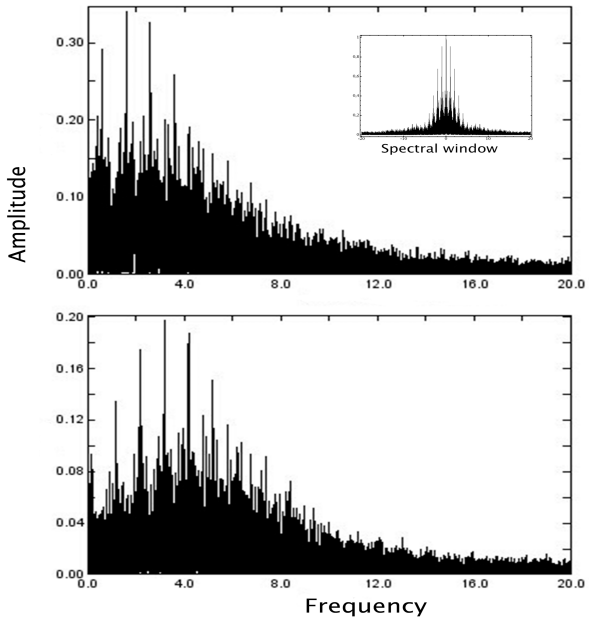

Figure 5: The Fourier amplitude spectrum of basic frequency and after prewhitening. The spectral window is shown inside first picture.

The power spectra of basic frequency and after prewhitening is shown in Fig. 5. After prewhitening of basic frequency the harmonics of basic frequency kf0 and f_m frequency responsible for modulation of light curves was found. The Fourier amplitude and phases of the pulsation component identified in the spectra of

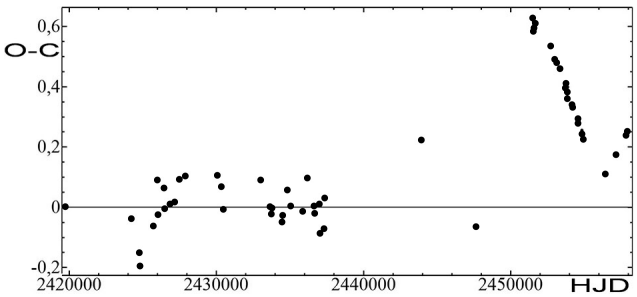

Figure 6: The mean O-C diagram of AE Leo during 100 years.

Table 1: Identified Fourier amplitude and phases of the pulsation and modulation frequencies in light curves of AE Leo.

Identif.	Frequency	Amplitude	Phase	S/N
f0	1.595519	0.370	0.86	5.3
2f0	3.191036	0.190	0.47	57.6
3f0	4.786535	0.117	0.95	40.0
4f0	6.380688	0.078	0.72	31.2
5f0	7.977561	0.044	0.15	18.3
6f0	9.573121	0.024	0.39	10.4
7f0	11.16721	0.019	0.40	8.3
f0-fm	1.51316	0.015	0.11	4.6

Table 2: The time of maxima AE Leo

Time HJD	Time HJD
2456416.467	2457165.440
2457835.449	2457840.464
2457847.355	2457872.429
2457899.380	

the light curves of AE Leo are presented in Table 1. The basic frequency denoted as f_0, the modulation frequency of Blazhko effect denote as f_m. We find seven frequencies, but, perhaps, there are more frequencies in the pulsation spectra of AE Leo.

From obtained data (Fourier analysis and the maxima height change) the preliminary value of Blazhko effect period is amount 12^d.

4. Pulsation-period variations, the O-C diagram

We have collected all available data from literature and WWW-resource for AE Leo maxima and constructed the updated O-C diagram, using the elements from GCVS. The resulting diagram is plotted in Fig. 6. These data indicate that AE Leo shows the secular period changes. The time of maxima from our observations, obtained by fitting pulsation light curves near the maxima, listed in Table 2.

References

APASS, Star catalog: 2010, *http://www.aavso.org.*
Benn D.: *http://www.aavso.org/vstar.*
Kurochkin N.E.: 1949, *Perem. Zvezdy*, **N6**, 303.
Lenz P., Breger M.: 2004, *Comm.in Asteroseismology* **144**, p.41.
Meinunger L.: 1961, *MVS N604-605.*
Morgenroth O.: 1935 *Astron. Nachr.*, **256**, 281.
Motl D.: 2009-17 *http://sourceforge.net/projects/c-munipack*
Paschke A., Martignoni M.: 2008 *http://www.ast.obs-mip.fr/users/leborgne/dbRR/*
Pojmanski G.: 2002, *Acta Astronomica*, **52**, 397.
Samus N.N., Durlevich O.V., Kazarovets E V., Kireeva N.N., Pastukhova E.N., Zharova A.V. et al.: 2011, *General Catalogue of Variable Stars* (GCVS database, Version 2011Jan).
Udovichenko S.N.: 2012, *Odessa Astron. Publ.*, **25**, 32.
Wozniak, P.R., Vestrand, W.T., Akerlof, C.W. et al.: 2004, *Astron. J.*, **127**, 2436.

DOI: http://dx.doi.org/10.18524/1810-4215.2017.30.117156

SPECTROSCOPICAL STUDY OF FAINT SOUTHERN CEPHEIDS WITH SOUTHERN AFRICAN LARGE TELESCOPE (SALT). FIRST RESULTS.

I. A. Usenko[1,2], A. Yu. Kniazev[3,4], V. V. Kovtyukh[1], S. I. Belik[1] and L. N. Berdnikov[5]

[1] Astronomical Observatory, Odessa National University, Marazlievska 1B, Odessa 65014, Ukraine, *vkovtyukh@ukr.net*
[2] Mykolaiv Astronomical Observatory, Obsevatorna 1, Mykolaiv 54030, Ukraine, *igus99@ukr.net*
[3] South African Astronomical Observatory, P.O. 7925, Cape Town, South Africa *akniazev@saao.ac.za*
[4] Southern African Large Telescope Foundation, P.O. 7925, Cape Town, South Africa
[5] Sternberg Astronomical Institute, Universitetskii pr. 13, Moscow 119991, Russia *lberdnikov@yandex.ru*

ABSTRACT. First Cepheids observations using echelle-spectrograph HRS fed by Southern African Large Telescope (SALT) were realized during 2016. All spectra have been obtained in the medium resoltion mode (R≈31000–41000) wth high S/N ratio near 50–220. All data were processed using package developed by authors based on the standard system of astronomical data reduction MIDAS. Using new echelle data we found the atmosphere parameters and chemical composition for 30 faint Cepheids of southern hemisphere, where for the most of theses stars these results we obtained for the first time. 28 stars are Cepheids after the first-dredge up stage, while ASAS 075842-25336.1 and ASAS 1131714-6605.0 having remarkable Li I 6707.8 Å absorption line and anomalous CNO and Na content could be consider as first crossing of the Cepheids instability strip.

Keywords: Stars: Cepheids: atmosphere parameters; Cepheids: chemical composition

1. Introduction

The abundance gradient for the Galaxy as observational characteristic of the galactic disk is the most input parameter in any theory of galactic chemical evolution. Many questions concerning the present-day abundance distribution in the galactic disk, its spatial properties and evolution with time remain to be answered. To answer these questions it would be reasonably to use the Cepheids as the quite suitable probes of metallicity in the Galactic disc.

According to results of investigations for iron, for example, its abundance gradient displays a multimodal structure: a rather flat part in vicinity of the Sun, a small gradient in the outer part of the disk (here the distribution shows some scatter and all the stars are metal-deficient comparing to the stars from the solar vicinity), and a quite large negative gradient in the inner part of the disk in the range from 4 to 7 kpc, but it with a very small number of investigated stars, and poorer statistics.

Even though elemental abundance increases towards the galactic center, there are arise two questions: 1) what is the real behavior of the abundance distributions within the inner parts (less than 7 kpc) of the galactic disk; 2) what is the real one for the galactocentric distances more than 10 kpc?

Therefore, the main objective of our program is to observe additional Cepheids situated closer to the galactic center and situated too much far away from it in order to:
1) Constrain the metallicity distribution and its gradient in these regions;
2) Find the properties of the abundance distribution at galactocentric distances of less than 7 kpc and more than 10 kpc.
3) To extract the possible objects belonging to the Population II.

To realize this program we have used Southern African Large Telescope (SALT). Our observational

Table 1: List of investigated Cepheids.

Object	Type	P (d)	R_G (kpc)	[Fe/H]	[C/H]	[N/H]	[O/H]	[Na/H]	[Mg/H]	[Al/H]
V1048 Cen	DCEP	1.300	7.44	–0.09	–0.35	+0.38	–0.35	+0.15	–0.12	+0.10
ASAS 114920-6600.6	DCEPS(B)	1.960	7.32	–0.04	–0.20	+0.34	+0.52	+0.12	–0.21	+0.15
ASAS 072424-0751.3	DCEPS	2.071	9.76	–0.19	–0.43	+0.22	-	+0.25	+0.18	+0.02
ASAS 073200-2529.3	DCEPS	2.421	9.25	–0.20	–0.47	+0.14	+0.05	+0.11	–0.20	–0.04
ASAS 174603-3528.1	DCEPS	2.573	6.02	+0.11	+0.04	+0.60	-	+0.41	–0.15	+0.43
ASAS 183652-0907.1	DCEP	2.590	6.55	+0.14	–0.21	+0.42	–0.15	+0.45	+0.16	+0.33
BD-10 4739	DCEP	3.058	6.63	+0.04	–0.24	+0.28	–0.29	+0.30	–0.18	+0.25
104130-5956.9	DCEPS	3.081	7.56	+0.00	–0.26	+0.39	+0.15	+0.18	–0.06	+0.18
V720 Car	DCEP	3.081	7.56	–0.03	–0.27	+0.36	–0.28	+0.17	–0.06	+0.13
ASAS 065851-1344.2	DCEPS	3.280	11.55	–0.29	–0.59	+0.18	–0.35	+0.06	–0.24	–0.09
FZ Car	DCEP	3.578	7.64	+0.05	–0.21	+0.51	–0.28	+0.29	+0.01	+0.21
HD 317966	DCEP	3.720	6.90	+0.08	–0.15	+0.64	–0.23	+0.40	+0.10	+0.23
ASAS 100814-5856.6	DCEPS	3.767	7.78	–0.07	–0.36	+0.24	–0.35	+0.11	+0.02	+0.16
HD 160473	DCEP	3.780	6.81	+0.04	–0.20	+0.51	–0.11	+0.23	+0.10	+0.21
V701 Car	DCEP	4.090	7.71	–0.01	–0.21	+0.51	-	+0.43	+0.00	+0.22
V690 Car	DCEP	4.150	7.85	+0.12	–0.18	+0.46	–0.04	+0.38	+0.04	+0.32
V1210 Cen	DCEP	4.320	6.88	+0.08	–0.08	+0.16	–0.25	+0.15	+0.39	+0.32
GI Car	DCEP	4.431	7.48	–0.04	–0.33	+0.34	–0.31	+0.18	–0.09	+0.13
CC Car	DCEP	4.760	7.76	+0.09	–0.17	+0.47	–0.28	+0.30	–0.06	+0.33
ASAS 182714-1507.1	DCEP	5.550	6.02	+0.32	–0.01	+0.90	–0.26	+0.67	+0.23	+0.58
ASAS 123617-6317.6	DCEPS	6.166	6.86	+0.09	–0.21	+0.47	-	+0.34	+0.22	+0.32
RS Nor	DCEP	6.198	6.26	+0.15	–0.11	+0.60	+0.32	+0.54	+0.11	+0.37
ASAS 070832-1454.5	DCEPS	6.388	9.58	–0.06	–0.38	+0.26	–0.52	+0.15	–0.26	+0.11
ASAS 092758-5218.9	DCEP	7.640	8.33	+0.05	–0.19	+0.35	-	+0.35	+0.22	+0.26
ASAS 093942-4931.5	DCEPS	7.754	8.08	–0.01	–0.24	+0.43	–0.28	+0.18	–0.00	+0.18
VX Cru	DCEP	12.213	6.78	+0.24	–0.03	+0.67	–0.09	+0.68	+0.25	+0.46
ASAS 083611-3903.7	DCEP	12.960	8.39	–0.08	–0.37	+0.13	–0.09	+0.10	–0.03	+0.08
VW Cen	DCEP	15.036	6.28	+0.38	+0.15	+0.74	–0.19	+0.67	+0.18	+0.53
ASAS 075842-2536.1	DCEPS(B)	0.580	9.03	–0.17	–0.30	–0.14	–0.06	–0.14	–0.46	+0.06
ASAS 131714-6605.0	DCEPS	1.290	6.85	+0.05	–0.17	+0.68	+0.01	+0.36	–0.05	+0.40

list contains 168 Cepheids located at galactocentric distances smaller than 7 kpc and more than 10 kpc (Mel'nik et al., 2015). They are to be bright enough to be accessible with SALT.

2. Observations, data reducing and objects selection

All observations have been **taken** using 11m SALT (Southern African Large Telescope) equipped by HRS (High Resolution Spectrograph). HRS is a dual-beam (3700-5500 & 5500-8900 ÅÅ) fiber-fed, white-pupil, echelle-spectrograph, employing VHP gratings as cross dispersers. We obtained even one spectrum for each Cepheid using *medium mode* spectral resolution (R = 40000), mean S/N = 100 and more, and it could be enough to resolve our observational tasks. These spectra will be used to obtain the atmosphere parameters and chemical composition of these unexplored yellow supergiants. The data were reduced using the *échelle* package which consist of huge amount of basic procedures for echelle data reduction. *FEROS* is another package and it was developed for the reduction of of echelle data from Fiber-fed Extended Range Optical Spectrograph (FEROS). FEROS looks very similar to HRS and both instruments have very close type of echelle data.

DECH30 package (Galazutdinov, 2007) allows to measure the line depths and radial velocities using spectra in FITS format. Lines depths were used to determine the effective temperature (a method based on the spectroscopic criteria, Kovtyukh, 2007).

78 objects with magnitude $10^m \leq V \leq 12.^m5$ have been selected from GCVS, ASAS and 2MASS catalogues. At now we have the results for spectra of 30 Cepheids. All these data are given in Table 1.

3. Atmosphere parameters and chemical composition

3.1. Methods

The effective temperatures T_{eff} were determined by a method based on the depth ratios of selected pairs of spectral lines most sensitive to the temperature. Several spectroscopic criteria (Kovtyukh, 2007) were used in this case. This method provide an internal accuracy of 10 – 30 K for T_{eff} (the error of the mean). The microturbulent velocity V_t was determined from the condition for the Fe I abundance derived from a set of lines being independent of their equivalent widths. The surface gravity $\log g$ was determined from the ionization equilibrium condition for Fe I and Fe II atoms.

When estimating the atmospheric parameters and chemical abundances, we used the VALD oscillator strengths (Kupka et al., 1999) and model atmospheres from Castelli & Kurucz (2004).

3.2. RS Nor as a testing object

We used RS Nor as a testing object **since** its atmosphere parameters and chemical composition were determined earlier by Luck (2014). Our carbon and oxygen abundances estimations are close to ones from Luck (2014) paper, thereas sodium and iron show

some less values ([Na/H] = +0.77 and [Fe/H] = +0.23 from Luck paper). All our data are given in Table 1.

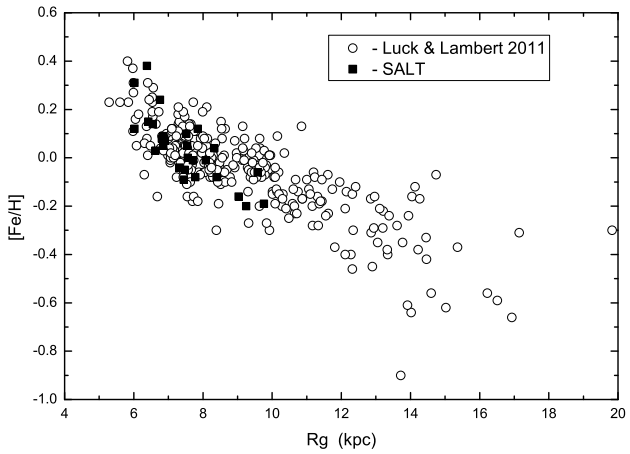

Figure 1: Metallicity gradient of Galaxy according to Cepheids [Fe/H] values. Open circles – Luck & Lambert (2011), filled squares – SALT data.

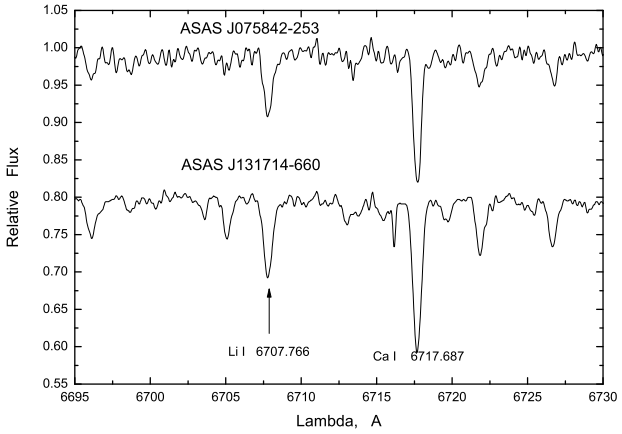

Figure 2: Spectral region around the 6707.8 Å Li I line in the spectra of ASAS 075842-2536.1 and ASAS 131714-6605.0.

4. Conclusions

Our analysis of the available spectra **results** to the following conclusions:

1. As seen from Table 1 all objects have metallicity values within the ranges of –0.3 – +0.4 dex that is an evidence of their belonging to Population I.

2. Our [Fe/H] estimates for these Cepheids are in good agreement with Luck & Lambert (2011) data for iron abundance gradient of Galaxy.

3. CNO- elements abundances in the whole show the typical values for yellow supergiants after first dredge-up stage. Carbon is in deficient, excepting ASAS 174603-3528.1, ASAS 182714-1507.1 and VW Cen. These Cepheids have metallicity overabundance and their [C/Fe] relation give the deficient too. Nitrogen demoinstrates overbundance except of case for ASAS 075842-2536.1. There are significant discrepancies of oxygen from the solar value.

4. Sodium is in overabundace, exept ASAS 075842-2536.1. Magnesium abundance shows discrepances and aluminium content is overabundant in most cases except for ASAS 073200-2529.3 and ASAS 065851-1344.2

5. Objects ASAS 075842-2536.1 and ASAS 131714-6605.0 have remarkable absorption line of lithium 6707.8 Å (see Figure 2), and anomalous CNO and Na content. Quite probably these stars are Cepheids, first time crossing the Cepheids instability strip (CIS).

References

Castelli F., Kurucz R.L.: 2004, *arXiv: astro-ph/ 0405087*.

Galazutdinov G.A.: 2007, *http://gazinur.com/DECH-software.html*.

Kovtuykh V.V.: 2007, *MNRAS* **378**, 617.

Kupka F., Piskunov N.E., Ryabchikova T.A., Stempels H.S., Weiss W.W.: 1999 *A&A*, **138**, 119.

Luck R.E.: 2014, *AJ*, **147**, 137.

Luck R.E., Lambert D.L.: 2011, *A*, **142**, 136.

Mel'nik A.M., Rautiainen P., Berdnikov L.N., Dambis A.K., Rastorguev A.S.: 2015, *AN*, **336**, 70.

DOI: http://dx.doi.org/10.18524/1810-4215.2017.30.114382

PULSATIONAL ACTIVITY OF THE SMALL–AMPLITUDE CEPHEID POLARIS (α UMi) IN 2016-2017

I. A. Usenko[1,2], V. V. Kovtyukh[1], A. S. Miroshnichenko[3], S. Danford[3]

[1] Astronomical Observatory, Odessa National University, Shevchenko Park, Odessa 65014, Ukraine, *vkovtyukh@ukr.net*

[2] Mykolaiv Astronomical Observatory, Obsevatorna 1, Mykolaiv 54030, Ukraine, *igus99@ukr.net*

[3] Dept. of Physics and Astronomy, University of North Carolina at Greensboro, P.O. Box 26170, Greensboro, NC 27402, USA, *a_mirosh@uncg.edu; danford@uncg.edu*

ABSTRACT. We present the results of an analysis of 49 spectra of α UMi (Polaris) obtained during August – December 2016 and January – March 2017. Frequency analysis displays an unexpected decrease of the pulsational period up to 17.3 min in comparison to the 2015 observational set. The radial velocity amplitude was reduced to 3.43 km s^{-1} in 2016 and to 3.31 km s^{-1} in the beginning of 2017 in comparison with 4.16 km s^{-1} in 2015. This result is also unexpected, because during the last decade a gradual amplitude growth has been observed. The average T_{eff} = 6021 K determined from the 2016–2017 data is close to the values determined for the 2001–2015 set.

Key words: Stars: radial velocities; Cepheids: effective temperatures; Cepheids: α UMi

1. Introduction

In our previous papers (Usenko et al., 2016; Usenko et al., 2017) we found that in 2015 the pulsational period and radial velocity amplitude of Polaris had increased. The former was 8.6 min longer compared to the 2007 data, and the latter became 4.16 km s^{-1} (twice the one of 2007 data). The average T_{eff} = 6017 K, and it is close to the value determined for the 2001–2004 set. These facts allow us to make a conclusion about the Cepheid movement to the red edge of the Cepheids instability strip (CIS). Since Polaris is a peculiar Cepheid demonstrating an increase of its pulsational activity after a long-term decrease, it needs high-quality continuous observations with both photometry and spectroscopy.

2. Observations and frequency analysis

Thirty seven spectra were taken in August–December 2016 and twelve in January – March 2017 with the 0.81 m telescope of the Three College Observatory (TCO), located in central North Carolina, USA. They were obtained with an échelle spectrograph manufactured by Shelyak Instruments[1] in a spectral range from 4250 to 7800 Å with a spectral resolving power of $R \sim 12000$ and no gaps between the spectral orders. The data were reduced using the *échelle* package in IRAF.

DECH30 package (Galazutdinov, 2007) allows to measure the line depths and radial velocities using spectra in FITS format. Lines depths were used to determine the effective temperature (a method based on the spectroscopic criteria, Kovtyukh, 2007).

Derived values of T_{eff} and radial velocity for each spectrum are given in Table 1.

In the next step, we used the PERIOD04 program (Lenz & Breger, 2005), which employs the Fourier and Fast Fourier Transform analysis and minimizes the residuals of sinusoidal fits to the data.

A Fourier amplitude spectrum was obtained over a frequency range of 0–1 d^{-1} with a resolution of 0.00002 d^{-1}. The highest amplitude of 1.97 corresponds to a frequency of 0.252403 ± 0.000255 d^{-1}, or a period of 3.96192 ± 0.004 days, respectively. This period is 17.3 minutes shorter compared to that of 3.97394 days determined from the 2015 data set. The systemic velocity (γ – velocity) is equal to -12.50 ± 1.48 km s^{-1}.

The following ephemeris has been computed based on the radial velocity values:

$$RV_{\min} = HJD\,2457685.737 + 3.96192 \times E \quad (1)$$

[1] http://www.shelyak.com

Table 1: Observational data of α UMi

HJD	T_{eff}	σ	Phase	RV (km s^{-1})					
2450000+	K	K		Metals	σ	NL	H_α	H_β	H_γ
7623.5721	6016	17	0.309	–12.52	1.31	165	–11.72	–12.34	–11.80
7627.5674	6003	19	0.318	–12.47	1.60	154	–12.56	–13.09	–12.24
7636.6104	6035	18	0.600	–13.28	1.40	173	–11.36	–11.64	–11.72
7637.6578	6075	23	0.865	–15.43	1.78	170	–14.57	–15.06	–15.21
7638.6128	6039	22	0.106	–15.04	1.52	151	–14.37	–14.15	–15.30
7640.5840	6046	25	0.603	–11.86	1.63	155	–10.62	–11.89	–12.73
7646.6272	6064	23	0.129	–13.66	1.67	167	–14.39	–14.29	–14.89
7656.5042	6039	16	0.622	–12.30	1.86	152	–11.70	–11.80	–12.27
7663.5326	5981	17	0.396	–11.33	1.52	151	–11.45	–11.94	–11.67
7666.5895	6058	20	0.167	–12.71	1.42	166	–14.23	–14.03	–13.95
7671.6202	6021	16	0.437	–10.97	1.37	143	–10.70	–11.38	–12.13
7672.5231	6054	17	0.665	–12.15	1.51	146	–12.49	–11.68	–11.78
7679.6214	5992	17	0.456	–11.38	1.70	165	–10.02	–10.81	–12.77
7684.5583	6017	15	0.703	–11.95	1.58	159	–12.27	–11.76	–12.44
7685.5899	6035	17	0.963	–14.60	1.65	164	–15.62	–15.05	–14.84
7686.5955	5998	15	0.217	–13.29	1.33	161	–13.02	–13.34	–13.76
7687.6101	6040	17	0.473	–10.92	1.52	165	–10.25	–10.54	–10.91
7690.6666	6020	19	0.244	–12.79	1.27	159	–13.16	–12.89	–13.75
7695.5187	5935	20	0.469	–11.06	1.37	168	–10.79	–10.27	–12.08
7697.5328	6017	15	0.977	–14.50	1.34	158	–14.20	–14.31	–14.05
7699.5794	6004	17	0.494	–10.39	1.43	169	–10.06	–10.64	–11.71
7703.5998	6011	18	0.509	–10.53	1.51	159	–9.71	–10.60	–10.71
7705.5479	6028	15	0.000	–14.72	1.43	164	–14.44	–14.70	–14.92
7708.6107	6079	19	0.773	–12.55	1.36	163	–12.80	–12.40	–13.18
7709.6391	6042	18	0.033	–14.46	1.44	158	–14.76	–14.48	–15.60
7710.6093	5966	14	0.278	–12.58	1.55	164	–12.41	–12.83	–13.83
7713.5625	6049	13	0.023	–14.40	1.33	167	–14.36	–14.20	–14.18
7714.5859	5997	14	0.282	–12.00	1.12	157	–11.64	–11.95	–11.32
7715.5773	5990	20	0.532	–10.55	1.53	159	–10.01	–10.47	–10.20
7719.5312	5984	17	0.530	–10.59	1.52	155	–9.94	–10.19	–10.88
7724.5379	6034	22	0.794	–12.85	1.39	163	–12.11	–13.02	–12.39
7725.6085	6024	19	0.064	–14.52	1.40	169	–14.20	–13.85	–13.55
7731.5661	6017	19	0.567	–10.66	1.58	164	–10.21	–10.42	–9.30
7732.5298	6045	17	0.811	–13.28	1.46	155	–13.47	–13.25	–14.03
7738.6107	5990	21	0.346	–11.97	1.23	169	–11.72	–11.79	–12.40
7743.5390	6016	21	0.589	–9.74	1.36	151	–9.79	–10.78	–9.87
7744.6051	6015	16	0.859	–12.37	1.32	163	–11.64	–11.95	–11.32
7772.5311	6031	16	0.907	–13.40	1.18	159	–13.07	–13.20	–13.05
7780.5681	6014	23	0.936	–13.41	1.28	164	–13.53	–12.99	–12.14
7782.5585	5995	19	0.438	–10.77	1.16	167	–10.41	–11.18	–10.44
7789.5451	6024	16	0.202	–12.69	1.34	159	–13.05	–12.80	–13.10
7794.5778	5997	21	0.472	–10.27	1.27	168	–9.92	–10.18	–10.59
7798.5661	5969	23	0.478	–10.34	1.25	165	–10.17	–11.54	–12.36
7802.5420	5995	13	0.482	–10.15	1.35	169	–9.75	–10.73	–10.51
7804.5477	6086	15	0.988	–12.90	1.39	158	–12.77	–13.16	–12.04
7808.6782	6058	20	0.031	–13.09	1.33	158	–14.09	–13.58	–13.96
7810.6837	5993	18	0.537	–10.11	1.23	168	–9.85	–10.06	–10.34
7815.6644	6040	13	0.794	–11.33	1.33	159	–11.43	–10.89	–8.42
7816.7154	6080	16	0.059	–13.19	1.13	164	–13.28	–13.25	–13.90

The effective temperature and radial velocity data for each spectrum along with the pulsational period phases are shown in Table 1.

Figure 1 represents phase curves of the Polaris radial velocity (lower panel) and effective temperature (upper panel) variations between August 2016 and March 2017.

As seen in this Figure, the 2016 data have a lager (within an uncertainty of 1.48 km s^{-1}) amplitude compared to the 2017 data. In case of the data approximations by sinusoidal curves, the mean amplitudes of the radial velocity curves are 3.43 km s^{-1} and 3.31 km s^{-1}, respectively.

The effective temperature variations show no significant changes, and the average values are 6021±18 K and 6024±18 K for the 2016 and 2017 data, respectively. These values are close to 6017 K derived for the 2015 and for the 2001 – 2004 set.

Figure 2 demonstrates the radial velocity amplitude variations in the last ∼125 years. As seen in this Figure, the 2016/2017 data are below that of 2015, but the amplitude growth tendency still remains.

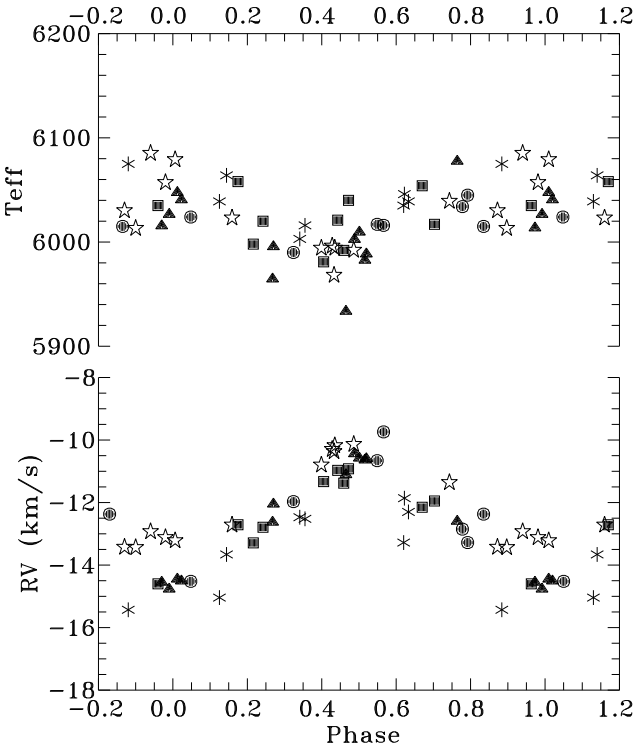

Figure 1: The effective temperature and radial velocity variations of Polaris during its pulsational period. Symbols of the data are: six-pointed stars - August–September 2016, squares - October 2016, triangles – November 2016, circles – December 2016, five-pointed stars – January–March 2017.

3. Summary

1. As seen from the results of our observations, the pulsational period of Polaris shows an abrupt decrease in comparison with the measurements obtained in 2015. This fact is very unusual and needs a careful verification. The last such a rapid pulsational period change took place in 1956 (Turner et al., 2005). Therefore in order to confirm this result, spectroscopic monitoring has to continue to obtain as many radial velocity measurements as possible.

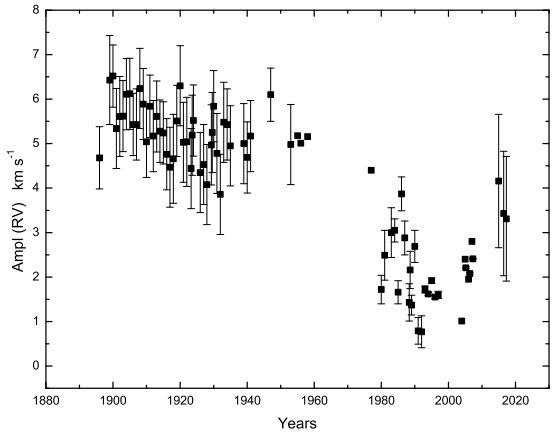

Figure 2: Radial velocity amplitude variations of Polaris over the last ∼125 years.

2. The mean amplitude of the radial velocity in 2016 – 2017 decreased by nearly 0.8 – 0.9 km s^{-1} compared to the 2015 data. Nevertheless, the pulsational amplitude growth tendency still remains.

3. The mean effective temperature of Polaris for this data set averages at 6017 – 6024 K. This value is close to 6015 – 6017 K determined for the set of 2001–2004 and 2015 data (Usenko et al., 2005; Usenko et al., 2016; Usenko et al., 2017).

References

Galazutdinov G.A.: 2007, *http://gazinur.com/DECH-software.html.*

Kovtuykh, V.V.: 2007, *MNRAS* **378**, 617

Lenz P. & Breger M.: 2005, *Commun. Astroseismology*, **146**, 53.

Turner D.G., Savoy J., Derrah J., Sabour M.A., Berdnikov L.N.: 2005, *AJ*, **117**, 207.

Usenko I.A., Miroshnichenko A.S., Klochkova V.G., Yushkin M.V.: 2005, *MNRAS*, **362**, 1219.

Usenko I.A., Kovtyukh V.V., Miroshnichenko A.S., Danford S.: 2016, *Odessa Astron. Publ.*, **29**, 100.

Usenko I.A., Kovtyukh V.V., Miroshnichenko A.S., Danford S.: 2017, *Nauka Innov.*, **13(1)**, 109.

DOI: http://dx.doi.org/10.18524/1810-4215.2017.30.114384

THE CHARACTERISTICS OF ELECTRON-NUCLEAR MODEL IN THE DEGENERATE DWARFS THEORY. EQUATION OF STATE

M.V. Vavrukh, D.V. Dzikovskyi

Department of Astrophysics of Ivan Franko National University of Lviv, Ukraine, *mvavrukh@gmail.com*

ABSTRACT. Within the microscopic theory the ground state energy of spatially homogeneous degenerate relativistic subsystem of electrons in the field of stationary nuclei of l-th sorts with charges $z_1, \ldots, z_l$ was calculated. In the two- and three-particle electron correlations approximation the contributions of Coulomb interactions to the equation of model state at low temperatures was analyzed.

Key words: electron-nuclear model, correlation functions, energy of model at $T = 0K$, equation of state.

PACS 97.20Rp, 97.60Bw

1. Introduction

The theory of internal structure of cold dwarfs was developed by S. Chandrasekhar in the 40-th years of the XX century, and it was based on the equation of state of ideal relativistic electron gas at $T = 0K$ [1, 2]. Generalization of this theory followed in the next decades, when in the works of many authors were investigated effects of such important factors as axial rotation [3, 4], Coulomb interactions [5], incomplete degeneration of electron subsystem [6, 7], effects of magnetic fields [8, 9], effects of general relativity [4, 10], processes of neutronization [11], etc. Interpretation of all the diversity of dwarfs properties obtained from the observations of space observatories [12, 13] requires constructing a general theory, which also takes into account the effects of these factors, among which are competing.

The effect of the interactions which play an important role in determining the structure of dwarfs at different masses and luminosities, and especially for the case of massive cold dwarfs is least studied. Basing on Wigner-Seitz, Thomas-Fermi approximations and nonrelativistic random phase approximation corresponding to the approximate accounting of two-particle electron correlations, E. Salpeter [5] showed, that Coulomb interactions lead to a small decrease of pressure of ideal degenerate relativistic electron gas at $T = 0K$, what is still considered as the basis of S. Chandasekhar's theory [9].

Due to the high density ($\sim 10^5$ g/cm^3) a matter in the internal ranges of degenerate dwarfs has the metal electron structure with completely collectivized electrons, and the Fermi momentum is of the order m_0c. Therefore the electron subsystem is weakly non-ideal, allowing to use the perturbation theory with regard to interactions. We have used the reference system approach, which is renormalized perturbation theory, formulated in terms of the n-particle correlation functions of the ideal as well as the interacting relativistic electron gas [14, 15].

2. The general relations

We consider a spatially homogeneous in the macroscopic sense electrically neutral model, which consists of N_e electrons and nuclei of l-th sorts (N_1 nuclei of charge $z_1, \ldots, N_l$ nuclei of charge z_l) in the volume V in thermodynamic limit $N_e,\ V \to \infty,\ N_e/V = const$ at the temperatures much lower than the temperature of the electron subsystem degeneration. The Hamiltonian of this model is

$$\hat{H} = \hat{H}_0 + \hat{V}_{ee} + \sum_{i=1}^{l} \hat{V}_{en}^{i} + \hat{V}_{nn}, \tag{1}$$

in which

$$\hat{H}_0 = \sum_{\mathbf{k},s} E_k \, a^{+}_{\mathbf{k},s} a_{\mathbf{k},s} \tag{2}$$

is the Hamiltonian of free electrons ($E_k = \{(m_0c^2)^2 + \hbar^2k^2c^2\}^{1/2} - m_0c^2$),

$$\hat{V}_{ee} = (2V)^{-1} \sum_{\mathbf{q}\neq 0} V_q \sum_{\mathbf{k}_1,s_1} \sum_{\mathbf{k}_2,s_2} \times \\ \times a^{+}_{\mathbf{k}_1+\mathbf{q},s_1} a^{+}_{\mathbf{k}_2-\mathbf{q},s_2} a_{\mathbf{k}_2,s_2} a_{\mathbf{k}_1,s_1} \tag{3}$$

is the operator of electron interactions,

$$\hat{V}_{en}^{i} = -V^{-1} z_i \sum_{\mathbf{q}\neq 0} V_q \, S^{(i)}_{-\mathbf{q}} \, \hat{\rho}_{\mathbf{q}},\ \hat{\rho}_{\mathbf{q}} = \sum_{\mathbf{k},s} a^{+}_{\mathbf{k}+\mathbf{q},s} a_{\mathbf{k},s} \tag{4}$$

is the operator of electron interactions with i-th nuclear subsystem,

$$\hat{V}_{nn} = (2V)^{-1} \sum_{\mathbf{q}\neq 0} V_q \sum_{i,j=1}^{l} z_i z_j \{S_{\mathbf{q}}^{(i)} S_{-\mathbf{q}}^{(j)} - N_i \delta_{i,j}\} \quad (5)$$

is the sum of direct nuclear interactions. Here $V_q = 4\pi e^2/q^2$, $S_{\mathbf{q}}^{(i)} = \sum\limits_{j=1}^{N_i} \exp\left[i(\mathbf{q}, \mathbf{R}_j^i)\right]$ is the structure factor of i-th nuclear subsystem, $a_{\mathbf{k},s}^{+}, a_{\mathbf{k},s}$ is the generation and destruction operators of electrons in quantum states with the given vector $\mathbf{k}$ and the spin orientation s, $\mathbf{R}_j^i$ is the radius-vector of j-th nucleus with the charge z_i.

We have used the subsystem of free relativistic electrons as the basis for calculating energetic and structure characteristics of model of interacting degenerate relativistic electron gas. In its turn the interacting electron gas is the basis system for consideration the electron-nuclear interactions. Energy of model with the Hamiltonian (1) is represented as the expansion by the correlation functions of model of interacting electron gas, that is:

$$\begin{aligned} E = E_e &+ \frac{1}{2V} \sum_{\mathbf{q}\neq 0} V_q \sum_{i,j=1}^{l} z_i z_j \{S_{\mathbf{q}}^{(i)} S_{-\mathbf{q}}^{(j)} - N_i \delta_{i,j}\} - \\ &- \sum_{n\geq 2} \{n! V^n\}^{-1} \sum_{i_1,i_2,\cdots,i_n=1}^{l} z_{i_1} z_{i_2} \cdots z_{i_n} \times \\ &\times \sum_{\mathbf{q}_1,\mathbf{q}_1,\cdots,\mathbf{q}_n\neq 0} V_{q_1} \cdots V_{q_n} S_{-\mathbf{q}_1}^{(i_1)} \cdots S_{-\mathbf{q}_n}^{(i_n)} \times \\ &\times \delta_{\mathbf{q}_1+\cdots+\mathbf{q}_n,0}\, \tilde{\mu}_n(\mathbf{q}_1 \cdots \mathbf{q}_n|0). \end{aligned} \quad (6)$$

Here E_e is the ground state energy of basis system of interacting relativistic electron gas, and $\tilde{\mu}_n(\mathbf{q}_1 \cdots \mathbf{q}_n|0)$ is the static limits of n-particle correlation functions of model of interacting electron gas. The modern theory of n-particle statics and dynamics correlation functions of the non-relativistic electron gas is developed in the work [14, 15] and based on the basis approach. One version of this approach is the so-called post RPA, in which the polarization operator is represented as

$$\begin{aligned} M_2(\mathbf{q}, -\mathbf{q}|0) =& \tilde{\mu}_2^0(\mathbf{q}, -\mathbf{q}|0) \Big[1 + \frac{V_q}{V} \times \\ &\times \tilde{\mu}_2^0(\mathbf{q}, -\mathbf{q}|0) G(q)\Big], \end{aligned} \quad (7)$$

where $G(q)$ is the static local field correction function.

This approach can be applied not only for weak non-ideal systems, but also for the systems with intermediate non-ideality [15]. In this approach

$$\mu_2(\mathbf{q}, -\mathbf{q}|0) = M_2(\mathbf{q}, -\mathbf{q}|0) \Big[1 + \frac{V_q}{V} M_2(\mathbf{q}, -\mathbf{q}|0)\Big]^{-1}. \quad (8)$$

Taking into account that the model we consider is non-ideal, for three-particle function we use the approximation RPA, in which

$$\begin{aligned} &\mu_3(\mathbf{q}_1, \mathbf{q}_2, \mathbf{q}_3|0) = \tilde{\mu}_3^0(\mathbf{q}_1, \mathbf{q}_2, \mathbf{q}_3|0) \prod_{i=1}^{3} \varepsilon_{RPA}^{-1}(q_i), \\ &\varepsilon_{RPA}(q) = 1 + \frac{V_q}{V} \tilde{\mu}_2^0(\mathbf{q}, -\mathbf{q}|0). \end{aligned} \quad (9)$$

The functions $\tilde{\mu}_n(\mathbf{q}_1 \cdots \mathbf{q}_n|0)$ are the partial case of dynamic correlation functions $\tilde{\mu}_n(\mathbf{q}_1 \cdots \mathbf{q}_n|\nu_1, \cdots, \nu_n)$, which are the spectral representation of n-particle correlation functions, given in the coordinate space. For example, the binary distribution electron function $F_2(\mathbf{r})$ is connected with the function $\tilde{\mu}_2(\mathbf{q}, -\mathbf{q}|\nu, -\nu)$ by expression

$$\begin{aligned} F_2(\mathbf{r}) =& 1 + [\beta N_e (N_e - 1)]^{-1} \sum_{\nu} \sum_{\mathbf{q}\neq 0} \times \\ &\times \tilde{\mu}_2(\mathbf{q}, -\mathbf{q}|\nu, -\nu) \exp\left[i(\mathbf{q}, \mathbf{r})\right]. \end{aligned} \quad (10)$$

where $\nu = 2\pi n \beta^{-1}$; $n = 0; \pm 1; \pm 2; \cdots$ is the Bose-Matsubara frequency. Therefore the energy of basis system of interacting electron gas it is convenient to calculate by expression

$$E_e = E_0 + (2\beta V)^{-1} \sum_{\nu} \sum_{\mathbf{q}\neq 0} V_q \int_0^1 \tilde{\mu}_2(\mathbf{q}, -\mathbf{q}|\nu, -\nu|\lambda) d\lambda, \quad (11)$$

where $\tilde{\mu}_2(\mathbf{q}, -\mathbf{q}|\nu, -\nu|\lambda)$ is the dynamic two-particle correlation function of auxiliary model of electrons with the potential of interaction λV_q:

$$\begin{aligned} \tilde{\mu}_2(\mathbf{q}, -\mathbf{q}|\nu, -\nu|\lambda) =& M_2(\mathbf{q}, -\mathbf{q}|\nu, -\nu|\lambda) \Big\{1 + \lambda \frac{V_q}{V} \times \\ &\times M_2(\mathbf{q}, -\mathbf{q}|\nu, -\nu|\lambda)\Big]\Big\}^{-1}, \\ M_2(\mathbf{q}, -\mathbf{q}|\nu, -\nu|\lambda) =& \tilde{\mu}_2^0(\mathbf{q}, -\mathbf{q}|\nu, -\nu) \Big[1 + \lambda \frac{V_q}{V} \times \\ &\times \tilde{\mu}_2^0(\mathbf{q}, -\mathbf{q}|\nu, -\nu) G(q, \nu)\Big]. \end{aligned} \quad (12)$$

It has been taken into account, that in the case of weak non-ideality of model the local field correction function does not depend on "coupling constant".

The static and dynamic correlation functions of non-relativistic ideal electron gas are well known. The analytical expression for $\tilde{\mu}_2^0(y, -y)$ was obtained in [16], the functions $\tilde{\mu}_3^0(\mathbf{q}_1, \mathbf{q}_2, -\mathbf{q}_1 - \mathbf{q}_2|0, 0, 0)$ and $\tilde{\mu}_4^0(\mathbf{q}_1, -\mathbf{q}_1, \mathbf{q}_2, -\mathbf{q}_2|0, \cdots, 0)$ were calculated in [17, 19]. The dynamic functions $\tilde{\mu}_3^0(y_1, y_2, -y_1 - y_2)$ and $\tilde{\mu}_4^0(y_1, -y_1, y_2, -y_2)$ were first calculated in [14]. Microscopic theory of the local field correction function, which is based on the summation of infinite series of convergent diagrams and created on the

functions $\tilde{\mu}_2^0(\mathbf{q},-\mathbf{q}|\nu,-\nu)$, $\tilde{\mu}_3^0(\mathbf{q}_1,\mathbf{q}_2,\mathbf{q}_3|\nu_1,\nu_2,\nu_3)$ and $\tilde{\mu}_4^0(\mathbf{q}_1,-\mathbf{q}_1,\mathbf{q}_2,-\mathbf{q}_2|\nu_1,-\nu_1,\nu_2,-\nu_2)$, are developed in the works [14, 20].

Correlation functions of relativistic interacting electron gas also satisfy the expressions (7)-(10), (12). In general they are similar to the relevant functions of non-relativistic model, but they have a significant dependence on the relativistic parameter $x = \hbar k_F (m_0 c)^{-1}$ ($k_F = (3\pi^2 N_e/V)^{1/3}$), and the calculation $\tilde{\mu}_n^0(\mathbf{q}_1,\cdots\mathbf{q}_n|0)$ at $n \geq 3$ is difficult, because the electron spectrum is not a quadratic function of the wave vector. The function $\tilde{\mu}_2^0(\mathbf{q},-\mathbf{q}|0)$ has the analytical representation [22]:

$$\tilde{\mu}_2^0(\mathbf{q},-\mathbf{q}|0) = 2\sum_{\mathbf{k},s} n_{\mathbf{k},s}\{E_{\mathbf{k}+\mathbf{q}} - E_{\mathbf{k}}\}^{-1} =$$

$$= \frac{3N_e}{m_0 c^2 x^2} J_2(q_*,0|x);$$

$$q_* x\, J_2(q_*,0|x) = \frac{2}{9}(R_+ - R_-)\left[1 + \frac{7}{4}x^2 - \frac{q_*^2}{8}\right] +$$

$$+ \frac{5}{72} q_* x (R_+ + R_-) + \frac{q_* x}{12} R_0 + \frac{1}{3} R_0^3 \times$$

$$\times \ln\left|\frac{R_+ - R_0}{R_- - R_0}\right| + \frac{1}{8} q_* \left(1 + \frac{q_*^2}{6}\right)\left\{2\ln|x + R_0| - \right.$$

$$\left. - \ln|(R_+ + x + q_*)(R_- + x - q_*)|\right\} + \frac{1}{6} S_q^3 \times \qquad (13)$$

$$\times \left\{\ln\left|\frac{1 + \frac{1}{2}q_*^2 + \frac{1}{2}x q_* + S_q R_+}{1 + \frac{1}{2}q_*^2 - \frac{1}{2}x q_* + S_q R_-}\right| - \right.$$

$$\left. - \ln\left|\frac{1 + \frac{1}{2}q_* x + S_q R_0}{1 - \frac{1}{2}q_* x + S_q R_0}\right| - 2\ln\left|\frac{x + \frac{1}{2}q_*}{x - \frac{1}{2}q_*}\right|\right\},$$

$$R_0 = (1 + x^2)^{1/2}, \quad S_q = \left(1 + \frac{1}{4}q_*^2\right)^{1/2},$$

$$R_\pm = [1 + (q_* \pm x)^2]^{1/2}, \quad q_* = \frac{|\mathbf{q}|x}{k_F}.$$

The behavior of the dimensionless factor $J_2(q_*,0|x)$ is illustrated in fig. 1. As in the non-relativistic case, the function $J_2(q_*,0)$ has a weak logarithmic peculiarity of the type $\left(x - \frac{1}{2}q_*\right)\ln\left|x - \frac{1}{2}q_*\right|$ in the vicinity to $q_* = 2x$ ($|\mathbf{q}| = 2k_F$) and the asymptotics:

$$\tilde{\mu}_2^0(\mathbf{q},-\mathbf{q}|0) \Rightarrow \begin{cases} \dfrac{3N_e(1+x^2)^{1/2}}{m_0 c^2 x^2} + \cdots & \text{by } q \to 0; \\ \dfrac{2N_e}{m_0 c^2 q_*} + \cdots & \text{by } q \to \infty. \end{cases} \qquad (14)$$

The function $\tilde{\mu}_3^0(\mathbf{q},-\mathbf{q},0|0)$, which is the partial case of the static three-particle function at $\mathbf{q}_2 = -\mathbf{q}_1$, has the simple analytical representation:

$$\tilde{\mu}_3^0(\mathbf{q},-\mathbf{q},0|0) = \frac{3N_e}{(m_0 c^2 x^2)^2} J_3(q,0|x),$$

$$J_3(q,0|x) = \frac{R_0}{\tilde{q}}\left\{\tilde{R}_+ - \tilde{R}_- + R_0 \ln\left|\frac{\tilde{R}_+ - R_0}{\tilde{R}_- - R_0}\right|\right\}, \qquad (15)$$

$$\tilde{R}_\pm = [1 + x^2(1 \pm \tilde{q})^2]^{1/2}, \quad R_0 = (1 + x^2)^{1/2}.$$

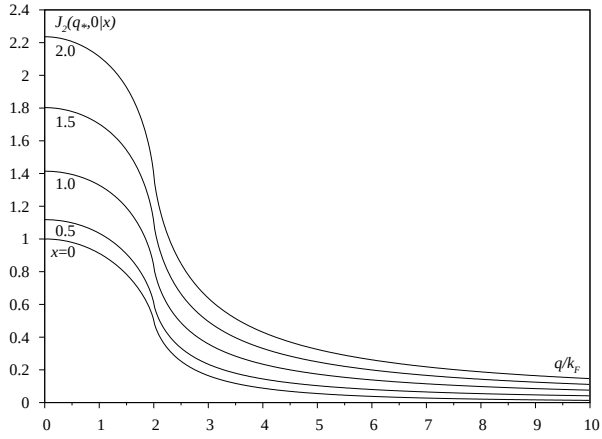

Figure 1: Dependence of the function $J_2(q_*,0|x)$ on the wave vector $\mathbf{q}$ at different values of the relativistic parameter.

In the formula (15) "non-relativistic" scale was used for the wave vector ($\tilde{q} \equiv |\mathbf{q}|/k_F$). In the long-wave limit

$$\lim_{\mathbf{q}\to 0} \tilde{\mu}_3^0(\mathbf{q},-\mathbf{q},0|0) \Rightarrow \frac{3N_e}{(m_0 c^2 x^2)^2}(1 + 2x^2). \qquad (16)$$

Dependence of dimensionless factor $J_3(q,0|x)$ on the wave vector and the relativistic parameter is illustrated in fig. 2. As in non-relativistic case, the function (15) has a logarithmic peculiarity at $q = 2k_F$.

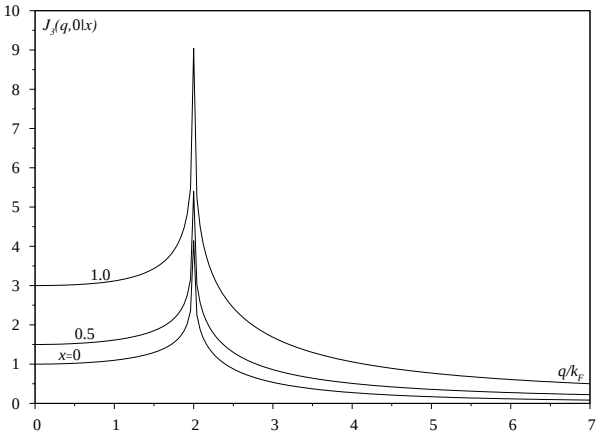

Figure 2: Dependence of the static function $J_3(q,0|x)$ on the wave vector $\mathbf{q}$ at different values of the relativistic parameter.

The formulae (13)-(15), and the fig. 1, 2 reveal the general property of correlation functions $\tilde{\mu}_n^0(y_1,\cdots,y_n)$ – steep decrease in the region of wave vectors ($|\mathbf{q}_i| > 2k_F$), providing convergence of integrals in the expand (6). In general for a rough estimate convergence of series (6) we consider a chemically homogeneous model ($z_i = z$, $z\sum_{i=1}^{l} N_i = N_n$), constrain

the integration for each independent vector $\mathbf{q}_i$ of the area $|\mathbf{q}_i| < 2k_F$, neglect screening interactions, replace the product of structural factors $S_{\mathbf{q}_1}, S_{\mathbf{q}_2} \cdots S_{\mathbf{q}_n}$ with N_n, and the functions $\tilde{\mu}_n^0(\mathbf{q}_1, \cdots \mathbf{q}_n|0)$ we replace with $3N_e(m_0c^2x^2)^{1-n}(1+x^2)^{\frac{1}{2}(n-1)}$, which approximately corresponds to the long-wave asymptotic. For the magnitude of n-th member of series (6) we obtain the estimate

$$N_e m_o c^2 z^{n-1} \alpha_0^n x^{2-n} (1+x^2)^{\frac{1}{2}(n-1)}, \tag{17}$$

where $\alpha_0 = e^2/\hbar c$ is the fine structure constant. Hence, the series (6) is expansion for dimensionless parameter $z\alpha_0$, which varies from 0,014 (helium dwarf) to 0,19 (iron dwarf). For the typical dwarfs, mainly consisting of nitrogen and oxygen, $z\alpha_0 \approx 0{,}1$. That is expansion parameter is a small value, which makes it possible to restrict ourselves to consideration of two- and three-electron correlations (we note, that correlation energy of basis system has the order α_0^2). Moreover, the three-electron function

$$\begin{aligned}
&\tilde{\mu}_3^0(\mathbf{q}_1, \mathbf{q}_2, \mathbf{q}_3|0) = \delta_{\mathbf{q}_1+\mathbf{q}_2+\mathbf{q}_3,0}\{\gamma_3(\mathbf{q}_1, -\mathbf{q}_2) + \\
&+ \gamma_3(\mathbf{q}_2, -\mathbf{q}_3) + \gamma_3(\mathbf{q}_3, -\mathbf{q}_1)\}, \\
&\gamma_3(\mathbf{q}_i, \mathbf{q}_j) = 2\sum_{\mathbf{k},s} n_{\mathbf{k},s}(\tilde{E}_{\mathbf{k}} + \tilde{E}_{\mathbf{k}+\mathbf{q}_i})(\tilde{E}_{\mathbf{k}} + \tilde{E}_{\mathbf{k}+\mathbf{q}_j}) \times \\
&\times (\hbar c)^{-4}\{2(\mathbf{k}, \mathbf{q}_i) + q_i^2\}^{-1}\{2(\mathbf{k}, \mathbf{q}_j) + q_j^2\}^{-1}; \\
&\tilde{E}_{\mathbf{k}} = E_{\mathbf{k}} + m_0c^2
\end{aligned} \tag{18}$$

can be calculated approximately, performing the substitution

$$\begin{aligned}
&\tilde{E}_{\mathbf{k}} + \tilde{E}_{\mathbf{k}+\mathbf{q}_i} \Rightarrow m_0c^2 C(\tilde{q}_i|\tilde{k}), \\
&C(\tilde{q}_i|\tilde{k}) = \{1 + x^2(\tilde{k}^2 + \tilde{q}_i^2)\}^{1/2} + \{1 + x^2\tilde{k}^2\}^{1/2},
\end{aligned} \tag{19}$$

which is asymptotically correct both at small and at large q_i. According to the Feynman identity [21]

$$\begin{aligned}
&\{2(\mathbf{k}, \mathbf{q}_i) + q_i^2\}^{-1}\{2(\mathbf{k}, \mathbf{q}_j) + q_j^2\}^{-1} = \\
&= \int_0^1 d\lambda\, F^{-2}(\mathbf{q}_i, \mathbf{q}_j|\mathbf{k}), \\
&F(\mathbf{q}_i, \mathbf{q}_j|\mathbf{k}) = \Omega_{ij} + 2(\mathbf{k}, \boldsymbol{\rho}_{ij}), \\
&\Omega_{ij} \equiv q_j^2 + \lambda(q_i^2 - q_j^2); \quad \boldsymbol{\rho}_{ij} = \lambda\mathbf{q}_i + (1-\lambda)\mathbf{q}_j.
\end{aligned} \tag{20}$$

Passing from the sum by vector $\mathbf{k}$ to integral, we use dimensionless variable $\tilde{k} = |\mathbf{k}|/k_F$, $\tilde{q}_i = |\mathbf{q}_i|/k_F$, and the spherical coordinate system, the Oz of which axis coincides with the vector $\boldsymbol{\rho}_{ij}$, we perform integration over the angular variables, reducing $\gamma_3(\mathbf{q}_i, \mathbf{q}_j)$ to one-dimensional integral:

$$\begin{aligned}
&\gamma_3(\mathbf{q}_i, \mathbf{q}_j) = \frac{3N_e}{4(m_0c^2x^2)^2}\int_0^1 dk\, C(q_i|k)\, C(q_j|k)\, f_{ij}(k), \\
&f_{ij}(k) = \frac{1}{\sqrt{-\delta(k)}}\ln\left|\frac{R_{ij} + (-\delta(k))^{-1/2}}{R_{ij} - (-\delta(k))^{-1/2}}\right| \text{ by } k < q_R; \\
&f_{ij}(k) = \frac{2}{\sqrt{\delta(k)}}\arctan\{\delta^{1/2}(k)R_{ij}^{-1}\} \qquad \text{by } k > q_R.
\end{aligned} \tag{21}$$

Here the following notations are was introduced:

$$\begin{aligned}
&R_{ij} \equiv R_{ij}(k) = 2(\mathbf{q}_i, \mathbf{q}_j) - \frac{q_i^2 q_j^2}{2k^2}; \\
&\delta(k) = \delta_{ij}(k) = \left(1 - \frac{q_R^2}{k^2}\right)\cdot 4q_i^2q_j^2(1 - t_{ij}^2); \\
&q_R = (\mathbf{q}_i - \mathbf{q}_j)^2\{4(1 - t_{ij}^2)\}^{-1};
\end{aligned} \tag{22}$$

$\delta(k)$ is the invariant of problem ($\delta_{12}(k) = \delta_{23}(k) = \delta_{31}(k)$), q_R is the radius of the circle, circumscribing the triangle constructed on the vectors $\mathbf{q}_1, \mathbf{q}_2, -\mathbf{q}_1 - \mathbf{q}_2$; t_{ij} is a cosine of the angle between the vectors $\mathbf{q}_i, \mathbf{q}_j$. In the formulae (21), (22) the variables k and q_i, q_j are dimensionless (in unit k_F). We use numerical integration over the variable k in the formula (21).

Integration over the angular variables of the vector $\mathbf{k}$ in the expression for the dynamic two-particle correlation function

$$\tilde{\mu}_2^0(\mathbf{q}, -\mathbf{q}|\nu, -\nu) = 2\sum_{\mathbf{k},s} n_{\mathbf{k},s}\frac{E_{\mathbf{k}+\mathbf{q}} - E_{\mathbf{k}}}{(E_{\mathbf{k}+\mathbf{q}} - E_{\mathbf{k}})^2 + \nu^2} \tag{23}$$

allows us to present it in the form of one-dimensionless integral:

$$\begin{aligned}
&\tilde{\mu}_2^0(\mathbf{q}, -\mathbf{q}|\nu, -\nu) = \frac{3N_e}{m_0c^2x^2}J_2(q_*, \tilde{\nu}|x), \\
&J_2(q_*, \tilde{\nu}|x) = (2xq_*)^{-1}\sum_s \int_0^\infty dk_* k_* n_{k_*,s} A(k_*|q_*, \tilde{\nu}), \\
&A(k_*|q_*, \tilde{\nu}) = \sum_{\sigma=\pm1}\sigma\{[1 + (k_* + \sigma q_*)^2]^{1/2} - \\
&- \tilde{\nu}\arctan[\tilde{\nu}^{-1}\eta_\sigma(k_*, q_*)] + \frac{1}{2}(1 + k_*^2)^{1/2} \times \\
&\times \ln[\tilde{\nu}^2 + \eta_\sigma^2(k_*, q_*)]\}, \\
&\eta_\sigma(k_*, q_*) = [1 + (k_* + \sigma q_*)^2]^{1/2} - [1 + k_*^2]^{1/2}.
\end{aligned} \tag{24}$$

Here appear the dimensionless variables

$$k_* = \frac{x|\mathbf{k}|}{k_F},\ q_* = \frac{x|\mathbf{q}|}{k_F},\ \tilde{\nu} = \frac{\nu}{m_0c^2}. \tag{25}$$

Fig. 3 illustrates the dependence $J_2(q_*, \nu|x)$ on the wave vector and the relativistic parameter.

It is well known from the non-relativistic electron fluid theory [14], that the dynamic local field correction

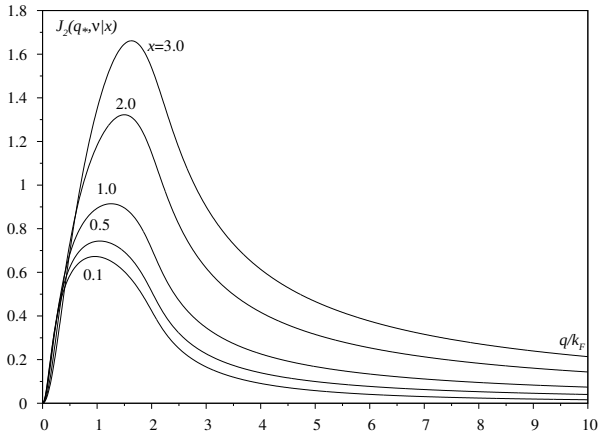

Figure 3: Dependence of the dynamic two-particle function $J_2(q_*,\nu|x)$ on the wave vector $\mathbf{q}$ at fixed values of the dimensionless frequency($\nu = 0.15m_0c^2x^2$) and different values of the relativistic parameter.

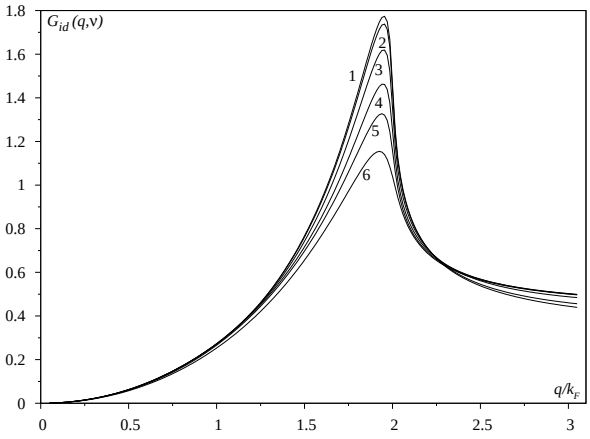

Figure 4: Dependence of the loclal field correction function $G_{id}(q,\nu)$ on the wave vector $\mathbf{q}$ and the relativistic parameter at the frequency $\nu = 0.01m_0c^2x^2$ (curve 1 – x=0.05; 2 – x=0.2; 3 – x=0.5; 4 – x=1.0; 5 – x=2.0; 6 – x=5.0).

function in the weakly non-ideal model is a universal function of the variable $y = (\mathbf{q},\nu)$, it does not depend on any parameters, and corresponds to the approximation

$$\begin{aligned} G_{id}(y) &= -(2\beta V_q)^{-1}\{\tilde{\mu}_2^0(y,-y)\}^{-2}\times \\ &\times \sum_{\mathbf{q}_1;\nu_1} V_{q_1}\tilde{\mu}_4^0(y,-y,y_1,-y_1), \\ \mu_4^0(y,-y,y_1,-y_1) &= \beta^{-1}\sum_{\mathbf{k},s}\sum_{\nu_*} G_{\mathbf{k},s}(\nu_*)\times \\ &\times G_{\mathbf{k}-\mathbf{q},s}(\nu_*-\nu)\sum_{\sigma=\pm1} G_{\mathbf{k}-\sigma\mathbf{q}_1,s}(\nu_*-\sigma\nu_1)\times \\ &\times \{2G_{\mathbf{k},s}(\nu_*) + G_{\mathbf{k}+\mathbf{q}+\sigma\mathbf{q}_1,s}(\nu_*+\nu+\sigma\nu_1)\}, \end{aligned} \tag{26}$$

where $G_{\mathbf{k},s} = \{i\nu_* - E_{\mathbf{k}} + \mu\}^{-1}$ is the spectral representation of the one-electron Green's function of the ideal model, $\nu_* = \pi\beta^{-1}(2n+1)$ is its chemical potential, $\nu_* = \pi\beta^{-1}(2n+1)$ is the Fermi-Matsubara frequency ($n = 0;\pm1;\pm2;\cdots$). After summarizing over the frequencies ν_* and $\nu_* \pm \sigma\nu_1$ according to the rule

$$\beta^{-1}\sum_{\nu_*} G_{\mathbf{k},s}(\nu_*) = n_{\mathbf{k},s} = \{1+\exp[\beta(E_k-\mu)]\}^{-1}, \tag{27}$$

we get the next representation:

$$\begin{aligned} G_{id}(y) &= -V_q^{-1}\{\tilde{\mu}_2^0(y,-y)\}^{-2}\sum_s\sum_{\mathbf{k}_1,\mathbf{k}_2} n_{\mathbf{k}_1,s}n_{\mathbf{k}_2,s}\times \\ &\times\big[V(\mathbf{k}_1-\mathbf{k}_2)f^-_{\mathbf{k}_1,\mathbf{k}_2}(\mathbf{q},\nu) - V(\mathbf{k}_1+\mathbf{k}_2+\mathbf{q})f^+_{\mathbf{k}_1,\mathbf{k}_2}(\mathbf{q},\nu)\big], \end{aligned}$$

$$\begin{aligned} f^{\mp}_{\mathbf{k}_1,\mathbf{k}_2}(\mathbf{q},\nu) &= Re\{[i\nu + E_{\mathbf{k}_1} - E_{\mathbf{k}_1+\mathbf{q}}]^{-1}\mp \\ &\mp[\pm i\nu + E_{\mathbf{k}_2} - E_{\mathbf{k}_2+\mathbf{q}}]^{-1}\}^2. \end{aligned} \tag{28}$$

In the work [22] were done numerical calculations in this approximation of the static the dynamic local field correction functions for the interacting relativistic electron gas. The asymptotics of the function at small and large values of the wave number $|\mathbf{q}|$ matches the asymptotics of corrections of the non-relativistic theory. The deviation of these functions is observed near the maximum and depends on the value of the relativistic parameter, as is shown in fig. 4 (the limit $G_{id}(q,\nu)$ at $x \to 0$ corresponds to the non-relativistic correction).

3. Ground state energy of a model

For the calculation of the interacting electron gas energy by formulae (11), (12) we should consider, that $G_{id}(q,\nu)$ does not depend on the "coupling constant" λ. From the integral term of the formula (11) it is convenient to extract the contribution of first-order perturbation theory

$$\begin{aligned} E_{HF}(x) &= -(2\beta V)^{-1}\sum_{\mathbf{q}\neq0} V_q\sum_{\nu}\tilde{\mu}_2^0(\mathbf{q},-\mathbf{q}|\nu,-\nu) = \\ &= -(2V)^{-1}\sum_{\mathbf{q}\neq0} V_q\sum_{\mathbf{k},s} n_{\mathbf{k}+\mathbf{q}/2,s}n_{\mathbf{k}-\mathbf{q}/2,s}, \end{aligned} \tag{29}$$

that allows to present E_e in a traditional form

$$E_e = E_0(x) + E_{HF}(x) + E_{corr}(x), \tag{30}$$

where

$$E_{corr}(x) = Nmc^2\alpha_0^2\left\{\frac{1}{\alpha_0^2}\frac{3}{4\pi x^3}\right\}\int\limits_0^\infty d\nu_* \int\limits_0^\infty dq_* q_*^2 \times$$
$$\times\left\{\frac{1}{2}\ln[1+L_0(y)(1+G(y)L_0(y))] - L_0(y)\right\} +$$
$$+\begin{cases} \dfrac{1}{2\sqrt{-\Delta}}\ln\dfrac{1+\frac{1}{2}L_0(y)(1+\sqrt{-\Delta})}{1+\frac{1}{2}L_0(y)(1-\sqrt{-\Delta})} & \text{by } \Delta<0 \\ \dfrac{1}{\sqrt{\Delta}}\arctan\dfrac{\frac{1}{2}L_0(y)\sqrt{\Delta}}{1+\frac{1}{2}L_0(y)} & \text{by } \Delta>0 \\ \dfrac{2G(y)L_0(y)}{1+2G(y)L_0(y)} & \text{by } \Delta=0, \end{cases} \quad (31)$$
$$\Delta\equiv\Delta(y) = 4G(y)-1, \quad L_0(y) = \frac{4\alpha_0 x}{\pi q_*^2}J_2(q_*,\nu_*|x).$$

is the so-called correlation energy. In the units m_0c^2

$$E_e = N_e m_0 c^2\left\{\varepsilon_0(x) - \frac{3}{4\pi}\alpha_0 x + \alpha_0^2\,\varepsilon_c(x)\right\}. \quad (32)$$

Here

$$\varepsilon_0(x) = (2x)^{-3}\big\{3x(1+x^2)^{1/2}(1+2x^2) - 8x^3 - \\ -3\ln\left[x+(1+x^2)^{1/2}\right]\big\} \quad (33)$$

is the contribution of an ideal system per one electron, $-3\alpha_0 x(4\pi)^{-1}$ is the contribution of interactions in the Hartree-Fock approximation, $\alpha_0^2\varepsilon_c(x)$ is the correlation energy. According to the results of numerical calculations $\varepsilon_c(x)$ can be approximated by the following expression:

$$\varepsilon_c(x) = -b_0\int\limits_0^x dt\,\frac{(b_1 a + t^{1/2})}{t^{3/2}+tb_1 a + b_2 t^{1/2}a^2 + b_3 a^3}\times \\ \times\frac{1+a_1 t + a_2 t}{1+td_0}, \quad (34)$$
$$a = (\alpha_0\eta)^{1/2};\ a_1 = 1{,}21954;\ a_2 = 1{,}33205;$$
$$d_0 = 1{,}18934;\ b_0 = 0{,}0621814;\ b_1 = 9{,}81379;$$
$$b_2 = 2{,}82214;\ b_3 = 0{,}73701.$$

At $a_1 = a_2 = d_0 = 0$ this expression matches the approximation [23] of the results of ground state energy calculation of non-relativistic electron fluid model $\varepsilon_c^{MC}(x)$ obtained using the Monte-Carlo method [24]. In the region $x \le 1$ the expression (34) is near to $\varepsilon_c^{MC}(x)$, and the deviation $\varepsilon_c(x)$ from $\varepsilon_c^{MC}(x)$ in $x > 1$ is caused by different asymptotics of these functions: $\varepsilon_c^{MC}(x) \to -b_0\ln x + \cdots$ by $x \gg 1$.

In order to calculate the contributions of electron-nuclear interactions in the products of structure factors in the formula (6) we have selected one-particle and two-particle sums by the coordinates of nuclei ignoring the three-nuclear effective interactions. In this approach

$$E \simeq E_e + E_{pol} + E_{conf}, \quad (35)$$

where E_{pol} is the polarization energy of electron fluid by nuclei, it does not depend on the structure of the nuclear subsystem,

$$E_{pol} = E_{pol}^{(2)} + E_{pol}^{(3)},$$
$$E_{pol}^{(2)} = -\frac{1}{2!}\sum_{i=1}^{l} z_i^2 N_i V^{-2}\sum_{\mathbf{q}} V_q^2\,\tilde{\mu}_2(\mathbf{q},-\mathbf{q}|0), \quad (36)$$
$$E_{pol}^{(3)} = -\frac{1}{3!}\sum_{i=1}^{l} z_i^3 N_i V^{-3}\sum_{\mathbf{q}_1,\mathbf{q}_2} V_{q_1}\times \\ \times V_{q_2}V_{-q_1-q_2}\,\tilde{\mu}_3(\mathbf{q}_1,\mathbf{q}_2,-\mathbf{q}_1-\mathbf{q}_2|0).$$

The configuration energy is determined by the structure of nuclear subsystem, and expressed through the effective two-particle potential of interactions of nuclei, which is formed by two- and three-electron correlations:

$$E_{conf} = \frac{1}{2!}\sum_{i=1}^{l}\frac{z_i^2}{V}\sum_{\mathbf{q}} V_q\Big\{1-\frac{V_q}{V}\,\tilde{\mu}_2(\mathbf{q},-\mathbf{q}|0) - \\ -\frac{z_i}{V^2}\sum_{\mathbf{q}_1} V_{q_1}V_{-q-q_1}\tilde{\mu}_3(\mathbf{q},\mathbf{q}_1,-\mathbf{q}-\mathbf{q}_1|0)\Big\}S_2^{(i)}(\mathbf{q},-\mathbf{q}) + \\ +\frac{1}{2!}\sum_{i\ne j=1}^{l}\frac{z_i z_j}{V}\sum_{\mathbf{q}} V_q\Big\{1-\frac{V_q}{V}\,\tilde{\mu}_2(\mathbf{q},-\mathbf{q}|0) - \frac{1}{2V^2}\times \quad (37) \\ \times(z_i+z_j)\sum_{\mathbf{q}_1} V_{q_1}V_{-q-q_1}\,\tilde{\mu}_3(\mathbf{q},\mathbf{q}_1,-\mathbf{q}-\mathbf{q}_1|0)\Big\}S_{\mathbf{q}}^{(i)}S_{-\mathbf{q}}^{(j)},$$
$$S_2^{(i)}(\mathbf{q},-\mathbf{q}) = \sum_{j_1\ne j_2=1}^{N_i}\exp\big\{i(\mathbf{q},\mathbf{R}_{j_1}-\mathbf{R}_{j_2})\big\}.$$

Let us rewrite the component $E_{pol}^{(2)}$, calculated in the local field approximation, in the form

$$E_{pol}^{(2)} = N_e m_0 c^2\frac{\langle z^2\rangle}{\langle z\rangle}\alpha_0^{3/2}\varepsilon_{pol}^{(2)}(x), \quad (38)$$

where the dimensionless function $\varepsilon_{pol}^{(2)}(x)$ is of the same order as $\varepsilon_c(x)$, and $\langle z^n\rangle = \left\{\sum\limits_{i=1}^{l} N_i\right\}^{-1}\sum\limits_{i=1}^{l} z_i^n N_i$. The function $\varepsilon_{pol}^{(2)}(x)$ can be approximated as

$$\varepsilon_{pol}^{(2)}(x) = -\int\limits_0^x\frac{c_0+c_1 t+c_2 t^2+c_3 t^3}{1+d_1 t+d_2 t^2+d_3 t^3}\,dt; \\ c_0 = 4{,}06151;\ c_1 = 32{,}6118;\ c_2 = -43{,}6587; \quad (39) \\ c_3 = 104{,}13;\ d_1 = 73{,}8252;\ d_2 = -67{,}1028; \\ d_3 = 189{,}781.$$

As is shown in fig. 5, $\varepsilon^{(2)}_{pol}(x)$ has the linear asymptotics at $x \gg 1$, as well as $\varepsilon_c(x)$. However, the polarization energy $E^{(2)}_{pol}$ exceeds the correlation energy of basis system by about $\langle z\rangle\alpha_0^{-1/2} \approx 10\langle z\rangle$ times, and for $\langle z\rangle \sim 10$ it is comparable with E_{HF}.

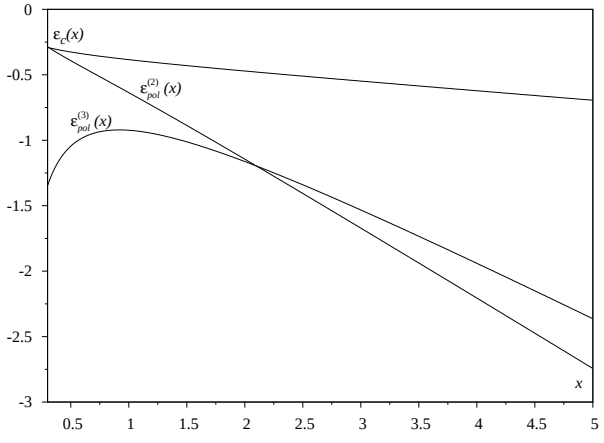

Figure 5: Dependence of functions $\varepsilon^{(2)}_{pol}(x)$, $10\cdot\varepsilon^{(3)}_{pol}(x)$ and $\varepsilon_c(x)$ on the relativistic parameter.

The contribution of three-particle correlations in the polarization energy is represented in the form

$$E^{(3)}_{pol} = N_e m_0 c^2 \frac{\langle z^3\rangle}{\langle z\rangle}\alpha_0^{5/2}\varepsilon^{(3)}_{pol}(x). \tag{40}$$

In the region $x > 1$ the ratio $\varepsilon^{(3)}_{pol}(x) \approx 0{,}1\varepsilon^{(2)}_{pol}(x)$ is satisfied. At sufficiently large values of nuclei charges $E^{(3)}_{pol}$ is not less than the correlation energy of basis system: at $\langle z\rangle \geq 6$ the contribution $E^{(3)}_{pol}$ is close to the correlation energy, at $\langle z\rangle \geq 12$ it exceeds the correlation energy by 5 times, and at $\langle z\rangle = 26$ – more than by 20 times. The result of numerical calculation of $\varepsilon^{(3)}_{pol}(x)$ is approximated by the expression

$$\begin{aligned}
&\varepsilon^{(3)}_{pol}(x) = -ax - c_0\int\limits_x^\infty \frac{1 + c_1/t + c_2 t}{1 + d_1 t + d_2 t^2 + d_3 t^3}\,dt,\\
&a = 0{,}0450;\ c_0 = 0{,}12607;\ c_1 = -0.93695;\\
&c_2 = 78{,}8552;\ d_1 = -23{,}2602;\ d_2 = 114{,}5030;\\
&d_3 = 164{,}060.
\end{aligned} \tag{41}$$

From the formulae (38), (40) it follows, that $E^{(3)}_{pol}/E^{(2)}_{pol} \sim 0{,}1z\alpha_0$, and it determines the order of three-electron correlations contribution function.

We have calculated the configuration energy in coordinate representation by introducing the effective two-nuclear potentials. In the two-particle correlations approximation they are determined by the expressions

$$\begin{aligned}
&V_2^{i_1,i_2}(\mathbf{R}^{(i_1)}_{j_1} - \mathbf{R}^{(i_2)}_{j_2}) = V^{-1}\sum_{\mathbf{q}} V_2(q)\times\\
&\times\exp\left\{i(\mathbf{q}, \mathbf{R}^{(i_1)}_{j_1} - \mathbf{R}^{(i_2)}_{j_2})\right\},\\
&V_2(q) = V_q\left\{1 - \frac{V_q}{V}\tilde{\mu}_2(\mathbf{q}, -\mathbf{q})\right\}.
\end{aligned} \tag{42}$$

In the formula (42) the sum of the vector $\mathbf{q}$ includes a component with $\mathbf{q} = 0$. We have done our calculation in the frame of model with two-sorts of nuclei. Therefore

$$\begin{aligned}
&E^{(2)}_{conf} = \frac{1}{V}\sum_{\mathbf{q}\neq 0} V_2(q)\left\{\frac{1}{2}\sum_{i=1,2} S^{(i)}_2(\mathbf{q}, -\mathbf{q}) z_i^2 + z_1 z_2\times\right.\\
&\left.\times S^{(1)}_{\mathbf{q}} S^{(2)}_{-\mathbf{q}}\right\} = \frac{1}{2}\sum_{i=1,2} z_i^2 \sum_{j_1\neq j_2=1} V_2(\mathbf{R}^{(i)}_{j_1} - \mathbf{R}^{(i)}_{j_2}) + z_1 z_2\times\\
&\times\sum_{j_1=1}^{N_1}\sum_{j_2=1}^{N_2} V_2(\mathbf{R}^{(1)}_{j_1} - \mathbf{R}^{(2)}_{j_2}) - \frac{1}{2}N_e^2\lim_{\mathbf{q}\to 0}\left\{V^{-1}V_2(q)\right\}.
\end{aligned} \tag{43}$$

To simplify the calculation of the lattice sum we adopt a simple model of nuclei distribution in the lattice, namely

$$\mathcal{N}^{(i)}_j = \mathcal{N}_j\left\{\sum_{i=1}^{l} N_i\right\}^{-1} N_i, \tag{44}$$

where $\mathcal{N}_j$ is the number of all knots on the j-th coordination sphere, and $\mathcal{N}^{(i)}_j$ is the number of the knots, occupied by nuclei with charge z_i. In this model

$$\begin{aligned}
&E^{(2)}_{conf} = \frac{N_e}{2}\langle z\rangle\sum_{j\geq 1}\mathcal{N}_j V_2(R_j) -\\
&-\frac{N_e m_0 c^2}{6}\left\{\frac{x^2}{(1+x^2)^{1/2}} - \frac{x\alpha_0}{\pi}\right\}
\end{aligned} \tag{45}$$

where R_j is the radius of the j-th coordination sphere.

The effective two-particle potential is screened, and at small and medium distances between nuclei it is close to the expression

$$V(R) = \frac{e^2}{R}\exp\{-R/R_0\}, \tag{46}$$

and the screened radius

$$R_0 = \frac{\sqrt{\pi}}{2}\alpha_0^{1/2} a_B\{x^{1/2}(1+x^2)^{1/4}\}^{-1} \tag{47}$$

has the order $0{,}1a_B$ (where $a_B = \hbar^2/m_0 e^2$ is the Bohr radius). At the large distances $V_2(R)$ oscillates, but with small amplitude,

$$V_2(R) \approx \frac{e^2}{a_B}\left(\frac{R_0}{2xR}\right)^3\cos(2xR/R_0). \tag{48}$$

The configuration energy for the simple cubic lattice of nuclei is calculated numerically and can be represented as

$$E^{(2)}_{conf} = N_e m_0 c^2 \langle z\rangle^{2/3} \alpha_0 \varepsilon^{(2)}_L(x|\langle z\rangle), \tag{49}$$

approximating dimensionless factor by expression

$$\varepsilon^{(2)}_L(x|\langle z\rangle) = -\int\limits_0^x \frac{a_1 + t a_2 + t^2 a_3}{1 + t a_4 + t^2 a_5 + t^3 a_6} t\, dt, \tag{50}$$

where all the coefficients $a_1, \cdots a_6$ are the functions of $\langle z\rangle$, that is

$$a_i(\langle z\rangle) = \frac{a_{i_0} + \langle z\rangle a_{i_1} + \langle z\rangle^2 a_{i_2}}{a_{i_3} + \langle z\rangle a_{i_4} + \langle z\rangle^2 a_{i_5}}. \tag{51}$$

Similar to the formula (42) we have calculated the correction to the effective two-nuclear potential by the three-electron correlations

$$V^{(3)}_2(R) = -V^3 \sum_{\mathbf{q}} V_q \sum_{\mathbf{q_1}} V_{q_1} V_{-q-q_1} \times \\ \times \tilde{\mu}_3(\mathbf{q}, \mathbf{q}_1, -\mathbf{q} - \mathbf{q}_1|0) \exp\{i(\mathbf{q}, \mathbf{R})\}, \tag{52}$$

where the sum over the vector $\mathbf{q}$ includes the compo-

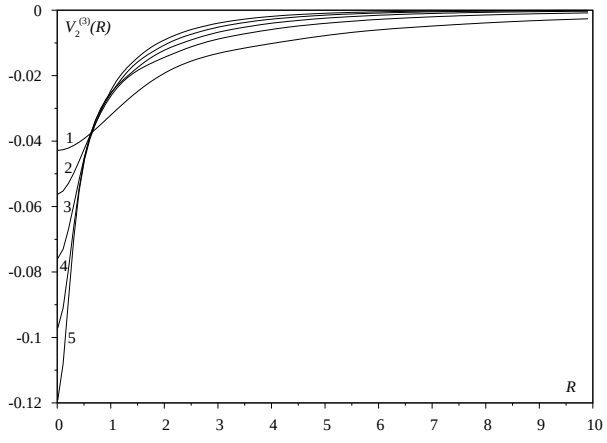

Figure 6: The effective potential of interactions $V^{(3)}_2(R)$ at different values of the relativistic parameter (curve 1 – $x = 1.0$, 2 – $x = 2.0$, 3 – $x = 3.0$, 4 – $x = 4.0$, 5 – $x = 5.0$).

nent $\mathbf{q} = 0$. As shown in fig. 6, $V^{(3)}_2(R)$ is the weak attracting potential of the type of quantum package screening potential, which is close to the expression

$$V^{(3)}_2(R) = -\frac{e^2}{R}\alpha_0^2\, A(x) \left\{1 - \exp\left[-\frac{R}{R_0}\gamma(x)\right]\right\} \times \\ \times \exp\{-R/R_0\}. \tag{53}$$

Contribution to the configuration energy of model by the three-particle correlations in the model (44) takes the form, similar to the formula (45):

$$E^{(3)}_{conf} = \frac{1}{2} N_e \langle z^2\rangle \sum_{j\geq 1} \mathcal{N}_j V^{(3)}_2(R_j) + \\ + \frac{4}{3\pi^2} N_e \alpha_0^2 \langle z\rangle m_0 c^2 (1 + x^2)^{-1/2} I_2(x), \tag{54}$$

$$I_2(x) = \int\limits_0^\infty \frac{dq}{q^2 \varepsilon^2(q)} J_3(q);\ J_3(q) = \frac{(m_0 c^2 x^2)^2}{3N_e} \tilde{\mu}^0_3(\mathbf{q}, -\mathbf{q}, 0|0);$$

This contribution is calculated for the simple cubic lattice of nuclei and represented

$$E^{(3)}_{conf} = N_e m_0 c^2 \alpha_0^2 \langle z^2\rangle \varepsilon^{(3)}_L(x|\langle z\rangle). \tag{55}$$

At sufficiently large nuclei charges $\langle z\rangle$ and $x \geq 2$ the function $\varepsilon^{(3)}_L(x|\langle z\rangle) \sim 0{,}1\varepsilon^{(2)}_L(x|\langle z\rangle)$, but it has a positive sign. It is approximated by the expression

$$\varepsilon^{(3)}_L(x|\langle z\rangle) = -a + xb - \int\limits_x^\infty \frac{c_0 + \frac{c_1}{y} + c_2 y + c_3 y^2}{1 + a_1 y + a_2 y^2 + a_3 y^3}\, dy. \tag{56}$$

4. Equation of state of model at $T = 0K$

For the well known dependence of model energy on the relativistic parameter we calculate the equation of state of cold degenerate matter using the expression

$$P(x) = \frac{dE}{dV} = \frac{x^4}{N_e}\left(\frac{m_0 c}{\hbar}\right)^3 (3\pi^2)^{-1} \frac{dE}{dx}. \tag{57}$$

Within accepted approximation in case of two-sorts of nuclei

$$P(x) = \frac{\pi m_0^4 c^5}{3h^3}\{\mathcal{F}(x) + f_2(x) + f_3(x)\}. \tag{58}$$

Here

$$\mathcal{F}(x) = x(2x^2 - 3)(1 + x^2)^{1/2} + 3\ln\left[x + (1 + x^2)^{1/2}\right] \tag{59}$$

is the contribution of the ideal degenerate relativistic spatially homogeneous electron gas;

$$f_2(x) = -2\alpha_0 x^4 \left\{\frac{1}{\pi} - \frac{4}{3}\frac{d}{dx}\left(\langle z\rangle^{2/3}\varepsilon^{(2)}_L(x|\langle z\rangle) + \right.\right. \\ \left.\left. + \frac{\langle z^2\rangle}{\langle z\rangle}\alpha_0^{1/2}\varepsilon^{(2)}_{pol}(x) + \alpha_0\varepsilon_c(x)\right)\right\} \tag{60}$$

is the contribution of Coulomb interactions in the two-electron correlations approximation;

$$f_3(x) = 8\alpha_0^2 x^4 \frac{d}{dx}\left\{\langle z^2\rangle\varepsilon^{(3)}_L(x|\langle z\rangle) + \frac{\langle z^3\rangle}{\langle z\rangle}\alpha_0^{1/2}\varepsilon^{(3)}_{pol}(x)\right\} \tag{61}$$

Table 1: Dependence of functions $\mathcal{F}(x)\cdot x^{-4}$, $f_2(x)\cdot x^{-4}$ and $f_3(x)\cdot x^{-4}$ on the relativistic parameter x according to the formulae (59), (60), (61).

x	$\mathcal{F}(x)\cdot x^{-4}$	$f_2(x)\cdot x^{-4}$				$f_3(x)\cdot x^{-4}$			
		$z=2$	$z=6$	$z_1=7;\ z_2=8$	$z=12$	$z=2$	$z=6$	$z_1=7;\ z_2=8$	$z=12$
0.5	0.737488	−0.0251212	−0.08993	−0.113385	−0.208688	0.00151018	0.00503624	0.00724728	0.0123084
0.6	0.857456	−0.0249004	−0.0898357	−0.113389	−0.209376	0.00144201	0.0045685	0.00653182	0.0107583
0.7	0.966234	−0.0247338	−0.0896419	−0.113228	−0.209565	0.00140653	0.00431288	0.00610532	0.00988929
0.8	1.06412	−0.0246166	−0.0894277	−0.11301	−0.209485	0.00138662	0.00415774	0.00582077	0.00935182
0.9	1.15175	−0.0245372	−0.0892269	−0.112785	−0.209267	0.00137469	0.00405367	0.00561505	0.00899025
1.0	1.22991	−0.0244844	−0.089051	−0.112575	−0.208985	0.00136685	0.00397618	0.00545736	0.00872662
1.1	1.29949	−0.0244498	−0.0889018	−0.11239	−0.208681	0.00136085	0.00391243	0.00533111	0.00851882
1.2	1.36139	−0.0244276	−0.0887769	−0.112229	−0.20838	0.00135532	0.00385556	0.00522669	0.00834323
1.3	1.41647	−0.0244137	−0.088673	−0.11209	−0.208093	0.00134944	0.00380207	0.00513813	0.00818666
1.4	1.46551	−0.0244055	−0.0885864	−0.111972	−0.207827	0.00134276	0.0037504	0.00506157	0.008042
1.5	1.50924	−0.0244011	−0.0885141	−0.111872	−0.207584	0.00133514	0.00370008	0.00499435	0.00790579
1.6	1.5483	−0.0243994	−0.0884535	−0.111786	−0.207364	0.00132663	0.00365119	0.00493463	0.00777667
1.7	1.58327	−0.0243994	−0.0884024	−0.111712	−0.207166	0.00131746	0.00360403	0.00488104	0.00765433
1.8	1.61463	−0.0244006	−0.0883592	−0.111649	−0.206988	0.00130788	0.00355898	0.00483256	0.00753897
1.9	1.64282	−0.0244027	−0.0883224	−0.111594	−0.206828	0.0012982	0.00351632	0.00478842	0.00743084
2.0	1.66822	−0.0244053	−0.0882909	−0.111547	−0.206686	0.00128866	0.00347628	0.00474798	0.00733015
2.5	1.7636	−0.0244211	−0.0881871	−0.111386	−0.206164	0.00124826	0.00331614	0.00458706	0.00693448
3.0	1.82417	−0.0244366	−0.0881333	−0.111299	−0.205853	0.00122235	0.00321213	0.00447214	0.00668381
3.5	1.86463	−0.0244497	−0.0881032	−0.111248	−0.20566	0.00120675	0.00314507	0.00438579	0.00652551
4.0	1.89283	−0.0244606	−0.0880853	−0.111216	−0.205535	0.00119715	0.0031007	0.00431866	0.00642247
4.5	1.91319	−0.0244697	−0.0880743	−0.111195	−0.205451	0.00119099	0.0030703	0.00426516	0.0063528
5.0	1.92833	−0.0244773	−0.0880673	−0.111182	−0.205393	0.00118685	0.00304877	0.00422167	0.00630395

is the three-particle electron correlations.

In the region $x \geq 1$ all contributions (with the exception of $\varepsilon_L^{(3)}(x|\langle z\rangle)$) to the model energy caused by interactions are negative monotonically decreasing functions of the relativistic parameter. The corrections $f_2(x)$, $f_3(x)$ are negative and decrease the pressure. In the two-electron correlations approximation the equation of state (58) numerically is very close to the result of Salpeter [5].

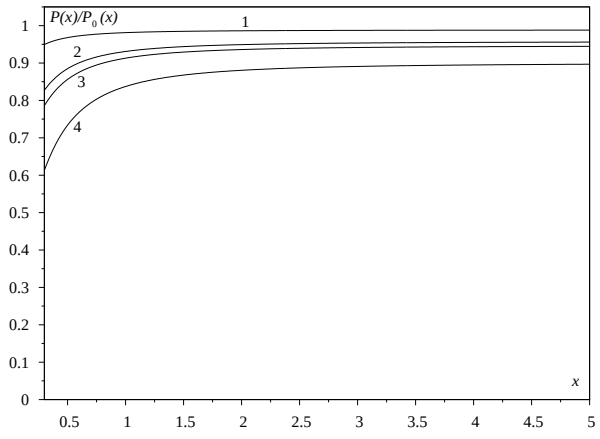

Figure 7: The ratio of pressure with Coloumb interactions $P(x)$ to the pressure of the ideal relativistic electron gas $P_0(x)$ as function of the relativistic parameter and nuclear charge (curve 1 – $z_1 = z_2 = 2$, 2 – $z_1 = z_2 = 6$, 3 – $z_1 = 7$; $z_2 = 8$; 4 – $z_1 = z_2 = 12$).

In table 1 is shown the dependence of terms $\mathcal{F}(x)$, $f_2(x)$, $f_3(x)$ on the relativistic parameter for the helium dwarf model ($z_1 = z_2 = 2$), carbon ($z_1 = z_2 = 6$), nitrogen-oxygen ($z_1 = 7$, $z_2 = 8$; $N_1 = N_2$) and magnesium ($z_1 = z_2 = 12$). The relative decrease of pressure by the interactions $\{\mathcal{F}(x) + f_2(x) + f_3(x)\}\mathcal{F}^{-1}(x)$ for the same models is illustrated in fig. 7.

5. Conclusions

Within the reference system approach, which was adapted for the description of degenerate relativistic electron subsystem, the energy of ground state of electron-nuclear model, as well as equation of state of the model, have been calclulated in a wide range of the relativistic parameter at absolute zero temperature. As it is shown in our calculation, the contributions of Coloumb interactions to the energy of ground state and pressure, caused by two-electron correlations are determinant and increase with increasing the nuclear charge. The contributions, caused by three-electron correlations are much smaller, but they exceed the contribution of correlation energy of electron fluid, especially at large values of nuclear charge.

Reference

[1] Chandrasekhar S.: 1931, *Astrophys. J.*, **74**, 81.
[2] Chandrasekhar S.: 1935, *Mon. Not. Roy. Astron. Soc.*, **95**, 676.
[3] James R.A.: 1964, *Astrophys. J.*, **140**, 552.
[4] Zeldovich Ya.B., Novikov I.D.: 1967, Relativistic astrophysics, Moskva: Nauka.
[5] Salpeter E.E.: 1961, *Astrophys. J.*, **134**, 669.
[6] Vavrukh M.V., Smerechinskii S.V.: 2012, *Astronomy Reports.*, **56**, n.5, 363.
[7] Vavrukh M.V., Smerechinskii S.V.: 2013, *Astronomy Reports.*, **57**, n.2, 913.
[8] Ostriker J.P., Hartwick F.D.A.: 1968, *Astroph. J.*, **153**, 797.
[9] Shapiro S.L., Teukolsky S.A.: Black Holes, White Dwarfs and Neutron Stars. Cornell University, Ithaca, New York, 1983.
[10] Kaplan S.A.: 1949, *Superdense stars. Scientific notes of the Lviv State Ivan Franko University. Series Mathematics*, **4**, 109.
[11] Hamada T., Salpeter E.: 1961, *Europ. Astrophys. J.*, **133**, 683.
[12] Tremblay P.-E., Bergeron P., Gianninas A.: 2011, *Astroph. J.*, **730**, 128.
[13] DeGennaro S., von Hippel T., Winget D.E. et al.: 2008, *Astrophys. J.*, **135**, 1.
[14] Vavrukh M., Krohmalskii T.: 1991, *Phys. stat. sol. (b)*, **168**, 519.
[15] Vavrukh M., Krohmalskii T.: 1992, *Phys. stat. sol. (b)*, **169**, 451.
[16] Gell-Mann M., Brueckner K.: 1957, *Phys. Rev.*, **106**, 364.
[17] Lloyd P., Sholl C.: 1969, *J. Phys. C*, **1**, 1620.
[18] Brovman E., Kagan Yu.: 1972, *Zh. Exp. Teor. Fiz.*, **63**, 1937.
[19] Brovman E., Holas S.: 1974, *Zh. Exp. Teor. Fiz.*, **66**, 1877.
[20] Vavrukh M., Vavrukh N.: 1996, *Low Temp. Phys.*, **22**, 767.
[21] Feynman R.P.: 1949, *Phys. Rev.*, **76**, 769.
[22] Vavrukh M., Dzikovskyi D., Solovyan V., Tyshko N.: 2015, *Visnyk of the Lviv University*, **50**, 104.
[23] Vosko S.H., Wilk L., Nusair N.: 1980, *Can. J. Phys.*, **58**, 1200.
[24] Ceperley D., Alder B.: 1980, *Phys. Rev. Lett.*, **45**, 566.

ASTROINFORMATICS

DOI: http://dx.doi.org/10.18524/1810-4215.2017.30.114411

ON THE CONCEPT OF THE ENHANCED FON CATALOG COMPILATION

V. Andruk[1], Q. Yuldoshev[2], I. Eglitis[3], L. Pakuliak[1], A. Mullo-Abdolov[4], I. Vavilova[1], Yu. Protsyuk[5], H. Relke[6], V. Golovnia[1], S. Shatokhina[1], O. Yizhakevych[1], Sh. Ehgamberdiev[2], M. Muminov[7], G. Kokhirova[4], L. Kazantseva[8]

[1] Main Astronomical Observatory NASU,Kyiv, Ukraine, *andruk@mao.kiev.ua*
[2] Ulugh Beg Astronomical Institute UAS,Tashkent, Uzbekistan, *q.astrin@gmail.com*
[3] Institute of Astronomy, University of Latvia,Riga, Latvia, *ilgmars@latnet.lv*
[4] Institute of Astrophysics of AS of Republic Tajikistan, Dushanbe, Tajikistan, *aziz.sherzod@gmail.com*
[5] Research Institute Mykolaiv Astronomical Observatory, Mykolaiv, Ukraine, *yuri@mao.nikolaev.ua*
[6] Walter Hohmann Observatory,Essen, Germany, *helena_relke@yahoo.com*
[7] Andijan State University,Andijan, Uzbekistan, *muminov1951@gmail.com*
[8] Astronomical Observatory of Kyiv Shevchenko National University, Kyiv, Ukraine, *kazl@ukr.net*

ABSTRACT. We suppose to compile the enhanced version of FON (Photographic Survey of the Northern Sky) catalog of stellar positions and B-magnitudes in the sky region from -20 to 90 degrees on declination. The photographic base of the project comprises about 5,700 plates obtained at three observatories of the former SU MAO NAS of Ukraine, Kitab observatory of Uzbekistan and Gissar observatory of Tajikistan. The mean epoch of the catalog is around 1988. The expected limited stellar magnitude is 17.5^m. More than 5,400 plates are processed to support the photometric part of the catalog. The plates were shot on the 1.2 m Schmidt telescope in Baldone, Latvia, in the U and V bands. Color data provide the possibility of catalog correction for the photometric color equation. Stars brighter than V $< 8.5^m$ will be supplemented with photoelectric U, B, V data. Proper motions will be obtained using GAIA data.

Keywords: star catalogs, digital image processing, photometry, UBV photometric system.

1. Introduction

In 1976 two scientists of MAO NAS of Ukraine I.G.Kolchinsky and A.B.Onegina proposed the project of the photographic survey of the northern sky (FON) (Kolchinsky & Onegina,1977). The idea arose after the acquisition of similar wide-angle astrographs of Carl Zeiss company with focal length 2 or 3 meters and aperture 40 cm in several observatories of the former USSR. The observational part of the project should have been run at 6 observatories. They are Kiev (Ukraine), Kitab (Uzbekistan), Zelenchuk (Russia), Abastumani (Georgia), Zvenigorod (Russia), Dushanbe (Tajikistan). Regular observations of the northern sky started in 1982. Unfortunately, for objective reasons, the idea of the four-fold overlapping of the sky with 6 astrographs was not fully implemented (Pakuliak et al., 2016). Here, in the final version of the enhanced catalog, we suppose to use plates from collections of three observatories from the previous list, namely Kiev, Kitab, and Dushanbe. In 2016 the processing of 5,400 plates was started for the providing the photometric part of the catalog with U, V magnitudes (Eglitis & Eglite, 2017b). Plates were shot on the 1.2 m. Schmidt telescope in Baldone, Latvia.

In MAO NAS of Ukraine, the FON project is carried out in the framework of UkrVO project (Vavilova et al., 2012a; 2012b; 2017; Vavilova, 2016).

2. Current status of the project

By now we have created the catalog of positions and B-magnitudes of stars for the Northern hemisphere (declination from -4° to 90°). The observational base of the catalog comprises 2260 digitized plates of MAO NASU 2-meters Carl Zeiss astrograph (Akhmetov, 2016; Andruk et al., 2014; 2015a; 2015b; 2016a; 2016c; Protsyuk, 2015a; Protsyuk & Relke, 2016).

Plates were digitized using two commercial scanners, Microtek ScanMaker 9800XL TMA and Epson Expression 10000XL. The resolution of images is 1200 dpi, linear dimensions of the most plates are 30x30 sm or 13,000x13,000 pixels (Protsyuk et al., 2014a; 2014b; 2014c). The catalog contains 24.7 million of stars and galaxies brighter than B = 16.5^m. The mean epoch of the catalog is 1988.2. Positions of catalog entries are given in the TYCHO-2 reference system, B-magnitudes are obtained in the system of photoelectric standards. The internal accuracy of the catalog for all objects is $\sigma_{\alpha\delta} = \pm 0.28$" and $\sigma_B = \pm 0.17^m$ (for stars in the interval B = 7^m -14^m these errors are $\sigma_{\alpha\delta} = \pm 0.13$" and $\sigma_B = \pm 0.08^m$). The convergence between calculated and reference positions is $\sigma_{\alpha\delta} = \pm 0.06$" and convergence with photoelectric B-magnitudes is $\sigma_B = \pm 0.14^m$ (Andruk et al., 2016b).

The result of the processing the Kitab FON photographic collection containing 1963 plates in the declination band from -20.5 to +2.5 degrees is the catalog of positions and B-magnitudes of 13.4 million stars and galaxies with B $\leq 17.5^m$ for the mean epoch 1985.0. (Yuldoshev et al., 2016a; 2016b). The digital images of plates were obtained on Epson Expression 10000XL commercial scanner with the same parameters of scanning (Muminov et al., 2013; 2014; 2017). Catalog positions are in the TYCHO-2 reference system and B-magnitude in the system of photoelectric standards. The internal accuracy of the catalog for all objects is $\sigma_{\alpha\delta} = \pm 0.23$" and $\sigma_B = \pm 0.15^m$ (for stars with B in the interval from 7^m to 14^m the errors are $\sigma_{\alpha\delta} = \pm 0.085$" and $\sigma_B = \pm 0.054^m$). The convergence between calculated and reference positions is $\sigma_{\alpha\delta} = \pm 0.042$" and convergence with photoelectric B-magnitudes is $\sigma_B = \pm 0.16^m$ (Yuldoshev et al., 2017).

Kiev and Kitab FON components have the overlapping area on declination from -4 to +2.5 degrees (Muminov et al., 2016). After the cross-identification of objects in two catalogs, the compiled catalog was created. The compiled catalog contains 36.7 million of stars and galaxies referred to the mean epoch 1987.0. For the objects measured twice or more times the errors are $\sigma_{\alpha\delta} = \pm 0.26$" and $\sigma_B = \pm 0.17^m$ ($\sigma_{\alpha\delta} = \pm 0.120$" and $\sigma_B = \pm 0.072^m$ for stars in the interval B = 7^m -14^m).

Dushanbe (Gissar) FON glass collection of the Institute of Astrophysics, the Academy of Sciences of Republic Tajikistan comprises near 1560 plates (Mullo-Abdolov et al., 2017). Before the start of plate collection digitizing, the commercial scanner Microtek ScanMaker 1000XL Plus has been investigated. The estimated errors of the scanner for stars brighter than B $\leq 13.5^m$ are $\sigma_x y = \pm 0.054$ px and $\sigma_m = \pm 0.020^m$ for rectangular coordinates and instrumental magnitudes respectively. The estimated astrometric accuracy obtained from the processing of the test plate with Pleiades in the system of TYCHO-2 is $\sigma_{\alpha\delta} = \pm 0.13$".

To enhance the photometric part of the catalog the collection of photographic plates shot on the 1.2 m. Schmidt telescope in Baldone, Latvia, in the U and V color bands are actively digitized and processed (Eglitis et al., 2016b; 2016c). The collection comprises near 780 U and 4660 Vplates. To date, the rectangular coordinates and photometric data of registered objects are obtained for almost the third part of the collection. The plate digitizing is made on the Epson Expression 10000XL scanner (Eglitis & Andruk, 2017a). It was tested for positional and photometric errors of the developed method of image processing by comparison between images with 8 and 16-bit grey scale color range. The instrumental errors found from the testing are ±0.0026 px and $\pm 0.0024^m$ for coordinates and magnitudes respectively. To estimate the astrometric and photometric accuracy, we processed 6 consecutive scans of the same plate with 1200 dpi resolution. The errors obtained for stars brighter than 13.5^m in U-band are $\sigma_x y = \pm 0.021 \div 0.027$ px and $\sigma_m = \pm 0.014^m \div 0.016^m$.

3. The photometric system of the catalog

The observational material in FON observational program was shot on refractors. The photometric data obtained as a result of digital image processing are distorted with the color equation, i.e.calculated photographic B_{ph} magnitudes are burdened with systematic errors depending on B-V color indices of stars. To obtain B_{ph} magnitudes, the characteristic curves were used, calibrated by reference stars with photoelectric data B_{pe} (Kornilov et al., 1991; Mermilliod, 1991; Andruk et al., 1995; 2017; Relke et al., 2015). The results of the comparison of photometric differences $\Delta B = B_{ph} - B_{pe}$ for calculated and reference stars are shown in Fig.1.

Panels **a** and **c** show the trend of differences ΔB with a stellar magnitude B_{pe}. Panels **b** and **d** demonstrate the dependence of differences ΔB on photoelectric values B-V for Kiev and Kitab components of FON catalog. The number of compared stars in catalogs is 29,776 and 6,135 for corresponding plots. RMS errors m of magnitude differences are 0.140^m and 0.156^m respectively. The presence of a color equation is noticeable on the panels **c** and **d**. Its value is approximately 0.16(B-V) of stellar magnitude.

4. Summary

In nearest perspective we plan the next steps:

1. Until 2019 to digitize and process the plates from the Dushanbe FON collection. To create the catalog of positions and B-magnitudes.

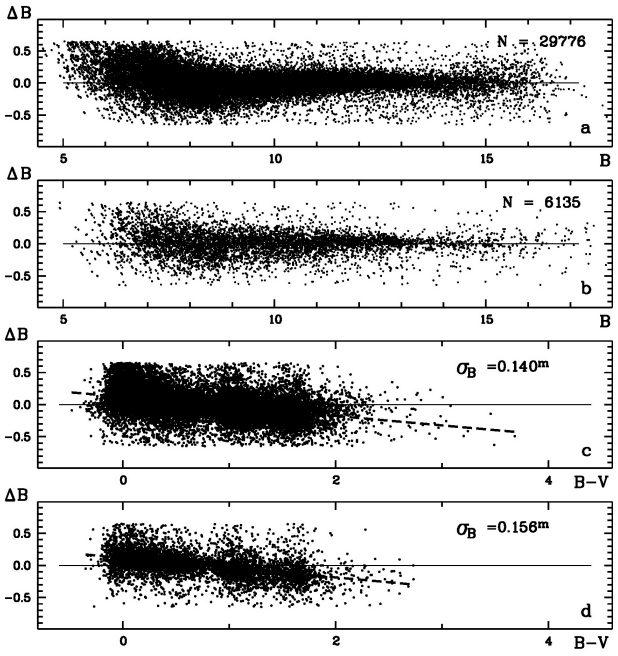

Figure 1: Photometric systems of FON catalog components

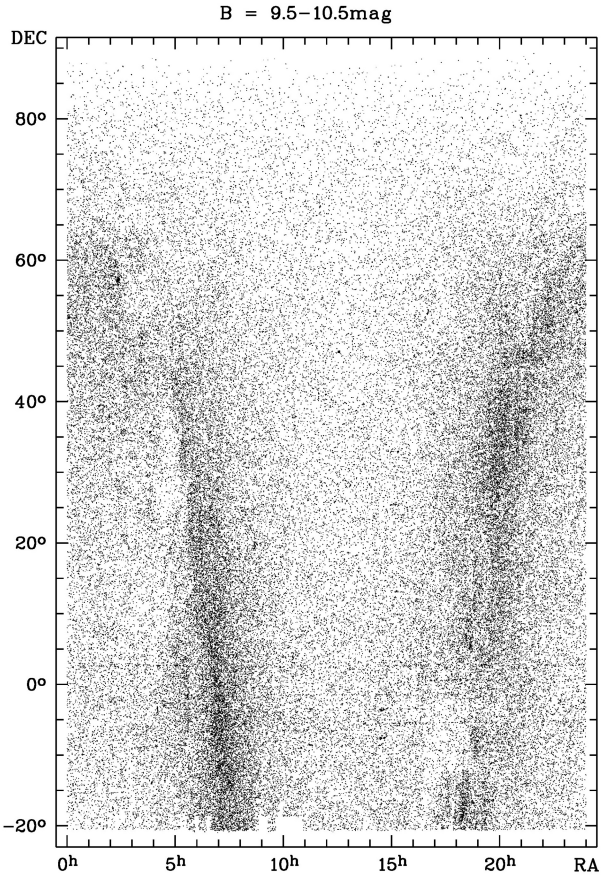

Figure 2: The star map on the data of enhanced FON catalog

2. Until 2020 to complete the digitizing and processing of U and V plates from the collection of 1.2 Schmidt telescope in Baldone. To obtain catalogs of positions and U, V magnitudes.

3. To supply the compiled catalog with bright stars data (down to V = 0^m) and to make the correct replacement for stars with V < 8.5^m with photoelectric U, B, V data.

4. To correct B-magnitudes of the compiled catalog for the color equation.

5. Using GAIA data to obtain proper motions of stars.

Fig. 2 demonstrates the distribution of stars from the catalog with =10±0.5^{m}on the hemisphere with the visible concentration of stars in the areas of Milky Way and the regions with the absorption of light in them.

The software created in the process of compilation Kiev and Kitab parts of the catalog was testes also in the processing of plates with Solar System bodies to determine their positions.(Eglitis et al., 2016a; Kazantseva et al., 2015; Protsyuk et al., 2015b; 2017; Shatokhina et al., 2016; Vavilova et al., 2014; Yizhakevych et al., 2014; 2015; 2016; 2017).

References

Akhmetov V.S.: 2016, *Odessa Astron. Publ.,* **29**, 116.

Andruk V., Kharchenko N., Schilbach E. et al.: 1995, *AN,* **316**, 225.

Andruk V.N., Golovnya V.V., Ivanov G.A. et al.: 2014, *Odessa Astron. Publ.,* **27**, 53.

Andruk V.N., Pakuliak L.K., Golovnya V.V. et al.: 2015, preprint (arXiv:1512.05535).

Andruk V.M., Pakuliak L.K., Golovnia V.V. et al.: 2015, *Odessa Astron. Publ.,* **28**, 192.

Andruk V.M., Golovnia V.V., Ivanov G.A. et al.: 2016, *Kinem. Phys. Cel. Bodies,* **32, N1**, 38.

Andruk V.M., Pakuliak L.K., Golovnia V.V. et al.: 2016, *Kinem. Phys. Cel. Bodies,* **32, N5**, 260.

Andruk V., Pakuliak L., Golovnia V. et al.: 2016, *Bull. T.Shevchenko Nat. Univ. Kyiv. Astron.,* **N54**, 24 (in Ukrainian).

Andruk V.M., Pakuliak L.K., Golovnia V.V. et al.: 2017, *Science and Innovation,* **13a**, N1, 17.

Eglitis I., Eglite M., Shatokhina S.V. et al.: 2016, *Odessa Astron. Publ.,* **29**, 123.

Eglitis I., Eglite M., Pakuliak L.K. et al.: 2016, *Odessa Astron. Publ.,* **29**, 126.

Eglitis I., Eglite M., Andruk V. et al.: 2016, *Bull. T.Shevchenko Nat. Univ. Kyiv. Astron.,* **N54**, 21 (in Ukrainian).

Eglitis I., Andruk V.: 2017, *Open Astronomy,* **26, N1**, 7.

Eglitis I., Eglite M.: 2017, *Science and Innovation,* **13a, N1**, 55.

Kazantseva L.V., Shatokhina S.V., Protsyuk Yu.I. et al.: 2015, *Kinem. Phys. Cel. Bodies,* **31, N1**, 37.

Kolchinsky I.G., Onegina A.B.: 1977, *Astrometry and Astrophysics,* **N33**, 11 (in Russian).

Kornilov V.G., Volkov I.M., Zakharov A.I. et al.: 1991, *Trudy GAIS,* **63**, 1 (in Russian).

Mermilliod J.C.: 1991, [online] Available at: *http://vizier.cfa.harvard.edu/viz-bin/VizieR?-source=II/168* .

Mullo-Abdolov A., Kokhirova G., Relke H. et al.: 2017, *Odessa Astron. Publ.,* **30, this issue**.

Muminov M.M., Kahharov B.B., Yuldoshev K.H. et al.: 2013, *Izvestija GAO. Pulkovo,* **220**, 517.

Muminov M.M., Yuldoshe Q.X., Ehgamberdiev Sh.A. et al.: 2014, *Odessa Astron. Publ.,* **27**, 57.

Muminov M.M., Ehgamberdiev Sh.A., Latipov A.A. et al.: 2016, *Izvestija GAO. Pulkovo,* **223**, 339.

Muminov M., Yuldoshev Q., Ehgamberdiev Sh. et al.: 2017, *Bulgarian Astron. J.,* **26**, 1.

Pakuliak L.K., Andruk V.M., Golovnia V.V. et al.: 2016, *Odessa Astron. Publ.,* **29**, 132.

Protsyuk Yu.I., Andruk V.N., Kazantseva L.V.: 2014, *Odessa Astron. Publ.,* **27**, 59.

Protsyuk Yu.I., Andruk V.N., Muminov M.M. et al.: 2014, *Odessa Astron. Publ.,* **27**, 61.

Protsyuk Yu.I., Kovylianska O.E., Protsyuk S.V. et al.: 2014, *Odessa Astron. Publ.,* **27**, 63.

Protsyuk Yu., Andruk V., Mazhaev A. et al.: 2015, *Odessa Astron. Publ.,* **28**, 202.

Protsyuk Yu., Yizhakevych O., Kovylianska O. et al.: 2015, *Odessa Astron. Publ.,* **28**, 204.

Protsyuk Yu., Relke E.: 2016, *Odessa Astron. Publ.,* **29**, 144.

Protsyuk Yu.I., Kovylianska O.E., Protsyuk S.V. et al.: 2017, *Science and Innovation,* **13a, N1**, 58.

Relke E., Protsyuk Yu.I., Andruk V.M.: 2015, *Odessa Astron. Publ.,* **28**, 211.

Shatokhina S., Kazantseva L., Kazantsev A. et al: 2016, *Odessa Astron. Publ.,* **29**, 151.

Vavilova I.B., Pakulyak L.K., Shlyapnikov A.A. et al.: 2012, *Kinem. Phys. Cel. Bodies,* **28, N2**, 85.

Vavilova I.B., Pakuliak L.K., Protsyuk Yu.I. et al.: 2012, *Baltic Ast.,* **21, N3**, 356.

Vavilova I., Golovnya V., Andruk V. et al.: 2014, *Odessa Astron. Publ.,* **27**, 65.

Vavilova I.B.: 2016, *Odessa Astron. Publ.,* **29**, 109.

Vavilova I.B., Yatskiv Ya.S., Pakuliak L.K. et al.: 2017, *IAUS,* **325**, 361.

Yizhakevych O., Andruk V., Pakuliak L. et al.: 2014, *Odessa Astron. Publ.,* **27**, 67.

Yizhakevych O.M., Andruk V.M., Pakuliak L.K.: 2015, *Odessa Astron. Publ.,* **28**, 213.

Yizhakevych O.M., Andruk V.M., Pakuliak L.K.: 2016, *Odessa Astron. Publ.,* **29**, 155.

Yizhakevych O.M., Andruk V.M., Pakuliak L.K.: 2017, *Kinem. Phys. Cel. Bodies,* **33, N3**, 142.

Yizhakevych O.,Andruk V., Pakuliak L. et al.: 2017, *Bull. T.Shevchenko Nat. Univ. Kyiv. Astron.,* **N55**, 9 (in Ukrainian).

Yuldoshev Q.X., Muminov M.M., Ehgamberdiev Sh.A. et al.: 2016, *Odessa Astron. Publ.,* **29**, 160.

Yuldoshev K., Usmanov O., Egamberdiev E. et al.: 2016, *Bull. T.Shevchenko Nat. Univ. Kyiv. Astron.,* **N54**, 28 (in Ukrainian).

Yuldoshev Q.X., Ehgamberdiev Sh.A., Muminov M.M. et al.: 2017, *Kinem. Phys. Cel. Bodies,* **33, N5**, 250.

DOI: http://dx.doi.org/10.18524/1810-4215.2017.30.114458

ASTRONOMICAL IMAGE PROCESSING FOR HIGH-ACCURATE ASTROMETRY DATA

A.M.Dmytrenko [1,2] , V.S.Akhmetov [1,2]

[1]Department of Astronomy and Space Informatics, V.N.Karazin National University, Kharkiv, Ukraine, 61022, *astronom.karazin007@gmail.com*

[2]Institute of Astronomy, V.N.Karazin National University, Kharkiv, Ukraine

ABSTRACT. This article presents the main results of the initial processing of some of the astronomical images obtained from the archive of the digitized photographics survey of the whole sky SuperCOSMOS. Using of the median filtering and gausian convolution procedure with the adaptive kernel allows to carry out the initial processing of astronomical images without calibration frames. After the initial processing, the photocenters of the celestial objects were identified by various methods. It has been concluded that after the use of the mathematical methods for the initial processing of the digitized photographics images, the position of objects is calculated with a higher random and systematic precision.

Keywords: astrometry; survey; image processing; big-data

1. Introduction

Huge strides in the development of telescope construction and radiation detectors have led to the exponential growth of the amount and quality of data in modern and future sky surveys. These factors have opened up new research horizons for astronomers, but they require new approaches to the processing of astronomical images. This article focuses on one of the most important computational problems of astronomy: the processing of raw astronomical data. Today, the resolution of the astronomical images resulting from the digitizing of photographic plates is up to several Gpixel. To processing such astronomical images, the use of large computational power and optimal algorithmic solutions is needed. At the present time, computer technology gives the ability to create and fully manage the files that contain several gigabytes of data.

For quality reduction, there are many different factors to consider from the observation and the specifics of the instruments up to atmospheric effects that are very difficult to describe. However, now there is a large number of different software packages, tools, and instruments in the automatic or semi-automatic mode designed for the high-quality initial processing of astronomical images. In modern observations with the using of CCD, high-quality results are achieved by means of calibration frames such as Offset, Dark, Flat. When such frames are absence, different mathematical methods have to be applied.

Today, computer technology makes it possible to effectively analyze the astronomical archives that contain even terabytes of astronomical images (Vavilova et al., 2012). For the processing of astronomical images, such software packs as IRAF, IDL, MIDAS, etc. have been developed and widely used. But since most of them have some particularities in use, in other words, they are targeted at specific purposes, apply-ing them to our purposes will not produce the desired results. Also, our research has shown that the software packs listed above cannot work with very large images or show very low performance. Therefore, it has been decided to develop our own software package that will effectively handle large amounts of astronomical image.

2. Photographic survey of the whole sky

In April 2018, there will be available the Gaia DR2 catalogue of over 1 billion stars position and proper motion (Gaia Collaboration, 2016). Precision in proper motions will be higher than 1 mas/year for the stars from 4 to 20.7 G mag. This catalogue will be based on the observations of the 5-year GAIA space mission. Short-term ground based astrometric surveys use Gaia DR1 as reference frame. Studying any complex motion or variable centroid objects, i.e. "time domain astronomy" requires observations at multiple, specific epochs or long time-line observations. To solve this problem, all digitized photographic whole sky surveys that were received from the 1950s up to 2000, as well as all available modern CCD surveys, have to be processed. This requires the creation of the software that will effectively processing digital photographic surveys at the modern astrometric precision levels.

In 2020, it is planned to launch an 8-meter LSST telescope that will be scaning the available sky over a few days. During only one night of observation with the use of the largest CCD matrix (3 Gpixel), about 15 TB of data will be received (Juric et al., 2015). The size of each image will be up to several GByts. Therefore the problems of software development, new processing algorithms, and new methods for analyzing the large amounts of data are especially acute.

In order to support the above listed tasks, a new software has been developed. The analysis of the efficiency

and correctness of the software operation was performed on images obtained from the digitizing of the northern photographic surveys of POSS and southern SERC, ESO, which are stored in Edinburgh SuperCOSMOS Scientific Archive (SSA) (Hambly et al., 2001, Hambly et al., 1998). One such FITS-image is an area of the celestial sphere of 6x6 degrees size, with a resolution of 0.67 arcseconds per pixel. The size of a FITS image is about 1Gpixel (32256x32256px), which is about 2 GByts of data in the digitized form.

3. Processing

3.1. Initial processing

The main peculiar properties of work with the photographic surveys is that they do not contain supporting calibration frames (Offset, Dark, Flat), so for the initial processing only the use of mathematical methods was needed.

To align the image field and to eliminate the noise, the median filtering with the variable (dynamic) kernel, as well as the mathematical convolution method with the Gaussian kernel were applied. Unfortunately, at this stage of the work some of the objects are not taken into account because of their irregular shape. For now, we are improving approaches to these methods in order to obtain undistorted data on the maximum number of objects.

The size of the median filter kernel ranged dynamically from the initial 3x3 pixels to the 50x50 pixels, and it includes the information of the part of the image which it overlaps while operating (Popowicz et al., 2015). The limitation of the maximum kernel size made it possible to exclude very bright objects (magnitude < 8) that could have obscured the surrounding weaker objects.

The convolution operation in our work helped to clarify the edges of the celestial objects, as well as "smooth" their brightness distribution on the field, which ultimately gives each of them a more "correct", Gaussian form.

3.2. Calculation photocenter of the objects

The position of the objects in the SuperCOSMOS was obtained by the fastest but at the same time the least accurate method known today (Center of Gravity, which is also referred to as the Moment method)

$$(x_b, y_b) = \left(\frac{\sum_{ij} W_{ij} I_{ij} x_{ij}}{\sum_{ij} W_{ij} I_{ij}}, \frac{\sum_{ij} W_{ij} I_{ij} y_{ij}}{\sum_{ij} W_{ij} I_{ij}} \right)$$

It's worth remarking that the improved kinds of this method exist, such as Weighted center of Gravity and Iterative center of Gravity. Their precision in finding centroids is several times higher.

Fig. 1 shows theoretical dependence the precision calculation of the photocenter from objects size in pixsels for some methods.

In our software, we suggest using a completely different method to measure an object's photocentre, which in theory and practice is already more precise than the above mentioned one; and what is important, it is only a little slower. This method is Least Squares Gaussian Fit

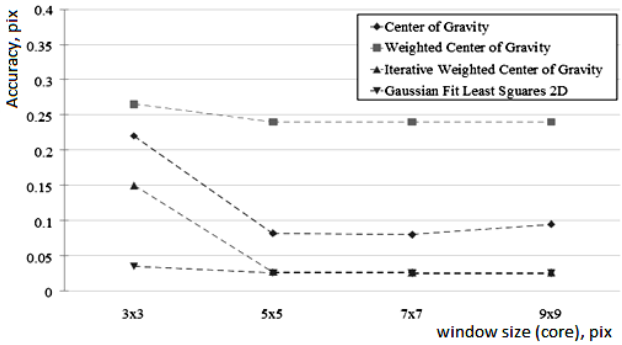

Figure 1: Accuracy of methods for searching photocentres comparing

2D (LSQ2) (Delabie et al., 2015). Its principle is to apply the least squares method to the two-dimensional function of the normal Gaussian distribution. This distribution was selected as a mathematical model because of its comparably high quality of celestial objects profile prediction to other simple functions.

The logarithm of the two-dimensional Gaussian function

$$I(x,y) = I_0 e^{-\left(\frac{(x-x_0)^2}{2\sigma_x^2} + \frac{(y-y_0)^2}{2\sigma_y^2}\right)}$$

was found for the possibility of using LSQ.

Next, after calculating and matching the most valid surface to the profile of each object from the resulting polynomial parameters, the coordinates of the celestial objects were calculated, as well as other parameters including maximum intensity

$$\ln I = x^2\left(-\frac{1}{2\sigma_x^2}\right) + x\left(\frac{x_0}{\sigma_x^2}\right) +$$

$$y^2\left(-\frac{1}{2\sigma_y^2}\right) + y\left(\frac{y_0}{\sigma_y^2}\right) + \left[\ln I_0 - \frac{x_0^2}{2\sigma_x^2} - \frac{y_0^2}{2\sigma_y^2}\right]$$

Among the drawbacks of the method, it is worth noting that it does not work with very faint celestial bodies with the size in the image in total less than 9 pixels. This problem is solved by artificially increasing (stretching) the objects using interpolation (sub-pixel image processing)

$$f = a_0 + a_1 x + a_2 y + a_3 x^2 + a_4 y^2$$

$$\begin{cases} a_0 = \ln I_0 - \frac{x_0^2}{2\sigma_x^2} - \frac{y_0^2}{2\sigma_y^2} \\ a_1 = \frac{x_0}{\sigma_x^2} \\ a_2 = \frac{y_0}{\sigma_y^2} \\ a_3 = -\frac{1}{2\sigma_x^2} \\ a_4 = -\frac{1}{2\sigma_y^2} \end{cases}$$

As a result of the work of our software, coordinates x, y of the photocentres were obtained for each of the objects on each of the images and then they were translated into the equatorial coordinate system. For astrometric reduction, the PMA catalog (Akhmetov et al., 2015) was used as a reference, with a precision of less than 10 mas on epoch 2015 year in position and 2-5 mas/yr in proper motions.

On Fig. 2 stars residuals distribution after reduction into PMA catalogue system is showed; distribution is built by positions during comparing data from present work with using Gausian Fit Least Squares 2D method and data from reference catalogue without any preprocessing of FITS-images (Fig 2.1). On Fig. 2.2 the same one is presented, but, before 'centroiding', the median correction were used. Finally, Fig. 2.3 shows distribution of uncertainties of positions after initial preprocessing including median filtering and convolutional.

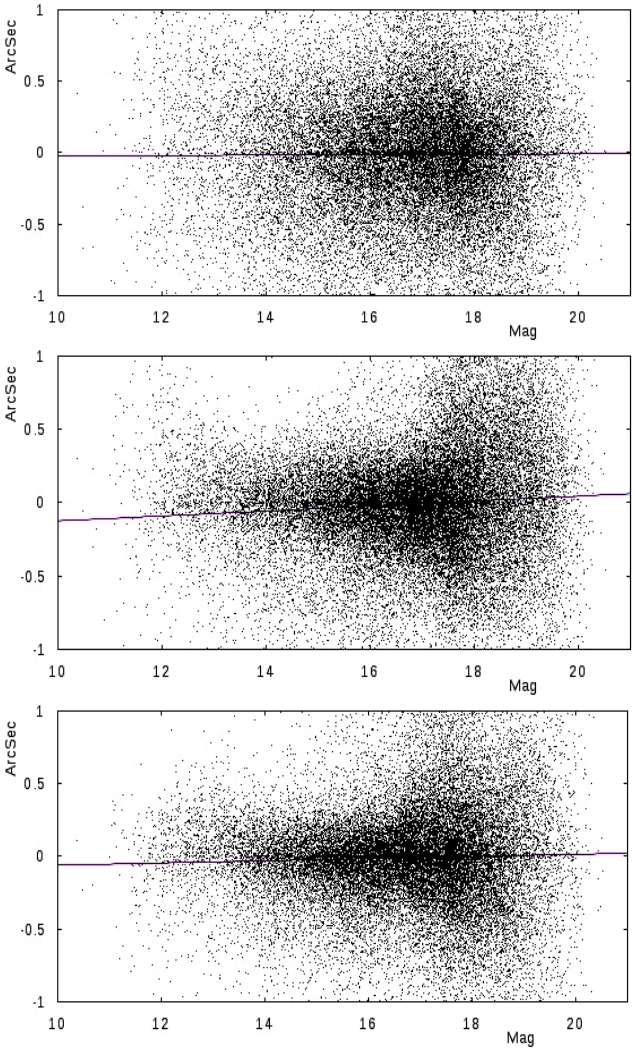

Figure 2: Here are two diagrams that show the deviation of the RA coordinate for SERCJ-602 plate when comparing the PMA catalog data and the data with the images 1) without initial processing, 2) with initial processing: median, 3) with initial processing: median and convolution.

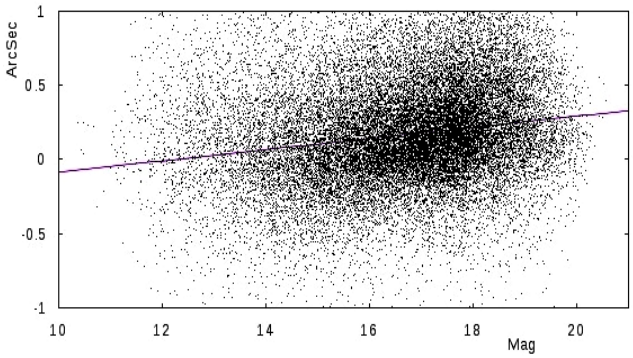

Figure 3: The results compare the SERCJ-602 plate and PMA catalogs by RA.

The mean residuals distribution after reduction into PMA catalogue system obtained in SuperCOSMOS is 630 mas. Using own software package with initial processing, we can calculated photocenter of objects with precision twice better than in SuperCOSMOS. Finally, the mean residuals distribution after reduction into PMA catalogue system after using this software is about 300 mas in both coordinate.

Obviously that obtained precision of positions determination is much better and allow to carry out astrometric reduction on new high level.

4. Conclusion

As result it can be demonstrated that the part of the analyzed data was successfully processed and then the positive results in valuation of the accuracy and acceptable processing speed were obtained.

An alternative method of searching for centroids of Gaussian shaped objects gives results that are much accurate than ones which were used earlier. This suggests that the data of the SCOSMOS plates collection, obtained relatively long ago, can still be useful in the modern approach of their processing.

References

Akhmetov V., Fedorov P., Velichko A. et al.: 2017, *MNRAS*, **469**, 1315.

Delabie T., De Schutter J., Vandenbussche B.: 2015, *JAnSc*, **61**, 60.

Gaia Collaboration: 2016, *A&A*, **595**, A1.

Gaia Collaboration: 2016, *A&A*, **595**, A2.

Hambly N., Davenhall A., Irwin M. et al.: 2001a, *MNRAS*, **326**, 1315.

Hambly N., Irwin M., MacGillivray H.: 2001, *MNRAS*, **326**, 1295.

Hambly N., Miller L., MacGillivray H. et al.: 1998, *MNRAS*, **298**, 897.

Juric M., Kantor J., Lim K.-T. et al.: 2015, *arXiv pre-print:1502.07915.*

Popowicz A., Smolka B.: 2015, *MNRAS*, **452**, 809.

Vavilova I. et al.: 2012, *Kinematics and Physics of Celestial Bodies*, **28**, N2, 85.

DOI: http://dx.doi.org/10.18524/1810-4215.2017.30.115454

METEOR OBSERVATIONAL DATA VISUALISATION IN THE EQUATORIAL COORDINATE SYSTEM USING INFORMATION TECHNOLOGY

V.A.Golovashchenko[1, 2], S.V.Kolomiyets [2]

[1] Kharkiv National University of Radio Electronics, Kharkiv, Ukraine, *vadym.holovashchenko@nure.ua*

[2] B.L. Kashcheyev Radio Astronomy Research Laboratory of Kharkiv National University of Radio Electronics, Kharkiv, Ukraine, *s.kolomiyets@gmail.com*

ABSTRACT. As a result of dynamic evolution of IT industry and astronomical research in the XXI century, which have resulted in obtaining large and complex data sets known as Big Data (e.g. data from the European Space Agency missions, such as GAIA mission, etc.), as well as due to rapid development of computer technologies, astronomy and computer science have become closely linked to each other. In the XXI century, Information technology has become an essential part of understanding the world around. This paper presents a solution to the problem of meteor data representation in the second equatorial coordinate (RA-Dec) system using Information Technology. Such a visualisation solution is needed to analyse the results of experiments based on the radar observations conducted in 1972-1978 (stage 1 – the data obtained in 1972 comprise 10,247 meteor orbits), which have been accumulated and stored in the Meteor Database of the Kharkiv National University of Radio Electronics (KNURE). A sample set of data with their characteristics and details about their delivery has been presented by (Kashcheyev & Tkachuk, 1980). An electronic calculator application was developed by employing the model of data visualisation in the form of celestial hemispheres using the object-oriented programming language C#.

Keywords: meteors, meteor map, data visualisation, databases, object-oriented programming, C#.

1. Introduction

It is thanks to Information Technology (IT) that scientific and technological capabilities have progressed so markedly in the XXI century (Butler 2012, etc.). The term "Information Technology" in its modern sense dates back to 1958. Information technology (IT) is the application of computers to store, study, retrieve, transmit and manipulate data for multiple various purposes to the advantage of users. This definition encompasses information processing techniques, as well as application of statistical and mathematical methods to decision-making and simulation of higher-order thinking using computer programmes. Information Technology, including internet-based technologies, is considered to be a subset of Information and Communications Technology (ICT). IT is designed to reduce the labour intensity of processes related to the utilisation of information resources. The current fourth phase of IT development is called electronic; it began in 1940. During this stage a gradual transition from procedural to object-oriented programming takes place (Graham 2004). Procedural programming is based on the concept of separating data from the code for their processing; this paradigm did not match the real world that consists of different objects which can be characterised simultaneously by their attributes (data) and behaviour (operations). Logical combination of data and procedures to perform operations on these data is the key concept of the object-oriented programming paradigm, which enabled to overcome the challenges of the procedural programming.

Meanwhile, mankind has entered the epoch of Big Data. For this reason, both the computer science and computer technology had to face fundamentally new challenges. Advances in astronomy over recent 20 years have contributed significantly in delivering a huge amount of data, and the flow of information is only expected to grow with promising new observations (Brescia *et al*., 2016). In this regard, the Global Astrometric Interferometer for Astrophysics (Gaia) mission of the European Space Agency (ESA), as well as the Large Synoptic Survey Telescope (LSST) and Square Kilometre Array (SKA) projects are worth particular attention. The goals of these projects are very ambitious; for instance, the LSST project is aimed to address profound scientific questions related to four research areas, such as probing dark energy and dark matter, taking an inventory of the Solar System, exploring the optical transient sky, and mapping the Milky Way.

Data centres (databases) and the Virtual Observatory are also important sources of Big Data in modern science (Brescia et al., 2016). A new trend of IT-mediated reasoning from data to the core of the subject has been emerging. There are also some new trends in the field of research methods, such as search for homogeneity in diversity and search for truth in the Information Technology itself as a manifestation of predicates of the Universe. Although these trends are quite typical for the process of learning the whole range of sciences, astronomy proves to be a specific area of knowledge for a variety of reasons,

conditions and circumstances. And all above-mentioned trends have been already detected, updated and even recorded in the proceedings of the International Astronomical Union (IAU) scientific convention under No 325. All these issues were discussed by the astronomers and IT experts during the afore-mentioned symposium called Astronomical Informatics held on 19-25 October, 2016, in Sorrento, Italy (Brescia et al., 2016). Among other topical issues, the participants of the symposium discussion stressed the need to combine the efforts of astronomers and programming experts in the field of data visualisation and transformation into analysis tools.

2. The study aim and objectives. Meteor data and processing technology. Results and discussion.

This study was aimed to develop convenient research tools to analyse the data obtained during meteor observations and presented as meteor data sets or databases with the function of meteor map visualisation in the second equatorial coordinate system.

To achieve the study objectives, the following tasks needed to be accomplished:

- taking specific sample sets of data from the KNYRE Meteor Database;
- creating an algorithm of links between the data available and the second equatorial coordinate system factoring in the relevant observation epoch;
- development of the software application "Astronomer's Reference Book – Calculator – Meteor Map" with the meteor map visualisation programmed in C#;
- testing and implementation of the software application "Astronomers' Reference Book" in the study of distribution of meteor radiants in the second equatorial coordinate system for meteoroids in prograde and retrograde orbits selected from the KNURE database.

It was expected that the task accomplishment would result in the practical IT implementation in astronomical meteor surveys through development of convenient virtual calculator with the meteor map visualisation option.

The study is focused on the examination of meteor data. The scope of the study covers the properties of meteor data adopted from special samples saved in the KNURE database.

The study was conducted using information technology, such as specific techniques and features of the object-oriented programming language C#.

A software product was created using integrated development environment Microsoft Visual Studio 2013, Windows Forms, .NET Framework 4.5 and programming language C#.

The novelty of the study is associated with independent development of specific IT tool "Astronomer's Reference Book – Calculator – Meteor Map", which can be used to analyse the specified meteor data and represent the results of their interpretation. This scientific paper also serves as the report on the results of the project "Astronomer's Reference Book" carried out by the students specialising in software engineering upon completion of the course within the academic discipline "Object-Oriented Programming" in the KNURE Department of Software Engineering.

2.1. Meteor data. Specific characteristics

In astronomy, meteor observational data, which are related to the celestial sphere and an observer in its centre, are specific. As seen from space, a terrestrial observer, whose position appears to coincide with the centre of the Earth, is able to record the true positions of the observed real physical objects; however, in meteoric astronomy, there is an imaginary point on the celestial sphere, called 'meteor radiant', which is the point of apparent intersection of the celestial sphere with the meteor path in the Earth's atmosphere when traced back. The position of this radiant is also related with the meteoroid, which is burning up in the atmosphere, at the instant of its burnout. Starting from the moment of observation of the meteor trail in the atmosphere at altitudes of 70-120 km, it is only the past tense that we can use to describe this meteoroid as an inhabitant of the Solar System; and its orbit in the Solar System could have been considered as ended if it was not for the assumption about the stochastic nature of meteors.

It is assumed that with a certain level of probability there might be at least one more real object which continues its motion in the Solar System along the same orbit as the burnt meteoroid did. There are also real physical meteor swarms comprised of meteoroids which travel around the Sun along similar orbits; and when observing periodic meteor showers from the Earth, it is because of these meteor swarms that a group of meteors in the atmosphere appear to emerge from one and the same radiant on the celestial sphere. Meteors which are not assigned to any of the known meteor streams are called sporadic. It is sporadic meteors that are discussed in this paper. Despite the afore-mentioned difference in determination of positions of meteor radiants and other celestial objects (such as stars, asteroids, comets, etc.), the night sky model (star map or chart) plays a significant role in meteoric astronomy; and this important analogy holds true for meteors with regard to their magnitudes. Hence, meteors with their radiants are assigned magnitudes in the same way as stars, i.e. when the meteor radiants are known, we say that meteors have magnitude "$+N^{m}$" or "$-N^{m}$"; and when meteor limiting magnitudes are recorded (in special cases), we say that meteors have magnitudes not higher than (or below) a certain value.

To describe a meteoroid as a Solar System object, its heliocentric orbit should be calculated, i.e. it is necessary to determine five orbital elements, namely semi-major axis a, eccentricity e, inclination i, argument of perihelion ω, and the longitude of the ascending node Ω. In some cases, other orbital parameters can be used: for instance, perihelion q and aphelion q' distances. The sixth orbital parameter – time t – defines the meteoroid position in its orbit. The time and date of meteor observation, meteor radiant position and velocity should be determined in order to calculate meteoroid's orbit in the Solar System. In this study, we used the guaranteed-accuracy algorithm for determination of meteor orbits which had been employed in radar observations in Kharkiv (Kolomiyets 2015).

2.1.2. Meteor data provided by the Kharkiv National University of Radio Electronics

Meteoric astronomy as a part of general line of meteor research in KNURE started developing in 1971. There is an electronic KNURE Meteor Database comprised of about 250,000 meteor orbits, which was created on the basis of radar observations of faint meteors with magnitudes below $+12^{m}$ carried out in 1972-1978 at the observation station in Balakliya. A sample data set with specified characteristics of meteor data and details about their delivery has been presented by (Kashcheyev & Tkachuk 1980). The KNURE Meteor Database is an electronic database with a statistically significant set of high-quality observational data; it serves as an IT tool and was used in the KNURE research activities many a time. It was required to refine the KNURE Meteor Database through development of specific functions to adjust the calculator to the standard epoch and to visualise the meteor map data. In this study, we adopted special sample sets of data from the KNURE Meteor Database in STATISTICA format. In order to test the software application "Astronomer's Reference Book – Calculator – Meteor Map", we used 10,247 meteor orbits obtained in 1972, as well as sample sets of prograde and retrograde meteor orbits.

2.2. Astronomical algorithm to create a calculator and meteor map

When creating the algorithm employed to develop the software application for meteor data processing, we used MAC recommendations for astrometric mathematical tools and techniques for data interpretation and analysis given in (Zharov, 2006).

2.2.1. The second equatorial coordinate system

In astronomical observations, the positions of celestial objects are defined by their coordinates on the celestial sphere. A coordinate system withthe origin lying at the centre of the Earth while its fundamental plane is a projection of the Earth's equator onto the celestial sphere is referred to as equatorial. In this study, we used the second equatorial coordinate system, for which δ is declination and α is right ascension. Declination δ varies from -90° to +90° relative to the equator towards the poles. Right ascension α of a celestial object is an angle between the two great circles, one of which passes through the celestial poles and the target object while the other one passes through the celestial poles and the vernal equinoctial point at which the ecliptic intersects the celestial equator. Right ascension α is measured in the direction opposite to the daily rotation of the celestial sphere (from 0 to 360°). An object's position $(\alpha,\delta)^0$ in the second equatorial (RA-Dec) system is not correlated to the daily rotation of the celestial sphere and changes slowly; that is important for plotting star maps and charts. It is equatorial coordinates $(\alpha,\delta)^0$ which are used in the software application "Meteor Map".

2.2.2. Calculating lunisolar precession

Lunisolar perturbations of the Earth's orbit result in a complex change in the Earth's rotation axis orientation in space. The axis slowly traces out a cone being constantly inclined to the orbital plane at an angle of 66.5^{o}. Such a motion is called precession; its period is about 26,000 years. Due to precession, the relative positions of the celestial poles continuously change. Positions of celestial objects change with time due to this lunisolar precession of the Earth's axis of rotation; hence, the adjustment to the standard epoch is needed. That is why the star maps should be regularly updated. Modern night sky maps date back to early 2000s (Equinox 2000). An annual shift of the mean pole position on the celestial sphere is about 50.3". There is a similar shift of the positions of equinoctial points as they move towards the apparent motion of the Sun. All the above has been taken into account when developing the application "Calculator"; nevertheless, the adjustments are still within the limits of accuracy.

2.2.3. Visualisation model

We used a conventional data-encoding scheme to create a 2D visualisation model ("Meteor Map") based on the projection of the physical model of the celestial sphere in the form of the globe with a constant radius onto the plane. The equatorial coordinate grid is illustrated by the beams radiating out from the centre and coaxial circles. Numbers in the margin of the map represent the right ascension (from 0 to 360°). The beam corresponding to the right ascension origin passes through the vernal equinoctial point. Fig. 1 depicts the distribution of a number of meteoroids in prograde and retrograde orbits for a sample set of orbital elements with aphelions within the range of 0.8-3.0 AU and eccentricities of 0.5-1.0. In other words, we have tested the application to visualise the space between the Earth and Ceres which orbits the Sun at a mean distance of 2.8 AU.

3. Conclusion

We have developed, tested and employed the software application "Astronomer's Reference Book – Calculator – Meteor Map" which enables to download meteor observational data and adjust meteor individual characteristics, such as unique numbers, orbital elements, time and date of observations, etc. It is feasible to create new lists of surveys, as well as to add, delete or adjust observational data. For this application, we have developed special functions, which enable to adjust the meteor data to the standard epoch, visualise meteor maps and save them in jpg format.

Acknowledgements. This study was conducted within the state-funded research 0116U002541 of the Ministry of Education and Science of Ukraine.

V.A.Golovashchenko is grateful to Y.Y.Cherepanova, a senior lecturer in the Department of Software Engineering of the Kharkiv National University of Radioelectronics.

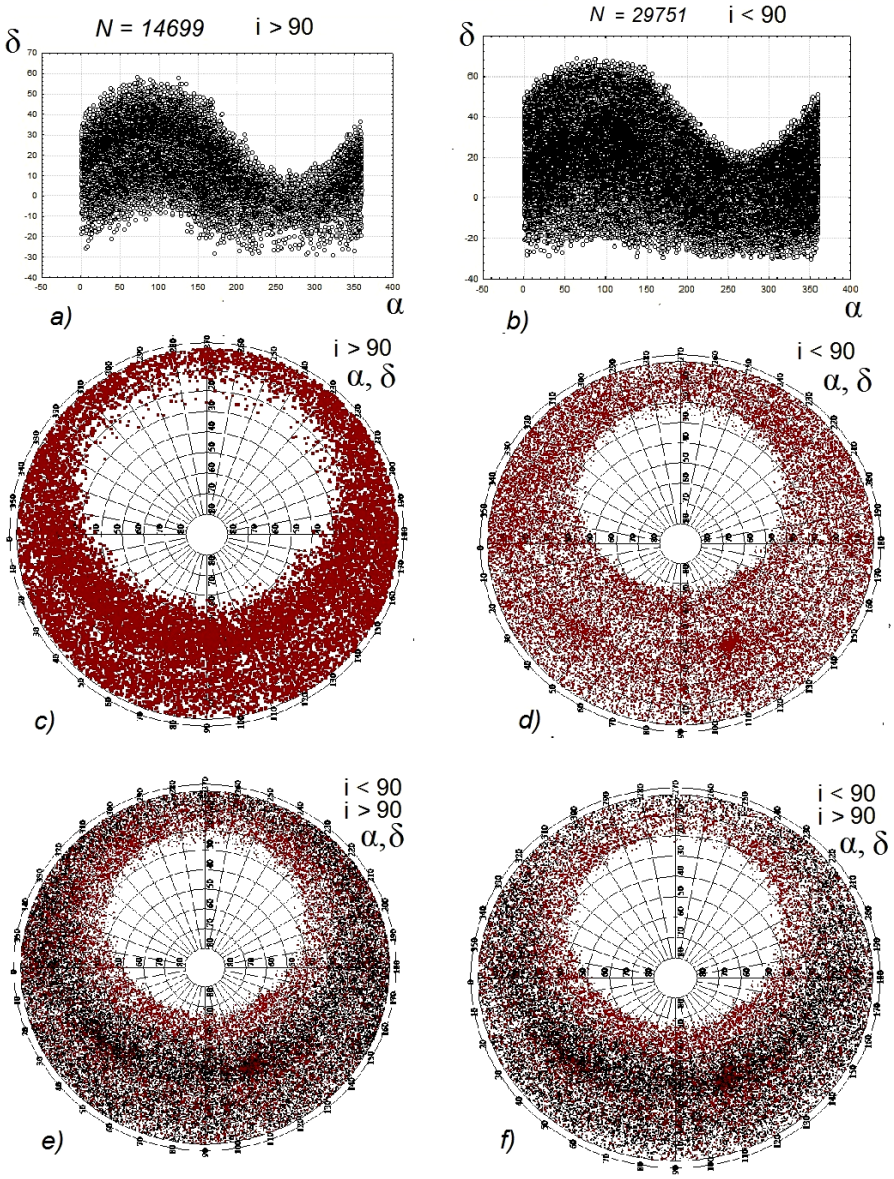

Figure 1: meteor data visualisation. The distribution of N meteoroids which orbit in the prograde $i < 90^0$ or retrograde sense $i > 90^0$ for a specific sample set of orbital elements $0.5 < e < 1$, $0.8 < q' < 3.0$ in the second equatorial (RA-Dec) system $(\alpha, \delta)^0$: a) $i > 90^0$ and b) $i < 90^0$ in the graphs plotted using STATISTICA software application; c) $i > 90^0$ and d) $i < 90^0$ in the meteor maps. Simultaneous distribution of prograde and retrograde orbits (marked with cerise and black conventional symbols, respectively) is presented on the maps: e) $-90^0 < \delta < 90^0$ (entire sphere) and f) $0^0 < \delta < 90^0$ (the Northern hemisphere).

References

Graham I.: 2004, Object-Oriented Methods: Principles & Practice. 3rd Edition. M.: Williams, p. 880.

Butle J.G.: 2012, A History of Information Technology and Systems, University of Arizona. Available online at: *https://tcf.ua.edu/AZ/ITHistoryOutline.htm* [Accessed 2 August, 2012].

Brescia M. et al.: 2016, Astroinformatics. Proc. IAU Symp. 325 (Cambridge Univ. Press), p. 403.

Zharov V.E.: 2006, Spherical Astronomy, Fryazino, p. 480.

Kashcheyev B.L., Tkachuk A.A.: 1980, Material Global Data Center B. Results of Radar Observation of Faint Meteors: Catalogue of Meteor Orbits to +12 m, Moscow, p. 232.

Kolomiyets S.V.: 2015, in *JASTP*, 124 March, p. 21.

DOI: http://dx.doi.org/10.18524/1810-4215.2017.30.114463

PHOTOGRAPHIC OBSERVATIONS OF SOLAR SYSTEM BODIES AT THE MAIN ASTRONOMICAL OBSERVATORY OF NAS OF UKRAINE: FINAL RESULTS

V. Golovnia, O. Yizhakevych, S. Shatokhina, V. Andruk

Main Astronomical Observatory of NASU, Kyiv, Ukraine, *golov@mao.kiev.ua*

ABSTRACT. Astrometric photographic observations of Solar system bodies in the frame of different programs were made at MAO NAN of Ukraine during 1950-2005. 9245 plates with the images of planets and their natural satellite, Moon, minor planets, comets and artificial satellites were obtained and processed in the late 20th century. At the beginning of the 21st century, the UkrVO Joint Digital Archive (JDA) was created, which is accessible at the MAO NAS resources (http://gua.db.ukr-vo.org/archivespecial.php).

To digitize the plate archive for the JDA database, flatbed scanners were used and the software was specially developed on the basis of the LINUX/MIDAS/ROMAFOT software for the processing of wide-field images, as well as searching for the images of minor planets and comets on the Northern sky survey program plates. Up to the present time, the photographic plates with images of outer planets and their satellites have been re-processed.

The final result of the long-lasting program of the photographic positional observations of Solar system bodies are summarized and presented in this publication.

Keywords: Solar system bodies, Astrometric photographic observations, UkrVO Joint Digital Archive.

1. Introduction

The article summarizes the results of re-processing of the old photographic observations of the Solar system bodies (SSB) at MAO NAS of Ukraine. The purpose of the observations was to obtain precise coordinates suitable for refining the SSB orbits and constructing new theories of motion, orientation of fundamental catalogs, studying the structure and evolution of the Solar system. The results, obtained by the team of the astrometry department, were the series of observations of Venus, Uranus, Neptune, Pluto, Mars, Jupiter, Saturn, natural satellites, minor planets, comets and Earth artificial satellites, which were later used for astrometric studies. The results of processing of the astrometric observations were published in different forms and placed in different sources (Onegina & Sereda, 1971; Gavrilov & Kislyuk, 1971; Duma & Kizyun., 1972; Sereda & Izhakevich, 1978; Gavrilov et al., 1980; Kislyuk et al., 1985, 1990, 1995; Duma et al., 2000; Kizyun, 2004). A part of the observations were published in editions, which are difficult to access now, such as “Manuscripts of VINITY”. Some observations still remain unpublished. Analysis of the data indicates the expediency of using of old photographic observations (Kiseleva 2007; Emelianov et al., 1999, 2006; Sergeeva et al., 2005). The modern approach to the processing of early photographic observations, which were collected in the UkrVO JDA, with new technologies is an effective tool for the reidentification of the SSB and correction of their orbits.

2. Telescopes and astroplates’ quantitative characteristics

The observation of the Solar system bodies was carried out using 11 instruments. The technique and methods of observations of the SSB were various. Table 1 shows the characteristics of the used telescopes: abbreviation for the telescopes and their original name in the JDA, scale of the telescope image ("/mm), location of telescopes and periods of the observations of the SSB on the corresponding telescopes. A list of telescopes, observational archives of the JDA prototype, list of emulsions, object types, observers list can be viewed at http://gua.db.ukr-vo.org/guides.php (Pakuliak, 2005, 2014; Pakuliak, Vavilova, 2014; Sergeeva, 2004, 2007, 2010).

The SSB observations were conducted with three "home" telescopes (DLA, DWA, DSA) of the Main Astronomical Observatory and seven expeditionary telescopes at Majdanak and Tashkent Observatory, Quito Astronomical Observatory and Comet Station (Ecuador), Astrophysical Observatories Abastumani and Byurakan (so-called “others” telescopes – Z-600, DAZ, CA, 2CAA, SCHC, 53/Sch and BYU (Kulyk et al., 2013). Figure 1 presents the distribution of the number of plates with the SSB according to the telescopes. As we can see 8802 plates were observed with “home” telescopes for 55 years. During eight years of the expeditions to other observatories 443 plates were received on seven “others” telescopes (see Figure 1, Table 2 and Table 4).

Table 1: List of the telescopes and periods of the observations of Solar System Bodies on the corresponding telescopes

Abbr.	Orig. name of the Istrument	"/mm	Observatory	Periods
DLA	Double Long-Focus Astrograph	38	Main Astron. Obs.,Kyiv, Ukraine	1950-1986
DWA	Double Wide-Angle Astrograph	103	Main Astron. Obs.,Kyiv, Ukraine	1976-2005
DSA	Double Short Focus Astrograph	295	Main Astron. Obs.,Kyiv, Ukraine	1950-1977
Z-600	Zeiss-600	28	Majdanak Obs., Mt. Majdanak, Uzbekistan	1986-1991
DAZ	Wide Angle Astrograph (Kitab)	69.8	Tashkent Ast. Obs. Kitab Station Uzbekistan	1986, 1988
CA	Ast. Photogr. Device AFU-75	281	Ast. Obs. end Comet Station, Quito, Ecuador	1986
2CAA	Two-camera astrograph	206	Astroph. Obs. Abastumani, Kanobili, Georgia	1990
SCHC	Schmidt camera	330	Astroph. Obs. Abastumani, Kanobili, Georgia	1987-1990
53/Sch.	53 cm Schmidt Telescope	113	Byurakan Astroph. Obs., Byurakan, Armenia	1983, 1985
BYU	1 m Schmidt Telescope	97	Byurakan Astroph. Obs., Byurakan, Armenia	1983

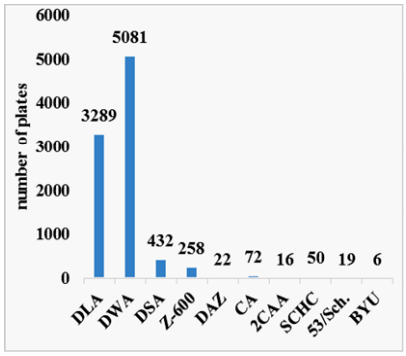

Figure 1: Distribution of the number of plates with the SSB according to the telescopes.

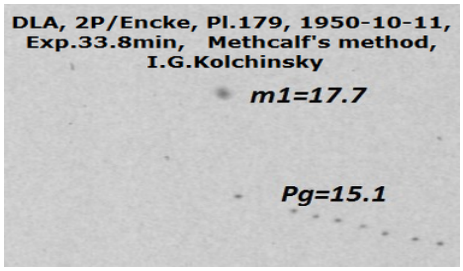

Figure 2: Comet Encke on the plate 179 DLA

Figure 3: Venus on the plate 181 DLA

3. Observational programs and observers

Regular observations of the SSB were conducted from 1950 to 2005 under different scientific programs including "Orbit", "Faint minor planets", "Selected minor planets", "Planets and their natural satellites"; "Mars, Phobos and Deimos – 1988"; "Mars – 1990-1993"; "Mars – 1994-1996"; "Comets", "SOPROG", "Moon", " Earth artificial satellites". Astrometric photographic observations of SSB began in 1950 at the astrographs DLA and DSA. First observers, I.G.Kolchinsky, T.A.Azarnova, A.A.Gorynia, R.I.Chupryna, started from the observations of the faint and selected minor planets and comets.

In Figure 2 the image of comet 2P/ Encke is presented. The comet had brightness of 17.7 magnitude and was observed by I.G.Kolchinsky.

The MAO NAS of Ukraine was the center for collecting information on the positions of comet 1P/Halley from around the world (Yatskiv et al., 1986; Major et al., 1987). Comet Halley was observed in the frame of the international program "International Halley Watch" and the Soviet program "SOPROG".

The plates of the Moon were obtained during the period between1950 and 1980 with DLA to determinate its accurate position and the absolute orientation of the selenodetic reference frame.

The major planets and their natural satellites were observed since 1951. In the Figure 3 the image of the Venus on the plate 181 DLA is presented.

Table 2: Distribution of the number of plates according to the observation programs and the telescopes

Object Type / Σ No. of plates	DLA	DWA	DSA	Other
Planets and their natural satellite **2065**	1508	263	17	277
Moon **657**	649	-	8	-
Minor planets **2037**	935	1063	39	-
Comets **1422**	197	693	366	166
Artific. Satellite **3064**	-	3062	2	-

The distribution of the number of plates with the SSB according to the telescopes and the observation programs is given in the Table 2 and Figure 4.

Table 3 gives the distribution of the number of plates obtained by the different observers in accordance with the observation period at the "home" telescopes. Additionally 47 plates were received by the following observers: 9 – L.L.Novoborskaya, 8 – A.N.Kur'yanova, 8 – D'jakonova, 6 – T.Ye.Majzlina, 6 – Ya.T.Kapko, 5 – L.K.Pakuliak, 5 – A.S.Duma; 31 plates were received one by one and 14 – by unknown observers.

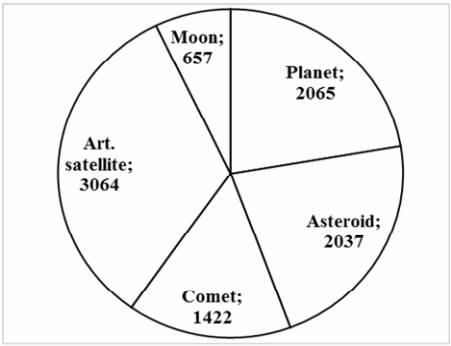

Figure 4: Distribution of the number of plates according to the observation programs.

Table 3: Observers at DLA, DWA, DSA

Observers, instruments (1-DLA, 2-DWA, 3-DSA)	Plates.	Observation period
L.M.Kizyun (Miz') (1+2)	1939	1960-2005
E.M.Sereda (1+2)	1180	1959-1987
I.V.Gavrylov (1)	816	1954-1966
Yu.I.Safronov (2)	646	1978-1991
G.V.Moroz (1+2)	595	1967-1983
A.B.Onegina (1+2)	470	1953-1977
S.P.Major (1+2)	410	1959-1986
Yu.M.Ivashchenko (2)	367	1983-1992
O.M.Yizhakevych (2)	347	1978-1988
Yu.V.Sizonenko (2)	287	1978-1997
R.F.Lysiakova (1)	196	1959-1965
I.M.Demenko (1)	114	1960-1971
I.V.Kulyk (Ledovskaya) (1+2)	114	1982-1988
I.G.Kolchinsky (1)	113	1950-1963
R.I.Chupryna (1+3)	112	1951-1956
G.A.Garazdo-Lesnykh (3)	103	1964-1970
M.R.Bocharova (2)	96	1985-1990
V.K.Rosenbush (Fartushnaya) (2+3)	95	1976-1979
V.I.Stupin (3)	92	1964-1968
V.V.Golovnya (2)	92	1985-1996
S.V.Shatokhina (1+2)	76	1984-1989
Yu.K.Philippov (1)	63	1971-1974
M.L.Divinskij (1)	44	1969-1972
A.V.Bolbochanu (1)	37	1960,1975
I.G.Zhdanova (3)	36	1954
A.E.Rosenbush (3)	33	1974
G.A.Ivanov (1+2)	25	1974-1983
A.A.Gorynia (1)	22	1950-1953
E.A.Herz (1+2)	21	1973-1981
T.A.Azarnova (3)	18	1950,1954
N.V.Kharchenko (1)	17	1982
O.V.Nazarenko (2)	17	1987
G.I.Balan (3)	16	1970
S.V.Kaltygina (2)	16	1984-1986
F.I.Lukatskaya (3)	15	1956-1963
A.F.Pugach (3)	15	1963-1964
V.S.Kysljuk (1)	15	1963-1970
D.P.Duma (Kotovych) (2)	14	1978-1983
V.P.Taraschuk (3)	13	1964-1966
A.I.Yatsenko (1+2)	13	1974-1983

Table 4: Observers at the "others" telescopes.

Observers	Plates.	Obs.period
Yu.V.Sizonenko	100	1983-1990
S.P.Major	98	1986-1991
I.V.Kulyk(Ledovskaya)	89	1985-1990
S.V.Shatokhina	46	1987-1991
G.N.Khimeridze	46	1990
O.M.Yizhakevych	23	1988-1991
E.M.Sereda	32	1986,1988
K.O.Major	9	1986

Table 4 gives the distribution of the number of plates obtained by individual observers in accordance with the observation periods at the Z-600, DAZ, CA, 2CAA, SCHC, 53/Sch and BYU telescopes**.**

Basically photographic observations of the SSB at MAO NAS of Ukraine have been finished in 1996. However, the date of complete cessation of the optical observations is 2005, when L. M. Kizyun (record holder in observations) completed observations of artificial satellites.

4. Catalogs of positions of the Solar system bodies

The results of elaborating of old observations, their analysis and methods of processing are presented in numerous publications (Kolchinskii & Onegina, 1977; Yizhakevych et al, 2001, Golovnya, 2000, 2001). However, the accuracy of the SSB positions based on old stellar catalogs is currently insufficient to refine modern motion theories and to reveal subtle effects in satellite motions. Creating the LINUX/MIDAS/ROMAFOT software and archive of digitized books – UkrVO JDA at MAO NASU made it possible to conduct a new astrometric treatment of some SSBs (Andruk et al, 2005, 2012, Protsyuk et al, 2014a, 2014b; Golovnya, 2010). On the basis of the digitization and reduction in a system of ICRS with a reference catalogue of TYCHO-2, new catalogues of the SSB positions have been created (Golovnya, 2000, Shatohina et al., 2016, 2017; Vavilova, 2016; Vavilova et al, 2014, 2017; Kazantseva et al, 2015; Protsyuk et al, 2015, 2016. 2017; Yizhakevych et al, 2014, 2015, 2017).

Table 5: The results of processing of the SSB observations

Name of SSB	Plates	Positions	Observation period
Venus	378	284	1959-1985
Moon	657	≈345	1950-1980
Mars+2sat (1318+831)	859	2149	1963--1988
J6, J7, J8	32	33	1987-1990
8 sat. of Saturn	209	1385	1961-1990
Uranus + 4 sat. (61+56)	33	117	1963-1990
Neptune+ 1 sat. (43+7)	29	50	1963-1990
Pluto	25	25	1961-1982
Minor planets	2037	≈1643	1950-1996
Comets	1422	≈447	1950-1996
Artificial satellite	3064	6024	1977-1981

Table 5 shows the distribution of the number of plates and number of positions received for the corresponding objects of the Solar system in the specified periods. Some positions of Minor planets are published in the "Manuscripts of VINITY", so the number of the positions in the table is given approximately.

Except for the plates with the SSB, the JDA includes about 18 thousands of direct sky area plates, which have been taken for various astronomical projects. Those plates also contain large number of the images of minor planets and others Solar system bodies (Shatohina et al., 2017).

5. Conclusions

The MAO NAS of Ukraine was the initiator and a participant of the international scientific programs and projects: astrometric observations of planets and their natural satellites, selected minor planets, minor planets, comets, Moon, artificial satellites.

9245 photographic plates with the images of the SSB were obtained and stored in the UkrVO JDA. For half a century, 12502 positions of the Solar system bodies were calculated and their catalogs were created.

The collected data were processed and used by IPA, Sternberg Institute and IMCCE, Minor Planet Center for the improvement of the ephemerides of minor planets, planets and their natural satellites, comets.

The result of many years of work has become a long, homogeneous series of observations of various Solar system bodies, obtained with the greatest possible accuracy and became the basis for further astrometric research. Some observations were made during the space missions such as VEGA, FOBOS, CORONAS.

References

Andruk V.M., Vid'Machenko A.P., Ivashchenko Yu.M.: 2005, *Kinem. Phys. Celestial Bodies*, Supl.N**5**, 544.

Andruk V.M., Ivanov G.A., Yatsenko A.I. et al.: 2012, *Bull. T. Shevchenko Nat. Univ*. Kyiv., Astron. **48**, 11.

Duma D.P., Kizyun L.N.: 1972, *Astr. Astrofiz*, **16**, 25.

Duma D.P. et al.: 2000, *Report of NANU*, Avail.et: http://www.mao.kiev.ua/docs/zvity/2000_tem**173**_Duma_Major, pp.40, (in Ukrainian).

Emelianov N.V. et al.: 1999, *VizieR On-line Data Catalog: J/A+AS/139/47*. 1999A&AS..139...47E.

Emelyanov N. V. et al.: 2006, CR, **44**, 2, 128.

Gavrilov I.V., Kislyuk V.S.: 1971, *The Moon*, **2**, 363.

Gavrilov I.V. et al.: 1980, *Report of AN USSR*, et: http://www.mao.kiev.ua/docs/zvity/1980_zv_tema**32**_Gavrilov_Major.pdf, pp.89, (in Russian).

Golovnya V. et al.: 2000, On-line Data Catalog: DBGPA 3/01. Avail.et: http://gua.db.ukr-vo.org/starcatalogs.php?whc=mphdcat.

Golovnya V. et al.: 2001, On-line Data Catalog: DBGPA 3/05. Avail.et: gua.db.ukr-vo.org/starcatalogs.php?whc=asteroids.

Golovnya V., Andruk V., Yatsenko A.: 2010, *Journal of Physical Studies,* **14**, N2, 2902, (in Ukrainian).

Kazantseva L.V., Shatokhina S.V., Protsyuk Yu.I. et al.: 2015, *Kinem. Phys. Celestial Bodies*, **31**, 1, 37.

Kiseleva T.P. et al.: 2007, *Solar Syst. Research*, **41**, 1, 72.

Kislyuk V.S. et al.: 1985, *Report of AN USSR*, Avail. et: http://www.mao.kiev.ua/docs/zvity/1985_Kislyuk_Major.pdf, pp.62, (in Russian).

Kislyuk V.S. et al.: 1990, *Report of AN USSR*, et: http://www.mao.kiev.ua/docs/zvity/1990_tema86_Kislyuk_Major.pdf, pp.28, (in Russian).

Kislyuk V.S. et al.: 1995, *Report of NANU*, Avail. et: http://www.mao.kiev.ua/docs/zvity/1995_zv_tema-102_Kislyuk_Major.pdf, pp.62, (in Ukrainian).

Kizyun L.M.: 2004, KFNT, **20**, 6, 540.

Kolchinskii I.G., Onegina A.B.: 1977, *Astrometry and Astrophysics,* **33**, 11 (in Ukrainian).

Kulyk I. et al.: 2013, *IMCCE. Int. Workshop NAROO-GAIA*, Paris Obs., Jun 2012, Paris, France. 153

Major S.P. et al.: 1987, *Report of AN USSR*, Avail. et: http://www.mao.kiev.ua/docs/zvity/zv_Halley_1983-1986_Major.pdf, pp.17, (in Russian).

Onegina A.B., Sereda E.M.: 1971, *Byull. ITA*, **732.**

Pakuliak L.K., Vavilova I.B.: 2014, *Report of NANU*, *DR* 0110U007859, **288**, 145 (in Ukrainian).

Pakuliak L.K.: 2005, *DBGPA V2.0*, Available et: http://gua.db.ukr-vo.org/archivespecial.php.

Protsyuk Yu.I, et al.: 2014a, Odessa Astron. Publ., **27**, 61.

Protsyuk Yu.I. et al.: 2014b, *Odessa Astron. Publ*., **27**, 63.

Protsyuk Yu. et al.: 2015, *Odessa Astron. Publ.*, **28**, N2, 204.

Protsyuk Yu. et al.: 2016, *Odessa Astron. Publ*, **29**, 147.

Protsyuk Yu.I. et al.: 2017, *Science and Innovation,* **13**, N1, 89.

Sereda E.M., Izhakevich E.M.: 1978, A i A, **36**, 72.

Sergeeva T.P., Golovnya V.V., Sergeev A.V. 2005, *Kinem. i Fizika Nebesnykh Tel*, Suppl, **5**, 577.

Sergeeva T.P. et al.: 2004, *Report of NANU, DR* 0101U006099, **198**,121, (in Ukrainian).

Sergeeva T.P. et al.: 2007, *Report of NANU, DR* 0105U000547, **222,** 101 (in Ukrainian).

Sergeeva T.P. et al.: 2010, *Report of NANU*, Avail. et: http://ukr-vo.org/documents/zvit_**249**_full.pdf, pp.121.

Shatohina S. et al.: 2016, *Bull. T.Shevchenko Nat.Univ. Kyiv.Astron.*, **53**, 24 (in Ukrainian).

Shatokhina S. et al.: 2017, *Bull. T.Shevchenko Nat.Univ. Kyiv.Astron.*, **55**, 6 (in Ukrainian).

Vavilova et al.: 2014, *Odessa Astron. Publ.*, **27**, 65.

Vavilova I.B.: 2016, *Odessa Astron. Publ*., **29**, 109.

Vavilova I.B. et al.: 2017, Astroinformatics, Proc. of the IAU Symposium, **325**, 361.

Yatskiv Ya.S. et al.: 1986, *Report of AN USSR*, d. r. No.01.83.0073650, (in Russian).

Izhakevich E.M. Shatokhina S.V., Golovnya V.V. et al., 2001, *Kinem. i Fizika Nebesnykh Tel*, **17**, 1, 65.

Yizhakevych O. et al.: 2014, *Odessa Astron. Publ*., **27**, 67.

Yizhakevych O.M., Andruk V.M., Pakuliak L.K.: 2015, *Odessa Astron. Publ.*, **28**, 213.

Yizhakevych O.M. et al.: 2017, *Kinem. Phys. Celestial Bodies*, **33**, N 3, 70.

DOI: http://dx.doi.org/10.18524/1810-4215.2017.30.114277

ON THE DIGITISATION OF ODESSA COLLECTION OF ASTRONOMICAL NEGATIVES. EXAMINATION OF THE EPSON PERFECTION V700 PHOTO SCANNER

S. Kashuba[1], V. Andruk[2], V. Kashuba[1]

[1] Astronomical Observatory of I. I. Mechnikov Odessa National University, Shevchenko park, Odessa 65014, Ukraine, *sv-k@onu.edu.ua*

[2] Main Astronomical Observatory of the National Academy of Sciences of Ukraine, Akad. Zabolotnoho St. 27, Kyiv 03680, Ukraine, *andruk1058@ukr.net*

ABSTRACT. This study was aimed to estimate the precision of the selected plate processing method and test the accuracy of the Epson Perfection V700 Photo scanner used to digitize astroplates from the Odessa Astronomical Observatory's collection. The processing of astroplates was performed using specific software developed in the LINUX/MIDAS/ROMAFOT environment. In order to estimate the repeatability of the scanner's astrometric and photometric errors, six consecutive scans of one and the same plate (No 17,000 — the Pleiades star cluster) were processed in two scanning modes with spatial resolutions of 1,200 and 2,400 dpi. The plate was exposed for 30 minutes with the fourth tube of the Seven Wide Angle (SWA) astrograph. The scan size was 18 x 24 cm (13 x 18 degrees). The following estimates of the scanner's accuracy were obtained for the stars brighter than B < 13 m in the two scanning modes: 1) $\sigma_{xy} = \pm 0.023$ px, $\sigma_m = \pm 0.013^m$; 2) $\sigma_{xy} = \pm 0.082$ px, $\sigma_m = \pm 0.042^m$ for the Cartesian coordinates and instrumental magnitude, respectively.

Keywords: astronegative, scanning, processing of digitized plates

1. Introduction

In the Odessa Astronomical Observatory they intend to digitise a unique collection of astronomical photographic plates amassed over many years of systematised patrol observations (Vavilova, 2011). The earliest plate is dated 1909, and the total number of plates exceeds 110 thousand. The collection has been acquired with various instruments and covers most of the northern hemisphere. Thus far, test scanning of several hundred of plates has been performed using Epson Perfection V700 Photo in order to assess the quality of scanning and suitability of digitised images for setting various research objectives.

2. Scanning results at 1200 and 2400 dpi

In this study aimed at testing the accuracy of the Epson Perfection V700 Photo scanner, the authors used a method which has already been employed earlier in a number of works (Golovnya, 2010; Eglitis, 2017; Mullo-Abdolov, 2017; Protsyuk, 2014b; Protsyuk, 2014c). The software specially developed for the FON project was used (Andruk, 2016a; Andruk 2016b; Kolchinskii, 1977; Pakuliak, 2016).

The programs and applications used to process digitized frames have been described in the studies (Andruk, 2015a; Andruk, 2015b; Andruk, 2017; Protsyuk, 2014a). In order to estimate the astrometric and photometric accuracy of the Epson Perfection V700 Photo scanner, six consecutive scans of the plate representing the Pleiades star cluster (No 17,000; ORWO-ZU21) were processed with the Seven Wide Angle Astrograph at the Astronomical Observatory of Odessa National University with 30-minute exposure and the resulting scan size of 18 x 24 cm. The scanning was performed in two scanning modes with spatial resolutions of 1,200 and 2,400 dpi, respectively. The computations for all objects recorded on the scanned plate (about 9,100 objects) were carried out as follows. The objects' characteristics, namely Cartesian X and Y coordinates and instrumental magnitudes m, averaged with respect to six scans were obtained for each scanning mode separately. A set of diagrams in Fig. 1 presents the following results of scanning at 1,200 dpi. Fig. 1a on the left depicts how the X-coordinates determined from each of six consecutive scans are spread out from the averaged ones (1a, 2a, 3a, 4a, 5a and 6a). The scatter of the X-coordinates about their means after systematic error reduction is illustrated in the diagrams on the right (1b, 2b, 3b, 4b, 5b and 6b). The standard deviation calculated for one of the differences between the estimated and averaged X-coordinates is indicated for all six scans. The bottom part

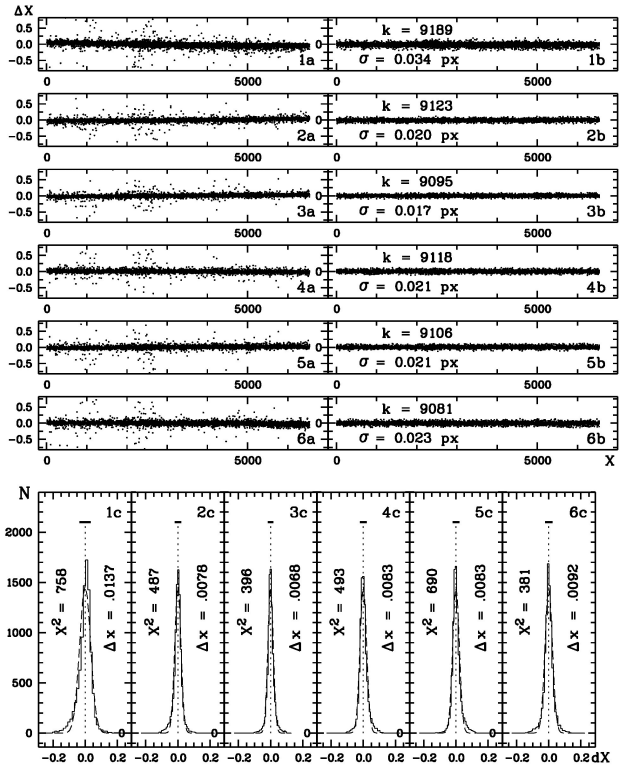

Figure 1a. Scanning at 1200 dpi. The scatter of X-coordinates determined from each of six consecutive scans about the averaged ones.

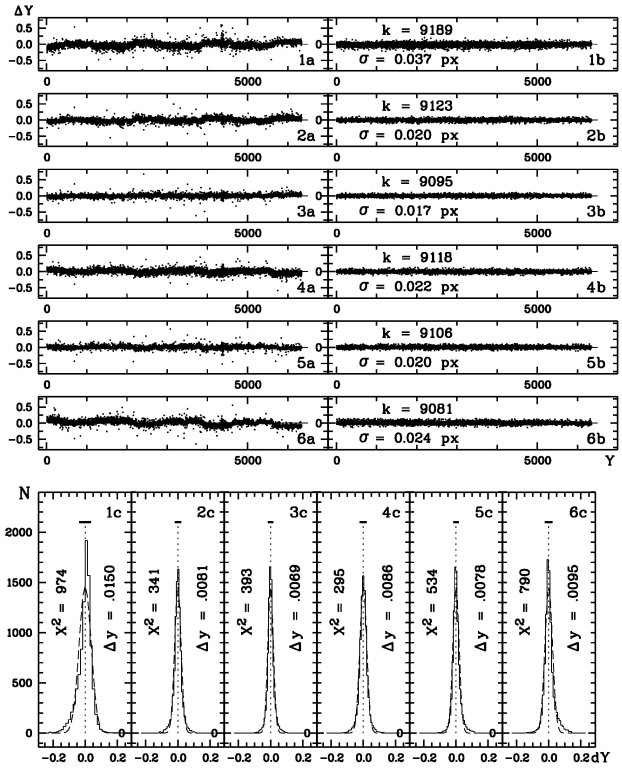

Figure 1b. Scanning at 1200 dpi. The scatter of Y-coordinates determined from each of six consecutive scans about the averaged ones.

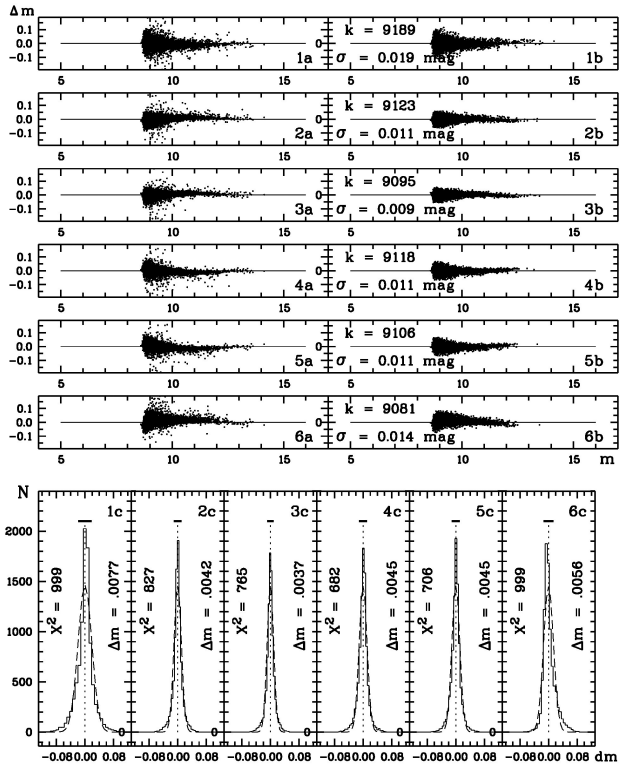

Figure 1c. Scanning at 1200 dpi. The scatter of instrumental magnitudes m estimated from each of six consecutive scans around the averaged ones.

of the figure shows the frequency distribution for these differences. The differences between the estimated and mean X-coordinates are presented as actual (solid lines) and theoretical (dashed lines) distribution functions over the respective intervals. The interval lengths ΔX and X^2 values are given on the left and right side of the bottom diagrams, respectively. Likewise, Figs. 1b and 1c demonstrate the scatter about the means and its characteristics for Y-coordinates and instrumental magnitudes, respectively. The results of processing of six scans at 2,400 dpi are plotted in a series of diagrams in Fig. 2.

Figs. 1a-1c and 2a-2c present the results obtained for the stars brighter than $B < 13^m$. The magnitude scale was calibrated using the compiled catalogue of photoelectric UBVR stellar magnitudes (Relke, 2015). Thus, the standard deviation (the root-mean-square deviation) of an estimate of the scatter of the Cartesian coordinates is $\sigma_{xy} = 0.023 \pm 0.007$ px and $\sigma_{xy} = 0.082 \pm 0.008$ px when scanning at 1,200 dpi and 2,400 dpi, respectively. The standard deviation of the difference between the estimated and averaged instrument magnitudes is $\sigma_m = 0.013^m \pm 0.004^m$ and $\sigma_m = 0.042^m \pm 0.003^m$ at 1,20 and 2,400 dpi, respectively.

The above standard deviation is the measure of the scanner's accuracy in the instrumental system. When converting to the equatorial coordinate system and Johnson system, the standard deviation will change by a scale

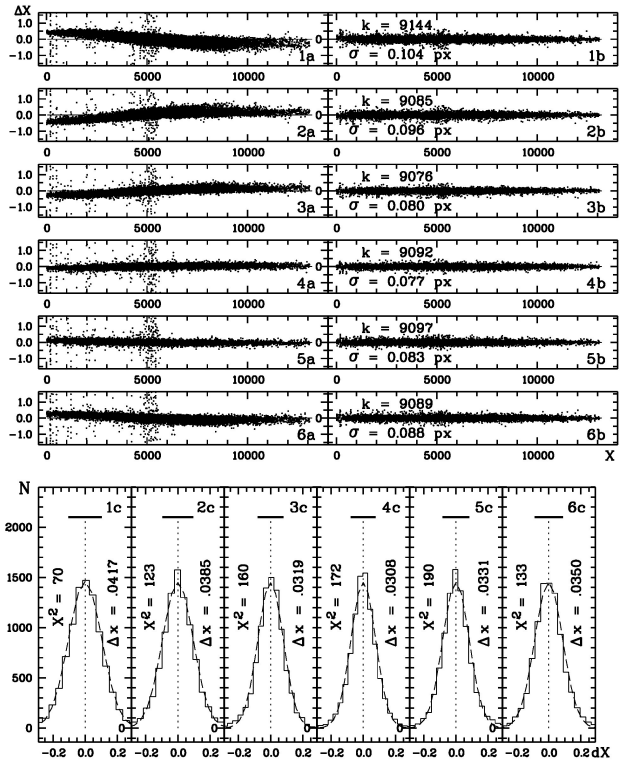

Figure 2a. Scanning at 2400 dpi. The scatter of X-coordinates determined from each of six consecutive scans about the averaged ones.

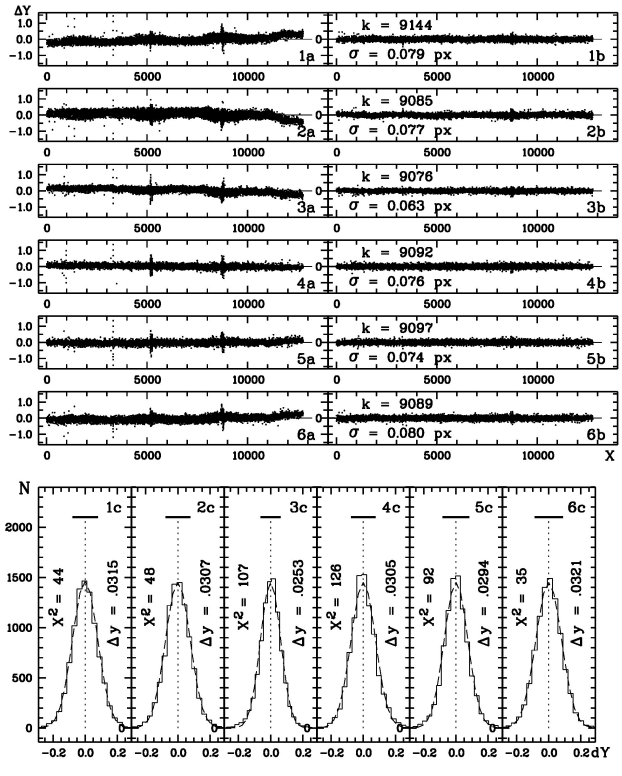

Figure 2b. Scanning at 2400 dpi. The scatter of Y-coordinates determined from each of six consecutive scans about the averaged ones.

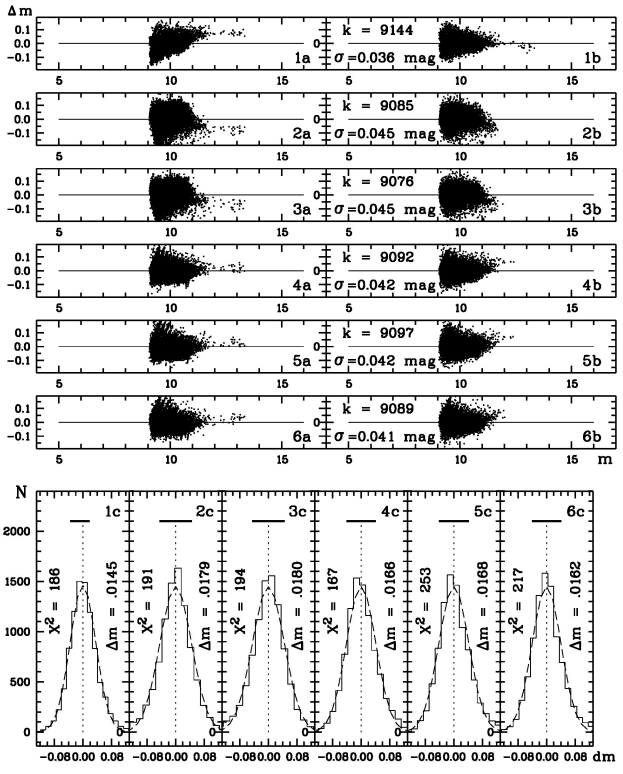

Figure 2c. Scanning at 2400 dpi. The scatter of instrumental magnitudes m estimated from each of six consecutive scans around the averaged ones.

factor for the Cartesian coordinates and by the photo emulsion contrast value for magnitudes.

The authors has drawn conclusion that the Epson Perfection V700 Photo flatbed scanner being used with the specially developed software enables digitising and processing astroplates, as well as obtaining characteristics of objects with an internal accuracy not greater than ± 0.15 arcseconds and ± 0.03 magnitude when scanning at 1,200 dpi. When scanning at 2,400 dpi, the internal accuracy is ± 0.25 arcseconds and ± 0.1 magnitude for Cartesian coordinates and instrumental magnitudes, respectively.

3. Conclusion

The study conducted to specify technical characteristics of processing astroplates digitised with the Epson Perfection V700 Photo scanner has produced the following results. Within the accuracy of estimates for the photographic plates, the Epson scanner is well suited to performing ground-based astrometric and photometric studies.

References

Andruk V. M. et al.: 2015, arxiv.org/abs/1512.05535.
Andruk V. M., Pakuliak L. K., Golovnia V. V., et al.: 2015, *Odessa Astron. Publ.,* **28**, 192.
Andruk V. M., Golovnia V. V., Ivanov G. A., et al.: 2016, *Kinem. Phys. Cel. Bodies,* **32**, **N1**, 38.
Andruk V. M., Pakuliak L. K., Golovnia V. V., et al.: 2016, *Kinem. Phys. Cel. Bodies,* **32**, **N5**, 260.
Andruk V. M., Pakuliak L. K., Golovnia V. V., et al.: 2017, *Science and Innovation,* **13a**, N1, 17.
Golovnya V., Andruk V., Yatsenko A.: 2010, *J. of Phys. Studies,* **14**, **N2**, 2902 (in Ukraine).
Eglitis I., Andruk V.: 2017, *Open Astronomy,* **26**, **N1**, 7.
Kolchinskii I. G., Onegina A. B.: 1977, *Astrometry and Astrophysics,* **N33**, 11 (in Ukraine).
Mullo-Abdolov A., Kokhirova G., Relke H. et al.: 2017, *Odessa Astron. Publ.,* 30, this issue
Pakuliak L. K., Andruk V. M., Golovnia V. V., et al.: 2016, *Odessa Astron. Publ.,* **29**, **N1**, 132.
Protsyuk Yu. I., Andruk V. N., Kazantseva L. V.: 2014, *Odessa Astron. Publ.,* **27**, **N1**, 59.
Protsyuk Yu. I., Andruk V. N., Kazantseva L. V., et al.: 2014, *Odessa Astron. Publ.,* **27**, **N1**, P..61.
Protsyuk Yu. I., Kovylianska O. E., Protsyuk S. V., et al.: 2014, *Odessa Astron. Publ.,* **27**, **N1**, 63.
Relke E., Protsyuk Yu.I., Andruk V.M., et al.: 2015, *Odessa Astron. Publ.,* **28**, 211.
Vavilova I. B., Pakuliak L. K., Protsyuk Yu. I., et al.: 2011, *Kosm. nauka tehnol,* **17**, **N3**, p. 74-91

DOI: http://dx.doi.org/10.18524/1810-4215.2017.30.114465

SUPERVISED AUTOMATIC IDENTIFICATION OF EXTRAGALACTIC SOURCES IN THE WISE×SUPERCOSMOS CATALOGUE

V. Khramtsov[1,2], V. Akhmetov[1,2]

[1]Institute of Astronomy of V.N. Karazin Kharkiv National University, Kharkiv, Ukraine

[2]Department of Astronomy and Space Informatics of V.N. Karazin Kharkiv National University, Kharkiv, Ukraine

vld.khramtsov@gmail.com, akhmetovvs@gmail.com

ABSTRACT. We present new catalogue of ~8,500,000 extragalactic objects as a result of automatic classification of WISE and SuperCOSMOS (SCOS) cross-identification product. The main goal is to create a set of candidates in extragalactic objects due to colour (photometric) features through machine learning techniques. Extragalactic sources were separated from stars in high-dimensional colour space using Support Vector Machine (SVM) classifier.

Construction of catalogue of the extragalactic objects is based on the four important procedures: 1. Cross-identification of the WISExSCOS catalogues. 2. Training set creation (Gaia DR1 and 2MASX\XSC data). 3. Feature engineering and colour-space constructing for further learning and classification. 4. Fine-tuning of SVM and separation and classification processes.

In result we got high-accuracy (~98%) algorithm for extragalactic source identification in built colour space. Product of algorithm realization is presented as photometric catalogue of the extragalactic objects and can be used for further astronomical investigations.

Keywords: Catalogues: statistics, extragalactic objects; Methods: machine learning, data analysis.

1. Introduction

Modern astronomical surveys include billions of objects, and with time amount of observed sources will increase. But not of all wide-field catalogues include spectroscopic information that allows us to study in detail these objects; at the same time, such catalogues almost always include photometric data. Therefore, the design of new algorithms to process large photometric data sets is an urgent task.

Particular problem of the catalogue analysis is a separation of extragalactic sources from the galactic ones. Without utilization of spectroscopic information, this problem usually can be solved by the most trivial way – with using morphological features (Peacock et al., 2016; Skrutskie et al., 2006); it is assumed that extragalactic sources, more often, are extended. Such approach has not to be applied successful to the deep-imagine catalogues because extragalactic sources (as active galactic nucleus (AGNs), quasars, faint distant galaxies, quasi-stellar objects (QSO) etc.) are unresolved or point-like – with photometric structure, similar to stars. Modern approach to solve this problem is separation of objects with high-dimensional diagrams representing different features (proper motion, colour, magnitude and others).

In current research we used high-dimensional colour space as feature space for star-galaxy separation. That was done from the reason that different types of objects, according to the shape of their spectral energy distribution, are in the different regions of colour diagrams. According to the fact, that galaxies are redder than stars (Pollo et al., 2010), we count on the infrared photometric information to separate stars and extragalactic sources. We choose photometric all-sky catalogues WISE and SCOS, cross-identification of which guarantees resolving sources up to $B < 20\,mag$ in the broad optical-

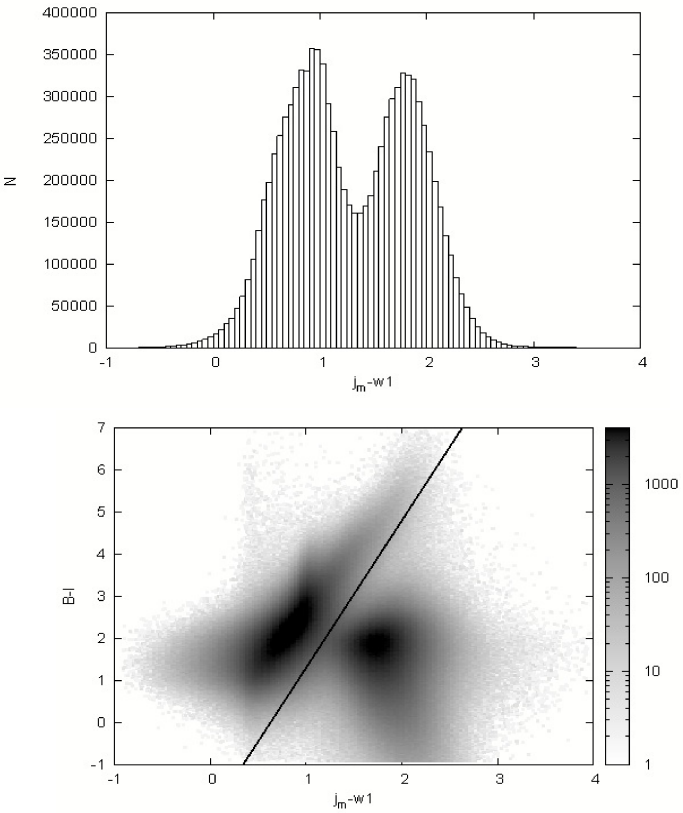

Figure 1: Colour histogram (J– W1) for PPMXL (up) and colour diagram (J– W1, B– I) for PMA (bottom). Objects in the right regions of the diagrams ($J - W1 > 1.3$) are extragalactic ones.

infrared range ($W1, W2, W3, W4, J, H, K$ (Vega), B, R, I (AB), where AB and Vega are photometry systems) and contains hundreds of millions of objects.

Method of using colour diagrams for the separation of objects into extragalactic and galactic sources was successfully applied in the creation of proper motion catalogues PPMXL (Vickers et al., 2016) and PMA (Akhmetov et al., 2017), where autors proposed to separation one- and two-colour diagrams respectively (Fig. 1).

Automatic object separation with using photometric data from the WISE and SCOS catalogues was successful carried out by several groups: (Solarz et al. 2017, in press), (Bilicki et al., 2016), (Kurcz et al., 2016), (Krakowski et al., 2016), (Kurcz et al., 2015).

The paper presents a result of classification of objects in high-dimensional colour space into two classes: candidates in extragalactic objects and galactic objects, with using linear separating classifier SVM (Vapnik, 1979). The paper is laid out as follows: the SVM method is describing in Sect.2; Sect.3 explains the procedure of data preprocessing; in Sect.4 we describe catalogue creation process (learning and classification).

2. Support Vector Machine (SVM)

For separation into classes we used Support Vector Machine (SVM) – linear supervised algorithm of classification based on building linear separating function between objects of different classes.

Classifier accepts a training set – sample of objects where each one is associated with certain feature vector and predetermined class. During learning process, the classification problem with SVM brings to finding equation of linear function that separating objects into the classes. Such function may be scalar (in 1-dimensional feature space), linear function (in 2-dimensional), plane (3-dimensional) or hyperplane (n-dimensional). After learning, unlabeled (without known class) object with the known feature vector enters into feature space and the class of this objects determines by its position relative to the separating function.

In our case, the classification problem of objects with adjusted colour indexes is a binary one. We define the labels $d = -1$ and $d = +1$ for objects, which are galactic and extragalactic objects respectively, and also, for convenience, we normalize all colour indexes $\bar{x}_i$ to the [0;1] interval. If stars and extragalactic objects are linear divided in colour space, it is obviously to select separating hyperplane, that is defined by equation: $\bar{w}^T \bar{x} + b = 0$, where $\bar{w}$ - is a normal to the hyperplane (so-called weight vector), b - is a bias. We can solve the binary classification problem using, actually, set of hyperplanes; those hyperplanes do not cross any sample of objects of different classes and, geometrically, locates between samples of stars and extragalactic objects. Width of the stripe, consisting set of hyperplanes, equals $\frac{2}{\|\bar{w}\|}$.

But it is possible to select optimal separating hyperplane, which provides equidistance to samples. We accept that optimality is observed if distance between two boundary hyperplanes (tangent to samples of stars and extragalactic sources respectively) from the set of solves, is a maximal one subject to non-existence of objects from training data between boundary hyperplanes in colour space. We can formulate conditions of optimality by follows:

$$d_i(\bar{w} \cdot \bar{x}_i + b) = 1$$

$$\Phi(\bar{w}) = \frac{1}{2} \|\bar{w}\|^2 \to \min$$

This optimization problem can be formulated in the Lagrangian:

$$J(\bar{w}, b, \alpha) = \Phi(\bar{w}) - \sum_i \alpha_i (d_i(\bar{w} \cdot \bar{x} + b) - 1)$$

where α_i – Lagrange multipliers for each object from training sample. Setting $\frac{\partial J}{\partial \bar{w}}, \frac{\partial J}{\partial b} = 0$, we obtain the solution:

$$\bar{w} = \sum_i \alpha_i d_i \bar{x}_i$$

$$\sum_i \alpha_i d_i = 0$$

allowing us to redetermine the optimization problem in the simpler, non-quadratic, form:

$$J(\alpha) = \sum_i \alpha_i - \sum_{i,j} \alpha_i \alpha_j d_i d_j \bar{x}_i \bar{x}_j$$

The weight vector $\bar{w}$ is a linear combination of the vectors from training sample, but summing occurs only for the objects for which $\alpha_i \neq 0$. This property is called sparsity and it is the main otherness of SVM from linear classifiers. Objects, for which $\alpha_i \neq 0$, are called support vectors.

In the case of linear indivisibility of samples, it is necessary to provide coordinate transformation to other one (Mercer, 1909), in which we can 1) provide search of linear separating hyperplane or 2) minimize the degree of blending of two samples. We can determine a parameter C for regulation of ratio of the minimization a classifying error and the maximization width separating stripe.

3. Data preprocessing

WISExSCOS cross-identification. Examined catalogue has been derived from the combination of two all-sky catalogues: WISE and SuperCOSMOS (SCOS). Considering the precision of determining position of sources — $< 0.15''$ for WISE (Wright et.al., 2010) and $< 0.30''$ for SCOS (Hambly et.al., 2010a), the catalogues were paired using a matching radius of $0.5''$. In the resulting cross-matched sample were held removing objects for which not all photometric information in bands $W1, W2, W3, W4, J, H, K$ (WISE), B, R, I (SCOS) is available. Wherein all 4 photometric bands from SCOS catalogue ($B, R1, R2, I$ (Hambly et.al., 2010b)) were used, but during filtration the averaging of $R1$ and $R2$ magnitudes for objects were done. After that, the resulting catalogue consisted of 235,232,381 objects.

Akhmetov et.al. (2017) proposed that interstellar extinction is an important application in separating plane building; to reduce false classifications, caused by interstellar reddening as distortion of colour space (Meingast et.al, 2017), we limited our WISExSCOS sample at galactic latitude $|b| > 7°$.

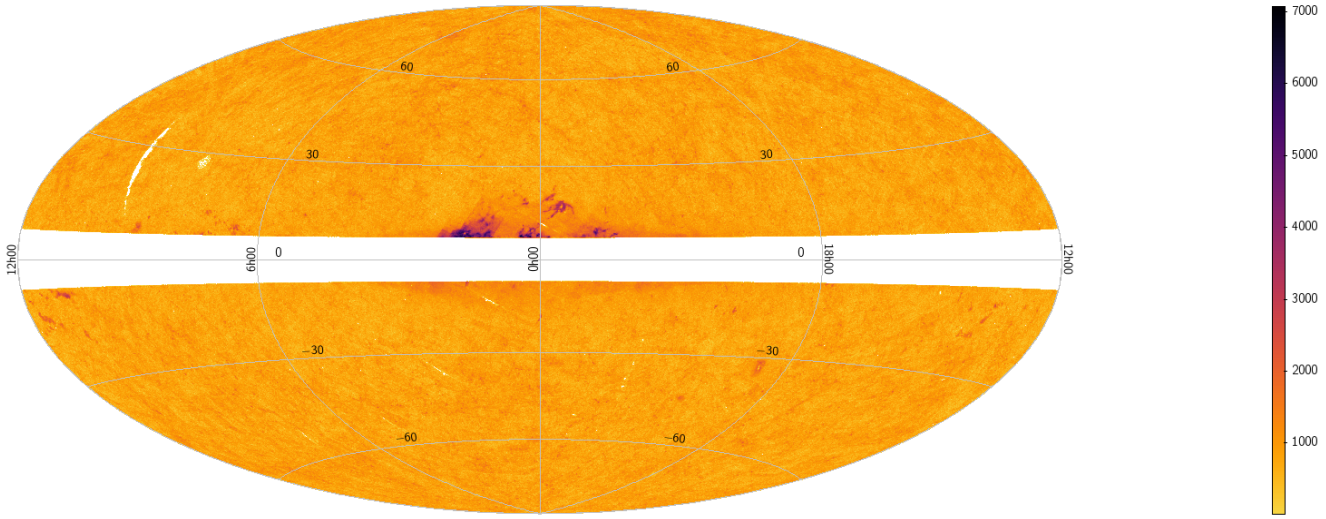

Figure 2: Aitoff density map in Galactic coordinates of 8 million objects, classified as extragalactic from WISExSCOS catalogue ($l = 0°, b = 0°$ at the centre)

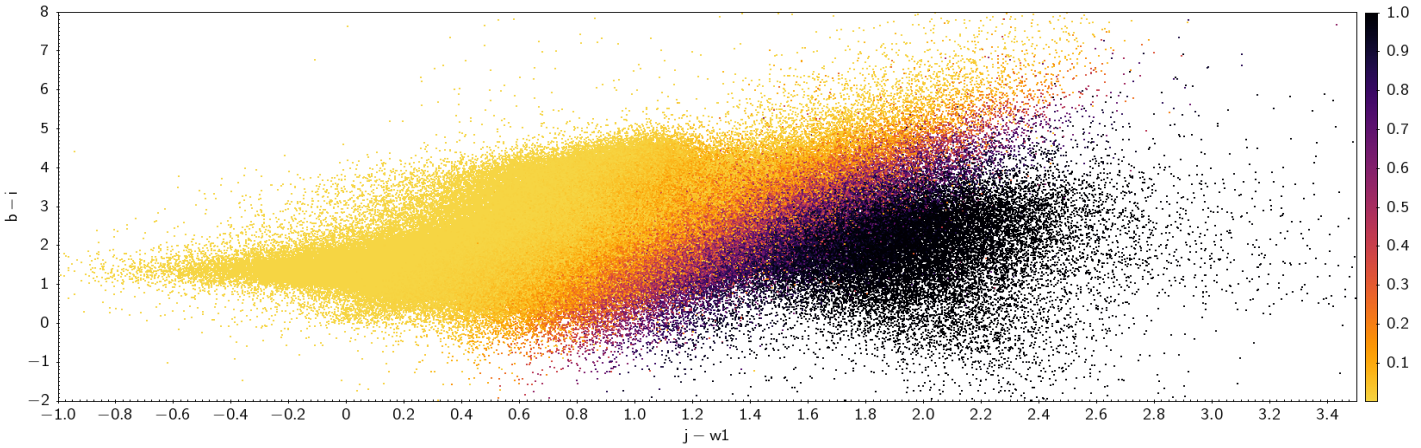

Figure 3: Colour-colour diagram (J− W1, B− I) of objects from training sample. Color bar representing the probability that object is extragalactic source.

Training set formation. Training sample was derived from 2MASX (Skrutskie et al., 2006) and GAIA DR1 (Gaia Collaboration, 2016) catalogues, assuming, that selected samples consists of the extragalactic and galactic objects respectively. We randomly extracted 50,000 objects, paired with WISExSCOS, for each catalogue. Resulting training sample included photometric information about 100,000 objects (labeled as star or extragalactic source) in 10 bands.

Colour space construction. We formed 45 colour indexes as pairwise differences of 10 magnitudes for each object from the training sample and from WISExSCOS catalogue. For building colour space for learning and classification, we produced visual feature selection of the colours of training sample as checking all two-colour diagrams.

In result we selected 6 colours, which provides clear separation of stars and extragalactic sources: $J-W1, B-I, W1-W2, W2-W3, J-W3, H-K$.

In constructed 6-dimensional colour space further learning within the training sample and classification of objects from WISExSCOS were performed. According to the selected colours it is seen, that lead role in separating extragalactic sources from stars belongs to infrared colours (Jarrett et al., 1998; Pollo et al., 2010).

4. Classification\separation process

To create the catalogue of candidates in extragalactic objects, we need to enter WISExSCOS objects alternately in the constructed colour space with existing separation hyperplane in it; the class of object determines by dint of position of the one in colour space relatively hyperplane, built during learning of SVM classifier.

Classifier were trained within 100,000 labeled objects (Gaia DR1 and 2MASX); learning was held by entering training sample and form of non-linear transformation (some kernel function). We selected Radial Basis Function (RBF) as kernel of space transformation: $\exp[-\gamma \| \bar{x}_i - \bar{x}_j \|^2]$, where $\| \bar{x}_i - \bar{x}_j \|$ - is an Euclidean distance in unreduced feature space.

Quality of learning, and also selecting parameters γ and C, were provided by classical methods of analysis of classification process – by the accuracy metric (accuracy score) using n-fold cross validation method (Kohavi, 1995).

Accuracy metric – is a way to quantify a proportion of the true classifications of the algorithm during training process:

$$acc_i = \frac{TS + TG}{TS + TG + FS + FG}$$

for i iteration, where the components of the equation are True Stars (TS), True Galaxies (TG) from the training sample, classified as stars and extragalactic objects respectively; False Stars (FS), which are real extragalactic objects from training sample, but classified as stars, and False Galaxies (FG) – labeled objects as `stars` in training data, but classified as extragalactic objects. Using n-fold cross validation, we used $n = 3$ meaning, that whole training data were split into three equal parts, and for one iteration classifier was trained on two of them; total accuracy of three-iteration learning process is defined as:

$$A_{total} = \frac{\sum_i acc_i}{3}$$

Classifier was trained with accuracy 97.9% within $C - \gamma$ combinated as $\gamma = 0.201$ and $C = 21$. For learning and classification, we used LIBSVM (Chang & Lin, 2011), integrated package for Support Vector Machine classification. Also we used Anaconda (Python distribution) – free open-source environment for large-scale data processing.

In result, we got catalogue of 8,290,477 objects (Fig. 2), identifying by SVM as extragalactic sources with probability $p > 0.5$ (Fig. 3).

5. Conclusion

Resulting photometric catalogue of candidates in extragalactic sources is one of the most accurate (in the sense of learning accuracy) catalogues of galaxies, that was got by automatic classification within colour indexes. Here we presented high quality of solving star-galaxy separation in analysis of modern deep-imaging all-sky photometric catalogues by automatic classification algorithm. However, the results obtained by us contradict the one presented earlier. Krakowski et al. (2016) showed, that final separation of galaxies from WISExSCOS catalogue consists ~15,000,000 objects; Bilicki et al. (2016) presented similar approach to identify ~19,000,000 extragalactic objects. Also, in these works the masking of high-extinction sky regions were provided much better than in this paper. Summing results, it is obvioulsy that portion of extragalactic objects in earlier investigations equals ~35% of all WISExSCOS objects; we got amount of extragalactic sources equaling ~4% of all objects. This fact can be explained by differences of training data and constructed colour space, so now a comparative analysis of the previously proposed methods with the method described in this paper is carried out.

In future we plan to focus on identification of specific extragalactic objects (quasars, AGNs, LRGs, ETGs, etc.) within our resulting catalogue of extragalactic sources.

References

Bilicki, M., Peacock, J., Jarrett, T., et al.: 2016, *ApJS*, **225**, 1, 5.

Chang, C.-C., Lin, C.-J.: 2011, *ACM Transactions on Intelligent Systems and Technology*, **2**, 27:1-27:27, software available at http://www.csie.ntu.edu.tw/cjlin/libsvm.

Gaia Collaboration: 2016, *A&A*, **592**, A2.

Hambly, N., Davenhall, A., Irwin, M., et al.: 2001a, *MNRAS*, **326**, 1315.

Hambly, N.; Irwin, M.; MacGillivray, H.: 2001b, *MNRAS*, **326**, 1295.

Jarrett, T., Chester, T., Huchra, J., et al.: 1998, *AAS*, **192**, 5515J.

Kohavi, R.: 1995, *Proceedings of the Fourteenth IJCAI*, **2 (12)**, 1137-1143.

Krakowski, T., Małek, K., Bilicki, M. et al.: 2016, *A&A*, **596**, A39.

Kurcz, A., Bilicki, M., Solarz, A. et al.: 2016, *A&A*, **592**, A25.

Kurcz, A., Krupa, M., Bilicki, M. et al.: 2015, *preprint (arXiv:1512.03604)*.

Meingast, S., Lombardi, M., Alves, J.: 2017, *A&A*, **601**, A137.

Peacock, J., Hambly N., Bilicki M., et al.: 2016, *MNRAS*, **462**, 2085.

Pollo, A., Rybka, P., Takeuchi, T.: 2010, *A&A*, **514**, A3.

Skrutskie, M., Cutri, R., Stiening, R., et al.: 2006, *AJ*, **131**, 1163-1183.

Solarz, A., Bilicki, M., Gromadzki, M. et al.: 2017, *A&A* [in press].

Mercer , J.: 1909, Philos. Trans. Roy. Soc. London, A, 209, 415-446.

Vapnik, V.: 1979, Estimation of Dependences Based on Empirical Data [in Russian], Nauka, USSR.

Vickers, J., Röser, S., Grebel, E.: 2016, *AJ*, **151**, 99.

Wright, E., Eisenhardt, P., Mainzer, A., et al.: 2010, *AJ*, **140**, 1868.

DOI: http://dx.doi.org/10.18524/1810-4215.2017.30.114488

ACCURACY OF MYKOLAIV ASTEROID OBSERVATIONS WITH DIFFERENT REFERENCE CATALOGUES

N.V.Maigurova, A.V.Pomazan, D.V.Bodryagin, L.E.Bondarchuk

Research Institute "Mykolaiv Astronomical Observatory", Mykolaiv, Ukraine
nadija@mao.nikolaev.ua

ABSTRACT. The results of astrometric reductions of main belt asteroid observations with usage of 3 different reference catalogues are presented. The high precision catalogs CMC15, UCAC4 and GAIA DR1 were used as reference catalogues for calculation asteroid equatorial coordinates. The asteroid observations were carried out at KT-50 telescope of the RI "MAO" Mobitel complex during 2016. The array contains 1666.positions of 68 asteroids mainly in range of (11 – 15) magnitudes. The differences (O – C) were calculated by comparing the obtained topocentric positions with the HORIZONS ephemerides of the JPL laboratory. The mean square errors of the (O – C) values were used for comparison of the different reductions model. The influence of the choice of the reference catalog on the random and systematic asteroid position errors is shown.

Keywords: CCD observations, reference catalogs, main belt asteroids, topocentric positions, ephemerids.

1. Reference Catalogs for Asteroid Astrometric Reductions

For a now the main source of asteroid positional data is the Minor Planet Center (MPC) database [http://www.minorplanetcenter.net/iau/mpc.html]. The database contains almost all available observations of asteroids beginning from 1896. The format of the records of modern observations includes information about of the reference catalog that was used to obtain the positions of the asteroids. Unfortunately, despite the recommendations of the MPC to use UCAC4 catalog [Zacharias et al., 2013] as the reference catalog, the number of used reference catalogs is increasing even for modern CCD observations. Although most of these catalogs nominally reproduce the ICRS system, the existing systematic differences between affect the uniformity of the data obtained by combining long-term observations to investigate slowly evolving effects. The previous study of the influence of the reference catalog on the accuracy of long –term time asteroid positional data showed that the errors of individual observatories exceed errors caused by the use of different reference catalogs [Maigurova rt al., 2017].The main goal of the presented work was to compare the results of the uniformly made astrometric reductions with 3 different high-precision reference catalogs: UCAC4, CMC15 [http://svo2.cab.inta-csic.es/vocats/cmc15/], GAIA DR1 [Gaia collaboration, 2016].

2. Asteroid Observations and Reductions

The array of main belt asteroid CCD observations obtained on the telescope KT-50 of the Mobitel complex RI "MAO" during 2016 was used to perform uniform astrometric reductions in 3 different reference catalogs. Mobitel complex was operated for observations since 2011. The telescope KT-50 (F = 3000mm, D = 500mm) is equipped with Alta U9000 camera (3Kx3K, 12x12mkm, 42.5'x42.5' FOV, 0.83"/pixel) in photometric band OG-14 (near standard R_c band). The detailed description of the complex is given in [Shulga et al., 2012]. The processing of the received observations was carried out by the package "Astrometrica" version 4.10.0.431 [http://www.astrometrica.at] with usage spherically symmetric Gaussian function as the PSF function, the fourth-degree polynomial as a model for linkage between measured and tangential coordinates and the usage of UCAC4 catalog as the reference one. 1666 positions of 68 asteroids were received during 2016 in UCAC4 catalog system, that sent to the MPC database. This array was reprocessed with usage the CMC15 and GAIA DR1 catalogs as reference one. The distribution of the obtained observations over the celestial sphere is shown in Fig. 1.

Uneven distribution is explained the fact that due to weather conditions and technical reasons, observations were only made during the period from April to October. Observations of each object were performed by series. The number of frames in the series was from 5 to 15. The histogram of the distribution of objects on the stellar magnitude is shown in Fig. 2. As can be seen from the histogram, the main part of the observed asteroids were objects in the range of (14 -16) magnitude.

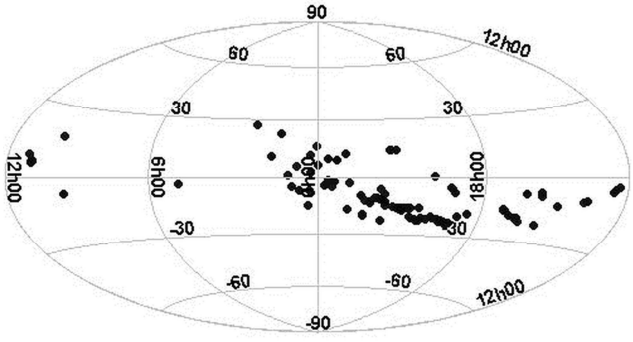

Figure 1: Distribution over the celestial sphere

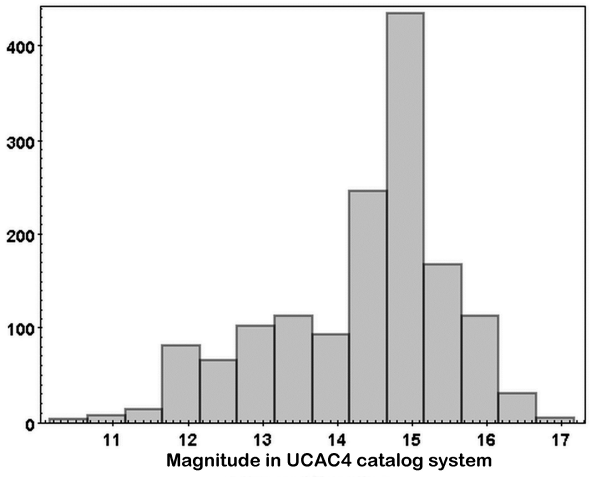

Figure 2: Histogram of the asteroids distribution on the stellar magnitude.

3. Accuracy Analysis

3.1. HORIZONS Ephemeris Comparison

The duration of a series of frames of one object usually didn't exceed 30 minutes, so the positions of the object in a series of frames were calculated with fixed set of reference stars on a small arc of the orbit. These circumstances make it possible to use the mean square error (MSE) of the residual differences (O-C), where (O) is the position obtained from the observations, (C) – the ephemeris position at the time of observation, as an estimate of the intrinsic precision of our measured positions. The online service HORIZONS of the NASA JPL laboratory [https://ssd.jpl.nasa.gov/?horizons] was used to obtain the ephemeris value (C).

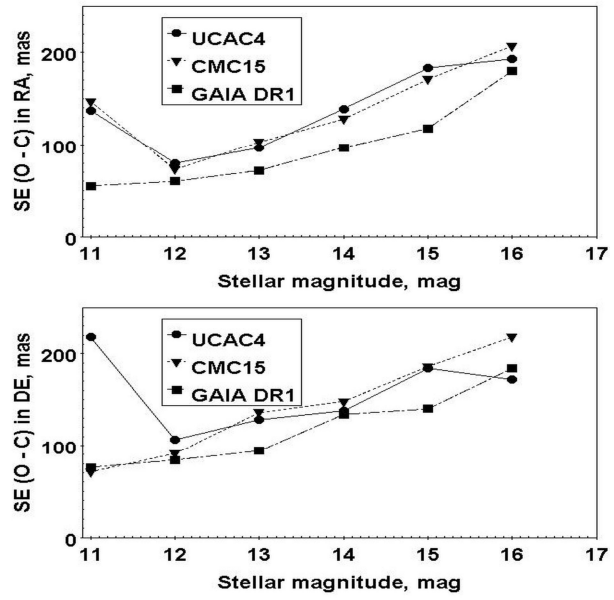

Figure 3: MSE on right ascension (up) and on declination (down) versus asteroid apparent magnitude

Fig. 3 shows the relation of the averaged MSE on the right ascension (up) and the declination (down) as a function of the asteroid stellar magnitude in the instrumental band for 3 different reference catalogs. As can be seen from the figure, in addition to the dependence on the stellar magnitude, there is a dependence on the reference catalog.

The results of comparing the residual differences (O-C) for individual asteroids with 3 reference catalogs are shown in Figure 4. Only asteroids with a number of observations more than 15 times were selected for the figure 4. The obtained results showed that the use of the GAIA DR1 catalog as a reference one in calculating topocentric positions reduces both random and systematic errors.

The mean values of residual (O-C) differences and their MSE obtained with usage different reference catalogs, when performing astrometric reductions, are shown in Table 1.

Table 1: The mean values of residual (O-C) differences and their MSE

Catalog	$(O-C)_{RA}$	CKO	$(O-C)_{DE}$	CKO
UCAC4	0.04	0.14	0.03	0.15
CMC15	0.02	0.13	0.13	0.14
GAIA DR1	0.02	0.10	0.05	0.13

The table data also show that the positions calculated with the reference catalogs UCAC4 and CMC15 have practically the same internal precision, but there is a significant difference from zero in values (O – C) in declination with reference catalog CMC15, that probably due to the lack of proper motions in the catalog. The position accuracy with the UCAC4 catalog is somewhat worse due to decreasing accuracy of the reference stars weaker than 15^{mag} in the UCAC4 catalog. As can be seen from the Table 1, the use of the GAIA DR1 as reference catalog allows improving the precision of the obtained positions by 15-20% compared with the use of UCAC4 and CMC15 catalogs. It should be noted, that UCAC4 is the MPC recommended catalog.

3.2. External Accuracy

In this paper, the results of performing of the astrometric reductions of the observational array of the main belt asteroids obtained at KT-50 Mobitel complex in 2016 are presented. As already noted above, all asteroid positions with UCAC4 catalog were sent to the MPC database. To estimate the external accuracy of our observations and compare them with the data of other observatories, we used the MPC statistics results for all observatories over 2011-2017 [http://www.minorplanetcenter.net/iau/special/residuals.txt]. Total 967 observatories were sent asteroid observations during this period. Only 486 of them had sent to MPC more than 100 asteroid positions during year. The Figure 4 shows the histogram of distribution of total MSE of the mean annual residual differences (O-C) for these observatories. It should be noted that value for RI "MAO" observations (Code MPC 089) is 0.35″ (0.23″ in right ascension and 0.26″ in declination).

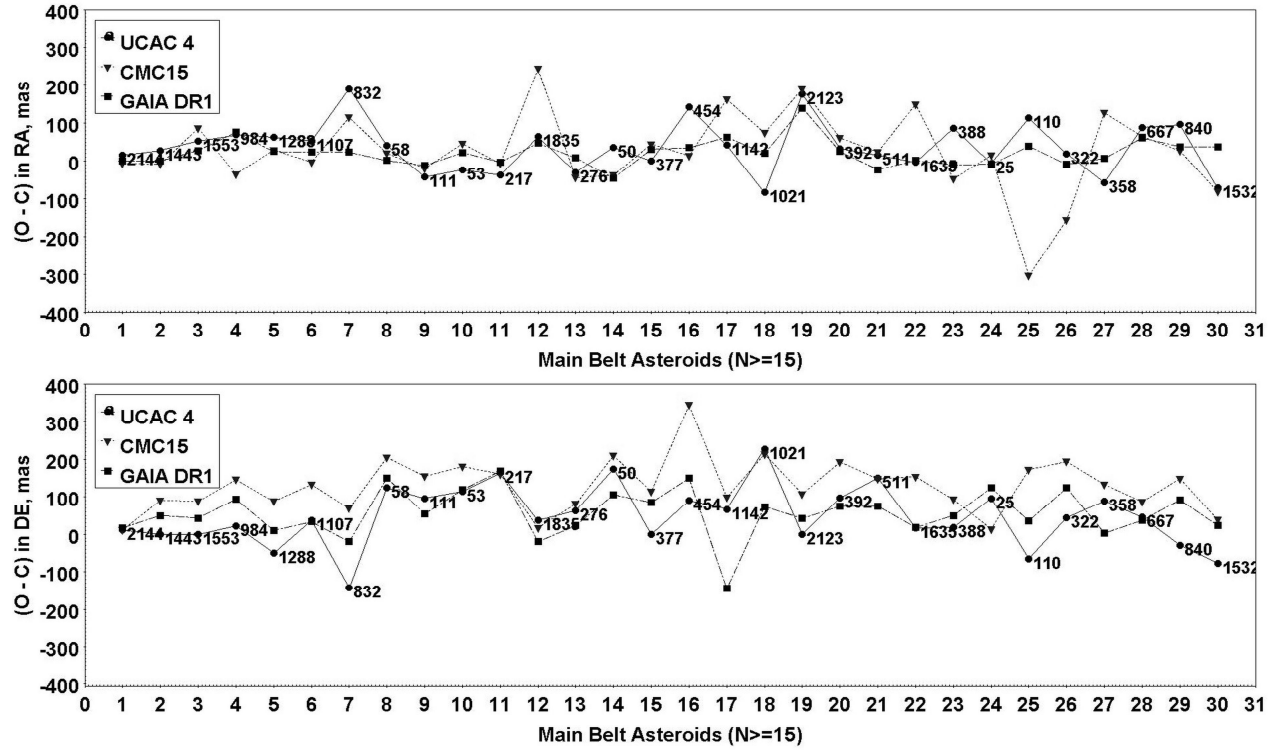

Figure 4: Residual differences (O – C) in right ascension (up) and declination (down) for asteroids with N>=15, calculated with different reference catalogs.

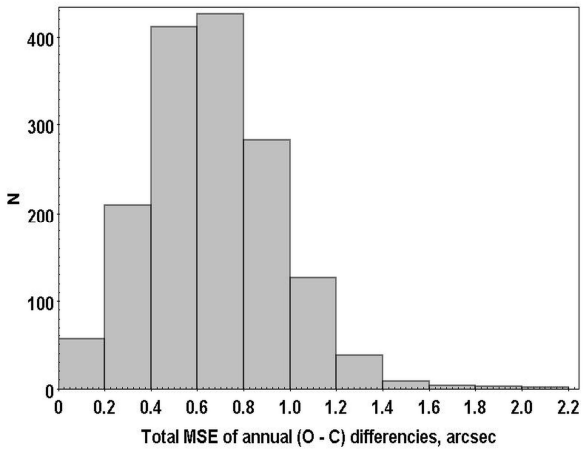

Figure 5: Distribution of total MSE of the mean annual residual differences (O – C) for the observatories with number of observations more than 100

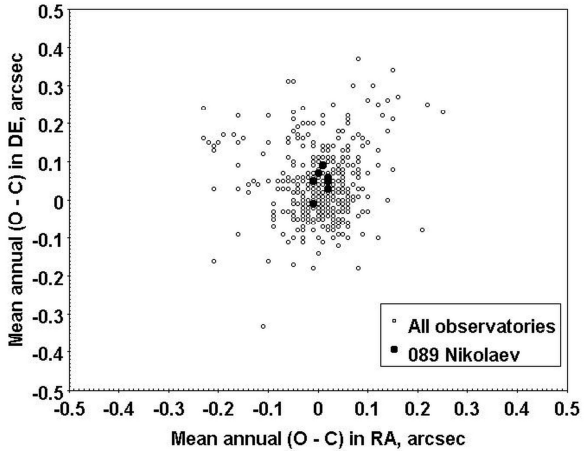

Figure 6: Mutual distribution of the mean annual (O – C) differences

The mutual distribution of the mean annual residual differences is shown in Fig. 5. Only 190 observatories with total MSE better than 0.5″ are presented in the figure. For these observatories, the mean values of the annual residual differences (O – C) are (-0.00 ± 0.08)″ and (0.04 ± 0.09)″. It can be seen from the Fig. 5 that (O – C) value in declination slightly differs from zero as for our data.

4. Conclusion

Topocentric equatorial coordinates referred to 3 modern astrometric catalogs were obtained for the array of asteroid observations at RI"MAO" during 2016. Results of astrometric reductions are shown that the use of the GAIA–DR1 catalog as reference one leads to a significant improvement in the position accuracy both for the random and for the systematic component. The positions obtained with the catalogs UCAC4 and CMC15 have practically the same accuracy in a random ratio, but in the system (O-C) in declination with usage CMC15 reference catalog, a significant non-zero difference have found.

Acknowledgements. This research has made use of the on-line service JPL HORIZONS, MPC database and TOPCAT software [Taylor, 2005]. The authors are grateful to colleagues who have taken part in observations of comets: N.Kulichenko, M.Kaliuzny, V.Kryuchkovskiy.

References

Astromerica, [on-line]. Available at: http://www.astrometrica.at
Carlsberg Meridian Catalog 15 (CMC15) [on-line]. Available at: http://svo2.cab.inta-csic.es/vocats/cmc15/
Gaia collaboration: 2016, *A&A*, **595**, A1-A7, A133.
HORIZONS System, [on-line]. Available at: https://ssd.jpl.nasa.gov/?horizons
Minor Planet Center, [online]. Available at: http://www.minorplanetcenter.net/iau/mpc.html
Minor Planet Center, [online]. Available at: http://www.minorplanetcenter.net/iau/special/residuals.txt
Maigurova N.V., Chernetenko Yu.A., Kryuchkovsky V.F.: 2017, *Sci. Innov*., **13**, 1, 75.
Shulga A.V., Kozyrev E.S., Sibiryakova E.S. et al.: 2012, *Space science and technology*, **18(4)**, 70 [in Russian]
Taylor M.: 2005,*ASPC*, **347**, 29T.
Zacharias N., Finch C., Girard T. et al.: 2013, *Astron. J.,* **145**, 44.

DOI: http://dx.doi.org/10.18524/1810-4215.2017.30.114407

INVESTIGATION OF THE MICROTEK SCANMAKER 1000XL PLUS SCANNER OF THE INSTITUTE OF ASTROPHYSICS OF THE AKADEMY OF SCIENCES OF THE REPUBLIC OF TAJIKISTAN

A.Mullo-Abdolov[1], G.Kokhirova[1], H.Relke[2], Q.Yuldoshev[3], Yu.Protsyuk[4], V.Andruk[5]

[1]Institute of Astrophysics of AS of Republic Tajikistan, *aziz.sherzod@gmail.com*

[2]Walter Hohmann Observatory, 159, 45133 Essen, Germany, *helena_relke@yahoo.com*

[3]Ulugh Beg Astronomical Institute of the Uzbek Academy of Sciences, 33 Astronomicheskaya St., 100052 Tashkent, Uzbekistan, *qudratillo@astrin.uz*

[4]Research Institute "Mykolaiv Astronomical Observatory", 1 Observatornaya St., 54030, Mykolaiv, Ukraine, *yuri@nao.nikolaev.ua*

[5]Main Astronomical Observatory of the National Academy of Sciences of Ukraine, 27 Akademika Zabolotnoho St., 03680 Kyiv, Ukraine, *andruk@mao.kiev.ua*

ABSTRACT. This work was done to estimate the accuracy of the processing method of photographic plates and the detailed study of the Microtek ScanMaker 1000XL Plus scanner, which plans to be used for the digitizing of about 1600 photographic plates of the Astrophysics Institute of the Academy of Sciences of the Republic of Tajikistan (Dushanbe) recorded for the FON project. For the processing of these photographic plates will be used software created in the LINUX/MIDAS/ROMAFOT environment. Six sequential scans of a single plate (1150, the Pleiades cluster) with a spatial resolution of 1200 dpi were processed to evaluate the repeatability of the scanner's astrometric and photometric errors. The size of photographic plates is 8 x 8 degrees (30 x 30 cm or 13000 x 13000 pixels). The estimated errors of the scanner for the stars brighter than $B < 13.5^m$ are $\sigma_{xy} = \pm 0.054$ pixels for the rectangular coordinates and $\sigma_m = \pm 0.020^m$ for the instrumental magnitudes. The estimated astrometric accuracy of the processing of stellar fields of photographic plates in the system of the Tycho-2 catalogue is $\sigma\alpha\delta = \pm 0.13"$.

Keywords: photographic plates, scanning, processing of digitized plates, astrometry, photometry, data analysis.

1. The Photographic Survey of the Northern Sky – FON project

The plan of the photographic observation of the Northern Sky (FON project) was proposed in 1976 by Main Astronomical Observatory of Ukraine (Goloseevo) scientists I.H.Kolchinskii and A.B.Onegina (Kolchinskii, 1977). The detailed overview of the current stage of the FON project was done by L.K.Pakuljak (Pakuljak, 2016). The idea of the FON project emerged from the state of photographic astrometry in the early 1970s. Suffice to say that the coordinate systems which were built in the past were significantly worsened because of the inaccuracies of the proper motions. It was necessary to create a homogeneous coordinate system that would be able to solve the problems of the modern astrometry, astronomy and cosmology. The main factors contributing to the development of the project were:

1. The completion of the Carte du Ciel project (CdC, Map of the Sky), started at the end of the 19th century and resulted with the creation of an accuracy stars catalog down to the 11th magnitude and a photographic stars atlas down to the 14th magnitude. As the result of the digitization of CdC data performed in the 1980s at the Sternberg Astronomical Institute (GAISh) was created an Astrographic Catalogue (AC) of 4 millions stars on the epoch 1950.0. The idea of the re-observing the sky with modern instruments was very attractive. Moreover the difference of more than 70 years between the observing epochs gave the opportunity to became proper motions for a large number of stars with the greatest accuracy at that time.

2. The development of an algorithm to handle an array of overlapping fields as a whole, using variables that describe the general as well as the individual parameters of the photographic plates (Google, Eichhorn & Lucas, 1970). As was shown by Eichhorn the solution of the system with tens thousands of unknowns taken into account the instrumental aberrations ensured on the best way the uniformly accuracy of the catalogue created on the base of overlapping fields.

3. Almost simultaneously in the 1970s some astronomical observatories of the former Soviet Union were equipped with the identical wide-angle Astrographs produced by the Carl Zeiss Company (Jena, Germany) with an aperture of 40 cm and focal distances of 2 or 3 meters. The observatories taking part in FON project: Holosievo, Zelentschuk, Zvenigorod, Dushanbe, Abastumani and Kitab were divided into four groups. The North Sky must be photographed four times with an overlapping. Each group photographed the sky independently according to a common schema with a shift of the centres of the fields on 2 degrees in such a way to get the fourfold overlapping. Observations were made with an exposure to became suitable for the measurement images of

stars down to 16-17 magnitude. Additional short exposure with a shift of the centre of the field on both coordinates was made on the same plate to correct the brightness equation. Such work distribution between the observatories gave advantages to the FON project compared with the zone observations. Each star would be photographed at least four times by different telescopes, which is very important to avoid systematic errors in the future catalogue.

2. History of the realization of the FON project on the GisAO, Dushanbe, Tadjikistan

The Gissar Observatory of the Institute of Astrophysics of the Academy of Sciences of the Republic of Tajikistan (GissAO) also participated in the implementation of the FON project. Regular observations began in 1985 and continued until 1992. The observations were carried out by Hamburg O., Mullo-Abdolov A., Relke E., Tsyhankova M., Kiselev N. The 1578 photographic plates were recorded. During this period by Relke H. was prepared a dissertation, which was successfully defended in April 1993 at the Goloseevo Observatory, Kyiv. In the frame of the thesis "Creating an astrometric standard in the Swan constellation" were developed and applied the algorithms for the reduction of the photographic plates of the FON project. The scientific leader of the dissertation was Dr. Kislyuk Vitaly Stepanovich, the head of the astrometry department of the Main Astronomical Observatory of Ukraine (Goloseevo). The main results were published in the following works (Kislyuk, Relke, 1992; Relke, Gamburg, 1993; Relke, 1993; Relke, 1991).

Owing to the unstable political situation of the 1990s, the lack of financial resources and the forced departure of almost 75 percent of the scientific staff, all scientific projects of the Institute of Astrophysics were interrupted including the observation for the FON project. During this time the observatories of the Institute of Astrophysics were plundered, almost all costly telescopes and equipment were severely damaged.

After the end of the Civil war the remaining staff of the Institute of Astrophysics with the help and support of russian specialists took over the rehabilitation of the institute's observatories. The telescopes of the GissAO and Sanglok observatory were repaired and equipped with modern technologies. Thanks to the staff of the Institute of Astrophysics all photographic plates of the FON project were retained and moved to a safe place, where they have been stored for more than 20 years. All photographic plates are in good condition. Over the years of the existent of the Institute of Astrophysics a huge photographic material was been accumulated. The modern technologies allow now the processing of all accumulated material on a new more higher level. Thanks to the support of the Academy of Sciences of Tadjikistan the Institute of Astrophysics was able to acquire a modern scanner, which plans to be applied for the scanning of the institute's photographic material to create a digital library. On the basis of the scanned photographic plates of the FON project is planned the creation of a catalogue of the Gissar Observatory. The scientists of the observatories of Goloseevo and Nikolayev (Ukraine), Kitab (Uzbekistan) and Walter Hohmann (Germany) have provided significant support in the instructing of using of scanner and processing of photographic plates for the FON project. So, at the Ulugh Beg Astronomical Institute of the Uzbek Academy of Sciences Mullo-Abdolov was trained in the using of the scanner and it's basis software. The scientists of the Goloseevo observatory have provided the software developed for the processing of scanned images. Digitized images are planned to be processed at Goloseevo, Nikolayev, Kitab, Walter Hohmann and GissAO observatories. The first step in the digitization and processing of photographic plates is the study of the astrometric and photometric characteristics of the scanner.

3. Errors of the Microtek ScanMaker 1000XL Plus scanner

In this work for the investigation of the astrometric and photometric characteristics of the Microtek ScanMaker 1000XL Plus scanner the authors used the procedures previously applied in the series of works (Golovnya, 2010; Eglitis, 2017; Muminov, 2013; Protsyuk, 2014b). The developed software for the processing of the digitized images is described in publications (Andruk, 2015a; Andruk, 2017; Protsyuk, 2014a). Six consecutive scans of the same plate number 1150 photographed with two exposures (1 and 27 minutes) were processed to estimate the astrometric and photometric errors of the scanner (Andruk, 2012).

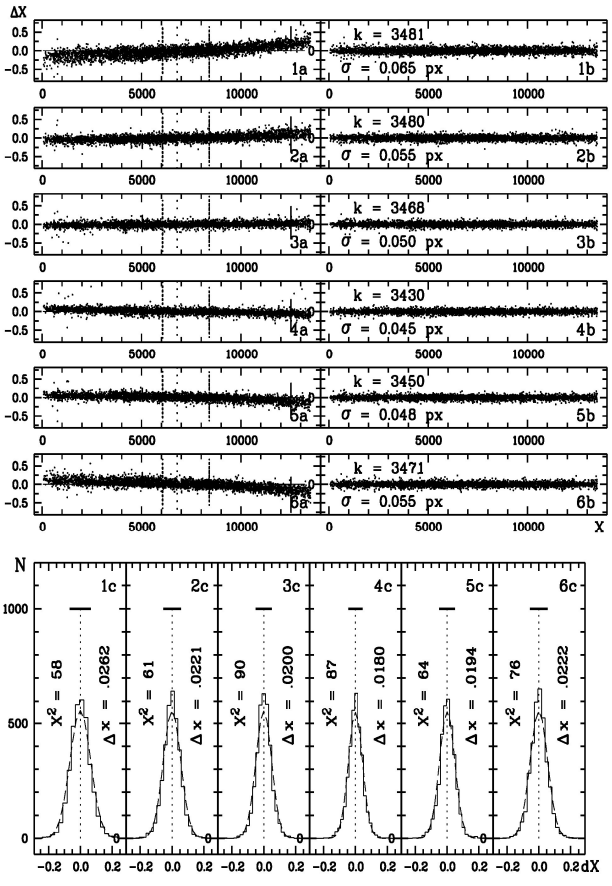

Figure 1: The trends of the differences between the sixconsecutive scans and the imaginary average scan for the X-coordinates.

The scanning was completed with a spatial resolution of 1200 dpi (Protsyuk, 2014c). The performing of calculations of all registered bright objects (approximately 3450) was done in the following way: the average values for the rectangular coordinates X, Y as well as for the instrumental magnitudes m of all objects were obtained by averaging of the corresponding valuesfor all objects over the six scans. On such a way we created an imaginary average scan. On the left side of Figure 1 are illustrated the trends of differences between the six consecutive scans and the imaginary average scan calculated for the X-coordinates (1a, 2a, 3a, 4a, 5a, 6a). After the correction of differences of each scan for the systematic errors we have results are shown on the right side of the Figure 1 (1b, 2b, 3b, 4b, 5b, 6b). The values of the standard deviation (SD) of one difference of coordinate for all six scans are indicated on the Y-axis. At the bottom of the Figure 1 are shown the frequency distributions of these differences. Differences are given in the form of real (continuous lines) and theoretical (dashed lines) distribution functions on appropriate intervals. The values of the length of intervals Δx and the values of X^2 are shown on the right and on the left respectively. The corresponding trends of the differences for the Y-coordinates are given in the Figure 2 and for the instrumental magnitudes m in the Figure 3.

The trends of the astrometric differences for the Y-coordinate have any breaks, which is probably due to the irregular movement of the carriage with the CCD linear. The results are shown in Figure 1, 2 and 3 were obtained for the stars having the B magnitudes brighter than 13.5^m. As you can see the errors of one definition of differences for the rectangular coordinates are σ_{xy} = 0.045 pixels and 0.066 pixels, errors in the definition of magnitudes do not exceed the values of $\sigma_m = 0.018^m$ and 0.022^m.

By transform to the equatorial coordinate system it is necessary to take into account the scale factor of 2.2. By transform to the Johnson system, the instrumental magnitudes should be corrected for the scale factor of 1.5 due to the contrast of the photo emulsion. Taking into account the scale factors the following conclusion can be made: The using of the flatbed Microtek ScanMaker 1000XL Plus scanner together with the developed software enables the digitizing and processing of the photographic plates as well as the obtaining of characteristics of the objects (high, moderate and faint brightness) with internal errors better than 0.1" and 0.04^m. For the more finer objects (B = 16^m – 17.5^m) these errors could be approximately twice worser. This result is based on the earlier studies for the photographic plates of the 30 x 30 cm size with the 1200 dpi scanning modes.

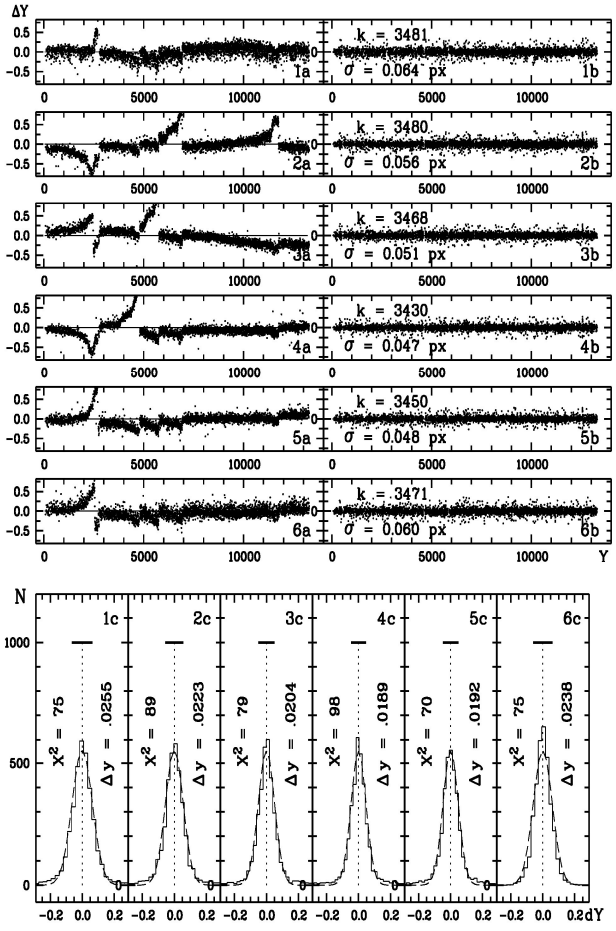

Figure 2: The trends of the differences between the six consecutive scans and the imaginary average scan for the Y-coordinates.

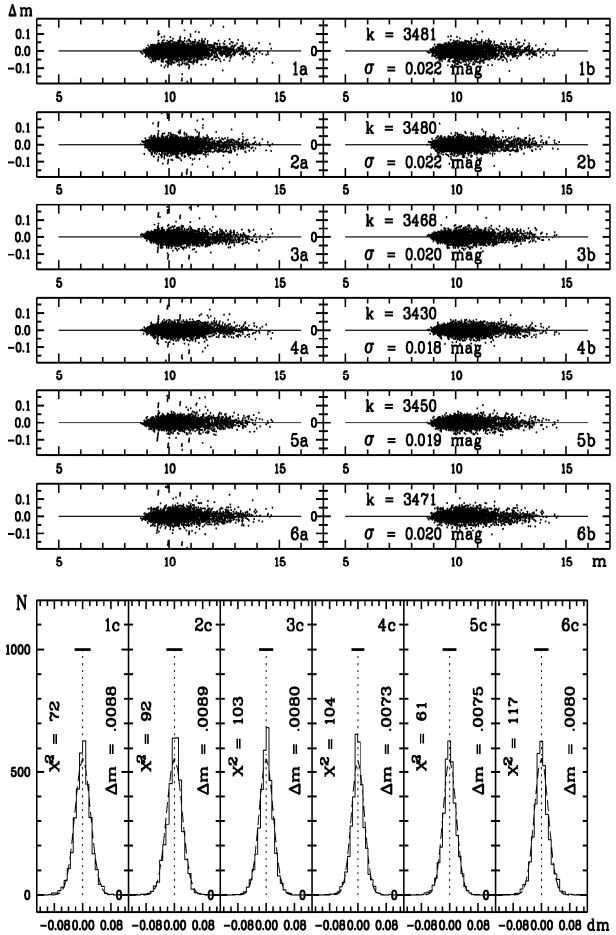

Figure 3: The trends of the differences between the six consecutive scans and the imaginary average scan for the instrumental magnitudes m.

The six top panels on the left of the Figure 4 show the trends of the scanner's systematic errors (1a, 1b, 1d, 1e) for the coordinates and the brightness equation (1 c, 1f) before the correction for the scanner's systematic errors. On the right the corresponding reduction errors after the correction for the scanner's systematic errors, brightness equation as well as for the aberrations of the telescope optics. Two lower panels illustrate the distribution of the reference stars from the Tycho-2 catalogue over the field of the plate No. 1150 (left) and the characteristic curve in the system of B-magnitudes Tycho-2 catalogue.

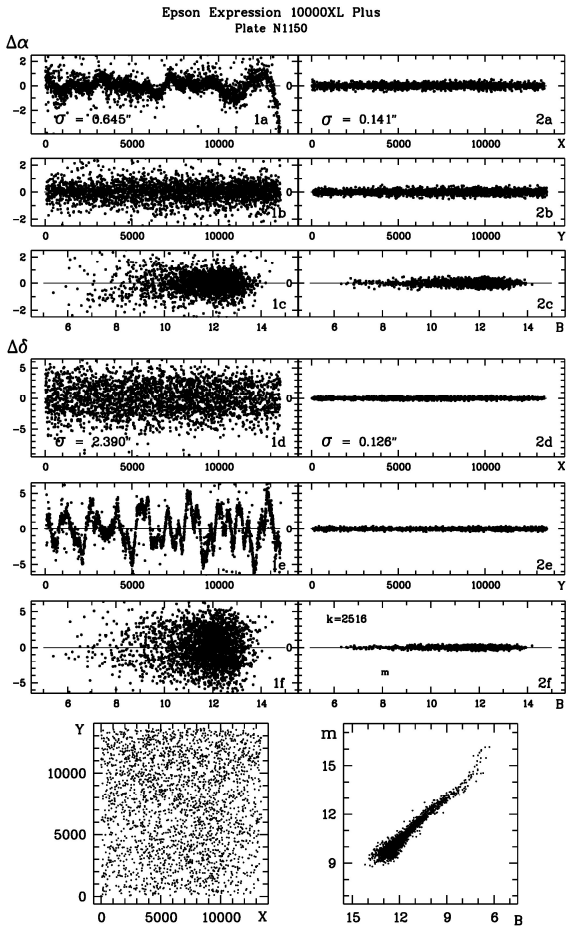

Figure 4: On the left: the trends of the systematic errors for coordinates (1a, 1b, 1d,1e) and the brightness equation (1 c, 1f) before the correction for the scanner's systematic errors. On the right: the corresponding reduction errors after the correction for the scanners systematic errors, brightness equation as well as for the aberration of the telescope optics. Two lower panels show the distribution of the reference stars from the Tycho-2 catalogue over the field of the plate No. 1150 (left) and the characteristic curve in the system of B-magnitudes Tycho-2 catalogue.

4. Conclusion

The results of the performed work concerning the astrometric and photometric characteristics of the processing of photographic plates digitized by the Microtek ScanMaker 1000XL Plus scanner allowed to make the following conclusion: Within the precision of reduction of photographic plates the scanner is suitable for the performing of astrometric and photometric works for the terrestrial astronomy and in particular for the FON project (Andruk, 2014; Andruk, 2015b; Andruk, 2016a; Andruk 2016b; Pakuliak, 2016; Relke, 2015; Yuldoshev, 2017). Errors of one measurement are 0.1 arc seconds for the equatorial coordinates and 0.04^m for the B-magnitudes.

Acknowledgements. The authors are thankful to academician Farhod Rahimi, the President of Academyof Sciences of the Republic of Tajikistan, for the supporting of the project "Creating of the digital archive of the GissAO" and help by the acquirement of the scanner. The photographic plates which were recorded for the FON project could be scanned and on the base of these digitized images will be created a new catalogue of the north sky down to the 17th magnitude.

References

Andruk V.M., Ivanov G.A., Yatsenko A.I. et al.: 2012, *Bull. T. Shevchenko Nat. Univ. Kyiv., Astron.* **N48**, 11 (in Ukraine)

Andruk V.N., Golovnya V.V., Ivanov G.A. et al.; 2014, *Odessa Astron. Publ.,* **27,** 53.

Andruk V.N., Pakuliak L.K., Golovnya V.V. et al.: 2015, preprint, *arxiv.org/abs/1512.05535.*

Andruk V.M., Pakuliak L.K., Golovnia V.V. et al.; 2015, *Odessa Astron. Publ.,* **28,** 192.

Andruk V.M., Golovnia V.V., Ivanov G.A. et al.: 2016, *Kinem. Phys. Cel. Bodies*, **32, N1,** 38.

Andruk V.M., Pakuliak L.K., Golovnia V.V. et al.: 2016, *Kinem. Phys. Cel. Bodies*, **32, N5,** 260.

Andruk V.M., Pakuliak L.K., Golovnia V.V. et al.: 2017, *Science and Innovation*, **13a, N1,** 17.

Eglitis I., Andruk V.: 2017, *Open Astronomy*, **26, N1**, 7.

Golovnya V., Andruk V., Yatsenko A.: 2010*, J of Phys. Studies,* **14, N2**, 2902 (in Ukraine).

Googe, W. D., Eichhorn, H., Lucas, C. F. Mon.Not.R. Astr. Soc., 1970, N 150, p. 35 – 44.

Kislyuk, V. S., Relke, H. 1992KFNT....8b..56K

Kolchinskii I.G., Onegina A.B.: 1977, *Astrometry and Astrophysics*, **N33**, 11 (in Ukraine).

Muminov M.M., Kahharov B.B., Yuldoshev K.H. et al.: 2013, I*zvestija GA Pulkovo*, 220, 517.

Pakuliak L.K., Andruk V.M., Golovnia V.V. et al.: 2016, *Odessa Astron. Publ.,* **29, N1**, 132.

Protsyuk Yu.I., Andruk V.N., Kazantseva L.V.: 2014, *Odessa Astron. Publ.*, **27, N1,** 59.

Protsyuk Yu.I., Andruk V.N., Kazantseva L.V. et al.: 2014, *Odessa Astron. Publ.*, **27, N1**, P..61.

Protsyuk Yu.I., Kovylianska O.E., Protsyuk S.V. et al.: 2014, *Odessa Astron. Publ.,* **27, N1**, 63.

Relke E., Protsyuk Yu.I., Andruk V.M. et al. 2015, *Odessa Astron. Publ*., **28, N2,** 211.

Relke, H., Gamburg, O. *Bulletin of the Institute of Astrophysics of the Academy of Science of Tadjikistan,* N. 81, 1993.

Relke, H., Gamburg, O. *Bulletin of the Institute of Astrophysics of the Academy of Science of Tadjikistan,* N. 81, 1993.

Relke, H. *Bulletin of the Institute of Astrophysics of the Academy of Science of Tadjikistan,* N. 81, 1993.

Relke, H. *1991ATsir1551...36R*

Yuldoshev Q.X., Ehgamberdiev Sh.A., Muminov M.M. et al.: 2017, *Kinem. Phys. Cel. Bodies*, **33, N5,** 250.

DOI: http://dx.doi.org/10.18524/1810-4215.2017.30.114490

THE ASTROMETRIC RESULTS OF OBSERVATIONS OF PERIODICAL COMETS AT KT-50 TELESCOPE IN RI "MAO"

A.V.Pomazan, N.V.Maigurova, O.V.Shulga

Research Institute «Mykolaiv Astronomical Observatory», Mykolaiv, Ukraine
antpomaz@gmail.com

ABSTRACT. The astrometric results of the observations of 10 periodical comets in 2017 are presented. The observations were made with telescope KT-50 telescope in RI «Mykolaiv Astronomical Observatory». The differences between the measured from observations (O) and calculated from ephemeris (C) positions and their mean square errors (MSE) were calculated. The ephemeris positions were taken from on-line computation service HORIZONS (JPL NASA, USA). For the measured positions the average MSE values are 0.17″ in right ascension and 0.18″ in declination respectively. Analysis of the values (O-C) before and after additions of obtained positions to Minor Planet Center (MPC) database revealed a gradual decrease of these differences with respect to the ephemeris. This indicates that the using of the new high-precision positions allows us to refine the calculated ephemeris. As well improvement and lengthening of the astrometric datasets play important role in the modeling of the cometary nongravitational effects.

Keywords: Astrometry, observations, comet, telescope.

1. Introduction

Comets originally formed in the cold outer planetary system and composed mostly of water ice with embedded dust particles. The scientific interest in comets and asteroids is due largely to their status as the relatively unchanged remnant debris from the solar system formation process. These objects may represent potentially catastrophic threats to our planet depending on their size and relative speed. The problem of asteroid-comet hazard is one of the priority tasks in modern astronomy. It is necessary to observe these objects regularly and as long as possible to reliably determine their orbits with better accuracy and produce more precise impact warnings. However, the comets like asteroids that are potentially the most hazardous because they can closely approach the Earth are also the objects that could be most easily exploited for their raw materials.

Comets observations in the Research Institute "Mykolaiv Astronomical Observatory" (RI MAO) have a long history. The earliest positions sent to the Minor Planet Center (MPC) database [http://www.minorplanetcenter.org/iau/mpc.html] refer to the observations of comet C/1882 R1-B in 1882. The observations carried out visually using a micrometer. Table 1 gives statistics data and accuracy of comets observations over whole history of observations at the RI «Mykolaiv Astronomical Observatory».

As can be seen from table 1, there are three main stages of observations of comets in the RI MAO: 1) visual observations using a micrometer with average accuracy (mean square error, MSE) 2.566″ in RA and 2.094″ in Dec; II) photographic observations with average accuracy 0.663″ and 0.543″ in RA and Dec respectively; III) CCD observation; mean accuracy of 0.230″ and 0.217″ in RA and Dec respectively.

The modern accuracy of comet positions allows us not only to refine the calculation of ephemerides, but also to make assumptions about the presence and magnitude of non-gravitational effects on the basis of comparison of the calculated and observed positions.

2. Instruments and observations

Newly open and periodic comets were observed at KT-50 telescope of Mobitel complex at RI «Mykolaiv Astronomical Observatory». The ephemerides of the HORIZONS system (JPL NASA, USA) [http://ssd.jpl.nasa.gov/horizons.cgi] were used to provide a list of observable comets.

The Mobitel complex was designed at the RI MAO under supervision of Shulga, A.V. (*Shulga et al., 2012*). Currently, the telescope has been equipped with only one optical glass OC-14 (GOST 9411-91) filter. The filter provides a bandwidth close to that of R_c standard filter of the Cousins system.

The specific feature of observations is the use of time delay integration (TDI) mode for all observations. The exposure was selected in such way as to achieve a good signal-to-noise ratio (SNR) based on the apparent magnitude presented in HORIZONS ephemeris system (JPL NASA, USA). The duration of exposure was 120 s for 80% of observations. It corresponds to a frame size of 3056 x 980 pixels and a field of view 42.4'×13.5'.

The 241 observations of 10 comets were obtained at RI MAO during 2017. The comet topocentric positions were sent to MPC database with observatory code 089 (*Kulichenko et al., 2017*).

Table 1: Statistics of comet's observations in RI «Mykolaiv Astronomical Observatory»

Year	Number of comets	Number of positions	O – C, ″		MSE, ″	
			RA	Dec	RA	Dec
1882	1	2	-1.769	0.550	-	-
1890	1	9	1.458	-0.189	1.895	1.735
1898	2	9	-4.174	-1.000	1.957	2.847
1900	1	10	-0.166	-0.620	3.847	1.701
Visual observations		**30**	**-1.163**	**-0.315**	**2.566**	**2.094**
1968	1	1	-0.869	-1.700	-	-
1974	1	9	-0.178	0.092	1.053	0.519
1985	2	131	-0.238	-0.189	0.602	0.562
1986	2	46	-0.634	-0.162	0.660	0.586
1990	1	5	-0.099	0.460	0.618	0.321
1996	2	50	-0.096	-0.232	0.241	0.660
1997	1	28	-0.343	-0.069	0.802	0.612
Photographic observations		**270**	**-0.265**	**-0.017**	**0.663**	**0.543**
2005	1	27	0.264	0.555	0.149	0.316
2011	5	163	-0.129	0.045	0.272	0.170
2012	14	222	0.235	0.064	0.402	0.244
2013	2	32	0.129	-0.025	0.112	0.212
2014	5	312	0.041	0.155	0.165	0.285
2015	2	30	0.626	-0.532	0.280	0.077
CCD observations		**786**	**0.194**	**0.044**	**0.230**	**0.217**

3. Processing and astrometric reductions

Accurate astrometric observations of comets are possible only during their approach to the Earth and the Sun. Unfortunately most comets have a large coma or areole at that time. This leads to an erroneous identification of the photometric center of brightness with the center of mass. According to research performed by *Chesley et al.* (2001) the true nucleus position of the comet was more accurately defined if the brightest pixel were used rather than positions based upon a best-fitting two-dimensional Gaussian fit to the photometric image. Based on this assumption, we have used brightest pixels only for measuring of comet's positions on images.

The "Astrometrica" software has been used for processing of obtained observations. Radially symmetric Gaussian function was used to getting instrumental coordinates of the reference stars in the system matrix. The 4-th order polynomial with GAIA DR1 (*Gaia collaboration, 2016*) as reference star catalog was chosen to connection model between the tangential and the measured coordinates. Astrometric reductions were made without bias, dark and flat corrections.

To compare such two measuring method we have made a test measuring of positions of the comet JOHNSON (C/2015 V2) observed on May 30, 2017. Measured positions presented in Table 2.

Presented *MSE* values of residuals between ephemerid (C) and measured (O) positions show better accuracy for those positions measured by picked up brightest pixels with aperture around 2 FWHM (it is correspond line with 8 pixels aperture). Such aperture was selected to measure of positions of all observed comets.

Table 2: Accuracy of positions measured by two different methods

Apeture, px	O – C, ″		MSE, ″	
	RA	Dec	RA	Dec
5	0.062	0.021	0.192	0.269
12	0.062	0.028	0.207	0.285
*5	0.048	-0.029	0.122	0.224
*8	0.075	-0.094	0.087	0.187

* The brightest pixels only were picked up for measuring the positions of comet.

4. Analysis of measured positions of comets

We have made the comparison of observed positions (O) with the calculated ephemeris (C) provided by on-line service HORIZONS (JPL NASA, USA) and have calculated the residuals (O − C) in both coordinates, which are listed in Table 3.

The Table 3 contains the date of observation, the number of frames, magnitude of the object, (O − C) differences and their standard errors (*MSE*) in both coordinates. The mean internal accuracy of single position is 0.169″ in right ascension and 0.184″ in declination. It was calculated using standard deviations (O − C) in positions for each series of observations.

The comparison of observed and calculated positions is given by distribution of single values of (O − C) and mean of the series of observations on Fig. 1 a) and b). On Fig. 1 b) each point represents the mean of the series of measurements of each comet per night. So, one can find points there which correspond to the same comet, but obtained in different observational periods. The error bars correspond to one-sigma interval.

Table 3: Astrometric accuracy of measured positions of observed comets

Comet	Number of positions	Date of observations	mag*, N-mag	RA		Dec	
				O – C, ″	MSE, ″	O – C, ″	MSE, ″
29P	3	27-06-2017	14.6**	-0.095	0.210	0.215	0.224
29P	9	30-07-2017	14.5**	0.104	0.085	0.057	0.147
29P	2	01-08-2017	14.5**	0.115	0.086	0.160	0.063
29P	9	13-09-2017	14.5**	0.465	0.174	0.084	0.256
29P	9	14-09-2017	14.5**	0.603	0.158	0.031	0.204
29P	9	17-09-2017	14.6**	-0.425	0.308	-0.072	0.328
29P	8	18-09-2017	14.6**	-0.322	0.158	0.060	0.168
41P	9	02-06-2017	14.3**	0.381	0.062	-0.017	0.072
41P	9	06-06-2017	14.5**	0.388	0.072	0.048	0.159
41P	9	26-06-2017	16.1**	-0.172	0.106	0.059	0.104
41P	8	30-06-2017	16.4**	-0.113	0.110	-0.066	0.177
65P	5	26-06-2017	16.2	-0.062	0.311	-0.952	0.368
65P	3	30-06-2017	16.3	-0.115	0.402	-0.565	0.372
C/2015 ER61	6	18-09-2017	16.5	0.380	0.186	0.053	0.200
C/2015 O1	9	01-06-2017	16.2	0.048	0.139	0.014	0.131
C/2015 O1	10	02-06-2017	16.2	0.090	0.060	-0.029	0.082
C/2015 O1	8	06-06-2017	16.2	0.023	0.111	0.230	0.214
C/2015 V2	10	30-05-2017	8.8**	0.158	0.091	-0.012	0.174
C/2015 V2	15	01-06-2017	8.8**	0.059	0.073	0.019	0.087
C/2015 V2	5	02-06-2017	8.8**	0.030	0.058	-0.151	0.071
C/2015 V2	9	06-06-2017	8.8**	0.040	0.087	-0.006	0.132
C/2015 VL62	6	13-09-2017	16.0	-0.463	0.392	0.191	0.180
C/2015 VL62	9	14-09-2017	16.0	0.022	0.335	0.029	0.573
C/2015 VL62	9	17-09-2017	16.1	-0.352	0.262	0.462	0.239
C/2015 VL62	9	18-09-2017	16.1	-0.124	0.513	0.133	0.232
C/2016 M1	6	14-07-2017	16.9	-0.003	0.094	-0.009	0.146
C/2016 M1	9	17-07-2017	16.9	0.018	0.092	0.128	0.089
C/2016 M1	5	18-07-2017	16.9	0.020	0.088	0.106	0.058
C/2016 M1	9	19-07-2017	16.9	0.006	0.135	0.151	0.157
C/2016 R2	6	03-10-2017	16.0	0.233	0.157	-0.235	0.123
C/2017 O1	9	03-10-2017	15.6	-0.171	0.115	-0.020	0.177

* Comet's approximate apparent visual nuclear magnitude.
** Comet's approximate apparent visual total magnitude (T-mag).

The comparison of observed and calculated positions is given by distribution of single values of (O – C) and mean of the series of observations on Fig. 1 a) and b). On Fig. 1 b) each point represents the mean of the series of measurements of each comet per night. So, one can find points there which correspond to the same comet, but obtained in different observational periods. The error bars correspond to one-sigma interval.

To estimate external accuracy of our observations and to compare our results with other observatories we have made analysis of "residuals.txt" file presented on IAU MPC site. We have selected two lists of observatories: I) those one have least (O – C) and their errors; II) those one have the largest number of observations. For analysis were selected only data since 2010. The observations of 10 comets observed in RI MAO in 2017 were taken for each observatory form those lists. Table 4 and 5 represent the (O – C) values and their errors for list I and II respectively.

5. Conclusions

The 241 positions of the 10 periodic comets were obtained from observations at KT-50 telescope in RI "MAO" in 2017.

The accuracy of obtained positions were analyzed to respect to ephemerides calculated by service HORIZONS (JPL NASA, USA). The mean values of (O – C) and MSE are $0.042'' \pm 0.200''$ in RA and $-0.087'' \pm 0.353''$ in Dec respectively.

Analysis of the values (O – C) before and after additions of obtained positions to Minor Planet Center (MPC) database revealed a gradual decrease of these differences with respect to the ephemeris. This indicates that the using of the new high-precision positions allows us to refine the calculated ephemeris. As well improvement and lengthening of the astrometric datasets play important role in the modeling of the cometary nongravitational effects.

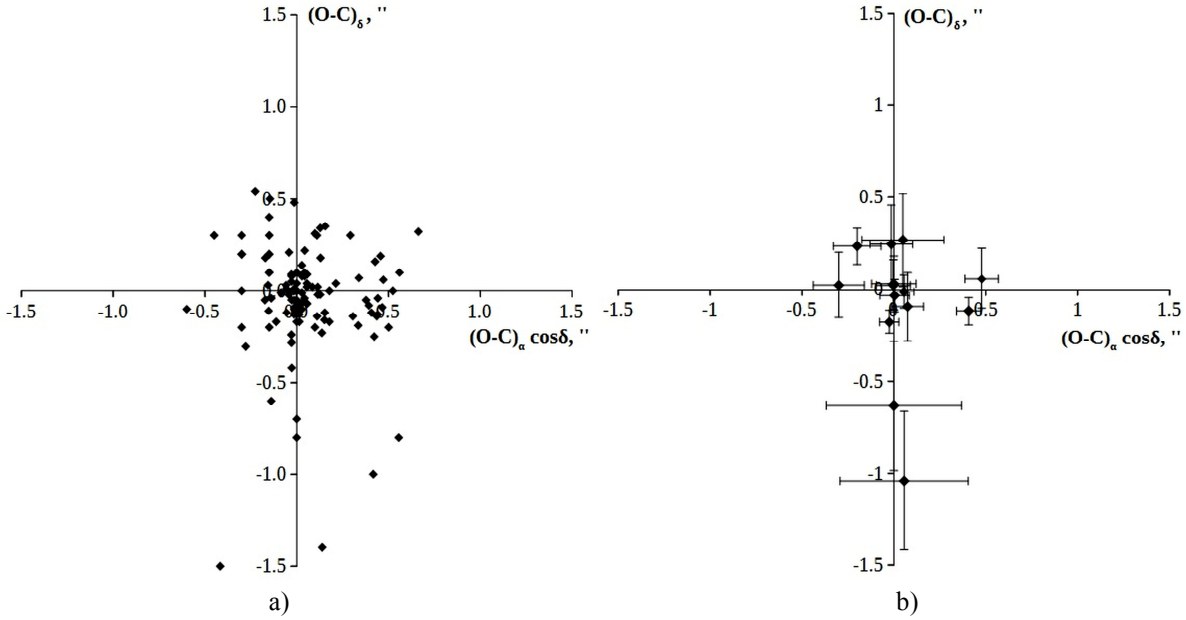

Figure 1: Distribution of: a) single values of (O – C); b) mean values of (O – C) for series.

Table 4: Comparison of O – C values and their errors for list of selected observatories with good accuracy of asteroids observations

Obs. code	Num of positions	RA		Dec	
		O – C, ″	MSE, ″	O – C, ″	MSE, ″
089*	241	0.025	0.169	0.003	0.184
168	33	-0.208	0.197	0.086	0.176
213	96	0.140	0.519	0.179	0.295
215*	63	0.166	0.302	0.000	0.237
987	36	-0.086	0.232	0.120	0.173
A71	47	0.002	0.290	0.362	0.385
B74	24	-0.013	0.395	0.046	0.152
C47	196	0.012	0.204	0.046	0.180
D95*	74	0.068	0.232	0.072	0.332
F51	34	0.056	0.144	-0.585	0.471
G40*	98	0.095	0.255	-0.044	0.217
I72	54	-0.088	1.476	0.478	1.504
J01	143	0.126	0.361	0.128	0.359

* The observatories which have the observations of 10 comets observed in RI MAO in 2017.

Table 5: Comparison of O – C values and their errors for list of selected observatories with a large number of asteroids observations

Obs. code	Num of positions	RA		Dec	
		O – C, ″	MSE, ″	O – C, ″	MSE, ″
160	297	0.017	0.294	0.037	0.213
585	477	0.070	0.210	0.192	0.308
703	32	-0.493	2.294	1.369	1.192
A77	302	0.117	0.962	-0.027	0.612
C23	300	0.007	0.256	0.101	0.179
F51	34	0.056	0.144	-0.585	0.471
H45	267	-0.023	0.174	-0.012	0.150
I81	211	0.008	0.422	0.133	0.472
J22	246	0.099	0.366	-0.083	0.517
K02	195	0.126	0.209	-0.042	0.173
Q11	138	0.134	0.247	0.035	0.273
T05	150	-0.107	0.212	0.018	0.257
T08	133	-0.081	0.204	-0.150	0.214

Acknowledgements. This research has made use of the on-line service JPL HORIZONS and database MPC. The authors are grateful to colleagues who have taken part in observations of comets: N. Kulichenko, M. Kaliuzny, V. Kryuchkovskiy, D. Bodryagin.

References

Astrometrica, [online]. Available at: http://www.astrometrica.at
Chesley S. R., Chodas P. W., Keesey M. S. et al.: 2001, *Bull. Am. Astron. Soc.*, **33**, 1090.
Gaia collaboration: 2016, *A&A*, **595**, A1-A7, A133.
JPL's On-Line Solar System Data Service, [online]. Available at: http://ssd.jpl.nasa.gov/horizons.cgi.
Minor Planet Center, [online]. Available at: http://www.minorplanetcenter.org/iau/mpc.html.
Minor Planet Circulars [online] Available at: http://www.minorplanetcenter.net/iau/ECS/MPCArchive/2017/MPC_20171005.pdf, MPC_20170709.pdf, MPC_20170609.pdf.
Minor Planet Electronic Circ., [online]. Available at: http://www.minorplanetcenter.net/mpec/K17/K17N58.html
Shulga A.V., Kozyrev E.S., Sibiryakova E.S. et al.: 2012, *Space science and technology*, **18(4)**, 70 [in Russian].

DOI: http://dx.doi.org/10.18524/1810-4215.2017.30.114495

COLITECVS – NEW TOOL FOR AUTOMATED REDUCTION OF PHOTOMETRIC OBSERVATIONS

V. E. Savanevych [1], O. B. Briukhovetskyi [1], S. V. Khlamov [2], A. V. Pohorelov [3], V. P. Vlasenko [1], P. A. Dubovský [4], I. Kudzej [4], Š. Parimucha [5]

[1] Western Radio Technical Surveillance Center, National Space Agency of Ukraine, Mukachevo, Ukraine, *vadym@savanevych.com, izumsasha@gmail.com*

[2] Uzhhorod National University, Laboratory of space research, Uzhhorod, Ukraine, *sergii.khlamov@gmail.com, colitec@neoastrosoft.com*

[3] Kharkiv National University of Radioelectronics, Kharkiv, Ukraine, *artempogorelov@gmail.com*

[4] Vihorlat Observatory, Humenné, Slovakia, *var@kozmos.sk, vihorlatobs1@stonline.sk*

[5] Faculty of Science, UPJŠ Košice, Slovakia, *stefan.parimucha@upjs.sk*

ABSTRACT. The capabilities of telescopes allow us to make the plotting of light curves a routine task. This one shifts the main attention of astronomer from the plotting to research. To achieve this goal, we developed a new tool for automated reduction of photometric observations, which includes the computational method for the brightness assessment of the investigated and comparison stars; brightness equalization of astronomical images using inverse median filter; light curve plotting and its processing using different tools.

Keywords: CCD, photometric observations, light curve, star's brightness, reduction, inverse median filter.

1. Introduction

At the present time the astronomers have to perform a lot of actions to plot the light curve. This is caused by the fact that the programs for plotting light curves use only the images of objects indicated by the astronomer in the frame. Otherwise, there are areas of the astronomical researches, where the frames are processed completely, with assumption of the different parameters of all objects in frames. For example, the programs those realize the full processing of the asteroid surveys results and automatic detection for asteroids and comets in the series of CCD-frames such as CoLiTec (Savanevych V. E. et al., 2015).

Authors combined existing methods of the light curves creation with the methods for full frames processing with the parameters estimation of all objects in these frames. Before the light curve plotting the anomaly pixels in CCD-frames are taken into account; the preliminary segmentation of celestial objects images is carried out as well as the assumption of the brightness and equatorial coordinates of objects with automatic selection of reference stars in the frame.

2. Brightness equalization of astronomical images

Astronomical digital images may be divided into coarse-grained and fine-grained components. Coarse-grained components correspond to the illumination of the image during astronomical observations at full moon or at sunrise/sunset and cover large part of frame. Fine-grained components correspond to the images of celestial objects. The size of them usually takes 5 ÷ 10 pixels and no more than 50 ÷ 60 pixels.

Coarse-grained components of the image correspond to low-frequency harmonics image spectrum, and fine-grained components correspond to high-frequency harmonics. To remove coarse-grained components from the image it is possible to use a high-pass filter. Difference in sizes of objects images and background (coarse-grained components of astronomical images) allows using median filtering of the image for coarse-grained components extraction. To equalize the image background, the coarse-grained component obtained after median filtering is subtracted from the original image.

The inverse median alignment is used in conjunction with service frames. It is especially important to use a master-dark frame. All master-frames are formed pixel by pixel. 10% of the largest and 10% of the smallest values of brightness of the each pixel is tentatively discarded. For the remaining values of calibration frames the average and RMS are calculated. Brightness of the master-dark frame pixel is considered equal to the mean value of the pixel brightness only for pixels that do not differ from the mean by more than three RMS.

In contrast to the flat-calibration of frames, inverse median filter removes coarse-grained components that are caused by the illumination from the moon, the sun, and illuminations of anthropogenic origin.

In this paper as the brightness equalization quality indicators we use the mean value and RMS of background brightness on a set of background pixels of the investigated local segment before and after operation of equalization. As a result of the brightness equalization the range of average background pixels brightness values has decreased in 131 times (quantiles of the indicated local means 0,95 and 0,05 differs in 131 times) for the segments of 30x30 pixels and in 145 times for the segments of 50x50 pixels. At the same time, the RMS of background pixels brightness in the investigated segments has not significantly changed. The value of quantiles of local RMS at the level of 0.95 decreases in 1.2 times in segments of 30x30 pixels and in 1.3 times for segments of 50x50 pixels.

3. Computational method for the brightness assessment of the investigated star

The computational method for the brightness assessment of the investigated star, comparisons stars and light curve creation includes the following operations.

1. Selection of the comparison stars by observer or automatically by proximity to investigated star by the attributes (distance, brightness and spectral class). Automatically selection is performed in two stages. At the first stage, selection of the stars, information about which is presented in APASS9 catalog and the image of which is single. On the second stage, sorting of the stars after first stage by the attributes. After that the first nearest stars are selected.

2. Introduction of the frame's window for every frame of series and determination of the average instrumental brightness and its RMS of every star in it:

$$\overline{m}_{IRjn} = \frac{1}{N_W}\sum_{n=1}^{N_W} m_{IRjn}\ , \qquad (1)$$

$$\sigma_{jn} = \sqrt{\sum_{n=1}^{N_W}\left(m_{IRjn}\right)^2 \Big/ \left(N_W - 1\right) - \left(\sum_{n=1}^{N_W} m_{IRjn} \Big/ N_W - 1\right)^2}\ , \qquad (2)$$

where n – CCD-frame's number, j – star's number, m_{IRjn} – reducted instrumental brightness of j-th comparison star in n-th frame, N_W – frames number in assessment window of the average and RMS of reducted instrumental brightness of comparison star.

3. Exclusion of photometric measurements of comparison stars with anomaly error of instrumental brightness in frame:

$$\sqrt{\left(m_{IRjn} - \overline{m}_{IRjn}\right)^2} > \gamma\sigma_{jn}\ , \qquad (3)$$

where $\gamma = 2 \div 4$ – proportionality coefficient.

4. Determination of the brightness of artificial comparison star (average instrumental brightness of all available comparison stars):

$$m_{synn} = \frac{1}{N_{reffsel}}\sum_{j=1}^{N_{reffsel}} m_{Ijn}\ , \qquad (4)$$

where m_{synn} – instrumental brightness of artificial comparison star in n-th frame, $N_{reffsel}$ – number of comparison stars, m_{Ijn} – instrumental brightness of j-th comparison star in n-th frame.

5. Picking the pair of two or more comparison stars.

5.1. Determination of the reduction coefficient of the instrumental brightness of comparison star ℓ-th pair of comparison stars for n-th frame:

$$\eta_{\ell n} = \sum_{j=1}^{N_{accept\ell}} m_{Ijn} \Big/ \sum_{j=1}^{N_{accept\ell}} m_{IBj}\ , \qquad (5)$$

where m_{IBj} – instrumental brightness of j-th comparison star in the base frame, $N_{accept\ell}$ – stars number in ℓ-th pair of comparison stars.

5.2. Reduction of the instrumental brightness of comparison stars to the base frame:

$$m_{IRj(\ell,n)} = \frac{m_{Ijn}}{\eta_{\ell n}}\ , \qquad (6)$$

where $m_{IRj(\ell,n)}$ – reducted instrumental brightness of j-th comparison star in n-th frame using ℓ-th pair of comparison stars, $\eta_{\ell n}$ – reduction coefficient of the instrumental brightness from n-th frame to the base one using ℓ-th pair of comparison stars.

5.3. Determination of the weight of every star in the current pair:

$$\upsilon_{\ell j} = \frac{1}{\nu_\ell \sigma^2_{m\ell j}}\ , \qquad (7)$$

where $\upsilon_{\ell j}$ – weight of j-th comparison star using ℓ-th pair of comparison stars.

$$\nu_\ell = \sum_{j=1}^{N_{accept\ell}} \frac{1}{\sigma^2_{m\ell j}}\ , \qquad (8)$$

$$\sigma^2_{m\ell j} = \frac{\sum_{j=1}^{N_{beg}} \left(m_{IRj(\ell,n)}\right)^2}{N_{beg} - 1} - \left(\frac{\sum_{j=1}^{N_{beg}} m_{IRj(\ell,n)}}{N_{beg} - 1}\right)^2 \qquad (9)$$

– dispersion of the reducted instrumental brightness of j-th comparison star using ℓ-th pair of comparison stars.

5.4. Determination of the star's brightness in each frame for the selected pair:

$$m_{I\beta\ell n} = \overline{m}_{I\beta\ell} + \frac{1}{\upsilon_{\Sigma\ell}}\sum_{j=1}^{N_{accept\ell}} \upsilon_{\ell j}\left(m_{Ijn} - \overline{m}_{Ij}\right), \qquad (10)$$

$$\upsilon_{\Sigma\ell} = \sum_{j=1}^{N_{accept\ell}} \upsilon_{\ell j}\ , \qquad (11)$$

$$m_{VS\ell n} = m_{IVSn} - m_{I\beta\ell n} + m_{cat\beta}\ , \qquad (12)$$

$$m_{syn\ell n} = m_{synn} - m_{I\beta\ell n} + m_{cat\beta}\ . \qquad (13)$$

6. Picking the best pair of comparison stars by the minimum of brightness RMS of the artificial comparison star on frames:

$$\sigma_{syn\ell} = \sqrt{\frac{\sum_{n=1}^{Nbeg}\left(m_{syn\ell n}\right)^2}{N_{beg}-1} - \left(\frac{\sum_{n=1}^{Nbeg} m_{syn\ell n}}{N_{beg}-1}\right)^2}, \qquad (14)$$

where $\sigma_{syn\ell}$ – brightness RMS of the artificial star using ℓ-th pair of comparison stars, $m_{syn\ell n}$ – measured brightness of the artificial star in n-th frame using ℓ-th pair of comparison stars, N_{beg} – number of the raw CCD-frames, $m_{VS\ell n}$ – measured brightness of star in n-th frame using ℓ-th pair of comparison stars, m_{IVSn} – instrumental brightness of star in n-th frame, $m_{cat\beta}$ – brightness assessment of main comparison star from catalog, $m_{I\beta\ell n}$ – measured instrumental brightness of the main comparison star in n-th frame using ℓ-th pair of comparison stars.

4. CoLiTecVS workflow for the automatic data reduction

CoLiTec project created the universal system for the automatic data reduction – CoLiTecVS (Savanevych V. E. et al., 2015). This system allows astronomer creating the light curve of investigated variable star without manual-data handling between processing steps.

At first, astronomer with a telescope and specified software takes images of the interesting sky areas where the investigated variable stars are located. These raw images will be moderated before its processing. At this stage faulty and unsupported frames will be rejected by OLDAS system as soon as they are formed. This technique allows greatly speeding up the processing and provides user immediate notification of emerging issues. Also OLDAS determines the frames affiliation to the series and telescopes.

CoLiTecVS has the following workflow: forming the series of frames with the investigated variable star; brightness equalization of frames using master-frames and inverse median filter; assessment of the brightness of investigated star using the developed computational method; preparing the task-file with selected comparison stars; processing of the photometric observations; light curve creation of the investigated variable star. Created light curves can be viewed and analyzed using the specific modules of CoLiTecVS – PlotViewer or Virtual Observatory (VO).

5. Representation of the photometric observations in CoLiTecVS

PlotViewer is the local tool of CoLiTecVS for light curves viewing of the different variable stars and formed by the different telescopes. You can moderate these light curves by removing the faulty photometric observations of the investigated variable stars. Also you can change scale of the plot for the accurate investigation of photometric observations. It's important that the plot represents photometric observations even during the processing by updating plot when the new data arriving (fig. 1).

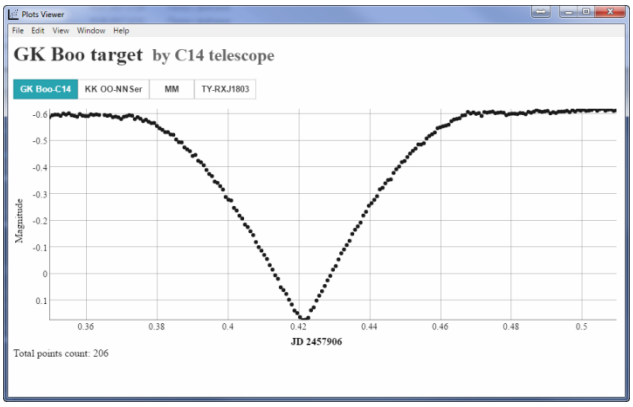

Figure 1: Light curve in PlotViewer

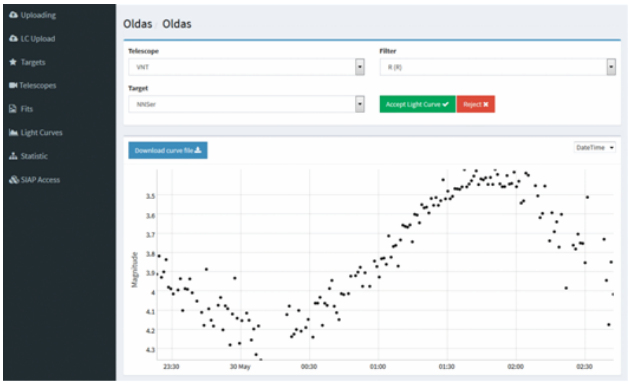

Figure 2: Light curve in VO

All processed photometric observations, light curves and even raw frames can be also sent to the Virtual Observatory (VO). These data are stored not only in the local database, but also published via SIAP protocol.

CoLiTecVS was designed according to IVOA recommendations for photometric data storing using cross-references. This one allows receiving all relevant information such as required frames, light curves or photometric observations. VO web-interface represents light curves as a graph of brightness measurements variation. It is plotted by measurements from storage, data from different catalogs and telescopes (fig. 2). Detailed information about the appropriate magnitude and dimension of this frame is displayed after clicking on a point of the graph that represents the specific measurement.

Light curves of the investigated variable stars should be moderated and accepted via web interface of VO. On this stage astronomer may review and edit all received light curves and specified data (filter, target name, measurements, etc.). Also, familiarization with the attached notes can help researcher with the analyze of investigated variable star. After editing and acceptance of the light curve the last one becomes publicity accessed.

6. Testing on real images

The CoLiTecVS software (Pohorelov et al., 2016) was developed in continuous testing on the archival images taken on the Astronomical Observatory on Kolonica Sad-

dle (Kudzej & Dubovský, 2010) with several instruments. We have compared the results of differential photometry acquired in usual way with the new automatic reduction.

6.1. Testing the influence of median filtering on the photometry results

Important part of the reduction process in CoLiTecVS is the calibration of the images. The user can choose various combination of processes like bias correction, dark-frame correction, flat-field correction and background brightness equalization by inverse median filter. We have already published the results of massive testing in Dubovský et al. (2017). The conclusion is that it can replace the master-flat application if there are no structures on the images background with size similar to the sizes of the stars. The ideal combination of calibration processes is: dark-frame, flat-field for removing the small structures and inverse median filtering for background equalization. If high quality flat-field is not available, then it is better to skip the flat-field calibration.

6.2. Testing the photometry tool of the CoLiTecVS

CoLiTecVS works as compact automatic toll. It takes raw images and provides light curves. It is not possible to cut one partial process and test it. But there is the possibility to take the images calibrated by CoLiTecVS and apply another photometry software on them. Exactly this was our approach. We have compared CoLiTecVS photometry of constant stars with the values obtained by conventional reduction process i.e. calibration and photometry performed with Muniwin software (Motl, 2009) and subsequently the ensemble photometry with MCV software (Kim et al., 2004). We have performed many comparisons with different instruments in different star fields. More than 100 time series were reduced. The typical result is shown on the Figure 3.

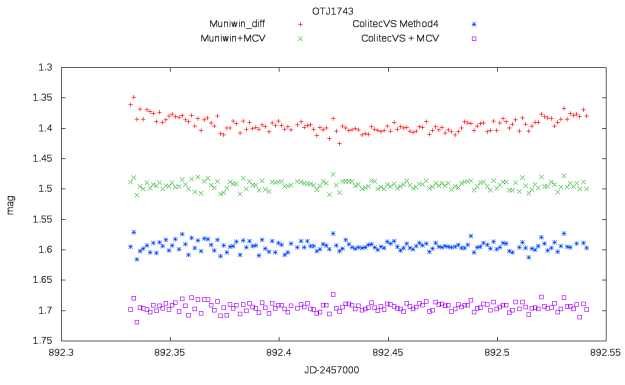

Figure 3: Comparison of photometry results of constant stars using different tools. The field of cataclysmic variable MASTER OT J174305.70+231107.8 was observed by Celestron 11" telescope equipped with MII G2-1600 CCD camera. The light curves are arbitrary shifted for clarity.

The meaning of the individual light curves is as follows: "Muniwin_diff" means single differential photometry with Muniwin software, one comparison star; "Muniwin + MCV" means ensemble photometry, instrumental magnitudes provided by Muniwin reduced by MCV software; "CoLiTecVS Method4" means ensemble photometry, fully automated output of CoLiTecVS; "CoLiTecVS + MCV" means ensemble photometry, instrumental magnitudes provided by CoLiTecVS reduced by MCV software.

The same result is presented also in numerical form in the Table 1.

Table 1: The means and standard deviations of the light curves depicted on the Figure 3.

	Mean	Standard deviation
Muniwin_diff	1.3935	0.0118
Muniwin + MCV	1.3935	0.0067
CoLiTecVS Method4	1.3939	0.0078
CoLiTecVS + MCV	1.3941	0.0070

The disadvantage of single comparison star is clearly visible. The trend with parabola shape is caused by extinction. The rest of the light curves are practically equal. So the CoLiTecVS can replace the conventional reduction process with the same precision and accuracy. If the user doesn't trust the automatic process completely, he has still the option to take instrumental output of CoLiTecVS and play with MCV. Especially removing the outstanding points on the light curves is still safer if doing manually.

7. Conclusion

New tool for automated reduction of photometric observations was developed. It includes the computational method for the brightness assessment of the investigated star, comparisons stars and light curve creation. The proposed method of inverse median filter application can be used for calibration of astronomical images without negative influence on the results of the photometry.

CoLiTecVS including VO technology is implemented in the Vihorlat Virtual Observatory (ViViO).

Acknowledgements. This work was supported by the Slovak Research and Development Agency under the contract No. APVV-15-0458.

References

Dubovský P.A., Briukhovetskyi O.B., Khlamov S.V. et al.: 2017, *OEJV*, **180**, 16.
Kim Y., Andronov I.L., Jeon Y.B.: 2004, *J. Astron. Space Science*, **21**, 191.
Kudzej I., Dubovský P.A.: 2010, *Odessa Astron. Publ.*, **23**, 70.
Motl D.: 2009, C-Munipack, [online] Available at: (http://cmunipack.sourceforge.net).
Pohorelov A.V., Khlamov S.V. et al.: 2016, *Odessa Astron. Publ.*, **29**, 136.
Savanevych V.E. et al.: 2015, *MNRAS*, **451**, 3287-3298.
Savanevych V.E. et al.: 2015, *Kinem. and Phys. of Cel. Bod.*, **31**, 302.

DOI: http://dx.doi.org/10.18524/1810-4215.2017.30.114510

ASTEROIDS SEARCH RESULTS IN LARGE PHOTOGRAPHIC SKY SURVEYS

S.V.Shatokhina[1], L.V.Kazantseva[2], O.M.Yizhakevych[1], I.Eglitis[3], V.M.Andruk[1]

[1]Main Astronomical Observatory of National Academy of Sciences
27 Akad. Zabolotnogo St., 03680, Kyiv, Ukraine, *svetash@mao.kiev.ua, andruk@mao.kiev.ua*
[2] Astronomical Observatory of Kiev National Taras Shevchenko University
3 Observatorna St., 04053, Kyiv, Ukraine, *KazL@ukr.net*
[3] Baldone Observatory, Institute of Astronomy, University of Latvia,
Raina blvd. 19, Riga, LV 1586, Latvia, *ilgnars@latnet.lv*

ABSTRACT. Photographic observations of XX century contained numerous and varied information about all objects and events of the Universe fixed on plates. The original and interesting observations of small bodies of the Solar system in previous years can be selected and used for various scientific tasks. Existing databases and online services can help make such selection easily and quickly.

The observations of chronologically earlier oppositions, photometric evaluation of brightness for long periods of time allow refining the orbits of asteroids and identifying various non-stationaries.

Photographic observations of Northern Sky Survey project and observations of clusters in UBVR bands were used for global search for small bodies of Solar system. Total we founded 2486 positions of asteroids and 13 positions of comets. All positions were compared with ephemeris.

It was found that 80 positions of asteroids have a moment of observation preceding their discovery, and 19 of them are chronologically the earliest observations of these asteroids in the world.

Keywords: photographic archive – asteroids – catalogs – positions

1. Introduction

The final result of the Northern Sky Survey (FON) project was the catalog of positions and B-magnitudes for more than 19 million stars and galaxies with B < 16.^{m} 5 (Andruk et al, 2016b). But processing results contains coordinates and stellar magnitudes for all registered objects on plates. They can be used for a global search for small bodies of the Solar system. We analyzed the results of digital processing of 2,260 photographic plates of FON project. As a result, 2399 images of asteroids and 11 images of comets from 8-16 magnitudes were found on these plates. The positions and magnitudes of searched asteroids and comets were composed into a catalogue.

This work started last year and detailed information about observations, photographic plates, and the first results was described in publication (Shatokhina et al, 2016, 2017). The techniques of astroplate digitization and further processing and determination of coordinates and magnitudes of stars are described in the series of publications (Andruk et al, 2005, 2007, 2010, 2014, 2015, 2016a, 2016b; Protsyuk et al, 2014a, 2014b). The results of the software testing for determination of Solar system bodies positions are described in (Kazantseva et al, 2015; Yizhakevych et al, 2014, 2015, 2016,2017; Protsyuk et al, 2014a, 2014b; Eglitis et al, 2016a, 2016b). Notice, that digitizing of astroplates has been performed using Microtek ScanMaker 9800XL TMA and Epson Expression 10000XL commercial scanners, with the resolution 1200 dpi. All scans of plates accumulated in Joint Digital Archive of Ukrainian virtual observatory (UkrVO). Standard images were processed using advanced complex LINUX / MIDAS / ROMAPHOT programs. The software was developed and implemented in MAO NASU to process the digitized astronomic negative plates as well as to obtain the final product in the form of a catalogue of positions and stellar magnitudes for all registered objects on the plate.

Earlier, in cooperation with the observatory of University of Latvia in Baldone a catalog of 89 positions and stellar magnitudes of asteroids and comets was obtained from processing observations of clusters in the UBVR spectral bands in 1967-1996. (Eglitis et al, 2016a, 2016c). The techniques of plate digitization and further processing were the same in both cases.

2. Results

The equatorial coordinates α, δ and stellar B-magnitudes of all objects on the plates were obtained in the reference system of Tycho-2 at the epoch of exposition of each plate. Photographic B-magnitudes of objects were calibrated with photoelectric standards (Andruk et al, 2016b).

A preliminary analysis of positions of the catalog's asteroids was carried out.

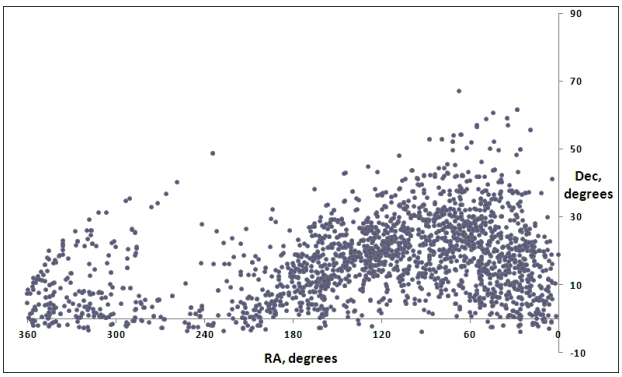

Figure 1: Distribution on coordinates RA, DEC for asteroids.

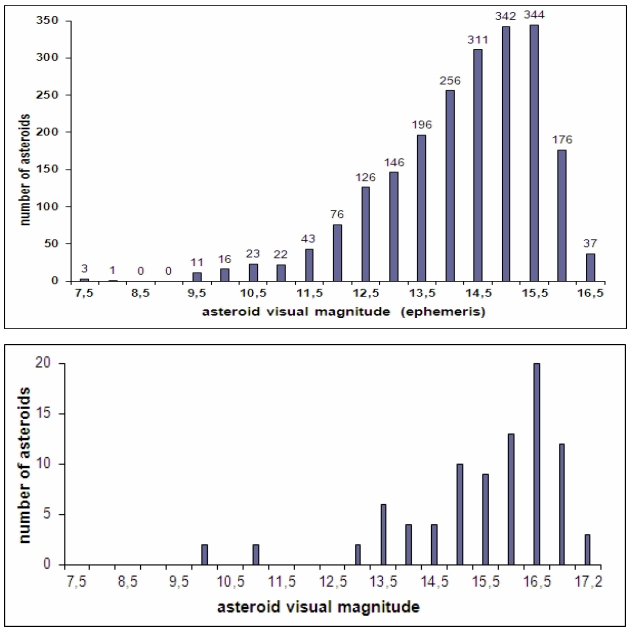

Figure 2: Distribution on magnitudes for asteroids from FON project (top) and Baldone archieve (bottom).

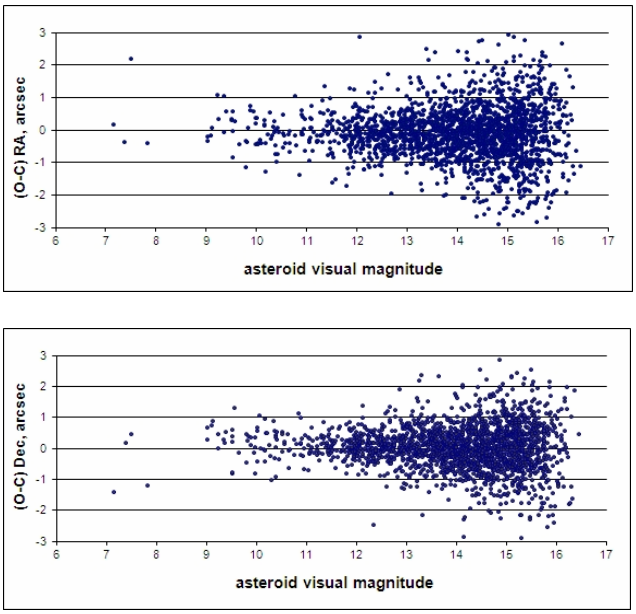

Figure 3: The scatter of O-C values for all asteroids.

The Fig. 1 shows the distribution on equatorial coordinates RA, DEC of all searching asteroids for all used plates. Notice, that the plates from FON project cover the area on celestial sphere from 0 to 24 hours in right ascention and from -4º to +90º in declination. Most asteroids are found in the declination zone up to 30 degrees. A significantly smaller number of asteroids are located in areas of high declination (up to 70 degrees).

The Fig.2 shows the distribution on visual magnitude for all asteroids. More faint asteroids with 15-16 magnitude were identified on the FON astronegatives with high atmospheric transparency and good observing conditions only. The faint asteroids up to 17.2 magnitudes were founded from observations in Baldone only. In addition, these observations were performed using V and R filters.

All positions of asteroids were compared with the ephemeris JPL DE431 (http://ssd.jpl.nasa.gov/horizons). Identification of asteroids was performed using JPL resources too. The differences O-C on both coordinates for all asteroids are presented on Fig. 3.

The scatter of O-C values increases for asteroids fainter than 13-14 magnitude. The Table 1 demonstrated increasing of root-mean-square errors of O-C for different selected intervals of magnitudes of asteroids. Therefore, the result of the inclusion of faint asteroids in the catalog leads to an increase in the root-mean-square errors of O-C values. As a final result, after exclusion of bad data the mean O-C values for 1987 asteroids from 8 to 16.5 magnitude were obtained, equal to -.09 .04, and their root mean square errors .67 .61 arcsec in both coordinates, respectively.

The Fig. 4 shows changes of observed B magnitudes for 2150 asteroids and comets. The scatter of B values for faint asteroids increases.

Digital processing of photographic plates of star fields allows to determine with high accuracy the coordinates and stellar magnitudes for all registered objects on these plates, such as stars, galaxies, small bodies, artificial satellites and artefacts. From digital processing of photographic plates of FON project were obtained the mean internal errors for stars equal 0.23 arcsec in both equatorial coordinates and $0.^{m}14$ in B magnitudes (Andruk et al, 2016b).

Table 1: Mean values of O-C and their root-mean-square errors σ for different selected intervals of magnitudes of asteroids

Interval of magnitudes	Number of positions	O-C RA, arcsec	O-C DEC, arcsec	σ RA	σ Dec
9-10	72	-.04	.19	.51	.49
9-11	187	-,08	.14	.54	.41
9-12	452	-.11	.11	.52	.44
9-13	898	-.09	.09	.57	.48
9-14	1512	-.09	.06	.64	.57
9-15	1985	-.09	.05	.70	.62
9-16	2022	-.09	.05	.70	.63

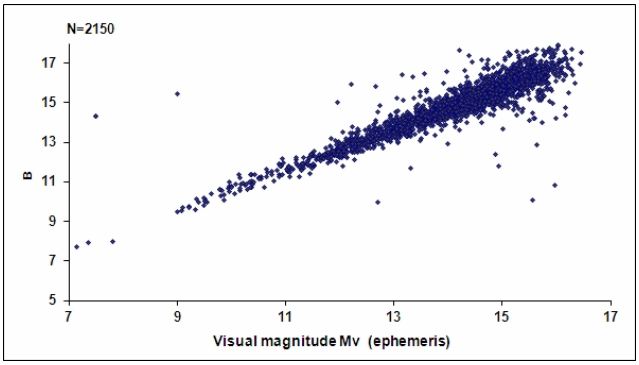

Figure 4: Changes of observed B magnitudes for 2150 asteroids and comets along visual asteroid's magnitude axis.

From the analysis of catalog data it was found that 80 positions of asteroids have a moment of observation preceding their discovery, and 19 of them are chronologically the earliest observations of these asteroids in the world. Most of them belong to the early oppositions of asteroids, which because of the lack of data are not involved in the

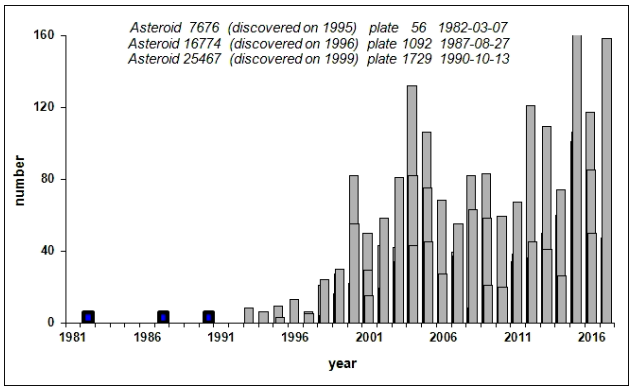

Figure 5: Distributions on time scale of all known observations in the world for 7676, 16774 and 25467 asteroids.

calculation of ephemerides. The more faint asteroids up to 17 magnitudes were identified on the plate in Baldone observatory. Therefore, among them are much more interesting asteroids which discovered much later than observed.

For asteroids 7676, 16774 and 25467 the distributions of all known observations in the world are presented on Fig. 5. Observational data took from Minor Planet Center (http://www.minorplanetcenter.net/db_search). With bold black color pointed asteroids from observations of FON project. These observations of asteroids are the earliest from all known observations in the world

3. Conclusion

Large photographic sky surveys can become a basis not only for creating a catalog of stars and galaxies, but also for compiling a catalog of the positions of small bodies of the Solar System. As an example, a catalog of 2410 positions and B-magnitudes of asteroids and comets was compiled from the photographic observations of the FON project in 1981-1996. Digital processing of photographic plates allows to determine with high accuracy the coordinates and stellar magnitudes for all objects. After comparing the catalog with ephemeris, the mean O-C values for asteroids from 8 to 16.5 magnitude were obtained, equal to -.09 .04, and their mean square errors .67 .61 arcsec in both coordinates, respectively. Quantitatively, the catalog is comparable with a total number of all positions of asteroids processed from observations of the ORBIT project in 1949-1996 at the MAO NASU.

Earlier, in cooperation with the observatory of University of Latvia in Baldone a catalog of 89 positions and stellar magnitudes of asteroids and comets was obtained from processing observations of clusters in the UBVR spectral bands in 1967-1996.

It was found that 80 positions of asteroids have a moment of observation preceding their discovery, and 19 of them are chronologically the earliest observations of these asteroids in the world. Most of them belong to the early oppositions of asteroids, which because of the lack of data are not involved in the calculation of ephemerides. The global search for such observations in the databases of the UkrVO and Baldone, followed by the processing of plates, will increase their number.

References

Andruk V.N., Ivanov G.A., Pogoreltsev M.T. et al.: 2005, *Kinem. Phys. Cel. Bodies*, **21**, N5, 396.

Andruk V., Pakuliak L.: 2007, *Journal of Physical Studies*, **11**, N3, 329.

Andruk V.M., Butenko G.Z., Yatsenko A.I.: 2010, *Kinem. Phys. Cel. Bodies*, **26**, N3, 146.

Andruk V.N., Golovnya V.V., Ivanov G.A. et al.: 2014, *Odessa Astron. Publ.*, **27**, N1, 53.

Andruk V.N., Pakuliak L.K., Golovnya V.V. et al.: 2015, arXiv151205535.

Andruk V.M. Golovnia V.V., Ivanov G.A et al.: 2016, *Kinem. Phys. Cel. Bodies*, **32**, N1, 38.

Andruk V.M., Pakuliak L.K., Golovnia V.V. et al.: 2016, *Kinem. Phys. Cel. Bodies*, **32**, N5, 260.

Eglitis I., Eglite M., Andruk V.M. et al.: 2016, *Odessa Astron. Publ.*, **29**, 126.

Eglitis I., Eglite M., Andruk V.M.: 2016, *Bull. T.Shevchenko Nat.Univ. Kyiv.Astron.*, **54**, 21 (in Ukrainian).

Eglitis I., Eglite M., Shatokhina S.V. et al.: 2016, *Odessa Astron. Publ.*, **29**, 123.

Kazantseva L.V., Shatokhina S.V., Protsyuk Yu.I. et al.: 2015, *Kinem. Phys. Cel. Bodies*, **31**, N1, 37.

Protsyuk Yu.I., Andruk V.N., Muminov M.M. et al.: 2014, *Odessa Astron. Publ.*, **27**, N1, 61.

Protsyuk Yu.I. Andruk V.N., Kazantseva L.V.: 2014, *Odessa Astron. Publ.*, **27**, N1, 59.

Shatokhina S. Kazantseva L., Kazantsev A.et al.: 2016, *Odessa Astron. Publ.*, **29**, 151.

Shatokhina S.V., Andruk V.N., Golovnya V.V.: 2017, *Bull. T.Shevchenko Nat.Univ. Kyiv.Astron.*, **55**, 6 (in Ukrainian).

Yizhakevych O., Andruk V., Pakuliak L. et al.: 2014, *Odessa Astron. Publ.*, **27**, N1, 67.

Yizhakevych O., Andruk V.M., Pakuliak L.K.: 2015, *Odessa Astron. Publ.*, **28**, N2, 213.

Yizhakevych O.M., Andruk V.M., Pakuliak L.K.: 2016, *Odessa Astron. Publ.*, **29**, 155.

Yizhakevych O. M., Andruk V.M., Pakuliak L.K.: 2017, *Kinem. Phys. Cel. Bodies*, **33**, N3, 70.

DOI: http://dx.doi.org/10.18524/1810-4215.2017.30.114529

CATALOGUE OF ASTROMETRIC POSITIONS OF JUPITER`S OUTER SATELLITES ON PHOTOGRAPHIC OBSERVATIONS IN MAO NAS OF UKRAINE IN 1987-1993

Yizhakevych O., Andruk V., Pakuliak L.

Main Astronomical Observatory of National Academy of Sciences,
27 Akad. Zabolotnogo St., 03680, Kyiv, Ukraine, *izhak@mao.kiev.ua*

ABSTRACT. The catalog of 33 topocentric positions of Jupiter's moons J6, J7, J8 has been created on photographic observations made in MAO NASU in 1987-1993. Positions are referred to the system of TYCHO-2 using the program package LINUX/MIDAS/ROMAFOT. The comparison of observed positions was made online with their theoretical data of IMCCE (www.imcce.fr/sat).

Key words: catalogues – planets and satellites; Jupiter; positional astrometry.

1. Introduction

Outer satellites of Jupiter J6 (Himalia), J7 (Elara) и J8 (Pasiphae) were discovered at the beginning of the XX century. They make a compact group of small moons with dimensions of several kilometers. Himalia, the largest of them has 170 km in diameter.

Outer moons rotate along highly elongated elliptical orbits at considerable angles to the equatorial plane of Jupiter. Some of them orbit Jupiter in the same direction (J7). The other part moves in the opposite direction, and such satellites are called retrograde. They are J6 and J8.

Because of the small dimensions, the outer satellites can only be observed with the help of large aperture telescopes. In addition, observations should be made in the most favorable periods of visibility. For photographic observations, the most favorable conditions emerged in 1986-1989. In these years, the maximum magnitude was expected for faint satellites, J6 ~ 14.6^m, J7~ 16.5^m, and J8 ~ 17.1^m.

The first photographic observations of outer moons of the Jupiter started in MAO NAS of Ukraine in September 1987 with double wide-angle astrograph (DWA).

Telescope parameters allowed us to obtain the images of most bright satellite only, J6 (Himalia). To observe J7 (Elara) and J8 (Pasiphae), more powerful telescopes are required with better resolution and more suitable location, remote from large settlements. These requirements were met by the telescopes of the southern observatories of Uzbekistan. They are the Zeiss double astrograph DAZ of Kitab latitude station and Zeiss reflector Z600 on the Mount Maidanak. Their technical parameters see in Table 1.

At these telescopes in 1987-1989, 4 series of observations were performed. After the processing of observations using the classical method, the catalog of 28 topocentric positions of three faint moons J6,J7,J8 was obtained. Positions were referred to the system of PPM (1950.0) (Izhakevich et al., 1991;1994).

The comparison of calculated positions with their ephemeris data was made by astronomers of Tomsk university L.E.Bykova and V.F.Jurga (Bordovytsina et al.,1978). The internal accuracy of the reduction estimated as unit weight RMS error was 0.44″ for DWA and 0.34″ for DAZ on both coordinates. For Z600 this value was 0.24″ to 0.34″ on right ascension and 0.15″ to 0.28″ on declination.

2. Observations

In the framework of Ukrainian virtual observatory project (UkrVO, JDA – Joint Digital Archive) (Vavilova, 2012a; Vavilova, 2012b; Vavilova, 2016, Vavilova, 2017) it was found expedient to make a revision of MAO NASU plate collection in its part containing the Solar System (SS) bodies observations. The main goal was to find plates never processed or with SS objects' images on the stellar fields of other observational programs. The objects of the most interest were the Jupiter moons. We found several plates of FON project made on DWA and thus extended the existing observational series to 1993,(see Fig. 1). The total number of plates involved into the processing is 33.

Table 1. The some parameters of telescopes

TELESCOPE, (Marsden's list):	DWA (083)	DAZ (186)	Z600 (188)
SPESIFICATIONS:			
Lens diameter (m)	0.4	0.4	
Diameter mirror (m)			0.6
Focal length (m)	2.0	3.0	7.5
Field of view (degr.)	8.5 x 8.5	5.5 x 5.5	0.5 x 0.5
Plate size (cm)	30 x 30	30 x 30	9 x 9
Scale value (arcsec/cm)	103. 3	68. 8	27. 5
Scale value (arcsec/px)	2.47	1.45	0.57

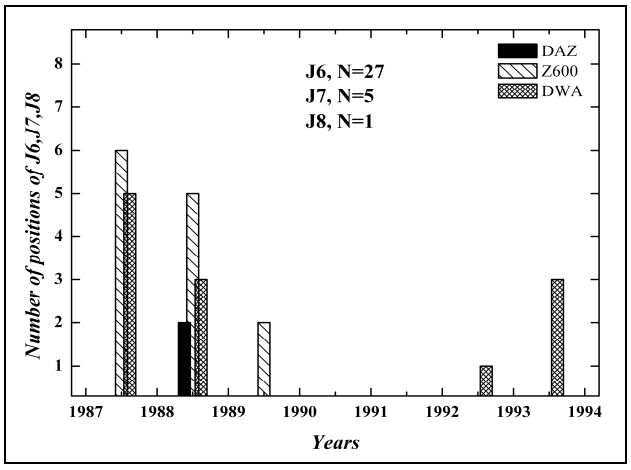

Figure 1: The distribution of J6, J7, J8 observations by years.

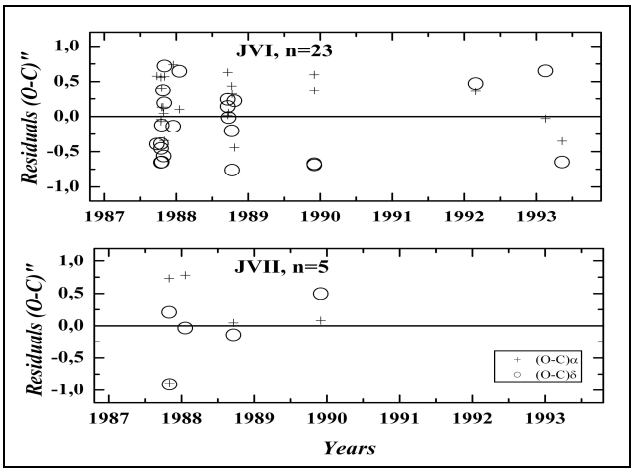

Figure 2: The dispersion of $(O-C)_i$ values for J6 and J7 over the total observational period.

The special attention was paid to re-checking of observational moments. The registration of start and finish of the exposure was made with the star chronometers. Further, their readings were referred to the time signals «Six points». After the revision of the corrections for the chronometer rate, UTC moments were calculated. The exposure time depended on moon brightness and could vary from 5 to 35 minutes. It is necessary to trace the object for a considerable time to fix its projection at the same point on the plate to obtain the images of faint moving objects like J7, J8. We calculated in advance the time intervals through which it was necessary to shift the telescope or the plate in the cassette holder at each coordinate separately (Metcalf's method). The guiding of the telescope was carried out manually by two observers. All the observations were made on the plates with the ORWO-ZU1 emulsion. To attenuate the brightness of the Jupiter on DWA we used the neutral filters.

3. Reduction

The processing of photographic observation can be divided into several steps. The first step is the plate digitizing to obtain its image in tif and fit formats. The preliminary image processing gives the rectangular coordinates ***x,y*** of all objects on the plate followed by the cross-identification with the objects in the reference catalogs (***α, δ)*** (Andruk et al., 2005; 2012; 2015). The connection between two coordinate systems can be presented in the form of infinite power series. In our case, the parameters of DWA and DAZ telescopes allowed us to restrict the model to a polynomial of the 6th degree. For plates of Z600 telescope the linear reduction model appeared to be optimal. The plate digitizing was carried out using Epson Expression 10000XL (EE) commercial scanner with resolution 1200 dpi. The reference catalog is TYCHO-2.

As a result of the reduction, a catalog was obtained the catalog of topocentric positions of Jupiter outer moons (see Table 2).

Table 2 shows the catalog of topocentric positions of Jupiter outer moons. The following columns are presented in the table: 1 – year, month, day, moment UTC in fractions of a day; 2,3 – Equatorial coordinates; 4 – values $(O-C)_i$ as a result of comparison of observations with theory DE431; 5 – the number of TYCHO-2 reference stars; 6 – indexes of plates in observational logs, identifiers of telescopes (DW -DWA, DZ –DAZ, Z –Z600); 7 – durations of exposure time in minutes of time; 8 – initials of the observer (Iv-Ivanov G., L-Ledovskaia (Kulyk) I., M-Major S., S-Sereda E., Sh-Shatokhina S., Ya-Yatsenko A., Yi-Yizhakevych O.). The last column contains some notes about the data character. Here, "1" means that average values of several reductions are presented, "2" shows the new result obtained from the first processed plate, "3" denotes positions with (O-C) exceeding 1 arcsec. Fig. 2. shows the dispersion of $(O-C)_i$ values for J6 and J7 over the total observational period.

The special attention was paid to the observations which in classical processing were successful, but their new reduction failed. For such problematic observation, we carefully tried to find the suitable reduction model. Various variants of the dimensions of the field of view and the number of reference stars on them were considered as well as the search of optimal criteria for noise level determination and noise misidentifications elimination. The bold font is used to highlight the plates for which the result is obtained as an average for several reductions. Nevertheless, on three plates (Z600, № 435,488,489), we failed to detect the images of satellites with the help of our program. One of them occurred to be half-overexposed. On the next one, the satellite J7 image almost merges with the image of the brighter star. The algorithm of the program failed to divide these two images and shifted to the brighter one. The image of the J8 moon on the third plate is so faint, that possibly «dive» in the noise too. In the previous successful classic method, the center of the satellite image was well estimated by eye even if it was the slight densifying of the emulsion. The program algorithm does not elaborate the limiting cases of recognition or too close neighborhood of the much brighter star. In those cases, the classical method with manual measurements became more successful.

Tables 3 and 4 present the statistical information of the reductions J6, J7 and J8 moons, which have $(O-C)_i$ better than 1 arcsec.

Table 2. Catalog of topocentric positions of Jupiter's outer moons J6, J7, J8 over the observational period 1987 – 1993.

DATE Year M Day UTC	RA.J2000 (h, m, s)	Dec.J2000 (°, ', ")	(O-C)al, (O-C)dl (arcsec)	N	Pl/Tel	exp min	Obs	mark
J6 (Himalia), 27 positions, 26plates, 23nights								
1987 09 23.080157	01 48 51.293	10 09 50.556	0.578 -0.392	1248	3179/DW	43	Yi	
1987 10 13.855550	01 37 48.101	09 07 47.401	0.559 -0.386	13	188/Z	5	M,L	
1987 10 13.918820	01 37 45.776	09 07 33.886	-0.071 -0.653	12	188/Z	5	M,L	
1987 10 14.903508	01 37 10.850	09 04 07.690	-0.042 -0.454	30	194/Z	10	M	
1987 10 17.955626	**01 35 21.918**	**08 53 17.694**	**0.132 -0.648**	**1560**	**3184/DW**	**25**	**Yi**	**1**
1987 10 17.982636	01 35 20.954	08 53 12.425	0.406 -0.123	1546	3185/DW	30	Yi	
1987 10 24.811301	01 31 16.864	08 28 27.629	0.133 0.374	38	235/Z	10	L,Sh	
1987 10 27.912917	**01 29 27.804**	**08 17 10.806**	**0.045 -0.563**	**1586**	**3208/DW**	**35**	**Yi**	**1**
1987 10 30.823393	01 27 47.528	08 06 42.720	-0.342 0.192	32	247/Z	10	L,Sh	
1987 10 31.811926	01 27 14.134	08 03 11.553	0.570 0.720	24	251/Z	10	L,Sh	
1987 12 15.767233	**01 12 34.796**	**06 19 32.367**	**0.737 -0.139**	**454**	**3219/DW**	**20**	**Yi**	**1,2**
1988 01 15.702904	01 18 45.201	06 47 09.531	1.634 0.493	624	3241/DW	30	Yi	3
1988 01 15.702968	01 18 45.099	06 47 09.698	0.070 0.667	1183	**3242**/DW	30	Yi	
1988 09 17.974690	04 16 10.784	20 03 50.657	0.020 0.140	515	0007/DZ	25	Sh,M	
1988 09 17.999275	04 16 10.857	20 03 49.843	0.630 0.243	631	0008/DZ	30	Sh,M	
1988 09 21.936897	04 16 12.562	20 01 01.671	0.522 1.829	34	323/Z	10	L,Sh	3
1988 09 21.947818	04 16 12.514	20 00 59.358	0.053 -0.016	5	324/Z	10	L,Sh	
1988 10 07.963328	04 14 17.707	19 46 09.057	0.438 -0.204	5	367/Z	9	L,Yi	
1988 10 09.825040	04 13 52.482	19 44 10.923	0.319 -0.763	4	386/Z	10	L,S	
1988 10 10.982953	04 13 35.375	19 42 57.744	-1.170 -0.233	51	402/Z	30	S,Yi	3
1988 10 22.032875	**04 10 13.862**	**19 31 07.712**	**-0.442 0.223**	**586**	**3297/DW**	**30**	**Sh**	**2**
1989 11 29.888139	06 45 16.710	23 18 30.458	0.598 -0.674	26	482/Z	12	L,Yi	
1989 11 30.880801	06 44 49.645	23 18 43.649	0.369 -0.689	528	487/Z	13	L,Yi	
1992 02 26.928932	10 50 57.194	08 33 13.638	0.358 0.472	1573	1956/DW	8	Ya	2
1993 02 16.043639	12 52 09.761	-03 37 02.540	-0.030 0.652	1391	2129/DW	22	Ya	2
1993 04 22.852408	12 29 40.928	-01 00 52.034	-1.060 0.217	1340	2196/DW	22	Iv	3
1993 05 10.832786	12 25 00.696	-00 42 21.360	-0.350 -0.648	1307	2207/DW	22	Yi	2
J7 (Elara), 5positions, 5plates, 5nights								
1987 10 29.822543	01 31 10.281	08 03 44.492	0.731 0.208	10	241/Z	30	L,Sh	
1987 10 31.830303	01 29 57.455	07 58 16.858	-0.895 -0.910	6	252/Z	30	L,Sh	
1988 01 18.581767	01 19 58.395	06 53 56.632	0.780 -0.035	17	265/Z	8	L	2
1988 09 17.999275	04 15 20.299	20 17 44.843	0.045 -0.140	288	008/DZ	30	Sh	
1989 11 29.920220	06 43 08.874	22 56 56.371	0.080 0.498	20	483/Z	30	L,Yi	
J8 (Pasiphae),1 position.								
1989 12 07.786099	06 39 33.759	23 21 29.889	0.579 0.080	29	492/Z	31	L,Yi	

Table 3. Results of the J6 reduction.

Tele--scope	n	O-Cα, O-Cδ"	Sd	Exp. min	Rmsα, Rmsδ	N star
DWA	10	+0.15 -0.05	0.38 0.52	8 – 43	0.09 0.08	454- -586
DAZ	2	+0.32 +0.19	0.43 0.07	25-30	0.11 0.10	515- -631
Z600	11	+0.24 -0.23	0.31 0.49	5-13	0.26 0.26	4- -528
Σ	**23**	**+0.21 -0.12**	**0.34 0.49**		**0.16 0.17**	

Table 4. Results of the J7, J8 reduction.

Tele-scope	n	O-Cα, O-Cδ	Sd	Exp. min	Rmsα, Rmsδ	N star
DAZ	1	+0.04 -0.14		30	0.08 0.08	288
Z600	4	+0.17 -0.06	0.78 0.61	30	0.27 0.20	6- -20
Σ	**5**	**+0.15 -0.08**	**0.68 0.53**		**0.16 0.17**	
J8 Z600	1	+0.58 +0.08	0.78 0.61	31	0.10 0.05	29

4. Brief summary

Thus, a catalog of 33 topocentric positions of outer Jupiter satellites was obtained by the method developed and proposed by GAO NASU (Andruk et al., 2005; 2012; 2015).

The catalog contains the coordinates of the satellites for the period from 1987 to 1993 and covers the orbit of Jupiter in the range from 1.5 to 12.8 hours on a right ascension.

The internal accuracy of the reduction of observations in the TYCHO2 star catalog system is much higher than the analogous values of the previous reduction in the PPM catalog.

This can be explained by the fact that, firstly, the reduction of a faint objects was performed on the basis of much brighter reference stars, and secondly, this may be the result of inaccuracy of manual guiding following the poorly visible object (Metcalf's method). Comparing our results with the similar research of other authors for the same period (Nakamura, 1991; Rocher, 1996; Shelus, 1991) we can state that the quality of our observations is not inferior in accuracy to the results of foreign colleagues.

Especially it should be noted that initially our programs were designed for processing photographic plates obtained with wide-angle astrographs, having one exposure and dense sharp images of motionless objects. Images of satellites do not meet these conditions. The use of these programs to determine the topocentric coordinates of the bodies of the Solar System became possible after the corresponding adjustment of the software package in order to treat poorly delineated images without strong central blackening. Nevertheless, when we had to process digitized plates with faint moving objects, such as the outer satellites of Jupiter, we found some flaws in the algorithm of our programs. The most serious are two ones, a problem of isolating a faint image of the object from the background noise and the problem of attenuation the neighboring bright star. The improvement of algorithms and programs will make it possible in the future to process any photographic observations of objects having a visible motion and not related to stellar fields.

References

Andruk V., Ivanov G., Pogorel'tsev M. et al.: 2005, *Kinem.Phys.Cel. Bodies*., **21**, **N5**, 396.

Andruk V., Ivanov., Yatsenko A. et al.: 2012, *Visn. Kyiv Nat. Univ., Astronomia*, **N48**, 11.

Andruk V.N., Pakuliak L.K., Golovnya V.V. et al.: 2015, preprint (arxiv.org/abs/1512.05535).

Bordovytsina T.V., Bykova L.E.: 1978, *Tomsk: Univ. Publ.*, 120.

Izhakevich E.M., Kaltygina S.V., Major S.P. et al: 1991, *Kinem.Phys.Cel. Bodies*., **7, N2,** 98. (in Russian).

Izhakevich E.M., Kaltygina S.V., Ledovskaia I.V. et al: 1994, *Kinem.Phys.Cel. Bodies.,* **10, N1,** 88 (in Russian).

Nakamura T., Kinoshita H., Kosai H., 1991**,** *AJ,* **101, N1,** 290.

Rocher P., Chapront J.: 1996, *A&A*, **311,** 710.

Shelus, P. J., Whipple, A. L. and Benedict, G. F.: 1991, *AJ*, **101, N4,** 1516.

Vavilova I.B., Pakulyak L.K., Shlyapnikov A.A. et al.: 2012, *Kinem. Phys. Cel. Bodies*, **28, N2**, 85.

Vavilova I.B., Pakuliak L.K., Protsyuk Yu.I. et al.: 2012, *Baltic Ast*., **21, N3,** 356.

Vavilova I.B.: 2016, *Odessa Astron. Publ*., **29,** 109.

Vavilova I.B., Yatskiv Ya.S., Pakuliak L.K. et al.: 2017, *IAUS*, **325**, 361.

DOI: http://dx.doi.org/10.18524/1810-4215.2017.30.114443

CATALOGUE OF COORDINATES AND B-MAGNITUDES IN -20º – +2º ZONE BASED ON THE ULUGH BEG ASTRONOMICAL INSTITUTE PART OF THE FON PROJECT

Q.X. Yuldoshev [1], M.M. Muminov[2], Sh.A. Ehgamberdiev[1],
H. Relke[3], Yu.I. Protsyuk[4], O.E. Kovylianska[4], S.V. Protsyuk[4], V.M. Andruk[5]

[1] Ulugh Beg Astronomical Institute of the Uzbek AS, Uzbekistan, *qudratillo@astrin.uz*

[2] Andijan State University, Uzbekistan, *muminov1951@gmail.com*

[3] Walter Hohmann Observatory, Germany, *helena_relke@yahoo.com*

[4] Research Institute "Mykolaiv Astronomical Observatory", Ukraine, *yuri@nao.nikolaev.ua*

[5] Main Astronomical Observatory NASU, Ukraine, *andruk@mao.kiev.ua*

ABSTRACT. Catalogue of 13.4 million stars down to 17.5^m was obtained in 2017 by using plates from the Kitab Observatory of Ulugh Beg Astronomical Institute (UBAI) of the Uzbek Academy of Sciences. Kitab's part of Photographic Sky Survey (Russian abbreviation is FON, in next contexts) project include more than 2600 photographic plates, exposed on the Double Astrograph of Zeiss (DAZ, D/F = 40/300, 69"/mm) from 1981 to 1996. Digitization of these plates was made by using Epson Expression 10000XL scanner with the 1200 dpi resolution. Catalogue includes objects from the 1963 plates in declination zone between -20° and +2° for middle epoch 1984.97. The equatorial coordinates of objects were determined in the Tycho-2 reference system and the B-magnitudes in the system of the photoelectric standards. Five participants from Uzbekistan, Germany and Ukraine have taken part in the processing of the digitized images. The average internal accuracy of the catalogue for one observation are 0.23" and 0.15^m for the equatorial coordinates and B-magnitudes respectively. For the stars brighter than 14^m the errors are 0.09" and 0.05^m respectively. The analysis of the catalogue and its comparison with the several astrometric catalogues was done.

Keywords: photometric – methods: data analysis – catalogs, virtual observatory tools – astrometry – techniques.

1. Introduction

Kitab observatory is the branch of UBAI and exists since 1930. This observatory was organized on the initiative of prof. M.F. Subbotin (1893-1968), appointed in 1922 by the director of the Tashkent Astronomical Observatory (formerly name of UBAI). This is only in the Central Asia and unique place of five world latitudinal stations where is located on the same geographical parallel. It is located on the +39°08' parallel.

In 1975, a double astrograph of Zeiss was installed to conduct observations in the Kitab and from 1980 to early 2000, several thousand observational data were obtained. Most of these data were obtained under the FON project.

Photographic Sky Survey (abbreviation in Russian is FON) project was initiated by the Main Astronomical Observatory of the National Academy of Sciences of Ukraine (MAO NANU, Kyiv, Ukraine) (Kolchinskii, 1977) and observations were made at six observatories such as Goloseevo, Zvenigorod, Dushanbe, Abastumani, Zelenchuk and Kitab. These observatories were equipped with 40 cm Double Astrograph of Zeiss (DAZ) and wide field astrographs with the same aperture, but focal length were 200 and 300 cm. The observations of the sky zone from -20° to +28° according to their declinations on the same astrograph (DAZ, D/F = 40/300) in Kitab, were made with a shift of the centers of photographic fields on two degrees by declination and four degrees by right ascension (Fig. 1). The photographing of each field was conducted with two exposures (long: from 22 to 28 minutes and short: from 40 to 75 seconds) on the same photographic plate with the shift on both coordinates. The duration of the long exposure was chosen in such a way to obtain images of stars down to 16-17 magnitude. During 1981-1996 more than 2600 astronegatives were taken under the project. The main part of these plates consists of the southern sky (more than 1900 plates with full overlapping) and selected fields in the northern sky. The Kitab observatory had successfully completed its task under the FON project.

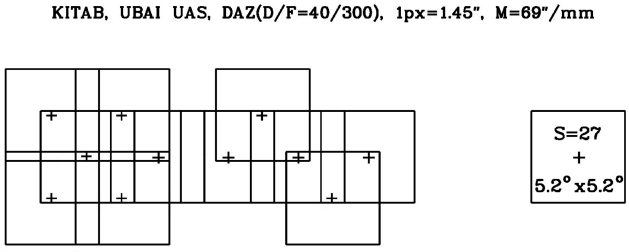

Figure 1: The overlapping scheme of photographic plates obtained in Kitab.

2. Processes of digitization and compiling the catalogue of the southern part of FON project in Tashkent

In 2014-2015 all astronegatives in Kitab were transferred to the UBAI in Tashkent (Uzbekistan) and digitization and systematization of these plates was started. In 2016, all plates of the project were scanned using flatbed scanner Epson Expression 10000XL. Totally 1963 astro negatives (cover sky by declination from -20° to +2°) were processed for compiling the catalogue. As before mentioned, for the digitizing of astronegatives a commercial scanner Epson Expression 10000XL was used. The spatial resolution is 1200 dpi (Protsyuk, 2014c, Protsyuk, 2014d) and size of the scanned images was up to 30x30 cm or 13000x13000 pixels (1px=1.45″). For obtaining useful information from digitized astronegatives following steps have been done and for processing the scanned images common method which was developed and has been applied in practice in the MAO NASU (Andruk, 2012, Andruk, 2015b) was used:

1. Image conversion from *tiff* to *fit* using the GIMP package after scanning astronegatives.
2. The processing of the scans using the LINUX/MIDAS/ROMAFOT package to obtain the rectangular coordinates *X*, *Y* and instrumental magnitudes of registered objects.
3. The separating of the registered objects into two exposures for each digitized plate (Andruk, 2012).
4. The creating of the files with the reference stars for each digitized plate using the Tycho-2 catalogue (Protsyuk, 2014b).
5. The creation of an additional file for the determination of the relationship between the rectangular and equatorial coordinate systems of reference stars.
6. Correction of the rectangular coordinates of registered objects for systematic errors.
7. Reduction of the rectangular coordinates *X, Y* of registered objects in the system of equatorial coordinates α, δ of the Tycho-2 catalogue.
8. Conversion of the instrumental photometric values of objects to the system of photoelectric B_{pe} stellar magnitudes of the Johnson's system (Andruk, 2017).

For the calibration of the characteristic curves of the photographic plates, the recording photometric field errors and the conversion of the instrumental photometric values to the system of photoelectric B_{pe} stellar magnitudes of the Johnson system were used data from the catalogues (Relke, 2015).

The equatorial coordinates and the photometric B-magnitudes of registered objects were obtained for all scans using specially developed software in the LINUX/MIDAS/ROMAFOT (Andruk, 2010), which was described in (Yatsenko, 2011, Muminov, 2012, Protsyuk, 2014a). This software has already been successfully applied for the processing of the scanned images of Kyiv's part of the FON project to create a new photographic catalogue down to 16-17 stellar magnitude (Andruk, 2016a, Andruk, 2016b).

2.1. Astrometric and photometric reduction

At the stage of diagnosing the systematic errors of the scanner $\Delta\alpha$ and $\Delta\delta$ and at the stages of reduction of the rectangular coordinates *X, Y* of the objects to the system of equatorial coordinates α, δ of the Tycho-2 catalogue, the tangential coordinates ξ, η and *B*-magnitudes were calculated using the method of least squares by formulas of the form (1) and (2), respectively:

$$\begin{cases} \xi_i = a_1 + a_2 X_i f_i + a_3 Y_i f_i + a_4 R_i m_i + a_5 f_i + \sum b_{lm} X_i^l Y_i^m \\ \eta_i = c_1 + c_2 X_i f_i + c_3 Y_i f_i + c_4 R_i m_i + c_5 f_i + \sum d_{lm} X_i^l Y_i^m \end{cases} \quad (1)$$

$$(l = 0 \div 6,\ m = 0 \div 6,\ l + m = n,\ n = 1 \div 6)$$

$$B_i = e_1 + e_2 X_i + e_3 Y_i + e_4 R_i + e_5 R_i^2 + \sum f_n m_i^n \quad (2)$$

$$(\mathrm{n} = 1, 2, \ldots 5)$$

where $i = 1, 2, \ldots N$ is the number of stars in the Tycho-2 catalogue on the plate; X_i, Y_i and R_i are the coordinates and distance of the image of the stars relative to the center of the plate; m_i is the instrumental photometric magnitudes of the stars; f_i is FWHM of the stars; the coefficients a_2, a_3, a_4 and c_2, c_3, c_4 are responsible to the coefficients of a_5, c_5 which are taken into account the influence of the light curve (calculated separately); the coefficients of the full sixth-degree polynomial (27 terms) b_{lm} and d_{lm} in the generalized case describe the aberrations of the telescope optics, weighed down by systematic scanner errors; the coefficients e_2, e_3, e_4, e_5 are responsible for the photometric equation (photometric error) of the field, and the coefficients f_1, f_2, f_3, f_4, f_5 correspond to the functional description of the type of characteristic curves themselves. The equation (2) is chosen as optimal, minimizing the photometric reduction errors in the B_{pe} photoelectric standards system.

2.2. Compiling the catalogue and its accuracy

The catalogue of Kitab consists near 13.4 million stars and galaxies up to 17.5^{m} for the middle epoch 1984.97. The equatorial coordinates were taken in the system of Tycho-2 and the photographic magnitudes in the system of Johnson. For compiling the catalogue 1963 astronegatives of Kitab observatory were processed. The quantities of the processed plates by zones are shown in Table 1. The linear size of the plates is around 30x30 cm or 13000x13000 px. The field of view of the telescope or sky area on the plates is roughly 5.5°x5.5°.

Table 1: Number of processed plates in zones

Zone	N	Zone	N
0	*179*	**-10**	*180*
-2	*174*	**-12**	*182*
-4	*234*	**-14**	*201*
-6	*228*	**-16**	*177*
-8	*240*	**-18**	*168*

In the second step of processing of 1963 plates, around 130.98 million objects were registered. After the procedures of mutual identifications, the average number of measurements of the stars and galaxies is l=4.4, and near

1.25 millon stars and galaxies (9.38% of the total number) are also added to the catalogue which were measured once.

The number of stars by magnitudes is given on Fig. 2.

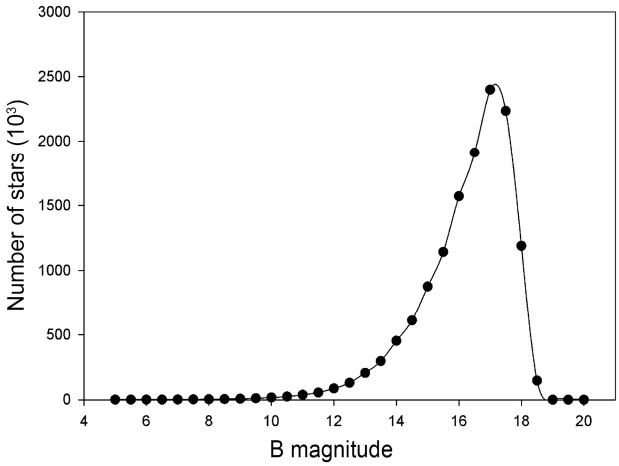

Figure 2: Number of stars by B-magnitudes.

The criteria of the identification and selection of candidates of the stars and galaxies in the overlapping zones is given below:

1) the difference between equatorial coordinates should not be greater than the size of the one pixel;

2) the difference between stellar magnitudes should not exceed ± 2^m (because of the accounting of variable stars).

If the candidate was identified at least on two plates it was according to the criteria, otherwise it was estimated as object of the catalogue.

In the Table 2 the distribution of internal errors of defined equatorial coordinates σ_α, σ_δ, photometric magnitudes σ_{Bph}, *FWHM*, intensity at the center of object and number of stars and galaxies on the intervals of stellar magnitudes of the catalogue are given. The average errors are provided at the top of the table 2 and their corresponding values are equal: σ_α=0.225"; σ_δ=0.234"; σ_{Bph}=0.154^m. Calculated errors of equatorial coordinates by declinations are shown on Fig. 3. The errors of equatorial coordinates and magnitudes as the function of B-magnitude are shown on Fig. 4.

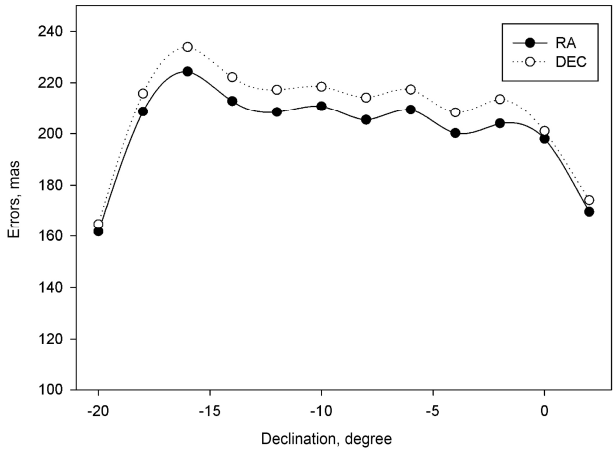

Figure 3: Estimated errors by declinations of the stars.

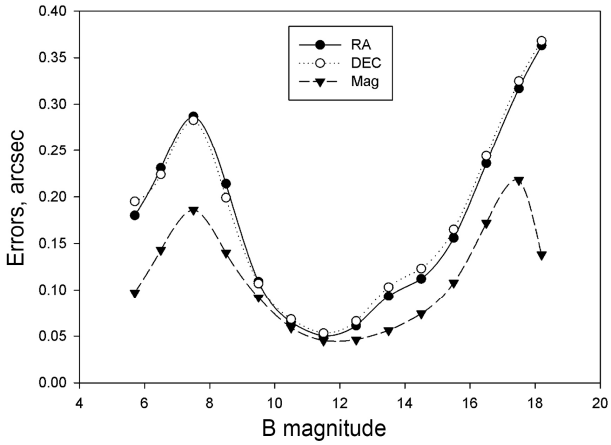

Figure 4: The errors of RA, DEC and magnitudes according to B-magnitudes.

Table 2. The internal errors of the defined equatorial coordinates and stellar magnitudes of the catalogue.

	B_{ph}	σ_α	σ_δ	σ_{Bph}	*FWHM*	*Intencity*	*k*
1	*5.72*	*0.180*	*0.195*	*0.097*	*83.4*	*113.7*	*226*
2	*6.57*	*0.231*	*0.224*	*0.143*	*79.2*	*109.2*	*1276*
3	*7.58*	*0.287*	*0.283*	*0.186*	*69.4*	*105.6*	*3828*
4	*8.56*	*0.214*	*0.199*	*0.140*	*54.1*	*100.4*	*9250*
5	*9.56*	*0.109*	*0.107*	*0.092*	*34.6*	*100.2*	*20863*
6	*10.56*	*0.065*	*0.068*	*0.059*	*21.4*	*95.3*	*48313*
7	*11.56*	*0.050*	*0.053*	*0.045*	*13.7*	*87.2*	*110290*
8	*12.57*	*0.061*	*0.066*	*0.046*	*9.7*	*74.0*	*259387*
9	*13.56*	*0.093*	*0.103*	*0.056*	*7.7*	*57.8*	*591427*
10	*14.55*	*0.112*	*0.123*	*0.074*	*6.8*	*40.1*	*1197019*
11	*15.54*	*0.156*	*0.165*	*0.108*	*6.3*	*23.9*	*2208206*
12	*16.53*	*0.236*	*0.244*	*0.172*	*5.9*	*13.1*	*3562269*
13	*17.55*	*0.317*	*0.325*	*0.218*	*5.6*	*7.8*	*3726545*
14	*18.15*	*0.363*	*0.368*	*0.138*	*5.3*	*5.6*	*416800*
Avg.	***16.17***	***0.225***	***0.234***	***0.154***	***6.4***	***20.6***	***12155699***

3. Conclusion

In 1981-1996 in frame of the FON project more than 2600 photographic plates with 30x30 cm in size corresponding to 5.5°x5.5° field of view were obtained in Kitab observatory and this archive is stored at the Astronomical Institute of the Uzbek Academy of Sciences in Tashkent, Uzbekistan. The archive includes between -20 and +28° of the sky by declination. As result of digitization and processing of 1963 plates of the Kitab's archive the catalogue of near 13.4 million equatorial coordinates and B-magnitudes of stars and galaxies down to 17.5^m was compiled for the middle epoch 1984.97 (Pakuliak L.K., 2016, Yuldoshev, 2017).

The coordinates were defined in the system of Tycho-2 and photographic B magnitudes in the Johnson's system. The internal accuracy of the catalogue is $\sigma_{\alpha\delta}$=0.23" and σ_B=0.15^m for all objects on the catalogue, $\sigma_{\alpha\delta}$=0.085" and σ_B =0.054^m for the objects in 5^m-14^m. The convergence of the coordinates with reference system of Tycho-2 and magnitudes with the photoelectric B magnitudes is $\sigma_{\alpha\delta}$=0.042" (for 356 665 objects) and σ_B=0.16^m (for 6 719 objects) respectively. The errors related to the UCAC4 catalogue are $\sigma_{\alpha\delta}$=0.26" (identified 9 892 697 or 73.75% objects).

In addition, it is planning to digitize and process of 1600 plates of FON project in Tajikistan. This archive covers from 0° to +90° of the sky (Mullo-Abdolov, 2017).

Interim results on the progress of compiling the catalogue of Kitab's part of FON program were reported at the Gamov-2015 (Andruk, 2015a), Gamov-2016 (Yuldoshev, 2016a), and other conferences (Muminov, 2013; Muminov, 2016; Yuldoshev, 2016b).

Acknowledgements. The authors express their gratitude to E. Rakhmatov and E. Mirmahmudov who carried out photographing of the Kitab's zone of the FON project in 1981-1996.

References

Andruk V.M. et al: 2010, *Kinem. Phys. Cel. Bodies*, **26, N3**, 146.

Andruk V.N., Ivanov G.A., Yatsenko A.I. et al.: 2012, *Bull. T. Shevchenko Nat. Univ. Kyiv., Astron*. **N48**, 11 (in Ukraine)

Andruk V.N., Relke H., Protsyuk Yu.I. et al.; 2015, *Odessa Astron. Publ.*, **28,** 188.

Andruk V.N., Pakuliak L.K., Golovnya V.V. et al.: 2015, preprint, *arxiv.org/abs/1512.05535*.

Andruk V.N., Golovnia V.V., Ivanov G.A. et al.: 2016, *Kinem. Phys. Cel. Bodies*, **32, N1**, 38.

Andruk V.N., Pakuliak L.K., Golovnia V.V. et al.: 2016, *Kinem. Phys. Cel. Bodies*, **32, N5**, 260.

Andruk V.N., Pakuliak L.K., Golovnia V.V. et al.: 2017, *Science and Innovation*, **13a, N1**, 17.

Kolchinskii I.G., Onegina A.B.: 1977, *Astrometry and Astrophysics*, **N33**, 11 (in Ukraine).

Mullo-Abdolov A., Kokhirova G., Relke H. et al.: 2017, *Odessa Astron. Publ.,* 30, this issue

Muminov M.M., Kahharov B.B., Yuldoshev K.H. et al.: 2013, *Izvestija GAO. Pulkovo*, **220**, 517.

Muminov M.M., Ehgamberdiev Sh.A., Latipov A.A. et al.: 2016, *Izvestija GAO. Pulkovo*, **223**, 339.

Pakuliak L.K., Andruk V.M., Golovnia V.V. et al.: 2016, *Odessa Astron. Publ*. **29, N1**, 132

Protsyuk Yu.I., Martynov M.V., Mazhaev A.E. et al.: 2014, *Kinem. Phys. Cel. Bodies*, **30**, **N6**, 296.

Protsyuk Yu.I., Andruk V.N., Kazantseva L.V. 2014 *Odessa Astron. Publ.,* **27**, **N1**, 59-60.

Protsyuk Yu.I., Andruk V.N., Kazantseva L.V. et al.: 2014, *Odessa Astron. Publ*., **27**, **N1**, P..61.

Protsyuk Yu.I., Kovylianska O.E., Protsyuk S.V. et al.: 2014, *Odessa Astron. Publ*., **27**, **N1**, 63.

Relke E., Protsyuk Yu.I., Andruk V.N. et al. 2015, *Odessa Astron. Publ*., **28, N2**, 211.

Yatsenko A.I., Andruk V.N., Golovnya V.V. et al.: 2011, *Kinem. Phys. Cel. Bodies*, **27**, **N5**, 249.

Yuldoshev Q.X., Muminov M.M., Ehgamberdiev Sh.A. et al.: 2016, *Odessa Astron. Publ*., **29,** 160.

Yuldoshev Q., Usmanov O., Ehgamberdiev E. et al.: 2016, *Bull. T. Shevchenko Nat. Univ. Kyiv., Astron.* **N54**, 28 (in Ukraine)

Yuldoshev Q.X., Ehgamberdiev Sh.A., Muminov M.M. et al.: 2017, *Kinem. Phys. Cel. Bodies*, **33**, **N5**, 250.

SUN AND SOLAR SYSTEM

DOI: http://dx.doi.org/10.18524/1810-4215.2017.30.114643

THE EFFECT OF MAJOR METEOR STREAMS ON THE TOTAL OZONE IN THE EARTH'S ATMOSPHERE

Yu. M. Gorbanev[1], I. A. Stogneeva[1], V. A. Shestopalov[1], E. F. Knyazkova[1], I. I. Kimakovskaya[1], S. R. Kimakovsky[1], A. V. Golubaev[2]

[1] The Research Institute "Astronomical Observatory" of the I.I. Mechnikov Odessa National University, Odessa, Ukraine, *skydust@ukr.net*

[2] Institute of Astronomy Kharkiv National University, Kharkiv, Ukraine, *Alexandr_sky@mail.ru*

ABSTRACT. The correlation between the total ozone and activity of major meteor streams, such as the Perseids, Geminids, Leonids and Orionids, has been found using the Total Ozone Mapping Spectrometer (TOMS) measurements of the global ozone distribution over the periods 1978 − 1993 and 1996 − 2001. The autocorrelation analysis of the total ozone time series for the period of about 20 years has confirmed the existence of regular changes in the ozone levels at the peaks of meteor shower activity. It has been established that TO decreases after the dates of peak activity of meteor streams (e.g. the Perseids) or during the whole periods of meteor shower activity (e.g. the Geminids, Orionids and Leonids). The analysis of the total ozone distribution (in the Southern and Northern Hemispheres), as well as the local distribution of ozone (over the selected surface area of several hundred square kilometres), was performed during the Leonid meteor shower in 1999. The atmospheric zones for which the ozone distribution pattern can be described as a result of interaction between the meteor shower material and the ozone layer were localised by applying the TOMS data. Such zones correspond to the regions where the highest Leonid activity has been observed. According to the radar observations (conducted in Kazan, Russian Federation), three activity maxima of the 1988 Geminid shower were reported: on the nights of 7^{th}, 12^{th} and 14^{th} December, 1988. The TO decrease was observed on the same dates. Thus, the analysis of the TO changes during the periods of intense meteor shower's activity enables to preliminary assess the maximum overall decline in the total ozone concentration which makes about 5 DU over two weeks. From the results obtained it can be inferred that the ozone layer can be used as an indicator of the interaction between the meteoric material and the Earth's atmosphere.

Key words: ozone; meteor; Total Ozone Mapping Spectrometer (TOMS)

1. Introduction

One of the important tasks of meteor astronomy is to estimate the global influx of interplanetary dust to the Earth's atmosphere. Various techniques of observations, including visual, photographic, television and radar ones, as well as theoretical methods, have been invoked to address this challenge adequately. All methods for observations involve selectivity due to non-regularity of monitoring, the location of a ground-based observation site, weather conditions, etc. Such selectivity of observations of meteor events in the Earth's atmosphere does not enable to obtain a global pattern of the interplanetary dust influx in meteor streams; hence, satellite observations which provide detailed monitoring of the atmospheric parameters over a long period of time are of great interest with regard to the meteor astronomy tasks. This paper presents an attempt to test the hypothesis about the effect of the meteoric influx on the total ozone (TO) using the TO geophysical satellite data.

Such an effect will be more pronounced, yet short-term for large meteoroids entering the Earth's atmosphere. For instance, as reported in (Gorkavyi et al., 2013), the bolide which exploded near Chelyabinsk (Russian Federation) on 15^{th} February 2013 had formed a new aerosol layer above the Junge layer in the Earth's atmosphere. That new aerosol layer remained in the atmosphere for more than three months. The present study results are based on the measurements by the limb profiler of the Ozone Mapping and Profiler Suite (OMPS) installed on the recently launched

NASA-NOAA Suomi NPP spacecraft. The presence and long lifetime of the stratospheric debris related to the Chelyabinsk bolide has been confirmed by the data obtained with the Optical Spectrograph and Infra-Red Imaging System (OSIRIS) on-board the Odin satellite and reported in the studies (Rieger et al., 2013; Rieger et al., 2014).

The ozone layer monitoring has shown that the TO undergoes significant regular or non-regular changes (Oltmans et al., 1998). The results of processing of the rocket-borne TO measurements reported in (Callis et al., 1979) are indicative of the correlation between the ozone concentrations at altitudes above 26 km and the solar activity. Solar proton flares can also cause the ozone depletion in the Earth's atmosphere (Stephenson et al., 1992; Shumilov et al., 1996; Kasatkina et al., 1998; Tassev et al., 1999; Krivolutsky et al., 2001; Kuznetsov, 2002). Volcanic eruptions are another natural factor affecting the TO. In the study (Deshler et al., 1996), by the example of the Mt. Pinatubo eruption, the authors showed the existence of a correlation between the ozone levels and volcanic aerosol at altitudes below 14 km.

Having analysed the extended TO data set obtained with the Solar Backscatter Ultraviolet instrument (SBUV) on the Nimbus-7 spacecraft and SBUV/2 on-board of the National Oceanic and Atmospheric Administration weather satellites NOAA-9 and NOAA 11 over the period from January 1979 to December 1995, the authors (McCormack et al, 1997) concluded that volcanic eruptions did affect the total amount of ozone in the Earth's atmosphere. The total-column ozone measurements using a Dobson spectrophotometer during a total solar eclipse occurred on 24^{th} October 1995 reported in (Chakrabarty, 1997) may serve as an example of the ozone layer sensitivity to the external effects. A sharp fall in the ozone column was observed 15 minutes before the total phase followed by a sharp rise 10 minutes upon its completion. The amplitude of the effect made $5 - 11$ % of the initial TO value.

Thus, the observations show that the ozone layer in the Earth's atmosphere is sensitive to the external effects. Meteor dust particles when entering and vaporising in the Earth's atmosphere also act as external factors affecting the TO. As reported in (Hedin et al., 2014), between a few tons to several hundred tons of meteoric material enters the Earth's atmosphere each day, and most of this material is ablated and vaporized in the $70 - 120$ km altitude region. The subsequent chemical conversion, re-condensation and coagulation of this evaporated material are thought to form nanometre-sized meteoric smoke particles (MSPs). It is also reported that such products of the meteoric material combustion are reckoned as a significant component of stratospheric aerosol and enhancers of the ozone depletion.

In the study (Link, 1976), the influence of the Orionid and Geminid meteor showers on the TO was concluded from the observational material of the Soviet satellite IK-3. In the meteor physics studies, the reactions between meteoric metal ions (Baggaley, 1977; Poole & Nicholson, 1975) or electrons (Poole, 1978) and ozone in the atmosphere were referred to explain the mechanisms of meteor trail luminosity. Such reactions result in decreased TO while there are also processes which may lead to the formation of meteoric ozone (Bibarsov, 1985). The impact of the sporadic meteors on the ozone layer is rather slight; it is enhanced under the effect of an intense meteor shower, and increases by many times when such phenomena as the Tunguska event occur. As reported in (Turco et al., 1981), in the early 1900s the Smithsonian Astrophysical Observatory conducted a long-term programme to estimate the variability of the solar constant. A spectrobolometer required to measure the relative solar radiation in the range of $0.35 - 1.6$ m was installed at Mount Wilson (California, USA, 34° N, 118° W).

Later, upon the introduction of the technique for the determination of ozone by the Chappuis-band absorption, it became possible to apply the above-mentioned measurements to calculate the ozone column concentrations during the period of the Tunguska event (about 70 % accuracy). The measurements of atmospheric transparency by the Smithsonian Astrophysical Observatory for the years 1909 to 1911 showed unusually low ozone levels in early 1909, implying a TO deficiency of 30 $\pm$15 % comparing to the seasonal mean ozone concentrations for the previous years. Based on the model calculations, the authors (Turco et al., 1982) concluded that as much as 30 million metric tons of nitric oxide (NO) might be generated in the stratosphere and mesosphere due to the Tunguska event, which resulted in the ozone reductions in the subsequent years. In another study (Park, 1978), it was also reported that the anomalous atmospheric phenomena after the Tunguska event could be attributed to the reactions of nitric oxide with atmospheric ozone. Therefore, it may be concluded from above that the effect of such a factor as the interplanetary matter influx on the ozone layer is likely to exist.

2. The search for the effect of annual meteor streams on the Earth's ozone layer

The main objective of this study is to test a hypothesis for the effect of major meteor streams on the Earth's ozone layer. In the study (Hughes & McBride, 1989), the resultant masses of the streams responsible for the Quadrantid, Perseid, Orionid and Geminid meteor showers were found to be $1.3{\cdot}10^{15}$, $3.1{\cdot}10^{17}$, $3.3{\cdot}10^{16}$ and $1.6{\cdot}10^{16}$ g, respectively. These results show that the Perseids are one of the most powerful

meteoroid streams whose contribution to the meteor material influx into the Earth's atmosphere exceeds the contribution of other streams by $1-2$ orders of magnitude. It is the amount of meteoric material which is expected to determine the pattern of a meteoroid stream's impact on the ozone layer. Thus, the Perseid, Geminid and Leonid streams were chosen as target ones to detect a correlation between the meteor shower activity (the meteoric dust influx in time or influx rate) and the ozone content in the Earth's atmosphere.

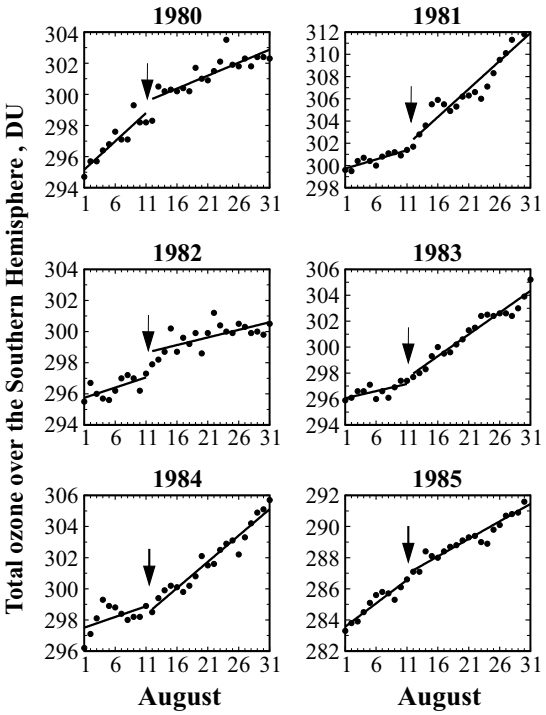

Figure 1: The total ozone over the Southern Hemisphere (SH) during the Perseid meteor shower in 1980-1985.

According to the visual, photographic and radar observations conducted over the recent decades, the peak activity of the Perseid meteor shower falls on the night of August 12. For example, as reported in the study of (Lindblad, 1986), the visual observations of the Perseid meteor streams during $1953-1981$ indicated the following specific features of the stream activity profile: the cross-section consisted of a long-duration, rather flat component and a sharp peak of activity with duration of $1-2$ days. The shower maximum for visual meteors occurred at solar longitude $139^{\circ}.4$ (the Equinox in 1950). The Perseid shower exhibited large variations in activity from year to year. In the study of (Russel, 1986), the Perseid meteor parameters were compared for the showers of 1977, 1978, 1980, 1981 and 1983. Sixteen years of observations of the Perseid meteor shower carried out with the patrol radar in Ottawa (Canada), reported in (Simek & McIntosh, 1986), showed that a sharp flux peak occurred at solar longitude $139^{\circ}.20 \pm 0^{\circ}.026$. It was also reported from the radar observations that the shower remained rather active over several days after the peak. The shift of the Perseid maximum with time was reported in the study (Lindblad & Porubcan, 1994) based on the photographic observations in the period $1937-1985$. The peak activity of the stream was located at approximately $139^{\circ}.5-139^{\circ}.6$ in $1940-1969$ and at $138^{\circ}.9-139^{\circ}.0$ in $1970-1989$. It is likely that there are two peaks of activity for the Perseid stream. Hence, to find a correlation between the Perseid meteor stream activity and the ozone layer of the Earth's atmosphere, it is necessary to pay attention to the TO change after the night of August 12 every year.

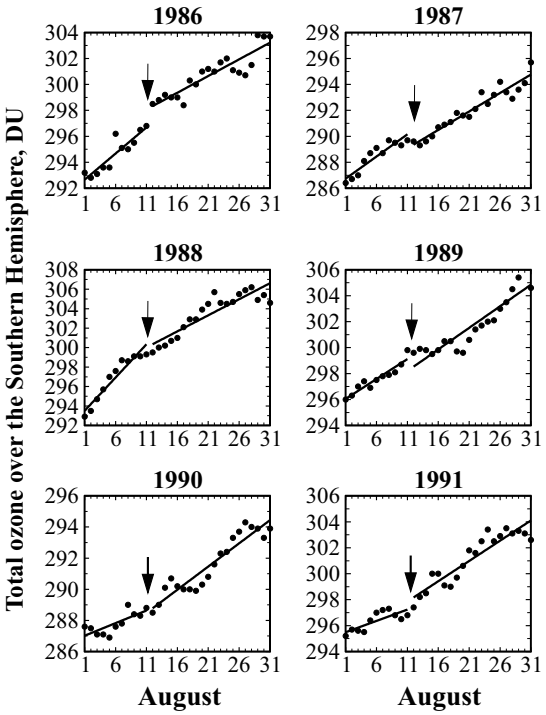

Figure 2: The total ozone over the Southern Hemisphere (SH) during the Perseid meteor shower in 1986-1991.

The measurements made by the Total Ozone Mapping Spectrometer (TOMS) (McPeters et al., 1996), which has been monitoring the Earth's atmosphere during 27 years, were used as observational material for this study. The satellite observation data are available on the web-site: $http://jwocky.gsfc.nasa.gov/$; in this study, we only used the total ozone values among all parameters measured by TOMS. A regular pattern of the total ozone behaviour was reported in our ear-

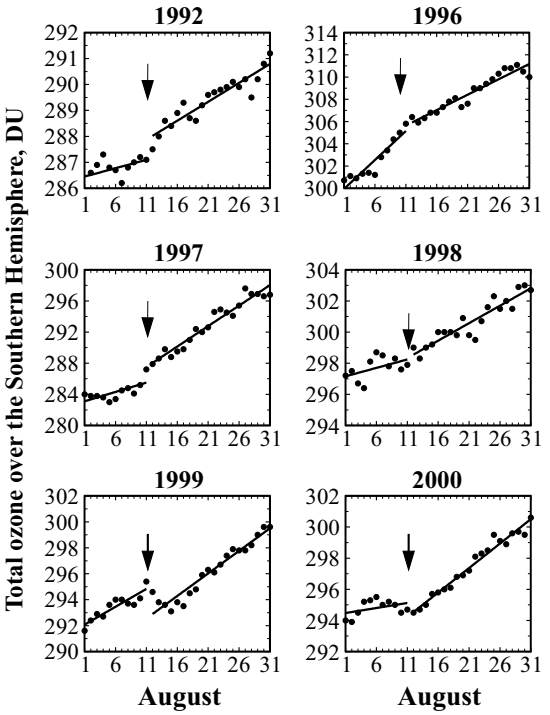

Figure 3: The total ozone over the Southern Hemisphere (SH) during the Perseid meteor shower in 1992-2000.

lier studies (Gorbanev et al., 2000; Gorbanev et al., 2001) which adopted the TOMS measurements of the global ozone distribution over the periods $1978-1993$ and $1996-2001$. The authors emphasise that there are specific features on the plotted total ozone seasonal variations which appear after the night of August 12 from year to year. The seasonal variations in the total ozone observed over the Southern Hemisphere (TO SH) in the month of August for a number of years are plotted in (Figs. $1-3$). The total ozone values in the text and figures are given in commonly used Dobson Units (DU). To provide better visualization of the figures, we have approximated the total ozone curve segments before and after the activity peaks by two straight lines. The following general conclusions about specific features of the profiles in (Figs. 1-3) can be made upon the comparison of these year-to-year straight lines with each other: the straight line constructed from the data covering the period before the activity peak, in fact, merges into the straight line built for the observations after the maximum (as observed in 1985, 1989 and 1996); either a noticeable parallel shift (as in 1982 and 1999) or more or less pronounced break (as in 1980, 1981, 1983, 1997 and 2000) is recorded between the straight lines. This is one of the methods for classifying specific features of the total ozone profiles during the period of the Perseid shower activity. The autocorrelation functions (ACF) were calculated to carry out a more detailed analysis of the data. The authors of this paper suggested that an intense influx of meteoric dust to the Earth's atmosphere occurs after the Perseid shower activity peak on August 12; this dust interacts with the ozone layer thereby changing its concentration.

A distinctive feature of annual meteor streams is the regularity of their activity: the peaks of activity fall on specific dates within a year. However, it should be taken into consideration that the meteor stream activity is regular, but not consistent which is reflected by meteor shower rate variations from year to year. Such pattern of the meteor activity depends on specific structural features of meteor swarms and also upon how the Earth intercepts these streams. The indicated non-uniform pattern of the impact of meteor showers on the Earth's atmosphere resulted in application of the ACF technique which enabled to detect the periodicity of meteor shower activity over a long time interval (about 20 years). We have generated a correlation between a total ozone series and the same series shifted by several time steps (in days) which can be called an autocorrelation function ($R\tau$) where τ is a time shift (or time lag). An absent of any annual periodic influence of the different natural phenomena on TO, including the cosmic dust influx from meteor streams, means that the total ozone profiles would only reflect seasonal variations (which are different in the Northern and Southern Hemispheres). In fact, due to a high sensitivity of the ozone layer, TO is subject to the different-amplitude fluctuations of either human or natural origin, as well as the influence of meteoric dust. From these considerations, the ozone curve segments corresponding to the periods of activity of major meteor streams were approximated by the simplest analytic functions which is consistent with the TO seasonal variations. An ACF which does not display the fluctuation contributions was developed by the approximate values. The most important information is carried by the differences ($\Delta R\tau$) between the ACF constructed by actual and smoothed time series. The dependencies of these differences on the time lag (Fig. 4) enable to point out that specific features of the plotted $\Delta R\tau$ (usually their maxima) correspond to the dates of the peak activity of the Perseid, Leonid, Orionid and Geminid meteor showers. That is indicative of the existence of regular variations in the TO profiles during the periods of meteor shower activity over recent 22 years. Such a tendency can be observed over both the Southern and Northern Hemispheres while it manifests itself to the different extent for the different showers. Another distinctive feature resulting from the correlation analysis is that the relevant local maxima on the plotted TO differences (Fig. 4), which are accurate to within 24 hours, can be observed for the meteor show-

ers with several peaks of activity (e.g. the Orionids and Geminids).

The search for correlations between the TO decline and meteor activity by applying the results of visual, photographic and radar observations is of a great interest. Such correlations were only obtained by the authors from the analysis of radar observations of the Perseid and Geminid activity for a number of years. The meteor radar rates for the period 1980-1985 (Simek, 1987) are presented in (Fig. 5a). The plotted activity profiles present the radar rates (R) for two groups of meteors, such as meteors with echo duration shorter than 1 s, which are small dust particles, and those with longer echo duration (up to 8 s), which are larger dust particles. Providing that the influence of the Perseid meteor stream on the ozone layer does exist, the difference of TO values before the shower's onset and during the peak of its activity should be correlated with the meteor rate at its peak. The difference in TO (D_{TO}) from July 18 to August 10 is plotted in (Fig. 5b). These dates were chosen as the onset date of intense dust influx in the Perseid stream to the Earth's atmosphere and the date preceding the shower's peak rate, respectively. The conducted analysis has shown that the highest correlation between the total ozone decline and meteor shower rate falls in this particular period. At that, the correlation coefficient is higher for the fine dust and reaches a value of 0.96.

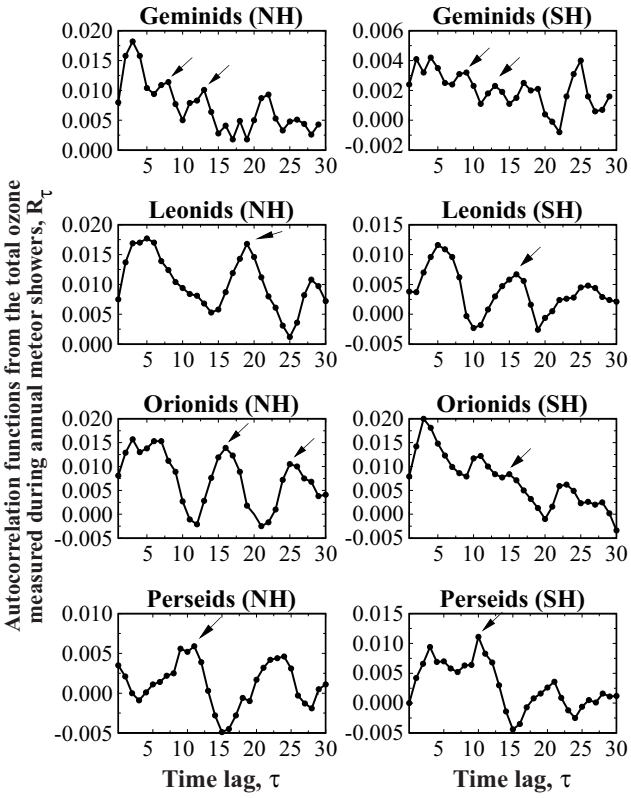

Figure 4: The autocorrelation functions from the total ozone measured during annual meteor showers.

3. The Geminid meteor stream pattern and total ozone

To investigate an interaction of the Geminid meteor shower with ozonosphere, the TO measurements over the Northern and Southern Hemispheres for the period of the shower activity from November 25 to December 25 in 1978 – 2001 were adopted in this study (Fig. 6a). To assess the magnitude of the TO decline, such a characteristic as the ozone deficiency (Δ_{TO}) was introduced. Taking such a decrease in TO as a result of the meteor shower activity and providing that the total ozone remains at the level prior the shower's onset, we define Δ_{TO} as the difference between the actual TO and approximated level of ozone obtained from the seasonal profile segments not affected by the shower's activity (Fig. 6b).

The structural features of the Geminid shower detected from the 1988 Δ_{TO} profiles have been confirmed by independent radar observations carried out in Kazan, Russian Federation (Karpov et al., 1998). The observation data processing has shown that the shower peaked three times during the period of its activity, in particular on the nights of 7^{th}, 12^{th} and 14^{th} December, 1988; it was likely due to the multiply-branched structure of the meteor swarm. The maximum rates of the Geminid meteor shower plotted in (Fig. 6b) are indicated by upward arrows. Three peaks were detected from the 1988 Δ_{TO} profiles falling on the nights of 6^{th}, 11^{th} and 13^{th} of December. It should be noted that the peaks of activity over the Northern Hemisphere were observed on December 6 and 11 while those over the Southern Hemisphere were observed on December 6 and 13. The dates of Δ_{TO} maxima are shifted relative to the dates of the meteor peak rates by a magnitude of one day. This fact can be explained by the asymmetry of the Geminid meteor influx curve, i.e. the Earth intercepts larger amount of meteoric particles before the shower's peak rather than after it (Belkovich et al., 1987).

As can be seen from Δ_{TO}, the TO decline is observed over both the Northern and Southern Hemispheres. Thus, it is reasonable to suggest that it accounts for the position of the Geminid radiant which is near the celestial equator and is being shifted (the daily shift is $\Delta\alpha = +1^\circ.1$; $\Delta\delta = -0^\circ.1$), so that meteoric particles get into the Southern Hemisphere. The Geminid individual radiant positions selected from a number of catalogues of photographic, radar and television monitoring data (Lindblad & Steel, 1993; Lindblad & Porubcan, 1994) were used to test this hypothesis. The selected sample of individual radiants was divided

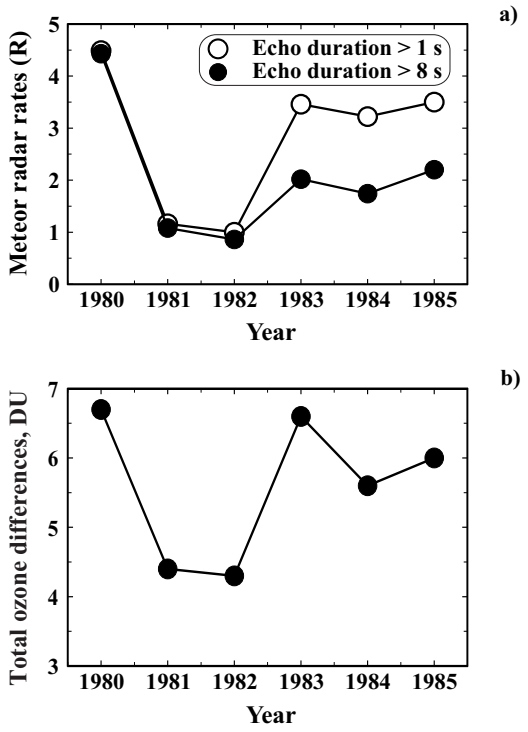

Figure 5: The correlation between the Perseid radar rates (R) and total ozone differences for the Northern Hemisphere (D_{TO} NH) for the period from July 18 to August 10 over 1980–1985.

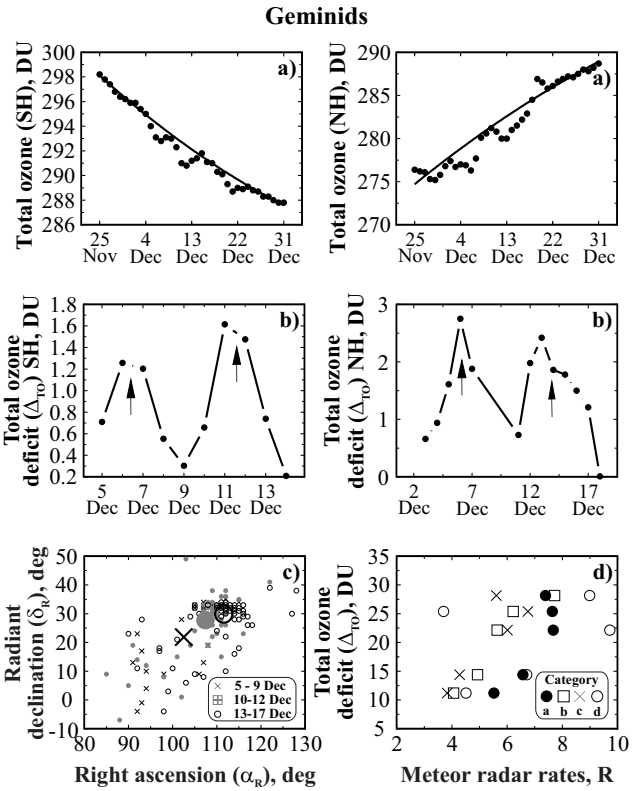

Figure 6: The Geminid meteor shower and total ozone over the Southern (SH) and Northern (NH) Hemispheres: a) the total ozone in November-December, 1988, during the Geminid meteor shower activity; b) the total ozone deficiency (Δ_{TO}); c) the Geminid meteor radiant positions in December; d) the correlation between the 1988 Geminid radar rates (R) and Δ_{TO}.

into three groups by the dates of their intersections with the Earth, including the periods of December 5 − 9, December 10 − 12 and December 13 − 17. A mean radiant for each of the three periods was determined within each group. Having plotted the data for three groups and calculated mean radiant positions for each of the groups, we found that the first group radiant was closer to the celestial equator than the others (Fig. 6c). This is likely why the peaks on the Δ_{TO} curves are observed on December 6 over both the Northern and Southern Hemispheres, i.e. meteoric particles get into both hemispheres. The second group radiant was shifted towards the north from the celestial equator; hence, there is a clear-cut peak on the Δ_{TO} curves for the Northern Hemisphere on December 11 while this peak is less pronounced on the ozone deficiency curve for the Southern Hemisphere. And, finally, the third group radiant position is the most distant from the celestial equator, so that the peak on December 13 can only be observed on the Δ_{TO} curves for the Northern Hemisphere. The effect of the Geminid shower activity on TO is also confirmed by a high correlation between the overall TO decline for the whole period of the shower activity and the Geminid integral radar rates (R) obtained by Czech astronomers (Pecina, 1999). The radar observations of the Geminids in the period 1958 − 1997 were presented in four echo duration categories, namely: a) 0.4 s $\leq T <$ 1.0 s; b) 1.0 s $\leq T \leq$ 8 s; c) $T \geq$ 1 s; and d) $T >$ 8.0 s. It was found from these data (Fig. 6d) that the highest correlation ($k = 0.96$) was observed for the b-category fine particles; hence, it can be concluded that the total ozone is the most affected by fine dust particles.

4. Possible display of the 1999 Leonid meteor shower activity in the ozone layer

The result obtained for the Leonid meteor storm can be reckoned as one of possible confirmations of the ozone layer role as an indicator of meteor activity. According to the visual observations reported in (Arlt et al., 1999), the 1999 Leonid meteor shower activity reached 3700 ±100 meteors per hour at the peak of the storm. Depending on the observation techniques and position of a ground-based observer, the meteor

rate varied from a hundred to 15,000 meteors per hour (Price & Blum, 1998). Such an increase in the stream activity is likely due to the passage of its parent Comet 55P/Tempel-Tuttle. The TO profiles corresponding to the period of the 1999 Leonid meteor stream activity are presented in (Fig. 7).

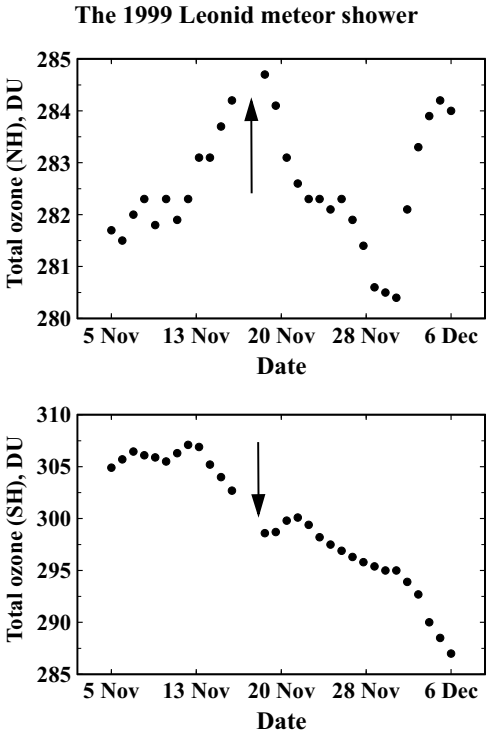

Figure 7: The total ozone over the Southern (SH) and Northern (NH) Hemispheres during the 1999 Leonid meteor shower.

A decrease in TO over the Northern Hemisphere can be observed just after November 18 which is the date of the meteor shower maximum. At this period of the year a seasonal increase in TO can be observed over the Northern Hemisphere while a decrease in TO can be observed over the Southern Hemisphere. The meteor stream activity interferes with the TO seasonal upward trend for the Northern Hemisphere and results in the TO decline after the date of the stream's peak with further re-establishment of the seasonal downward trend within approximately 10 days, which is illustrated in (Fig. 7). The influence of the meteor stream on the total ozone over the Southern Hemisphere is less significant. This is due to the fact that the maximum meteoric material influx during the Leonid shower activity occurred over the Northern Hemisphere of the Earth. Such intense meteor activity should have affected not only the total ozone, but also individual regions of the ozone layer.

A relatively lower activity of meteor showers (with meteor rate up to 100 meteors per hour) results in the TO variations, but does not affect individual regions of the ozone layer. Let us introduce the concept of the local ozone (LO) which is the ozone concentration measured through the atmospheric column over a surface area of a $1^\circ.25$ of longitude and 1° of latitude grid cell. The satellite observation data sets have such a grid-spacing covering the entire globe, and the local ozone distribution is measured by TOMS over each of these areas. The LO change during a meteor storm occurs in the regions where the maximum amount of dust material is carried into the atmosphere, i.e. where the mean orbit of the meteor swarm intersects the Earth's orbit. To localise such regions, we used both preliminary ephemerides of the meteor shower activity and actual observation data, such as: the major peak of the 1999 Leonid shower on 18.11.1999 at 02^h03^m UT (Molau, 1999); at 02^h02^m $\pm 02^m$ UT (Arlt et al., 1999; Rendtel et al., 2000); 01^h55^m $\pm 04^m$ UT (Brown et al., 2002); the secondary peaks on 18.11.1999 at 01^h25^m, 01^h43^m, 01^h50^m, 02^h33^m, 03^h17^m and 03^h29^m UT (Arlt et al., 1999); the radian positions at $\alpha = 153^\circ.65$ $\pm 0^\circ.1$, $\delta = 21^\circ.80$ $\pm 0^\circ.0$ (Molau, 1999); $\alpha = 153^\circ.6$ $\pm 0^\circ.1$, $\delta = 21^\circ.9$ $\pm 0^\circ.1$ (Rendtel et al., 2000); $\alpha = 153^\circ.1$ $\pm 0^\circ.1$, $\delta = 21^\circ.5$ $\pm 0^\circ.2$ (Brown et al., 2002).

The mean orbit of the meteor stream traces an arc in the Earth's atmosphere due to the Earth's rotation and its orbital motion. The dusty cloud responsible for the major peak of the 1999 Leonid meteor storm entered the Earth's atmosphere on November 18 at about 02^h00^m UT at altitudes of $95 - 123$ km (Brown et al., 2002). It is feasible to localise the surface site where the storm radiant position was at the zenith at this instant of time. The geographic coordinates of this point are $\phi = +22^\circ$, $\lambda = 66^\circ$ of east longitude, which coincides with the calculations made by other authors (McNaught & Asher, 1999). Let us assume that the meteoric material influx into this region of the Earth's atmosphere will be the largest at the shower's activity peak. After the meteor event, i.e. the combustion of interplanetary dust particles, the micron-sized products of disintegration in the atmosphere descend from altitudes of $95 - 120$ km to those of 40 km and below.

In astronomy, the activity of a meteor shower is defined as Zenithal Hourly Rate (ZHR), i.e. the number of meteors recorded within an hour. As reported in (Arlt et al., 1999), the Leonid storm was observed with a peak equivalent ZHR of $80 - 100$ for 6 hours. Thus, (Fig. 8) presents the LO maps for different regions of the Earth's atmosphere which cover the area with coordinates $\phi = 66^\circ$ $\pm 60^\circ$, $\lambda = +22^\circ$ $\pm 22^\circ$ where the radiant position of the meteor shower was shifting along the latitude $\phi = +22^\circ$ for 6 hours. Slanting lines with no LO data in (Fig. 8) are related to hardware specific features of data reception by a satellite.

The LO decreased due to fluctuations, but did not

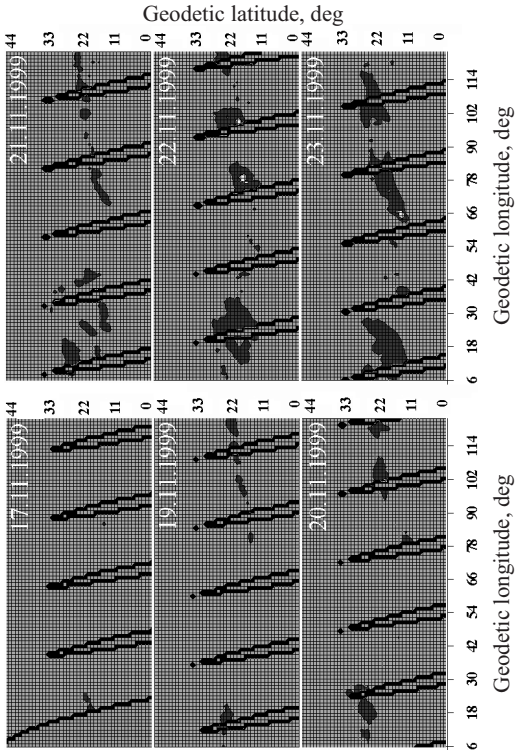

Figure 8: The 1999 Leonid meteor shower display in the Earth's atmosphere. The local ozone isoline maps for different dates during the period of the shower activity.

fall below the level of 253 DU till the peak activity on November $14-16$; hence, the LO isocurves for the other selected six dates were plotted on the maps in the range from 200 to 250 DU. The lower level is determined by the minimum LO values in this region. Distinctive decreases in LO can be tracked along the latitude $\phi = +22°$ which correlates with the latitude of the surface sites where the radiant position is at the zenith during the whole period of the stream activity. It should be noted that these LO drops appear after the Leonid meteor shower activity on November 18, i.e. the date of the peak activity. The increased area and depth of these local formations in the ozone layer after 20.11.1999 can be described as the process of slow deposition of products of combustion and fragmentation of meteoric particles upon their entering the Earth's atmosphere and interacting with the atmospheric ozone.

In the author's opinion, the results presented in this article enable to assert that the ozone layer in the Earth's atmosphere can be an indicator of the activity of meteor showers, in particular, annual major meteor streams, such as the Perseid, Geminid, Leonid and Orionid ones. The kinematic and structural features of meteor swarms can be obtained from the responses of the ozone layer. It is suggested that further studies of the ozone concentration just in the meteor region of the Earth's atmosphere, as well as its responses on the meteor shower activity, should be carried out in the future.

5. Kinetics of Interaction between Meteoric Matter and Ozone Layer

In order to understand the mechanism of the correlation revealed between the activity of meteor showers and variations in the ozone concentrations, let us first get down to observations. Recent studies of the upper atmosphere composition have shown the existence of a secondary ozone layer at an altitude of about $80-90$ km. For instance, radio observations performed with the BLM radar in $1992-2000$ proved the existence of a secondary ozone layer at atmospheric altitudes of $85-90$ km along with the known stratospheric ozone shield at heights up to 40 km (Cevolani & Pupillo, 2003). The authors have associated the observed variations in the mesospheric ozone concentrations with the activity of meteor showers as a result of interaction of the ablated dust particles with ozone. Meteoric ablation is the source of the metal atoms – Na, Fe, Mg, etc. – which occur in the mesosphere at altitudes between 80 and 105 km. At altitudes below 85 km these metals are converted mainly to hydroxides and carbonates through reactions involving O_3, O_2, CO_2 and H_2O (Plane et al., 2014). The study (Dunker et al., 2013) investigated a possible connection between the Geminid meteor shower and mesospheric sodium layer. The results of the observations have shown that the sodium column density during the Geminid meteor shower is lower than the winter average value at the same latitude. Based on the observations conducted on 13^{th} and 19^{th} December, 2010, the authors have come to the conclusion that the daily meteoric Na flux is about 121 kg while the total daily meteoric mass flux into the Earth's atmosphere is about 20 t.

Therefore, physical and chemical parameters of the atmosphere, including the ozone concentrations, at meteor altitudes are expected to correlate with the meteoric mass delivered. For instance, meteor radar observations at the Sodankylä Geophysical Observatory (SGO - $67°22'N$; $26°38'E$, Finland) reported by (Kozlovsky et al., 2016) have indicated that the mesospheric temperature at an average altitude of 91 km is systematically underestimated by $20-50$ K during the Geminid meteor shower (with the peak activity on the 13^{th} of December). According to the SGO meteor radar observations and data obtained with the Earth Observing System (EOS) Microwave Limb Sounder (MLS) onboard the NASA Aura satellite during the Geminid meteor shower in $2008-2014$ the peak night meteor rate accounted for $15,000-20,000$ mete-

ors d^{-1}. A similar temperature effect has been found for the Quadrantids whereas there is no such effect for the other investigated meteor showers. The latter is likely to be associated with the chemical and physical properties of meteoric particles of the given meteor showers.

It should be noted that it would be more effective to search for a correlation between the mesospheric ozone concentration variations and such a meteor shower activity characteristic as the flux density of meteoroids within a given mass range rather than the Zenithal Hourly Rate (ZHR). According to the results reported by (Molau, 2016), the flux density at the peak of the Lyrid meteor shower activity (see Fig. 1 in the paper referred above) is about $4{\cdot}10^{-3}$ meteoroids $km^{-2}h^{-1}$ (which is four times higher than the flux density of the sporadic background). The activity profile of the Lyrids obtained from the IMO Network video observations in $2012 - 2015$ was rather smooth without year-to-year variations while the Quadrantid meteor shower showed interannual variations in the flux density (see Fig. 2 in the paper referred above) which accounted for 10^{-2} to $5{\cdot}10^{-2}$ meteoroids $km^{-2}h^{-1}$ (according to the reported data the indicated flux density is 10 to 50 times higher than that one of the sporadic background). The authors have also reported that the meteor shower sporadic activity is likely to correlate with the lunar phase (± 15 % relative to the average sporadic meteoroid flux density). This could explain the secondary peaks on the correlation curves presented in this paper (see Fig. 4). According to the optical observations carried out in 2011 (Molau & Barentsen, 2014) the meteoroid flux density of another meteor shower, namely the Draconids, was $(118 \pm 10){\cdot}10^{-3}$ $km^{-2}h^{-1}$. However, it should be taken into account that the aforementioned flux density value was reported for the meteors with a limiting magnitude of $+6.5^m$. The flux density for the fainter meteor showers may be orders of magnitude higher (there is a well-known power-law which defines that the dust trail density increases with decreasing mass of dust particles). The calculations based on the observational data obtained by other authors (Trigo-Rodriguez et al., 2013) have shown that the meteoroid flux density over six hours of the Draconid meteor shower averaged to $65.8{\cdot}10^{-3}$ particles $km^{-2}h^{-1}$. The total meteoric mass delivered to the Earth's atmosphere at altitudes up to 85 km in 2011 (on the 8^{th} of October) was 950 ± 150 kg. As reported in the paper (Ye et al., 2014), an intense outburst of the Draconid meteor shower was recorded by the Canadian Meteor Orbit Radar (CMOR) on 8^{th} October, 2012. The peak activity level was equivalent to a ZHR max of 9000 ± 1000 meteors h^{-1} (the peak flux density of the meteoroids heavier than 10^{-7} kg was about 2.4 ± 0.3 $km^{-2}h^{-1}$) whereas the ZHR reported by visual observers was just about 200 meteors h^{-1}. According to the analysis carried out by the International Meteor Organisation (IMO) the peak ZHR was 324 ± 66 meteors h^{-1}.

It was not our aim to thoroughly examine the kinetics of interaction between meteoric matter and ozone layer as it will be the subject of our further research. However, the afore-mentioned published papers of other scientists enable to gain a rather comprehensive understanding about how meteoric matter affects the atmospheric ozone concentrations.

6. Conclusion

The correlation between the total ozone and activity of major meteor streams, such as the Perseids, Geminids, Leonids and Orionids, has been found using the Total Ozone Mapping Spectrometer (TOMS) measurements of the global ozone distribution over the periods $1978 - 1993$ and $1996 - 2001$. The autocorrelation analysis of the total ozone time series for the period of about 20 years has confirmed the existence of regular changes in the ozone levels at the peaks of meteor shower activity. It has been established that TO decreases after the dates of peak activity of meteor streams (e.g. the Perseids) or during the whole periods of meteor shower activity (e.g. the Geminids, Orionids and Leonids). The analysis of the total ozone distribution (in the Southern and Northern Hemispheres), as well as the local distribution of ozone (over the selected surface area of several hundred square kilometres), was performed during the Leonid meteor shower in 1999. The atmospheric zones for which the ozone distribution pattern can be described as a result of interaction between the meteor shower material and the ozone layer were localised by applying the TOMS data. Such zones correspond to the regions where the highest Leonid activity has been observed. According to the radar observations (conducted in Kazan, Russian Federation), three activity maxima of the 1988 Geminid shower were reported: on the nights of 7^{th}, 12^{th} and 14^{th} December, 1988. The TO decrease was observed on the same dates. Thus, the analysis of the TO changes during the periods of intense meteor shower's activity enables to preliminary assess the maximum overall decline in the total ozone concentration which makes about 5 DU over two weeks. From the results obtained it can be inferred that the ozone layer can be used as an indicator of the interaction between the meteoric material and the Earth's atmosphere.

References

Arlt R., Bellot Rubio L., Brown P., Gyssens M.: 1999, *WGN (JIMO),* **27(6)**, 286.

Baggaley W.J.: 1977, *Nature,* **270**, 588.

Belkovich O.I., Kondratieva E.D., Reznikov E.A.: 1987, *Kinemat. & phys. of celest. bod.,* **3(2)**, 34.

Bibarsov R.SH.: 1985, *Akad. N. Tadzhikskoi SSR, Doklady,* **28(9)**, 510.

Brown P., Campbell M.D., Hawkes R.L., Theijsmeijer C., Jones J.: 2002, *PSS,* **50(1)**, 45.

Callis L.B.:1979, *New Scientist,* **84**, 532.

Cevolani G., Pupillo G.: 2003, *An. Geophys.,* **46**, 247.

Chakrabarty D.K., Shah N.C., Pandya K.V.: 1997, *Geophys. Res. Let.,* **24(23)**, 3001.

Deshler T., Johnson B.J., Hofmann D.J., Nardi B.: 1996, *Geophys. Res. Let.,* **23(21)**, 2931.

Dunker T., Hoppe U.-P., Stober G., Rapp M.: 2013, *An. Geophys.,* **31(1)**, 61.

Gorbanev Y.M., Stogneeva I.A., Shestopalov V.A.: 2000, *Collected Works of the First International Conference CAMMAC 99 The Modern Issues Related to Comets, Asteroids, Meteors, Meteorites, Astroblemes and Craters. Vinnitsa,* 268.

Gorbanev Y.M., Stogneeva I.A., Shestopalov V.A., Knyazkova E.F., Golubaev A.V., Ivanova I.I., Kimakovsky S.R.: 2001, *Collected Works of the International Conference the Fourth All-Saint Readings. The Modern Issues in Physics and Dynamics of the Solar System. Kiev,* 90.

Gorkavyi N., Rault D.F., Newman P.A., Silva A.M., Dudorov A.E.: 2013, *Geophys. Res. Let.,* **40(17)**, 4728.

Hedin J., Giovane F., Waldemarsson T.. et al.: 2014, *J. Atmosph. & Sol.-Ter. Phys.,* **118**, 127.

Hughes D.W., Mcbride N.: 1989, *MNRAS,* **240**, 73.

Karpov A.V., Stepanov A.M., Kazakov M.V.: 1998, *Astron. Newslet.,* **32(2)**, 177.

Kasatkina E.A., Shumilov O.I., Raspopov O.M., Henriksen K.: 1998, *Geomagn. & Aeron.,* **38(2)**, 152.

Kozlovsky A., Lukianova R., Shalimov S., Lester M.: 2016, *J. Geophys. Res. Space Phys.,* **121(2)**, 1669.

Krivolutsky A.A., Kuminov A.A., Repnev A.I.: 1999, *Magn. & Aeron.,* **39(3)**, 3.

Krivolutsky A.A., Kuminov A.A., Repnev A.I., Vyushkova T.Y., Pereyaslova N.K., Nazarova M.N., Bazilevskaya G.A.: 2001, *Magn. & Aeron.,* **41(2)**, 246.

Kuznetsov I.V.: 2002, *Magn. & Aeron.,* **42(5)**, 649.

Lindblad B.A.: 1986, *IN: Asteroids, comets, meteors II; Proc. of the International Meeting, Uppsala, Sweden, June 3-6, 1985. Uppsala, Sweden, Astronomiska Observatoriet,* 531.

Lindblad B.A.: 1988, *The IAU Meteor Data Center in Lund at Second GLOBMET Symp., Kazan, USSR, pre.,* 1.

Linblad B.A., Steel D.I.: 1993, *The Meteoroid orbits available from the IAU Meteor Data Center. at Millani et al., Asteroids, Comets, Meteors,* 497.

Lindblad B.A., Porubcan V.: 1994, *PSS,* **42(2)**, 117.

Link F.: 1976, *Eclipses of the IK-3 satellite Transl. into ENGLISH from Compt. Rend., Series B - Sci. Phys.(France),* **282(17)**, 415.

McCormack J.P., Hood L.L., Nagatani R., Miller A.J., Planet W.G., McPeters R.D.: 1997, *Geoph. Res. Let.,* **24(22)**, 2729.

McNaught R.H., Asher D.J.: 1999, *Meteorit. & Planet. Sc.,* **34(6)**, 975.

McPeters R.D., P.K. Bhartia, A.J. Krueger, and Herman J.R.: 1996, *Nimbus-7 Total Ozone Mapping Spectrometer (TOMS) Data Products User's Guide NASA Ref. Publ.,* 73.

McPeters R.D., P.K. Bhartia, A.J. Krueger, Herman J.R.: 1998, *Earth Probe Total Ozone Mapping Spectrometer (TOMS) Data Products User's Guide NASA Ref. Publ.,* 73.

Molau S., Rendtel J., Bellot Rubio L.R.: 1999, *Earth, Moon & Planets,* **87(1)**, 1.

Molau, S.: 2016, *WGN, Proc. of the International Meteor Conference, Egmond, the Netherlands, 2-5 June 2016, Eds.: Roggemans A.; Roggemans P., ISBN 978-2-87355-030-1,* 185.

Molau S., Barentsen G.: 2014, *Earth, Moon & Planets,* **112(1-4)**, 1-5. DOI: 10.1007/s11038-013-9425-3.

Oltmans S.J., Lefohn A.S., Scheel H.E., Harris J.M. et al. 1998, *Geoph. Res. Let.,* **25(2)**, 139.

Park C.: 1978, *Acta Astronautica,* **5**, 523.

Pecina P., Simek M.: 1999, *A & A.,* **344**, 991.

Plane John M. C., Saunders Russell W., Hedin Jonas, et al.: 2014, *J. Atmosph. & Sol.-Ter. Phys.,* **118**, 151.

Price C., Blum M.: 1998, *Earth, Moon, & Plan.,* **82/83**, 545.

Poole L.M.G., Nicholson T.F.: 1975, *PSS,* **23**, 1261.

Poole L.M.G.: 1978, *PSS,* **26**, 697.

Rendtel J., Molau S., Koschny D., Evans S., Okamura O., Nitschke M.: 2000, *WGN (JIMO),* **28(5)**, 150.

Rieger L.A., Bourassa A.E., Degenstein D.A.: 2013, *Atmosph. Measur. Techn.,* **6(5)**, 8435.

Rieger L.A., Bourassa A.E., Degenstein D.A.: 2014, *Atmosph. Measur. Techn.,* **7(3)**, 777.

Russell J.A.: 1986, *A.J.,* **91**, 640-645.

Shumilov O.I., Kasatkina E.A., Raspopov O.M., Henriksen K.: 1996, *Magnet. & Aeron.,* **36(6)**, 15.

Simek M., Mcintosh B.A.: 1986, *Bulletin,* **37(3)**, 146.

Simek M.: 1987, *Bulletin,* **38**, 1.

Stephenson J.A.E., Scourfield M.W.J.: 1992, *Geoph. Res. Let.,* **19(24)**, 2425.

Tassev Y.K., Yanev T.K., Velinov P.I.Y., Mateev L.N.: 1999, *Advanc. in Sp. Res.,* **24(5)**, 607.

Trigo-Rodriguez, Jose M. Madiedo, I.P.Williams, et al.: 2013, *MNRAS,* **433(1)**, 560.

Turco R.P., Toon O.B., Park C., Whitten R.C., Pollack J.B., Noerdlinger P.: 1981, *Science,* **214**, 19.

Turco R.P., Toon O.B., Park C., Whitten R.C., Pollack J.B., Noerdlinger P.: 1982, *Icarus,* **50**, 1.

Quanzhi Ye, Paul A. Wiegert, Peter G. Brown, Margaret D. Campbell-Brown, Robert J. Weryk: 2014, *MNRAS,* **437(4)**, 3812.

DOI: http://dx.doi.org/10.18524/1810-4215.2017.30.115456

SOFTWARE FOR ADAPTING DSPZ RECEIVERS TO THE URAN INTERFEROMETER NETWORK

E.A.Isaeva[1], O.A.Lytvynenko[1], V.A.Shepelev[2]

[1]URAN-4 Observatory of IRA NASU, Odessa, Ukraine, *uran4@te.net.ua*

[2]Institute of Radio Astronomy, NASU, Kharkov, Ukraine, *shep@rian.kharkov.ua*

ABSTRACT. More than 10 years ago, URAN interferometer network (Megn A.V.,1997; Konovalenko A.A., 2014) had been equipped with newly designed receivers with a pass band extended up to 250 kHz and software rejection of interferences (Rashkovskii, 2012). The broadening of bandwidth of received signal increase the sensitivity of the receivers significantly and let us to investigate the angular structure about one hundred radio sources. A software package had been developed that allows: preparing a program of observations, carrying out observations automatically, making data cross-correlation, calculating visibility functions for all pairs of antennae, and fitting models of an angular structure of the sources. Data storage formats were elaborated for each stage of recording or processing.

At present, new digital radio astronomy receiver DSPZ have been developed by IRA NASU (Zakharenko, 2016). The receiver allows recording an entire bandwidth of signals of a decameter range from 8 to 32 MHz. It is used at UTR-2 and URAN radio telescopes operated in a single dish mode. Application of the receivers for interferometer observation with the URAN network provides additional advantages in accuracy and sensitivity of studies. In this report we consider the data formats and synchronization methods used in URAN equipment and DSPZ receivers, and discuss algorithms of their transformation. Newly elaborated software is described, that allows selecting a set of frequency bands of signals recorded with DSPZ and converting them to the form used by the URAN software. This approach allows us to carry out the interferometer observations in an the extended frequency range provided by DSPZ and to use as much as possible the software package developed for the URAN network for data reduction.

Keywords: URAN network, interferometer observation, DSPZ receiver, frequency bands, time marker

1. Introduction

The UTR-2 radio telescope is currently equipped with digital DSPZ receivers with a wide dynamic range determined by 16-bit ADCs. They allow to record all frequency range of signals received by the radio telescope 8 to 30 MHz. These receivers are very versatile and can be used in various observational programs, including interferometric studies.

URAN interferometers used set of receivers with narrower pass band which operate simultaneously at two selected frequencies of the range.

Extending of the pass band and / or increasing the number of operating frequencies using DSPZ would be very useful for improvement of the quality of the interferometer studies of radio sources structure. A software package for data correlation and reduction has been worked out for the URAN earlier and using of these developments will accelerate application of the DSPZ receivers to interferometer studies.

The purpose of this work is to create software for conversion of data collected by DSPZ broadband receivers to the format used in the URAN. It makes possible to carry out the data reduction using the software elaborated for these interferometers.

2. Date formats and conversion data files

The data recorded by DSPZ receiver are stored in files of *.jds format. The format of data recorded by URAN receiver is *.itm. The difference of signals recorded by the receivers is presented in the Table 1. Therefore a structure of data stored, service information, and synchronization methods used in these formats are quite different.

Table 1: data parameters of two formats

Parameters	Format *.jds	Format *.itm
Signal bandwidth, MHz	16,33	0,25
Sampling frequency, MHz	33,66	1
ADC resolution, bits	16	8
Output channels	2	4

Let's consider a structure of a computer program developed to transform of the data stored in *.jds data files recorded by DSPZ to format of *.itm data files used by the URAN receiver. The program consists of two independent modules: dsp_transform.exe and dsp_fft.sav. The main module dsp_transform.exe is written in Delphi while IDL is used for called program module dsp_fft.sav. The program module dsp_transform.exe contains a user interface to manage the data conversion program and visualize process of conversion.

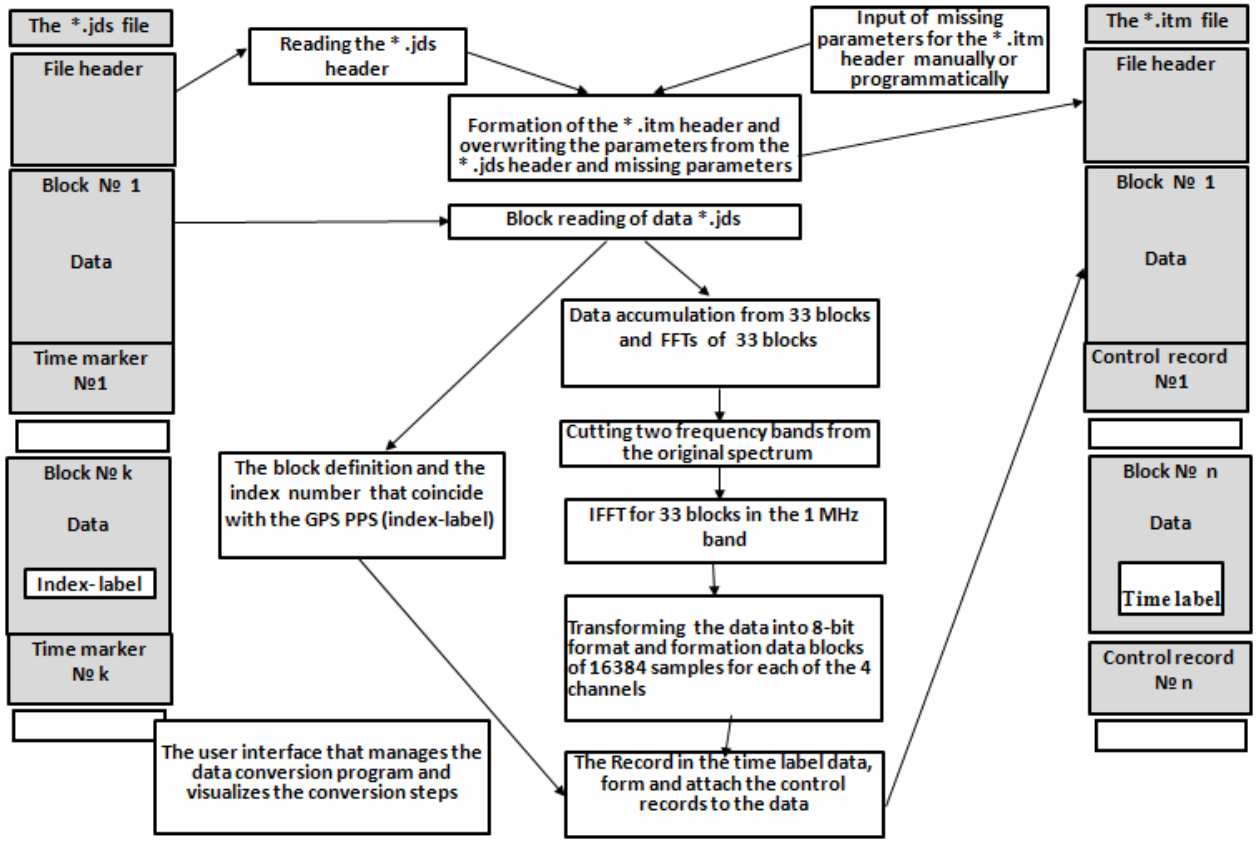

Figure 1: Diagram of the data conversion by the program dsp_transform.exe

The program module dsp_fft.sav allows to transform data recorded in *.jds format to *.itm format.

In general, conversion of data in *.jds format to * .itm format can be represented as the following scheme (see Figure 1).

3. Spectral transformations

For radio interferometer observations with DSPZ receivers, the frequency band of the input signal can be limited to range from 16,5 MHz to 30MHz. In this case, the Nyquist condition will be satisfied if the sampling frequency of DSPZ is 33 MHz. That range contains operating frequencys of URAN receivers (usually 20 and 25 MHz).

After performing of the Fast Fourier Transform (FFT) of the DSPZ receiver output signal, an inverted spectrum in the range 0 – 16.5 MHz will be obtained. In this case it is necessary to consider that the current frequency f in the spectrum of the original signal corresponds to the current frequency f_{FFT}=33MHz-f in the inverted spectrum (see Figure 2a). Thus, in order to obtain the original spectrum, it is necessary to invert the indexes of counts in the obtained inverted spectrum. Figure 2 shows the results of signal transform of the DSPZ receiver test record (from *.jds format to *.itm format).

The next step of format conversion is extracting of narrow bands from the original spectrum and reducing sampling frequency. These narrow bands should correspond to the band of recorded signals in *.itm files. The bandwidth of the URAN receiver recorded signal is 250 kHz, and the sampling frequency of a signal is 1 MHz.

The second procedure after FFT is cutting out two band of 1 MHz width from the inverted spectrum of the original DSPZ signal.

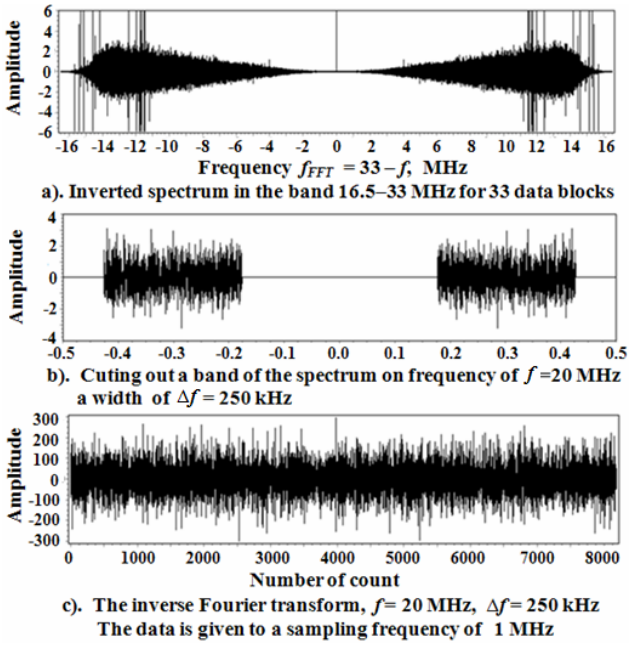

Figure 2: Cutting the frequency band and converting the data to the new sampling frequency.

Each of bands must include one of the operating frequencies of the URAN receivers. In extracted band, all spectral components must be zeroed apart from those corresponding to the recorded signal of the URAN receiver.

This procedure of cutting out the band of the spectrum from the data in the *.jds format automatically reduces the sampling rate by 33 times, which corresponds to a sampling frequency in the *.itm format (1 MHz). Figure 2b shows an example of cutting out and shifting a 250 kHz band with a center frequency f = 20 MHz, which corresponds to f_{FFT}=13 MHz in inverted spectrum.

Then, using the Inverse Fourier Transform (IFFT) of the extracted frequency band, we obtain a signal in the *.itm format. Figure 3c shows a signal in the *.itm format which was obtained from the DSPZ receiver test record.

4. Formation of data blocks and their synchronization

The data in the formats *.jds and *.itm differ in the size of the data blocks, the number of channels, and the service information recorded at the end of each block, and also the ADC resolution.

The data block in *.itm format has the dimension equal to array[i= 0..16383, j=0..3], and in the format *.jds array[i= 0..8189, j=0..1], where i is the number of count, and j is the channel number. Thus, the next step of the data conversion is the formation of data blocks of a correct size, which corresponds to *.itm format. Then a control record must be generated for each block and inserted at the end of the block. The control record contains the parameters which are necessary for the data synchronization. These parameters are calculated using an information from time markers of *.jds blocks.

The DSPZ receivers use 16-bit ADCs while the URAN data are stored in 8-bit. For the purpose of transformation, the standard procedure in IDL BYTSCL is used, which allows scaling the signal at specified boundary values. Three options for converting data to an 8-bit format for different situations and tasks are provided.

The first option uses an absolute scaling of the signal over the maximum and minimum amplitude values for the entire record. This option cannot work properly when spikes occur with amplitude which exceeds several times the maximum operating range of a useful signal. In this case the useful signal will be significantly suppressed. The second option is the most universal. It uses a specified boundary values of BYTSCL procedure associated with the roof-mean-square deviation of the signal that was calculated for the entire record. The third option is direct clipping of higher bits of a binary signal. This option can be used when the signal recording mode of DSPZ receivers is limited to 8 bits.

Data in the formats *.jds and *.itm differ in the way of synchronization. In the *.jds format, a time marker is recorded at the end of each data block, containing seconds of the day and a phase of the seconds equal to the number of samples passed since the beginning of each second. Unlike the *.jds format, in *.itm format, the time label is embedded directly into the data block instead of some sample. Thus, knowing the phase of a second in the *.jds format, one can calculate the index of sample in the data stream in the *.itm format, taking into account the reduction in the sampling rate by 33 times. Now you can insert time labels into the generated *.itm file.

5. Conclusion

The software for the conversion of DSPZ data to the format used in the VLBI URAN has been developed. This software was tested in the long-baseline interferometer observations with the URAN-2 interferometer (Shepelev V.A., 2017). The standard URAN interferometers equipment and DSPZ receivers were used simultaneously in this experiment. Obtained results demonstrate the effectiveness of the application of the programs developed.

References

Konovalenko A.A., Kalinichenko N.N., Lytvynenko O.A. et al.: 2014, *VarSITI_Newsletter*, **2**, 1.

Megn A.V., Braude S.Ya., Rashkovskii S.L. et al.: 1997, *Radiophys. and Radioastron.*, **2**, 385 (in Russian).

Rashkovskii S.L., Belov A.S., Ivanov A.S. et al.: 2012, *Radiophys. and Radioastron.*, **17**, 201 (in Russian).

Zakharenko V., Konovalenko A., Zarka P. et al.: 2016, *J. Astron. Instrum.*, **5**, no. 4. id1641010.

Shepelev V.A., Konovalenko A.A., Lytvynenko O.A. et al.: 2017, in *17-th Odessa International Astronomical Gamow Conference-School Abstracts 2017*, Odessa, Ukraine, p. 30.

DOI: http://dx.doi.org/10.18524/1810-4215.2017.30.114670

MICROWAVE EMISSION OF SOLAR FLARES: CORONAL MASS EJECTIONS AND SHOCK WAVES

E.A.Isaeva[1], Yu.T.Tsap [2,3]

[1] Institute of Radio astronomy of NAS of Ukraine, URAN-4 observatory, *isaevaode@gmail.com*

[2] Crimean Astrophysical Observatory

[3]Pulkovo Observatory

ABSTRACT. Coronal mass ejections (CMEs) mostly affect the geomagnetic field. These structures are observed and studied with coronagraphic images therefore we don't see the corona in the plane of the sky and the measurements of the propagation speed for solar disk events are not accessible to coronagraphic observations. This suggests that microwave emission of solar flares that can be attributed to the gyrosynchrotron mechanism of mildly relativistic electrons can be used. In turn, the relationship between coronal shock waves and CMEs also remains unclear.

The data set that we use in this study is based on microwave (μ) observations of spectral fluxes F_μ at 8.8 GHz obtained with the Radio Solar Telescope Network for the 124 proton solar events . The correlation coefficient r between the CME velocities V_{CME} and integral fluxes of microwave emission $\int F_\mu dt$ achieves of about 0.8 while it does not exceed 0.36 between V_{CME} and the shock wave velocities. It has been found the quite strong correlation between the growth rate of microwave emission and the deceleration of frequency drift in the frequency range of 25-180 GHz ($r \approx 0.66$). The obtained results suggest that microwave observation can be used to predict V_{CME} and the shock wave generation occurs in the region of flare energy release.

Keywords: Coronal mass ejections (CMEs), shock waves.

1. Introduction

The data set includes 124 proton events recorded from 06-11-1997 to 20-09-2015 with proton energies > 1-100 MeV, which were simultaneously accompanied by the microwave IV type bursts (μ-bursts) and coronal mass ejections (CME).

This data set contains a large number of overlapping proton events, which were separated and identified by the authors themselves. In this connection, some of these events are absent in the world data center (WDC), where a list of proton events with proton energies > 10 MeV is given and where overlapping events are not always separated. Among the 124 proton events 76 ones are present in the proton events directory ftp://ftp.swpc.noaa.gov/pub/indices/SPE.txt, and 48 events have been identified by us independently. As a result, the list includes superimposed proton events with energy E > 1-100 MeV.

When identifying proton events with flares, we were guided by generally accepted criteria. However, we do not exclude the mistakes made by us in the separation and identification of complex overlapping events.

The most important criterion for the proton flares is the presence of a *U*-shaped and *W*-shaped type of the frequency radio spectrum of continual radio bursts of IV type in the range of 25-25000 MHz. Such types of frequency radio spectrum have a deep minimum in the decimeter range and the pronounced maxima in the centimeter and meter ranges. Earlier it was shown by a number of authors that we can estimate the total number of accelerated particles based on the parameters of microwave bursts whereas the conditions of particle escape follow from the parameters of meter-decameter bursts (Akin'yan et al., 1977, 1978, Chertok 1982; Chertok et al., 1987; Melnikov et al., 1990; 1991; Lipatov et al., 2002). The sufficiently powerful meter-decameter component of the continuum radio bursts of the IV type suggests the favorable conditions (Daibog et al., 1987) and vice versa.

Another important criterion of for proton flares is the effective duration of microwave bursts at the frequency of a microwave spectral maximum. Using this parameter, we can estimate the enrichment of the solar energetic particles (SEP) by protons with respect to electrons. In particular, Daibog et al. (1989, 1993) have shown that the acceleration of sub-relativistic protons requires significantly more time than electrons.

The next important criterion of proton flares is the heliographic longitude of the proton flare λ, counted to the east and west of the central meridian on the Sun. It is known that there is a very strong dependence of the parameters of proton fluxes on the heliographic longitude of flares (Ochelkov, 1986), since the direction of propagation of the proton flux is determined by the spiral structure of the interplanetary magnetic field.

Thus, to identify proton events with flares, it is necessary to know the heliographic longitude of the flare and the type of the frequency radio spectrum.

It is known that the microwave IV type bursts (μ-bursts) are always accompanied by bursts of soft X-ray emission. Therefore, based on the time of the flare maximum and coordinates in X-rays, it is possible to identify the radio bursts on the solar disk with proton events.

Using the coordinates of the X-ray flare, we can estimate the arrival time of the first protons at the near-Earth orbit. In this case, it is necessary to take into account the time delay between the first protons detected near-Earth orbit and the peak of the X-ray flare emission. The corresponding delay time largely depends on the heliographic longitude of the flare. The shortest delay time is observed

for western proton events with heliographic longitude in the range from 60 to 90 degrees, measured from the central meridian on the Sun. High-energy protons with E > 100 MeV are registered the first in about 20 minutes after the peak of X-ray flare emission. However, the delay time for the eastern events is much longer than the delay time for the western ones and can range from a few hours to three days. The delay time, or the geometry of propagation of the proton flux in the interplanetary space, is determined by the degree of diffuse scattering of the proton flux. The longer proton path is caused by the more diffuse scattering, and as a consequence, the decrease in the intensity of the proton flux in the Earth's orbit. It should be taken into account that the fluxes of high-energy protons undergo the greatest attenuation. As a result that, the energy spectrum of the protons becomes steeper, that is, for eastern events, an increase in the exponent of the energy spectrum of the protons is observed. Moreover, the higher the degree of diffuse scattering of the proton flux, the greater the rise time of the proton flux, which in turn affects the temporal profiles of the proton flux. Therefore, for eastern events, the temporal profile of the intensity of the proton flux becomes smooth, and for the eastern events on the limb of the Sun, the growth time can be even longer than the decay time. At the same time, for western proton events a sharp increase in the intensity of the proton flux is observed for several hours.

The identification of proton events with flares, for single western proton events, is not very difficult. However, for a series of overlapping proton events, the identification procedure can be ambiguous, because in a series of overlapping events, both western and eastern events can be present, spread over time from several hours to 3 days. But, despite this, the vast majority of overlapping proton events can be divided and identified with flares.

To identify proton events with flares, we used the original data of X-ray emission from the Sun and the proton fluxes using GOES data, as well as the original records of the radio emission of the Sun in the range 25-15400 MHz.

2. Background data

The original data of the intensity of the proton flux with energy > 1-100 MeV and the X-ray emission in the ranges 0.05-0.4 and 0.1-0.8 nm (https://satdat.ngdc.noaa.gov/sem/goes/data/new_avg/).

Dynamic spectra in the range 25-180 MHz (http://www.ngdc.noaa.gov/stp/space-weather/solar-data/solar-features/solar-radio/rstn-spectral/).

Solar radio emission at frequencies of 245, 410, 610, 1415, 2695, 4995, 8800, 15400 MHz (https://www.ngdc.noaa.gov/stp/space-weather/solar-data/solar-features/solar-radio/rstn-1-second/).

Tabular data of the shock wave velocities detected in the range 25-180 MHz (http://www.ngdc.noaa.gov/stp/space-weather/solar-data/solar-features/solar-radio/radio-bursts/tables/spectral-sgd/).

Tabular data of velocities of coronal mass ejections (CME) (https://cdaw.gsfc.nasa.gov/CME_list/UNIVERSAL/text_ver/univ_all.txt) .

3. Relationship between CME velocities and parameters of continual radio bursts

In this paper, the relationship between the CME velocities V_{CME} and the parameters of continual radio bursts in the range 245-15400 MHz is investigated. Comparative analysis has shown that there is a strong correlation between V_{CME} and the integral flux of microwave bursts $\int F_\mu dt$ in the range of 2695-15400 MHz. Fig. 1a shows the relationship between V_{CME} and $\int F_\mu dt$ at 8800 MHz, where N is the number of events, and r is the correlation coefficient between these values. For the vast majority of proton events, indicated by black circles, the correlation coefficient r between V_{CME} and $\int F_\mu dt$ is about 0.80. The gray line in Fig. 1a shows the linear regression (1), which is described by the equation

$$\log_{10} V_{CME,\mu} = 0.2322 \cdot \log_{10} \int F_\mu dt + 4.8603 \qquad (1),$$

where $V_{CME,\mu}$ is the calculated value. The light circles in Fig. 1a are most likely related to errors in the identification of proton events with flares and CMEs. Among 14 events marked with light circles, 7 ones were identified by the authors, the rest were taken from the WDC catalog. But, out of these 7 events, 3 in the microwave range 4995-15400 MHz were accompanied by bursts of GRF type, but they had a sufficiently powerful continual burst in the range 245-2695 MHz. In connection with this, these events were included in the sample of proton events. If 7 events identified by the authors and 3 events that were

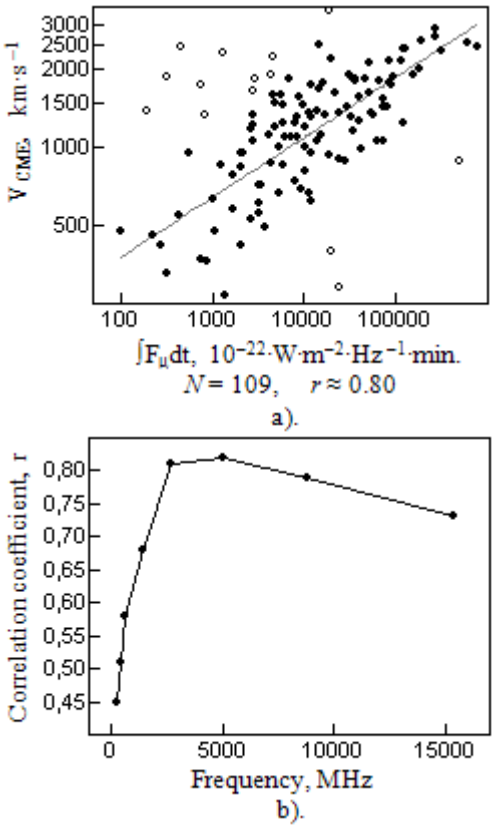

Figure 1: The relationship between the CME velocities V_{CME} and the integral fluxes of continual radio bursts $\int F_\mu dt$.

accompanied by GRF bursts, to exclude from this sample, then only 4 events will remain for which there is a poor correlation between V_{CME} and the integral flux of μ-bursts.

It is also seen that the correlation between the V_{CME} and the integral flux $\int Fdt$ decreases significantly with decreasing frequency, and the correlation coefficient r between V_{CME} and $\int Fdt$ does not exceed 0.45 in the meter range at 245 MHz, (see Figure 1b).

4. Relationship between coronal shock waves and CMEs

To study the correlatiobetween shock waves and CMEs, the tabular data of the shock wave and CME velocities, as well as original dynamic spectra in the range 25-180 MHz, were used.

It is known that shock waves can be generated both by solar flares and coronal mass ejections. The II type bursts in the decimeter-meter ranges are associated with shock waves caused by flares (Wagner et al., 1983, Vrsnak et al., 1995), while the decameter-hectometre bursts is related to the propagation of interplanetary shock waves generated by CMEs (Gopalswamy et al., 1998; Classen et al., 2002). The most reliable indicator of shock waves in the solar corona are the slowly drifting type II bursts. It is believed, that the plasma mechanism of radio emission is responsible for their generation (Cairns et al., 2003).

In this paper, the following approximation of the dependence of the frequency $f_{i,j}$ on the time t_i is used

$$\log_{10} f_{i,j} = a_j \cdot \overline{t_i} + b_j \qquad (2)$$

where t_i is the time of the maximum intensity of the II type burst at the frequency $f_{i,j}$, a_j and b_j are the linear regression coefficients, $i = 1 \ldots n$ is the account number, $j = 1,2$ is the harmonic number. The zero point of time for all events corresponds to the beginning of the first harmonic at a frequency of 180 MHz. The approximation (2) allows us to estimate the frequency $f_{i,j}$ in the range 25 -180 MHz for 95% of the events quite precisely. In particular, the correlation coefficient r between the calculated $f_{i,j}$ and observed frequency values f turned out to be greater than > 0.98 for selected events (see Figure 2c). Fig. 2 shows the histograms of the distribution of the number of events for which the correlation coefficient r between the observed value of f and the calculated value of the frequency $f_{i,j}$ lies in a specified range of values. Other approximations (3,4)

$$\log_{10} f_{i,j} = a_j \cdot \log_{10} t_i + b_j \qquad (3)$$
$$\log_{10} f_{i,j} = a_j \cdot t_i + b_j \qquad (4)$$

of the frequency dependence on time was previously used, which gave a lower accuracy of frequency estimation (see

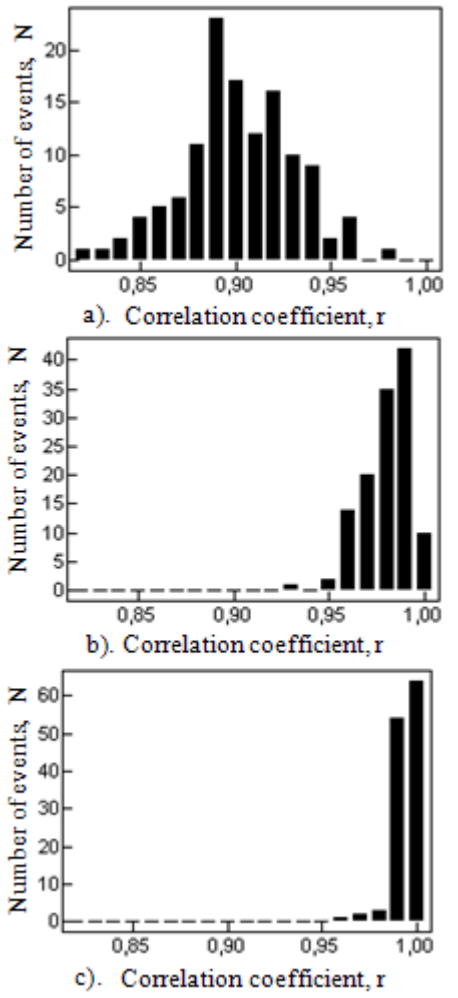

Figure 2: The comparison of the different approximations describing the dependence of the frequency $f_{i,j}$ on the time t_i

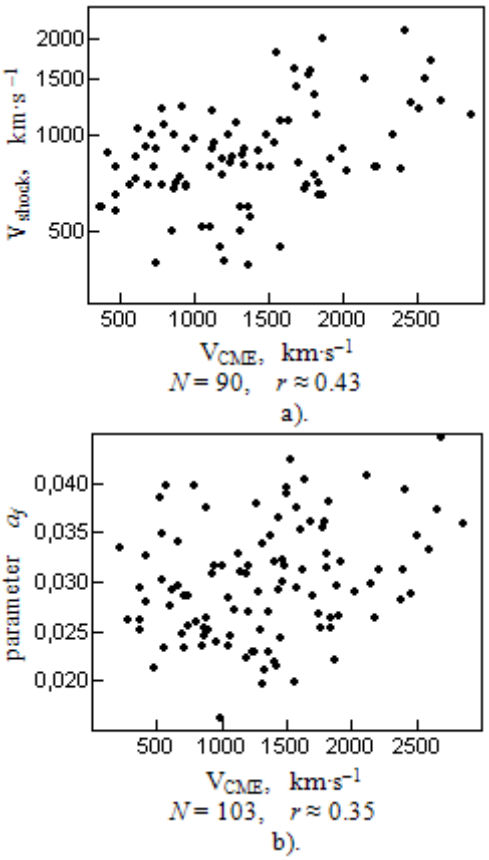

Figure 3: The relationship between shock wave velocities V_{shock} and CME velocities $V_{CME.}$

Figure 2a,b). In Fig. 3a,b shows the relationship between the CME velocities V_{CME}, shock wave velocities V_{shock}, and the parameters a_j, which characterize the slowdown of frequency drift in the model (2). It is clear that the corresponding correlations are weak. At first glance, this can explain by different time of registration of shock wave velocities and CME. However, the correlation between the CME velocities V_{CME} and the frequency drift velocities $V_{II} = \frac{df}{dt}$, calculated at the time of CME detection turned out to be weak.

5. Relationship between shock waves and solar flares

Let us consider the correlation between shock waves and the parameters of μ-bursts in terms of the original radio data at 8 fixed frequencies in the range 245-15400 MHz. A comparative analysis has shown that there is a relatively good correlation between the parameters a_j and the rise time t_μ of μ- bursts at the frequency of 8800 MHz. The correlation coefficient between t_μ and a_j is ≈ 0.66 (see Figure 4a). Note that we took into account that flares differ significantly in intensity and duration we therefore expressed the rise time t_μ as a percentage of the duration (100%) of μ-bursts.

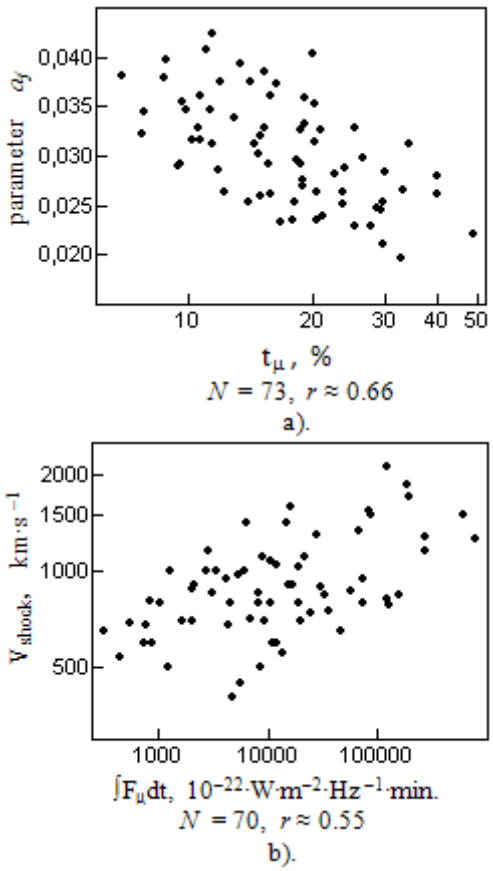

Figure 4: Relationship between shock wave velocities V_{shock} and parameters of microwave bursts

The correlation between the shock wave velocities V_{shock} and the integral fluxes $\int F_\mu dt$ of μ-bursts at the frequency of 8800 MHz was also investigated. The correlation coefficient between $\int F_\mu dt$ and $V_{shock} \approx 0.55$ (see Fig. 4b). The weak correlation between V_{shock} and $\int F_\mu dt$ is most likely due to the fact that different stations give averaged estimates of the velocity of shock waves at different time a fairly large dispersion should be observed. Despite this, the correlation between $\int F_\mu dt$ and V_{shock} can by quite clearly seen for the majority of proton events (see Fig. 4b).

References

Akin'yan S.T. et al.: 1977, *Geomagnetizm i Aeronomiia*, **17**, 10.
Akin'yan S.T. et al.: 1978, *Geomagnetizm i Aeronomiia*, **18**, 577.
Cairns I.H. at al.: 2003, *Space Sci. Rev*., **107**, 27.
Chertok I.M.: 1982, *Geomagnetizm i Aeronomiia*, **22**, 182.
Chertok I.M. et al.: 1987, *Geomagnetizm i Aeronomiia*, **27**, 362.
Classen H.T. et al.: 2002, *A&A*, **384**, 1098.
Daibog E.I. et al.: 1987, *Izv. AN SSSR, ser.ph.*, **51**, 1825.
Daibog E.I. et al.: 1988, *Izv. AN SSSR, ser.ph.*, **52**, 2403.
Daibog E.I. et al.: 1989, *Letters to the Astron. J.*, **15**, 991.
Daibog E.I. et al.: 1993, *Solar Phys*., **144**, 361.
Gopalswamy et. al.: 1998, *J. Geophys. Res*., **103**, 307.
Lipatov B.N. et al.: 2002, *Izv. of HEIs, Radiophysics*, **65**, № 2, 83.
Melnikov V.F. et al.: 1990, *Solar-Terrestrial Predictions, US Dep. Of Comm., NOAA, Boulder, Co.*, **1**, 533.
Melnikov V.F., et al.: 1991, *Space Research.*, **29**, 95.
Ochelkov Yu.P.: 1986, *Geomagnetism and Aeronomy*, **26**, № 6, 1007.
Vrsnak B. et al.: 1995, *Solar Phys*., **158**, 331.
Wagner W.J. et al.: 1983, *A&A*, **120**, 136.

DOI: http://dx.doi.org/10.18524/1810-4215.2017.30.117655

UKRAINIAN DATABASE AND ATLAS OF LIGHT CURVES OF ARTIFICIAL SPACE OBJECTS

N.Koshkin [1], V.Savanevych [2], A.Pohorelov [3], L.Shakun [1], V.Zhukov [4], E.Korobeynikova [1], S.Strakhova [1], S.Moskalenko [2], V.Kashuba [1], A.Krasnoshchokov [2]

[1] Astronomical Observatory of Odessa I.I.Mechnikov National University, Ukraine, *nikkoshkin@yahoo.com*

[2] The National Center of Space Facilities Control and Test (SCC NCSFCT), Ukraine

[3] The Kharkiv National University of Radio Electronics, Ukraine

[4] Skyline Electronics Ltd. Co., Odessa, Ukraine

ABSTRACT. This paper describes the Ukrainian database of long-term photometric observations of resident space objects (RSO). For the purpose of using this database for the outer space monitoring and space situational awareness (SSA) the open internet resource has been developed. The paper shows examples of using the Atlas of light curves of RSO's for analyzing the state of rotation around the center of mass of several active and non-functioning satellites in orbit.

Key words: Database, space object, photometry, light curve, rotation period.

1. Introduction to the problem

The significance and functions of resident space objects in near-Earth orbits is continuously growing. In the same time the debris of outer space is also increasing. Especially dangerous collisions involve large massive objects that can produce a large number of fragments. An effective way to prevent this is removing the most dangerous space debris (SD) from the Earth's orbit. Removing an object from the orbit requires an accurate prediction of its motion and RSO orientation parameters. The important characteristics of the removing object are the period of its rotation and orientation in space at any moment in time. Rotating objects periodically change their brightness. So, the photometric monitoring is a real approach for remote diagnostics of satellite rotation around its center of mass. This information is also very useful, for example, in emergency cases when operating spacecraft is involved. Also in the numerical integration of non-spherical bodie's moving it's important to take into account their orientation (for example, for large defunct RSO) especially in case of predicting close approaches with other RSO.

There are several centers that carry out photometric monitoring of near-Earth RSOs in Ukraine. These are several university observatories of MOSU (first of all the Astronomical Observatory of Odessa National University) and Space control centers of State Space Agency of Ukraine (now located in Mukachevo and Dunaevtsi). The database of light curves of AO ONU contains results of more than 10-years monitoring of the satellites functioning and large space debris objects in near-Earth orbits. The KT-50 telescope (main mirror diameter of 500 mm) is used to track of RSOs on low Earth orbit (Shakun & Koshkin, 2014). High-orbit RSOs have been observed using automated OMT-800 telescope (with main mirror diameter of 800 mm) at the observation station in Mayaki (Andrievsky et al., 2013).

2. Ukrainian Database and Atlas on-line

In 2016, AO ONU and the Space control center (SCC) created Ukrainian "Photometric Data Storage Portal for RSOs" as the specialized part of the Ukrainian Virtual Observatory (UkrVO). The results of RSOs photometric observations provided by the national optical observation devices are coming for storing and online access to the "Portal", and are used by the SCC to perform it tasks.

The software complex is intended to store photometric data and includes function of accumulation and archiving of light curves and other priori RSOs information. Uploading and viewing of existing data is carried out using an interactive web interface (Fig. 1-2). Due to the large amount of data, the interface provides filtering and searching features by all the most important criteria. The results of the RSO brightness measurements are available both as text file and as an interactive light curve chart with zooming features (Fig. 3). The available opportunities allow conducting preliminary expert evaluation of the RSOs behavior based not only on the latest observations results, but also on retrospective data. This is very important feature for SCC because it allows determining RSO type (spacecraft, rocket carrier, SD or its fragment, etc.) as well as identifying the spacecraft activity periods and making conclusions about their functional purposes and statuses.

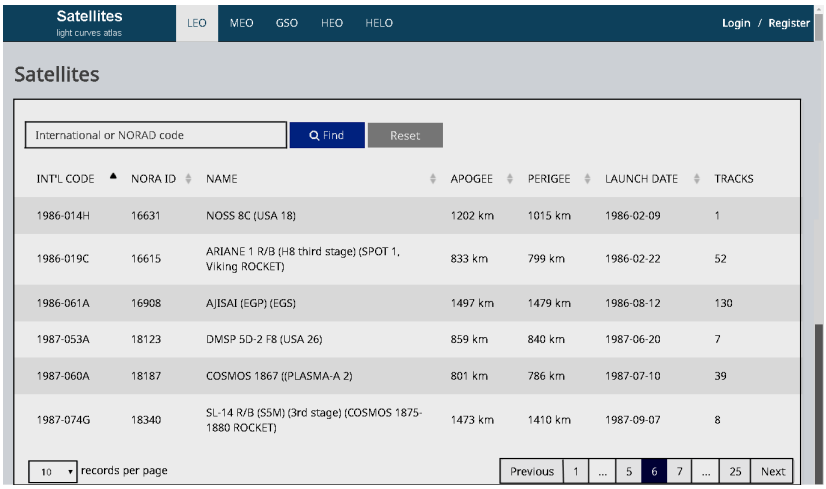

Figure 1: Ukrainian Database and Atlas of light curves of artificial space objects (RSO selection window).

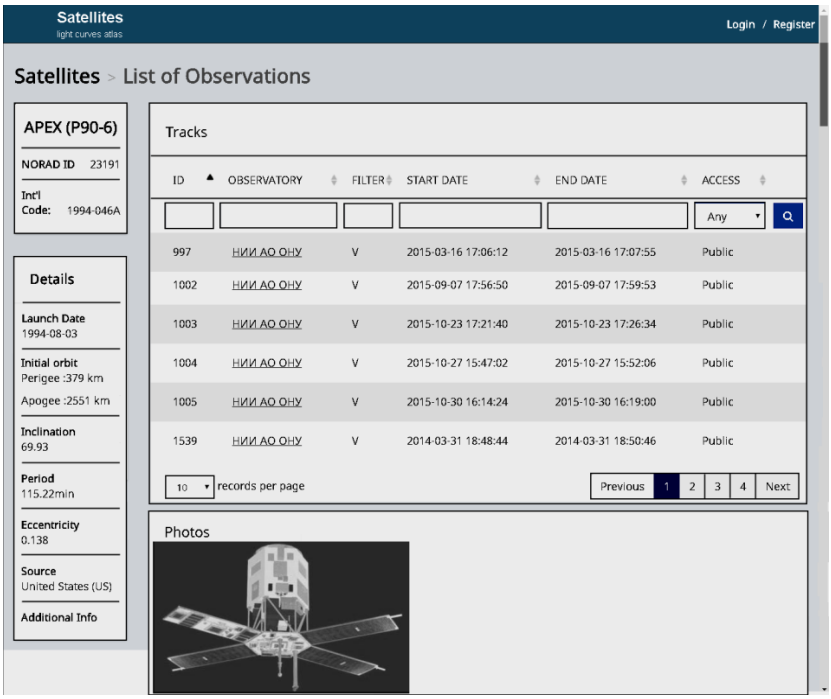

Figure 2: Ukrainian Database and Atlas (Track selection window).

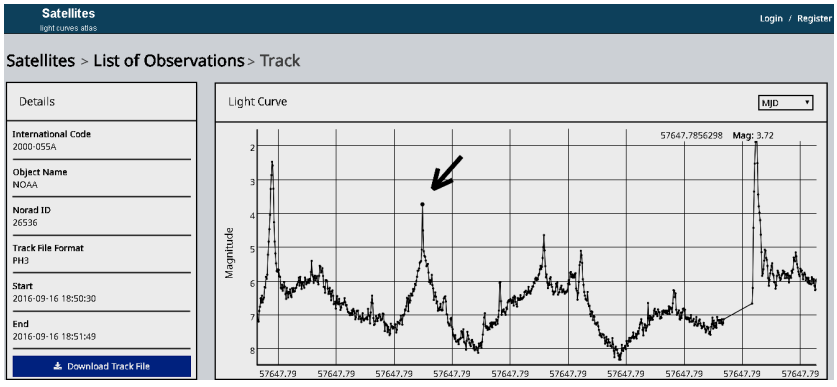

Figure 3: Ukrainian Database and Atlas (Light curve presentation window).

Based on the "Portal" data specialists have possibility to make conclusion about the stabilization and spatial orientation of the spacecraft, to assume the geometric shape, the presence and location of external antennas, optics and other equipment. Analysis results are used by SCC to track and regular update actual RSO classifiers that incorporate the signs confirmed or refined based on latest photometric measurements. Processed data are than passed to NCSFCT.

We can conclude that the creation of the "Photometric Data Storage Portal for RSOs" and its using for space surveillance purposes made it possible to significantly expand the functional capabilities of the SCC and provided possibility to online access data in cooperative mode.

3. Usage of database

As an example of the analysis of photometric material from the AO ONU database let's consider the brightness variations of two Cosmos satellites. The first one (Kondor-E, 2013-032A) is launched into low Earth orbit on June 27, 2013, the second (Kondor-E2, 2014-084A) on December 19, 2014. Both satellites are intended for obtaining images of the Earth's surface and oceans monitoring. They have an orbit height of about 500 km above the ground, inclination of 74.75° and their planned operation time is 5 years. The Kondor-E satellites are equipped with a large parabolic antenna measuring 6 × 7 m in the S-band synthetic aperture radar (SAR), which can perform both survey in strip mode and detailed selective spot surveys. We do not know about any serious problems with these satellites. However, analysis of the light curves of these RSOs shows a different character of their motion about center of mass. Fig. 4,a shows the light curve of the 2013-032A RSO, obtained on May 29, 2017 using the telescope KT-50 in Odessa. Changes in the brightness of the satellite have a pronounced periodic nature, which may indicate its rotation. The apparent rotation period in this case is approximately 8.7 seconds.

Fig. 4,b shows the light curve of RSO 2014-084A, obtained also on May 29, 2017 using the telescope KT-50. The changes in the satellite brightness have an aperiodic showing (although in two zones of the light curve we can see a repeat of a short-term increase in brightness at an interval of about 6 sec. The may be caused by the design element movement, for instance, by the movement of scanning antenna) In general, this light curve is usual for stabilized spacecraft on its orbit.

In some cases, long-term photometric monitoring of RSO's orbital behavior makes it possible to reveal the evolution of its rotation. Fig. 5,a shows the light curve of the US weather satellite 1994-089A NOAA-14 (on orbit since December 1994, orbit altitude of about 850 km, inclination is 98.7°), obtained on May 17, 2017. Fig. 5,b shows light curve of the satellite 2000-055A NOAA-16 (on orbit since September 21, 2000, orbit altitude of about 840 km, inclination - 98.8°), received on August 1, 2017. Both spacecraft are inactive, so it's actually space debris. The light curves are similar in character, periodic and display the rotation of the satellites. For now, NOAA-14 shows a rotation with a visible period of about 19.4 seconds (4 peaks per full revolution). The NOAA-16 spacecraft seems to be rotating faster – the full synodic period at the beginning of August 2017 was about 7.6 seconds.

It is known that around November 25, 2015 NOAA-16 collided with another body in orbit, that is caused the formation of 136 new small fragments, including the main body of the satellite.

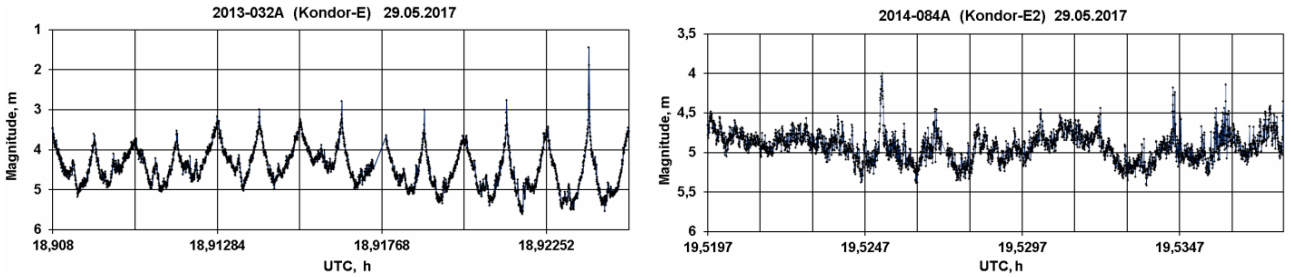

Figure 4: (a) The light curve of the RSO 2013-032A (Kondor-E). Vertical lines correspond to a time interval of 8.7 s. (b) The light curve of RSO 2014-084A (Kondor-E2). Vertical lines correspond to a time interval of 6 s. Both light curves obtained on May 29, 2017 with using the telescope KT-50 in Odessa.

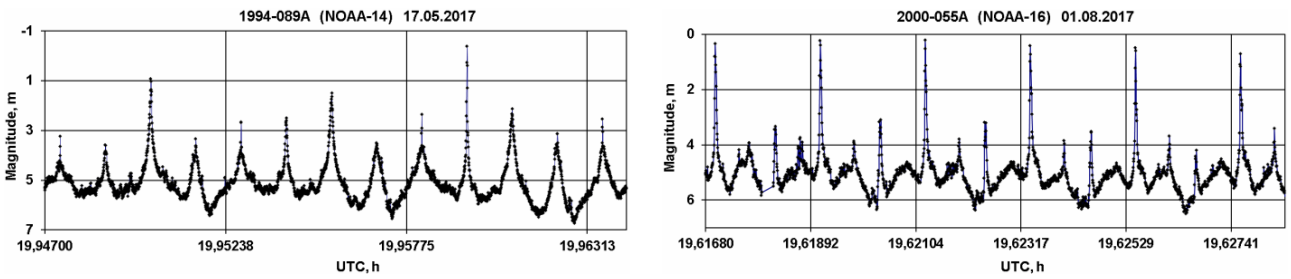

Figure 5: (a) The light curve of NOAA-14 (1994-089A), obtained on May 17, 2017. Vertical lines correspond to a time interval of 19.4 seconds. (b) The light curve of NOAA-16 (2000-055A), obtained on August 1, 2017. Vertical lines correspond to a time interval of 7.6 seconds. Both light curves obtained with using the telescope KT-50 in Odessa.

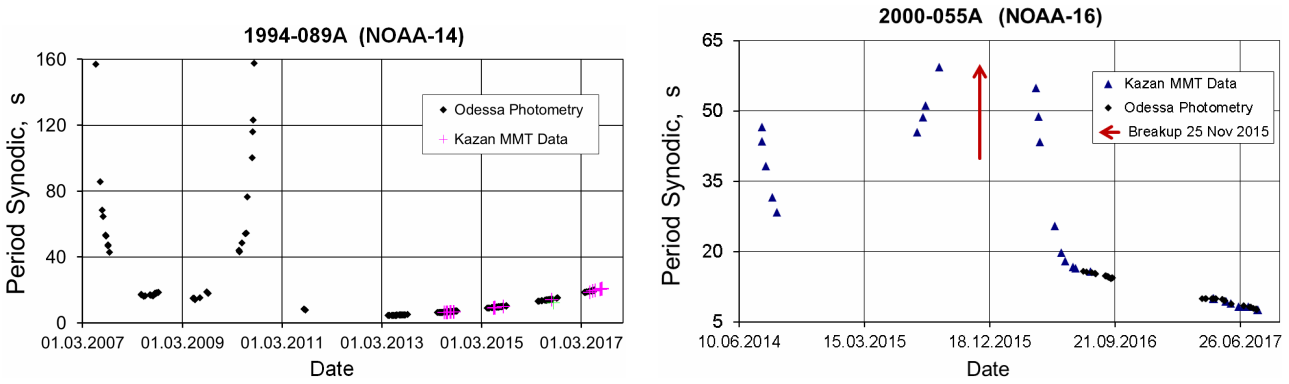

Figure 6: Change in the observed synodic rotation period of two non-functioning RSO: (a) NOAA-14; (b) NOAA-16.

Rotational speed of NOAA-14 did not remain constant. Fig. 6,a shows a complex history of the rotation period evolution of this RSO during 2007 - 2017 according to our measurements obtained with the telescope KT-50 and the Russian MMT project (Biryukov et al., 2015). However, starting from 2013 the satellite slows down in a stable mode. Fig. 6,b shows the change in the rotation period of NOAA-16 at different times in the interval from 2014 to 2017 according to MMT and our measurements on the KT-50. It's obvious that the angular velocity of rotation also experienced great changes and after a catastrophic collision on the orbit the rotation has accelerated. During 2016-2017 the period of rotation of this satellite monotonously decreased with small variations which are typical for objects of space debris. These objects are subjected, for example, to the pressure of solar radiation (Kucharski et al., 2017).

4. Conclusion

Last years, interest in studying the rotation of satellites has been continuously growing (primarily, defunct satellites, i.e. space debris). The Multichannel monitoring telescope (MMT, Kazan, Russia) has been active since 2014 (Biryukov et al., 2015). ESA runs the "Debris Attitude Motion Measurements and Modeling" project, led by the Astronomical Institute of the University Bern (AIUB) (Kanzler et al., 2015). The Space Research Institute of Austrian Academy of Sciences (Graz, Austria) in cooperation with Space Environment Research Centre (SERC, Australia) and a number of other centers of Satellite Laser Ranging (SLR) perform a large program to determine the satellites attitude and their spin properties (Kucharski et al., 2017).

The Ukrainian Light Curves database will be contain results of more than 10-year monitoring (now is added data only by the AO ONU) of the behavior of functioning satellites and large objects of space debris in orbit. Some of this data is already available on-line within digital Atlas of light curves and they continue to grow. The functioning of the database is supported by the program of the Ukrainian space agency for ensure of the space situational awareness. The paper describes the database structure and capabilities of working with it. The example of four RSOs demonstrates the use of photometric data for a preliminary analysis of the state and evolution of their rotation around center of mass.

References

Andrievsky S. et al.: 2013, *Odessa Astron. Publ.*, **26**, 6.

Biryukov A. et al.: 2015, *Baltic Astronomy*, **24**, 100. Available at: (https://arxiv.org/pdf/1411.2552.pdf)

Database and Atlas of RSO light curves: http://193.193.221.52:3000/satellites

Kanzler R. et al.: 2015, *Adv. Maui Optical and Space Surveillance Tech. Conf.* (AMOS-2015). Available at: (https://amostech.com/TechnicalPapers/2015/Orbital_Debris/Kanzler.pdf)

Kucharski D. et al.: 2017, *Earth and Space Science*, **4**, 10, 661. DOI: 10.1002/2017EA000329

MMT: http://astroguard.ru/satellites

Shakun L., Koshkin N.: 2014, *Adv. in Space Res.*, **53**, 1834.

DOI: http://dx.doi.org/10.18524/1810-4215.2017.30.114685

DOUBLE STATION OBSERVATION OF METEORS WITH LOW BASELINE IN MYKOLAIV

M.O.Kulichenko, O.V.Shulga

Research Institute «Mykolaiv Astronomical Observatory»,
Mykolaiv, Ukraine, *niiko4kulichenko@gmail.com, shulga-av@ukr.net*

ABSTRACT. Results of single and double station observations of meteors using TV CCD techniques which were conducted in 2013-2016 in Mykolaiv astronomical observatory (RI MAO) are shown in the article.

Keywords: meteor, combined observational method, meteoroid heliocentric orbit.

1. Introduction

Meteor observational campaign using TV CCD unintensified techniques was started in 2013 in Mykolaiv astronomical observatory (RI «MAO») (Kulichenko et al., 2014; 2015). The main accent of the research is made on precise astrometry and meteoroid orbits calculation.

2. Observation facilities

System of meteor telescopes includes 6 optical telescopes (4 lenses: f = 85 mm, f/1.8; 2 lenses: f = 100 mm, f/2.0) equipped with a TV CCD cameras WAT-902H2 (768×576, 8.6×8.3μ). The field of view of 4 telescopes is 3.2°×4.2° and 2.7°×3.6° for 2 telescopes. The length of baseline is 11.8 km. Cameras work in the interlace mode with rate 50 half-frames per second for better time resolution. The observations were conducted in completely automatic mode using on-line meteor detection software developed at RI «MAO». The method of meteor registration is based on combined observation method (Shulga et al., 2008; 2011). Limiting magnitude for stars is in (11-12)^m. Mean accuracy of positional measurement for reference stars is (6-8)". The method of double station synchronization is based on using PPS-impulse from GPS receiver Resolution-T as reference impulse. Accuracy of time synchronization is 10^{-4} s.

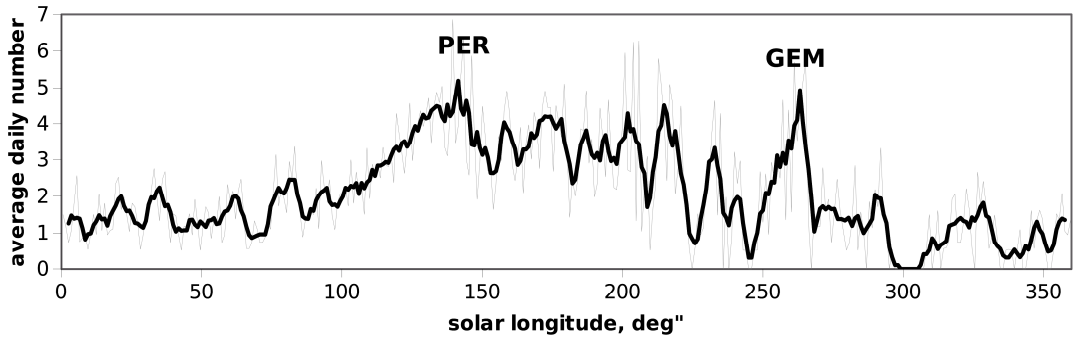

Figure 1: Meteor number variation per year. Averaged data 2013-2016

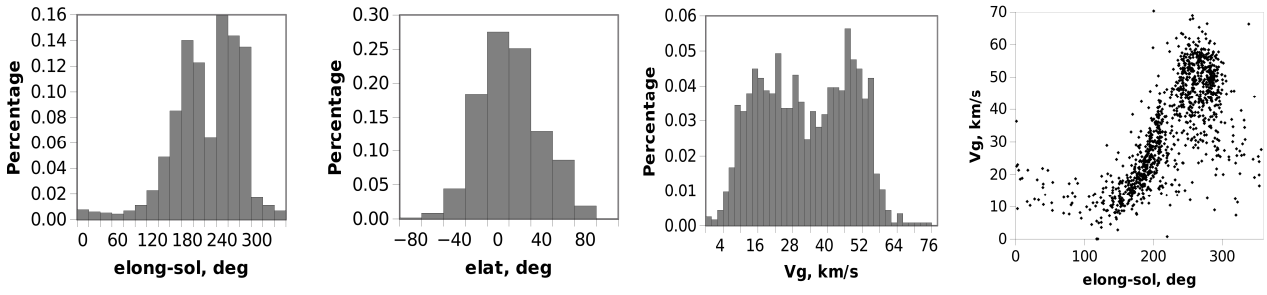

a) b) c) d)

Figure 2: Distributions of: a) ecliptic longitude of radiant position relative to solar longitude; b) ecliptic latitude of radiant position; c) geocentric velocity of meteors; d) diagram geocentric velocity – ecliptic longitude reduced to the solar longitude.

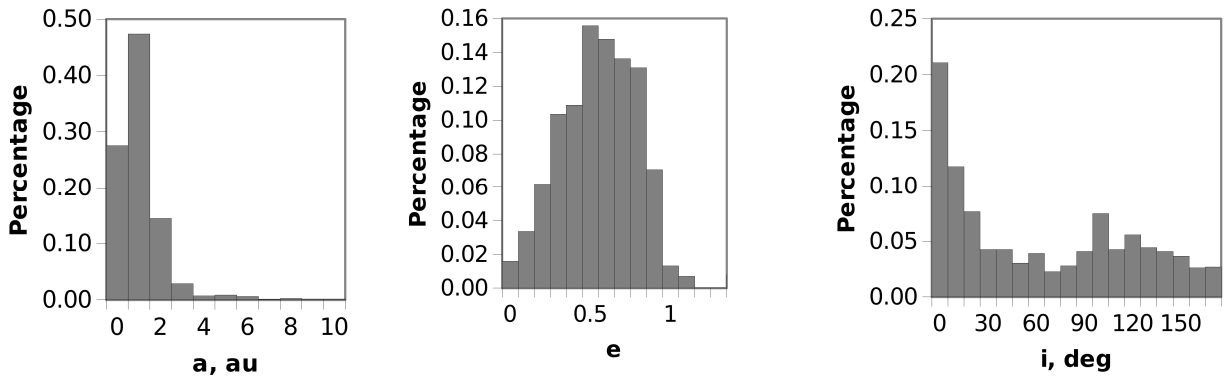

a) b) c)

Figure 3: Distribution of some meteoroid orbit elements: a) semi-major axis; b) eccentricity; c) inclination.

3. Results

3.1. Single station observation

In 2013-2016 9110 single station meteors were registered. Due to weather conditions, narrow fields and technical problems the meteor quantity distribution over solar longitude for single camera is not representative. However it is possible to obtain average smoothed annual variation using sum of all 6 cameras observations for 3 years (Fig. 1).

This single station statistics shows increase of meteors number in the second part of year and strict peaks of main meteor showers such as Perseid and Geminid. The mean duration of observed meteor trajectories is in 0.05-0.6 s. The distributions of meteors over meteor magnitude and arc length have their maxima at 2^m and (0.75-1)° and include meteors with range from -2^m to 7^m. 85% of meteor trajectories are partial because of narrow field of view but due to high time resolution >60% of detected trajectories have >5 frames.

3.1. Double station observation

In 2013-16 1148 double station meteors were observed. Several meteor showers both major (Perseid, Geminid etc) and minor (e.g. Southern delta Aquariids) were matched. More than 80% of meteors are sporadic.

Double station trajectories have atmospheric path length range in 1.2-15 km with maximum at 4-5 km. Atmospheric heights range is in 60-120 km. The average accuracy of visible radiant estimation is less 0.5º with baseline 11.8 km. The accuracy of geocentric velocity estimation is 0.5 km/s. Maximum of heliocentric radiants (ecliptical coordinates of radiant) distribution is near the ecliptic plane (Fig. 2, b). Heliocentric radiants distribution has two typical maximums near the apex point and Antihelion source point which are most power sources of sporadic meteors in optical range (Fig. 2, a). Geocentric velocity distribution has two peaks at 15 and 50 km/s which is corresponding with heliocentric radiant distribution: first peak is average velocity of sporadic meteors from Antihelion source, second peak belongs to sporadic meteors from apex (Fig. 2, c, d). Orbital elements distributions show that most of meteoroid orbits belong to near Earth object with eccentricities 0.5-0.8 and have low inclinations (Fig. 3, a-c). Local maximum in inclination distribution near 110º corresponds with Perseid meteor shower.

4. Conclusion

Based on the results of meteor observation in 2013-2016 catalog containing heliocentric orbital elements of meteoroids and kinematic parameters for their atmospheric path has been obtained.

References

Kulichenko N., Shulga O., Kozyryev Y. et al.: 2014, in Gyssens M., Roggemans P., Zoladek, P., eds., PIM3, 50. (2014pim3.conf...50K)

Kulichenko N., Shulga O., Kozyryev Y. et al.: 2015, JIMO, **43**, 81. (2015JIMO...43...81K)

Shulga O., Kozyryev Y., and Sybiryakova Y.: 2008, in IAU Symp., 248, 128. (2008IAUS..248..128S)

Shulga O., Kozyryev Y., and Sybiryakova Y.: 2011, in Tanga P., Thuillot W., eds., GFUN, 97. (2011gfun.conf...97S)

DOI: http://dx.doi.org/10.18524/1810-4215.2017.30.114690

ESTIMATIONS OF LOCAL MAGNETIC FIELDS IN SOLAR FLARES: BASIC METHODS AND SOME RESULTS

V.G. Lozitsky[1], E.A. Baranovsky[2], N.I. Lozitska[1], V.P.Tarashchuk[2]

[1] Astronomical Observatory of the Taras Shevchenko National University of Kyiv, Kyiv, Ukraine, *lozitsky@observ.univ.kiev.ua, nloz@observ.univ.kiev.ua*

[2] Crimea Astrophysical Observatory, Nauchny, Crimea
edward@craocrimea.ru , veratar4@gmail.com

ABSTRACT. We consider three methods for estimations of local magnetic fields in solar flares: (1) analysis of bisectors of $I \pm V$ profiles (Lozitsky, 2015); (2) search for Zeeman-like effects in cores of spectral lines with very low Lande factors, $g_{\rm eff} \approx 0.01$ (Lozitsky, 1993, 1998); (3) semi-empirical modeling using many spectral lines and two-component models (see, e.g., Lozitsky et al., 2000). We illustrate the application of named methods to different observational data and to different spectral lines. Our main conclusions are following: (a) upper limit of local magnetic fields in solar flares is, at least, ~10^4 G, (b) such extremely strong fields can occur in very small, spatially unresolved scales, (c) lifetime of such fields is, at least, a few minutes.

.

Keywords: Sun, solar activity, solar flares, magnetic fields, spectral lines, the Zeeman effect, diagnostics of spatially unresolved structures, extremely strong fields.

1. Introduction

Solar magnetic fields have very fine structure, with size of smallest elements under the instrumental limit for modern solar telescopes. In fact, this limit is on level of 50-70 km at present (see, e.g., Varsik et al., 2014) whereas the smallest magnetic elements on the Sun, likely, have the size about 15-20 km (Stenflo, 2011, Botygna et al., 2016). Due to this reason, direct magnetic observations allow to obtain some average (effective) magnetic field $B_{\rm eff}$ which can be very differ from local magnetic field $B_{\rm loc}$. For non-flare regions, $B_{\rm loc}$ is of kilogauss range (see, e.g. Stenflo, 1973; Rachkovsky et al., 2005) whereas $B_{\rm eff}$ can be 1-3 orders weaker, and it reflects, in general, the magnetic flux rather than true local field.

The diagnostics of spatially unresolved magnetic fields in solar flares is more complicated than in unperturbed regions outside flares. For non-flare regions, one can apply the line ratio method or its modification (see, e.g., Stenflo, 1973, Rachkovsky et al., 2005). For flares, especially for wide emission line profiles, this method is not suitable. Therefore, it is necessary to use other methods, which are also quite informative, but are based on other approaches to the problem of estimating local fields. Below, three such methods will be considered, with a brief summary of the results obtained and their discussion.

2. Analysis of bisectors of $I \pm V$ profiles

In a general case, the diagnostics of spatially unresolved magnetic structures requires the application of at least two-component models for interpretation of observations. However, in this case number of free parameters is greatly increased (till about ten), which makes the final conclusions very vague, dependent on some simplifying assumptions. One can try to apply a simplified approach based on fixing and analyzing explicit deviations from the case of a weak one-component magnetic field. This is the main idea of the method for analyzing the bisectors of $I \pm V$ profiles of magnetosensitive spectral lines.

In weak-field approximation, Stokes V parameter could be presented via formula

$$V \propto (dI/d\lambda)\Delta\lambda_{\rm H}\,, \qquad (1)$$

where $dI/d\lambda$ is Stokes I gradient, $\Delta\lambda_{\rm H}$ – Zeeman splitting

$$\Delta\lambda_{\rm H} = 4.67\times10^{-13} g_{\rm eff}\lambda^2 B, \qquad (2)$$

where $\Delta\lambda_{\rm H}$ and λ are in Å, and B in gauss (G); $g_{\rm eff}$ – effective Lande factor. In fact, formula (1) follows from the condition that $I + V$ and $I - V$ profiles have analogous shape, but they are shifted mutually on $2\Delta\lambda_{\rm H}$. This means that their bisectors should be parallel mutually, if $\Delta\lambda_{\rm H} << \Delta\lambda_{1/2}$, where $\Delta\lambda_{1/2}$ is half-width of a spectral line.

As to real observed profiles, bisectors are often not parallel even in case if $\Delta\lambda_{\rm H} << \Delta\lambda_{1/2}$. There are two main types of nonparallelism: (1) a monotonous increase in the splitting of bisectors as the line center is approached and (2) the non-monotonic course of this splitting, such as "loop" or "bulb". Both cases do not correspond to the approximation of a weak one-component magnetic field and require consideration in the framework of inhomogeneous magnetic fields. Figs. 1-3 present the examples of observations with non-parallelism of bisectors of (2) type.

One can see that splitting of bisectors $\Delta\lambda_B$ has a maximum on distances $\Delta\lambda_{max} \approx 200$-$350$ mÅ. Let us remember, in weak-field approximation should be $\Delta\lambda_B = \text{const}$.

Accoding to modelling data, similar spectral peculiarities are possible in two cases: (a) two-component model, with weak and strong fields, with quasi-gaussian profiles in both components, and very narrow spectral lines in second (spatially unresolved) component with strong field, (b) also two-component model, but with non-gaussian profiles in strong component. In (a) case, observed value $\Delta\lambda_{max}$ corresponds, approximately, the Zeeman splitting $\Delta\lambda_H$ in strong component (Gordovskyy and Lozitsky, 2014). This criterium gives very strong field in second component, in range of $\sim 10^4$ G. At heights of about 40 Mm (Fig. 2), such fields are unlikely.

Consideration of case (b) allows us to reduce the value of local fields in sub-telescopic structures. Namely, then the "loop" of bisectors appears not because of the large Zeeman splitting, but because of the non-Gaussian profiles with a flat top having a steep intensity gradient at a certain distance from the center. However, this requires the presence of a large optical thickness in sub-telescopic structures with an amplified field.

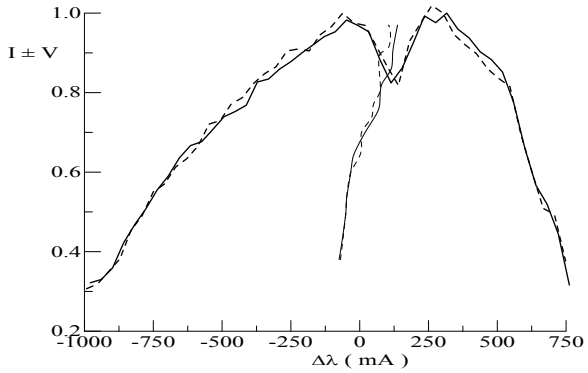

Figure 1: Observed $I + V$ and $I - V$ profiles and bisectors of Hα line ($g_{eff} = 1.05$) in limb solar flare of 19 July 2012 of M 7.7 class (Kirichek et al., 2013).

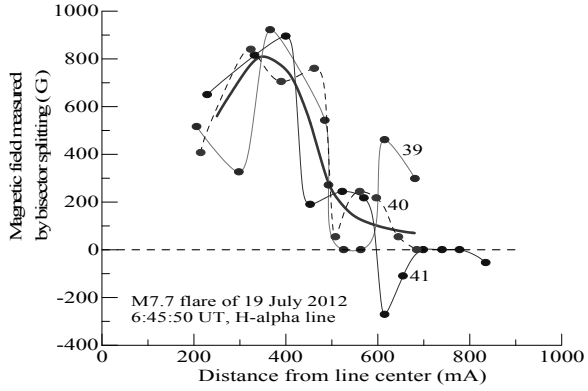

Figure 2: Observed splitting of bisectors of $I \pm V$ profiles versus distance from line center for limb solar flare of 19 July 2012 of M 7.7 class. Numbers 39-41 correspond to distance of the place under study from the solar limb (Kirichek et al., 2013).

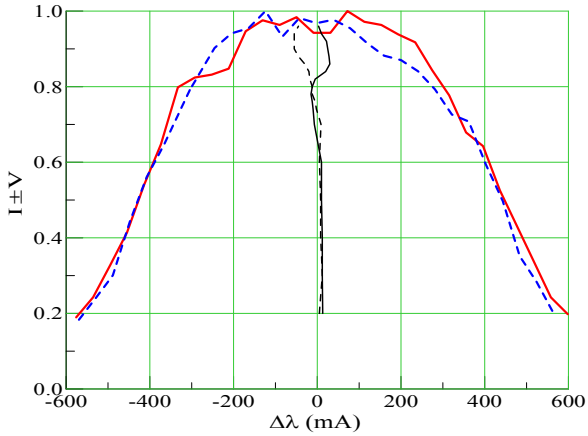

Figure 3: The same as on Fig. 1, but for quiet prominence of 09 November 2011 (Lozitsky et al., 2015).

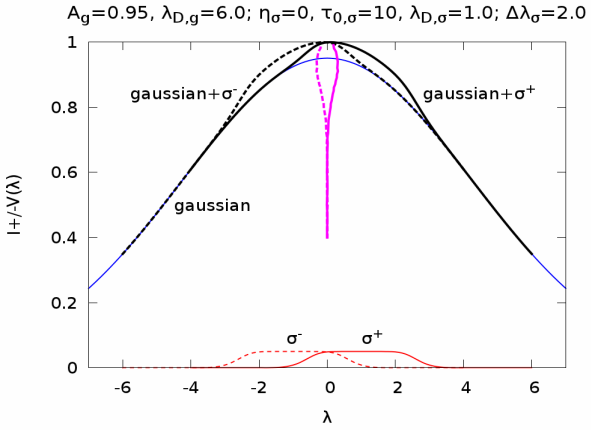

Figure 4: Theoretical $I \pm V$ profiles and their bisectors for two-component magnetic field (Lozitsky et al., 2015).

Fig. 4 illustrates case (b) with such parameters: the filling factor of the small-scale component is 5%, and the optical thickness in it is 10. The Doppler width in this component is 6 times smaller than in the background component that indicates the reduce of kinetic temperature. It was also believed that the magnetic field in the background component is zero, and the field in the small-scale component is purely longitudinal.

Comparing Figures 3 and 4, we see their good qualitative correspondence. If the horizontal scale of Figure 3 is attached to Figure 4, then the Zeeman splitting in the small-scale component should be approximately 100 mA. This gives the magnitude of the magnetic field in the strong component of about 5 kG. Of course, this is also a very strong field for the level of the lower corona. Another thing is paradoxically here: the plasma density in regions with such a strong field should be substantially increased. Obviously, this poses an acute problem of the equilibrium of such structures: it is not clear what can compensate the huge magnetic and gas pressures inside the small-scale component. Perhaps there exists some specific topology of the magnetic field, for example, in the form of a vortex (Soloviev, 2013). Notice, earlier Kurochka and Tel'njuk-Adamchuk (1978), using data in unpolarized light, also came to the conclusion that the emission elements of the flare should be dense, optically opaque.

2. Spectral effects in lines with $g_{eff} \approx 0.01$

A simple test for testing the hypothesis of the existence of especially strong magnetic fields is as follows. Spectral lines with very small Lande factors, about 0.01, should not show signs of Zeeman effect if the signal-to-noise ratio for observations is about 50-100, and the magnetic field value does not exceed 5 kG. In the visible region of the solar spectrum, there are at least three iron lines, very convenient for such a check. These are FeI lines λ = 5123.723, 5434.527 and 5576.099 Å.. Theoretically, for *LS* coupling, their effective Lande factors are $g_{LS} = 0.000$, but experimental values, determined in a laboratory, are $g_{Lab} = -0.013$, -0.014 and -0.012, respectively (Landi Degl'Innocenti E.L.: 1982).

The first results of this kind were obtained by Lozitsky (1984) for the photosphere of the active region outside the spots. The photometric profiles were averaged over a large area on the Sun (≈ 25 Mm) to increase the signal-to-noise ratio. It turned out that in the nuclei of lines 5123 and 5576 there is a weak splitting, which for their Lande factors should correspond to a magnetic field of about 3 kG.

For flares, a similar result was obtained nine years late (Lozitsky, 1993). It turned out that the emission peaks in lines FeI 5123.7 and FeI 5434.5 are also sometimes split, the value of the corresponding magnetic field reaching 90 kG.

Till present, the splitting effect in the nuclei of lines with very low Lande factors (about 0.01) was found in six solar flares. Some examples of the observed effects are shown in Figs. 5-7.

Although in most cases the splitting effects mentioned above appear in the cores of the lines ($\Delta\lambda \le 100$ mÅ), there are also cases when $I + V$ and $I - V$ profiles are very different and at great distances from the center, 130-180 mÅ (Lozitsky, 2009). Perhaps this indicates the existence of even stronger fields in flares.

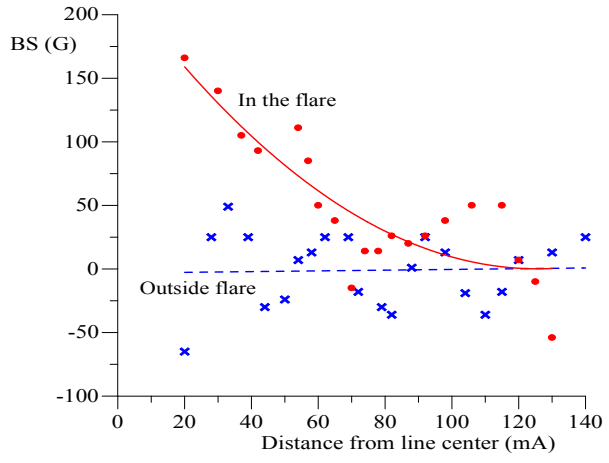

Figure 5: Observational manifestation of the Zeeman effect in core of FeI 5576 line in flare of 5 November 2004: crosses and dashed line – splitting of bisectors of $I \pm V$ profiles in this line, *BS*, formally calibrated to case of FeI 5233 line ($g_{eff} = 1.261$), outside the flare; filled circles and solid line – observed *BS* splitting in bright knot of flare (Lozitsky and Staude, 2008).

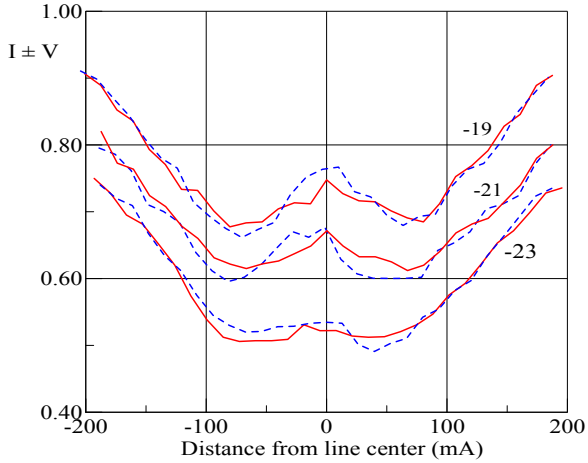

Figure 6: Observed Stokes $I \pm V$ profiles of FeI 5434.5 line in flare of 17 July 2004 (Lozitsky, 2011). The numbers from -17 to -21 correspond to the numbers of the photometric sections; adjacent cuts are located at a distance of 1 Mm.

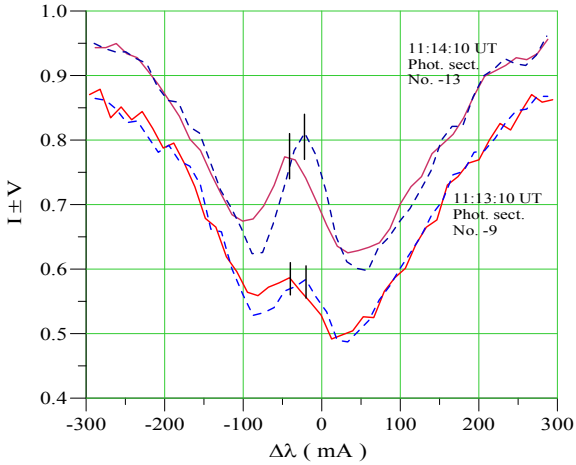

Figure 7: The same as on Fig. 6, but for X17.2/4B flare of 28 October 2003 (Lozitsky and Lozitska, 2017). The spectral splitting of the emission peaks, marked by vertical dashes, corresponds to a magnetic field of about 50 kG.

One of the problems of 10^4 G magnetic fields is that their enormous magnetic pressure exceeds by many orders of magnitude the pressure of the surrounding plasma (Lozitsky, 2015). Such fields should exist either in some special magnetic configurations of the type, perhaps a magnetic vortex (Solov'ev, 2013) or, in general, there may exist a very short time. Concerning the latter, observational data were obtained that the spectral manifestation of these fields exist for at least several minutes (Lozitsky, 1998).

It is highly unlikely that these extremely strong fields form at the same height, where they are observed. Likely, these fields form somewhere in convective zone and they lift on the Sun surface in the ready form. At least in some flares a violet Doppler shift is observed, indicating a lifting of plasma with velocities of about 2 km/s (see Fig. 7).

3. Semi-empirical models

The construction of semi-empirical models allows one to increase the spatial resolution in depth and, in addition, makes it possible to obtain altitude profiles of the magnetic field and thermodynamic conditions. This approach requires Stokes-metric data in many spectral lines and also the use of program codes for the calculation of line profiles in a perturbed atmosphere. This gives a lot of important and interesting information about the physical conditions in solar flares. Here we note only one problematic point.

There is no complete clarity in how the magnetic field varies with altitude in solar flares. In some papers, a non-monotonic change in the magnetic field with altitude has been obtained (see, e.g., Lozitsky et al., 2000), while in others a monotonous attenuation with altitude was obtained (see, e.g. Abramenko and Baranovsky, 2004; Baranovsky et al., 2009).

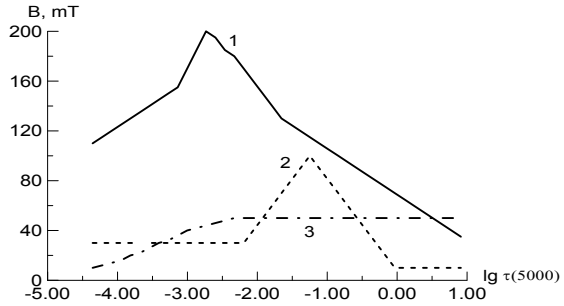

Figure 8: Semi-empirical models of magnetic field for M4.1/1B flare of 5 November 2004 for three moments: 1 – peak of flare, 2 – 4 min after peak, and 3 – 10 min after peak (see details in paper by Kurochka et al., 2008).

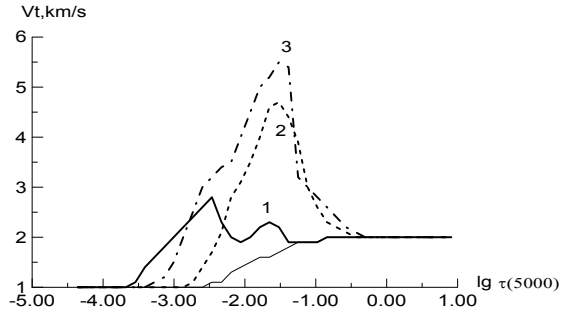

Figure 9: Evolution of the macro-turbulent velocity in M4.1/1B flare of 5 November 2004 (Kurochka et al., 2008).

Perhaps this depends on the phase of the flare development. Thus, in paper by Kurochka et al (2008), a high-altitude peak of the field was obtained at the flare maximum, which gradually "blurred" into the usual monotonous distribution of the magnetic field within 10 minutes (Fig. 8). This issue requires careful study in the future.

It is interesting to note that the macroturbulent velocity changed in the flare on 5 November 2004 differently than the magnetic field (Fig. 9). At maximum phase of the flare this velocity did not exceed 2.5 km/s, whereas in 10 minutes it increased to 5.5 km/s. Apparently, these data directly indicate that the energy of the magnetic field has been transformed into the energy of turbulent motions.

4. Conclusions

Our main conclusions are following: (a) upper limit of local magnetic fields in solar flares is, at least, ~10^4 G, (b) such extremely strong fields can occur in very small, spatially unresolved scales, (c) lifetime of such fields is, at least, a few minutes. Probably, the sub-telescopic regions in flares with such very strong fields have a sharply reduced temperature and an increased plasma density. Local non-monotonous distribution of magnetic field strength versus height are possible in flares, their lifetime is also several minutes.

Acknowledgements. This study was funded by the Taras Shevchenko National University of Kyiv, project No. 16БФ023-01, and by Crimea Astrophysical Observatory, project "Physical relationships of solar formations", grant РФФИ № 16-42-910467 р-аэ.

References

Abramenko V.I., Baranovsky E.A.: 2004, *Solar Phys*., **220**, 81.
Baranovsky E.A., Lozitsky V.G., Tarashchuk V.P.; 2009, *Kinem. Phys. Celest. Bodies*, **25**, 373.
Botygina O.O., Gordovskyy M.Yu., Lozitsky V.G.: 2016, *Adv. Astron. Space Phys*., **6**, 20.
Gordovskyy M., Lozitsky V.G.: 2014, *Solar Phys*., **289**, 3681.
Kirichek E.A., Solov'ev A.A., Lozitskaya N.I. et al.: 2013, *Geomagn. Aeronomy*., **53**, 831.
Kurochka L.N., Tel'njuk-Adamchuk V.V.: 1978, *Solar Phys*., **59**, 11.
Kurochka E.V., Lozitsky V.G., Osyka O.B.: 2008, *Kinem. Phys. Celest. Bodies,* **24***,* 308.
Landi Degl'Innocenti E.L.: 1982, *Solar Phys.,* **77**, 285.
Lozitsky V., Masliukh V., Botygina O.: 2015, *Bull. Taras Shevch. Nat. Univ. of Kyiv. Astronomy*, **52**, 7.
Lozitsky V.G., Staude J.: 2008, *J. Astrophys. Astron*., **29**, 387.
Lozitsky V.G.,, Lozitska N.I.: 2017, *Bull. Taras Shevch. Nat. Univ. of Kyiv. Astronomy*, **55**, 51.
Lozitsky V.G.: 1984, *PhD Thesis*, Kiev, 164p.
Lozitsky V.G.: 1993, *Kinem. Phys. Celest. Bodies*, **9**, 18.
Lozitsky V.G.: 1998, *Kinem. Phys. Celest. Bodies*, **14**, 401.
Lozitsky V.G.: 2009, *J. Phys. Studies*, **13**, 2903-1.
Lozitsky V.G.: 2015, *Adv. Space Res*., **55**, 958.
Lozitsky, V.G., Baranovsky, E.A., Lozitska, N.I. et al.: 2000, *Solar Phys*. **191**, 171.
Lozitsky, V.G.: 2011, *Int. J. Astron. Astrophys*., **1,** 147.
Rachkovsky D.N., Tsap T.T., Lozitsky V.G.: 2005. *J. Astrophys. Astron*., **26**, 435.
Solov'ev A.A..:2013, *Solar Phys*., 286, 441.
Stenflo J.O.: 1973, *Solar Phys*., **32**, 41.
Stenflo J.O.: 2011, *A & A*, **529**, id.A42, 20 pp.
Varsik J., Plymate C., Goode P et al.: 2014, *Proc. of SPIE*, **9147**, id.91475D 10pp.

DOI: http://dx.doi.org/10.18524/1810-4215.2017.30.114640

EVOLUTION FEATURES OF GIANT SOURCES WITH LINEAR AND BREAK STEEP RADIO SPECTRA

A.P. Miroshnichenko

Institute of Radio Astronomy, NAS of Ukraine,
Kharkiv, Ukraine, *a.p.miroshnichenko@gmail.com*

ABSTRACT. In the framework of the cosmological model ΛCDM the features of properties of giant radio sources with steep low-frequency spectra of linear (S) and break (C+) types are examined. Our estimates of characteristic age of galaxies and quasars with steep spectrum from the UTR-2 catalogue have values 10^7-10^8 years. We consider that steep radio spectra may be formed at the transient injection by synchrotron losses of relativistic electrons. Earlier we have determined two evolution branches in relation of the characteristic age and ratio of emission of torus and accretion disk crown for sources with steep spectra S and C+. To further examination of evolution features of giant sources with steep spectra we consider ratio of emission of radio lobes and accretion disk (and disk crown) versus velocity of jet propagation and characteristic age of these objects. Analysis of obtained relations testifies to periodical activity of giant low-frequency steep spectrum radio sources.

Keywords: Galaxies – Quasars – Radio sources: giants

1. Introduction

Non-thermal spectra of extragalactic sources have a number of features at the low-frequency band. Near 30 per cent of objects from the UTR-2 catalogue of extragalactic sources have steep radio spectra (the value of spectral index is greater 1) (Braude et al, 1981, 2003). To consecutive study of identified sources with low-frequency steep radio spectra we use corresponding data (http://ned.ipac.edu) at high–frequency range – centimetre, infrared, optical, X-ray bands. This gives the advantage in obtaining of many astrophysical characteristics of objects and in determination of their evolution effects. We have identified 130 galaxies and 91 quasars with steep low-frequency spectrum at selection criteria (low-frequency spectral index exceeds 1, and flux density is more than 10 Jy at the frequency 25 MHz) in two fields of UTR-2 catalogue. So, the compiled sample includes 78 galaxies with linear steep spectrum (S) and 52 galaxies with break steep spectrum (C+), 55 quasars with linear steep spectrum (S) and 36 quasars with break steep spectrum (C+) (Miroshnichenko, 2014). We use for calculations of physical parameters of considered sources the ΛCDM – Universe model with cosmological parameters $\Omega_m = 0.27$, $\Omega_\Lambda = 0.73$, $H_0 = 71$ km/s·Mpc.

The goal of this work is further examination of relations of emission contribution of structure components of giant steep-spectrum sources versus other physical characteristics.

2. Evidences for long evolution of sources with steep low-frequency spectra

When study of radio sources with steep low-frequency spectra from the UTR-2 catalogue we have determined that all these objects have giant structure (~ Mpc) (Miroshnichenko, 2012). Our estimates of characteristic age of galaxies and quasars with steep spectrum from the UTR-2 catalogue have values 10^7-10^8 years (Miroshnichenko, 2013). At these great time scales the steep radio spectra of sources may be formed at the transient injection of relativistic electrons by their long synchrotron losses (Kardashev, 1962).

From the relation of initial and present spectral indices (Gorbatsky, 1986) we derive estimation of time (t_{STI}) necessary for observed steepness of radio spectrum of source at the case of transient injection of relativistic electrons:

$$t_{STI} = \frac{\left(\frac{\nu_2}{\nu_1}\right)^{(\alpha-\alpha_0)/(2\alpha_0-1)} - 1}{\mu B_x^2 \left[\left(\frac{\nu_2}{\nu_1}\right)^{(\alpha-\alpha_0)/(2\alpha_0-1)} E_2 - E_1\right]} \qquad (1)$$

where α_0 - is initial spectral index,

α - is present spectral index,

ν_1, ν_2 – are limit frequencies of the frequency interval,

$\mu = 1{,}57 \cdot 10^{-3}$,

$B_x^2 = B^2 + B_{CMB}^2$,

B - is magnetic field strength of source, in 10^{-5} Gauss,

$B_{CMB} = 0{,}32(1+z)^2$ – is equivalent magnetic field strength corresponding to intensity of microwave background, in 10^{-5} Gauss,

$$E_i = \left(\frac{\nu_i}{1{,}41 \cdot 10^{18} B_x}\right)^{1/2}.$$

We consider the initial spectral index of sources in our sample has value $\alpha_0 = 0{,}8$ and the present spectral index of these sources has value $\alpha = 1{,}2$ (in case of S steep spectrum) and $\alpha = 2$ (in case of C^+ steep spectrum). As a result, at the frequencies $\nu_1 = 10$ MHz and $\nu_2 = 80$ MHz we obtain from (1) the estimation of synchrotron decay times at transient injection $t_{STI} \sim 10^8$ years (at the typical magnetic field strength B (Miroshnichenko, 2012) of examined sources $B \sim 10^{-5}$ Gauss). This estimate is near to value of characteristic age t (Miroshnichenko, 2013) for considered sources. So, the low frequency steep spectra of radio sources correspond to long evolution of these objects.

At process of synchrotron losses by relativistic electrons at their propagation in jets the radio lobes are formed with linear size of order near Mpc. Radio emission of these giant structures has maximum intensity at low-frequency band, particularly, at frequencies of decametre band.

For continuing study of evolution features of giant radio-sources with steep spectrum we examine ratio of emission of their radio lobes and accretion disk ($lg(S_{25}/S_{opt})$) versus jet propagation velocity V_j . Also, we consider ratio of emission of radio lobes and accretion disk crown ($lg(S_{25}/S_X)$) versus V_j . The value $lg(S_{25}/S_{opt})$ characterizes the ratio of monochromatic luminosities of source at the decameter band (at the frequency 25 MHz) and the optical band (V). Analogously, $lg(S_{25}/S_X$ corresponds to ratio of monochromatic luminosities of source at the frequency 25 MHz and te X-ray band (1 keV).

The jet propagation velocity of source V_j (Miroshnichenko, 2016a) is determined from our estimates of linear size of radio structure R (Miroshnichenko, 2012) and characteristic age of source t (Miroshnichenko, 2013) as

$$V_j = R/2t \quad . \tag{2}$$

Note, that derived estimate of jet propagation velocity of examined giant sources V_j are subrelativistic ($\sim 0{,}1c$) (Miroshnichenko, 2016a). We obtained above-mentioned relations $\left[\lg\left(\frac{S_{25}}{S_{opt}}\right)\right](V_j)$, $\left[\lg\left(\frac{S_{25}}{S_X}\right)\right](V_j)$ for galaxies and quasars with linear steep spectrum S and break steep spectrum C^+ (Figure 1, Figure 2).For galaxies of both spectral types (G_S and $G_C{}^+$) the positive trend is visible in relation $\left[\lg\left(\frac{S_{25}}{S_{opt}}\right)\right](V_j)$, that is, for greater values V_j the greater values of radio emission of radio lobes and accretion disk are observed (Figure 1). Besides, it follows from Figure 1, that the relation for each spectral type of galaxies (S and C^+) looks as separate branch.

Quasars in our sample (Q_S and $Q_C{}^+$) also display the positive trend in relation $\left[\lg\left(\frac{S_{25}}{S_{opt}}\right)\right](V_j)$ (Figure 2). Appreciably, that quasars with linear steep spectra (Q_S) are located at the region of greater V_j , while the most of quasars with spectrum C^+ occupy the region of smaller jet velocities V_j (Figure 2). The ratio of emission of radio lobes and accretion disk crown ($lg(S_{25}/S_X)$) for galaxies and quasars of both spectral types (G_S , $G_C{}^+$, Q_S , $Q_C{}^+$) versus V_j indicate on positive trend localization of jets with linear steep spectrum (G_S , Q_S) in region of greater values V_j (Figure 3, Figure 4).

For contribution of emission of radio lobes relatively of accretion disk versus the characteristic age $\left[\lg\left(\frac{S_{25}}{S_{opt}}\right)\right](t)$ shows clustering of objects (G_S , $G_C{}^+$) , (Q_S , $Q_C{}^+$) in two regions of ages (Figure 5, Figure 6). Galaxies and quasars with break steep spectrum ($G_C{}^+$, $Q_C{}^+$) have characteristic age t by one order greater than it for galaxies and quasars with S steep spectrum (G_S, Q_S). Mean values of characteristic age (Miroshnichenko, 2013; Miroshnichenko, 2016a,b) for objects of our sample are: $\langle t_{G_S} \rangle = 5{,}22(\pm 0{,}36)\cdot 10^7$ years, $\langle t_{Q_S} \rangle = 5{,}80(\pm 0{,}34)\cdot 10^7$ years, $\langle t_{G_{C^+}} \rangle = 4{,}66(\pm 0{,}41)\cdot 10^8$ years, $\langle t_{Q_{C^+}} \rangle = 2{,}92(\pm 0{,}25)\cdot 10^8$ years.

Relation of ratio of emission of radio lobes and accretion disk crown versus characteristic age of sources for examined galaxies and quasars (Figure 7, Figure 8) has form similar to relation $\left[\lg\left(\frac{S_{25}}{S_{opt}}\right)\right](t)$, $\left[\lg\left(\frac{S_{25}}{S_X}\right)\right](t)$ (Figure 5, Figure 6).

Note, that the mean value of ratio of emission of radio lobes and accretion disk of source $\left\langle \lg\left(\frac{S_{25}}{S_{opt}}\right)\right\rangle$ has greater value for galaxies and quasars with linear steep spectrum S as compared to objects with spectrum C^+. Namely, these values are: $\left\langle \lg\left(\frac{S_{25}}{S_{opt}}\right)_{G_S}\right\rangle = 5{,}64(\pm 0{,}12)$,

$\left\langle \lg\left(\frac{S_{25}}{S_{opt}}\right)_{Q_S}\right\rangle = 5{,}33(\pm 0{,}06)$,

$\left\langle \lg\left(\frac{S_{25}}{S_{opt}}\right)_{G_{C^+}}\right\rangle = 5{,}15(\pm 0{,}12)$,

$\left\langle \lg\left(\frac{S_{25}}{S_{opt}}\right)_{Q_{C^+}}\right\rangle = 5{,}00(\pm 0{,}10)$. As well, the mean value of ratio of emission of radio lobes and accretion disk crown $\left\langle \lg\left(\frac{S_{25}}{S_X}\right)\right\rangle$ has greater value for considered objects with linear steep spectrum S as compared to these with break steep spectrum C^+:

$\left\langle \lg\left(\frac{S_{25}}{S_X}\right)_{G_S}\right\rangle = 9{,}03(\pm 0{,}23)$,

$\left\langle \lg\left(\frac{S_{25}}{S_X}\right)_{Q_S}\right\rangle = 8{,}45(\pm 0{,}14)$,

$$\left\langle \lg\left(\frac{S_{25}}{S_X}\right)_{G_{C^+}} \right\rangle = 7{,}89(\pm 0{,}33),$$

$$\left\langle \lg\left(\frac{S_{25}}{S_X}\right)_{Q_{C^+}} \right\rangle = 7{,}78(\pm 0{,}17)\ .$$

Thus, the greater contribution of emission of radio lobes is observed for more young sources (with linear steep spectrum S) than for more old sources (with break steep spectrum C^+). Alternative reason of difference of these parameters may be the increase of contribution of emission of accretion disk and accretion disk crown for sources with steep spectrum C^+. Probably, this is connected with activity recurrence of nuclei of giant sources.

3. Conclusion

The examined giant radio sources – galaxies and quasars with both types of steep spectra (S and C^+) from the UTR-2 catalogue reveal a number of evolution features:

1. Positive correlation is determined for the ratio of emission of radio lobes and accretion disk versus jet propagation velocity of sources. Analogous correlation is observed for the ratio of emission of radio lobes and accretion disk crown versus jet propagation velocity. At that, the greater jet propagation velocities are typical for galaxies and quasars with steep linear spectra S.
2. Values of ratio of emission of radio lobes and accretion disk of examined sources are clustered in two regions of sources ages. Sources with C^+ type of steep spectrum have characteristic age by one order greater than these with steep spectrum S.
3. Contribution of emission of radio lobes relatively accretion disk decreases at the increasing of age of steep spectrum sources (or the contribution of accretion disk or crown increases) testifying to their activity recurrence.

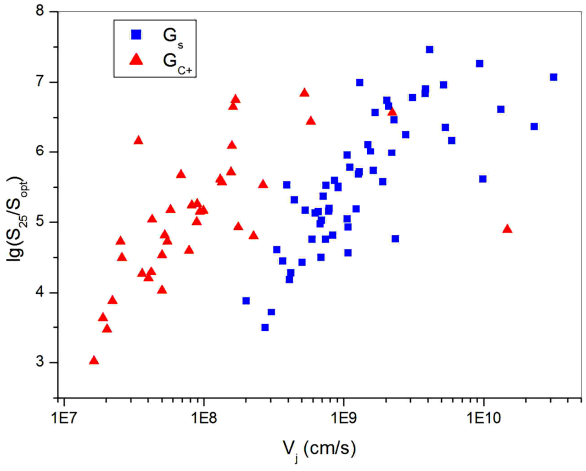

Figure 1: Ratio of emission of radio lobes and accretion disk versus jet velocity for galaxies with steep radio spectra of both types (S and C^+)

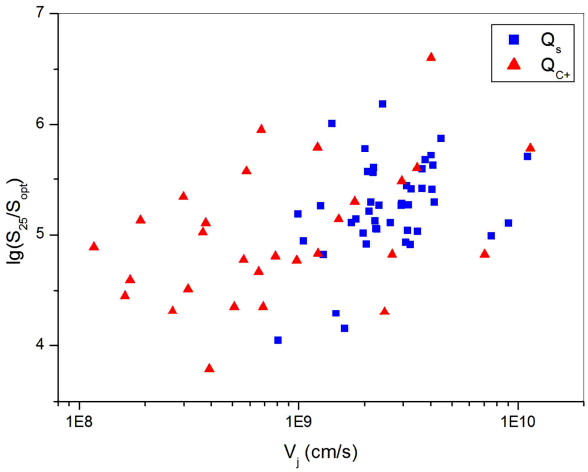

Figure 2: Ratio of emission of radio lobes and accretion disk versus jet velocity for quasars with steep radio spectra of both types (S and C^+)

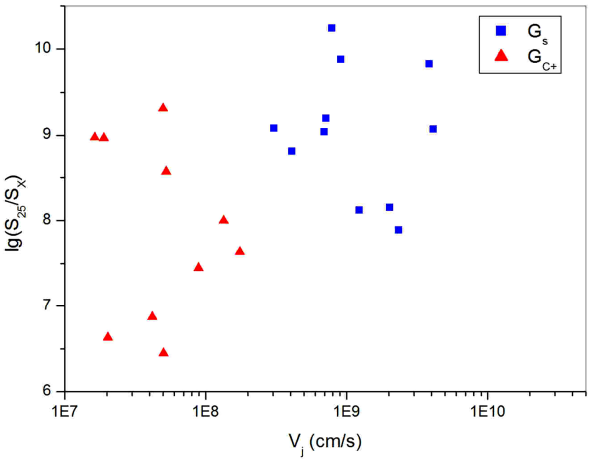

Figure 3: Ratio of emission of radio lobes and accretion disk crown versus jet velocity for galaxies with steep radio spectra of both types (S and C^+)

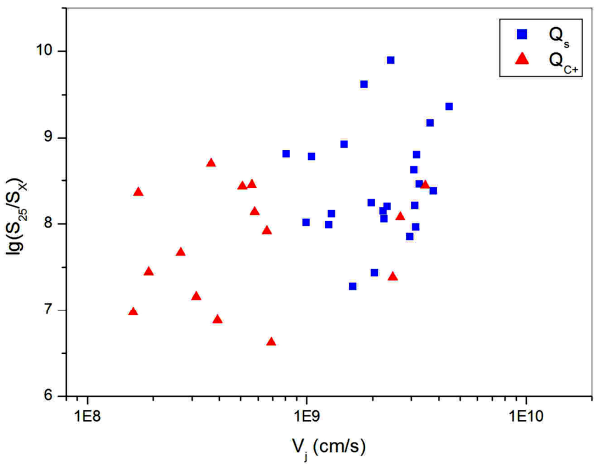

Figure 4: Ratio of emission of radio lobes and accretion disk crown versus jet velocity for quasars with steep radio spectra of both types (S and C^+)

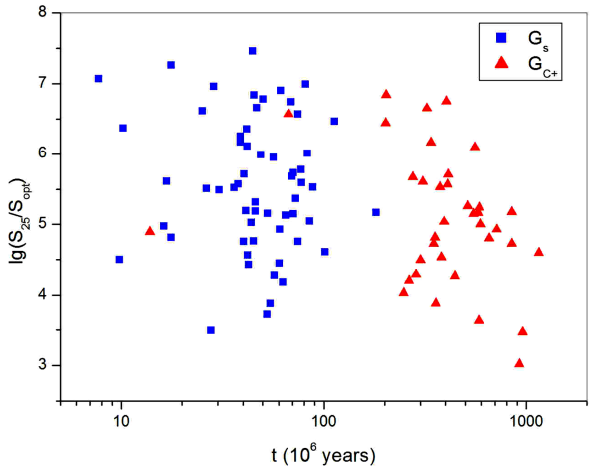

Figure 5: Ratio of emission of radio lobes and accretion disk versus characteristic age for galaxies with steep radio spectra of both types (S and C^+)

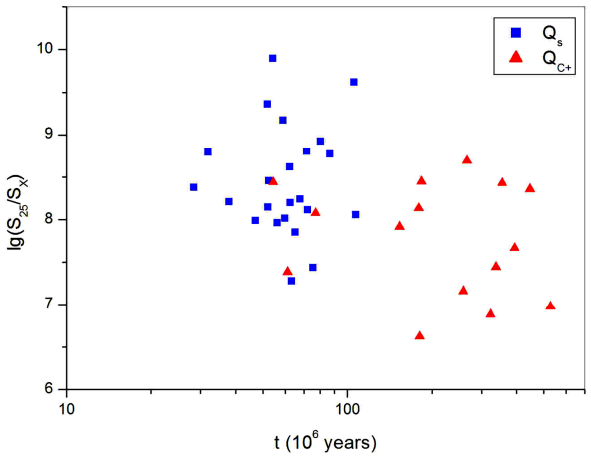

Figure 8: Ratio of emission of radio lobes and accretion disk crown versus characteristic age for quasars with steep radio spectra of both types (S and C^+)

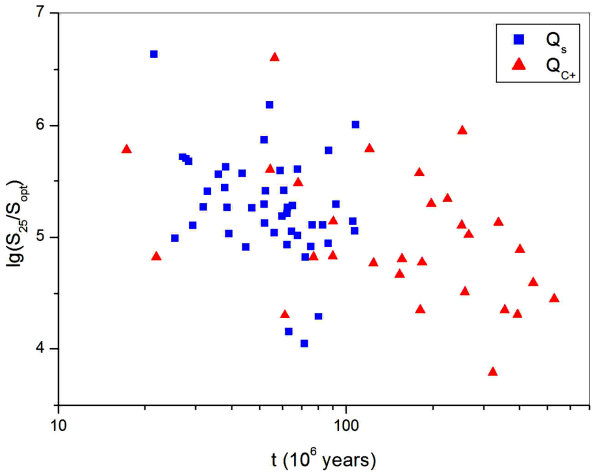

Figure 6: Ratio of emission of radio lobes and accretion disk versus characteristic age for quasars with steep radio spectra of both types (S and C^+)

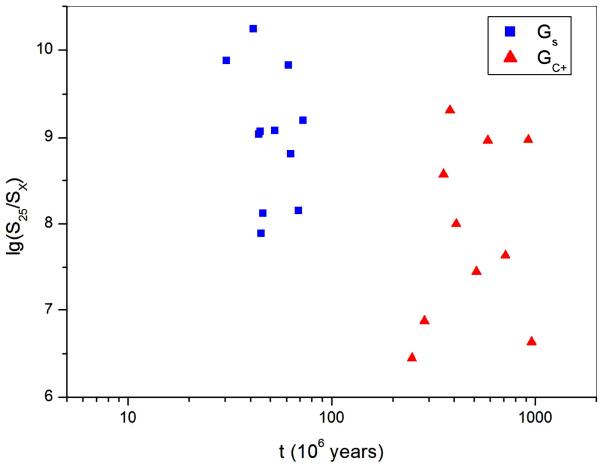

Figure 7: Ratio of emission of radio lobes and accretion disk crown versus characteristic age for galaxies with steep radio spectra of both types (S and C^+)

References

Braude S.Ya, Miroshnichenko A.P., Sokolov K.P. & Sharykin N.K.: 1981, *Astrophys.Space Sci.*, **76**, 279.

Braude S.Ya., Miroshnichenko A.P., Rashkovski S.L. et al.: 2003, *Kinem.&Phys.Celest.Bodies*, **19**, 291.

Gorbatsky V.G.: 1986, Introduction to Physics of Galaxies and Clusters of Galaxies. (Nauka, Moscow).

Kardashev N.S.: 1962, *Sv.Astron.*, **6**, 317.

Miroshnichenko A.P.: 2012, *Radio Phys.&Radio Astron.*, **3**, 215.

Miroshnichenko A.P.: 2013, *Odessa Astron.Publ.*, **26/2**, 248.

Miroshnichenko A.: 2014, Independent Estimates of Energies of Steep-Spectrum Radio Sources, in Multiwavelength AGN Surveys and Studies, eds. A. Mickaelian & D. Sanders, (Cambridge University Press, Cambridge), 96.

Miroshnichenko A.P.: 2016a, Abstracts of VIII Conference "Selected Issues of Astronomy and Astrophysics", I.Franko National University of Lviv, 20.

Miroshnichenko A.P.: 2016b, *Odessa Astron. Publ.*, **29/2**, 173.

DOI: http://dx.doi.org/10.18524/1810-4215.2017.30.114691

ERYTHROCYTES FUNCTIONAL FEATURES IN THE 11-YEAR SOLAR CYCLE

Parshina S.S.[1], Tokayeva L.K.[1], Dolgova E.M.[1], Afanas'yeva T.N.[1], Samsonov S.N.[2], Petrova V.D.[1], Vodolagina E.S.[1], Kaplanova T.I.[1], Potapova M.V.[1]

[1] Saratov State Medical University n.a. V.I. Razumovsky of the Ministry of Health of Russia, St. B. Kazach'ya, 112, Saratov, Russia, *parshinasvetlana@rambler.ru*

[2] Institute of Cosmophysical Research and Aeronomy n.a. U.G. Shafer, Russian Academy of Sciences, Lenin Avenue, 31, Yakutsk, Russia, *s_samsonov@ikfia.ysn.ru*

ABSTRACT. There had been studied features of rheological blood failures in patients with unstable angina (UA) in periods of the high (HSA) and low solar activity (LSA) in the 23rd 11-year solar cycle. This category of patients is characterized by prethrombotic blood state, although they don't have coronary thrombosis. The research aimed to study compensatory mechanisms which block thrombosis development at the solar activity increase. There had been established that the period of the solar activity increasing in the 11-year solar cycle is characterized by an increase of a blood viscosity, comparing with the period of a low solar activity. Though, erythrocytes functional features in this case are compensatory mechanisms – erythrocyte aggregation paradoxically reduced and their deformability increases. It is probably connected with the revealed fibrinogen decrease in the period of the high solar activity. We can see that the change of a solar activity is accompanied not only by the progressing of pathologic processes, but also by an activation of adaptive changes in erythrocyte membrane so0 as to prevent thrombosis. Though, the required compensatory mechanisms were found invalid, which were shown in the decrease of an oxygen delivery to tissues, and the effectiveness decrease of the medical treatment in the period of a HSA.

Keywords: solar activity, unstable angina, blood rheological properties, erythrocytes functional features.

1. Introduction

Unstable angina (UA) is an exacerbation of an ischemic heart disease and is characterized by developing of a prethrombotic state, and rheological blood properties (blood viscosity and erythrocytes functional features), in this case, are of prime importance (Voskoboi, 1995). The external influense on haemorheological defects at UA are considered only in a few studies (Parshina, 2006). Although it is known that the cosmic weather influences significantly on a cardiovascular system condition (Samsonov et. al., 2016).

The research aimed studying erythrocytes functional features (aggregation and deformability) in the 11-year solar cycle in order to reveal compensatory mechanisms which prevent thrombosis at the solar activity (SA) increase.

2. Results and discussion

200 patients with UA had been examined. 120 of them were in the group of the high solar activity (HSA). They had been examined in the period from the 2nd up to the 5th year of the 11-year solar cycle. This period is characterized by an increment of a solar activity (SA) and high values of the Wolf's numbers (112,0±2,9). The group of the low SA (LSA) consisted of 80 patients, who had been examined in the period from the 6th up to 11th year of the solar cycle. The second half of the 11-year solar cycle was characterized by the decrease of a SA and by the low value of the Wolf's numbers (62,4±3,9; $p<0,05$ with the period of a HAS).

In the group of a HAS a higher blood viscosity (BV) had been noted in vessels of a medium diameter (on the 100 s^{-1} rates of shear), than at patients in the period of a LSA ($p<0,05$) (Table 1). At the same time the increase of a SA had not influenced on a blood fluidity in vessels of big and small diameters (on the 200 s^{-1} and 20 s^{-1} rates of shear) ($p>0,05$) (Table 1).

Table 1. Blood rheological properties, hematocrit index and fibrinogen level at patients with unstable angina in the high and low solar activity (M±m)

Parameters	Unstable angina	
	High SA (n=120)	Low SA (n=80)
BV 200 s^{-1}, mPa·s	6,58±0,13	6,38±0,13
BV 100 s^{-1}, mPa·s	10,50±0,44 *	7,19±0,18
BV 20 s^{-1}, mPa·s	11,73±0,45	10,59±0,39
EA, c.u.	1,18±0,03 *	1,46±0,03
ED, c.u.	1,55±0,06 *	1,10±0,08
Ht/ η, c.u.	6,51±0,02 *	7,09±0,16
Ht, %	40,3±0,5 *	42,9±0,3
FG, g/l	3,69±0,08 *	3,97±0,11

Notes: SA – solar activity;

* – the difference between the group of the HSA and the LSA is statistically valid, $p<0,05$.

It had been found that erythrocyte functional features are very sensitive to SA change. So, in the high SA there is lower erythrocyte aggregation activity (EAA) than in the low SA ($p<0,05$) (Table 1).

It is known that a high EAA increases a local BV in postcapillary venules, slows down the blood velocity, increases capillary tension. This leads to extravasation of fluids, tissue hypostasis, ischemia, capillars rupture, it also causes a decrease of oxygen delivery to tissues (Korkushko & Lishnevskaya, 2005). That is why revealed decrease of EAA in increase of a SA at patients with UA is an important compensatory mechanism which prevents progressing of myocardial ischemia.

Besides, there had been noted a fast growth of erythrocyte deformability (ED) in a HSA comparing with the period of a LSA ($p<0,05$) (Table 1). That is ED which let erythrocytes go through vessels the diameter of which is commensurately to their sizes. As even a 10% decrease of ED leads to serious failures in tissue oxygenation (G. Cicco, A. Pirelli, 1999), a hypothesis for a leading role of the non-ischemic hypoxia caused by ED defect, in atherosclerosis pathgenesis (Korkushko & Lishnevskaya, 2005). An increase of ED can be connected with the decrease of fibrinogen (FG) level as well, in the increase of SA (Table 1).

Hematocrit (Ht) parameter had been decreased in the group of a HSA comparing with the group of a LSA ($p<0,05$) (Table 1), which can be considered as another compensatory mechanism preventing further defect of a blood fluidity in microcirculation zone, in increase of a SA.

The analysis of the study results shows that the basic factor of a haemorheological decompensation in the SA increase at patients with UA is an increase of a blood viscosity. Erythrocytes functional features in this case serve as a compensatory mechanism – erythrocyte aggregation paradoxically reduced and their deformability increases.

At the same time the tissue oxygen delivery (Ht/η) in the HAS was lower than in the period of a LSA ($p<0,05$) (Table 1). This means that despite of the activation of compensatory haemorheological mechanisms in the increase of a SA (EA decrease and ED increase), adaptative ability at patients with UA are not enogh to eradicate an ischemic heart disease hypoxia. Taking to account the given results, we should consider haemorhelogical changes at patients with UA in the period of a HSA as a compensatory mechanism failure.

The hypothesis finds endorsement in the study of treatment effectiveness in the periods of HSA and LSA. We had established that medical treatment effectiveness depends on the period of a SA: in the LSA antianginal effect was more evident than in the HSA ($2,27\pm0,16$ points and $1,75\pm0,12$ points, $p<0,05$).

From there, an increase of a SA at patients with UA is accompanied by not only pathological processes developing, but also by an activation of compensatory changes in erythrocyte membrane which prevent thrombosis. Though, the required compensatory mechanisms were found invalid, which were shown in the decrease of an oxygen delivery to tissues, and the effectiveness decrease of the medical treatment in the period of a HSA.

References

Voskoboi I.V.: 1995, *Author's abstract*, 28.

Parshina S.S.: 2006, *Author's abstract*, 48.

Samsonov S.N. et al.: 2016, *Psychosomatic and Integrational Res.*, **2**, 1 (http://pssr.pro/).

Korkushko O.V.: 2005, *Materials of a conference Clinical gemostaziologiya and haemorheology in cardiovascular surgery, Moscow*, 176.

Cicco G.: 1999, *Clin. Hemorheology and Microcirculation*, **21**, 169.

DOI: http://dx.doi.org/10.18524/1810-4215.2017.30.117660

ACCURACY OF SATELLITE OPTICAL OBSERVATIONS AND PRECISE ORBIT DETERMINATION

L.Shakun, N.Koshkin, E.Korobeynikova, S.Strakhova, V.Dragomiretsky, A.Ryabov, S.Melikyants, T.Golubovskaya, S.Terpan

Astronomical Observatory of Odessa I.I.Mechnikov National University, Odessa, Ukraine, *leomspace@gmail.com*

ABSTRACT. The monitoring of low-orbit space objects (LEO-objects) is performed in the Astronomical Observatory of Odessa I.I. Mechnikov National University (Ukraine) for many years. Decades-long archives of these observations are accessible within Ukrainian network of optical observers (UMOS). In this work, we give an example of orbit determination for the satellite with the 1500-km height of orbit based on angular observations in our observatory (Int. No. 086). For estimation of the measurement accuracy and accuracy of determination and propagation of satellite position, we analyze the observations of Ajisai satellite with the well-determined orbit. This allows making justified conclusions not only about random errors of separate measurements, but also to analyze the presence of systematic errors, including external ones to the measurement process. We have shown that the accuracy of one measurement has the standard deviation about 1 arcsec across the track and 1.4 arcsec along the track and systematical shifts in measurements of one track do not exceed 0.45 arcsec. Ajisai position in the interval of the orbit fitting is predicted with accuracy better than 30 m along the orbit and better than 10 m across the orbit for any its point.

Keywords: artificial satellite, LEO, optical observation, short-exposition observations, analysis of measuring precision, orbit estimation, Ajisai, Orekit, UMOS.

1. Introduction

The increase of occupation of the near-Earth orbits with the space debris constitutes a significant danger for active near-Earth satellites. The monitoring of near-Earth cosmic objects allows predicting the dangerous rendezvous of these objects. The optical observations of the objects on low-Earth orbits (LEO) are regularly performed in the Astronomical Observatory of Odessa I.I. Mechnikov National University (Ukraine) (Shulga et al., 2015).

For the observations, we use the telescope with the aperture of 50 cm and focal length 2 m on the azimuthal mounting. There is the television camera WACOM902H that works with the frequency of 50 interlace half-frame per second in the focal plane. Field of view of the telescope is about 10 arcmin. The LEO-objects are observed in tracking mode and this allows to obtain both the coordinate and the unique photometric information with high time resolution simultaneously (Koshkin et al., 2017). Shakun & Koshkin (2014) give the detailed description of the methods of objects position measurements on the frame and time tagging of the frames. In that paper is shown that the accuracy of one measurement is about 0.8 arcsec and accuracy of time measurement from frame to frame is better than 0.0001 seconds.

However, in addition to the measurement accuracy caused by the method of frame measurements and features of the time tagging, observations may contain other errors that can be detected only by means of independent comparison of measurements and positions of the well-known object.

In this paper, we compare the accuracy of our measurements of Ajisai (EGS) position that has the well-determined orbit with theoretical estimates of its visible position. We also estimate the orbit calculated by using our measurements with applying of the numerical model of satellite motion and compare the obtained orbit with the daily predictions that provided by International Laser Ranging Service (ILRS).

2. The estimate of measurement accuracy

To compare with our measurements, we need the estimates of satellite position that are significantly more precise than ones we get. The source of such estimates may be the prediction of Ajisai position provided by ILRS. For Ajisai such predictions are provided by Japan Aerospace Exploration Agency (JAXA) and NERC Space Geodesy Facility (see: CPF predictions). Every provider gives its prediction once a day for five days ahead. We joined successive predictions in one sequence and used only data of prediction for the first day (as the most reliable ones) for the calculation of the satellite position. So we gained these positions in the continuous range for the first eleven months of 2017. The comparison of the position in JAXA's range of prediction (jax) and ones of NERC Space Geodesy Facility (sgf) (Table 1) show that with rare exceptions difference between these predictions is less than 1 m. In visible coordinates, it means that deviation between the predictions is less than 1 arcsec. We expect such predictions are suitable for our further analysis. We chose the JAX prediction, because it had smaller shifts of positions between daily forecasts and these shifts are also much less than 1 m.

Table 1: Comparison of Ajisai positions by JAX and SGP propagations for months of 2017. In the columns marked as „std" the estimates of the standard deviation of the difference between predictions are given, in the columns, marked as "max abs" are maximal absolute values of differences. dV corresponds to the difference along the velocity vector, dR – in the perpendicular direction to the velocity vector in the orbital plane, dN – in the perpendicular direction to the orbital plane.

Year. Month	std			max abs		
	dV (m)	dR (m)	dN (m)	dV (m)	dR (m)	dN (m)
2017.01	0,305	0,080	0,311	1,532	0,248	0,909
2017.02	0,254	0,045	0,324	1,151	0,138	0,958
2017.03	0,245	0,049	0,299	1,520	0,184	0,796
2017.04	1,408	0,072	0,260	9,006	0,348	0,679
2017.05	0,256	0,043	0,284	1,154	0,164	0,747
2017.06	0,449	0,076	0,324	2,562	0,220	0,904
2017.07	0,282	0,050	0,340	2,519	0,211	1,076
2017.08	0,229	0,067	0,328	1,002	0,224	1,127
2017.09	0,495	0,072	0,493	2,733	0,224	1,557
2017.10	0,241	0,038	0,251	0,863	0,144	0,901
2017.11	0,600	0,060	0,259	2,691	0,233	0,879

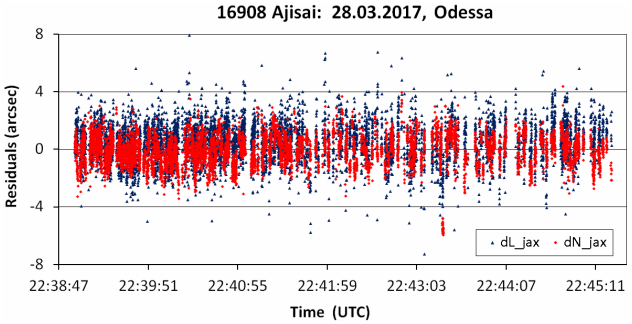

Figure 1: Residuals between measurements and calculated visible coordinates of Ajisai according to the prediction of JAX for 28.03.2017. dL are the residuals along the visible trajectory, dN are the residuals across the visible trajectory.

In Figure 1 the residuals between measurements and calculated visible coordinates according to the prediction of JAX are shown for the typical satellite track. The residuals are considered in terms of along the visible trajectory and across it. The coordinate system necessary for decomposition of the vector of residuals can be obtained on the basis of theoretical topocentric values of position vector (r) and velocity vector (v) of a satellite as

$$\vec{i} = \frac{\vec{r}}{r}, \quad \vec{j} = \left[\vec{k}, \vec{i}\right], \quad \vec{k} = \frac{[\vec{r}, \vec{v}]}{\left|[\vec{r}, \vec{v}]\right|},$$

where unit vector ***i*** is directed along the vector observer-satellite, unit vector ***j*** is codirectional to the tangent line to the visible trajectory and unit vector ***k*** is perpendicular to visible trajectory in given point. The visible angular velocity of a satellite is determined by projecting of velocity vector on the vector ***j***.

This coordinate system for representation of the residuals usually is better connected with the causes of errors appearance and it allows to understand them easier than the traditional representation of residuals in the equatorial or the horizontal system of coordinates.

Since when we observe LEO-objects their visible angular velocity is high, the images of reference stars or the objects become drawn-out along the motion direction and this requires the correct alignment of the position of the center or the edges of the stroke with the moment of time. In addition, due to the high angular velocity of the object, even small errors in registration of moments of time when the image was taken, lead to significant shifts in the estimate of coordinates along the trajectory. Both causes lead to the perceptible difference in behavior of errors along and across the trajectory. Among other things, detecting of the systematic errors in time registration is the most difficult if we consider the observations solely.

For the estimation of measurement accuracy and estimation of the orbit, we take 13 tracks of Ajisai from 23.03.2017 to 12.04.2017. In Table 2 the statistical parameters of residuals between observations and theoretical values based on the JAX predictions are given separately for every track.

One can see, that the estimate of the standard deviation across the track is stable in the range from 0.9 to 1.1 arcsec, but the error along the track is 1.4 times higher. The mean of all residuals of the whole track usually is significantly biased from zero. The theoretical difference of the mean bias of residuals between two predictions (sgf-jax) is given in Table 1 for comparison. There the residuals are calculated for the same moment of time when the observations were made. Thus, it is obvious, that obtained biases of the tracks cannot be explained by differences in predictions assuming a prediction error is of the order of 1 m. For the explanation of these mean biases, the residuals between satellite positions and theoretical predictions must be about 10 m and more.

In the end, we give the estimates of biases in terms of time moments shifts along the trajectory dT that accentuates the extreme importance of thorough measuring of the timing of images obtaining. Taking into account, that Ajisai is the satellite with relatively slow visible velocity, we expect that for very low orbit satellites these requirements will be even more essential.

3. The estimation of orbit

Now, for considering the observations presented in Table 2, we estimate the satellite's orbit using the numerical model of motion.

For integration of equations of motion and astrometric transformations, we used low-level astrodynamics library Orekit 9.0. But for the model of observations and in the algorithm of optimization of the satellite motion model we used our own code in the programming language Kotlin.

Table 2: Statistics of measurements of the Ajisai positions. dL are the residuals along the trajectory; dN are residuals across the trajectory; dT are residuals along the trajectory in terms of time-lags. avg are mean values of bias for the whole track; std are the estimate of the standard deviation for one measurement; sgf-jax are the mean values of residuals between two theoretical ILRS-predictions.

Date and Time of Track	Numbers of measurements	dL (arcsec)			dN (arcsec)			dT (sec)	
		avg	std	sgf-jax	avg	std	sgf-jax	avg	sgf-jax
23.03.2017 20:03	7483	0,0019	1,32	0,0010	-0,2710	0,95	0,0410	0,00001	0,000001
28.03.2017 20:35	10273	0,1294	1,25	-0,0101	-0,4648	1,00	0,0164	0,00010	-0,000017
28.03.2017 22:38	7482	0,4377	1,32	-0,0069	-0,1131	1,00	0,0072	0,00059	-0,000009
29.03.2017 21:43	6808	0,2556	1,29	0,0006	-0,1398	0,99	0,0188	0,00032	0,000002
30.03.2017 20:48	7670	0,2906	1,21	0,0092	-0,2450	0,90	0,0069	0,00040	0,000013
31.03.2017 20:01	2460	0,4214	1,30	0,0035	-0,7009	1,09	0,0047	0,00073	0,000005
31.03.2017 21:58	8156	0,3957	1,35	0,0152	0,0876	1,05	-0,0053	0,00056	0,000021
03.04.2017 21:17	10555	0,3479	1,40	0,0041	-0,0574	1,08	0,0115	0,00048	0,000005
10.04.2017 21:02	5435	0,3074	1,28	-0,0008	0,3626	0,88	-0,0203	0,00043	-0,000001
10.04.2017 23:03	7168	-0,0057	1,15	0,0054	0,4526	1,05	-0,0267	-0,00001	0,000010
11.04.2017 20:16	1667	0,0091	1,52	0,0008	-0,2164	1,09	-0,0240	-0,00012	0,000002
11.04.2017 22:09	10610	0,1735	1,31	0,0121	0,1367	1,11	-0,0233	0,00027	0,000020
12.04.2017 21:16	7050	0,3338	1,28	0,0177	0,1667	0,95	-0,0185	0,00050	0,000025

The process of orbit determination includes the following stages:

1. A primary estimate of Kepler orbits parameters from three observations for one track.
2. Optimization of the Keplerian orbit for all observations of the single track.
3. Optimization of position and velocity for a given epoch for the numerical model of satellite motion for one track.
4. Optimization of the position and velocity of the satellite for a given epoch for the numerical model of satellite motion for one or several tracks on close days
5. Optimization of the position, the velocity of the satellite for a given epoch, and parameters of the ratio of cross-section to mass, in terms of correction for the influence of sunlight pressure and correction for the influence of the atmosphere.

Thus, to determine the orbit, we did not use any a priori information about the satellite's orbital motion.

In the numerical integration of the equations of satellite motion, the following perturbing forces were taken into account:

1. The Earth gravity field was calculated by using the model Eigen6s (Furste et al., 2011) truncated to the 51st degree and the 51st order. The contribution of the harmonics was derived in accordance with the algorithm Holmes & Featherstone (2002).
2. Ocean tides in accordance with the model FES2004 (Lyard et al., 2006).
3. Gravitational perturbation from the Moon and the Sun according to the model DE-430.
4. Tides in the solid body of the Earth from the Moon and the Sun.
5. The force of solar radiation pressure with considering umbra and penumbra regions in the term of an effective cross-section of the satellite.
6. Atmospheric drag force in accordance with DTM2000 (Bruinsma et al., 2003) in the term of the effective cross-section. The level of the solar radiation flux was taken as an average one.
7. The general relativity term.

For integrating the equation, we used the method Dormand-Prince 5(3) (Hairer et al., 2011), with the variable step and accuracy control 0.001 m on a step and the maximal value of step 120 sec.

The effective cross-sections of the satellite fitted independently in cases of solar radiation pressure and the atmospheric drag force.

The results of these fitting are presented in Figure 2 in the form of differences between the satellite position (dV, dR, dN) according to the orbit optimized by us and the positions predicted by JAX.

As one can see, in the interval of fitting, the differences along the satellite trajectory are not more than 30 m, and in the perpendicular direction are not more than 10 m.

In the month interval of the propagation, the differences along the trajectory are not more than 100 m. And only a month later the differences have a linear trend along the orbit. Three months after the fitting interval, the time lag of the satellite along the orbit is about 0.4 sec.

4. Discussion and conclusion

Thus we have shown that

- The accuracy of the one measurement of object positions across the visible trajectory is from 0.9 to 1.1 arcsec, and along the visible path from 1.2 to 1.4 arcsec.
- The mean values of the residuals of the coordinates both along and across the visible trajectory are of several tenths of an arcsecond and require the further analysis and elimination.

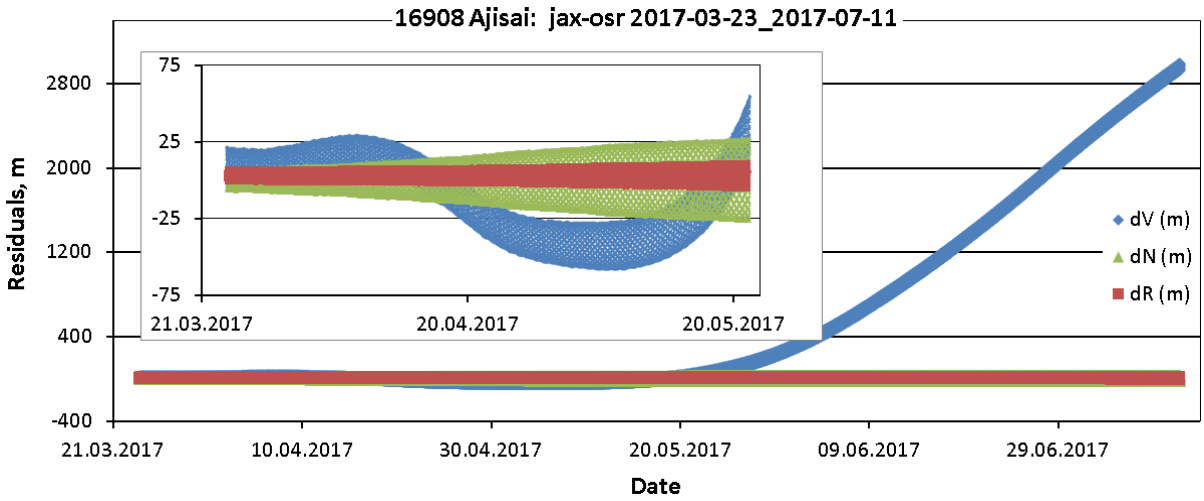

Figure 2: The difference between the positions of the satellite according to the optimized orbit and positions according to the prediction of JAX. dV are the differences along the direction of the velocity vector; dN are the differences in the perpendicular direction to the instantaneous plane of the orbit; dR are the differences in the perpendicular direction to the velocity vector in the instantaneous plane of the orbit.

- Observations of such quality make possible to predict positions within the interval of fitting with accuracy to dozens of meters along the orbit and better than 10 meters in the perpendicular directions to the orbit.
- The monthly prediction of the satellite positions is suitable for planning automated observations.

The causes of the significant bias of the mean residuals from zero can be both systematic biases along the orbit and the correlation of close observations. Taking to account the similarity of the value of bias along and across the orbit in our case, most likely we deal with the second cause. Sure, very short exposures and a small field of view of the telescope results in a small number of reference stars, that in many frames does not allow to restore the coordinate system completely. The use of the mean coordinate system moving from frame to frame without the doubt should result in a correlation of close measurements. The result of this is the significant bias of the mean values of the residuals from zero.

The conclusions of Section 2 on the accuracy of the measurements are in good agreement with the residuals between the fitting orbit and the JAX prediction obtained in Section 3. Relatively larger deviations in the difference of positions along the orbits are probably related to the fact that all observations were obtained at one observation point in approximately the same time of day, and this fact allows to see only a small part of the orbit.

After 2-3 months, the difference between the predicted and the real position of the satellite along the orbit grows up to several arcminutes, which is quite high and can go beyond the field of view of the telescope. However, almost whole deviation lies along the visible motion of the satellite. Correction of the initial moment of observations allows us to remove the major part of the accumulated deviation along the orbit. Thus, the prediction based on our observations can be successfully used to detect and to track the satellite for several months later than the orbit was fitted.

Acknowledgements. We are thankful to the authors of Orekit for the development and long-term development improvement of such useful engineering solution. Without Orekit, this work would take considerably greater effort.

References

Bruinsma S., Thuillier G., Barlier F.: 2003, *Journal of Atmospheric and Solar-Terrestrial Physics,* **65**, 1053.
CPF predictions: ftp://edc.dgfi.tum.de/pub/slr/cpf_predicts/2017/ajisai/.
EGS (Ajisai): http://global.jaxa.jp/projects/sat/egs/.
Hairer E., Norsett S., Wanner G.: 1993, *Solving Ordinary Differential Equations (Springer)*, 528.
Holmes S., Featherstone W.: 2002, *Journal of Geodesy*, **76**, 279.
ILRS: https://ilrs.cddis.eosdis.nasa.gov/.
Furste C., Bruinsma S., Shako R. et al.: 2011, *Geophysical Research Abstracts*, **13**, EGU2011-3242-2.
Kaminski K., Koshkin N., Shakun L. et al.: 2017, *Proc. of 7th Eur. Conf. on Space Debris*, ESA/ESOC, Darmstadt, 18-21 Apr. 2017. Available at: (https://conference.sdo.esoc.esa.int/proceedings/sdc7/paper/721/SDC7-paper721.pdf).
Koshkin N. et al.: 2017, *Adv. in Space Res.*, **60**, 1389.
Lyard F. et al.: 2006, *Ocean Dynamics*, **56**, 394.
Orekit: https://www.orekit.org/.
Shakun L., Koshkin N.: 2014, *Adv. in Space Res.*, **53**, 1834.
Shulga A.V. et al.: 2015, *Space Science and Technology*, **21**, 3, 74.
UMOS: http://umos.mao.kiev.ua/eng/, https://en.wikipedia.org/wiki/Ukrainian_Optical_Facilities_for_Near-Earth_Space_Surveillance_Network.

DOI: http://dx.doi.org/10.18524/1810-4215.2017.30.114695

INFLUENCE OF SOLAR RETROGRADE MOTION ON TERRESTRIAL PROCESSES

N.S.Sidorenkov [1], Ian Wilson [2]

[1] Hydrometcenter of the Russia, Moscow, *sidorenkov@mecom.ru*

[2] The Liverpool Plains Daytime Astronomy Centre, Curlewis, NSW, Australia, *irgeo8@bigpond.com*

ABSTRACT. The influence of solar retrograde motion on secular minima of solar activity, volcanic eruptions, climate changes, and other terrestrial processes is investigated. Most collected data suggest that secular minima of solar activity, powerful volcanic eruptions, significant climate changes, and catastrophic earthquakes occur around events of solar retrograde motion.

Keywords: barycentric motion of the sun; secular minima of solar activity, volcanic eruptions, climate changes; the historical process of humankind.

1. Barycentric motion of the sun

The amplitude of the 24th 11-year cycle of solar activity was found to be the smallest over the last 200 years. Even smaller amplitudes of 11-year sunspot cycles were observed only during the Dalton Minimum. What is the cause of this decay of the amplitude of the 11-year sunspot cycle? The most plausible explanation of this phenomenon can be provided by the Jose cycle (Jose, 1965), which he obtained by calculating the trajectory of solar motion around the center of mass of the solar system. Let us look at his work more closely.

The planets rotate around the Sun. The Sun moves around the center of inertia of the solar system, which is hereafter called the barycenter. The trajectory of the Sun (cardioid) has the form of a fourth-order quasi-periodic curve (conchoid of a circle). It usually moves counterclockwise around the barycenter. However, at very rare times, the center of the Sun moves so that the barycenter turns out to be outside the cardioid. In these cases, the Sun passes the barycenter clockwise, so Jose called these events solar retrograde motion. The last event was observed about the year 1990 (Fig. 1). Jose (1965) showed that such events happen every 178.7 years. Earlier events of solar retrograde motion occurred about the years 1811, 1632, 1454, 1275, 1096, 918, 739, 560, 382, 203, 24, –154, and –333.

Jose (1965) found the relation between the 179-year period of solar retrograde motion and the similar cyclicity of solar activity. At present, solar activity records are available over the last thousand years. Amplitude beats between the 11-year solar activity cycle and its secular maxima and minima have been established. The minima are given the names of scientists who made the greatest contribution to their study (see the first column in Table 1). The second and third columns list approximate times of beginning and end of solar spot minima, and the fourth column gives the times of solar retrograde motion. The differences between the beginning (middle) of a solar activity minimum and solar retrograde motion is given in the sixth column. A comparison of them shows that, in all five cases, the secular minima of solar activity approximately agree with the times of solar retrograde motion (with a delay of approximately 18 years). Unfortunately, this sample is too small for the hypothesized relation between the secular solar activity minima and the events of solar retrograde motion to be justified statistically, but there is no ground to reject it, especially as, on small scales (as compared with the solar system), the influence exerted by features of the Earth's monthly rotation around the center of inertia of the Earth–Moon system can easily be observed in weather and climate variations (Sidorenkov, 2016).

Taking into account what was said above, it can be concluded that the amplitude decay for the 24th 11-year cycle suggests the onset of a new secular minimum of solar activity, which was predicted, together with its consequences, by Landscheidt (2003).

2. Volcanic explosions

It is well known that secular minima of solar activity are associated with climate cooling on the Earth. Climatologists explain them by stratospheric sulfur compound pollution caused by explosive volcanic eruptions.

In volcanic explosions, eruption products are injected into the stratosphere, spread over the globe, and gradually descend, specifically, on the Antarctic and Greenland ice sheets. As snow falls, they get buried progressively deeper and the snow turns into ice. An analysis of ice cores produced by drilling provides information on volcanic eruptions over the globe in the far past.

Data on volcanic activity and the stratospheric annual content of sulfate aerosol (sulfate ion SO^{2-}_4) were obtained by Traufetter et al. (2004) by analyzing ice cores drilled in Queen Maud Land in western Antarctica. These data can

be found at http://www.ncdc.noaa.gov/paleo/icecore/antarctica/domec/domec**.** New data on volcanic aerosol concentrations in the stratosphere over the last 2000 years were obtained in (Clausen et al., 2012; Sigl et al., 2013). Below, we use data from (Sigl et al., 2013).

The stratospheric aerosol consists, to a large degree, of tiny droplets of sulfuric acid. It reflects solar radiation in the lower stratosphere and the upper troposphere, thereby reducing the surface air temperature (Borzenkova and Bruk, 1989). Figure 2 illustrates temperature variations in the Northern Hemisphere extratropical zone (upper curves) and variations in the stratospheric SO^{2-}_4 concentration (lower histogram).

In the period between the years 700 and 1200, the volcanic activity was weak, so the stratospheric aerosol concentrations were low. As a result, the Medieval Warm Anomaly (MWA) was observed.

In the middle of the 13th century (near the solar retrograde motion event in 1275) there was a powerful eruption of the Samalas volcano (Indonesia) (1258–1261) along with a prolonged series of less intense eruptions. As a result, a thick aerosol layer formed in the stratosphere, which led to strong absorption of solar radiation and, as a consequence, to a decrease in surface air temperature. In the 14th century, volcanic eruptions were few, so the transparency of the atmosphere increased and the surface air temperature rose. Near solar retrograde motion in 1454, a powerful eruption of the Kuwae volcano (1458–1461) again led to strong cooling. The retrograde motion events in 1633 and 1811 were also accompanied by strong volcanic eruptions facilitating climate cooling.

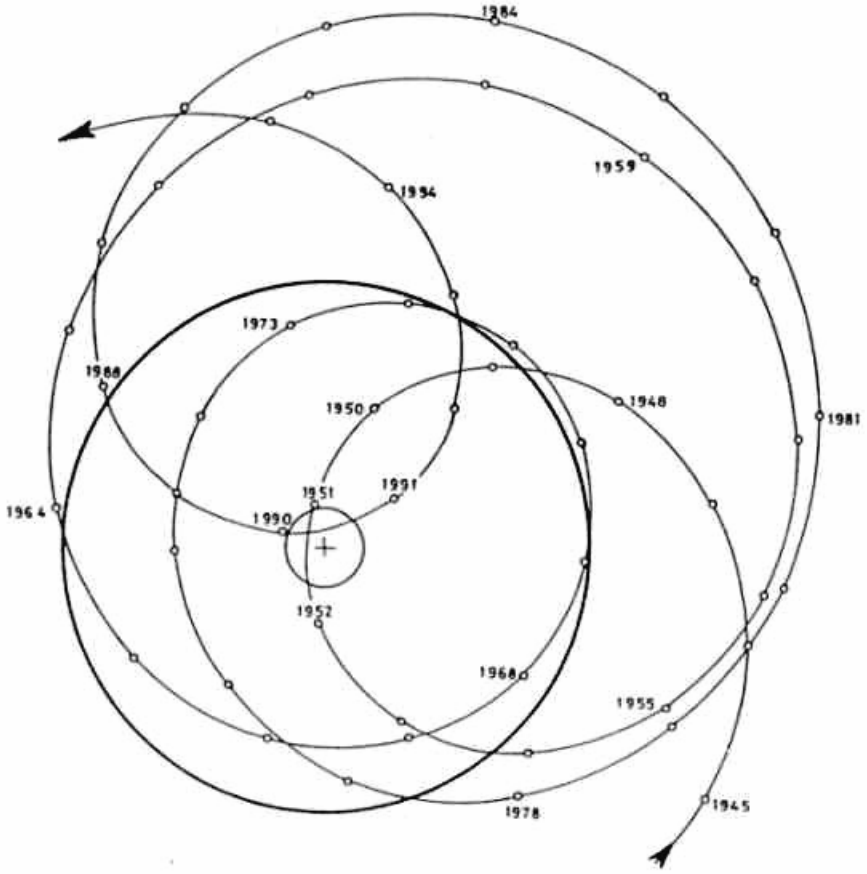

Figure 1: Path of the Sun in the barycentric ecliptic coordinate system for the period from 1945 to 1995. The solar system barycenter is denoted by + (Landscheidt, 2003).

Table 1. Secular minima of solar activity and times of solar retrograde motion

Minimum name	Start	End	Retrograde motion	Difference
Oort	1040	1080	1096	–36
Wolf	1280	1350	1275	40
Spörer	1450	1550	1454	46
Maunder	1645	1715	1632	48
Dalton	1790	1820	1811	–6
Landscheidt	2009	2040	1990	–
	Average			18

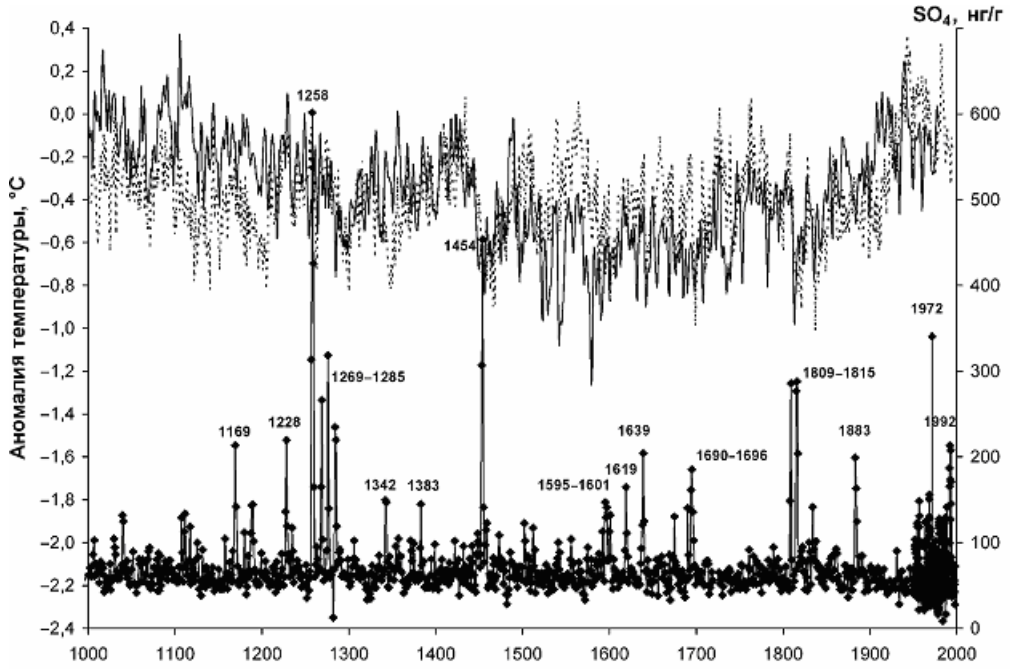

Figure 2: Annual air temperature anomalies in the Northern Hemisphere (data from (Moberg et al., 2005) are shown by solid lines, and the data from (D'arrigo et al., 2006), by dotted lines) and the stratospheric so^{2-}_4 concentrations inferred from antarctic ice core data (Traufetter et al., 2004) over the last 1000 years [http://www.ncdc.noaa.gov/paleo/icecore/antarctica/domec/domec]. The plot is taken from (Borzenkova et al., 2011)

3. Centuries cold period

The period from 1600 to 1840 was the longest cold period in the Northern Hemisphere over the last 1000 years. Climate warming did not begin until 1840, and it still persists with small oscillations.

Borzenkova et al. (2011a) identified long periods (1260–1350, 1420–1570, 1620–1710, and 1780–1830) when volcanic eruptions had the largest effect on the global air temperature. All of them coincide with the corresponding events of solar retrograde motion in 1275, 1454, 1632, 1811! The same periods of reduced transparency in the upper atmosphere are associated with the cases of most significant cooling in the Northern Hemisphere, which are part of the longest (over the last 1000 years) cooling epoch known as the Little Ice Age. This long cold period was caused by persistently high stratospheric aerosol concentrations maintained by intense volcanic activity (powerful eruptions in the years 1452/1453, 1458/1459, 1600/1601, 1809/1815, 1835, etc.).

Until the middle of the 19th century, the air temperature variations in the Northern Hemisphere were determined by transparency oscillations in the upper troposphere and the lower stratosphere caused by the presence of aerosol of mainly volcanic origin (Borzenkova et al., 2011). Inspection of Fig. 2 shows that the highest peaks of stratospheric volcanic aerosol can be associated with events of solar retrograde motion. The spectral analysis of series of sulfate aerosol concentration reveals a period of about 180 years (Borzenkova et al., 2011) coinciding with a Jose cycle (Jose, 1965).

4. The last 1990 event

Windelius and Tucker (1988), noting the increased seismic and volcanic activity during the previous events of solar retrograde motion in 1811 and 1632, warned of the danger of its recurrence in connection with the approaching event of solar retrograde motion in 1990.

Indeed, the last 1990 event of solar retrograde motion can be associated with the eruptions of El Chichón (Mexico) in 1982 and Pinatubo (Philippines) in 1991. In the latter case, as much as 25.4±2.8 kg/km^2 of sulfate ion SO^{2-}_4 was injected into the stratosphere. The effects of the Pinatubo eruption were felt worldwide. It ejected more aerosols into the stratosphere than any eruption since Krakatau in 1883. Over the following months, a global layer of sulfuric acid haze was observed in the atmosphere. Global temperatures dropped by 0.5 °C, and ozone layer depletion increased substantially; specifically, an especially large ozone hole was formed over Antarctica.

Catastrophic earthquakes were observed only on December 24, 2004, in the Indian Ocean (magnitude of about 9.3; the loss of life was estimated to be between 225 and 300 thousand people). An earthquake of magnitude of 9.0 to 9.1 occurred on March 11, 2011, in Japan. It was followed by a strong tsunami and led to the Fukushima nuclear disaster.

In 1990, there began a weak El Nino event, which continued extremely long until June, 1995. The strongest El Nino events in historic times occurred in 1983, 1987, and 1998.

Landscheidt (2003) believes that a new little ice age is to be expected instead of global warming.

5. Historical processes

A hundred years ago, Chizhevsky (1924) hypothesized that solar activity affects historical processes. The collapse of the Soviet Union and Yugoslavia occurred about the event of solar retrograde motion in 1990, the Napoleonic wars broke out about the event of 1811, the Time of Troubles in Russia and the splitting of the Russian Orthodox Church were about the event of 1632, and the Mongol invasion of Russia happened about the event of 1275. This evidence suggests that historical processes in Russia are possibly connected with events of solar retrograde motion. There are similar comparisons of historical events in China with secular minima of solar activity, which suggest nearly the same connection.

6. Conclusion

Unfortunately, the events of solar retrograde motion covered by available series of empirical data are insufficient for the hypothesized dependence of terrestrial events on solar retrograde motion to be justified statistically. However, most collected data suggest that secular minima of solar spots, powerful volcanic explosions, catastrophic earthquakes, substantial climate changes, and significant historical social events happen most frequently around events of solar retrograde motion.

The variability of terrestrial processes and events are usually tried to be connected with solar activity. However, solar activity cannot affect the motion of the Sun around the solar system barycenter. Therefore, from a physical point of view, it is more natural to suppose that processes occurring on the Sun, the Earth, and solar system planets are affected by the barycentric motion of the Sun governed by gravitation. This conclusion is also supported by the author's results obtained in the study of effects produced by the Earth's monthly motion around the Earth–Moon system barycenter (Sidorenkov, 2016).

Acknowledgments. I am grateful to I.I. Borzenkova for her assistance with this work.

This study was supported by the Russian Foundation for Basic Research, project 15-05-075590.

References

Borzenkova I.I. and Bruk S.A.: 1989, *Trudy. Gos. gidrol. inst.*, **347**, 40.

Borzenkova I.I., Zhil'tsova E.L., Lobanov V.A.: 2011, In: *Problems in ecological modeling and ecosystem monitoring (Planeta, Moscow)*, 131.

Chizhevsky A.L.: 1924, Physical factors of historical processes (Kaluga, 1924) [In Russian].

Clausen H.B., Vinther B.M., Mayewski P.A.: 2012, *Climate of the past*, **8**, 19291940.

D'arrigo R., Wilson R., Jacoby G.: 2006, *J. Geophys. Res.*, **111**, No. D03103. DOI: 10.29/2005JD006352.

Jose P.B.: 1965, *A. J.*, **70**, No. 3, 193.

Landscheidt T.: 2003, *Energy and Environment,* **14**, 4.

M'berg A., Sonechkin D. M., Holmgren K. et al.: 2005, *Nature*, **433**, No. 7026, 613.

Sigl Michael, McConnell Joseph R., Layman Lawrence, et al.: 2013, *J. Geophys. Res.,* **118**, 1151, doi:10.1029/2012JD018603

Traufetter F., Oerter H., Fischer H. et al.: 2004, *J. Glaciology,* **50**, No. 168, 137.

Sidorenkov N.S.: 2016, *Izvestiya, Atmospheric and Oceanic Physics*, **52**, No. 7, 667, Pleiades Publishing, Ltd., DOI: 10.1134/S0001433816070094.

Windelius G., Tucker P.: 1988, Solar motion, Seismicity, Climate. Drottning Holm, Sweden, 41 p.

DOI: http://dx.doi.org/10.18524/1810-4215.2017.30.117157

RESONANCES IN SATURN'S SYSTEM

A.S.Voitko[1], V.V.Troianskyi[2]

[1] Department of Theoretical Physics and Astronomy, Odessa National University, Odessa, Ukraine, *a.voitko@onu.edu.ua*

[2] Astronomical Observatory, Odessa National University, Odessa, Ukraine, *v.troianskyi@onu.edu.ua*

ABSTRACT. One of principal tasks of celestial mechanics is study of motion of natural satellites of planets. In this work, the authors have examined resonances in system of satellites and rings of Saturn. They have showed presence of resonances between all the regular satellites and satellites – rings.

Key words: Saturn, satellites, rings, resonance.

1. Introduction

Saturn is the sixth planet of Solar system and second biggest gas giant. 62 satellites and system of bright rings of the planet are known today.

Galileo was the first one who saw Saturn rings and Christian Huygens in 1655 has discovered the biggest one in Saturn system and second in Solar system satellite Titan (Lorenz et al., 2002). Actually, Titan is unique because it is the only planetary satellite with own dense atmosphere and was proved that only it and Earth have stable presence of liquid on its surface in all Solar system (Lorenz, 1994). After Huygens, Jean-Dominique, comte de Cassini has discovered 4 satellites: "two-faced" Iapetus (1671) with one light and second dark sides (Denk et al., 2010), Rhea (1672) that has own rings (Tiscareno et al, 2010), Dione and Tethys (1984), both of these have two co-orbital satellites moving in Lagrange points (Fulchignoni, 1986; Mourão et al., 2010). William Hershel has contributed to the study of the system by discovering of Mimas and Enceladus in 1789. This is the two of the smallest inner satellites (orbits of inner satellites limited by F ring). Satellites were capture in resonance by relatively massive Tethys and Dione respectively. At the same time they are different, Mimas has a large crater and tectonically unactive, but Enceladus has more plane surface and source of inner heat, geysers (Cuk et al., 2015). Eighth satellite Hyperion was found much later in 1848 (Memories of the Royal Astronomical Society, 1850). Later in 1899 was found the first irregular satellite Phoebe (Pickering, 1899). It is worth to say that regular satellites move by orbits with small eccentricity and their orbit planes lie in equator plane of the planet. Orbits of irregular satellites have big eccentricity between 0.11 and 0.58 and inclination of orbit plane between 34º and 179º, that is why most of them are retrograde (regress orbital motion) (Jewitt, 2007).

Saturn ring system causes serious difficulties in searching of satellites, because of that reason next satellite Janus was discovered by Audouin Dollfus in 1966 (Dollfus et al, 1981). Three days later, 18th of December 1966, had found that another satellite moves by very similar orbit. That way Epimetheus was discovered by Richard Walker (Gingerich, 1967). Satellite discovering has continued in 1980 with help of Voyager-1, Voyager-2 and Cassini-Huygens (Morrison, 1982; Russell, 2003).

Among all the satellites there are 24 regular and 38 irregular, which probably are captured asteroids. Lastly discovered 62nd satellite named S/2009 S1 is poorly researched now.

In the text were mentioned famous Saturn rings. They are composed of icy and dust particles and moving in accordance to the Kepler`s laws. There are highlighted main rings in all rings which were named with English letters as highlighted. For example: A and B rings, which are separated by Cassini division, C ring in the brightest B ring. At the same time, results of the named missions show that main rings are composed of great number of thin rings. (Pollack, 1975).

2. Orbital resonances between satellites

There are large numbers of a resonance phenomenon in Saturn satellite system. Let`s add that mean motion is the mean orbital angular speed (n):

$$n = \frac{360^\circ}{T} \qquad (1),$$

where T – orbital period of celestial body in days (Murray & Dermot, 2010). System of two satellites, which move around main body, is in resonance, if their mean motions are related as two small natural numbers (Peale, 1976).

This topic is often examines in works about natural satellites (Peale, 1976; Dermott et al, 1988; Callegari et al, 2008; Fuller et al, 2016; Troianskyi, 2016; Luan et al, 2017). So orbital resonances among regular Saturn satellites and other bodies of Solar system are well known. Examining combinations of satellites in pairs shows that

all satellites have pare in resonance. As a result, the authors first wrote a formula:

$$
\begin{aligned}
&-2\times\left(\begin{array}{c} P_{Pan}+P_{Daphnis}+P_{Atlas}+ \\ +P_{Prometheus}+P_{Pandora}+P_{Epimetheus}+P_{Janus}+ \\ +P_{Aegaeon}+P_{Anthe}+P_{Telesto}+P_{Hyperion} \end{array}\right)- \\
&-1\times\left(\begin{array}{c} P_{Mimas}+P_{Methone}+P_{Pallene}+P_{Tethys}+ \\ +P_{Calypso}+P_{Halane}+P_{Rhea}+P_{Titan} \end{array}\right)+ \\
&+1\times\left(P_{Enceladus}+P_{Dione}+P_{Iapetus}\right)+ \\
&+2\times P_{Polydeuces}=0.00(days)
\end{aligned}
\qquad (2)
$$

There were considered orbital periods (Sheppard, 2017) for 23 regular satellites in the formula (2). There is an ability to search orbital resonances of irregular satellites only in their group, because relations about 1:100 with regular satellites, gaps and rings contradict orbital resonance definition (Murray & Dermot, 2010). But among pairs of irregular satellites no resonances. It confirms that they wasn`t formed with the other bodies of the system, but captured (Gladman et al, 2001).

3. Orbital resonances between satellites and rings

This topic was studied in already published works (Lissauer et al, 1982; Gordon et al, 2006; Colwell et al, 2009; Crida et al, 2016).

Orbital resonances with rings and gaps specify shepherd satellites in rings. For example: Pan that forms Encke gap or Prometheus and Pandora both form ring F. For wide rings like main A, B, C, D orbital resonances have poor accuracy. It is difficult to highlight a thin ring that is why the authors used distances between two edges of neighbor gaps. Orbital periods of ring particles were calculated in accordance to third Kepler`s law, where ring mass wasn`t taken in account. Actually, shepherd satellites have 1:1 relations with ring material or middle of gap.

4. Results

The authors studied all possible combinations: 252 pairs among regular, 703 pairs among irregular satellites, 529 pairs among rings and regular satellites, 414 pairs among gaps and regular satellites.

As a result first earned formula (2) that describes orbital resonances between all the regular satellites.

Authors shown orbital resonances between regular satellites and rings. Orbital resonances show conformity between gaps and satellites that form it.

Orbital resonances between irregular satellites and satellites – rings, authors wasn`t found.

References

Callegari N., Yokoyama T.: 2008, *Bulletin of the American Astronomical Society*, **40**, 479.

Colwell J. E., Nicholson P. D., Tiscareno M. S., Murray C. D., French R. G., Marouf E. A.: 2009, *Springer Science+Business Media B.V.*, 375.

Crida A., El Moutamid M.: 2016, *American Astronomical Society*, DPS meeting, **48**.

Cuk M.: 2015, *American Astronomical Society*, **46**, 400.01.

Denk T., Neukum G., Roatsch T., Porco Carolyn C., Burns Joseph A., Galuba Götz G., Schmedemann N., Helfenstein P., Thomas Peter C., Wagner Roland J., West Robert A.: 2010, *Science*, **327/5964**, 435.

Dermott S.F., Malhotra R., Murray C.D.: 1988, *Icarus*, **76**, 295.

Dollfus A., Brunier S.: 1981, *Icarus*, **48**, 29.

Fulchignoni M.: 1986, *The Solid Bodies of the Outer Solar System*, (Proc. of a conf. held at Vulcano, Italy).

Fuller J., Luan J., Quataert E.: 2016, *MNRAS*, **458/4**, 3867.

Gingerich O.: 1967, *IAU Circular,* **1991**.

Gladman B., Kavelaars J.J., Holman M., Nicholson P.D., Burns J.A., Hergenrother C.W., Petit J.-M., Marsden B.G., Jacobson R., Gray W., Grav T.: 2001, *Nature*, **412/6843**, 163.

Gordon M.K., Murray C.D., Showalter M.R.: 2006, *Bulletin of the American Astronomical Society*, **38**, 560.

Lissauer J.J., Cuzzy J.N.: 1982, *AJ*, **87**, 1051.

Lorenz Ralph D.: 1994, *Planetary and Space Science*, **42/1**, 1.

Lorenz R., Mitton J.: 2002, *Cambridge University Press*, 4.

Luan J., Goldreich P.: 2017, *AJ*, **153/1**.

Memories of the Royal Astronomical Society: 1850, **18**, 21.

Mourão D., Winter O.C.: 2010, *Bulletin of the American Astronomical Society*, **42**, 958.

Morrison D.: 1982, *NASA Special Publications*, **451**.

Murray C.D., Dermot S.F.: 2010, *Solar System dynamics*. (Cambridge, University press).

Partridge E. A., Whitaker H. C.: 1896, *Popular Astronomy*, **3**, 408.

Peale S.J.: 1976, *A&A*, **14**, 215.

Pickering E.C.: 1899, *Harvard College Observatory Bulletin*, **49**, 1.

Pollack J.B.: 1975*, Space Science Reviews*, **18**, 3.

Russell C.T.: 2003, *Space Science Reviews*, **104/1-4**, 2002.

Sheppard S.S.: 2017, The Giant Planet Satellite and Moon Page, [online] Available at: (*http://home.dtm.ciw.edu/users/sheppard/satellites/satsatdata.html*) [Accessed 01 Nov 2017].

Tiscareno M.S., Burns J.A., Cuzzi J.N., Hedman M.M.: 2010, *Geophysical Research Letters*, **37/14**.

Troianskyi V.V.: 2016, *Odessa Astron. Publ.*, **29**, 221.

Jewitt D., Haghighipour N.: 2007, *A&A*, **45/1**, 261.

MEMORIAL

DOI: http://dx.doi.org/10.18524/1810-4215.2017.30.118686

ODESSA SCIENTIFIC SCHOOL OF RESEARCHERS OF VARIABLE STARS: FROM V.P.TSESEVICH (1907-1983) TO OUR DAYS

Andronov I.L.
Department of Mathematics, Physics and Astronomy, Odessa National Maritime University
tt_ari@ukr.net

ABSTRACT. The biography of Vladimir Platonovich Tsesevich (11.11.1907 – 28.10.1983), a leader of the astronomy in Odessa from 1944 to 1983, is briefly reviewed, as well as the directions of study, mainly the highlights of the research of variable stars carried out by the members of the scientific school founded by him. The directions of these studies cover a very wide range of variability types – "magnetic" and "non-magnetic" cataclysmic variables, symbiotic, X-Ray and other interacting binaries, classical eclipsers and "extreme direct impactors", pulsating variables from DSct and RR through C and RV to SR and M. Improved algorithms and programs have been elaborated for statistically optimal phenomenological and physical modeling.

Initially these studies in Odessa were inspired by ("with a capital letter") Vladimir Platonovich Tsesevich. who was a meticulous Scientist and brilliant Educator, thorough Author and the intelligibly explaining Popularizer, persevering Organizer and cheerful Joker – a true Professor and Teacher. He was "the Poet of the Starry Heavens".

Keywords: *variable stars; eclipsing binary;interacting binary, cataclysmic, pulsating; Personalia: V.P.Tsesevich*.

1. V.P. Tsesevich (11.10.1907 – 28.10.1983)

Vladimir Platonovich Tsesevich was born in Kiev on 11.10.1997. His father Tsesevich Platon Ivanovich was a famous opera singer (bass voice). His beautiful songs may be found in the Internet. His mother Kuznetsova Elisaveta Aleksandrovna was an opera actress, later a pedagogue. V.P. Tsesevich started education on the Leningrad State University at the age of almost 15, and chosen variable stars as the main direction of his studies.

The first paper based on his observations (but he was not a co-author) appeared also in 1922, but the first his own paper appeared next year (totally 42 during his studentship). The name was written as "W.Zessewitsch" in the papers published in the "Astronomische Nachrichten".

The supervisor of his PhD studies was G.A.Tikhov, a famous astronomer. After Leningrad, in 1933-1937, he was a Director of the Tadjik Astronomical Observatory (now Institute of Astrophysics). In 1937-1942, worked in Leningrad. Evacuated to Dushanbe, where worked as a professor, and finally moved to the Odessa State University in 1944.

Under his supervision, the initially small astronomical observatory in Odessa has become one of the leading astronomical organizations.

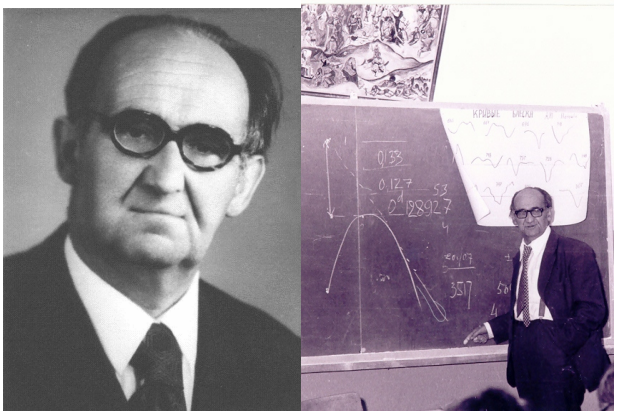

In 1948-50, his talent of an organizer was effectively realized in being a director of the Main Astronomical Observatory of the Ukrainian Academy of Sciences (1948-1950). In 1948, he was elected to be a corresponding member of the Ukrainian Academy of Sciences.

In our memory, remained a deep impression of his tremendous energy and enthusiasm of Vladimir Platonovich Tsesevich. He was not only an outstanding scientist and organizer of science, the founder of the scientific school of investigators of variable stars, but also a brilliant lecturer and popularizer of astronomy. The list of his 730 publications was compiled by Dziubina & Rikun (1988). However, in the ADS there is only a small part of them (142 for "Tsesevich", 31 "Tsessevich", 44 "Zessewitsch").

His lectures for students were bewitching and exciting. Among them, there were "Additional Chapters of Mathematical Physics" and two semesters of "Relativistic Astrophysics". He had read the lectures, as a poem, and it was exciting. He deduced numerous formulae without lecture notes, neglecting the bells, and consequently stopped, when difficult transition to some formula, sometimes lasting of few pages, came to the end. He taught not to be afraid of challenges and showed a process of creativity. Exacting to himself, he was exacting to others. He followed numerous new discoveries and ideas in astronomy, and proposed new directions of study. His last scientific passion was the magnetic cataclysmic binary system AM Herculis. The first papers showing its extreme exotic nature were published 40 years ago.

V.P.Tsesevich supervised more than 40 PhDs graduates, creating an effective scientific school and supported different scientific directions. V.P. Tsesevich was very different, somehow similar to the variable stars he studied.

Besides being a director of the Astronomical observatory of the I.I. Mechnikov Odessa State (currently Na-

tional) University (ONU) and the Chair of the Astronomical Department of the Physical Faculty of ONU, he lectured in some other institutes – of the Refrigerator Industry, in the Odessa Higher Engineering Marine School, in the Odessa Institute of Marine Fleet Engineers (currently Odessa State Maritime University (ONMU)). In the last institute, he lectured for 15 years and even was a Chair of the Department of Higher Mathematics (currently the Department of Mathematics, Physics and Astronomy).

Among these publications, there were numerous monographs, which may be subdivided into "printed catalogues" and "classical" monographs like "Variable Stars and Methods of Their Observations" (Tsesevich, 1970, 1980), famous collective monographs "Eclipsing variable Stars" (Tsesevich, 1971), "RR Lyrae-type Stars" (Tsesevich, 1969), both translated to English.

The most popular book is "What and How to Observe in the Sky" (Tsesevich, 1984). It has been issued six times, last time in 1984, and even now is one among the best books.

Not all readers became astronomers, but many people remember the book, and many students remember talented and emotional professional and public lectures. This had initiated passion to astronomy (and science generally) of many scientists, who now represent the base of our majestic science.

The asteroid 2498 (discovered on 23.08.1977 by N.S.Chernykh in the Crimean Astrophysical Observatory) was named "Tsesevich". "Named in honor of Vladimir Platonovich Tsesevich (1907–1983), former director of the Odessa University Observatory, renowned for his research on variable stars. He also studied the brightness variations of {433} Eros and is the author of a handbook for amateur astronomers".

The Google search for V.P.Tsesevich (in Russian) gives 3300 entries, from which we would like to point out some memories by Volyanska, Karetnikov & Mandel (2007), Vavilova (2017), Andronov (2003), Samus' (1988, 2007). The compilation of memories was prepared to his 100-th anniversary (Tsesevich, 2007).

2. After V.P. Tsesevich

During the last years of life of Vladimir Platonovich Tsesevich (11.11.1907 – 28.10.1983), the Astronomical observatory of the I.I.Mechnikov Odessa National (previously "State") University (ONU) became a widely known University center, which worked in a close connection with the Department of Astronomy.

Odessa was the only place in the country, where the director of the observatory and the chair of the Department of Astronomy was the same person (1871-2016).

At that time, there were few departments and smaller "sectors", which covered various directions of astronomy, so the students had a wide choice, and later worked in varies observatories and academic institutes.

Besides ONU, in different years, astronomers worked in other organizations in Odessa (N.I.Divari, O.E.Mandel in the Polytechnical Institute (now Odessa National Polytechnical University), V.A.Smirnov, L.V.Glazunova in the Odessa National Academy of Telecommunications, I.A.Klyus, V.V.Mikhalchuk in the Odessa State Maritime Academy, 5 astronomers in the Odessa National University; there is an Odessa Department of the Radioastronomical Institute of NASU). The astronomers from various organizations participate in events organized by the Odessa Astronomical Society (chair – M.I.Ryabov (56 papers)).

The secretary of the Department of Astronomy was V.G.Karetnikov (in 1983-2006 – the chair), who had a scientific working group at the observatory with a main direction on photometrical and spectrospoic study of classical eclipsing binary systems. The current number of publications listed in the ADS is 182. V.G.Karetnikov was a supervisor of the PhD Theses by E.V.Menchenkova (23 joint (only) papers/49 totally), V.V.Nazarenko (15/62), L.V.Glazunova (8/46), F.V. Sirotkin (4/27), G.V.Volkova-Manilova (2/13), S.M.Andrievsky (2/194), I.Kudzej (1/60), K.A.Antoniuk (0/102). Also in this group, worked S.V.Kutsenko (9), O.G.Lakinskaja (2). 16 papers were published with Yu.A.Medvedev. This group continued studies of eclipsing systems, started in Odessa by V.P.Tsesevich and A.M.Shulberg.

V.G.Karetnikov was the Chair of the Department of Astronomy (1983-2006), the Director of the Astronomical Observatory (1990-2006). During this period, the following Doctors of Science were graduated: N.S.Komarov (1990), I.S.Shestaka (1994), I.L.Andronov (1995), S.M.Andrievsky (2002), T.V.Mishenina (2005).

The traditionally largest department of the observatory on "Variable Stars" was supervised by Yu.S.Romanov (68 papers in the ADS) with collaborators working on analysis in Odessa and observing in Mayaki at the 7-th camera astrograph (V.P.Bezdenezhnyj (11), B.A.Murnikov (12), A.I.Pikhun (19), S.V.Kashuba). The majority of papers were devoted to photometrical, and spectral studies of the RR Lyr-type stars. In this Department, also actively worked in the Mayaki observational station, having own directions at 20" and AZT-3 telescopes, but with a monitoring th the 7-camera astrograph. Yu.S.Romanov was a supervisor of PhD theses of S.N.Udovichenko (13/48), A.V.Yushchenko (1/119), D.E.Mkrtichian (1/167), G.A.Garbuzov (2/34). Other active collaborators were Z.N.Fenina (16/41), L.P.Zaikova (5/9), A.N.Rudenko (3), O.P.Paramonova (2/11), L.E.Lysova (2/13), V.P.Murnikova (1/10), B.A.Murnikov (1/12) A.I.Movchan (1/16), A.S.Gadun (1/73) et al.

The first number is the number of joint paper in collaboration wit the head of the Department. A special program on studies of the Blazhko effect and determination of the moments of brightness maxima of RR Lyr-type stars was carried out by B.N.Firmanyuk (54) et al.

The second largest department "Astrospectroscopy" was supervised by N.S.Komarov (168 papers), where PhD theses defended T.V.Mishenina (159 papers), V.F.Gopka (83), T.N.Dorokhova (73), D.N.Doikov (11).

N.I.Dorokhov (71) had multiple trips to Dushak-Eregdag for photometrical observations of TT Ari, lambda Boo-type and other stars according to the international campaigns.

Later on, the largest Departments "Variable Stars" and "AstroSpectroscopy" were merged into one Department of "Physics of Stars and Galaxies", initially supervised by N.S.Komarov, and, since 2003, by T.V.Mishenina. The

scientific secretary of AO is A.V.Dragunova (25). An important contribution made S.I.Belik (40), V.A.Pozigun (25), V.F.Karamysh (14), L.F.Orlova (14) et al.

In this Department, currently work all Doctors of Sciences of the Observatory – S.M.Andrievsky (194), V.V.Kovtyukh (172), T.V.Mishenina (159), A.I.Zhuk (147), S.A.Korotin (113). Traditionally partially worked the Professors of the Department of Astronomy – V.G.Karetnikov (182), I.L.Andronov (363, before 2006), E.A.Panko (64, after 2016). In recent decade, PhDs habilitated T.I.Gorbaneva (34), A.Chepizhko (7), L.L.Chinarova (88), V.A.Yushchenko (17), F.A.Chekhonadskikh (14), M. Eingorn (66), A. Chopovsky (11), A.L.Sukharev (21), A.I.Donskykh (11).

Not surprizingly, that astronomers – Doctors of Science posess top places at the scientific rating in the I.I.Mechnikov National University and give the highest contribution to the scientific outcome.

The third large Department from the times of V.P.Tsesevich is on "Space Research", initially supervised by Yu.A.Medvedev (50) and currently by N.I.Koshkin (50). Currently there work PhDs P.P.Sukhov (50), V.V. Troianskyi (13) the Associate Professor A.A.Bazey (5), and actively working L.S.Shakun (26), S.L.Strakhova (16), S.M.Melikyants (10), V.V.Dragomiretsky (10), E.A. Korobeinikova (5) and others. The major direction is on astrometry photometry of satellites and asteroids.

In the times of V.P.Tsesevich, there was a separate sector of astrometry, where worked M.Yu.Volyanskaya (21), M.I.Myalkovskiy (12), A.P. Chelombit'ko (6), V.V.Zhukov (16), O.S.Shakhrukhanov (3), N.V.Bazey (2). There was a sector of "Astronomical Instrument Making". N.N.Fashchevskiy (21) got his PhD in Astrophysics based on the observations obtained at the telescope he designed. E.A. Depenchuk (21), V.N.Ivanov (13), M.G.Arkhipov (8), L.S.Paulin (4), A.F.Pereverzentsev (5), A.V.Ryabov (21) made a great contribution in creating telescopes of the Odessa Observatory.

The supervisor of the special sector on "Meteors and comets" was professor E.N.Kramer (135), also there worked I.S.Shestaka (98), A.K.Markina (33), V.I. Musij (22), and later Yu.M.Gorbanev, who is the current leader of the working group.

It should be mentioned that these reminiscenses do not follow all the collaborators working in ONU or graduated in ONU, but working in other institutions.

I.L.Andronov (363) is the last PhD student (No.~41), who habilitated under the supervision of V.P.Tsesevich. He continued the direction of studies of variable stars – initially magnetic (and non-magnetic) cataclysmic, later X-Ray binaries, classical eclipsing binaries, rare "Extreme Direct Impactors", symbiotic, Mira-type, Semi-regular, RV, RR and other pulsating and newly discovered variables. The observations are carried out within a campaign "Inter-Longitude Astronomy" (ILA), which is based on temporarily working groups from different countries. Besides, an expert system for advanced modeling of the time series was elaborated, which is oriented onto general tasks, as well as on the specifics of different types of variability of stars. Generally 1900+ stars were studied in this group. The following eight PhD theses were habilitated: L.S.Kudashkina (1997, 55 papers), S.V.Kolesnikov (2000, 79), V.I.Marsakova (2000, 54), A.V.Halevin (2000, 36), A.V.Baklanov (2005, 65), V.V.Breus (2013, 25), L.L.Chinarova (2014, 88), M.G.Tkachenko (2017, 13). Currently, this group (4 in the Odessa National Maritime University, 3 in the Odessa National University; 2 effectively work in astronomy outside), together with S.N.Udovichenko (48 papers, supervisor Yu.S.Romanov), represent in the Ukrainian Universities the main direction of studies of V.P.Tsesevich – the photometric variability of stars of different types. There are prominent graduates from Odessa, now actively working outside Ukraine.

3. "Inter-Longitude Astronomy" (ILA) Campaign

3.1. The ILA Group

Continuing the scientific school founded by V.P. Tsesevich, the variable stars of different types are studied on the base of temporarily working groups in collaboration with astronomers from Korea, Germany, USA, Greece, France, Poland, Slovakia, Hungary, Spain, Portugal, Kazakhstan and other countries.

For the time series analysis, we make long-term photometric and polarimetric monitoring of the group of selected "key" objects as well as use the data from orbital and ground-based observatories.

In Ukraine, this group consists of 4 astronomers in the Odessa National Maritime University (Prof. Dr. Ivan L. Andronov, Dr. Vitalii V. Breus, Dr. Larysa S. Kudashkina, Dr. Mariia G. Tkachenko), 3 staff members in the Odessa National University (Dr. Lidiia L. Chinarova, Dr. Sergei V. Kolesnikov and Dr. Vladyslava I. Marsakova) and 2 students (Kateryna D. Andrych, Dmytro E. Tvardovskyi).

The total number of the stars studied in this group exceeds 1900, the number of articles of coauthors of this project, referred in the database "Astronomy Data System" (ADS), exceeds 400 (for the leader of group: 370 since 1980, 24 in 2015-2017). Members of the group from Odessa defended 9 PhD Theses and a 1 of Dr. Sci.

This project is called "Inter – Longitude Astronomy" (ILA), the funding to the participants is due to corresponding universities. The reviews of highlights of the project were published by Andronov et al. (2003, 2010, 2017). Also results are included in the national projects "Ukrainian Virtual observatory" (UkrVO) (Vavilova et al., 2011, 2012) and "AstroInformatics" (Vavilova et al., 2017).

3.2. "Polar" (Gravi-Magnetic Rotators)

Study of cataclysmic binary systems with magnetic white dwarfs (AM Her, QQ Vul, BY Cam, V1432 Aql, V808 Aur). This monitoring started in 1978 photometrically and in 1989 polarimetrically (Kolesnikov and Andronov, 2017). Every year new observations of magnetic cataclysmic variables with quickly rotating white dwarfs are carried out to study rotational evolution and check model of precession proposed earlier and also to study observational appearance of dependence of structure of the accretion stream on the angle between the magnetic axis and the line of centers. Systems for long-term monitoring are intermediate polars: BG CMi, MU Cam =1RXS J062518.2+733433, FO Aqr, AO Psc, 1RXS J063631.9 +353537, 1RXS J070407.9 +262501, 1RXS J180340.0 +401214, 1RXS J192626.8 +132153, 1RXS J213344.1 +510725, PQ Gem, V405 Aqr, EX Hya.

Recently, the spin-up of the magnetic white dwarf is discovered in the system MU Cam with characteristic with characteristic time-scale of $\tau = P/|dP/dt| = (170 \pm 1.5)$ thousand years. This value is 30 times less than 4.71 million years, which is observed in other intermediate polar EX Hya, but only twice less than 290 thousand years in BG CMi (Andronov et al., 2017).

3.3. "SuperHumper"

Cataclysmic binary systems (nova-like and dwarf novae) with precessing accretion disks and QPOs. Main target for the international monitoring: TT Ari, where we studied transitions between positive and negative superhumps and discovered a state of "excitation of quasi-periodic oscillations" (Kim et al., 2008). Other important targets are MV Lyr and V1084 Her. Very interesting are "Transient Periodic Oscillations" in DO Dra (Andronov et al., 2008).

3.4. "SSS" (Super-Soft Sources)

Research of rapid variability of the interacting binary systems – s*uper-soft sources* of X-ray radiation (V Sge, QR And).

3.5. "NewVar" (New Variable)

Discovery and complete study of new variables in the selected fields on the base of the new special observations. Initially, the studies of new variables were carried out on photographic plates of the Odessa, Moscow and Sonneberg plate collections. Then we studied 863 faint variable candidates from the Hipparcos-Tycho mission. Currently, we study newly discovered variables in the field of the main targets (e.g. Kim et al., 2004).

3.6."Eclipser"

Mathematical modeling of the asymmetric interactive binary systems. The method NAV was elaborated, which allows phenomenological modeling of complete light curve. For detached MS systems, it allows to determine physical parameters as well (Andronov et al., 2015). The minima are fitted not only for EA-type systems, but also for EB and EW (Tkachenko et al., 2016). Especially interesting are "Extreme Direct Impactors" (Andronov and Richter, 1987, Andronov et al., 2010).

3.7."Stellar Bell"

Careful photometric researches and modeling of the known variables, including pulsating variables with "combined", or "alternatively operating" types. The review paper with results of our researches of long-period variables was presented by Andronov et al. (2014).

3.8."TSA" (Time Series Analysis)

Elaboration and improvement of the algorithms and programs for the analysis of multicomponent signals. The algorithms allow studies of irregularly spaced data, which are characteristic for photometrical surveys from space and ground-based observatories, and provide determination of phenomenological characteristics with much better accuracy (Andronov, 2005; Andronov, Tkachenko & Chinarova, 2016).

4. Other current variable star researches in Odessa

Astronomical Observatory of ONU has a great "Sky Patrol" plate collection, which is the third in the world according to the number of plates after Harvard (USA) and Sonneberg (Germany).

Hundreds of papers were published from 1956, the last one (in the epoch of visual estimates of brightness on plates) by Chinarova & Andronov (2000). As the best accuracy is ~0.08^m, this is a great resource for studies of historical light curves of large-amplitude (>0.5^m) stars.

Active CCD observations of DSct and RR pulsating variables (and stars in the field) are carried out at the 48-cm telescope AZT-3 by S.N.Udovichenko (2012, 2015). Among his 48 papers, 18 are based on the CCD observations since 1997.

References

Andronov I.L.: 2003, *Odessa Astron. Publ.*, **16**, 5.
Andronov I.L.: 2005, *ASPC*, **335**, 37.
Andronov I.L. et al.: 2003, *Astron.Astroph.Trans.*, **22**, 793.
Andronov I.L. et al.: 2008, *A&A*, **486**, 855.
Andronov I.L. et al.: 2010, *Odessa Astron. Publ.*, **23**, 8.
Andronov I.L. et al.: 2014, *AASP*, **4**, 3.
Andronov I.L. et al.: 2015, *JASS*, **32**, 127.
Andronov I.L. et al.: 2017, *ASPC*, **511**, 43
Andronov I.L., Richter G.A.: 1987, *AN*, **308**, 235.
Andronov I.L., Tkachenko M.G., Chinarova L.L.: 2016, *OEJV*, **176**, 35.
Chinarova L.L.; Andronov I.L.: 2000, *KFNTS*, **3**, 397.
Dziubina S.V., Rikun I.E.: 1988, "Uchenye Odessy. Vladimir Platonovich Tsesevich" (1907-1983) ("The Scientists of Odessa. Vladimir Platonovich Tsesevich (1907-1983)), Odessa, 1988, 110p.
Kim Yonggi et al.: 2004, *JASS*, **32**, 127.
Kim Yonggi et al.: 2008, *A&A*, **496**, 765.
Kolesnikov S.V., Andronov I.L.: 2017, *ASPC*, **510**, 502.
Samus N.N.: 1988, *IAIss*, **20**, 216.
Samus N.N.: 2007, *Odessa Astron. Publ.*, **20**, 193.
Tkachenko M.G., Andronov I.L.: Chinarova L.L.: 2016, *JPhSt*, **20**, 4902.
Tsesevich V.P.: 1969, "RR Lyrae Stars", Moskva, Nauka, 1969rls..book.....T
Tsesevich V.P.: 1970, "Peremennye zvezdy i sposoby ikh issledovaniia.", Moskva: Nauka, 240 p.
Tsesevich V.P.: 1971, "Instationary stars and methods of their investigation. Eclipsing variables", Moskva: Nauka, 352 p. 1971isme.conf....T
Tsesevich V.P.: 1980," Peremennye zvezdy i ikh nabliudenie", Moskva, Nauka, 1980pzn..book.....T
Tsesevich V.P.: 1984, "What and How to Observe in the Sky", Moskva, Nauka, 1984cknr.book.....T
Tsesevich V.P.: 1984, "O Vremeni i o Sebe: Vospominaniya i Dokumenty", Odessa, Astroprint, 80pp.
Udovichenko S.N.: 2012, *Odessa Astron. Publ.*, **25**, 32.
Udovichenko S.N.: 2015, *Odessa Astron. Publ.*, **28**, 186.
Vavilova I.B.: 2017, *Odessa Astron. Publ.*, **30**, 256.
Vavilova I.B. et al.: 2011, *KosNT*, 17d, 74V.
Vavilova I.B. et al.: 2012, *KPCB*, **28**, 85.
Vavilova I.B. et al.: 2017, *IAUS*, **325**, 361.
Volyanska M.Yu., Karetnikov V.G., Mandel O.E.: 2007, *Odessa Astron. Publ.*, **20**, 6.

DOI: http://dx.doi.org/10.18524/1810-4215.2017.30.118718

SCIENTIFIC ASTRONOMICAL SCHOOL BY PROFESSOR VOLODYMYR P. TSESEVICH ON THE PHYSICS OF VARIABLE STARS

I.B. Vavilova
Main Astronomical Observatory, National Academy of Sciences of Ukraine,
27 Akademika Zabolotnogo, Kyiv, 03143, Kyiv, Ukraine
irivav@mao.kiev.ua

ABSTRACT. This paper is dedicated to the Prof. Volodymyr Platonovych Tsesevich (1907–1983), an outstanding scientist and legendary personality of the XX century.

We describe briefly the Kyiv period of his life and activity taken from his Personal Dossier from the Archive of the Presidium of the NAS of Ukraine. A particular attention is paid to the role by V.P. Tsesevich in the development of astrophysical research at the Main Astronomical Observatory of the Academy of Sciences of UkrSSR, when he served as the Director (19.11.1948–03.05.1951), and to the fruitful cooperation between Kyiv and Odesa astronomers.

We present briefly a "tree" of the scientific astronomical school by Prof. V.P. Tsesevich on the physics of stars. The data were obtained from different archives (Astronomical Observatory of the I.I. Mechnikov National University of Odesa, Main Astronomical Observatory of the NAS of Ukraine, Archive of the Vernadsky National Library, Archive of the Russian AS, and other institutions). The full database contains of a brief information on the about 100 representatives of this school as follows: name, title and year of thesis's defense, past/present affiliation). The scientific school is formed since 1950-ies till now having its greatest continuation in the work of such astronomers as N.S.Komarov, V.G.Karetnikov, Yu.S. Romanov, and I.L.Andronov (a branch of this school after V.P. Tsesevich), as well as S.M.Andrievsky as the follower by V.G. Karetnikov and T.V. Mishenina, V.F. Gopka, V.V. Kovtykh as the followers by N.S. Komarov.

The given information on the school by V.P. Tsesevich is not absolutely full, for example, 1) there are no the data on thesis's defense under his supervision before 1948; 2) information on the astronomical school developed by A.M. Stafeev and some other scientists is a very poor; 3) some shortcomings may be presented. We will grateful for all the additions and corrections to update a tree of this scientific school, which played and plays a prominent role in the development of our knowledge on physics of stars.

Keywords: variable stars, scientific school, personalities: V.P. Tsesevich.

1. Introduction

Prof. Volodymyr Platonovych Tsesevich (11.11.1907, Kyiv – 28.10.1983, Odesa) was outstanding scientist in the fields of astrophysics and astronomical instrumentation of the XX century. His main studies from student years till the last days of a life were concerned with the physics of variable stars (observation and theory). Being a great enthusiast of astronomy, brilliant lecturer and popularizer, V.P. Tsesevich has engaged many young people and collaborators in this research and was able to create a world recognized scientific astronomical school of his own. He was a foremost organizer of science, for example, his activity in frame of the International Astronomical Union was as follows: Past Vice-President of Com. 42 Close Binary Stars (1961–1967), Past Organizing Committee Member of Commission 42 Close Binary Stars (1967–1973).

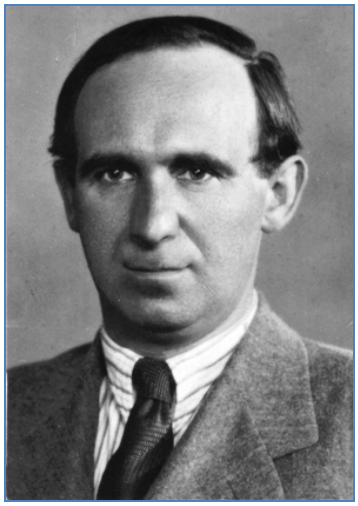

Figure 1: Professor V.P. Tsesevich, 1948.
Photo is taken from "The Personal Dossier of the Corresponding Member of the Academy of Sciences of UkrSSR. V.P. Tsesevich", Archive of the Presidium of the NAS of Ukraine

The biography of V.P. Tsesevich and his scientific work and activity as the Director of the Observatory in Dushanbe in 1933–1937 (now – Institute of Astrophysics of the Academy of Sciences of the Republic of Tajikistan) and the Director of the Astronomical Observatory of the I.I. Mechnikov National University of Odesa in 1944–1983 is fully described by his colleagues (see, for example, Karetnikov (1996), Pozigun (1996), Karetnikov (1997), Andronov (2003), Koshkin & Mishenina (2007), Fenina & Romanov (2008), Andronov (2017)).

By this reason, in this paper, we underline briefly the Kyiv period of his life and activity (Chapter 2), namely his role in the development of astrophysical research at the Main Astronomical Observatory of the Academy of Sciences of UkrSSR (MAO NASU), when he served as the Director (19.11.1948–03.05.1951) as well as was elected as the Corresponding Member of the Academy of Sciences of the UkrSSR in 1948 (Figure 1).

During the 20th century in Ukraine several recognized astronomical centers were established and scientific school were developed thanks to the activity of such prominent astronomers as A.Ya. Orlov in Odesa, Poltava, Kyiv (see, Yatskiv et al., 2005); N.P. Barabashov in Kharkiv (see, Shkuratov, 2008); S.K. Vsekhsvyatsky in Kyiv (see, Andrienko & Zosimovich, 2005; Vavilova et al., 2011); S.Ya. Braude in Kharkiv (see, Konovalenko, 2000; Vavilova et al., 2007); and V.P. Tsesevich in Odesa (see, references, in the previous paragraphs). The modern educational and scientific system of Ukraine in field of astronomy and astrophysics has been provided due to their extensive work (Pavlenko et al., 2006; Yatskiv et al., 2003). In this context, we present also briefly a "tree" of the scientific astronomical school by V.P. Tsesevich on the physics of variable stars (Figure 2, Chapter 3).

2. The Kyiv period of life and activity of Prof. V.P.Tsesevich

In 1944, V.P. Tsesevich was appointed to the position of professor of the Odesa University and Director of the Astronomical Observatory of this university. In 1944, December 30, he defended Dr. Sci. Thesis "On the methods of determining the orbits of Algol type stars" at the Kazan State University.

In 1948, Prof. V.P. Tsesevich was elected as the Corresponding Member of the Academy of Sciences of the UkrSSR (AS UkrSSR). His Personal Dossier in the Archive of the Presidium of the NAS of Ukraine contains of the characteristics and recommendation letters signed by Dr. Sh. Gordeladze (MAO AS UkrSSR, 11.05.1948), Dr. L. Shaposhnikova (Odesa State University, 20.05.1948), Prof. S. Orlov and Prof. B. Kukarkin (AstroSovet AS SSSR, 05.11.1946), Prof. D. Martynov (Kazan University, 23.05.1948), Prof. A. Mikhailov (AstroSovet AS SSSR, 23.05.1948). These letters give additional support to the recognition of V.P. Tsesevich's results in those years. We can read, for example: "In 1931, together with B. Okunev, he organized a regular observational service for RR Lyra-type stars, which continues to the present day. Studying the Blazhko effect, he established the relationship between the nature of changes in their periods and the spatial-kinematic characteristics. Tsesevich V.P. conducted a series of studies of stars such as RV Tauri, cepheids (periods, light curves), eclipsing variable stars. He improved the methods of determining the elements of orbits and other characteristics of eclipsing stars by their light curves (method of differential corrections), developed a method for taking into account the annularity of eclipses. In 1939-1940 he published tables of special functions for solving light curves for various types of eclipses, which till now are considered the best and unsurpassed in accuracy…".

A great support in this election was played by A.Ya. Orlov, Member of the AS UkrSSR, Director-Founder of the Main Astronomical Observatory of the AS UkrSSR. He invited Volodymyr Platonovych to Kyiv to replace him for the post of Director.

In 1948–1951, Prof. V.P. Tsesevich headed (part-time) MAO AS UkrSSR, being at the same time the Director of the Astronomical Observatory of the Odesa University (OAO). There are no documents, which shed light what has caused his decision. But years later, one can say that this decision was the only true and wise one. Although V.P. Tsesevich was the Director for only three years, he significantly influenced the development of astrophysical research as well as initiated a number of scientific and organizational reformations at the Main Astronomical Observatory of the AS UkrSSR:

– *suggested new research fields*: Photographic Astronomy (sky survey); Variable Stars; Structure of the Galaxy;

– o*rganized the Scientific Council of the Main Astronomical Observatory*: the first meeting was held in 1949;

– *established the journal "Izvestiya GAO AN UkrSSR"* ("News of the MAO AS UkrSSR"): the first issue was published in 1950;

– *held the IX Plenum of the Commission for Research on Variable Stars* of the AstroSovet of the Academy of Sciences of the USSR in 1950.

– *invited the students graduated from the Odesa University, Department of Astronomy*, to begin their scientific career and research at the Main Astronomical Observatory in Kyiv: the first student, who has responded to this initiative, was Raisa Chupryna. She worked at the observatory in 1949–1957 and afterwards at the Odessa Department of the MAO NASU.

– *initiated postgraduate courses for future Candidates of Science* (PhDs) in astrophysics at the Faculty of Physics of the Kyiv University: the first Candidates of Sciences, who defended their theses under V.P. Tsesevich's supervision and began to form a Kyiv's branch of his scientific astronomical school, were I.G. Zhdanova and F.I. Lukatskaya in 1953 (see, Figure 2).

Later on, the "Odessa landing" of post-graduated students has arrived to the MAO NASU. Some of them defended their theses under Tsesevich's supervision as well as have formed the department of physics of stars: M.Ya. Orlov (research of RCrB type stars with anomalous chemical composition, worked in 1960–1998), T.V. Orlova (research in solar physics, worked in 1960–1985), L.R. Lisina (photometric research of the Moon, worked in 1960-1994), M.G. Rodriges (research of stars of late spectral classes, worked in 1960–2002), A.F. Pugach (research of physics of non-stationary stars, worked in 1962–2011), E.S. Kheilo (variable stars in globular clusters, astronomical instrumentation).

The new round of cooperation between observatories fell on 1972–1983 years and related to the initiatives by Ya.S. Yatskiv and V.P. Tsesevich:

– in 1972, the Odessa Department of Astrophysical Instrumentation of the MAO NASU ("Zeiss-Sevich" firm) was established; the telescope (diameter 0.8 m, Cassegren's focus F = 10 m) of the Astronomical Observatory of the Odesa University was installed at the Peak Terskol (Kabardino-Balkaria, Russia). Prof. V.P. Tsesevich was the Head of this department on a voluntary basis;

– in 1978, the Bureau of the Presidium of the Academy of Sciences of the UkrSSR decided to create a network of decameter radio telescopes "URAN", including telescope "URAN-4" in Mayaki, near Odesa, where the OAO Observational Station is located. Now this antenna belongs to the Institute of Radio Astronomy of the NAS of Ukraine.

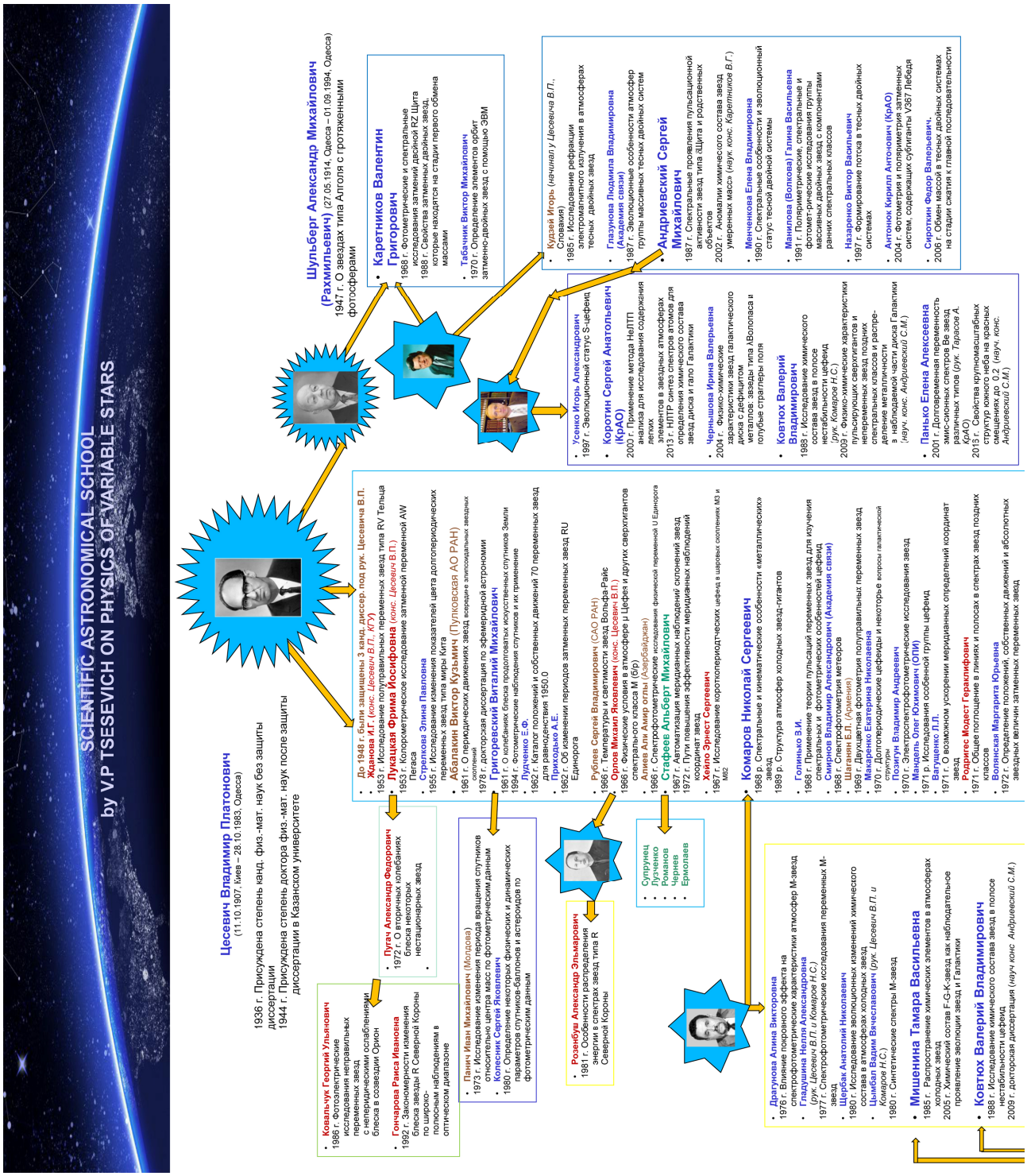

Figure 2: The tree of the scientific astronomical school by Professor V.P. Tsesevich on variable stars.

This poster (in Russian) was presented during the Gamow Conference-School in Odesa, August 14–19, 2017, at the Memorial Session dedicated to the 110-anniversary of Prof. V.P. Tsesevich' birthday.
Since then it was slightly changed after the helpful remarks by Prof. V.G. Karetnikov.

- **Мотрич Валерий Демьянович**
1988 г. Фундаментальные характеристики звезд-гигантов поздних спектральных классов
- **Гопка Вера Федоровна**
1990 г. Содержание тяжелых элементов в атмосфере звезд К-гигантов
- **Дорохова Татьяна Николаевна**
2003 г. Астросейсмология звезд нижней части полосы нестабильности: наблюдательный аспект

- **Ющенко Александр Владимирович (Юж. Корея)**
1998 г. Содержание тяжелых элементов в звездных атмосферах
- **Ющенко, Владимир Александрович.**
2017 г. Тяжелые элементы в атмосферах пекулярных звезд

- **Чехонадских Федор Анатольевич**
2012 г. Химический состав, нормальные показатели цвета и светимости F-G-K сверхгигантов

- **Горбанева Татьяна Ивановна**
2008 г. Наблюдательные проявления процессов перемешивания в звездах малых масс

- **Удовиченко Сергей Михайлович**
1987 г. Исследование переменных пульсирующих звезд с магнитным полем
- **Мкртичян Давид Эгишович (Таиланд)**
1993 г. Фотометрические и спектральные проявления пульсационной активности звезд нижней части полосы нестабильности

- **Кудашкина Лариса Сергеевна**
1997 г. Характеристики долгопериодических переменных звезд - источников космического мазерного излучения
- **Колесников Сергей Вячеславович**
2000 г. Периодические и апериодические изменения поляризации и блеска катаклизмических переменных звезд
- **Марсакова Владислава Игоревна**
2000 г. Переменность характеристик индивидуальных циклов пульсаций долгопериодических звезд
- **Халевин Александр Викторович (Греция)**
2000 г. Свойства аккреционного потока в магнитных тесных двойных системах
- **Бакланов Алексей Владимирович (КрАО)**
2005 г. Нестабильность аккреционных структур в катаклизмических двойных звездах
- **Бреус Виталий Витальевич**
2013 г. Орбитальная и вращательная переменность магнитных катаклизмических двойных звездных систем
- **Чинарова Лидия Львовна**
2014 г. Многокомпонентная переменность долгопериодических симбиотических и катаклизмических звезд
- **Ткаченко Мария Геннадиевна**
2017 г. Экспертный программный комплекс статистически оптимального определения параметров двойных систем

- **Синческул В.Н.** (Полтава)
1972 г. Фотометрические исследования звезд в области большой Туманности Ориона и ее окрестностей
- **Медведев Юрий Александрович**
1973 г. Спектрофотометрические исследования звезд-гигантов спектрального класса М
- **Казанасмас Михаил Степанович** *(рук. Цесевич В.П. и Харадзе Е.К.)*
1973 р. Исследования межгалактического поглощения и пространственного распределения звезд в одной области Млечного Пути в созвездии Ориона

- **Романов Юрий Сергеевич**
1974 р. Исследование эффекта Блажко в переменных звездах RR Лиры

- **Токтогулов Мусур** (Киргизия)
1974 г. Исследование световых кривых метеоров
- **Шодиев Умар** (Таджикистан)
1975 г. Исследование метеорных следов по электронно-оптическим и фотографическим наблюдениям
- **Сатыволдиев Васыджан** (Таджикистан)
1975 г. Исследование переменных звезд в области Т ассоциации Скорпиона-Змееносца
- **Кынчев Петр Здравков** (Болгария)
1975 г. Исследование эффекта Блажко у переменной звезды Xz' Лебедя
- **Фенина Земфира Николаевна**
1976 г. Количественная спектральная классификация звезд спектральных классов B8-G0 в применении к пульсирующим переменным звездам типа RR Лиры
- **Гладушина Нелля Александровна** *(рук. Цесевич В.П. и Комаров Н.С.)*
1977 г. Спектрофотометрические исследования переменных М-звезд
- **Нудженко Александра Григорьевна**
1977 г. Изменяемость периодов долгопериодических переменных звезд
- **Иванов Виталий Никонович**
1977 г. Электрофотометрия быстро меняющих блеск объектов
- **Фирманюк Богдар Несторович**
1980 г. Исследование нестабильности периодов изменения блеска звезд типа RR Лиры
- **Цымбал Вадим Вячеславович** *(рук. Цесевич В.П. и Комаров Н.С.)*
1980 г. Синтетические спектры М-звезд
- **Клюс Иван Алексеевич (ОВИМУ)**
1982 г. Исследование изменения блеска переменных звезд методами статистики

- **Андронов Иван Леонидович**
1984 г. Исследование влияния магнитного поля на аккрецию в тесных двойных системах
1995 г. Строение и эволюция магнитных тесных двойных систем

- **Гарбузов Геннадий Александрович**
1984 г. Фотометрические и спектральные исследования группы пульсирующих звезд с короткими периодами изменений блеска
- **Кошкин Николай Иванович**
1988 г. Фотометрический метод определения оси вращения и других кинематических и оптических характеристик астероидов с большими амплитудами изменения блеска
- **Фащевский Николай Николаевич**
1988 г. Новый трехзеркальный телескоп и его астрофизическое применение

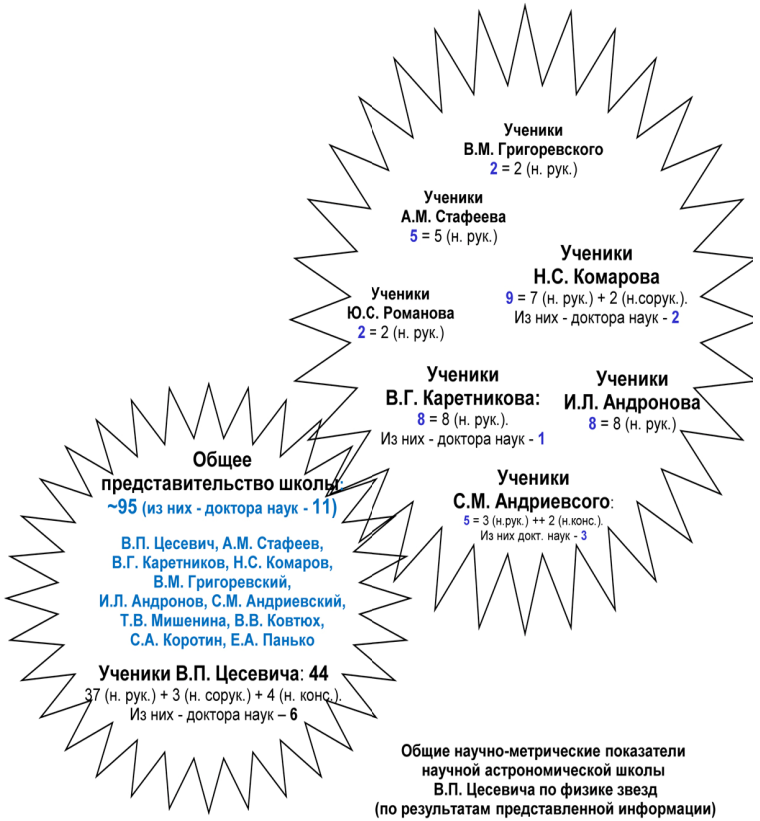

Общие научно-метрические показатели научной астрономической школы В.П. Цесевича по физике звезд (по результатам представленной информации)

АО ОНУ ГАО НАНУ ОНМУ Другие страны

This cooperation continues to this day in frame of such projects as follows:

– *Ukraine Network of Optical Stations* (UMOS) for near-Earth space research, responsible persons for these observations from the OAO are N.I. Koshkin and V.V. Troyansky (http://umos.mao.kiev.ua/);

– *Ukrainian Virtual Observatory* (UkrVO), responsible person for this research field from the OAO is S.V. Kashuba (http://ukr-vo.org), see, for example, Vavilova et al. (2013);

– *"CosmoMicroPhysics"*, Target Complex Scientific Program of the NAS of Ukraine, which was conducted in 2017–2013; responsible person for this research from the OAO was Prof. A.I. Zhuk. It is concerned with a study of the structure and evolution of the Universe on galactic and cosmological scales, dark energy and dark matter problem (see, for example, Novosyadlyj et al., 2013; Yatskiv et al., 2014; Alexandrov et al., 2016);

– *joint research in field of physics of stars* (see, for example, Gopka et al. (2013));

– *participation in the Gamow conferences-schools*, including membership in the organizing committee.

In 2017, a newest round of cooperation obtained a legal confirmation: "The Odesa Scientific & Educational Complex" was established by the Astronomical Observatory of the I.I. Mechnikov National University of Odesa and the Main Astronomical Observatory of the NAS of Ukraine. It was initiated by Prof. Ya.S. Yatskiv and Prof. S.M. Andrievsky and was supported by Prof. I.M. Koval', the Rector of this University.

3. Scientific Astronomical School by V.P. Tsesevich on variable stars

A *scientific school* is one of the forms of organization of scientific research, which is extremely productive for the development of science, especially in the so-called scientific growth points. This form of organization of scientific activity presupposes availability:

– the presence of an informal structured scientific or engineering community;

– the ability of this informally structured community to offer a new field in research, create new knowledge, formulate new ideas and concepts, solve a number of problems at the global avant-garde level, that is, the ability to create a *high science*;

– the ability of this informally structured community to create itself or use high-tech equipment and knowledge from related scientific fields or industries;

– the founder of the scientific school, leader-scientist/ the design engineer, who for the first time forvarded a new problem or a new field, developed it himself and with his students and followers;

– a special style of work and thinking, a special atmosphere, a respect for the students and the opportunity for them to work together, a pedagogical work on selecting students and improving their knowledge, that is all that lays the foundations of continuity of the school.

Scientific school is an organism with its life cycle, but this cycle may be limited. The final of a scientific school is due to various factors, in particular: the educational resources have been exhausted; innovations have been lost; there have been revolutionary changes in the scientific field and the scientific school does not have time to reorganize own research, and so on. As a result, the school can "dissipate", turn into smaller research groups and laboratories that keep traditions, and maybe give birth to new scientific idea. We note that scientific schools have a greater level of professionalism and experience to reach scientific results as compare with level of mobility and ability to rapid changes in methods of investigation. At the same time, the growth of experience prevents mobility, and the growth of mobility leads to loss of experience.

The scientific astronomical school by Prof. V.P. Tsesevich on physics of variable stars meets the aforementioned definitions of scientific school. Its tree is presented in Figure 2. The data were obtained from various archives (Astronomical Observatory of the I.I. Mechnikov National University of Odesa, MAO NASU, Archive of the Vernadsky National Library, Archive of the Russian AS, and other institutions). The full database contains of brief information on the about 100 representatives of this school as follows: name, title and year of thesis's defense, past/ present affiliation).

The scientific school has been formed since 1950-ies and had a greatest continuation in the work of such astronomers as V.G. Karetnikov, N.S. Komarov, Yu.S. Romanov, and I.L.Andronov (a branch of this school after V.P. Tsesevich), as well as S.M. Andrievsky as the follower by V.G. Karetnikov, and T.V. Mishenina, V.F. Gopka, V.V. Kovtykh as the followers by N.S. Komarov.

The research fields, where V.P. Tsesevich, his postgraduate students and followers make foremost results, could be compiled (in period till 1980-ies) as follows:

– physics of variable stars of different type (epoch 1 – before observations with the 7th camera astrograph, and epoch 2 – after its installation at the observational station in Mayaki);

– systematical monitoring and photography of the sky with the help of multi-camera short-focus astrographs, which was provided in Ukraine and Tajikistan;

– catalogues and atlases of variable stars and other cellestial bodies;

– Blazhko effect testing for different type of variables;

– definition of the orbits of binary stars with extended atmospheres (A.M. Shulberg and his followers);

– astronomical ground-based instrumentation.

The most of results of this period were integrated in monographs and books (Tsesevich, 1969; Tsesevich & Kazanasmas, 1971; Tsesevich, 1971; Tsesevich, 1973; Tsesevich, 1976). A full biobibliography by V.P. Tsesevich was issued by Dziubina & Rikun (1988).

New investigations, which were initiated in 1957 under the program of the International Geophysical Year since the beginning of space research, are provided till now:

– Sky Patrol, studies of changes in the brightness of the artificial satellites of the Earth (see, for example, Grigorevskii, 1979; Koshkin, 2017);

– observations of meteors (see, for example, Gorbanev & Kramer, 1994); we note that V.P. Tsesevich initiated together with E.N. Kramer the All-Union Fireball Service.

Since 1980-ies his followers have formulated new ideas and concepts and strengthened the success and international cooperation of the scientific school at a higher level:

– *photometrical and spectroscopic study of variables* (see, for example, Karetnikov, 1986; Cherepashuk, 2003);

– *astrospectroscopy* (see, for example, Komarov, 1985; Gopka, 2004; Yushchenko, 2002; Mishenina, 2016; Andrievsky, 2018; Kovtyukh, 2006; Korotin, 2015);

– *astroseismology* (see, for example, Mkrtichian, 2017);

– "*Inter-Longitude Astronomy*" (Andronov, 2003);

– and *other research fields*, which are integrated with scientists who is not belonging to this scientific school (*extragalaxy astronomy*, *cosmology* etc.).

The international campaign "Inter-Longitude Astronomy" collects smaller campaigns on different objects of numerous types – "magnetic" and "non-magnetic" cataclysmic variables, classical eclipsing and interacting binary systems, pulsating and eruptive variable stars. Review on the theoretical models vs observational evidence of gravi-magnetic rotators (classical, asynchronous and intermediate polars) and on the methods for statistically optimal phenomenological modelling using "special shapes" are given by Andronov (2008, 2016).

At the end of this Section we would like to give several commentaries. First of all, about the greatest collections, which are at the disposal of the OAO: 1) the glass collection that ranks the third in the world after Harvard and Sonneberg Observatories and numbers 105 000 photoplates. This collection was formed due to the efforts of astronomers of Odesa during long-term observations mainly with 7th camera astrograph in Mayaki; 2) the unique part of glass collection, which is stored in Mayaki, is the so-called Simeiz collection of astronegatives. It contains of the observational data (since 1909) on small bodies of the Solar System, which were obtained at the Simeiz Observatory in Crimea. This collection was saved by V.P. Tsesevich and moved to Odessa after he accidentally found it discarded at the Crimean Astrophysical Observatory, – a great respect to Prof. Tsesevich for this decision.

A commentary to the tree of scientific school is related to the personalities and questions, which are raised when you consider abstracts of their Cand. Sci. Theses. The abstracts of theses until the 1960's have consisted of several pages and did not always contain information on the name of the scientific supervisor. In such cases, one who is a supervisor has to judge from the subject of the dissertation, from the comments of colleagues, as well as from own knowledge of the history of astronomy in Ukraine.

A very important argument in the compilation of a science school's tree is the discussion with representatives of the school, as it gives an opportunity to better understand the role of each of them in the formation of the school, international cooperation, the ideas and methods proposed, etc. One example of the necessity of such approach is the candidate's dissertation by V.K. Abalakin, the outstanding astrophysicist of the XX century, one of the best graduates of the Odessa University, member of the Russian Academy of Sciences. The supervisor of his postgraduate courses and Cand. Sci. Thesis was V.P. Tsesevich, but the actual supervisor and the personality, who inspired Abalakin by celestial mechanics, was Professor K.N. Savchenko, of which Viktor K. Abalakin himself wrote brilliantly in his essay (Abalakin, 1995).

So, one can analyze scientometric indicators, which are given in Figure 2.

We can conclude that the age of the scientific school by V.P. Tsesevich is about 70 years; the averaged effectiveness of defense of Cand. Sci. Theses is 6 persons per 5 years; 11 persons among 95 representatives of this school defended Dr. Sci. Theses and 8 of them were supervisors at least 1 Cand. Sci. The Scientific School is living!

Figure 3: Memorial plaque in honor of V.P. Tsesevich, which was installed at the building of the MAO NAS of Ukraine on October 25, 2017. Sculptor – A. Kusnetsov

Figure 4: Ceremonial of the opening of the Memorial plaque in honor of V.P. Tsesevich, which was installed at the building of the MAO NAS of Ukraine. From left to right: Dr. M.I. Ryabov, Dr. A.A. Korsun', Prof. Ya.S. Yatskiv, Dr. M.G. Rodriges, Prof. M.V. Strikha (Deputy-Minister for Education and Science of Ukraine). Kyiv, October 25, 2017.

We note that the given information on the scientific school by V.P. Tsesevich (Figure 2) is not absolutely full,

for example, 1) there are no the data on thesis's defense under his supervision before 1948; 2) information on the astronomical school developed by A.M. Stafeev or scientists from other countries is a very poor; 3) some shortcomings may be presented. We will grateful for all the additions and corrections to update a tree of this scientific school, which played and plays a prominent role in the development of our knowledge on physics of stars.

4. Instead of Conclusion

On 25 October, 2017, a special session dedicated to the 110-anniversary of the Volodymyr Tsesevich birthday was organized in Kyiv in frame of the meeting of the Ukrainian astronomer named after "AstroAutumn in Holosiyiv".

Ya.Yatskiv, I. Vavilova and A. Korsun' have presented the report "Volodymyr Tsesevich and his activity as the Director of the Main Astronomical Observatory of Academy of Science of the UkrSSR". Mikhail Ryabov has told his impression on the V. Tsesevich's role for development of astronomical instrumentation "30 years of radio astronomical research at the Odessa Observatory URAN-4" (see, for example, Ryabov, 1993).

Afterwards the participants from Chernivtsi, Dnipro, Kharkiv, Kyiv, Mykolaiv, Odesa took part in the opening the Memorial plaque in honor of Tsesevich V.P., which was installed at the building of the MAO NAS of Ukraine (Figure 3 and 4).The photo gallery is available through http://mao.kiev.ua/index.php/ua/?option=com_content&view=article&id=270.

Acknowledgements. The author thanks Professors Ya.S. Yatskiv, V.G. Karetnikov and I.L. Andronov for useful remarks and Vavilov S.S. for technical assistance.

References

Abalakin V.K.: 1995, *Professor K.N. Savchenko*. In: "*The Pages of the History of Astronomy in Odessa*", Part 2, Ed. V.G. Karetnikov, Odessa: Astroprint, p.33–39.
Alexandrov A.N. et al.: 2016, *General Relativity Theory: Recognition through Time*, Kyiv: Naukova Dumka, 332 p.
Andrienko D.A., Zosimovich I.D.: 2005, in "*Sergei Vsekhsvyatsky*", Kyiv: Kyiv University, 8-38.
Andrievsky S. et al.: 2018, *MNRAS*, **473**, Is. 3, 3377.
Andronov I.L.: 2003, *Odessa Astron. Publ.*, **16**, 5.
Andronov I.L.: 2008, *JPhSt*, **12**, 2902.
Andronov I.L. et al.: 2003, *A&AT*, **22**, 793.
Andronov I.L., Tkachenko M.G., Chinarova L.L.: 2016, *PhysJ*, **2**, 140.
Andronov I.L.: 2017, *Odessa Astron. Publ.*, **30**, 252.
Cherepashchuk A.M., Karetnikov V.G.: 2003, *ARep.*, **47**, Is. 1, 38
Dziubina S.V., Rikun I.E. (Comp.): 1988, *Vladimir Platonovich Tsesevich. Biobibliography*, Ed. Yu.S. Romanov, in "*Scientists of Odessa*", is. 17, 110 p.
Fenina Z.N., Romanov Yu.S.: 2008, *Vladimir Platonovich Tsesevich or the Golden Age of the Odessa Astronomical Observatory*. Kiev: LOGOS.
Gopka V.F. et al.: 2004, *ARep.*, **48**, Is. 7, 577.
Gopka V. et al.: 2013, *Odessa Astron. Publ.*, **26/1**, 54.
Gorbanev Yu.M., Kramer E.N.: 1994, *Solar System Research*, **27**, No. 4, 376.
Grigorevskii V.M.: 1979, *Pisma AZh*, **5**, 482.
Karetnikov V.G., Kovtyukh V.V.: 1986, *AZh*, **63**, 1144.
Karetnikov V.G.: 1996, *A&AT*, **10**, 21.
Karetnikov V.G. (Ed.): 1997, *The Pages of the History of Astronomy in Odessa*. Collection, Part 4, Odessa: Astroprint, 208 p.
Komarov N.S.: 1985, *AZh*, **62**, 740.
Konovalenko A.A.: 2000, *Geophys. monograph*, **119**, 311.
Korotin S.A. et al.: 2015, *A&A*, **581**, id.A70, 10 pp.
Koshkin N.I., Mishenina T.V. (Eds.): 2007, "*Vladimir Platonovich Tsesevich. About time and me*". Reminiscences and documents, Odessa: Astroprint, 80 p.
Koshkin N. et al.: 2017, *Adv. Sp. Res.*, **60**, Is.7, 1389.
Kovtyukh V.V.: 2006, *ARep.*, **50**, Is. 2, 134.
Mishenina T. et al.: 2016, *MNRAS*, **462**, Is. 2, 1563.
Mkrtichian D.E.: 2017, *IBVS*, No. **6210**, #1.
Novosyadlyj B. et al.: 2013, *Dark Energy: Observational Evidence and Theoretical Models*, Kyiv: Nauk. Dumka.
Pavlenko Ya.V., Vavilova I.B., Kostiuk T.: 2006, In: *Organizations and Strategies in Astronomy*, Vol. **7**, Ed. A. Heck (Berlin: Springer), p. 71.
Pozigun V.A.: 1996, "*Astronomical Observatory of the Odessa State University*", Odessa: Astroprint, 32 p.
Ryabov M. I., Serokurova N. G.: 1993, *A&AT*, **4**, Is. 1, 29
Shkuratov Yu.G. (Ed.): 2008, "*200 years of astronomy in the Kharkov University*", Kharkov: Kharkov National University, 632 p.
Tsesevich V.P.: 1980, *Activities of A. Ya. Orlov in Odessa*. In: *Geodynamics and astrometry. Foundations, methods, results*, p. 24-27.
Tsesevich V.P.: 1969, *RR Lyrae stars* (Jerusalem: Israel Program for Scientific Translations (IPST))
Tsesevich V.P.; Kazanasmas M.S.: 1971, *Atlas of finding charts of variable stars*, Moskva: Nauka, 350 p.
Tsesevich V.P.: 1971, *Instationary stars and methods of their investigation. Eclipsing variables*, Moskva: Nauka, 352 p.
Tsesevich V.P.: 1973, *Eclipsing variable stars*, New York: J.Wiley.
Tsesevich V.P.: 1976, *Investigation of variable stars in selected regions of the Milky Way*, Kiev: Nauk. dumka, 256 p.
Vavilova I.B., Karetnikov V.G., Konovalenko A.A. et al.: 2001, In: "*Preserving the Astronomical Sky*", Eds. R.I. Cohen, W.T. Sullivan III, Proc. IAU Symp. **196**, 153.
Vavilova I.B. & Yatskiv Ya.S.: 2003, *Teaching of Astronomy in Asian-Pacific Region*, **19**, 47.
Vavilova I.B., Konovalenko A.A., and Megn A.V.: 2007, *Astron. Nachr.*, **328**, 420.
Vavilova I.B. et al.: 2012, *Kinemat. Physics Cel. Bodies*, **28**, is. 2, 85.
Shkuratov Yu.G. (Ed.): 2008, "*200 years of astronomy in the Kharkov University*", Kharkov: Kharkov National University, 632 p.
Yatskiv Ya.S., Vavilova I.B.: 2003, *Kinemat. Physics Cel. Bodies*, **19**, 569.
Yatskiv Ya.S., Korsun A.A. & Vavilova I.B.: 2005, *Kinemat. Physics Cel. Bodies*, **21**, 403.
Yatskiv Ya.S. et al.: 2014, *General Relativity: Horizons for Tests*, Kyiv, MAO NASU, 264 p.
Yushchenko, A.: 2002, Journal of the Korean Astronomical Society, **35**, 4, 209.

Наукове видання

Одеські Астрономічні Публікації

том 30 (2017)

Англійською мовою

Технічний редактор *В. В. Ковтюх*
Комп'ютерна верстка *С. Л. Страхова*

Підписано до друку 24.12.17.
Формат 60x84/8. Папір офсетний. Друк різограф.
Ум. друк. арк. 30,46. Обл.-вид. арк. 28.0. Тираж 300 екз. Зам. № 230.

Друкарня ТОВ Компанія ВАІТЕ
01402, Київ, вул. П. Лумумби, 7
Свідоцтво про внесення до Держреєстру суб'єкта видавничої справи
серія ДК №2570 від 27.07.2006 р.